EDITORIAL STAFF
Editor, **J. J. JAKLITSCH, JR.**
Production Editor,
STELLA ROBINSON
Editorial Prod. Asst.,
BETH DARCHI

HEAT TRANSFER DIVISION
Chairman, **R. L. WEBB**
Secretary, **C. J. CREMERS**
Senior Technical Editor, **E. M. SPARROW**
Technical Editor, **B. T. CHAO**
Technical Editor, **D. K. EDWARDS**
Technical Editor, **R. EICHHORN**
Technical Editor, **M. EPSTEIN**
Technical Editor, **J. S. LEE**
Technical Editor, **V. E. SCHROCK**
Technical Editor, **R. SIEGEL**

POLICY BOARD, COMMUNICATIONS
Chairman and Vice-President
I. BERMAN

Members-at-Large
J. W. LOCKE
J. E. ORTLOFF
M. J. RABINS
W. J. WARREN

Policy Board Representatives
Basic Engineering, **F. LANDIS**
General Engineering, **A. A. SEIREG**
Industry, **R. K. HAMPTON**
Power, **R. E. REDER**
Research, **G. P. COOPER**
Codes and Stds., **L. L. ELDER**
Computer Technology Com.,
A. A. SEIREG
Nom. Com. Rep.,
S. P. ROGACKI

Business Staff
345 E. 47th St.
New York, N. Y. 10017
(212) 644-7789
Mng. Dir., Publ., **C. O. SANDERSON**

OFFICERS OF THE ASME
President, **DONALD N. ZWIEP**
Exec. Dir. & Sec'y, **ROGERS B. FINCH**
Treasurer, **ROBERT A. BENNETT**

EDITED and PUBLISHED quarterly at the *offices of* The American Society of Mechanical Engineers, United Engineering *Center, 345 E. 47th St., New York, N. Y.* 10017. ASME TWX No. 710-581-5267. Second-class postage paid at New York, N. Y., and at additional mailing offices.

CHANGES OF ADDRESS must be received at Society headquarters seven weeks before they are to be effective. Please send old label and new address.

PRICES: *To members, $25.00, annually; to* nonmembers, $50.00. Single copies, $15.00 each. *Add $1.50 for postage to countries outside the* United States and Canada.

STATEMENT from By-Laws. The Society shall not be responsible for statements or opinions advanced in papers or . . . printed in its publications (B 13, Par. 4).

COPYRIGHT © 1979 by the American Society of Mechanical Engineers. Reprints from this publication may be made on conditions that full credit be given the TRANSACTIONS OF THE ASME, SERIES C—JOURNAL OF HEAT TRANSFER, *and the author and date of* publication stated.

INDEXED by the Engineering Index, Inc.

transactions of the ASME

Published Quarterly by
The American Society of
Mechanical Engineers
Volume 101 • Number 4
NOVEMBER 1979

journal of heat transfer

ANNOUNCEMENTS

TECHNICAL PAPERS

(continued on page 616)

Downloaded 04 Feb 2011 to 194.85.80.107. Redistribution subject to ASME license or copyright; see http://www.asme.org/terms/Terms_Use.cfm

TECHNICAL NOTES

E. M. Sparrow
Fellow ASME
J. W. Ramsey
R. G. Kemink

Department of Mechanical Engineering,
University of Minnesota
Minneapolis, Minn. 55455

Freezing Controlled by Natural Convection

Experiments were performed for freezing under conditions where the liquid phase is either above or at the fusion temperature (i.e., superheated or nonsuperheated liquid). The liquid was housed in a cylindrical containment vessel whose surface was maintained at a uniform, time-invariant temperature during a data run, and the freezing occurred on a cooled vertical tube positioned along the axis of the vessel. The phase change medium was n-eicosane, a paraffin which freezes at about 36°C (97°F). In the presence of liquid superheating, the freezing process is drastically slowed and ultimately terminated by the natural convection in the liquid. The terminal size of the frozen layer and the time at which freezing terminates can be controlled by setting the temperature parameters which govern the intensity of the natural convection. The stronger the natural convection, the thinner the frozen layer and the shorter the freezing time. In the absence of liquid superheating, a cylindrical frozen layer grows continuously as predicted by theory, but the growth rate is higher than the predictions because of the presence of whisker-like dendrites on the freezing surface.

Introduction

Freezing and melting are companion processes that occur consecutively in numerous heat transfer applications. For example, the projected use of liquid/solid phase change as a means of storing thermal energy is based on the cyclic freezing and melting of the phase change medium. Not only are freezing and melting frequently interrelated via applications, but it has also been customary to analyze them by a common analytical model. Indeed, the voluminous literature on the Stefan and Neumann phase-change problems (and their variants) deal interchangeably with freezing and melting.

The standard model for freezing envisions a liquid initially at a uniform temperature, either at or above the fusion point. Then, at a specified instant of time, a cooling process is initiated at a wall which bounds the liquid such that the wall temperature drops below the fusion point and freezing begins. The freezing front propagates into the liquid, and the heat released by the freezing process is carried across the frozen layer to the wall by conduction. If the liquid temperature is above the fusion point, heat is transported from the liquid to the moving freezing front by conduction (the freezing front is at the fusion temperature). With the passage of time the thickness of the frozen layer continues to increase, albeit at a slower rate because of the growing resistance to heat conduction across the layer.

An identical scenario, with appropriate changes of wording, can be written to describe the standard model used for the analysis of melting. On the other hand, recent experiments, for instance [1–3], have demonstrated that natural convection, rather than conduction, is the dominant heat transport mechanism in the melting process. The experimental results revealed two characteristics which should be noted for subsequent comparison with those for freezing, namely (1) the melting process is accelerated by the presence of natural convection and (2) natural convection occurs regardless of whether the initial temperature of the medium is equal to or different from the fusion value.

The freezing process is the main focus of interest in the present research. Experiments were undertaken to explore the heat transfer mechanisms which occur when a liquid is brought into contact with a surface whose temperature is maintained at a value lower than the fusion temperature. The experimental conditions included both the case where the liquid was initially at the fusion temperature and the case where the liquid temperature exceeded the fusion value (i.e., superheated liquid). For reasons which will become apparent shortly, greater emphasis was placed on the superheated liquid case, but the nonsuperheated case also yielded interesting results.

The contrasts in the freezing patterns for the two cases were found to be truly remarkable. These contrasts encompassed (1) differences in the growth pattern of the frozen layer (continuous growth versus growth which stopped after a finite time interval), (2) shape of the frozen layer (straight phase boundary versus contoured phase boundary), and (3) texture of the frozen layer surface (whisker-like dendrites versus smooth). Aside from the presence of the dendrites, the freezing of the nonsuperheated liquid followed the classical scenario; in contrast, the experiments on the freezing of superheated liquid yielded an entirely different scenario—one in which the freezing is controlled by natural convection. These freezing patterns will be described later.

The experiments were performed utilizing n-eicosane, a paraffin which freezes at about 36°C (97°F). The paraffin was contained in a test chamber which, in turn, was situated in a constant-temperature water bath. Freezing was initiated when a cooled vertical cylinder, whose temperature was held constant by thermostatically controlled circulating water, was introduced into the test chamber. For given values of the temperatures of the liquid and the cooled tube, a succession of data runs of various durations was performed. At the conclusion of each such data run, the frozen paraffin was removed from the cooled tube and stored. The temperatures of the liquid and of the tube were varied parametrically during the course of the investigation.

For each of the frozen paraffin specimens, both the mass and the surface contour were measured in order to provide quantitative information about the freezing patterns. Photographs were also taken to provide a visual record. Comparisons with the literature were made whenever possible. This included comparing the measured frozen layer thicknesses for the nonsuperheated case with theoretical predictions based on a pure conduction model. Also, for the superheated case, heat transfer rates deduced from the measured thicknesses were compared with values from a natural convection boundary layer model.

A search of the archival heat transfer literature failed to unearth experiments of the type reported here. In fact, when the research was undertaken, the authors were unaware of some related analytical work which had been published about a decade earlier. This oversight was due, at least in part, to the fact that the most recent heat transfer publications dealing with freezing (e.g., [4–6]) continue to employ a heat conduction model and ignore natural convection. In [7], which also summarizes related analyses, an analysis was performed which identifies the role of natural convection in the freezing process which takes place on a cooled vertical wall which bounds an infinite region containing a superheated liquid. The relationship of the present results to those of [7] will be discussed later, when other comparisons are made.

Contributed by the heat transfer division for publication in the JOURNAL OF HEAT TRANSFER. Manuscript received by the Heat Transfer Division May 23, 1979.

The Experiments

Experimental Apparatus. The heart of the experimental apparatus is the test cell in which the freezing takes place. In addition to the test cell itself, the apparatus includes auxiliary systems for controlling the temperature of the cooled tube on which freezing occurs and the temperature of the environment surrounding the phase-change medium.

A schematic diagram of the test cell is presented in Fig. 1. As shown there, a cylindrical stainless-steel vessel situated in a temperature-controlled water bath is used to contain a paraffin, n-eicosane, which is in its liquid state. The vessel is 15.2 cm (6 in.) in diameter and 17.8 cm (7 in.) high. During a data run, freezing takes place on a cooled cylindrical tube which is immersed in the liquid paraffin. The tube, which is 2.49 cm (0.982 in.) in diameter, is concentric with the containment vessel.

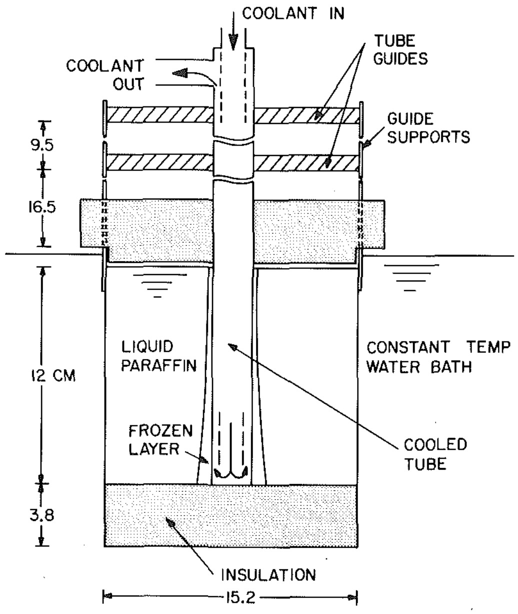

Fig. 1 Schematic diagram of the test cell

To isolate the lower reaches of the frozen layer from possible thermal interactions with the lower wall of the containment vessel, a 3.8-cm ($1\frac{1}{2}$ in.) thick styrofoam insulation layer was positioned at the bottom of the vessel. The insulation was covered with plastic-coated contact paper to insure a smooth surface. Furthermore, to minimize the possibility of extraneous heat transfers at the upper surface of the paraffin, a plastic-coated styrofoam cap was fitted to the top of the containment vessel.

The cooled tube is, in actuality, a tube within a tube. The outer tube, purposefully selected of thick-walled brass (0.33 cm, 0.130 in. in thickness) to promote temperature uniformity, was capped at its lower end; the inner tube is of thin-walled copper. As shown in the figure, the coolant enters at the top of the inner tube and passes axially downward. Upon reaching the bottom of the tube, it reverses direction and flows upward through the annular gap between the tubes, ultimately exiting at the top.

To facilitate measurement of the temperature of the cooled tube, three thermocouples were installed on its surface, respectively at axial stations situated 1.27, 6.35, and 11.4 cm ($\frac{1}{2}$, $2\frac{1}{2}$, and $4\frac{1}{2}$ in.) from the lower end. These thermocouples were laid in axial grooves machined into the surface. The grooves were filled with copper oxide cement (a relatively good heat conductor) and, after a finishing operation, it was impossible to detect any discontinuity between the brass surface and the cement.

Controlled vertical positioning and guided vertical movement of the cooled tube was accomplished by the support and guide structure shown at the top of Fig. 1. Vertical supports, anchored to the side of the containment vessel, positioned a pair of guides through which the tube is threaded. Each guide is a 1.27-cm ($\frac{1}{2}$-in.) thick aluminum disk machined with a center hole whose diameter exceeds that of the tube by a few thousands of an inch. The spacing between the disks was chosen large enough to insure true vertical alignment of the tube. Each disk was equipped with a set screw which enabled the cooled tube to be locked in place, and this feature was employed to position the tube above the containment vessel during non-data-run periods.

The containment vessel was situated in a temperature-controlled water bath. The water was housed in a stainless steel tank, 38 cm (15 in.) deep, and 51 × 38 cm (20 × 15 in.) in horizontal cross section. Temperature control and uniformity was achieved by a thermostatically activated heating device which also served to circulate the water throughout the bath. Heat losses from the bath were minimized by an insulation blanket covering the walls of the tank and by a thin film of liquid paraffin on the water surface—which inhibited evaporation. Spatial temperature uniformity throughout the bath was within 0.1°C, and timewise constancy was held to even closer tolerances.

The temperature of the cooled tube was maintained at a pre-selected level by water which circulated in a closed loop. The loop included a thermostatically activated device capable of heating, refrigerating, and pumping. Preliminary data runs indicated that the pumping capability was not sufficient for the attainment of the desired temperature control. Therefore, a supplementary pump was installed in the loop, downstream of the cooled tube.

The instrumentation for the experiments included a digital voltmeter, which could be read to 1 μV, for detecting the thermocouple outputs and an analytical balance with a smallest scale division of 0.1 mg for weighing the frozen paraffin specimens. The diameters of the specimens were measured with a vernier caliper to within 0.01 mm.

Experimental Procedure. There are three temperature parameters that play a decisive role in the freezing process: (1) the temperature T_i ($i \sim$ inner) of the cooled tube on which the freezing occurs, (2) the temperature T^* of the freezing front (i.e., solid-liquid interface), and (3) the surface temperature T_0 ($0 \sim$ outer) of the containment vessel. Of these, the freezing front temperature is fixed by nature, 36°C (96.8°F) for 99 percent pure n-eicosane. The other two temperatures constitute, along with the duration time of a data run, the main prescribable parameters of the experiments. Rather than work directly with these temperatures, the experiments were parameterized by a pair of temperature differences, namely,

$$\Delta T_i = T^* - T_i, \qquad \Delta T_0 = T_0 - T^* \tag{1}$$

These quantities will, in subsequent discussion, be referred to respectively as the inner and outer temperature differences. Thus, each data run was defined by given values of ΔT_i and ΔT_0, plus the duration time of the run.

To examine the freezing pattern for given thermal conditions, a succession of data runs of different duration times was performed for fixed values of ΔT_i and ΔT_0. Each data run was preceded by a pre-

Nomenclature

D = diameter of cooled tube
h = natural convection heat transfer coefficient
k_s = thermal conductivity of solidified material
q_i = local heat flux per unit tube surface area
r_i = radius of cooled tube
r^* = local radius of solid-liquid interface
T_i = temperature of cooled tube
ΔT_i = inner temperature difference, $T^* - T_i$
T_0 = surface temperature of containment vessel and initial temperature of liquid
ΔT_0 = outer temperature difference, $T_0 - T^*$
T^* = fusion temperature
x = axial distance measured from top of frozen specimen

Subscripts

cond = conduction across solidified layer
conv = natural convection to the interface from the liquid
freeze = freezing at the interface

paratory period during which thermal equilibria were separately established in the liquid paraffin and in the cooled tube, respectively at the preselected values of T_0 and T_i. During this period, the tube was positioned above the paraffin containment vessel, and the top of the latter was closed (with its insulation cap) to prevent heat losses. The attainment of equilibrium was detected by means of the surface thermocouples of the tube and by a thermocouple immersed in the liquid paraffin.

The data run was initiated by opening the top of the vessel and then lowering the cooled tube into the paraffin. Insertion of the tube was accomplished within about a second, and a frozen layer formed immediately. The top of the containment vessel was then capped and the data run was permitted to proceed for a preselected duration.

Immediately prior to the scheduled termination of the run, the insulating cap of the containment vessel was removed. Then, at the appointed moment, the cooled tube, along with the attached frozen paraffin layer, was rapidly raised upward and out of the containment vessel. With the set screws on the guide disks, the tube was locked in place so that the upper edge of the frozen layer very nearly contacted the lower guide disk. This positioning left a clearance of $3\frac{3}{4}$–5 cm ($1\frac{1}{2}$–2 in.) between the lower edge of the frozen layer and the top of the containment vessel. The clearance facilitated the manual operations associated with the separation of the frozen specimen from the tube.

The technique used to accomplish the separation was to heat the tube to the melting point of the paraffin. As a first step, a metal plate was placed on the top of the containment vessel as a closure, and on this was placed a bowl-like plastic piece which served to collect fragments of solid paraffin on those few occasions when perfect separation was not achieved. To obtain the hot water necessary for the melting, it was deemed best to use the building supply (and mix hot and cold water from the taps) rather than to employ the heater/refrigerator/circulator device as the heat source. This decision was made with a view to avoiding the time loss involved with raising the thermal mass of the *h*/*r*/*c* device to the melting temperature of the paraffin and subsequently lowering it to T_i.

In the actual separation procedure, the tube was carefully brought to the melting temperature, using the digital read-out of the tube wall thermocouples as a guide. Just prior to the attainment of melting, the set screws were released and the tube was supported manually within its guides. Then, at the precise moment that melting was initiated, the tube was moved rapidly upward, leaving the separated specimen in the hand of the experimenter.

Each frozen specimen was weighed immediately after separation. Photographs were taken later, when a family of specimens had been assembled. Measurement of surface contours was performed still later because surface markings, made to ensure the precision of the contour measurements, would have marred the photographs.

Results and Discussion

The patterns of freezing in both nonsuperheated and superheated liquids will first be displayed photographically, and the physical mechanisms which give rise to these patterns will be identified and discussed. Then, quantitative data on the timewise evolution of the frozen layer (i.e., on the frozen mass and on the position of the freezing front) will be presented, as will surface heat transfer rates. These data will be compared, wherever possible, to literature information.

Photographic Record of Freezing Patterns. The first case to be dealt with is that in which the freezing occurred in a nonsuperheated liquid, that is, the liquid paraffin was at the fusion temperature so that $\Delta T_0 = 0$. In preparation for a data run at this operating condition, the temperature of the water bath surrounding the containment vessel was set at about 0.1°C below the fusion value. This resulted in the formation of a very thin layer of frozen paraffin on the inner wall of the vessel. Sufficient time was allowed for the liquid paraffin to come to thermal equilibrium with this frozen layer, whereupon the data run was initiated in the manner described earlier.

Three data runs were performed for the nonsuperheated case, all for $\Delta T_i = 27.8°\text{C}$ (50°F), with respective run times of 15, 45, and 90 min. The frozen paraffin specimens that resulted from these runs are shown in Fig. 2 where they are arranged from left to right according to increasing run time.

From the figure, it is seen that at any instant of time, the frozen layer is essentially a perfect cylinder, aside from a small-scale surface structure that will be discussed shortly. With the passing of time, the thickness (and diameter) of the layer increases continuously, but the rate of growth diminishes. These characteristics coincide precisely with those of a model where the only heat transport mechanism is radial conduction across the frozen layer—carrying the heat liberated at the solid-liquid interface to the cooled tube. Thus, for freezing in the absence of liquid superheat, the experimental findings validate the heat conduction basis that underlies all analytical treatments of freezing. Quantitative comparisons between experiment and analysis will be made later, subsequent to the presentation of other photographic results.

The small-scale surface structure mentioned in the preceding paragraph is worthy of elaboration. To this end, a close-up view of a portion of the surface of the rightmost element of Fig. 2 is presented in Fig. 3. The figure reveals that the surface is covered with a whisker-like (i.e., dendritic) growth. The presence of such dendrites is rarely, if ever, accounted in the analytical treatment of freezing, and with good reason in view of the complexities involved. It can be conjectured that the greatly enlarged solid-liquid contact area afforded by the dendrites, relative to that of the nominal cylindrical surface, should lead to a higher rate of freezing. This issue will be revisited later.

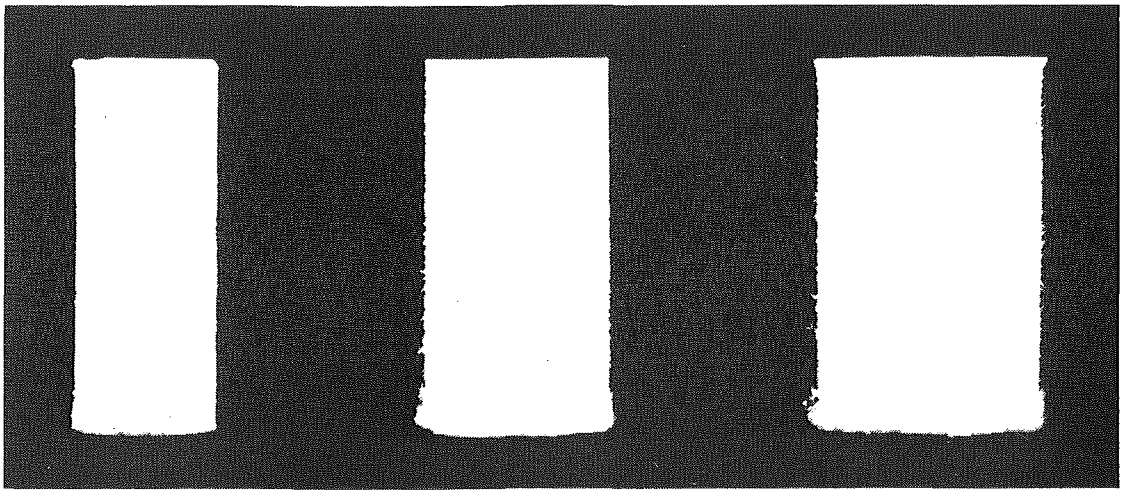

Fig. 2 Pattern of freezing in a nonsuperheated liquid. $\Delta T_i = 27.8°\text{C}$ (50°F). Run times (left to right) = 15, 45, and 90 min

Attention will now be turned to the pattern of freezing in the presence of a superheated liquid. A succession of data runs were made at the same inner temperature difference ΔT_i as before (i.e., 27.8°C, 50°F), but now, the outer temperature difference ΔT_0 was set at 17.8°C (32°F) rather than at zero. These runs ranged in duration from 15 to 180 min. A sequence of frozen specimens from these runs is shown in Fig. 4, corresponding, from left to right, to run times of 15, 30, 60, 90, 120, and 180 min.

The freezing pattern in evidence in the figure is dramatically different from that of Fig. 2. Three major areas of difference can be identified: (1) In the presence of liquid superheating, the freezing does not continue indefinitely as in the nonsuperheating case. Rather, the freezing stops after a finite period of time. By comparing corresponding frozen specimens at equal run times, it is seen that the amount of frozen material is sharply reduced when superheating is present. (2) Quite apart from differences in size, there are interesting differences in the shapes of the two groups of frozen specimens. In contrast to the near-perfect cylinders for the nonsuperheating case, freezing in the presence of superheating yields a gently contoured surface, with the thickness of the frozen layer increasing from top to bottom. (3) The whisker-like dendrites, which overlay the freezing front when there is no superheating (Fig. 3), disappear altogether when superheating is present.

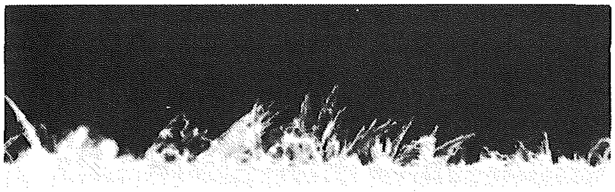

Fig. 3 Close-up view of whisker-like dendrites

As will shortly be made plausible, all of the aforementioned differences in the freezing patterns are due to natural convection in the superheated liquid. However, before that, it is appropriate to present additional photographs in order to identify trends which result from changes in the inner and outer temperature differences.

For the next series of data runs, the inner temperature difference ΔT_i was fixed at 13.9°C (25°F), which is just half the value of ΔT_i for the frozen specimens of Fig. 4; the value of ΔT_0 was maintained unchanged at 17.8°C (32°F). The first six specimens of Fig. 5 show the freezing pattern for the new thermal conditions and are arranged from left to right with run times of 15, 30, 60, 90, 120, and 180 min. From the figure, it is seen that all of the qualitative influences of the superheating, as outlined in connection with Fig. 4, continue in force, but there are interesting differences in detail. The most striking difference is that at any instant of time, there is a marked reduction in the amount of freezing at the lower ΔT_i: this observation also pertains to the final size of the solidified layer. In addition, the time required to attain the final size diminishes with a decrease in ΔT_i (this observation will be buttressed later by data on the mass of frozen material).

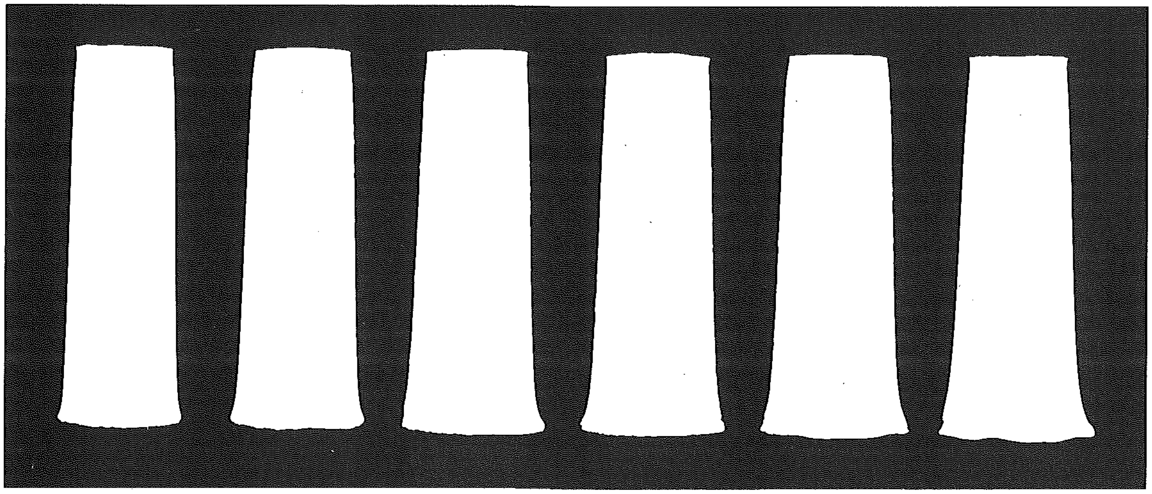

Fig. 4 Pattern of freezing in a superheated liquid. ΔT_i = 27.8°C (50°F), ΔT_0 = 17.8°C (32°F). Run times (left to right) = 15, 30, 60, 90, 120, and 180 min

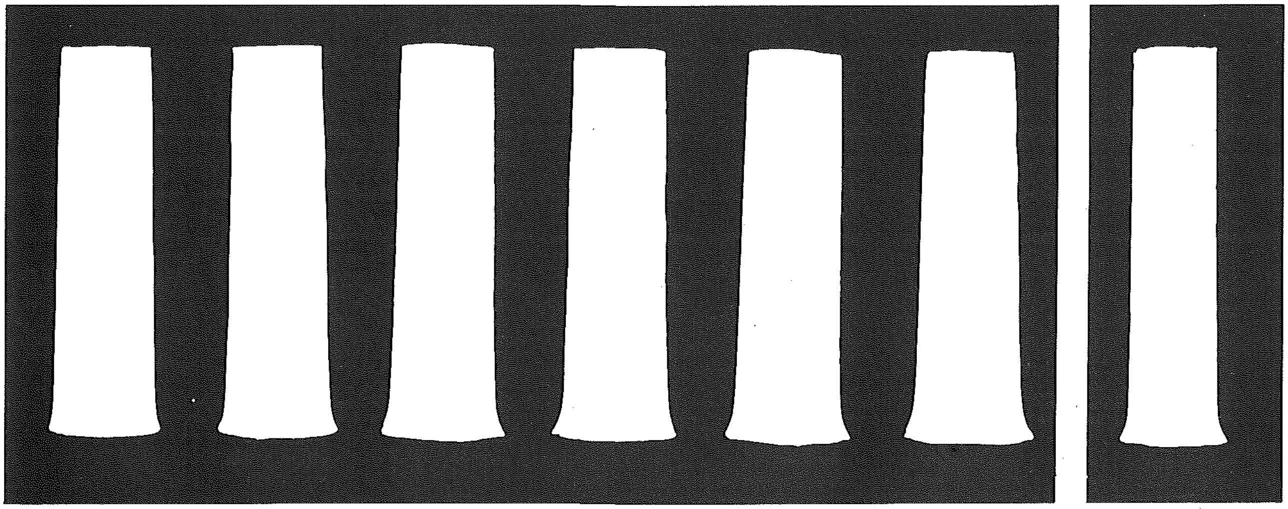

Fig. 5 Pattern of freezing in a superheated liquid. Main part of figure: ΔT_i = 13.9°C (25°F), ΔT_0 = 17.8°C (32°F); run times (left to right) = 15, 30, 60, 90, 120, and 180 min. Right-most photo: ΔT_i = 13.9°C (25°F), ΔT_0 = 35.6°C (64°F); run time = 30 min

To further explore the effects of the imposed thermal conditions, still another series of runs was made. For these runs, ΔT_i was maintained the same as for the previous set (13.9°C, 25°F), but the outer temperature difference ΔT_0 was doubled to attain the value 35.6°C (64°F). The resulting frozen specimens were so thin that in certain cases, some fragmentation occurred during separation from the cooled tube. All of the fragments were collected and correct mass measurements were made, but a full set of intact specimens was not available for photography. A typical specimen (30 min run time) from this set of data runs is shown at the right of Fig. 5. The sharp decrease in the frozen mass relative to the other specimens in Fig. 5 is clearly in evidence. Another feature of these runs was the very rapid completion of freezing—within about 60 min.

It is now appropriate to rationalize and explain the various findings that were evidence by Figs. 2–5.

The Participating Phenomena. To begin, it is relevant to consider the natural convection flow in the liquid paraffin. In the presence of superheat, there is a radial temperature variation in the liquid, ranging from the fusion temperature T^* at the solid-liquid interface to T_0 at the wall of the containment vessel, with $T_0 > T^*$. As a result of this horizontal temperature variation, a natural convection flow will be induced. The highest temperature surface contacted by the liquid is the wall of the containment vessel; correspondingly, there will be a natural convection upflow along this wall. On the other hand, the lowest temperature surface contacted by the liquid is the solid-liquid interface, and a downflow occurs along that surface.

In this manner, a closed-loop natural circulation is established in the liquid. In the downflowing liquid adjacent to the interface, it is reasonable to expect that the convective heat transfer coefficients will decrease in the flow direction, with the highest coefficients occurring near the top of the surface.

Next, attention will be directed to the heat transfer across the frozen layer. From a calculation comparing the latent heat liberated by the freezing process to the sensible heat liberated by the subcooling of the solid below its fusion temperature, it was found that the latter was 5–10 percent of the former. Thus, for the qualitative arguments to be made here, it is entirely adequate to ignore the latter. Therefore, at any instant of time, the heat flow through the solid behaves like steady-state conduction. Then, if r^* denotes the instantaneous radius of the solid-liquid interface at an axial station x, and r_i is the radius of the cooled tube, the instantaneous radial heat flux q_i at x, per unit tube surface area, is

$$(q_i)_{\rm cond} = k_s \Delta T_i / r_i \ln (r^*/r_i) \tag{2}$$

where k_s is the thermal conductivity of the solid. During the course of a given data run, k_s, ΔT_i, and r_i are constants, so that $(q_i)_{\rm cond} \sim 1/\ln(r^*/r_i)$, and this relationship is plotted as line 0–0 in Fig. 6. This line describes the conduction in the solid at any station x. Since r^* increases during the freezing process, $(q_i)_{\rm cond}$ decreases.

With the aforementioned neglect of the sensible heat effect, $(q_i)_{\rm cond}$ has to be balanced by heat flows entering the solid at the interface. These include the latent heat liberated by the freezing process and the heat transferred to the interface by natural convection from the liquid. With regard to the natural convection, r^* is sufficiently large so that the natural convection coefficients are not influenced by curvature effects; furthermore, the effect of surface mass transfer associated with the freezing was found to be on the order of 1/2 percent. In view of these facts and since the establishment of the natural convection is relatively rapid and ΔT_0 is constant, it is appropriate to regard the convective coefficient h as a constant at any fixed x during a data run. Therefore,

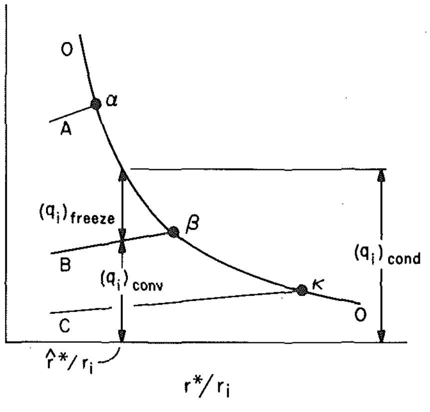

Fig. 6 Heat transfer quantities related to the melting process

$$(q_i)_{\rm conv} = (r^*/r_i) h \Delta T_0 \tag{3}$$

For concreteness, equation (3) may be envisioned as being evaluated at a specific value of x and plotted as curve B in Fig. 6.

Consider now a time t at which the frozen layer thickness at station x is $\hat{r}^*$. At $\hat{r}^*$, the values of the solid-layer conduction and the natural convection heat flux to the interface are identified in Fig. 6. From the figure as well as the foregoing discussion, it is clear that

$$(q_i)_{\rm freeze} = (q_i)_{\rm cond} - (q_i)_{\rm conv} \tag{4}$$

that is, the admissible heat flux contribution of the freezing process is a residual between conduction in the solid and natural convection.

Now, let time pass so that r^* increases. From Fig. 6, it is seen that $(q_i)_{\rm cond}$ decreases while $(q_i)_{\rm conv}$ increases, with the result that the freezing contribution diminishes. Finally, at point β, there is a precise balance between the solid-phase conduction and the interfacial natural convection, and freezing ceases altogether.

The foregoing discussion rationalizes the finite freezing periods encountered in the superheated liquid experiments. Consideration will next be given to the contoured shape of the interface. For this purpose, attention may be focused on a station x where the convective heat transfer coefficient is higher than that for curve B of Fig. 6. Let the curve corresponding to the higher h be denoted by A. It is evident from the figure that the intersection point α of curve A with the conduction line 0–0 corresponds to a smaller r^* value than does the point β. Furthermore, the intersection point κ, which belongs to a curve C having relatively low heat transfer coefficient, corresponds to a larger radius r^*.

It is, therefore, clear that high convection coefficients yield thinner frozen layers and low coefficients yield thicker frozen layers. Since the convective coefficients decrease from the top to the bottom of the frozen layer, the observed increase in layer thickness with downward distance is rationalized.

It remains to discuss the influences of the inner and outer temperature differences ΔT_i and ΔT_0. First, consider the effect of decreasing ΔT_i while ΔT_0 is maintained fixed. According to equation (2), a decrease of ΔT_i would result in a downward movement of the heat conduction curve 0–0 in Fig. 6, while the natural convection curves A, B, and C remain as they were. The points α, β, and κ marking the intersections of curves A, B, and C with the shifted conduction curve all lie to the left of their prior positions. Thus, a decrease in ΔT_i at a fixed ΔT_0 decreases the final thickness of the frozen layer, with a consequent decrease in the freezing time. This deduced result agrees with the experimental findings as evidenced by the comparison of Fig. 4 with the leftmost six photographs of Fig. 5.

Finally, consideration may be given to the effect of increasing ΔT_0 at a fixed value of ΔT_i. Equation (3) then calls for an upward movement of the natural convection curves A, B, and C, with curve 0–0 remaining as is. This results in a leftward shift in the intersection points α, β, and κ. Thus, an increase in ΔT_0 at a fixed ΔT_i brings about a decrease in the final thickness of the frozen layer and a shorter freezing time. Comparison of the representative frozen specimen at the far right of Fig. 5 with the other specimens in that figure affirms this deduction.

Thus, all of the trends displayed in Figs. 4 and 5 have been rationalized.

Frozen Mass, Interface Position, and Heat Transfer. Further confirmation of the cessation of freezing in superheated liquids after a finite period of time is afforded by the measurements of the frozen

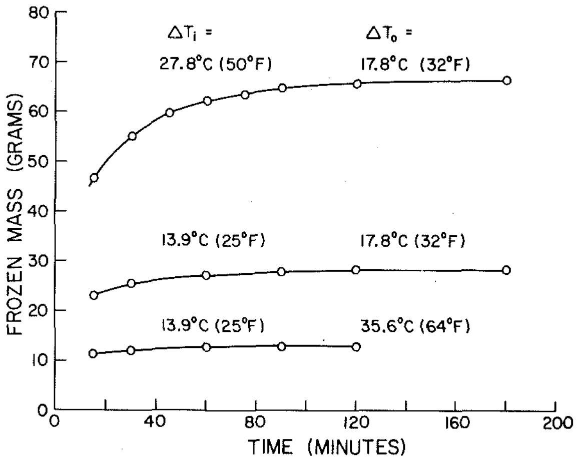

Fig. 7 Mass of the frozen layer as a function of time

mass. Mass versus time results for the aforementioned three sets of operating conditions are plotted in Fig. 7. Curves have been passed through the data to provide continuity, and each curve is parameterized by the corresponding values of ΔT_i and ΔT_0.

All of the curves display a common trend whereby an initial rapid growth of the frozen layer (note that the frozen mass = 0 at time = 0) gives way to a more gradual growth, which ultimately ceases altogether. The zero growth state is attained more rapidly as ΔT_i decreases and ΔT_0 increases. These same conditions (i.e., low ΔT_i and high ΔT_0) result in relatively thin, low-mass frozen layers. It is thus apparent that a frozen layer of any desired terminal size can be obtained by adjustment of ΔT_i and ΔT_0.

Quantitative information about the growth pattern of the frozen layer in the presence of liquid superheating is provided by the successive positions of the solid-liquid interface. The diameters of the frozen specimens of Figs. 4 and 5 were measured as a function of axial position, and representative results from these measurements are presented in Fig. 8. To achieve a compact presentation, the successive interfaces for one set of operating conditions are plotted on the left side of the tube and those for a second set of operating conditions are plotted on the right side of the tube. To preserve clarity, only the interfacial positions at three times, 15, 30, and 180 min, are shown for each case. It should also be noted that different scales have been used for the axial and radial distances to facilitate the plotting.

Inspection of Fig. 8 indicates that the evolution of the frozen layer and the attainment of the final thickness is different depending on the axial station being considered. Near the top, the final thicknesses are small and they are attained in a relatively short time, as witnessed by the overlap of the data points. With increasing downward distance, the final thicknesses are larger, and the spread among the data points indicates that a longer time is required to reach the nonfreezing state. In addition, by taking note of the greater data-point overlap on the left-hand side of the figure, it can be concluded that the cessation of freezing occurs at an earlier time than for the operating condition of the right-hand side. All of the aforementioned trends fit precisely with the phenomenological discussion that was centered on Fig. 6.

Interface positions were also measured for the case of no liquid superheating, and these results can be compared with the theoretical predictions of [8]. The predictions, which are given in [8] in dimensionless form, were specialized to the conditions of the present experiments by making use of the properties of 99-percent pure n-eicosane that are given in [9] and [10]. A comparison of the data with the predictions is presented in Fig. 9.

From the figure, it is seen that the data tend to fall above the predictions, but in the view of the authors the agreement is remarkably good. This appraisal is based on the presence of whisker-like dendrites during the freezing experiments (Figs. 2 and 3), while, in contrast, the theory assumes a completely smooth interface. It is readily understood that the additional solid-liquid contact area provided by the dendrites should increase the freezing rate, as is evidenced in Fig. 9. Also, it may be noted that the size and density of the dendrites increased markedly with time (as suggested by inspection of Fig. 2 but better seen by direct inspection). Therefore, it can be expected that the gap between the theoretical and experimental results should increase with time and this, too, is verified by Fig. 9.

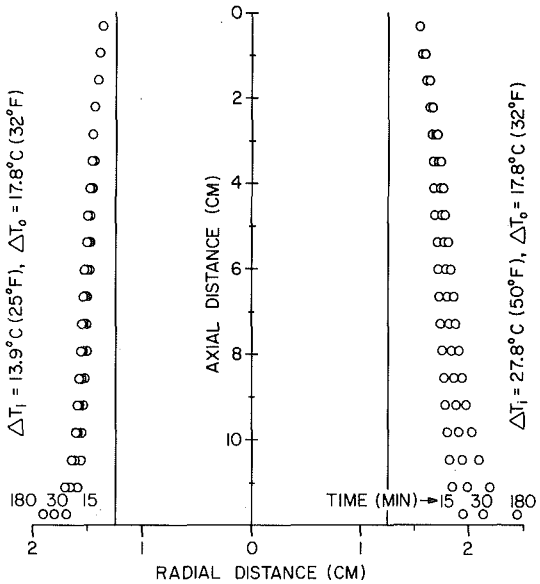

Fig. 8 Position of the solid-liquid interface at various times for freezing in a superheated liquid

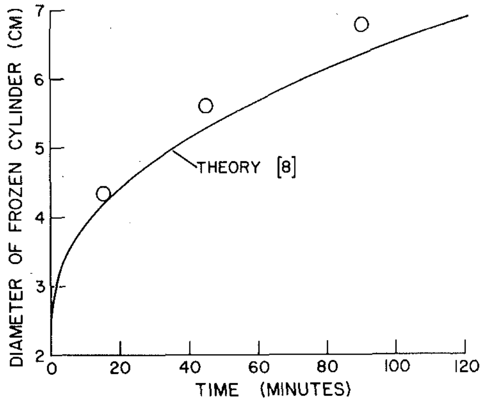

Fig. 9 Position of the solid-liquid interface as a function of time for freezing in a nonsuperheated liquid

In retrospect, the authors are somewhat surprised that the spread between theory and experiment was not greater than that shown in the figure. It is also noteworthy that others [11], albeit in a different type of freezing experiment, have found "that numerous tiny crystals grow out ahead of the main interface during freezing."

The final topic to be considered in the presentation of results is the natural convection heat transfer from the superheated liquid to the interface during the post-freezing period. When freezing has ceased, a local energy balance at the interface requires that the heat delivered by natural convection is equal to the radial conduction in the solid (under the assumption of negligible axial conduction). Thus, from the measured thicknesses of the frozen layer and with the thermal conductivity k_s of solid n-eicosane [9], the natural convection heat flux has been determined at various axial stations for the two operating conditions ΔT_i = 27.8°C, ΔT_0 = 17.8°C and ΔT_i = 13.9°C, ΔT_0 = 17.8°C.

If note is taken of the fact that these two operating conditions have a common value of ΔT_0, it might be conjectured that the natural convection heat flux, per unit interface area, should be the same for the two cases. Indeed, the only reasons why the fluxes might be different are possible differences in the size of the layer and the shape of the interface. In the opinion of the authors, these differences should not play a major role except, perhaps, in the immediate neighborhood of the bottom of the specimen.

To examine this issue, the interface heat fluxes for the second case were ratioed with those for the first, giving representative values of 1.06, 1.01, 1.01, 1.03, and 1.05, respectively at $x/D = 0.65, 1.6, 2.7, 3.4$, and 4.5 (x = axial distance from top of tube, D = tube diameter). These results affirm the insensitivity of the natural convection to the geometrical differences between the terminal specimens for the two cases.

It is of interest to compare the natural convection coefficients with analytical predictions. There are, however, no predictions available for the buoyancy-driven recirculating flow that prevails in the experiments. As an alternative, local heat transfer coefficients were evaluated from the formula for a flat plate situated in an infinite domain (e.g., equation (12–14) of [12]). A comparison was made by ratioing these values with the experimental results for the first of the two cases, yielding 1.33, 1.43, 1.58, 1.69, and 2.31 at the same x/D cited in the preceding paragraph. The experimentally determined heat transfer coefficients decreased from the top to the bottom of the frozen layer, as expected.

This comparison shows that there is no correlation between the present natural convection results and those for the classical vertical plate case. This outcome is, in fact, expected on the basis of conclusions reached by Ostrach [13] in a survey article on natural convection in enclosures. The most direct impact of this outcome is that the analysis of [7], which pertains to freezing on a vertical plate situated in an infinite domain, is inapplicable to finite domains where the flow recirculates.

Concluding Remarks

The experiments reported here have demonstrated that freezing in the presence of a superheated liquid can be drastically slowed and ultimately terminated by natural convection in the liquid. The final size of the frozen layer and the time at which freezing terminates can be controlled by fixing the values of two temperature differences—an inner difference which involves the temperatures of the interface and the cooled surface, and an outer difference involving the temperatures of the outer boundary of the system and the interface.

It is interesting to compare the effects of natural convection on the freezing and melting processes. In the case of melting, natural convection actually accelerates the phase change process, whereas for freezing the opposite effect prevails. Furthermore, for melting, natural convection occurs regardless of whether the initial temperature of the medium is equal to or different from the fusion value. On the other hand, in the case of freezing, the initial temperature must be different from the fusion value in order that natural convection occurs. These contrasting characteristics underscore the differences in the role played by natural convection in the two processes.

Acknowledgment

The research reported here was performed under the auspices of the U.S. Department of Energy, contract DE-AS-0279ER10343.A000.

References

1 White, R. D., Bathelt, A. G., Leidenfrost, W., and Viskanta, R., "Study of Heat Transfer and Melting Front from a Cylinder Imbedded in a Phase Change Material," ASME paper No. 77-HT-42, 1977.

2 Sparrow, E. M., Schmidt, R. R., and Ramsey, J. W., "Experiments on the Role of Natural Convection in the Melting of Solids," ASME JOURNAL OF HEAT TRANSFER, Vol. 100, 1978, pp. 11–16.

3 Abdel-Wahed, R. M., Ramsey, J. W., and Sparrow, E. M., "Photographic Study of Melting About an Embedded Horizontal Cylinder," *International Journal of Heat and Mass Transfer*, Vol. 22, 1979, pp. 171–173.

4 Ockendon, J. R. and Hodgkins, W. R., editors, *Moving Boundary Problems in Heat Flow and Diffusion*, Clarendon Press, Oxford, 1975.

5 Wilson, D. G., Solomon, A. D., and Boggs, P. T., *Moving Boundary Problems*, Academic Press, New York, 1978.

6 Eckert, E. R. G., et al., "Heat Transfer—a Review of 1977 Literature," *International Journal of Heat and Mass Transfer*, Vol. 21, 1978, pp. 1270–1271.

7 Lapudula, C. A. and Mueller, W. K., "The Effect of Buoyancy on the Formation of a Solid Deposit Freezing on a Vertical Surface," *International Journal of Heat and Mass Transfer*, Vol. 13, 1970, pp. 13–25.

8 Sparrow, E. M., Ramadhyani, S., and Patankar, S. V., "Effect of Subcooling on Cylindrical Melting," ASME JOURNAL OF HEAT TRANSFER, Vol. 100, 1978, pp. 395–402.

9 Griggs, E. I. and Yarbrough, D. W., "Thermal Conductivity of Solid Unbranched Alkanes from n-Hexadecane to n-Eicosane," *Proceedings, 14th Southeastern Seminar on Thermal Sciences*, 1978, pp. 256–267.

10 Humphries, W. R. and Griggs, E. I., *A Design Handbook for Phase Change Thermal Control and Energy Storage Devices*, NASA technical paper 1074, 1977.

11 Thomas, L. J. and Westwater, J. W., "Microscopic Study of Solid-Liquid Interfaces During Melting and Freezing," *Chemical Engineering Progress Symposium Series*, Vol. 59, No. 41, 1963, pp. 155–164.

12 Eckert, E. R. G. and Drake, R. M., *Analysis of Heat and Mass Transfer*, McGraw-Hill, New York, 1972.

13 Ostrach, S., "Natural Convection in Enclosures," in *Advances in Heat Transfer*, Vol. 8, 1972, pp. 161–227.

N. Shamsundar
Assoc. Mem. ASME

R. Srinivasan[1]
Department of Mechanical Engineering
University of Houston
Houston, Texas 77004

A New Similarity Method for Analysis of Multi-Dimensional Solidification

There are many multi-dimensional phase change problems which are of interest in applications but cannot be solved by even the powerful computational techniques that are available today. A new similarity rule is presented in this paper to make the solution of such problems possible. The similarity rule applies to problems in which sensible heat contributions are much smaller than latent heat contributions, and the heat flux distribution on the surface of the phase change substance is more or less uniform. After a derivation of the similarity rule is given, it is verified by application to some problems arising in latent heat storage for which finite-difference computations have been performed previously. The similarity rule is easy to apply, and greatly reduces the effort needed in analysing phase change problems. In conjunction with the energy conservation principle, the similarity rule provides an efficient tool for analysing the time-response of a phase change system to arbitrarily varying heat loads, as is demonstrated by examples.

Introduction

Interest in phase change dominated by thermal conduction has been kept alive over many years because of the many fields of application. More recently, this interest has been given a boost because of its relevance to thermal energy storage in molten salts. Excellent methods for treating one-dimensional problems have been developed over the years (see the survey paper by Muehlbauer and Sunderland [1]) and, during the past five years, finite-difference and finite-element methods for solving transient multidimensional problems became available [2, 3]. However, the computational effort and expense, as well as the requirements of computer core, are often so large as to strain the resources available, and may even prevent the solution of certain problems, as illustrated below. In this paper, a new similarity rule is developed that will drastically cut down the computational effort, and the application of the rule is demonstrated in connection with some heat exchangers for thermal energy storage.

Problem Description

The computational difficulties that are confronted may be illustrated by considering the solidification of a phase change material (PCM) in long tubes of square ($2L \times 2L$) cross section when subjected to uniform convective cooling on the outer surface. This problem, with saturated liquid PCM filling the tube initially, was solved in considerable detail by Shamsundar and Sparrow [4] by using an enthalpy based model and an implicit finite-difference scheme. It is reported there that the fineness of the grid that is required to obtain results of a specified accuracy varies with the Biot number, Bi_L. It was found, for example, that a 40×40 grid was adequate for a Biot number of 0.1 to give heat flux results accurate to three digits. When the Biot number is raised to 10, obtaining results of the same accuracy necessitates a 4000×4000 grid during the initial stages of solidification, although the grid can be much coarser for the later stages. Clearly, a grid of this degree of fineness is impossible to implement on even the most powerful computers available today. Nor, by any means, can a Biot number of 10 be considered too large. Much higher values are encountered in applications where the heat extraction rates are fast.

The reasons for this drastic change in step-size requirements are explained in detail in the thesis [5] on which the paper [4] is based. The difficulty just illustrated arises in any solidification problem in which the heat transfer rates are high, and results concerning heat fluxes are desired. It does not occur if one is interested only in the rate of phase change with respect to time. In [4], this problem was overcome by employing an ad hoc procedure that skirts the issue. Reduced accuracy was settled for, but the calculation for Bi = 10 still took five times the computer time as the one for Bi = 0.1. For most problems, such a procedure would not be possible to devise.

A second area of concern and difficulty relates to ascertaining the thermal response to convective cooling when the heat transfer coefficient and the bulk temperature of the coolant vary with time in an arbitrary manner. Obviously, it will be too expensive to compute the response to every conceivable input by making a finite-difference computation. On the other hand, results of this type are indispensable for engineering calculations.

Formulation of Similarity Rule

Prior to stating and deriving the similarity rule that is the focus of this paper, we shall make a few comments to motivate the search for such a rule, and explore the conditions that must be satisfied for the rule to be valid.

Motivation of Search for Similarity Rule. Consider a mass of PCM in a container of arbitrary shape. The surface of the container loses heat by convection to a cooling fluid. The convective coefficient and the coolant temperature can vary with time, but are assumed to be spatially uniform. It is required to calculate the instantaneous surface-integrated heat flux and the fraction of PCM in the solid phase, both as functions of time. Such results have been obtained for many different shapes, and the following observations are derived from them. In many applications, particularly in thermal energy storage, the temperature differences are so small that sensible heat effects are negligibly small compared to latent heat effects. The quantitative criterion related to this statement is the Stefan number Ste. For Ste much smaller than unity, heat capacity can be ignored: this is the well-known quasi-steady situation.

The appropriate nondimensional variables by means of which the results are expressed are the heat flux ratio $\hat{Q} \equiv$ (instantaneous heat flux at time t/instantaneous heat flux when the entire surface is at T_{sat}), the nondimensional time $\tau = \mathrm{Ste\,Fo}$, and the frozen fraction $F \equiv$ (amount of PCM frozen/total amount of PCM). For any specified geometrical configuration, the solution is a pair of curves for each constant value or specified time-dependence of the Biot number. These are the curves of $\hat{Q}$ against τ and F against τ. Although, strictly speaking, there will be a pair of curves for each value of the Stefan number, the curves for an entire range of Stefan numbers coincide with one another over all except the very last stages of solidification. Past experience shows that one may ignore the Stefan number influence, that is, the quasi-steady approximation is valid, for Ste < 1

---

[1] Presently with Airesearch Inc., Phoenix, Arizona.

Contributed by the Heat Transfer Division for publication in the JOURNAL OF HEAT TRANSFER. Manuscript received by the Heat Transfer Division June 23, 1978.

and $F < 0.9$. These ranges correspond to the conditions governing many applications such as thermal energy storage.

Since one still needs to compute a pair of curves for each value of Bi, it is logical to inquire if there is some means of correlating the results for different values of Bi. Naturally, one looks to the simplest cases for guidance as to the correlation. For the simple one-dimensional problem of solidification inside a cylinder by convective cooling at the wall, the quasi-steady approximation [6] results in the following formulae for $\hat{Q}$ and F in terms of the dimensionless interface position $\eta^* = r^*/R$.

$$\hat{Q} = 1/(1 - \mathrm{Bi}_R \ln \eta^*), \tag{1}$$

$$F = 1 - \eta^{*2}. \tag{2}$$

The interface position η^* can be eliminated between these two equations, yielding

$$(1/\hat{Q} - 1)/\mathrm{Bi}_R = -(1/2) \ln (1 - F). \tag{3}$$

Thus, we have obtained an equation between the dimensionless flux $\hat{Q}$ and the solid fraction F that *does not involve the time variable* τ. For any particular value of F, the extent of freezing, the left hand side of this equation is independent of Bi. We may obtain a better interpretation of the quantity on the left hand side of (3) by using the definitions for Bi and $\hat{Q}$ as given in the Nomenclature. Then, we get

$$\frac{1}{\mathrm{Bi}_R}\left(\frac{1}{\hat{Q}} - 1\right) = \frac{k}{hR}\left(\frac{T_{\mathrm{sat}} - T_b}{T_w - T_b} - 1\right)$$
$$= \frac{k}{hR}\left(\frac{T_{\mathrm{sat}} - T_w}{T_w - T_b}\right) = \frac{2\pi k(T_{\mathrm{sat}} - T_w)}{Q'}$$

if Q' is the instantaneous heat flux per unit length of the tube. By employing the shape factor concept [7], we can replace Q' by $kS(T_{\mathrm{sat}} - T_w)$, S being the shape factor for the solid PCM. With these manipulations, equation (3) becomes

$$S = -4\pi/\ln (1 - F). \tag{4}$$

Equation (4) states that the shape factor is solely dependent on the frozen fraction, and is the same at a given value of F for all rates of cooling, that is, for all values of Bi.

Equation (3) is the similarity rule that we have sought. It is natural to expect a similar rule to hold for two and three- dimensional problems. For multidimensional problems with convective cooling, the shape factor is usable only when the surface temperature and, therefore, the surface flux, is approximately uniform. Then, considering the conductive and convective thermal resistances in series, we get the approximate relation

$$Q \approx \frac{T_{\mathrm{sat}} - T_w}{1/(kS)} \approx \frac{T_w - T_b}{1/(hA)} \approx \frac{T_{\mathrm{sat}} - T_b}{1/(kS) + 1/(hA)}.$$

Thus,

$$\hat{Q} \equiv \frac{Q}{hA(T_{\mathrm{sat}} - T_b)} \approx \frac{1}{(hA)/(kS) + 1},$$

and

$$(1/\hat{Q} - 1)/\mathrm{Bi}_L \approx A/(LS). \tag{5}$$

The crucial question now is the following. Is S a function of F alone? In other words, is the shape of the solidified region defined solely by F, regardless of current and previous values of Bi? If so, equation (5) would reaffirm the similarity rule for multi-dimensional problems. We conjecture an affirmative answer to this question, and we seek to establish the conjecture as true by two different approaches. In the first approach, we give a mathematical proof based on the governing equations of conduction phase change. In the second, we employ numerical results. The mathematical proof brings to light the circumstances under which the similarity rule is valid. It is definitive to a degree that numerical verification cannot attain. The latter, on the other hand, provides graphic evidence, and establishes that the effectiveness of the rule is not impaired when actual circumstances deviate considerably from those required by the mathematical proof.

Assumptions. The similarity rule that we are about to derive will apply to the solidification of two and three-dimensional bodies when the following assumptions are fulfilled, at least approximately.

1 Heat capacity is negligible, that is, the Stefan number is small.

2 The specific heat, thermal conductivity and density of the substance change little with temperature.

3 The temperature of the PCM as well as that of the coolant next to the cooled surface is, instantaneously, uniform over the surface. The convective heat flux and, therefore, the heat transfer coefficient are also uniform over the surface.

4 After solidification commences, superheat in the liquid is negligible and may be neglected in writing the energy balance equation at the interface.

All these assumptions except the third are reasonable in the context of many applications. Assumption 3 is rather restrictive and satisfied exactly in only some configurations. In general, one cannot specify uniform wall temperature simultaneously with uniform wall heat flux without introducing overdeterminancy. However, we shall show that mild violations of Assumption 3 do not have severe effects on the application of the rule. Assumption 4 is justified because natural convection in the liquid smooths out any nonuniformities in temperature that are initially present. Therefore, before solidification can start, the substance will be almost everywhere at the solidification temperature. However, very fast cooling or simultaneous heating and cooling will invalidate this assumption.

On the basis of these assumptions, the similarity rule may be stated as follows.

Similarity Rule. For any specified multidimensional geometrical configuration, the process of solidification is such that the quantity $(1/\hat{Q} - 1)/\mathrm{Bi}$ is a function of the frozen fraction F only; it is independent of Bi and T_b, whether or not they vary with time.

Proof. Define the temperature variable θ as

$$\theta \equiv \left(\frac{T_{\mathrm{sat}} - T}{T_w - T_b}\right)\frac{k}{hL}. \tag{6}$$

Nomenclature

A = surface area
Bi_D, Bi_L, Bi_R = Biot numbers, hD/k, hL/k, hR/k
c = specific heat of solid PCM
C = constant related to geometry
D = diameter of cylinder
F = fractional volume of solid PCM
Fo_D, Fo_L, Fo_R = Fourier numbers, $\alpha t/D^2$, $\alpha t/L^2$, $\alpha t/R^2$
h = surface heat transfer coefficient
k = thermal conductivity of solid PCM
L = characteristic length; half of side of square
n = normal coordinate (dimensionless)
n' = normal coordinate
$\hat{q}$ = dimensionless local wall flux, $(T_w - T_b)/(T_{\mathrm{sat}} - T_b)$
Q = instantaneous wall flux
$\hat{Q} = Q/[hA(T_{\mathrm{sat}} - T_b)]$
Q' = instantaneous wall flux per unit length
R = radius of cylinder
r^* = radius of interface
S = shape factor; horizontal half-spacing
Ste = Stefan Number, $c(T_{\mathrm{sat}} - T_b)/\lambda$
t = time
T = temperature
T_b = coolant bulk temperature
T_{sat} = solidification temperature of PCM
T_w = wall temperature of container
W = vertical half-spacing
α = thermal diffusivity of solid PCM
$\eta^* = r^*/R$
θ = dimensionless temperature variable
λ = latent heat
ρ = density of solid PCM
τ = dimensionless time variable
ϕ = correlation function, equation (16)

Then, the governing equations for the quasi-stationary conduction (because of Assumptions 1–4) are the following:

$$\text{In the solid, } \nabla^2\theta = 0. \tag{7}$$

$$\text{At the interface, } \theta = 0. \tag{8}$$

$$\text{At the convectively cooled boundary, } \frac{\partial\theta}{\partial n} = 1. \tag{9}$$

Note that, in the quasi-stationary case, the transient nature of the situation is not observed during the solution for the temperature field; it comes into play only in the calculation of the motion of the interface by employing the energy conservation condition at the interface. Equations (7–9) represent a straightforward Dirichlet-Neumann boundary-value problem for the variable θ; the solution is unique, independent of Bi and T_b, and determined only by the shape and size of the solid PCM. At the cooled surface, $T = T_w$ and θ assumes the value given by equation (6) as

$$\theta_w = \left(\frac{T_{\text{sat}} - T_w}{T_w - T_b}\right)\frac{k}{hL} = \left(\frac{T_{\text{sat}} - T_b - T_w + T_b}{T_w - T_b}\right)\frac{k}{hL} = \left(\frac{1}{\hat{Q}} - 1\right)\frac{1}{\text{Bi}}.$$

Since we just showed that θ_w is independent of Bi, so is $(1/\hat{Q} - 1)/\text{Bi}$. It is important to note that, at this stage, the development is unrelated to any phase change problem.

The second part of the proof consists of showing that, for a given value of the frozen fraction, the shape of the phase boundary is independent of the Biot number. To do so, consider two solidification problems which have the same specifications except that the Biot number and the fluid temperature may vary with time differently in the two cases. Let us assume that the solid-liquid interfaces of the two problems coincide at some instant of time t. In the applications we consider, the interface coincides with the convectively cooled boundaries at the instant when solidification starts, satisfying this assumption.

Now, consider the motion of the interface and the change in the frozen fraction during a differential interval of time dt. In general, the local normal n' to the interface moves by an amount dn' which depends on the local position $\mathbf{r}'$, dt and Bi. Similarly, dF depends on dt and Bi. By considering n' to be a function of $\mathbf{r}'$, F and Bi, and eliminating dt, we find that, with constant Bi,

$$\partial n'/\partial F = (\partial n'/\partial t)/(\partial F/\partial t). \tag{10}$$

Now, the energy conservation condition at the interface is that

$$k(\partial T/\partial n') = \rho\lambda(\partial n'/\partial t). \tag{11}$$

By combining equations (10) and (11), and by using $n = n'/L$, we get

$$\partial n/\partial F = (k/\rho\lambda L^2)(\partial T/\partial n)/(\partial F/\partial t). \tag{12}$$

Next, the instantaneous global energy balance for the PCM is represented by

$$\rho\lambda L^2(\partial F/\partial t) = C\hat{Q}\,hL(T_{\text{sat}} - T_b), \tag{13}$$

where C is a geometrical constant. By eliminating $\partial F/\partial t$ between equations (12) and (13), we see that

$$\frac{\partial n}{\partial F} = \frac{k}{\rho\lambda L^2 C}\,\frac{\partial T}{\partial n}\,\frac{\rho\lambda L^2}{\hat{Q}hL(T_{\text{sat}} - T_b)}.$$

We now replace T in terms of θ using equation (6) to reduce the last equation to

$$\frac{\partial n}{\partial F} = \frac{k}{\hat{Q}hLC(T_{\text{sat}} - T_b)}\left(-\frac{\partial\theta}{\partial n}\right)(T_w - T_b)\frac{hL}{k}.$$

But $\hat{Q} = (T_w - T_b)/(T_{\text{sat}} - T_b)$, so that

$$\partial n/\partial F = -(\partial\theta/\partial n)/C. \tag{14}$$

In the first part of the proof, we showed that θ is independent of Bi. Therefore, equation (14) proves that $\partial n/\partial F$ is independent of Bi. To conclude the proof, observe that

$$dn' = (\partial n'/\partial F)dF + (\partial n'/\partial \text{Bi})d\text{Bi}$$

at any location $\mathbf{r}'$ and that, since the interfaces for the two problems coincide at time t, $\partial n'/\partial\text{Bi}$ is equal to zero. Therefore, dn', the change in the location of the interface, is independent of Bi for a given change in F.

We emphasize that the above proof is valid even when T_b and Bi vary with time. This is important with respect to practical applications of the similarity rule.

Numerical Verification

We shall now examine the usefulness and validity of the similarity rule in situations that do not satisfy Assumption 3, that is, the wall heat flux is not uniform. Naturally, the smaller the nonuniformity, the more closely is the similarity rule obeyed. We shall look at three configurations; the first two have nearly uniform wall flux, and the third has very nonuniform flux distributions.

The first two examples are derived from a commonly considered heat exchanger for thermal energy storage. In this shell and tube type of heat exchanger, the phase change material fills the shell side, while the tubes contain a flowing coolant. A systems type of study of this exchanger has been made by the Grumman Corporation [8], and a detailed thermal analysis of the same has been performed in [9]. Sketches of the two tube layouts are shown in Fig. 1; the two layouts are, respectively, an in-line and a staggered arrangement. The curves of $\hat{Q}$ against τ with Bi = constant for the in-line arrangement with $S = W = D$, obtained from finite-difference calculations, are shown in Fig. 2 for Bi ranging from 0.1 to 100. The dashed lines show $\hat{Q}$ plotted against Bi τ, since it may be argued that one should expect faster freezing with higher Bi, and therefore the time variable should reflect the effect of Bi. Plots of $\hat{Q}$ against F for the same case are shown in

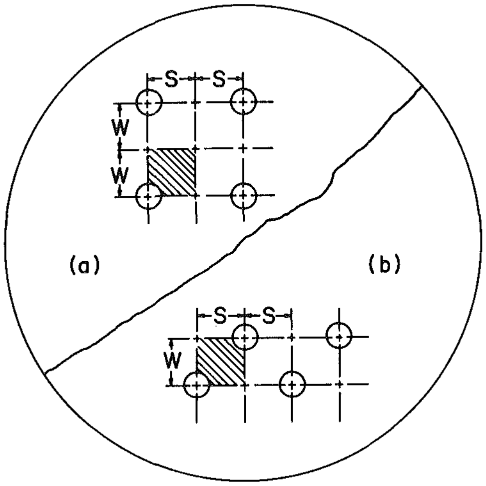

Fig. 1 Diagrams of (*a*) in-line and (*b*) staggered tube layouts

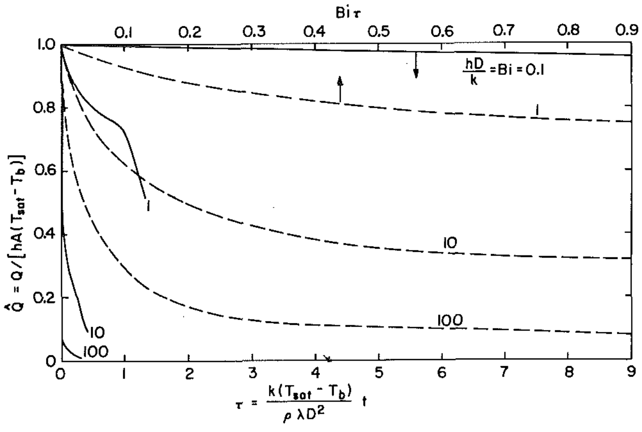

Fig. 2 Timewise variation of heat flux for solidification around tubes in an in-line array: Bi_D = 0.1 to 100

Fig. 3. These results apply to the solidification of PCM initially at T_{sat}, and are for a Stefan number of 0.1, which is small enough to validate Assumption 1 over most of the solidification period. Figs. 2 and 3 show that the variation of heat flux with time is markedly affected by the Biot number, as is the variation of heat flux with extent of freezing. We shall now show that the results of both figures are correlated by the similarity variables defined previously.

Fig. 4 shows $(1/\hat{Q} - 1)/Bi_D$ plotted against F, the full line representing the results for $Bi_D = 0.1, 1, 5, 10, 25$ and 100. The various sets of results correlate to within plotting accuracy except for values of F approaching 1. In view of this excellent correlation, it is of interest to inspect how well this problem satisfies Assumption 3. Since the liquid is always at the melting point, solidification and heat transfer occur around each tube independently of other tubes until the solid layers growing around adjacent tubes make contact with one another. Before this event occurs, the solidification is radially symmetric and, therefore, one-dimensional. The flux and the temperature are uniform at the surface of the tube, and Assumption 3 is valid exactly. Therefore, it is no surprise that the results correlate so well. Beyond the knee of the curve, which corresponds to the instant when the interfaces around adjoining tubes intersect, the transient becomes two-dimensional, and Assumption 3 is not exactly satisfied. In fact, inspection of the local flux distributions, which were obtained from the finite-difference computations, shows that the ratio of maximum to minimum local flux varies from less than 1.01 for Bi = 0.1 to 1.2 for Bi = 100. Therefore, although the flux is nonuniform, the violation of Assumption 3 is not so severe as to impair the usefulness of the similarity rule.

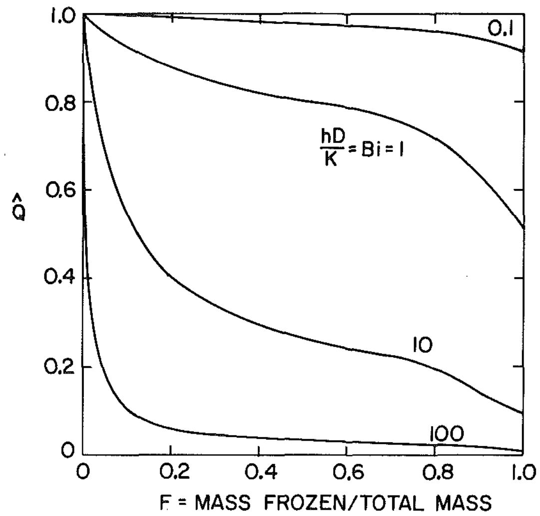

Fig. 3 Variation of heat flux with frozen fraction for solidification around tubes in an in-line array: Bi_D = 0.1 to 100

For Bi = 100, the heat flux variation with time is so rapid that it cannot be shown well on Fig. 2. The heat flux cannot be obtained with even modest accuracy unless a very fine grid is used, as stated earlier. However, the similarity rule enables this task to be done by using the correlation curve.

An additional figure, Fig. 5, shows the raw output from the computer program for the array of round tubes, for Bi = 0.1 and Bi = 100. Both runs were made with the same moderately sized grid. The curves of heat flux and frozen fraction against time are totally different for the two cases, as seen from Figs. 2 and 3. While the curve of $\hat{Q}$ against τ is very smooth for Bi = 0.1 (see Fig. 2), that for Bi = 100 shows numerous and large discontinuous jumps and the error in reading $\hat{Q}$ is very large. When the similarity variable $(1/\hat{Q} - 1)/Bi$ is computed, these discontinuities are greatly reduced.

Fig. 5 has the interesting feature that the curve for Bi = 0.1 meanders just as much as that for Bi = 100! The explanation of this is quite simple. When Bi = 0.1, $\hat{Q}$ is very close to unity, and calculating $(1/\hat{Q} - 1)/Bi$ involves evaluating the difference between two nearly equal numbers, and then dividing the result by a small number. Clearly, this procedure accentuates even undetectable (by plotting) errors in $\hat{Q}$. For Bi = 100, on the other hand, $1/\hat{Q}$ is much larger than unity, and the error in $1/\hat{Q} - 1$ is about the same as in $\hat{Q}$, which is a large error. However, division by Bi, which is large, greatly cuts down the jumps. The similarity curve, then, has the advantage of placing results for different Bi on an equal footing. A smooth curve may be drawn with confidence through the raw data points. To get a $\hat{Q}$ versus τ curve with equally small fluctuations would require an impossibly small grid size.

The broken line in Fig. 4 is for the staggered arrangement, plotted using results given in [10]. Again, the correlation is excellent.

In order to study the applicability of the similarity rule to various geometries, solidification around square ducts arranged in a square grid (half-spacing equal to side of square) was analyzed. For this geometry, the solidification is never one-dimensional. The heat flux distribution is fairly nonuniform, especially near the reentrant corners. The results are shown by using long and short dashes in Fig. 4. The difference between the curves for Bi = 0.1 to 100 is, again, indistinguishable. The closeness of the similarity curve for freezing outside square ducts to that for freezing outside cylindrical tubes is remarkable.

Thus, we conclude that the similarity rule remains almost exactly true even when moderate nonuniformities are present in the heat flux

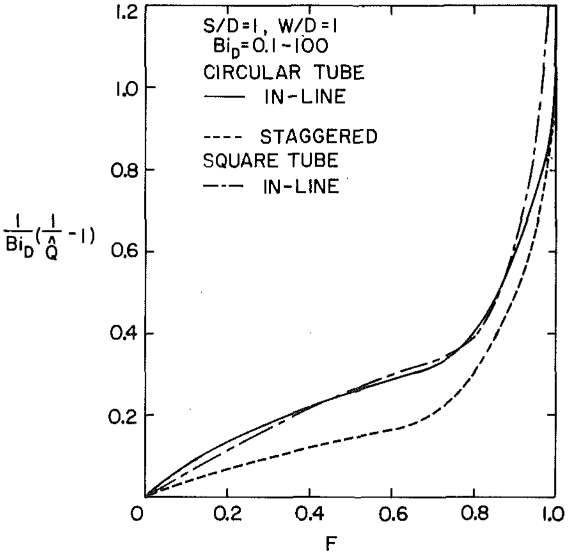

Fig. 4 Similarity curves for solidification around tubes in in-line and staggered arrays

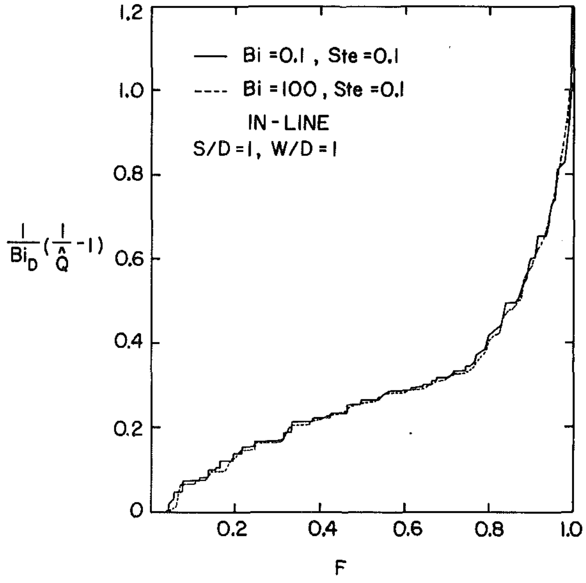

Fig. 5 Comparison of similarity curves for Bi = 0.1 and Bi = 100

distribution. In order to subject the rule to a more severe test, we shall apply it to a problem which is at no time one-dimensional and involves rather large nonuniformities in heat flux. This is the problem of solidification in square tubes that was touched upon in Problem Description; the solutions for this problem were given in [4]. Figs. 6 and 7 are the $\hat{Q} - \tau$ and $F - \tau$ results for $\mathrm{Bi}_L = 0.1$ and $\mathrm{Bi}_L = 10$, respectively. Again, the Biot number is observed to have a marked effect on the curve of heat flux against time as plotted with the variables $\hat{Q}$ and τ. *Fig. 8 is an additional figure for the* $\mathrm{Bi}_L = 10$ *case, intended to show* the extent of nonuniformity in heat flux. The dimensionless *local* flux $\hat{q}$, defined analogously to $\hat{Q}$, is shown plotted against the dimensionless position on the side of the container at various instants of time. In the later stages of solidification, the heat flux at the center of a side is as much as four times the flux at the corner. Notwithstanding this severe nonuniformity, the similarity rule remains surprisingly useful. We can explain in part why this happens. Although the flux distribution is very non-uniform, the Biot number is so high that, relative to $T_{\mathrm{sat}} - T_w$, the change in $T_w - T_b$ from one point on the boundary to another is very small. Therefore, Assumption 3 is justifiable even though the flux is non-uniform.

Fig. 9 shows the results of Figs. 6 and 7 and also the results for $\mathrm{Bi}_L = 1.0$, plotted in terms of the similarity variables. Because of the large nonuniformities in local flux, the curves for $\mathrm{Bi}_L = 0.1$, and 10 do not coincide except at the ends. To this extent, the similarity rule is only approximately obeyed. However, the separation between the curves is small and results sufficient for engineering purposes could be obtained by using just the mean curve of the three. More importantly, the results for an intermediate Bi, say $\mathrm{Bi}_L = 5$, for which computed results are not available, may be obtained by interpolation.

For purposes of comparison, the curve pertaining to axisymmetric solidification in a cylinder, as given by equation (3), is plotted in Fig. 9 using dashes. The apparent insensitivity of the correlating curve to the shape of the PCM container is remarkable.

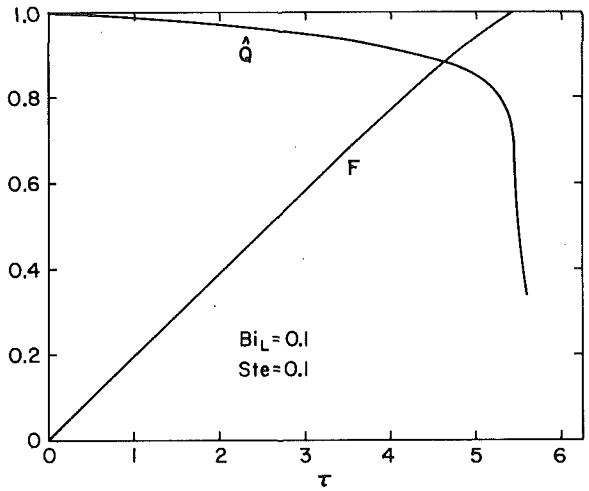

Fig. 6 Timewise variation of heat flux and frozen fraction for solidification in a square tube: $\mathrm{Bi}_L = 0.1$

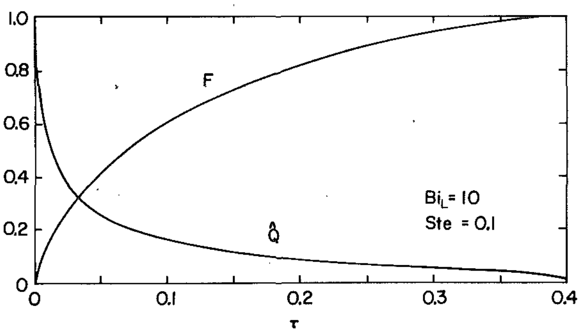

Fig. 7 Timewise variation of heat flux and frozen fraction for solidification in a square tube: $\mathrm{Bi}_L = 10$

Method of Application

In this section, we shall discuss how the similarity rule we have established and verified may be employed as a tool for the analysis of phase change in new configurations with heat loads for which no results are available and conventional analyses are troublesome.

For any new configuration (by "configuration" we mean all layouts that are different only in geometrical scale), a finite-difference or finite-element calculation is necessary for a few benchmark cases. The benchmark cases are those that satisfy the assumption that the heat

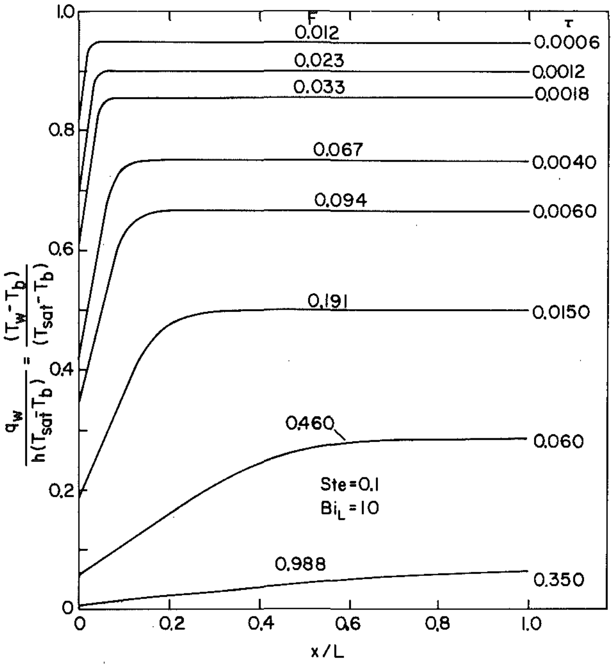

Fig. 8 Local heat flux along the wall of a square tube: $\mathrm{Bi}_L = 10$

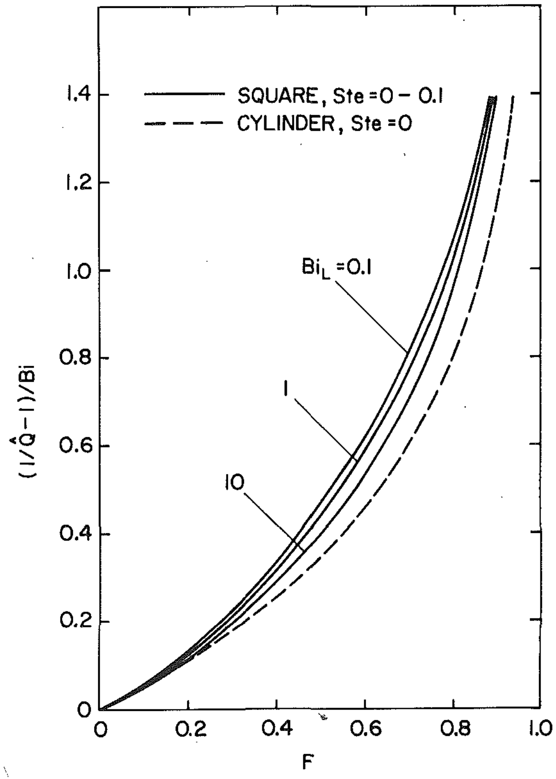

Fig. 9 Similarity curves for solidification inside a square and a circular tube

transfer coefficient and the bulk temperature of the coolant are constant in time. Results should be obtained for a low value of Bi, and also for the highest *feasible* Bi. Then, a plot of $(1/\hat{Q} - 1)/\mathrm{Bi}$ against F is made for the two Biot numbers, and the quality of the correlation is assessed. If the correlation is good, the similarity rule is accepted as valid. If the correlation is not good, the plot is still useful for obtaining $\hat{Q} - F$ results for intermediate values of the Biot number by interpolation. It is also possible to envision instances where results for high Bi are not possible to obtain, such as for the square container considered in the previous sections. Then, the only hope left for using the similarity rule is to examine the local flux distributions that are available. If these distributions are fairly uniform, then the similarity rule is again acceptable as valid. Thus, we see that the similarity rule is useful for all cases except those in which the fluxes are nonuniform and, at the same time, it is not possible to perform finite-difference calculations for large Biot numbers.

Once the similarity curve has been obtained, it may be employed to find the curves of $\hat{Q}$ and F against τ by employing the energy balance principle. For example, for the in-line array of tubes shown in Fig. 1, the equation expressing energy conservation (with sensible heat contributions neglected) is

$$\mathrm{Bi}_D\hat{Q} = \left(\frac{4}{\pi}\frac{S}{D}\frac{W}{D} - \frac{1}{4}\right)\frac{dF}{d\tau} = C\frac{dF}{d\tau} \tag{15}$$

where C is a number that depends on the configuration only. Let the correlation curve be expressed as

$$(1/\hat{Q} - 1)/\mathrm{Bi}_D = \phi(F) \tag{16}$$

where ϕ is independent of Bi_D but may depend on geometrical parameters such as S/D and W/D. Then, from equations (15) and (16), we get

$$d\tau = C\left[\frac{1}{\mathrm{Bi}_D} + \phi(F)\right]dF. \tag{17}$$

For constant Bi, this equation may be integrated, with the initial condition $F = 0$ at $\tau = 0$, to get

$$\tau = CF/\mathrm{Bi}_D + C\int_0^F \phi(F)dF$$

Thus, the graph of F versus τ *for any* Bi_D is obtained by numerical evaluation of a simple integral. From this, the graph of $\hat{Q}$ versus τ may be obtained by cross-plotting.

It should be noted that the computation of the results of $\hat{Q}$ and F against τ can also be performed in an alternative way, by eliminating F between equations (15) and (16). This alternative procedure will yield the $\hat{Q} - \tau$ curve directly without the need for any cross-plotting. However, it involves evaluating the derivative of the inverse function to ϕ. This is likely to introduce fairly large errors into the results. Therefore, the first procedure is to be preferred.

Application to Calculation of Response to Time-Dependent Cooling Rates. To conclude the discussion regarding applications, we shall now show how the new similarity rule may be employed in finding the heat flux and extent of freezing as functions of time when both the heat transfer coefficient and the coolant temperature vary with time in a general way. In this case, which is the one encountered in practice, neither Bi nor Ste is constant as time proceeds. The results of Q' and F as functions of t can be obtained in this general case without having to make finite-difference calculations. All that one needs to do is to obtain the similarity curve by making finite-difference computations for the case of constant Bi and Ste, using a low Bi for convenience. If necessary, the validity of the similarity rule for the particular geometry should be established.

When Bi and Ste are not constant, the nondimensional variables $\hat{Q}$ and τ are no longer useful as indicators of thermal performance. Instead, we must revert to the dimensional heat flux Q' and the physical time t. To obtain Q' and F as functions of t we note that, because the similarity rule is applicable, equations (15) and (16) are valid even for the present case, where Bi is not a constant. These equations, when written in terms of dimensional quantities, result in the relations

$$Q' = \pi CD^2\rho\lambda\frac{dF}{dt} = \frac{\pi k[T_{\mathrm{sat}} - T_b(t)]}{\phi(F) + \dfrac{k}{h(t)D}}. \tag{18}$$

In these, we have written h and T_b as functions of time explicitly. The only input to this equation that comes from finite-difference calculations is the function $\phi(F)$. By virtue of the similarity rule, and because heat capacity contributions are negligible, we can state the following rule for the general case we are now considering.

The similarity function $\phi(F)$ is independent of the history of the load on the solidifying system.

According to this rule, the $\phi(F)$ in equation (18) is the same for any $h(t)$, $T_b(t)$; therefore, $\phi(F)$ may be obtained by subjecting the case of constant, low, Bi and constant Ste to finite-difference analysis. After substituting this into equation (18), integration with respect to t gives the desired results, namely, the curves of Q' and F against t.

Example 1. To illustrate the usefulness of the similarity rule, we shall apply it to the freezing of PCM around a square duct when the Biot number varies according to the equation

$$\mathrm{Bi} = 5 + 4\sin(2\pi F). \tag{19}$$

Thus, the Biot number varies between 1 and 9 as the freezing progresses. From integrating equation (17), we have

$$\tau = C\int_0^F \frac{dF}{\mathrm{Bi}} + C\int_0^F \phi(F)dF. \tag{20}$$

The second integral here is independent of the specified Bi, and could be calculated by numerical integration of the similarity function, which was shown in Fig. 4. However, the calculation can be simplified even more by using the following short cut. Let τ_c be the value of τ corresponding to solidification with Bi = constant = Bi_c. Then, equation (20) reduces to

$$\tau_c = \frac{CF}{\mathrm{Bi}_c} + C\int_0^F \phi(F)dF. \tag{21}$$

Subtracting (21) from (20), we get

$$\tau = \left(\tau_c - \frac{CF}{\mathrm{Bi}_c}\right) + C\int_0^F \frac{dF}{\mathrm{Bi}}. \tag{22}$$

For Bi as given by equation (19), the remaining integral can be evaluated analytically to be

$$\int_0^F \frac{dF}{5 + 4\sin(2\pi F)} = \frac{1}{3\pi}Atn\left[\frac{3}{5\cot(\pi F) + 4}\right],$$

where $Atn(\chi) = \tan^{-1}(\chi)$ for $\chi > 0$, $Atn(\chi) = \pi - \tan^{-1}(-\chi)$ for $\chi \leq 0$.

The quantity τ_0 is available from the finite-difference computations for $\mathrm{Bi}_0 = 1, 10, 100$, etc. from which the similarity curve was plotted. Thus, the evaluation of the performance for the variation (19) of Bi reduces to simple manipulations that can be performed on a desk calculator. The results are shown plotted in Fig. 10 for $\mathrm{Bi}_0 = 10$ (full lines) and $\mathrm{Bi}_0 = 1$ (broken lines). The ordinate variable on the left is Bi $\hat{Q}$ rather than $\hat{Q}$ because the former is independent of Bi. The agreement between the two curves is good. To obtain further evidence in support of the similarity rule, a finite-difference calculation was made in which the Biot number was recalculated at each time interval from equation (19). The results are shown by the little circles in Fig. 10. The agreement with the predictions of the similarity rule is excellent. The small differences are caused by many factors, among which are heat capacity effects, moderate grid size, and violations of the uniform heat flux assumption. At any rate, the differences are small enough to be ignored.

If the Biot number is specified as a function of time rather than frozen fraction, as would be the case when the coolant flow is given as a function of time, it would become necessary to solve a first order, nonlinear ordinary differential equation.

Example 2. Another useful application of the similarity rule would be to enquire how the coolant flow should be regulated so as to obtain

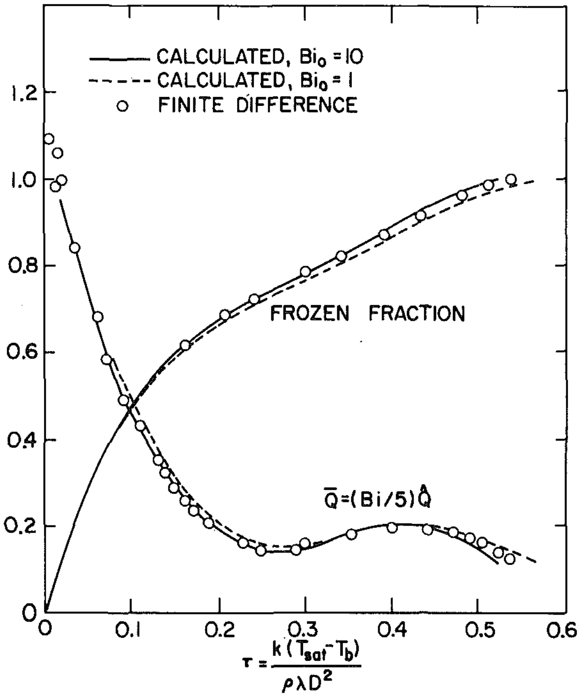

Fig. 10 Application of similarity rule to solidification with variable coolant flow rate

a specified heat flux-time curve. For example, suppose that the heat flux is required to be constant over the entire operating period. Then, if the coolant temperature itself is constant, Bi $\hat{Q}$ has to be constant,[2] and the frozen fraction is proportional to time elapsed. Considering freezing outside square ducts, let the constant heat load be such that complete freezing corresponds to $\tau = 2$, and $F = 0.5\,\tau$. Then, from

$$\frac{1}{C}\frac{d\tau}{dF} = \frac{1}{\mathrm{Bi}} + \phi(F),$$

it is possible to calculate Bi as a function of time. For the case considered, the spacing between the ducts is twice the duct size, and $C = 0.75$. Thus,

$$\mathrm{Bi} = \frac{1}{8/3 - \phi\,(0.5\tau)}.$$

The resulting variation of Bi is shown in Fig. 11. From the Bi, it is possible to obtain the appropriate coolant flow rate by using the proper correlation for convective heat transfer.

On the same figure, results are shown for another case of constant heat flux, in which $F = 2\tau$, the time for complete freezing being $\tau = 0.5$. The curve of Bi for this case shows that the Biot number has to increase rapidly after $F = 0.8$, and becomes infinite at $F = 0.91$. Thereafter, it becomes impossible to supply the heat demanded!

Conclusions

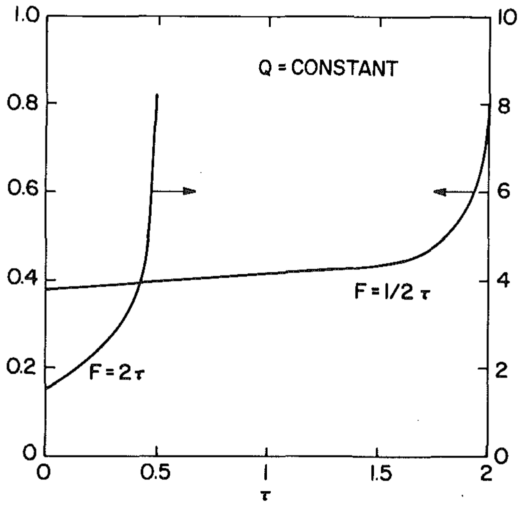

Fig. 11 Variation of Biot number with time required to maintain constant heat output

A similarity rule has been developed for assisting in the analysis of multidimensional transient solidification problems. The rule allows large reductions in computational effort for some problems, and enables the solution of some otherwise intractable problems. For the rule to be applicable, heat capacity contributions should be small, and the instantaneous surface temperature distribution should be more or less uniform. These conditions are satisfied in many applications, thermal storage being an example. The similarity rule allows inexpensive calculation of the thermal response to complicated variations of heat loads. Expensive finite-difference calculations need be made only for a few reference cases. From the results of these calculations, the thermal response to any specified heat load can be calculated by carrying out rather simple operations, the most complex of which are numerical evaluations of some integrals and solution of a single ordinary differential equation.

By numerical testing, it has been shown that even when the assumptions behind the similarity rule are violated to a moderate degree, its usefulness is not much impaired. Similarly, the success of the method in solving problems involving time-dependent loads has been demonstrated. Therefore, the rule can be used in many different ways as a powerful aid to systems analyses.

Although the examples used to illustrate the rule were two-dimensional, the rule is equally valid and beneficial for three-dimensional problems. No new features emerge when one proceeds from two to three-dimensional problems. Extensions of the methods discussed in this paper to problems that involve surface heat transfer methods other than forced convection are being investigated.

Acknowledgments

The research on which this paper is based was performed under Contract EG-77-C-04-3974/EFT-5 for the U.S. Department of Energy and the Energy Foundation of Texas. We are grateful to the journal referee for suggesting additional calculations for validating the similarity rule.

References

1 Muehlbauer, J. C., and Sunderland, J. E., "Heat Conduction with Freezing or Melting," *Applied Mechanics Reviews*, Vol. 18, No. 12, Dec. 1965, pp. 951–959.

2 Wilson, D. G., Solomon, A. D., and Boggs, P. T., (editors), *Moving Boundary Problems*, Academic Press, 1978.

3 Comini, G., del Guidice, S., Lewis, R. W., and Zienkiewicz, O. C., "Finite-element Solutions of Non-linear Heat Conduction Problems with Special Reference to Phase Change," *International Journal for Numerical Methods in Engineering*, Vol. 8, 1974, pp. 613–624.

4 Shamsundar, N., and Sparrow, E. M., "Analysis of Multidimensional Conduction Phase Change via the Enthalpy Model," ASME JOURNAL OF HEAT TRANSFER, Vol. 97, 1975, pp. 333–340.

5 Shamsundar, N., "Multidimensional Conduction Phase Change with Density Change, and Application to Thermal Energy Storage," Ph.D. Thesis, University of Minnesota, Minneapolis, 1975.

6 London, A. L., and Seban, R. A., "Rate of Ice Formation," Trans ASME, Vol. 65, 1943, pp. 771–778.

7 Eckert, E. R. G., and Drake, R. M., *Analysis of Heat and Mass Transfer*, McGraw-Hill, 1972, p. 111.

8 Grumman Aerospace Corporation, "Thermal Energy Storage Heat Exchanger," NASA CR 135245, 1977.

9 Shamsundar, N., and Srinivasan, R., "Analysis of Energy Storage by Phase Change with an Array of Cylindrical Tubes," paper presented at 1978 ASME Winter Annual Meeting.

10 "Heat Transfer in Thermal Storage Systems—Design Procedures for Latent Heat Storage," Final Report for ERDA Contract EG-77-C-04-3974/EFT-5, University of Houston, Department of Mechanical Engineering, 1978.

---

[2] $\mathrm{Bi}\hat{Q} = [hD/k][Q/hA(T_{sat} - T_b)] = \text{constant} \times Q$

L. T. Yeh[1]
Assoc. Mem. ASME

B. T. F. Chung
Associate Professor,
Mem. ASME

Department of Mechanical Engineering,
The University of Akron,
Akron, OH 44325

A Variational Analysis of Freezing or Melting in a Finite Medium Subject to Radiation and Convection

The objective of this work is to develop an approximate analytical solution for the heat transfer in a finite medium with a change in phase. The medium is subjected to radiative and aerodynamic cooling (or heating) at one side and is thermally insulated at the other side. Furthermore, the initial temperature is different from the fusion (or melting) temperature. It is assumed that all the physical properties are constant for each phase but may be different (except density) for different phases. In this analysis, Biot's variational method is employed. With this technique, the complicated nonlinear problem is reduced to an initial value problem which is then solved by the Runge Kutta method. The calculated temperature histories at both surfaces and the time variant fusion (or melting) line are in terms of dimensionless parameters such as radiation number, Biot's number, Stefan number, ratio of freezing (or melting) to initial temperatures and the thermal properties ratios in both phases. Some limiting solutions of the present work are found to agree with the earlier analysis.

Introduction

Problems of transient heat transfer in a finite medium with a phase change arise frequently in the areas of food processing, polymer production, metal casting, frost and ice formations, and nuclear reactor operations. Due to the complexity involved, previous solutions of heat transfer with a change in phase were restricted to either of the following categories: (1) the temperature of the material under consideration is initially at the melting or fusion temperature, and (2) the fixed surface of the material is subjected to a linear boundary condition. The first category is essentially under the assumption that the material is semi-infinite. The analysis based on this assumption tends to underpredict the melting and solidification rate because of the finite dimension of the actual structure. The second category excludes the situation involving radiative heating or cooling at the boundary, a case of practical significance such as metal casting at high temperature and thermal storage devices in space vehicles. Apparently, solutions of general nature have not yet been available in the literature.

Heat conduction with phase change differs from heat conduction without phase change in that the interface between the solid and liquid phases is moving and hence the boundary condition at this interface is nonlinear. Therefore, exact analytical solutions are limited to a few cases [1–5]. It is felt that when a great accuracy is not required, approximate analytical solutions are desirable and practical. One of the useful approximate techniques is the variational method due to Biot [6, 7]. This method has been successfully applied by many investigators [8–12] to various phase change problems involving a linear boundary condition at the fixed surface of the material. Recently, the present authors [13, 14] have studied heat transfer in material accompanied by solidification and freezing due to thermal radiation and convection at the boundary. However, the authors assumed that material under consideration is initially at the fusion or melting temperature. More recently Yan and Huang [15] solved the same problem as presented in [13] using a regular perturbation method. The authors defined a small parameter $\epsilon = c_p(T_i - T_e)/L$ which can be rewritten in terms of the inverse of Stefan number, B as $\epsilon = (1 - U_e)/B$ where $B = L/c_pT_i$. The values of B for most metals and liquids of practical interest in engineering lie between 0.1 and 1.0 as tabulated in [13]. Since ϵ has to be less than unity, their perturbation solution is of practical use in a limited range of parameters. For an example, in the case of solidification of water ($B \doteq 0.3$) the solution is valid only when $U_e > 0.7$. In particular, the perturbation solution is inadequate at $U_e = 0$, a case of radiation in space.

All papers mentioned above deal with phase change in a semi-infinite domain with initial temperature equals to fusion or melting temperature. Goodman and Shea [16] and Weinbaum, et al. [17] have attacked the problem of melting or freezing in a finite medium initially not at fusion temperature. The former employed heat balance integral method while the latter applied the singular perturbation technique. Both solutions are restricted to their applications to certain physical parameters. The perturbation solution in [17] is limited to the condition of $c_p(T_i - T_f)/L \leq 0.5$; the differential equations obtained based on integral method in [16] are further linearized by power series expansion and hence additional approximation is introduced. Furthermore, none of these analyses treat either convective or radiative boundary condition at the surface.

The purpose of this work is to develop a variational analysis for freezing or melting in a finite medium; the medium is subjected to radiative and aerodynamic cooling (or heating) at one side and is thermally insulated at the other side. Furthermore, the initial temperature is different from the fusion (or melting) temperature.

It should be pointed out that the same problem can be solved using heat balance integral method. However, for a strongly nonlinear phase change problem, Biot's variational method appears to be somewhat advantageous over the Goodman's integral method as illustrated in [13] for the case of initial temperature equal to the fusion temperature; the integral method yields two simultaneous ordinary differential equations while the Biot's variational method gives one differential equation and one simple algebraic equation. Further, the variational method yields numerical results which are a few percent more accurate than that of integral method. This has been previously demonstrated for the case of pure conduction without phase change [18–19] and heat transfer with a phase change [13].

Mathematical Analysis

Consideration is given to a finite region of liquid (or solid) which is initially at a uniform temperature, T_i, but is different from its fusion (or melting) temperature, T_p. Due to radiative and aerodynamic cooling (or heating) at one surface, phase change takes place, while the other side is thermally insulated. It is assumed that during the period of phase change, there exists, at all times, a sharply-defined line of division between the solid and the liquid, the thermal properties are temperature independent but they may be different for

---

[1] Research Assistant, Presently with Technical Applications, The Babcock and Wilcox Co., Barberton, Ohio.

Contributed by the Heat Transfer Division for publication in the JOURNAL OF HEAT TRANSFER. Manuscript received by the Heat Transfer Division March 19, 1979.

different phases. Furthermore, heat transfer due to free convection in the liquid region is assumed negligibly small and the newly formed phase is assumed to be opaque. Depending upon thermal condition at the boundary and the transport properties of the material, the problem is treated by considering three consecutive time domains. *The sequence of events that are likely to occur is shown in Fig. 1, e.g.,* for the case of solidification.

First Time Domain ($0 \le \tau \le \tau_\ell$ or $0 \le \tau \le \tau_p$). In this period, the effect of radiative and aerodynamic cooling (or heating) has penetrated into a position ($x' = q_4$) which is less than the thickness of the slab, ℓ. Because no phase change takes place in the entire region, the problem can be treated as heat transfer in a semi-infinite body subjected to radiation and convection. Equations describing the system are given by

$$\frac{\partial T_1'}{\partial t} = \alpha \frac{\partial^2 T'}{\partial x'^2} \quad \tau > 0, \quad 0 \le x \le q_4 \qquad (1)$$

$$T_1' = T_i \quad x' > 0 \quad t = 0 \qquad (2a)$$

$$k \frac{\partial T_1'}{\partial x'} = \sigma F(T_1'^4 - T_e^4) + h_0(T_1' - T_e) \quad x' = 0, \quad t > 0 \qquad (2b)$$

$$\frac{\partial T_1'}{\partial x'} = 0 \quad x' = q_4, \quad t > 0 \qquad (2c)$$

Where T_1' is the absolute temperature, q_4 is the depth of penetration, σ is Stefan-Boltzman constant, F is the overall radiation shape factor and h_0 is the convective heat transfer coefficient.

Using Biot's variational principle, we first define a heat flow vector, $\vec{H}$, whose time rate of change, $\dot{H}$ is the heat flux across an area normal to $\vec{H}$. The energy balance represented by equation (1) can be in terms of $\vec{H}$ as

$$\operatorname{div} \vec{H} = -cT \qquad (3)$$

Where c is heat capacity and T is the temperature above the initial temperature. We then assume the following temperature profile in the region of $0 \le x' \le q_4$

$$T_1 = (q_1 - T_i)\left(1 - \frac{x'}{q_4}\right)^2 \qquad (4)$$

Where T_i is the absolute initial temperature of materials under consideration, q_1 is the absolute temperature at the heat transfer surface.

Employing equation (4), the heat flow vector $\vec{H}_1$, is immediately obtained from equation (3),

$$\vec{H}_1 = \frac{1}{3} c_1 q_4 (q_1 - T_i)\left(1 - \frac{x'}{q_4}\right)^3 \qquad (5)$$

Once the heat flow vector, $\vec{H}_1$ is found, the following generalized Lagrangian equation which represents the energy balance in each phase is employed [3]

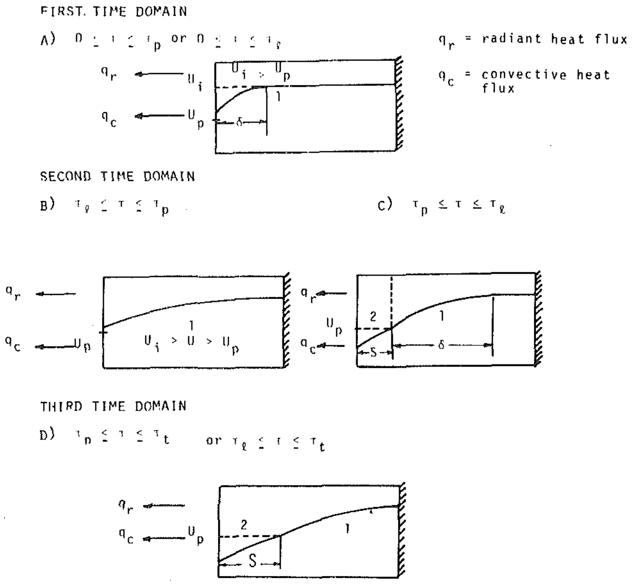

Fig. 1 Sequence of events occurring during solidification

$$\frac{\partial V}{\partial q_i} + \frac{\partial D}{\partial \dot{q}_i} = Q_i \quad i = 1, 2, \ldots m \qquad (6)$$

where

$$V = \tfrac{1}{2} \int_v cT^2 dv$$

$$D = \tfrac{1}{2} \int_v \frac{1}{k} \dot{H}^2 dv$$

$$Q_i = -\int_A T \frac{\partial \vec{H}_j}{\partial q_i} \cdot \vec{n} dA \qquad (7)$$

and m is the number of generalized coordinates involved in the problem. ($T = T_1$ or T_2 and $\dot{H} = \dot{H}_1$ or $\dot{H}_2$ depending on old or new phase under consideration).

Substituting equations (4) and (5) into equation (6) gives

$$10 q_4^2 \dot{q}_1 + 15 q_4 \dot{q}_4 (q_1 - T_i) = 84 (q_1 - T_i) k_1 / c_1 \qquad (8)$$

Equations (4) and (2*b*) give the following relationship between the surface temperature and the penetration depth

$$q_4 = -\frac{2(q_1 - T_i)k_1}{\sigma F(q_1^4 - T_e^4) + h_0(q_1 - T_e)} \qquad (9)$$

Combining equations (8) and (9) yields

Nomenclature

A = surface area
B = fusion or melting parameter or the inverse of Stefan number, $B = L/c_pT_i$ for solidification, $B = L/c_pT_e$ for melting
$\mathrm{B_0}$ = Biot's number, $h\ell/k$
c = heat capacity, ρc_p
c_p = specific heat
F = radiation overall shape factor
h_0 = heat transfer coefficient
k = conductivity
ℓ = total length of the slab or liquid
L = latent heat
Nr = radiation parameter, $Nr = F\sigma T_i^3 \ell/k$ for solidification, $Nr = F\sigma T_e^3 \ell/k$ for melting
$\vec{n}$ = unit normal vector
p = phase change parameter $p = 1$ for solidification, $p = -1$ for melting
q_1 = absolute temperature at the free surface
q_4 = depth of penetration
q_8 = solidification depth or the position of interface
s = dimensionless solidification depth, q_8/ℓ
t = time
T = temperature above the initial temperature
T' = absolute temperature
T_p = melting or fusion temperature
T_1 = temperature above the initial temperature for the old phase
T_2 = temperature above the initial temperature for the new phase
u = dimensionless absolute temperature $u = T'/T_i$ for solidification, $u = T'/T_e$ for melting
u_p = dimensionless melting or fusion temperature, e.g., $u_p = T_p/T_i$ for solidification
v = volume
x = dimensionless distance, x'/ℓ
x' = distance along the slab or liquid
α = thermal diffusivity
δ = dimensionless thermal layer or penetration depth, q_4/ℓ
ρ = density
σ = Stefan-Boltzmann constant
τ = $\alpha_1 t/\ell^2$

Subscripts

e = environment condition
i = initial condition
ℓ = condition when $q_4 = \ell$
p = phase change condition
t = condition at the end of process
1 = condition at the old phase, e.g., liquid for solidification process
2 = condition at the newly formed phase, e.g., solid for solidification process

$$\dot{u}_s = \frac{\frac{21}{25}[N_r(u_s^4 - u_e^4) + \mathrm{B}_0(u_s - u_e)]^3}{(u_s - u_i)[N_r(u_s^4 - u_e^4) + \mathrm{B}_0(u_s - u_e)] - 0.6(u_s - u_i)^2(4N_r u_s^3 + \mathrm{B}_0)}$$

where $u_s = q_1/T_i$ for cooling and $u_s = q_1/T_e$ for heating.

This equation is solved numerically with the aid of $u_s(0) = u_i$. The solution becomes invalid when either of the following conditions is reached: (1) when $\tau = \tau_p$, i.e., solidification or melting begins at the front surface; and (2) when $\tau = \tau_\ell$, i.e., the penetration depth reaches the insulated surface.

Second Time Domain ($\tau_\ell \le \tau \le \tau_p$ or $\tau_p \le \tau \le \tau_\ell$). There are two possible paths that the transfer process may take place during this time period: (1) the phase change takes place at $x = 0$ after the depth of penetration reaches the insulated surface. This is graphically shown in Fig. 1(*b*). (2) The phase change takes place before the depth of penetration reaches the insulated surface as shown by Fig. 1(*c*). They will be analyzed separately below:

1 *Case with* $\tau_\ell \le \tau \le \tau_p$. Since no phase change takes place in this time interval while the penetration depth already arrived at the insulated surface, the solution for temperature distribution is identical to that of second time domain in a slab without phase change. The transit time, τ_ℓ, and the corresponding surface temperature can be found by solving equations (9) and (10) simultaneously with q_4 set equal to ℓ. This condition will serve as the starting point for the differential equation for u_s derived below. Note that the boundary condition represented by equation (2*c*) is replaced by

$$\frac{\partial T_1'}{\partial x'} = 0 \quad \text{at} \quad x' = \ell \tag{2d}$$

We again assume a parabolic temperature profile for this time domain

$$T_1 = (q_1 - q_2)\left(1 - \frac{x'}{\ell}\right)^2 + q_2 - T_i \tag{11}$$

where q_2 is the absolute temperature at the insulated surface. With the above specified temperature, the heat flow vector, $\vec{H}_1$ is determined from equation (3). Substituting $\vec{H}_1$ and T_1 into equation (6) and combining equation (2*b*) yields the following first order differential equation

$$\frac{du_s}{d\tau} = \frac{-[N_r(u_s^4 - u_e^4) + \mathrm{B}_0(u_s - u_e)]}{1 + \frac{8}{21}(4N_r u_s^3 + \mathrm{B}_0)} \tag{12}$$

The dimensionless insulated surface temperature, u_ℓ is found directly from the boundary condition at $x = 0$ and is given by

$$u_\ell = u_s + \frac{1}{2}[N_r(u_s^4 - u_e^4) + \mathrm{B}_0(u_s - u_e)] \tag{13}$$

where $u_\ell = q_2/T_i$ for cooling and $u_\ell = q_2/T_e$ for heating.

2 *Case with* $\tau_p \le \tau \le \tau_\ell$. In this case, phase change occurs before the penetration depth reaching the insulated surface. Under this condition, both liquid and solid phases exist simultaneously. Let us designate the old phase and the newly formed phase by subscripts 1 and 2, respectively. The energy balance at the interface gives

$$K_2\frac{\partial T'_2}{\partial x'} - K_1\frac{\partial T'_1}{\partial x'} = p\rho L\frac{dq_8}{dt} \tag{14}$$

where L is the latent heat and q_8 is the solidification or melting distance, and

$$p = \begin{cases} 1 \text{ for solidification} \\ -1 \text{ for melting} \end{cases}$$

We assume that the temperature profiles in both regions take the forms

$$T_1 = (T_p - T_i)\left(\frac{q_4 - x'}{q_4 - q_8}\right)^2 \tag{15}$$

and

$$T_2 = (q_1 - T_p)\left(1 - \frac{x'}{q_8}\right) \tag{16}$$

where q_1, q_4, and q_8 are the absolute surface temperature at $x = 0$, the depth of penetration and the time variant interface position respectively. T_p, T_1, and T_2 are the absolute phase change temperature (fusion or melting temperature), the temperature of region 1 above the initial temperature and the temperature of region 2 above the phase change temperature, respectively. Note that the choice of linear temperature profile in the newly formed phase has been shown to yield quite satisfactory results in the earlier studies [11, 12, 20].

From equation (3) the heat flow vectors in each region are then determined. They are

$$\vec{H}_1 = \frac{1}{3}c_1(q_4 - q_8)(T_p - T_i)\left(\frac{q_4 - x'}{q_4 - q_8}\right)^3 \tag{17}$$

and

$$\vec{H}_2 = \frac{1}{2}c_2(q_1 - T_p)q_8\left(1 - \frac{x'}{q_8}\right)^2 + \frac{1}{3}c_1(q_4 - q_8)(T_p - T_i) - p\rho Lq_8 \tag{18}$$

The substitution of equations (17) and (18) into equation (6) yields

$$\frac{1}{42}(\delta - s)\left(\frac{d\delta}{d\tau} - \frac{ds}{d\tau}\right) + \frac{4}{45}\left(\delta\frac{ds}{d\tau} - s\frac{d\delta}{d\tau}\right) + \frac{1}{630}\left(\frac{d\delta}{d\tau} - \frac{ds}{d\tau}\right)(11\delta + 45s) = \frac{7}{30} \tag{19}$$

and

$$\begin{aligned}
&\left[\frac{3}{40}s(u_s - u_p)\frac{du_s}{d\tau} + \frac{2}{15}(u_s - u_p)^2\frac{ds}{d\tau} - \frac{2}{3}pB(u_s - u_p)\frac{ds}{d\tau} - \frac{1}{6}pBs\frac{ds}{d\tau} + B^2\frac{ds}{d\tau}\right] \\
&+ \frac{1}{9}\frac{c_1}{c_2}(u_s - u_p)\left(\frac{d\delta}{d\tau} - \frac{ds}{d\tau}\right)(u_p - u_i) \\
&- \frac{1}{9}\frac{c_1}{c_2}(u_s - u_p)(u_p - u_i)\frac{ds}{d\tau} \\
&- \frac{1}{18}\frac{c_1}{c_2}(u_p - u_i)\frac{du_s}{d\tau} + \frac{1}{3}\frac{c_1}{c_2}pB(u_p - u_i)\frac{ds}{d\tau} \\
&- \frac{1}{9}\left(\frac{c_1}{c_2}\right)^2\left(\frac{d\delta}{d\tau} - \frac{ds}{d\tau}\right)(u_p - u_i)^2 \\
&- \frac{1}{3}\frac{c_1}{c_2}pB\left(\frac{d\delta}{d\tau} - \frac{ds}{d\tau}\right)(u_p - u_i) \\
&= -\frac{\alpha_2}{\alpha_1}[Nr(u_s^4 - u_e^4) + \mathrm{B}_0(u_s - u_e)] \\
&\quad \times\left[\frac{1}{3}(u_s - u_p) - pB - \frac{1}{3}\frac{c_1}{c_2}(u_p - u_i)\right]
\end{aligned} \tag{20}$$

respectively, where $s = q_8/\ell$, $\delta = q_4/\ell$ and the parameter B corresponds to the inverse of Stefan number and is defined by, for solidification,

$$B = \frac{L}{c_{p2}T_i}$$

From the boundary condition at $x = 0$, we have

$$s = \frac{u_p - u_s}{Nr(u_s^4 - u_e^4) + \mathrm{B}_0(u_s - u_e)} \tag{21}$$

The three time dependent variables, u_s, δ and s are solved simultaneously from equations (19–21) with the aid of the initial conditions

$$\left.\begin{aligned} u_s &= u_p \\ s &= 0 \\ \delta &= \delta_p \end{aligned}\right\} \quad \text{at } \tau = \tau_p \tag{22}$$

where δ_p (or q_4/ℓ) can be obtained from equation (9) by setting $u_s = u_p$. (or $q_1 = T_p$)

3 *Third time domain* ($\tau_p \leq \tau \leq \tau_t$ *or* $\tau_\ell \leq \tau \leq \tau_t$). During this period, both liquid and solid exist simultaneously and a definite line of division between the liquid and the solid also exists. Temperature profiles in the liquid and solid regions are assumed to be the forms

$$T_1 = (T_p - q_2)\left(1 - \frac{x' - q_8}{\ell - q_8}\right)^2 + q_2 - T_i \tag{23}$$

and

$$T_2 = (q_1 - T_p)\left(1 - \frac{x'}{q_8}\right) \tag{24}$$

where q_2 is the absolute temperature at $x = 1$. The heat flow fields in both regions are found to be

$$\begin{aligned} \vec{H}_1 = \frac{1}{3} c_1 (T_p - q_2)(\ell - q_8)\left(1 - \frac{x' - q_8}{\ell - q_8}\right)^2 \\ + c_1 \ell (q_2 - T_i)\left(1 - \frac{x'}{\ell}\right) \end{aligned} \tag{25}$$

and

$$\begin{aligned} \vec{H}_2 = -p\rho L q_8 + (\ell - q_8) c_1 \left[\frac{1}{3}(T_p - q_2) + (q_2 - T_i)\right] \\ + \frac{1}{2} c_2 q_8 (q_1 - T_p)\left(1 - \frac{x'}{q_8}\right) \end{aligned} \tag{26}$$

The substitution of equations (23–26) into equation (6) yields

$$\begin{aligned} (1 - s)\left[\frac{17}{21}\frac{du_\ell}{d\tau}(1 - s) + \frac{8}{21}(u_p - u_\ell)\frac{ds}{d\tau}\right] \\ = -2(u_\ell - u_p) \end{aligned} \tag{27}$$

and

$$\begin{aligned} &\Big[\frac{3}{40} s (u_s - u_p)\frac{du_s}{d\tau} + \frac{2}{15}(u_s - u_p)^2 \frac{ds}{d\tau} \\ &\qquad - \frac{2}{3} pB (u_s - u_p)\frac{ds}{d\tau} - \frac{1}{6} pBS \frac{du_s}{d\tau} + B^2 \frac{ds}{d\tau}\Big] \\ &- \frac{2}{3}\frac{c_1}{c_2}\left(\frac{2}{3}u_\ell + \frac{1}{3}u_p - u_i\right)(u_s - u_p)\frac{ds}{d\tau} \\ &\qquad + \frac{2}{9}\frac{c_1}{c_2}(1 - s)(u_s - u_p)\frac{du_\ell}{d\tau} \\ &\quad + 2\frac{c_1}{c_2} pB \left(\frac{2}{3}u_\ell + \frac{1}{3}u_p - u_i\right)\frac{ds}{d\tau} - \frac{2}{3}\frac{c_1}{c_2} pB (1 - s)\frac{du_\ell}{d\tau} \\ &\qquad - \frac{1}{6}\frac{c_1}{c_2}\left(\frac{2}{3}u_\ell + \frac{1}{3}u_p - u_i\right) s \frac{du_s}{d\tau} \\ &- \left(\frac{c_1}{c_2}\right)^2 \left[\frac{2}{3}(1 - s)\frac{du_\ell}{d\tau} - \left(\frac{2}{3}u_\ell + \frac{1}{3}u_p - u_i\right)\frac{ds}{d\tau}\right] \cdot \left(\frac{2}{3}u_\ell + \frac{1}{3}u_p - u_i\right) \\ &\quad = -\frac{\alpha_2}{\alpha_1}\left[Nr(u_s^4 - u_e^4) + \mathrm{B}_0(u_s - u_e)\right]\left[\frac{1}{3}(u_s - u_p) - pB\right] \end{aligned} \tag{28}$$

Equations (21, 27) and (28) are solved numerically with the following initial conditions:

$$\left.\begin{aligned} u_s &= u_p \\ s &= 0 \\ u_\ell &= u_{\ell_p} \end{aligned}\right\} \quad \text{at } \tau = \tau_p \tag{29}$$

where u_{ℓ_p} can be determined from equation (13) by letting $u_s = u_p$. Equations (21, 27) and (28) are still valid for the period $\tau_\ell \leq \tau \leq \tau_t$, except that the initial conditions are

$$\left.\begin{aligned} u_\ell &= u_i \\ u_s &= u_{s\ell} \\ s &= s_\ell \end{aligned}\right\} \quad \text{at } \tau = \tau_\ell \tag{30}$$

Both $u_{s\ell}$ and s_ℓ are determined from equations (19–21) at $\tau = \tau_\ell$. The temperature histories at both surfaces and the time variant fusion (or melting) line are presented in terms of dimensionless parameters such as radiation number, Biot's number, Stefan number, ratio of freezing (or melting) to initial temperatures and the thermal properties ratios in both phases. Details of numerical solution can be found in [21].

Results and Discussion

Although the present analysis is applicable to both melting and freezing, the numerical computations are presented for the case of solidification only, i.e., $p = 1$. Figs. 2–8 illustrate the temperature curves and solidification rate. The parameters chosen in Figs. 2–5 are $u_e = 0.25$, $\mathrm{Nr} = 10$, $\mathrm{B}_0 = 0$ and $B = 1$. Fig. 2 shows the surface temperature histories for $u_p = 0.72u_i$. The solid lines represent the radiative surface temperature and the dash lines correspond to the insulated surface temperature. The process takes place along the paths shown by sketch *a-c-d* in Fig. 1. The curve 1 in this figure represents the case that both heat capacity and thermal conductivity ratios between solid and liquid phases are unity, i.e., $c_2/c_1 = k_2/k_1 = 1$; curve 2 represents the case with $c_2/c_1 = 1.5$ and $k_2/k_1 = 1$ and curve 3 corresponds to the temperature history for $c_2/c_1 = 1$ and $k_2/k_1 = 1.5$. Due to radiative cooling the surface temperature at $x = 0$ gradually decreases from the initial value to the point P indicated in Fig. 2. At this point the surface reaches the fusion temperature and begins to solidify. At the same time, the depth of penetration continues to increase in the liquid region and finally reaches the insulated surface. This condition is designated by point T. From this moment, the temperature of the insulated surface starts to decrease as shown by dash lines. The point G represents the condition at which the insulated surface reaches the fusion temperature. Since the material is finite in extent, all curves end at the point E corresponding to the situation where $s = 1$. The time indicated at the end of each curve represents the total solidification time. T_2, G_2 and E_2 in dash line denote the projected points from the corresponding T, G and E on Curve 2. (In a similar way, we can locate T_1, G_1, E_1, T_3, G_3 and E_3. They are not shown in the figure for clarity.)

Fig. 3 illustrates a different situation in which the transport process follows the path *a-b-d* in Fig. 1. The fusion temperature is relatively low ($u_p = 0.5u_i$) in this case, hence the depth of penetration reaches the insulated surface before the solidification taking place at the front surface. Again the curves designated by 1, 2 and 3 represent different thermal properties ratios between the newly formed and the old phases. It is found in both Figs. 2 and 3 that the curve 3 drops most rapidly, then follows curve 1 and finally curve 2. This implies that the material with a high heat capacity ratio (solid to liquid for the case of solidification) cools more slowly than that of a lower heat capacity ratio. The case with a higher thermal conductivity ratio (solid to liquid) cools faster in the solidification.

As can be seen in both Figs. 2 and 3 that there is no temperature change at the back surface during the early stage, because the penetration depth is less than the thickness of the material. The insulated surface temperatures start to decrease at point T and finally reach the fusion temperature. This surface then remains at fusion temperature until the solidification process completes.

It should be pointed out that all curves in Figs. 2 and 3 terminate at the condition when the interface reaches $x = \ell$. The temperature at the insulated boundary continues to decrease after the interface has reached $x = \ell$. We did not continue the calculation and plotting, since beyond that point the problem is reduced to the heat transfer in one phase. The horizontal dash lines G_2-E_2, G_1-E_1 and G_3-E_3 (the projected points from the corresponding solid lines) represent the time intervals that the insulated surface maintains at the fusion temperature for various thermal conditions. The point G denotes the onset when the insulated surface is cooled to the fusion temperature but still maintains at liquid phase. During the cooling process the liquid

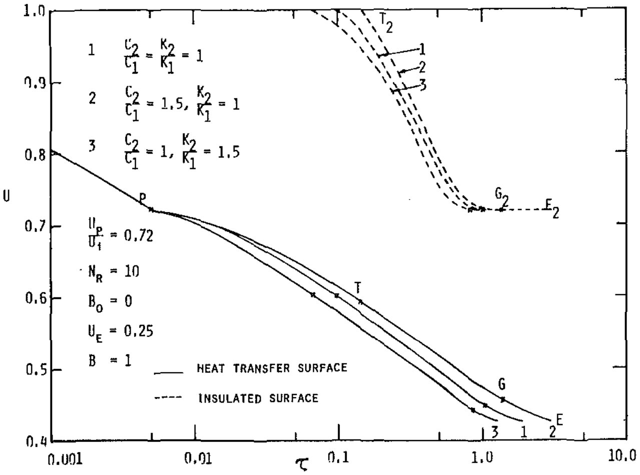

Fig. 2 Temperature history at radiative surface and insulated surface during solidification

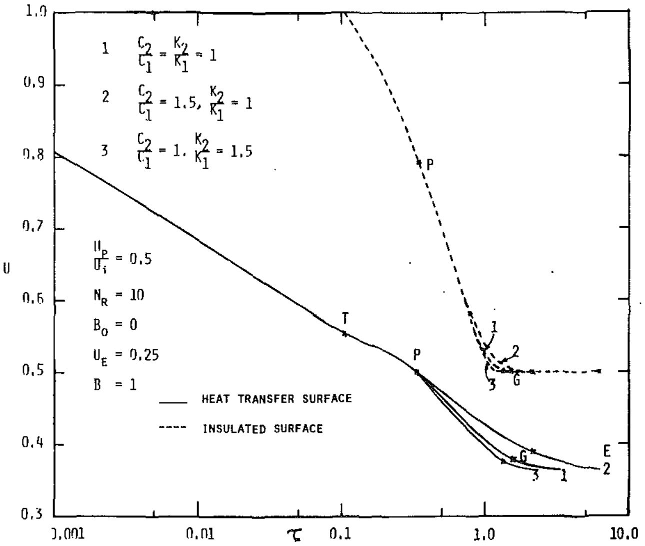

Fig. 3 Temperature history at radiative surface and insulated surface during solidification

phase temperature continues to decrease to the fusion temperature while the interface is moving toward the insulated surface. Unless the rate of fusion is extremely fast, the insulated surface will always stay at fusion temperature for certain amount of time.

Fig. 4 illustrates typical temperature profiles in both liquid and solid regions at some specific times. The same parameters given by the curve 1 of Figs. 2 and 3 are used. Solid lines represent the case with $u_p = 0.5u_i$ and dash lines with $u_p = 0.72u_i$. The four curves in each group represent the temperature profiles at the four different times which are chosen from the time periods *I-P*, *P-T*, *T-G* and *G-E* shown in Fig. 2 and *I-T*, *T-P*, *P-G* and *G-E* shown in Fig. 3. (*I* = initial state.)

The horizontal lines marked by *G-E* in Fig. 4 imply that part of the liquid still maintains at fusion temperature at certain time. The length of time that the liquid is at fusion temperature may be seen from the segment *G-E* in Figs. 2 and 3 and is quite long. Note that the time is plotted in log scale in these figures.

Fig. 5 shows the time variant fusion line, $s(\tau)$ for various heat capacity ratio and thermal conductivity ratio between the solid and the liquid regions. Solid lines represent the case with $u_p = 0.5u_i$ and dash lines imply $u_p = 0.72u_i$. The same parameters as those of Figs. 2 and 3 are employed. All curves start from the point *P* indicated in Figs. 2 and 3. At a given time, *s* increases when the ratio of k_2/k_1 increases or when c_2/c_1 decreases. The total solidification time increases as the ratio of k_2/k_1 decreases. Numerical computations show that the fusion front moves slower if u_p/u_i is smaller.

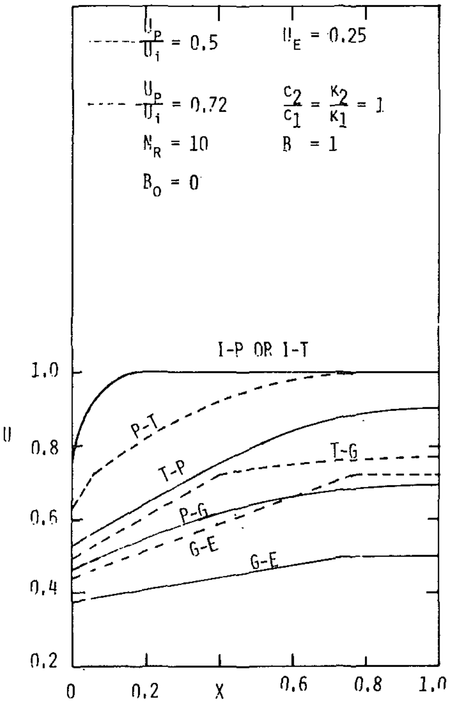

Fig. 4 Temperature distribution in liquid and solid regions during solidification

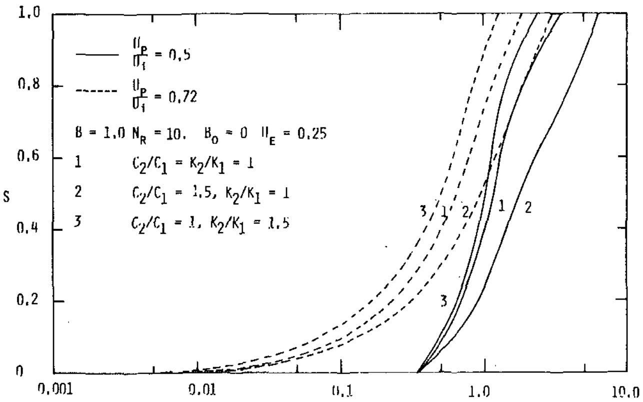

Fig. 5 Solidification front movement with time

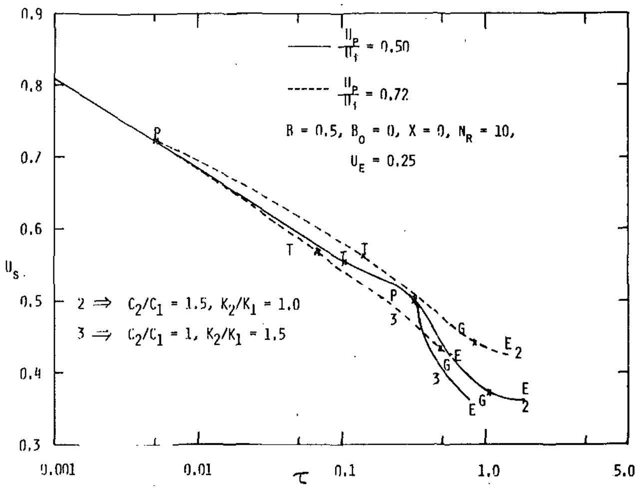

Fig. 6 Temperature history at radiative surface

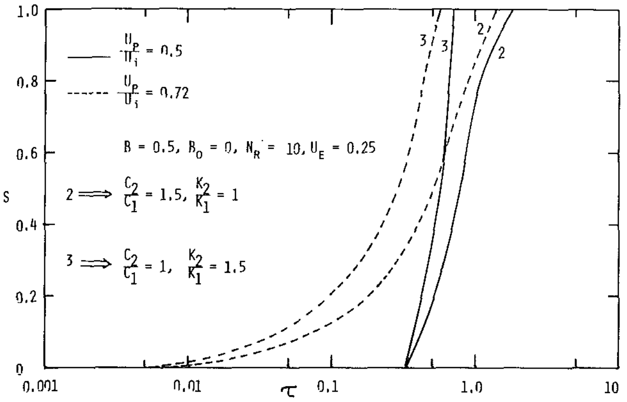

Fig. 7 Solidification front movement with time

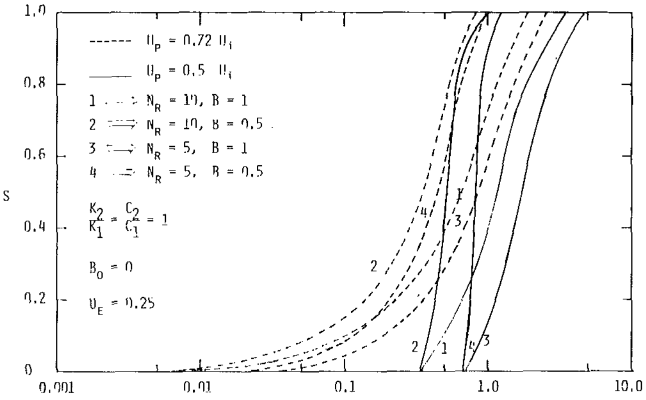

Fig. 8 Solidification front movement with time

Fig. 6 shows radiation surface temperature histories for the fusion parameter, B equal to 0.5 with two different values of u_p/u_i. It is seen that temperature histories under these two conditions are identical before the fusion starts. The solid lines follow the path shown by the sketch a-b-d in Fig. 1, and dash lines follow the path shown by a-c-d in Fig. 1. From Figs. 2, 3 and 6, it is found that the total solidification time decreases as B decreases. In the case of $c_2/c_1 = 1$, $k_2/k_1 = 1.5$ and $B = 0.5$ the freezing rate is so fast that the insulated surface only maintains at the fusion temperature for a very short period before the solidification process completes. This implies that point G coincides with point E in Fig. 6.

Fig. 7 illustrates the interfacial position versus dimensionless time during solidification. All curves for both $u_p/u_i = 0.72$ and 0.5 start at the point which corresponds to point p in Fig. 6. This is due to the fact that the surface temperature is higher than the fusion temperature before this point.

Fig. 8 depicts solidification front movement with time for various values of Nr, B and u_p/u_i. It is seen that s increases as Nr increases at a given value of B. Consequently, the time required to complete the solidification process decreases. The onset of the solidification process is independent of Stefan number, $1/B$. However, the total solidification time is greatly affected by Stefan number.

If the material under consideration is semi-infinite, the heat transfer process follows the path a-c shown in Fig. 1. For this case, only equation (10) in the first time domain, and equations (19–22) in the second time domain are employed. Note that both s and δ approach infinity when ℓ approaches infinity, and the total solidification time, τ_t, is meaningless physically.

Due to the general nature of the present problem, no previous solution is available for comparison. Although the work of Weinbaum, et al. [17] also dealt with phase change in a finite medium, it is difficult to compare the present numerical solutions with that of [17] because of different parameters, variables, and boundary conditions involved in the two papers. In fact, the perturbation solution fails to handle the case with $B = 0.5$ and $U_p/U_i = 0.5$, a numerical example presented in this work because the small parameter ϵ becomes unity under the above conditions. Note that $\epsilon = 1/B\ (1 - U_p/U_i)$ in term of our notations. However, the predicted trends of temperature profile and solidification rate are consistent with that given in [17]. Figs. 5, 7 and 8 have shown that the interface does not advance until certain length of time of cooling. This time lag depends on the initial temperature of the liquid, thermal properties of liquid and solid and the environment conditions. Comparisons of Figs. 5 and 7 reflect that the smaller the value of B the faster the interface travels. This agrees with other investigators' findings [15, 22] for the case of initial temperature equal to the fusion temperature.

It is of interest to examine the following limiting condition from the present solution. Consider the case that the initial temperature and the fusion temperature are identical and the properties of solid and liquid phases are same. The solution for solidification depth and surface temperature can be directly obtained from equations (21, 27) and (28) by letting $u_p = u_\ell = u_i =$ constant, $c_1 = c_2$ and $\alpha_1 = \alpha_2$. We then obtain an expression which is identical to equation (12) in [13].

References

1 Carslaw, H. S. and Jaeger, J. C., *Conduction of Heat in Solids,* 2nd Ed., Clarendon Press, Oxford, 1959.

2 Ruoff, A. L., "An Alternate Solution of Stefan's Problem," *Quarterly of Applied Math,* Vol. 16, 1958, p. 197.

3 Cho, S. H. and Sunderland, J. E., "Heat Conduction Problem With Melting and Freezing," ASME JOURNAL OF HEAT TRANSFER, Vol. 91, 1969, p. 421.

4 Mikhailov, M. D., "Exact Solution for Freezing of Humid Porous Half Space," *Int. Journal Heat Mass Transfer,* Vol. 19, 1976, p. 651.

5 Özisik, M. N. and Uzzell, J. C., "Exact Solution for Freezing in Cylindrical Symmetry With Extended Freezing Temperature Range," ASME JOURNAL OF HEAT TRANSFER, Vol. 101, 1979, p. 331.

6 Biot, M. A., "New Methods in Heat Flow Analysis With Application to Flight Structure," *Journal Aero. Sci.,* Vol. 24, No. 12, 1957, p. 857.

7 Biot, M. A., "Further Developments of New Methods in Heat Flow Analysis," *Journal Aerospace Sci.,* Vol. 26, No. 6, 1959, p. 367.

8 Biot, M. A. and Agrawal, "Variational Analysis of Ablation for Variable Properties," ASME JOURNAL OF HEAT TRANSFER, Vol. 86, 1964, p. 437.

9 Biot, M. A. and Doughaday, H., "Variational Analysis of Ablation," *Journal of Aerospace Sci.,* Vol. 29, 1962, p. 227.

10 Lardner, T. J., "Approximate Solutions to Phase-Change Problems," *AIAA,* Vol. 5, 1967, p. 2079.

11 Prasad, A., and Agrawal, H. C., "Biot's Variational Principle for Aerodynamic Ablation of Melting Solids," *AIAA,* Vol. 12, 1974, p. 250.

12 Prasad, A. and Agrawal, "Biot's Variational Principle for a Stefan Problem," *AIAA,* Vol. 10, 1972, p. 325.

13 Chung, B. T. F. and Yeh, L. T., "Solidification and Melting of Materials Subject to Convection and Radiation," *Journal of Spacecraft and Rockets,* Vol. 12, 1975, p. 329.

14 Yeh, L. T. and Chung, B. T. F., "Phase Change in a Radiating and Convecting Medium With Variable Thermal Properties," *Journal of Spacecraft and Rockets,* Vol. 14, 1977, p. 118.

15 Yan, M. M. and Huang, P. N. S., "Perturbation Solutions to Phase Change Problem Subject to Convection and Radiation," ASME JOURNAL OF HEAT TRANSFER, Vol. 101, 1979, p. 96.

16 Goodman, T. R. and Shea, J. J., "The Melting of Finite Slabs," *Journal of Applied Mechanics,* Vol. 82, 1960, p. 16.

17 Weinbaum, S. and Jiji, L. M., "Singular Perturbation Theory for Melting or Freezing in Finite Domains Initially Not at the Fusion Temperature," *Journal of Applied Mechanics,* Vol. 44, 1977, p. 25.

18 Costello, F. A., "An Evaluation of Several Methods of Approximating Solution to the Heat Conduction Equation," ASME Paper No. 63-HT-44, 1963.

19 Chung, B. T. F. and Yeh, L. T., "Analysis of Heat Transfer in Slabs with Variable Properties Subjected to Radiation and Convection," ASME Paper No. 75-WA/HT-67, 1975.

20 Hrycak, P., "Problems of Solidification with Newton's Cooling at the Surface," *A.I.Ch.E.J.,* Vol. 8, 1963, p. 585.

21 Yeh, L. T., Ph.D. Dissertation, Department of Mechanical Engineering, The University of Akron, Akron, OH, 1976.

22 Goodling, J. S. and Khader, M. S., "Inward Solidification with a Radiative Boundary," *Proceedings 10th Southeastern Seminar on Thermal Sciences,* 1974, p. 286.

K.-S. Hsu
Bechtel, Inc.
Houston, TX

F. A. Locher
Bechtel, Inc.
San Francisco, CA

J. F. Kennedy
Iowa Institute of Hydraulic Research
The University of Iowa
Iowa City, IA

Forced-Convection Heat Transfer from Irregular Melting Wavy Boundaries

The problem of turbulent flow past freezing or melting ice is formulated for the case of random boundary waves, with particular attention to the distribution of heat-transfer rate along wavy surfaces. Relations are obtained for the celerity and unsteady spectrum of the boundary waves. The results of 21 laboratory experiments are reported and used to establish the values of certain quantities appearing in the heat-transfer relation adopted. The velocity Reynolds number of the phase shift between the boundary waves and heat-transfer variation is found to have a nearly constant value of 4×10^4.

Introduction

In an earlier study [1] the instability that is responsible for the formation of ice ripples on the underside of river ice was examined mathematically and experimentally. The analytical model treated the interfacial waves as monochromatic, and demonstrated that the stability of the interface between a turbulent liquid flow and a boundary composed of the frozen liquid is critically dependent on the distribution of the local heat-transfer rate along the wavy boundary. However, in the experiments the waves were found to be quite irregular, and the interfacial profiles to be heavily influenced by effects that arose at the joints in the refrigeration plates from which the flume walls and floor were fabricated. Consequently, the earlier investigation failed to establish conclusively the relationship among the flow characteristics, the interface topography, and the streamwise distribution of heat transfer rate between the flow and the boundary. Herein the problem is formulated for a random wavy interface, and additional experiments conducted utilizing improved procedures are reported. Analysis of the experimental results within the analytical framework leads to verification of the heat transfer relation utilized in the analysis and evaluation of the parameters it includes.

Analysis

The flow to be analyzed is shown in Fig. 1, which depicts an ice cover on a flowing stream. The heat-balance relation at the interface is

$$q_w(x,t) - q_i(x,t) = \rho_i \lambda \eta_t \tag{1}$$

where, in addition to the quantities identified in Fig. 1, ρ_i and λ are the density and heat of fusion of the ice; t is time; and $q_{i,w}$ are, respectively, the rates of heat transfer by conduction from within the ice to the interface, and from the ice to the flow. The subscripts, x, y, and t signify partial differentiation with respect to the corresponding variable. Note that for the sign convection of Fig. 1, $q_{i,w} \leq 0$, because $T_c \leq T_m \leq T_w$, where T_m is the melt temperature. The ice thickness at any time is expressed as the sum of two components

$$\eta(x,t) = \bar{\eta}(t) + \eta'(x,t) \tag{2}$$

where

$$\eta'(x,t) = \int_{-\infty}^{\infty} A(k,t)\exp[ik(x-ct)]dk \tag{3}$$

in which $k = 2\pi/L$ is the wave number; $A(k,t)$ and $c(k)$ are the amplitude and celerity of the component with spatial frequency I/L; and an overbar and a prime denote spatially averaged quantities and local deviations therefrom.

The temperature distribution within the ice is assumed to be described by

$$T_{xx} + T_{yy} = 0 \tag{4}$$

which requires, in addition to the usual restrictions of homogeneity and isotropy, that the boundary temperatures be constant and η_t sufficiently small for T to be quasi-steady. In some experiments, calibrated thermistors were frozen into the ice. Temperature measurements made with these showed that the temperature distribution in the ice was indeed quasi-steady, and in fact nearly linearly distributed across the ice. For the values of T_c used in the experiments, the sensible heat taken up by the ice as its temperature distribution changed during the melting phase was very small compared to the heat of fusion. A first-order perturbation solution of (4) subject to the boundary conditions illustrated in Fig. 1 is

$$T = T_c + (T_m - T_c)\left\{\frac{y}{\bar{\eta}} - \int_{-\infty}^{\infty} \frac{A}{\bar{\eta}}\frac{\sinh ky}{\sinh k\bar{\eta}}\exp[ik(x-ct)dk]\right\} \tag{5}$$

provided $k\eta' \ll \tanh k\bar{\eta}$. Substitution of (5) into the linearized heat conduction relation for the ice at the interface

$$q_i = -K_i T_y(x, \bar{\eta}, t) \tag{6}$$

which requires that the interfacial slope be very small, yields

$$\bar{q}_i = -\frac{K_i(T_m - T_c)}{\bar{\eta}} \tag{7}$$

and

$$q_i' = -\bar{q}_i \int_{-\infty}^{\infty} \frac{kA(k,t)}{\tanh k\bar{\eta}}\exp[ik(x-ct)]dk \tag{8}$$

where K_i is the thermal conductivity of the ice.

It is well established that the mean heat-transfer rate between a turbulent flow and a boundary may be expressed as

$$\bar{N} = C_0 P^m R^n \tag{9}$$

where

$$\bar{N} = \frac{\bar{q}_w d}{(T_m - T_w)K_f}$$

$$R = \frac{Ud}{\nu}$$

and

$$\mathrm{P} = \frac{C_p \mu}{K_f}$$

are, respectively, the Nusselt, Reynolds, and Prandtl numbers; C_0 is a constant; and K_f, C_p, ν, and μ are the conductivity, specific heat, and kinematic and dynamic viscosities of the liquid, respectively; and d is a characteristic dimension of the flow. Equation (9) will be generalized to express the local heat transfer rate in terms of the local potential-flow velocity at the mean interface

---

Contributed by the Heat Transfer Division for Publication in the JOURNAL OF HEAT TRANSFER. Manuscript received by the Heat Transfer Division January 25, 1979.

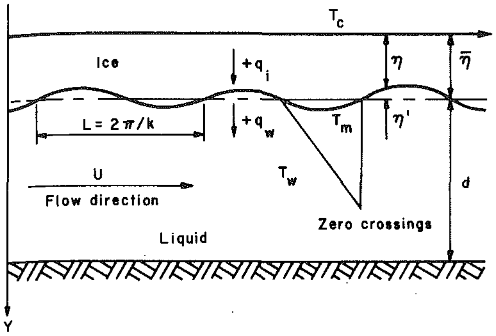

Fig. 1 Definition sketch for flow beneath river ice. Note that in experiments, the ice was beneath the flow

$$\frac{q_w(x,t)d}{(T_m - T_w)K_f} = N(x,t) = C_0 P^m \left(\frac{d}{\nu}\right)^n [U + B\phi_x(x - \Delta, \bar{\eta}, t)]^n \quad (10)$$

where

$$\phi = -iU \int_{-\infty}^{\infty} \frac{A \cosh k(y - d - \bar{\eta})}{\sinh kd} \exp ik(x - ct)dk \quad (11)$$

is the linearized velocity potential for the flow between the ice cover and horizontal bed, as depicted in Fig. 1. The quantity Δ is the lag distance between the streamwise distributions of local heat-transfer rate and local potential-flow velocity at the mean level of the interface, and B is a factor to allow for a local velocity perturbation due to a boundary wave and an equal change in the mean velocity not necessarily producing the same variation in the heat-transfer rate.

Justification of extension of (9), a relation for the rate of heat transfer between a steady uniform flow and its boundary, to predict the spatial distribution of the local heat flux between a nonuniform flow and a wavy boundary is in order here. Turbulent flows past smooth boundaries are homologous, or self-similar, when expressed in suitable nondimensional form, as in the well known power-law and logarithmic relations. For example, the former of these may be written

$$\frac{n'}{n'+1} \frac{u(y)}{U} = (2y/d)^{1/n'} \quad (12)$$

where $u(y)$ is the velocity at a distance y from the boundary, d is the height of a rectangular conduit (see Fig. 1) or the diameter of a circular pipe, and the reciprocal exponent, n', is only slightly sensitive to R (n' varies only from about 6 to 10 as R is varied from 10^3 to 10^6). Because of the similar form of the velocity profiles given by, for example, (12), U could be replaced in (9) by the velocity at any fixed fraction of d from the wall; this would affect only the value of C_0. In the case of heat transfer between a wavy boundary and a turbulent flow, it seems reasonable to relate the local heat flux to a near-wall velocity, for it is these velocity variations that will most heavily influence the transfer process. Because the boundary-wave-induced velocity variations are the result of a balance between inertial and pressure forces, they can be estimated from a potential-flow formulation, as has been shown by Hsu and Kennedy [2]. The velocity perturbations so calculated for the mean position of the wavy wall then are incorporated into (9) to obtain an expression for the local boundary heat-flux, (10). It is advantageous to utilize U instead of a near-wall velocity in (9), because U is the velocity which can be readily determined. Moreover, in the boundary-stability analysis retaining U affects only the value of C_0, which will be seen to be incorporated into the mean (streamwise-averaged) heat flux which arises in the relations describing the interface stability and ice-ripple characteristics.

Expansion of (10) in a Taylor series, dropping of higher order terms, and substitution of (11) yields

$$N(x,t) = \bar{N}\left\{1 + nB \int_{-\infty}^{\infty} \frac{kA}{\tanh kd} \exp[ik(x - ct - \Delta)]dk\right\} \quad (13)$$

Here it should be pointed out that $\bar{N}$ calculated by integration of $N(x, t)$ is independent of A; this is a consequence of the linearizations used in deriving (13).

Substitution of (2, 3, 8), and q_w given by (13) into (1) yields

$$A(k,t) = A(k,0) \exp\left\{\frac{kt}{\rho_i} \lambda \left[\frac{n\bar{q}_w}{\tanh kd} B \cos\theta + \frac{\bar{q}_i}{\tanh k\bar{\eta}}\right]\right\} \quad (14)$$

$$c = \frac{n\bar{q}_w}{\rho_i \lambda \tanh kd} B \sin\theta \quad (15)$$

in which $\Delta = \theta/k$.

The spectrum, Φ, of the interfacial profile given by (3) and (14) can be calculated following the procedure described by Kinsman [3], with the result

$$\Phi(k,t) = \Phi(k,0) \exp\left[\frac{2kt}{\rho_i \lambda}\left(\frac{n\bar{q}_w}{\tanh kd} B \cos\theta + \frac{\bar{q}_i}{\tanh k\bar{\eta}}\right]\right. \quad (16)$$

It is seen from (16) that a wave component with circular frequency k will be unstable, neutrally stable, or stable according as the argument of the exponential term is positive, zero, or negative.

The angular phase shift, θ, will be expressed, following Ashton and Kennedy [1], as the sum of the two components,

$$\theta = \alpha + k\delta \quad (17)$$

where α is a fixed fraction of the wavelength and δ is a fixed distance. The wave number for which the amplification rate is greatest is given by

$$\Phi_{kt}(k, 0) = 0 \quad (18)$$

Nomenclature

A = amplitude of spectral component
B = amplification factor of local heat transfer rate
c = celerity of ice ripples
C_0 = coefficient in heat-transfer relation
C_p = specific heat of liquid
d = characteristic length in Reynolds and Nusselt numbers
h = depth of free-surface flow
$k = 2\pi/L$ = wave number
K_f = thermal conductivity of liquid
K_i = thermal conductivity of ice
L = wavelength of ice ripples
L_0 = L determined from zero-crossings count
L_s = L determined from spectra of ice ripples
m, n = exponents in heat transfer relation
n' = reciprocal of exponent in power-law velocity distribution
N = Nusselt number
P = Prandtl number
q_i = rate of conductive heat transfer in ice
q_w = rate of heat transfer between ice and the flow
R = Reynolds number
t = time
T = Temperature
T_c = temperature of upper surface of ice cover
T_m = temperature of melt
T_w = temperature of flowing water
$u(y)$ = velocity at distance y from boundary
u_* = shear velocity
U = mean-flow velocity
x, y = spatial coordinates
$(\bar{\ })$ = spatial average of ( )
α = component of heat-transfer angular phase shift
δ = component of spatial heat-transfer phase shift
Δ = spatial phase shift of local heat-transfer rate
η = ice thickness
$\bar{\eta}$ = spatially averaged η
η' = deviation of η from $\bar{\eta}$
$\theta = k\Delta = \alpha + k\delta$, the angular phase shift of local heat transfer rate
λ = heat of fusion
μ = dynamic viscosity
ν = kinematic viscosity
ρ_i = mass density of ice
ϕ = velocity potential
Φ = spectrum

Table 1 Summary of experimental conditions and computed results

Experimental Conditions									Ice-Profile Data			Heat-Flux Data		Parameters Appearing in Heat Transfer Relation						
Run No.	T_w (°C)	T_c (°C)	U (cps)	h (cm)	$R_h \times 10^{-4}$	u_* (cps)	Melting stage duration (hrs)	Number of profiles analyzed	L_o (cm)	L_s (cm)	$c \times 10^5$ (cps)	$\bar{q}_w \times 10^2$ $\frac{\text{cal}}{\text{sec cm}^2\,{}^\circ\text{C}}$	$\bar{N} \times 10^{-2}$	B cos θ	B	θ (rad)	Δ_o (cm)	δ (cm)	α (rad)	$R_{\Delta_o} \times 10^{-4}$
*H17	0.93	-1.1	9.1	7.6	0.40	0.555	18	19	106.4	99.7	56.7	-1.45	0.50	-3.36	4.16	3.77	73.2	5.9	3.47	3.83
H 4	1.00	-3.0	9.1	15.2	0.80	0.521	20	21	***	95.7	19.8	-1.42	0.91	-4.20	4.86	3.67	56.1	11.4	2.79	2.93
H 5	2.00	-1.0	9.1	15.2	0.80	0.519	9	10	***	93.9	***	-2.90	0.93	-4.55	5.17	3.64	54.3	12.5	2.67	2.94
H12	1.41	-1.2	12.2	15.2	1.07	0.672	9	10	89.9	81.4	46.6	2.61	1.19	-3.80	4.52	3.71	53.0	3.7	3.43	3.28
H11	0.87	-1.1	15.2	15.2	1.34	0.816	13	14	77.1	81.4	32.3	-1.90	1.39	-3.20	4.03	3.80	46.6	6.2	3.31	4.07
H16	0.40	-1.1	30.5	7.6	1.34	1.603	12	13	35.4	48.8	34.1	-1.76	1.41	-2.27	3.34	3.97	22.3	.61	3.89	1.84
H18	0.41	-1.0	30.5	21.3	3.74	1.465	16	17	29.3	34.7	33.5	-1.43	3.16	-2.59	3.57	3.90	18.0	2.1	3.51	3.10
H 7	0.43	-8.5	36.6	15.2	3.21	1.764	16	17	31.7	30.5	31.7	-2.05	3.05	-2.45	3.46	3.93	19.8	1.8	3.55	4.09
H 8	0.15	-1.6	36.6	15.2	3.21	1.766	38	20	30.8	30.5	12.8	-.623	2.66	-2.32	3.37	3.95	19.2	2.3	3.48	3.95
H 2#	0.29	-7.5	75.3	15.5	6.74	3.313	12	13	14.6	14.3	33.8	-2.37	5.40	-2.16	3.26	3.99	9.1	1.6	3.28	3.85
H 3#	0.29	-2.8	75.3	15.5	6.74	3.313	8	9	14.3	14.3	45.7	-2.67	5.94	-2.26	3.32	3.97	9.1	1.4	3.34	3.85
H13#	0.27	-1.0	83.2	15.2	7.22	3.621	7	8	13.1	13.4	***	-2.26	5.30	-1.84	3.06	4.07	8.5	***	***	3.97
**A16	1.03	-6.4	14.6	15.2	1.28	0.788	13	13	65.5	81.4	45.7	-2.23	1.38	-2.92	3.81	3.84	43.9	3.2	3.60	3.68
A18	1.00	-6.8	18.9	15.5	1.69	0.986	11.5	13	50.9	81.4	57.9	-2.77	1.81	-3.04	3.91	3.82	34.7	3.8	3.52	3.77
A14	0.25	-7.1	24.4	15.2	2.14	1.238	189	18	43.9	48.8	15.8	-.852	2.18	-2.36	3.40	3.95	28.3	4.0	3.44	3.88
A10	0.65	-2.1	36.6	15.2	3.21	1.763	7	7	33.5	40.5	51.8	-3.15	3.14	-2.51	3.51	3.91	21.9	.91	3.77	4.55
A11	0.43	-8.6	36.6	15.2	3.21	1.764	12	12	34.7	40.5	33.5	-2.11	3.13	-2.59	3.56	3.90	21.6	.61	3.81	4.47
A12	0.24	-7.8	36.6	15.2	3.21	1.765	33	14	33.8	40.5	17.7	-1.15	3.07	-2.60	3.57	3.90	21.6	3.7	3.33	4.44
A13	0.25	-7.8	45.4	15.5	4.07	2.128	89	14	28.7	27.1	22.3	-1.46	3.81	-2.38	3.42	3.94	18.3	1.7	3.55	4.67
A17	0.40	-6.5	50.9	15.5	4.56	2.351	11	13	25.9	30.5	36.6	-2.56	4.18	-2.74	3.68	3.87	15.8	1.0	3.66	4.54
A15	0.30	-7.2	75.3	15.5	6.74	3.313	11	15	21.6	18.9	26.5	-2.49	5.41	-2.52	3.51	3.91	13.4	.43	3.77	5.67

*H indicates experiments conducted by authors.

** A indicates experiments conducted by Ashton and Kennedy [1].

***Not possible to define from bed profile data.

\# Runs with strongly three-dimensional interface relief.

which yields, after substitution of (16) and (17),

$$\left[\frac{\cos\theta - k\delta\sin\theta}{\tanh kd} - \frac{kd\cos\theta}{\sinh^2 kd}\right] + \frac{\bar{q}_i}{n\bar{q}_w B}\left[\frac{1}{\tanh k\bar{\eta}} - \frac{k\bar{\eta}}{\sinh^2 k\bar{\eta}}\right] = 0 \qquad (19)$$

If kd is sufficiently large that $\tanh kd \simeq 1$ and $\sinh^2 kd \gg kd$, and $k\bar{\eta}$ is small enough that $\tanh k\bar{\eta}$ and $\sinh k\bar{\eta}$ may be replaced by their arguments, (19) reduces to

$$\tan(\alpha + k\delta) = 1/k\delta \qquad (20)$$

a result of Ashton and Kennedy [1] obtained from their analysis of monochromatic waves.

Experiments

The experiments were conducted in the refrigerated flume of the Low Temperature Flow Facility at the Iowa Institute of Hydraulic Research. This tilting, recirculating flume is 12.20 m (40 ft) long, 0.61 m (2 ft) wide, and 0.30 m (1.0 ft) deep; has temperature-controlled walls and bed; and is located in a temperature-regulated room. For each experiment a 9 cm (3.5 in.) thick ice sheet was frozen on the flume bed, mechanically planed, and brought to its steady-state temperature for the conditions of the run before liquid water, which had been prechilled to the value of T_w selected for the experiment, was introduced into the flume in the quantity required to give the desired flow depth. Note that the experiments were conducted using free-surface flows over an ice bed, instead of as depicted in Fig. 1, to facilitate measurement of interfacial profiles. Comparison [1] of data on ripples formed beneath flowing water and those generated beneath a floating ice cover have revealed no discernible differences between the two types. This is a consequence of the Richardson number being so small that density-stratification effects, due to temperature variations in the flow near the ice, are negligible. The pump then was started, the pump speed adjusted to give the required discharge, and the water heater adjusted to maintain the selected T_w. Interfacial profiles were measured at intervals of 1 to 2 hrs, depending on the melting rate, by means of a linear potentiometer and appurtenant electronic circuitry which transduced displacements to voltages. The potentiometer was mounted on a motorized carriage which moved along the flume at constant velocity. The voltage output was sampled at a spatial frequency of 420 per meter (128 per foot) by an on-line IBM computer which placed the digitized profile data on cards for subsequent calculation of the spectra and other quantities of interest. Profiles were measured along a 762 cm (25.0 ft) reach commencing 244 cm (8.0 ft) downstream from the flume inlet. The vertical accuracy of the bed-measurement system was ±0.015 cm (0.0005 ft). Water was drained from the flume periodically as required to maintain the desired flow depth. Each experiment was continued until the spectrum of η' had become steady or until the floor of the flume became exposed at some locations. During each experiment T_c and T_w were maintained within ±0.3°C (0.5°F) and ± 0.01°C (0.02°F), respectively, of the desired values. Further details of the experimental procedure are given by Hsu [4]. The air temperature in the room was maintained at very nearly 0°C (32°F) during the melting stage of each experiment.

Twelve experiments were conducted during this investigation. In addition, the digitized profiles from nine of Ashton and Kennedy's [1] experiments were available on computer cards and were included in the data analysis. The principal results of these experiments are summarized in Table 1. The flow depth in the free-surface experiments is denoted by h and used as the characteristic dimension in computing the Reynolds and Nusselt numbers.

Results

The primary objectives of the study were to verify the relation for the spectral evolution of the interfacial waves, (16); to evaluate the quantities n, B, α, and δ appearing in the local heat-transfer relation, (10) and (17); and by inference to validate the heat-transfer relation itself. Evaluation of the four parameters proceeded as follows: The mean heat-transfer rate, $\bar{q}_w$, for each period between profile measurements was computed from (1) averaged along the bed,

$$\bar{q}_w - \bar{q}_i = \rho_i \lambda \bar{\eta}_t \qquad (21)$$

with $\bar{q}_i$ given by (7) for average conditions between profile measurements and $\bar{\eta}_t$ computed from successive measured mean-bed elevations. A plot of these results for profiles with variances σ^2 (the variance of η' about $\bar{\eta}$) less than 0.065 cm^2 (0.01 in.^{2}) in the format of (9), with the Reynolds number based on the depth, h, yielded the result shown in Fig. 2, from which one obtains $n = 0.85$, and $C_0 = 0.019$ for $P_r = 13.44$ (the value for water at 0°C) and m = 1/3; this value of C_0 is close to the experimentally determined one of 0.020 given by Bird, et al. [5] if the pipe diameter is replaced by the pipe hydraulic radius in their relation. However, the value of n obtained from the slope of the line in Fig. 2 is slightly greater than the generally accepted exponent, 0.80. For σ^2 less than about 0.065 cm^2 (0.01 in.^{2}), $\bar{q}_w$ was found to be constant in each experiment, as (13) indicates, but for larger σ^2 was found to increase with further development of the bed waves; this was judged to be due to nonlinear effects not included in the derivation, or to separation in the case of bed waves approaching their equilibrium configuration.

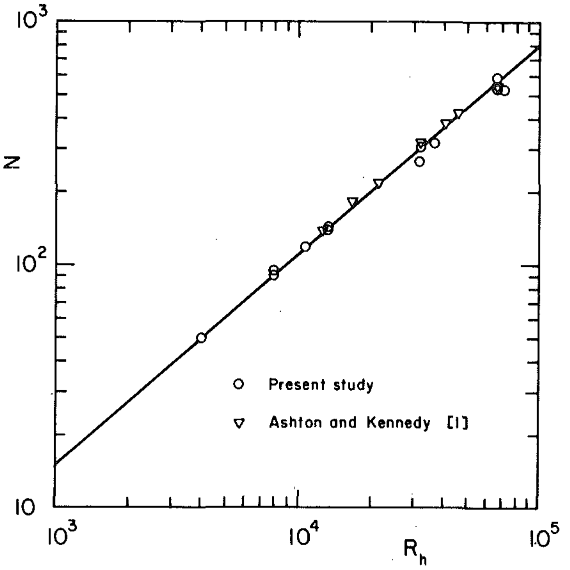

Fig. 2 Mean bed heat-transfer rate (Nusselt number) as a function of Reynolds number for flume experiments with free-surface flow

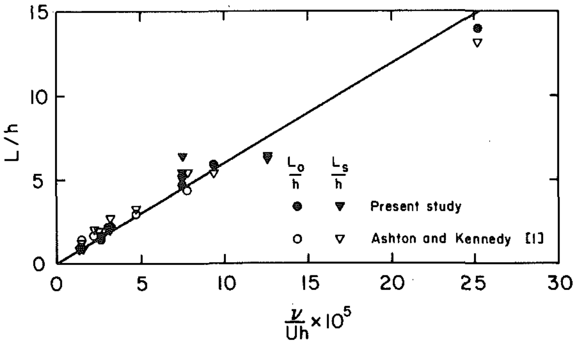

Fig. 3 Normalized ice-ripple wavelength as a function of $1/R_h$

The characteristic or dominant wavelength of each profile was determined in two ways: from a zero-crossings (see Fig. 1) count along each bed-profile record, which yielded L_0 and k_0; and from the peak of the spectrum estimate computed for each profile, which gave L_s and k_s. These are summarized in Table 1, where it is seen that the two values are nearly equal in most cases. A nondimensional plot of L_0/d and L_s/d versus $1/R_h$ is given in Fig. 3, which indicates the relation between U and L is

$$\frac{UL}{\nu} = 5.9 \times 10^4 \tag{22a}$$

while the arithmetic average of Reynolds numbers based on L_0 and L_s gave

$$\frac{UL}{\nu} = 6.7 \times 10^4 \tag{22b}$$

The normalized standard deviations of the L_0 and L_s Reynolds numbers are 0.14 and 0 .18, respectively. Thorsness and Hanratty's [6] mathematical model of melting and dissolution boundary waves has shown that waves with shear-velocity Reynolds number, $u_* L/\nu$, greater than about 2100 are unstable, and that the fastest growing waves occur at a shear-velocity Reynolds number of about 3500. In the present experiments a mean value of

$$\frac{u_* L_0}{\nu} = 3180 \tag{23}$$

was found, with a normalized standard deviation of 0.12. The celerities of individual prominent interfacial waves were determined from successive profiles and plotted in the format of (15) with $k = k_0$; the result is shown in Fig. 4. Note that results from two of Ashton and Kennedy's [1] experiments (their Nos. A7 and A9) not included in Table 1 are plotted in Fig. 4, to provide data at larger c. From Fig. 4 and (15) there results

$$B \sin \theta = -2.45 \tag{24}$$

in which the minus sign has arisen because $\overline{q}_w < 0$. Use of k_s instead of k_0 has practically no effect on the estimate of $B \sin \theta$, because in both cases the term tanh kd in (15) is nearly unity.

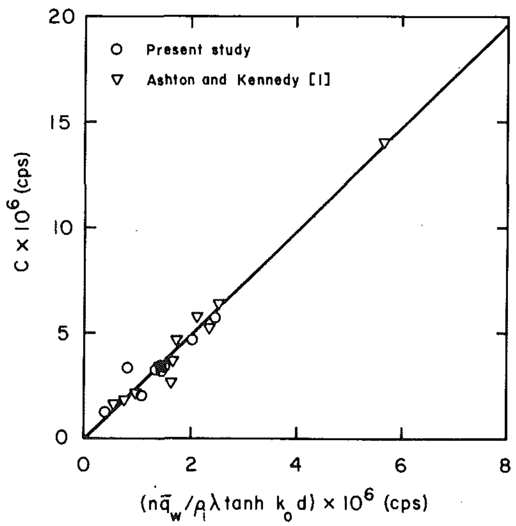

Fig. 4 Ice-ripple celerity plotted in format of (15) to determine B sin θ

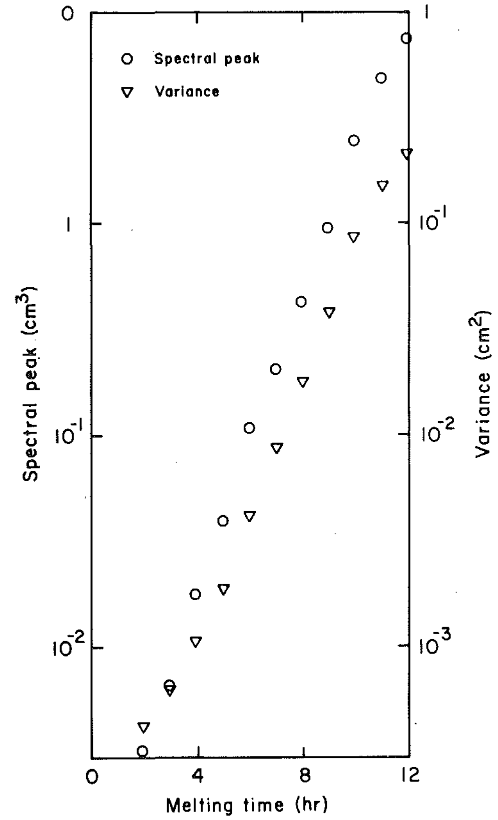

Fig. 5 Temporal development of spectral peak and of ice-ripple variance; Run K-2

The quantity B cos θ was determined for each experiment by plotting the peaks of the spectral estimates as a function of time; a typical result is shown in Fig. 5, which also includes the variance of η'. Both are seen to increase exponentially with time, and at nearly equal normalized rates for the duration of this experiment. It was found that the exponential growth rate remained nearly constant until the ripples reached equilibrium, whereupon it dropped abruptly to zero. From (16), the slopes of straight lines fitted to the measured

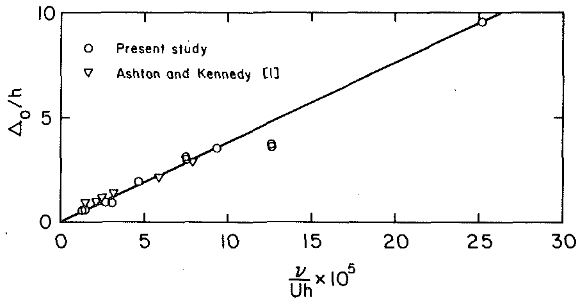

Fig. 6 Normalized heat-transfer phase shift as a function of $1/R_h$

points in plots like Fig. 5, and the measured or computed values of the other quantities appearing in (16), the values of $B\cos\theta$ given in Table 1 were determined. These and (24) gave the values of B and θ.

The quantities $\Delta_0 = \theta/k_0$ and $R_{\Delta_0} = U\Delta_0/\nu$ also are included in Table 1. Dimensional analysis indicates that Δ_0 is a function of h, ν, and u_* (the shear velocity; U may be used in place of u_* if the friction factor is constant). It was found that Δ_0/h is a linear function of the reciprocal of R_h, as shown in Fig. 6. The dimensional analysis just outlined indicates that R_{Δ_0} should be a constant, and the data presented in Table 1 show that its range of variation is not great. Its average value from Table 1 is

$$\frac{U\Delta_0}{\nu} = 4.0 \times 10^4 \qquad (25)$$

with a normalized standard deviation of 0.15. In Table 1, B is seen to decrease with increasing U and to level off at about $B = 3.4$ for velocities larger than roughly 30 cm/s (1.0 ft/s).

The total phase shift, θ, is expressed in (17) as the sum of two components: α and $k\delta$. These were determined as follows: A value of δ was selected and the corresponding α was calculated from (17) and the experimentally determined θ. The spectra at different times were calculated from (16) using these values of α and δ, the value of B for the run, and as an initial spectrum one measured at a time such that the ripples had developed to the point that an accurate estimate of the spectrum could be made (i.e., such that bed-elevation fluctuations were within the resolution of the measuring system). The spectrum of the last measured profile with $\sigma^2 < 0.065$ cm^2 (0.01 in.^{2}) then was compared with that calculated from (16) for the measured $\Phi(0, k)$ and the selected α and δ. These two quantities, α and δ, then were adjusted until the sum of the squared differences between measured and computed spectra was minimized. The resulting values of α and δ are given in Table 1. The Reynolds number based on δ was found to have a value of

$$R_\delta = \frac{U\delta}{\nu} \cong 0.41 \times 10^4 \qquad (26)$$

although it exhibited considerable variation (normalized standard deviation = 0.48).

A maximum-growth-rate hypothesis was used to obtain a relation, (19), between $k\delta$ and θ. For the ranges of variables covered in the present experiments, (19) and (20) are nearly identical. Fig. 7 presents comparison of (20) and experimentally determined values of θ and $k\delta$ and demonstrates generally satisfactory agreement.

Finally, it should be mentioned that the calculated spectra using the best-fit values of α and δ were in very good conformity with the measured ones except over the low and high frequency tails. Detailed comparisons are given by Hsu [4].

Concluding Remarks

Spatial phase shifts between streamwise distributions of flow properties and of local boundary displacement are known to be responsible for the instabilities that lead to the formation of various types of waves. For example, the phase shifts between small water waves and the distributions of pressure and shear stress on the waves are responsible for the extraction of energy from wind by the waves and the consequent growth of the waves. The phase shift between local sediment-transport rate and small bed disturbances causes the formation and growth of sediment ripples and dunes. The methodology developed herein provides a means for determining the phase shifts between the streamwise distributions of turbulent transfer between wavy boundaries and the flows past them. It has also been demonstrated that turbulent transfer relations for whole flow sections can be applied locally by making suitable assumptions concerning the effect of boundary undulations on the magnitude and streamwise distribution of the turbulent transfer variations they produce.

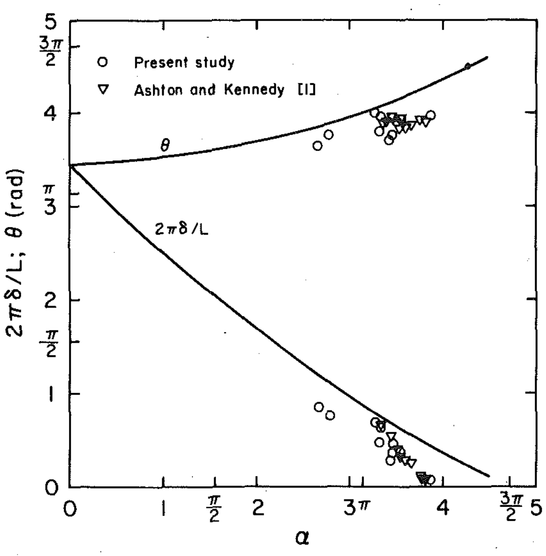

Fig. 7 Verification of (18), the relation between the phase-shift components for the fastest growing wave

For application, it is recommended that $\bar{q}_w$ be obtained from Fig. 2 or an equivalent heat transfer relation. The dominant wavelength is taken from Fig. 3 or computed by means of (22). The phase shift Δ_0 is obtained from (25), and the corresponding $\theta_0 = k\Delta_0$ substituted into (24) to obtain B. The wave velocity then can be obtained from (15). The validity of these quantities for related problems (e.g., wavelike dissolution patterns resulting from mass transfer [6]; ice ripples formed by gas flows; etc.) remains to be verified.

Acknowledgments

This study was sponsored by the National Science Foundation under Grants GK-17698 and ENG77-12176.

References

1 Ashton, G. D., and Kennedy, J. F., "Ripples on Undersides of River Ice Covers," *J. Hyd. Div., Proc. ASCE*, Vol. 98, No. HY9, Sept. 1972, pp. 1603–24.

2 Hsu, S.-T., and Kennedy, J. F., "Turbulent Flow in Wavy Pipes," *Journal Fluid Mechanics*, Vol. 47, Part 3, 1971, pp. 481–502.

3 Kinsman, Blair, *Wind Waves*, Prentice-Hall, Englewood Cliffs, NJ, 1965.

4 Hsu, K.-S., "Spectral Evolution of Ice Ripples," Ph.D. Thesis, Dept. of Mechanics and Hydraulics, The Univ. of Iowa, Iowa City, Dec. 1973.

5 Bird, R. B., Stewart, W. E., and Lightfoot, E. N., *Transport Phenomena*, Wiley, New York, 1960.

6 Thorsness, C. B., and Hanratty, Thos. J., "Wavelike Dissolution Patterns," Manuscript transmitted in private communication, Jan. 1978.

H. Tanaka

Associate Professor,
Department of Mechanical Engineering,
The University of Tokyo,
Bunkyo-ku, Tokyo, Japan

Further Developments of Dropwise Condensation Theory

The high rates of heat transfer of dropwise condensation as well as its limits are explained on the basis of the behaviors of submicroscopic active drops. The expression for the substantial growth rate of a single drop valid down to the thermodynamic critical size is incorporated into a set of basic equations from [8] whose capability to describe the process of coalescence and growth of drops in dropwise condensation has been demonstrated in [9]. Consideration of the nondimensionalized forms of the basic equations with the aid of numerical analysis results in an expression of the Nusselt number for dropwise condensation in terms of a few characteristic parameters. Comparison of the predicted Nusselt numbers with available experimental data suggests that the condensation coefficient of water is around 0.2 provided the nucleation site density is infinitely high. Otherwise, if the condensation coefficient should be unity, we have to accept that the nucleation sites are fairly scattered.

Introduction

Mechanism of dropwise condensation has attracted considerable interest, since the heat-transfer coefficient for dropwise condensation is much higher than that for filmwise condensation. It has been established that under dropwise condensation vapor condenses at discrete nucleation sites on a bare surface and that films greater than a monolayer in thickness do not form on the area between the drops [1, 2]. A very wide range of drop sizes exists on the condensing surface, extending from the primary drops to the largest departing drops. A thorough understanding of the mechanism of dropwise condensation requires the knowledge of the distribution of drops by sizes and that of the heat transfer through a single drop of a given size. Considerable progress has been made on the latter problem [1, 3]. Effects of liquid conduction, curvature of the interface and interfacial mass-transfer resistance can be accounted for. In attempting to calculate the average heat-transfer rate, different workers have dealt with the problem of the drop-size distribution in a variety of ways. A rational overall model of dropwise condensation was first put forward by LeFevre and Rose [3]. They intuitively assumed a form for the time-averaged distribution function which had the correct behavior for the limiting cases of very large and very small drops. Later Rose and Glicksman [4] proposed a universal form of the time-averaged distribution function for large drops which grow primarily by coalescence with smaller drops, by introducing a simplified model of the sequence of events occurring during the time interval between successive sweepings by departing drops, on the basis of high magnification cine film observations. Difficulty in the problem of drop-size distribution arises from how to deal with numerous coalescences between drops. Thus several investigators [5–7] have attempted to simulate the entire process of dropwise condensation, namely growth, coalescence and renucleation of drops, by using a computer.

While most of the earlier works seem to be concerned with time-averaged features of dropwise condensation, the present author has put forward a new theory of heat transfer by dropwise condensation [8], from the viewpont that the so-called steady dropwise condensation on a vertical surface is in reality composed of transient dropwise condensation occurring repeatedly on the tracks left by departing drops. A fundamental set of simultaneous integrodifferential equations describing the process of transient dropwise condensation in terms of the drop-size distribution function and the drop growth rate function was derived theoretically from statistical and geometrical considerations. Instantaneous drop-size distributions during the transient dropwise condensation beginning simultaneously throughout a considerably large, initially bare surface were actually measured in a range of comparatively large drops [9]. The measured distributions agreed satisfactorily with the predictions from [8]. Further, the theoretical time average of the instantaneous distribution over the sweeping period showed a good agreement with experimental time-averaged drop-size distributions reported in [17, 22]. While in [8] the distribution function was primarily calculated by using a computer, analytical discussions of the various characteristics of the distribution function were also made. The analytical substantiation of the mathematical form of distribution function will be accomplished in this present paper.

In [8], the governing heat-transfer resistance through a single drop was assumed to be simply represented by heat conduction through itself, and the heat-transfer coefficient was considered to be determined principally by the number density of nucleation sites. Then, for the case of dropwise condensation of steam at atmospheric pressure, it was estimated that the mean spacing between nucleation sites amounted to a few microns and that approximately ten percent of the surface was bare on a time average. Glicksman and Hunt, from computer simulation [7], and Graham and Griffith, by analyzing the drop-size distributions obtained experimentally [17], have come up to similar conclusions [32]. Although they took into account the effects of curvature and interfacial mass transfer on substantial growth rate of a single drop, the resultant resistance due to these effects was considered to occupy a minor part in the total heat-transfer resistance measured under dropwise condensation. As compared with the foregoing estimation of the spacing between nucleation sites, the size of the thermodynamic critical drop is approximately 0.02 μm in its radius for a water droplet on a surface of 1.0°C subcooling. Therefore, when the surface is newly swept by a departing drop, there should exist broad bare spaces between the primary drops. Then it seems likely that surface roughness and promoter which are considered to govern the nucleation site density have a considerable effect on the heat-transfer coefficient of dropwise condensation. Contrary to expectation, however, experimental evidences show measurable but only small effects of promoter used and surface finish [12, 13, 33]. The present investigation is partly motivated by this contradiction.

Further, Glicksman and Hunt [7] and Graham and Griffith [17, 32] explained the tendency of the heat-transfer coefficient to decrease with a decrease in the saturation temperature of steam, observed in [17], as caused mainly by the decrease in the number density of nucleation sites with decreasing the steam pressure. This, however, seems implausible because the variation of the saturation temperature causes little change in the size of the thermodynamic critical drop (see equation (10) and Table 1), presumably with almost the same number of nucleation sites being activated irrespective of the saturation

---

Contributed by The Heat Transfer Division for publication in the JOURNAL OF HEAT TANSFER. Manuscript received by The Heat Transfer Division January 31, 1979.

temperature on the condensing surface at a constant subcooling. On the other hand, as the interfacial mass-transfer resistance varies greatly with the saturation temperature (see equation (6) and Table 1), this resistance is expected to be concerned with the foregoing decrease of heat transfer with decreasing the saturation temperature, probably having some effect even on the heat transfer of atmospheric pressure steam. Another motivation of the present investigation is to substantiate this expectation.

In this paper, a clear theoretical forecast of the behavior of the heat-transfer coefficient of dropwise condensation in terms of possibly important parameters concerning the nucleation of primary drops as well as the substantial growth rate of submicroscopic drops is first deduced on the theoretical basis established in [8]. During the deducing process intimate references are made to the actual values of those characteristic parameters of condensing substances used in the existing experiments. With the purpose of examining the effect of the interfacial mass-transfer resistance in especial, the following physically idealized condition which is opposite to that assumed in [8] is introduced as for the nucleation of primary drops in the numerical analysis described later; namely, the nucleation sites are so densely distributed on the condensing surface that the primary drop can nucleate almost everywhere. A critical comparison of the predictions from the theory with available experimental data of several condensing substances at various pressures is made in the final section of this paper.

Basic Equations

A transient dropwise condensation starting simultaneously at time $t = 0$ throughout a considerably large, initially bare, surface is considered. A drop is assumed to have a spherical segment geometry and its size is defined by the radius of its base. Taking an average over the surface at an instant t, there may be $N(r, t)dr$ drops per unit area having sizes in the interval $[r, r + dr]$. The sizes of those drops grow at a mean rate $\dot{r}_a(r, t)$ both by coalescence and by direct condensation on themselves. This substantial growth rate is denoted by $\dot{r}_e(r)$. The following equations hold between N and $\dot{r}_a$ [8].

$$\frac{\partial N}{\partial t} = -\frac{\partial N\dot{r}_a}{\partial r} - \int_r^{R_{\max}} 2\pi\rho\{\dot{r}_a(r) + \dot{r}_a(\rho)\}\psi(r; N)N(r)N(\rho)d\rho + \pi R_{\max}{}^2 N(R_{\max})\dot{r}_a(R_{\max}) \cdot N(r) \quad (1)$$

$$\int_{R_{\min}}^{r} \frac{S}{3}\pi\rho^3 \cdot 2\pi r\{\dot{r}_a(r) + \dot{r}_a(\rho)\}\psi(\rho; N)N(\rho)d\rho = S\pi r^2(\dot{r}_a - \dot{r}_e) \quad (2)$$

where

$$\psi(r, t; N) = 1 \Bigg/ \left[\left\{1 - \int_r^{R_{\max}} \pi p^2 N(p, t)dp\right\}\left\{1 - \frac{r}{r_E(r, t)}\right\}\right] \quad (3)$$

$$r_E(r, t) = 2\left\{1 - \int_r^{R_{\max}} \pi p^2 N(p, t)dp\right\} \Bigg/ \int_r^{R_{\max}} 2\pi p N(p, t)dp \quad (4)$$

$R_{\min}$ and $R_{\max}$ are the size of the primary drop and that of the departing drop, respectively. S is the following shape factor:

$$S = (2 - 3\cos\theta + \cos^3\theta)/\sin^3\theta$$

where θ is the contact angle of the liquid. Details of the derivation of the foregoing equations are presented in [8]. The following description is not very strict but may be comprehensible. Equation (1) is derived from a balance of the number of drops having a size r. The first term on the right-hand side of equation (1) denotes the net increase in the number of drops with the size r due to the shift of drop size by drop growth. The second term expresses the number of drops with the size r which become extinct captured by drops larger than r. Thus, the first term less the second term must equal the left-hand side. The last term on the right-hand side of equation (1) stands for a modification of the surface area after drop departure begins. Equation (2) represents a balance of the volume of a drop having a size r. The left-hand side of equation (2) is the total volume of smaller drops which are captured by the drop with the size r. The right-hand side expresses the apparent volume increase due to coalescence. ψ in equation (3) is concerned with the geometrical condition that drops can not intersect but exclude one another and that, between two drops, the larger one takes precedence of the smaller one. When small drops with a size r are considered in contrast to drops larger than r, they can reside only in a limited region with an area of $\{1 - \int_r^{R_{\max}} \pi p^2 N(p, t)dp\}$ left unoccupied by drops larger than r. Then, the effective distribution density of the small drops with the size r in the region where they are recognized is higher than the apparent distribution density $N(r)$ over the

Nomenclature

a = dimensionless drop growth rate, defined in equation (15)
D = equivalent radius of the bare space necessary for the primary drop to originate
e = dimensionless rate of substantial growth of a single drop, defined in equation (21)
h = heat-transfer coefficient for dropwise condensation
h_{fg} = heat of vaporization
h_i = interfacial heat-transfer coefficient
m = exponent of ξ in the expression of n in the equilibrium region of small drops, see equation (31)
N = distribution density of drops by sizes
Nu = Nusselt number for dropwise condensation, defined in equation (27)
n = dimensionless distribution density of drops, defined in equation (15)
p = exponent of ξ in the expression of a in the equilibrium region of small drops, see equation (30)
p_s = saturation pressure
Q = heat-transfer rate through a drop
R = gas constant
$R_{\max}$ = base radius of the departing drop
$R_{\min}$ = base radius of the primary drop
r = base radius of the drop
r_{cri} = radius of curvature of the thermodynamic critical drop
r_E = equivalent radius of the space left unoccupied by drops greater than r, defined in equation (4)
r_1 = characteristic drop size at which the interfacial mass-transfer resistance and the conduction resistance become equivalent, defined in equation (8)
r' = radius of curvature of the drop
$\hat{r}$ = instantaneous effective maximum drop size
$\dot{r}_a$ = drop growth rate
$\dot{r}_e$ = substantial growth rate of a single drop
S = shape factor
T_s = saturation temperature
ΔT = difference between saturation temperature and condensing surface temperature
t = time
t_0 = period of sweeping
V_0 = volume per unit area of condensate removed at every sweeping
υ = dimensionless volume of condensate per unit area
υ_g = specific volume of vapor
υ_l = specific volume of liquid
α = condensation coefficient
$\tilde{\alpha}$ = fraction of the area covered by drops with sizes greater than ξ
λ_l = thermal conductivity of liquid
σ = surface tension
θ = contact angle
ϕ = geometrical factor expressed by dimensionless variables, see equation (18)
ψ = geometrical factor, defined in equation (3)
τ = dimensionless time, defined in equation (14)
τ_0 = dimensionless period of sweeping
ξ = dimensionless drop size = $r/R_{\max}$
$\xi_{\text{cri}} = r_{\text{cri}}/R_{\max}$
$\xi_D = D/R_{\max}$
$\xi_E = r_E/R_{\max}$, see equation (19)
$\xi_{\min} = R_{\min}/R_{\max}$
$\xi_1 = r_1/R_{\max}$
$\xi = \hat{r}/R_{\max}$

whole surface by a factor represented by $\psi(r)$. ψ was derived from approximation and it needs to be slightly modified in case the contact angle θ is much greater than $\pi/2$. Finally, $r_E(r)$ defined by equation (4) represents an equivalent radius of the foregoing region where the drops of the size r are recognized.

As for the initiation of primary drops, it is assumed that when any bare space with an equivalent radius of a prescribed value D appears between drops a primary drop originates without delay and fills the space. Then the equivalent radius $r_E(R_{\min})$ of the bare area on the surface is maintained at the constant value D:

$$r_E(R_{\min}, t) = D \tag{5}$$

With respect to the initial condition, any assumed drop-size distribution at time zero whose density is concentrated near the primary drop size yields the same results except for the very early stage of the process [8]. Then, we used the following form in the numerical analysis.

$$N(r, 0) = \begin{cases} Cr^{-6} & R_{\min} \leqq r < 10R_{\min} \\ 0 & 10R_{\min} \leqq r \end{cases}$$

where a numerical constant C is determined in conformity with the condition (5).

Growth Rate of a Single Drop. Considerable progress has been made to calculate the heat transfer through a single drop of a given size. The interfacial mass-transfer resistance can be represented by the following interfacial heat-transfer coefficient [10].

$$h_i = \frac{2\alpha}{2-\alpha} \frac{1}{(2\pi R T_s)^{1/2}} \frac{h_{fg}^2}{v_g T_s} \tag{6}$$

where α is the condensation coefficient, R the gas constant, T_s the saturation temperature, h_{fg} the heat of vaporization, and v_g the specific volume of the vapor. Umur and Griffith [1] achieved an analysis of heat conduction through a single drop of hemispherical shape of radius r, with a uniform subcooling ΔT at the base and the heat-transfer coefficient h_i at the liquid-vapor interface. Mikic [11] has shown that the exact solution derived by Umur and Griffith can be well approximated by the following expression which formally assumes that the heat-transfer rate Q from vapor to the solid surface is controlled by two resistances in series, namely the interfacial resistance $1/(2\pi r^2 \cdot h_i)$ and the conduction resistance through the drop $1/(\pi r^2 \cdot 4\lambda_l/r)$ (λ_l is the thermal conductivity of the liquid).

$$\Delta T = \left(\frac{1}{2\pi r^2 h_i} + \frac{1}{4\pi r \lambda_l}\right) Q \tag{7}$$

Here, it must be noted that the interfacial resistance and the conduction resistance become equivalent at the following characteristic size.

$$r_1 = 2\lambda_l/h_i \tag{8}$$

Curvature of the liquid-vapor interface results in an equilibrium saturation temperature which is lower than the saturation temperature at a planar interface [3]. The difference is given by

$$\Delta T_c = \frac{2\sigma v_l}{h_{fg}} \frac{T_s}{r'} \tag{9}$$

where r' is the radius of curvature, σ the surface tension, and v_l the specific volume of the liquid. Then, for a given wall subcooling ΔT, no drops below the following critical radius of curvature are possible.

$$r_{\mathrm{cri}} = \frac{2\sigma v_l}{h_{fg}} \frac{T_s}{\Delta T} \tag{10}$$

Substituting this into equation (9) yields

$$\Delta T_c = \frac{r_{\mathrm{cri}}}{r'} \Delta T \tag{11}$$

LeFevre and Rose [3] have shown that there is no cross effect between the phenomenon of the interfacial mass transfer and that of the interfacial curvature and that the two resultant temperature differences can be simply added. Then, including ΔT_c, the overall temperature difference can be written instead of equation (7) as

$$\Delta T = \left(\frac{1}{2\pi r^2 h_i} + \frac{1}{4\pi r \lambda_l}\right) Q + \frac{r_{cri}}{r} \Delta T \tag{12}$$

In the end, the substantial growth rate of a single drop, $\dot{r}_e$, appearing on the right-hand side of equation (2), can be found for the case of hemispherical shape as [7]

$$\dot{r}_e = \frac{1}{2\pi r^2} \frac{v_l}{h_{fg}} Q = 2 \frac{\lambda_l v_l}{h_{fg}} \frac{\Delta T}{r} \cdot \frac{1 - r_{\mathrm{cri}}/r}{1 + r_1/r} \tag{13}$$

Nondimensionalized Forms and Basic Parameters

Taking $R_{\max}$ and $R_{\max}^2/\{(\lambda_l v_l/h_{fg})\Delta T\}$ as characteristic scales for length and time, respectively, dimensionless drop size ξ and dimensionless time τ are defined by

$$\xi = r/R_{\max}, \quad \tau = t \cdot (\lambda_l v_l/h_{fg}) \Delta T/R_{\max}^2 \tag{14}$$

Distribution density N and drop growth rate $\dot{r}_a$ are as well nondimensionalized by

$$n(\xi, \tau) = N \cdot R_{\max}^3, \quad a(\xi, \tau) = \dot{r}_a \cdot R_{\max}/\{(\lambda_l v_l/h_{fg})\Delta T\} \tag{15}$$

Then, the basic equations (1) and (2) can be made dimensionless as follows.

$$\frac{\partial n}{\partial \tau} = -\frac{\partial n a}{\partial \xi} - \int_\xi^1 2\pi\eta\{a(\xi) + a(\eta)\}\phi(\xi; n) n(\xi) n(\eta) d\eta + \pi n(1) a(1) \cdot n(\xi) \tag{16}$$

$$\int_{\xi_{\min}}^{\xi} \frac{S}{3} \pi\eta^3 \cdot 2\pi\xi\{a(\xi) + a(\eta)\}\phi(\eta; n) n(\eta) d\eta = S\pi\xi^2(a - e) \tag{17}$$

where

$$\phi(\xi, \tau; n) = 1 \Bigg/ \left[\left\{1 - \int_\xi^1 \pi\zeta^2 n(\zeta, \tau) d\zeta\right\}\{1 - \xi/\xi_E\}\right] = \psi(r, t; N) \tag{18}$$

$$\xi_E(\xi, \tau) = 2\left\{1 - \int_\xi^1 \pi\zeta^2 n(\zeta, \tau) d\zeta\right\} \Bigg/ \int_\xi^1 2\pi\zeta n(\zeta, \tau) d\zeta = r_E(r, t)/R_{\max} \tag{19}$$

$$\xi_{\min} = R_{\min}/R_{\max} \tag{20}$$

In this place the substantial growth rate for hemispherical geometry given in equation (13) is transformed to

$$e = \dot{r}_e \cdot R_{\max}/\{(\lambda_l v_l/h_{fg})\Delta T\} = \frac{2}{\xi} \frac{1 - \xi_{cri}/\xi}{1 + \xi_1/\xi} \tag{21}$$

where

$$\xi_{\mathrm{cri}} = r_{\mathrm{cri}}/R_{\max}, \quad \xi_1 = r_1/R_{\max} \tag{22}$$

We note that the reciprocal of ξ_1 is a kind of Biot number. The boundary condition in equation (5) becomes

$$\xi_E(\xi_{\min}, \tau) = \xi_D \tag{23}$$

where

$$\xi_D = D/R_{\max} \tag{24}$$

Equations (16) and (17) along with equations (21) and (23) fully describe the process of transient dropwise condensation. Then, it is obvious from those equations that the process in the nondimensionalized space and time is determined by the following four basic parameters.

$$\xi_1, \ \xi_{\mathrm{cri}}, \ \xi_{\min} \text{ and } \xi_D$$

We may equally choose

$$\xi_1, \ \xi_{\mathrm{cri}}/\xi_1 = r_{\mathrm{cri}}/r_1, \ \ \xi_{\min}/\xi_{\mathrm{cri}} = R_{\min}/r_{\mathrm{cri}}, \ \text{ and } \xi_D/\xi_{\min} = D/R_{\min}$$

Here, the second parameter defines another kind of Biot number than $1/\xi_1$.

The so-called steady dropwise condensation on a vertical surface is composed of the transient dropwise condensation occurring repeatedly on the tracks left by departing drops. A typical point on the condensing surface will be swept by departing drops almost periodically at time intervals of t_0 and will be cleared of condensate of the following volume per unit area at the time of each sweeping.

$$V_0 = \int_{R_{\min}}^{R_{\max}} \frac{S}{3}\pi r^3 N(r, t_0)dr$$

where $N(r, t)$ is the foregoing instantaneous drop-size distribution in the case of transient condensation. The time-averaged heat-transfer coefficient during the steady condensation is given by

$$h = \frac{h_{fg}V_0}{v_l \Delta T t_0}$$

If the process of the steady condensation on a vertical surface is also made dimensionless by transformation (14), the heat-transfer coefficient is expressed in terms of the quantities in the dimensionless space and time as follows.

$$h = \frac{h_{fg}}{v_l}\frac{1}{\Delta T}\frac{\upsilon(\tau_0)\cdot R_{\max}}{\tau_0 \cdot R_{\max}{}^2/\{(\lambda_l v_l/h_{fg})\Delta T\}} \tag{25}$$

where τ_0 is the dimensionless period of sweeping and υ is the dimensionless volume of condensate per unit area in the case of transient condensation:

$$\upsilon(\tau) = \int_{\xi_{\min}}^{1} \frac{S}{3}\pi \xi^3 n(\xi, \tau)d\xi$$

Equation (25) is rearranged as

$$\frac{hR_{\max}}{\lambda_l} = \frac{\upsilon(\tau_0)}{\tau_0} \tag{26}$$

We may define the Nusselt number of dropwise condensation by the left-hand side of equation (26):

$$\mathrm{Nu} = \frac{hR_{\max}}{\lambda_l} \tag{27}$$

Here, we should note that the sweeping cycle is controlled by one and the same process of transient dropwise condensation occurring near the top of the surface, where the transient condensation will come up to a fairly developed stage with a number of drops grown up near the departing size. Then, since the process of transient dropwise condensation in the dimensionless space and time is determined by the foregoing four basic parameters, we have

$$\mathrm{Nu} = \upsilon(\tau_0)/\tau_0 = \mathrm{Func}(\xi_1, \xi_{\mathrm{cri}}/\xi_1, \xi_{\min}/\xi_{\mathrm{cri}}, \xi_D/\xi_{\min}) \tag{28}$$

A simple model to calculate the cycle of drop departure is presented in [8]. Exactly, the dimensionless sweeping period τ_0 increases slightly with the dimensionless distance from the top of the condensing surface, $x/R_{\max}$ (x is the actual distance). However, the quotient $\upsilon(\tau_0)/\tau_0$ is scarcely affected by $x/R_{\max}$ as explained in [8].

Available Experimental Data. When the condensing substance, system pressure p_s (correspondingly, saturation temperature T_s) and surface subcooling ΔT are given, two characteristic drop sizes in the substantial growth rate expression (13), r_1 and r_{cri}, are determined from equations (6, 8) and (10). Further, under a given gravitational force field, the departing drop size $R_{\max}$ is fixed. Thus two of the four basic parameters, namely $\xi_1 = r_1/R_{\max}$ and $\xi_{\mathrm{cri}}/\xi_1 = r_{\mathrm{cri}}/r_1$, appearing in the nondimensionalized form (21) of the substantial growth rate, are determined. In Table 1 actual values of those characteristic parameters as well as experimental Nusselt numbers defined by equation (27) are listed for three condensing substances, for which reliable experimental data taken for the so-called steady dropwise condensation on a vertical surface are available. While a number of experimental works for steam at atmospheric pressure have been published [12–14], there exist only limited number of measurements over a range of pressures [15–17]. Entries of water data in Table 1 are restricted to those which were obtained by using copper surfaces promoted with dioctadecyl disurphide. Except for water systematic and reliable measurements are limited to a few organic compounds [18] and mercury [19, 20]. Of the organic compounds only the data of ethylene glycol were adopted in Table 1, because physical properties of the other test fluids are not sufficiently available nor measurements of the departing drop size exist. A main source of the physical properties of ethylene glycol was Reference [21]. The departing drop sizes for water and ethylene glycol were taken from [17, 22] and [23], respectively, although observation in [22] and [23] were performed on condensing surfaces promoted with different promoters than the systems in Table 1. Measurements of the departing drop size with varying pressures are very few. As for water, Graham and Griffith [17] reported that $2R_{\max}$ = 2.5 mm at T_s = 373 K while $2R_{\max}$ = 3.0 mm at T_s = 304 K. Then it seems tolerable to assume $R_{\max}$ as a constant irrespective of the system pressure in the reduction of Table 1. Here, it should be noted that in calculating the interfacial heat-transfer coefficient h_i from equation (6) the condensation coefficient α for immediate need was assumed to be unity. While it seems to be generally accepted that the condensation coefficients of liquid metals are near unity up to moderate pressures [24, 25] and so is that of water at very low pressures [10, 26, 27], behaviors of condensation coefficients with the pressure and the condensation rate seem to have not yet been established [28].

Table 1 Available experimental data

System	Literature	T_s K	p_s N/m^2	Typical ΔT K	Measured h W/m^{2}K	Experimental Nu	h_i W/m^{2}K	r_1 mm	ξ_1	r_{cri} mm	ξ_{cri}/ξ_1 = r_{cri}/r_1	Symbol in Fig.4
Water;	[15]	295	2.7×10^3	1.0	5.7×10^4	113	8.55×10^5	1.42×10^{-3}	1.18×10^{-3}	1.74×10^{-5}	1.23×10^{-2}	● 1
Copper surface promoted with dioctadecyl disulphide;	[17]	304	4.5×10^3	1.0	7.3×10^4	142	1.32×10^6	9.35×10^{-4}	7.79×10^{-4}	1.78×10^{-5}	1.91×10^{-2}	● 2
	[16]	306	5.0×10^3	1.0	8.4×10^4	162	1.45×10^6	8.56×10^{-4}	7.13×10^{-4}	1.79×10^{-5}	2.09×10^{-2}	● 3
		321	1.1×10^4	2.0	1.3×10^5	244	2.78×10^6	4.60×10^{-4}	3.83×10^{-4}	9.26×10^{-6}	2.01×10^{-2}	● 4
		342	3.0×10^4	2.0	1.7×10^5	308	6.10×10^6	2.17×10^{-4}	1.81×10^{-4}	9.64×10^{-6}	4.44×10^{-2}	● 5
		359	6.0×10^4	2.0	2.0×10^5	355	1.05×10^7	1.28×10^{-4}	1.07×10^{-4}	9.93×10^{-6}	7.74×10^{-2}	● 6
R_{max} observed =1.2mm [17,22]	[12-14,17]	373	1.01×10^5	2.0	2.4×10^5	422	1.57×10^7	8.69×10^{-5}	7.24×10^{-5}	1.01×10^{-5}	1.17×10^{-1}	● 7
	[14]	373	1.01×10^5	8.0	3.2×10^5	563	1.57×10^7	8.69×10^{-5}	7.24×10^{-5}	2.54×10^{-6}	2.92×10^{-2}	● 8
Ethylene glycol; Copper plate coated with ptfe 0.01mm thick; R_{max}obs.=0.8mm[23]	[18]	334	2.64×10^2	20	7.5×10^3	23	5.64×10^4	9.22×10^{-3}	1.15×10^{-2}	1.50×10^{-6}	1.63×10^{-4}	▲ 1
		369	1.85×10^3	20	1.7×10^4	52	3.08×10^5	1.70×10^{-3}	2.13×10^{-3}	1.58×10^{-6}	9.30×10^{-4}	▲ 2
		386	4.19×10^3	20	2.3×10^4	70	6.24×10^5	8.44×10^{-4}	1.05×10^{-3}	1.61×10^{-6}	1.91×10^{-3}	▲ 3
		399	7.47×10^3	20	2.6×10^4	79	1.02×10^6	5.14×10^{-4}	6.43×10^{-4}	1.64×10^{-6}	3.18×10^{-3}	▲ 4
		423	1.98×10^4	20	3.0×10^4	91	2.34×10^6	2.25×10^{-4}	2.82×10^{-4}	1.67×10^{-6}	7.41×10^{-3}	▲ 5
Mercury; Copper block plated with stainless steel 0.25mm thick; R_{max} obs. =0.15mm [19]	[19]	393	1.00×10^2	5.0	9.9×10^3	0.136	8.32×10^3	2.62	17.5	1.83×10^{-5}	6.97×10^{-6}	◪ 1
		473	2.30×10^3	5.0	7.6×10^4	0.92	1.20×10^5	0.205	1.37	2.15×10^{-5}	1.05×10^{-4}	◪ 2
		553	2.11×10^4	5.0	1.4×10^5	1.56	7.47×10^5	0.0361	0.241	2.41×10^{-5}	6.67×10^{-4}	◪ 3
	[20]	378	4.75×10	20	2.2×10^3	0.031	4.35×10^3	4.88	32.5	4.42×10^{-6}	9.06×10^{-7}	■ 4
		412	2.35×10^2	20	1.2×10^4	0.159	1.74×10^4	1.30	8.67	4.76×10^{-6}	3.66×10^{-6}	■ 5
		452	1.13×10^3	5.0	6.0×10^4	0.75	6.62×10^4	0.362	2.41	2.07×10^{-5}	5.71×10^{-5}	■ 6
		492	4.12×10^3	2.0	3.0×10^5	3.6	1.95×10^5	0.129	0.860	5.54×10^{-5}	4.29×10^{-4}	■ 7
		531	1.23×10^4	2.0	4.5×10^5	5.1	4.82×10^5	0.0548	0.365	5.86×10^{-5}	1.07×10^{-3}	■ 8

The thermodynamic critical radius r_{cri} in equation (10), being inversely proportional to ΔT, becomes very small even for moderate experimental ΔT, and is roughly of a similar order between the three condensing fluids in Table 1. On the other hand, the range of the characteristic size r_1 defined by equation (8) extends wide apart. Water at atmospheric pressure has the smallest r_1, which is still an order of magnitude larger than r_{cri}. Then water at atmospheric pressure has the smallest ξ_1. In this case the dimensionless substantial growth rate e in equation (21) becomes conduction-controlled to be approximated as $e \fallingdotseq 2/\xi$ in a very wide range of the dimensionless drop size: $\xi_1 < \xi \leqq 1$. In contrast to this, mercury at low pressures has ξ_1 which is far larger than unity. Then, the substantial growth rate of a mercury drop at low pressures becomes interfacial mass-transfer controlled and is expressed as $e \fallingdotseq 2/\xi_1 = \mathrm{const.}$ in the entire domain of the dimensionless drop size: $\xi_{\mathrm{cri}} < \xi \leqq 1$ except the vicinity of ξ_{cri} at which e rapidly vanishes. In case of ethylene glycol and low pressure water, ξ_1 is considerably small but ξ_{cri} is further smaller than ξ_1. Then a large drop in $\xi_1 < \xi \leqq 1$ is conduction-controlled, while a small drop in $\xi_{\mathrm{cri}} < \xi < \xi_1$ is interfacial mass-transfer controlled.

Effect of Each Basic Parameter

Numerical Analysis. Numerical analysis was first performed for the case of transient condensation of steam at atmospheric pressure on an initially bare surface at a uniform subcooling of $\Delta T = 1.0^\circ\mathrm{C}$. In this case, $\xi_1 = 7.24 \times 10^{-5}$ and $\xi_{\mathrm{cri}}/\xi_1 = 0.233$ as is understood from Table 1. Two other basic parameters concerning the nucleation of primary drops were assumed as

$$\xi_{\mathrm{min}}/\xi_{\mathrm{cri}} = 1.2 \quad \text{and} \quad \xi_D/\xi_{\mathrm{min}} = 2.1 \tag{29}$$

Namely, the primary drop was assumed to be 1.2 times as large as the thermodynamic critical size, and to originate when and where a fresh bare surface of an area 4.4 times as large as the base of the primary drop is exposed. As stated in the introduction, in order to examine the effect of interfacial mass-transfer resistance in especial, the nucleation site density is assumed to be infinitely high throughout the numerical analysis. Then the ratio ξ_D/ξ_{min} is taken as a constant which is not different from unity by too much, irrespective of the value of the thermodynamic critical size r_{cri}.

The calculated variation with time τ of the profile of drop growth rate a is shown by solid lines in Fig. 1. As was explained and demonstrated in [8] and [9], a short time after the beginning of the transient condensation, a *universal distribution for large drop range* develops. This corresponds to a characteristic peak of the growth rate curve at $\tau = 1.59 \times 10^{-8}$ in Fig. 1. As the characteristic peak shifts to the larger side with time, a straight part expressed by the following form appears in a range of smaller drops.

$$a = B\xi^{-p} \tag{30}$$

On the growth rate curve at $\tau = 8.45 \times 10^{-5}$, the straight part is seen to extend from $\xi = 10^{-3}$ to 10^{-1}. We referred to this part as an *equilibrium region of small drops* in [8]. In the drop-size range smaller than the equilibrium region of small drops, drops nucleate, grow and coalesce in the geometrical circumstances provided by drops belonging in the equilibrium region of small drops; and they develop another characteristic part of drop-size distribution—*a steady distribution for microscopic drops* [8]. Drop departure from the surface begins at about $\tau = 1.6 \times 10^{-4}$. From this time on, the universal distribution for large drop range breaks down and a stationary distribution over the whole drop range develops at about $\tau = 5 \times 10^{-4}$, as shown for $\tau = 1.26 \times 10^{-3}$ in Fig. 1.

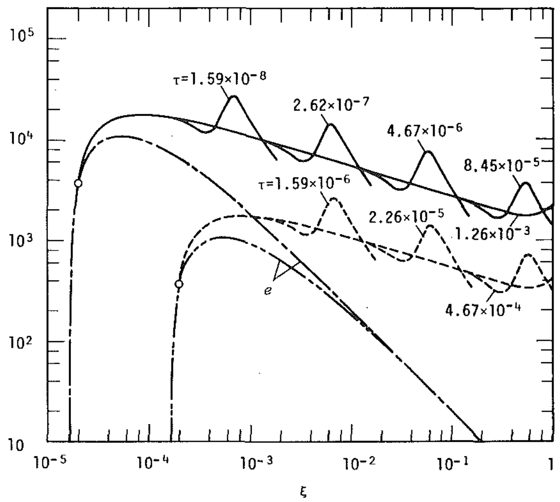

Fig. 1 **Variation with dimensionless time τ of dimensionless drop growth rate a against dimensionless drop size ξ; solid lines: steam at atmospheric pressure and at $\Delta T = 1.0^\circ\mathrm{C}$, $\xi_1 = 7.24 \times 10^{-5}$, $\xi_{\mathrm{cri}}/\xi_1 = 0.233$, $\xi_{\mathrm{min}}/\xi_{\mathrm{cri}} = 1.2$, $\xi_D/\xi_{\mathrm{min}} = 2.1$; broken lines: $\xi_1 = 7.24 \times 10^{-4}$, $\xi_{\mathrm{cri}}/\xi_1 = 0.233$, $\xi_{\mathrm{min}}/\xi_{\mathrm{cri}} = 1.2$, $\xi_D/\xi_{\mathrm{min}} = 2.1$**

An explanation of the method of calculation on a digital computer will be given here. The principle is the same as described in [8]. First, when a drop-size distribution $n(\xi, \tau)$ at times τ is given, equation (17) reduces to Volterra's integral equation with respect to $a(\xi, \tau)$, and is solved by rewriting it to simultaneous linear equations by using trapezoidal rule. At this point, nodal points of calculation on ξ-axis were chosen to form a geometrical progression with a common ratio of $10^{1/100} = 1.0233$. Namely, one order of magnitude of ξ was divided into 100 equal intervals in a logarithmic scale. Substitution of $n(\xi, \tau)$ and $a(\xi, \tau)$ so-obtained into the right-hand side of equation (16) using difference analogue and trapezoidal rule yields $(\partial n/\partial \tau)(\xi, \tau)$. Then, by choosing a proper time increment, $\Delta\tau$, a new distribution at $\tau + \Delta\tau$ is obtained as

$$n(\xi, \tau + \Delta\tau) = n(\xi, \tau) + (\partial n/\partial\tau)(\xi, \tau) \cdot \Delta\tau$$

A time increment $\Delta\tau$ has to satisfy the following condition for any set of neighboring nodal points (ξ_i, ξ_{i+1}), lest the drop with the size ξ_i at time τ grows in excess of the size ξ_{i+1} in the time interval $\Delta\tau$.

$$\Delta\tau \leqq (\xi_{i+1} - \xi_i)/a(\xi_i, \tau)$$

The right-hand side of this condition decreases sharply with decreasing ξ_i. So selection of $\Delta\tau$ is controlled by the behaviors of microscopic drops comparable to the primary drop, and a formidable number of time steps will be needed in order to advance a computer run until dominating drops grow near to the departing size. We know, however, from Fig. 1 that a stationary distribution develops in a small drop range starting first as the steady distribution for microscopic drops and then extends progressively towards the larger drop side in company with the development of the equilibrium region of small drops. Then, in order to save computer time in the actual calculation, the lower bound of a drop-size range of iterative computation was shifted to a larger ξ step by step according to the development of the stationary distribution in the smaller drop range.

By assuming the same model as [8] to calculate the cycle of drop departure (surface height was assumed to be 50 times R_{max}), the Nusselt number defined by equation (27) was calculated as Nu = 1620 for the present case of the so-called steady dropwise condensation of steam at atmospheric pressure on a vertical surface at $\Delta T = 1.0^\circ\mathrm{C}$. This prediction is nearly four times as large as the experimental value of Nu =422 for water vapor under similar conditions of $T_s = 373$ K and $\Delta T = 2.0^\circ\mathrm{C}$ in Table 1. Further comparison with experiments and discussion will be given later.

Effect of ξ_1. The equilibrium region of small drops is important since it covers a main portion of the drop-size distribution as time goes by. In this region, the distribution density n and the fraction $\tilde{\alpha}$ of the area covered by drops with sizes greater than ξ can be expressed in a set with expression (30) as [8]:

$$n(\xi, \tau) = A\xi^{-m} \tag{31}$$

$$\tilde{\alpha}(\xi, \tau) = 1 - \left(\frac{\xi}{\hat{\xi}}\right)^{3-m} \tag{32}$$

Expression (32) gives complete coverage of the surface by drops when the equilibirum region of small drops be extended to zero radius. The same form as expression (32) was intuitively assumed and applied to the time-averaged drop-size distribution by LeFevre and Rose [3]. Here, $\hat{\xi}(\tau) = \hat{r}/R_{\max}$, and $\hat{r}(t)$ may be called as an *instantaneous* effective maximum drop size in the terminology used by LeFevre and Rose. Using

$$\tilde{\alpha}(\xi, \tau) = \int_{\xi}^{\hat{\xi}} \pi\eta^2 n(\eta, \tau) d\eta$$

a factor A in expression (31) is related to $\hat{\xi}$ as

$$A(\tau) = \frac{3-m}{\pi}\hat{\xi}^{m-3} \tag{33}$$

Every drop in the equilibrium region of small drops, irrespective of its size, is always in a geometrically similar condition relative to its surroundings [8]. In this region drops grow primarily by coalescence and, in equation (1) concerning the balance of drop number, the first term on the right-hand side is virtually in keeping with the second term. These facts reduce the basic equations (16) and (17) to the following two equations which hold between the exponents p and m appearing in expressions (30) and (31).

$$\frac{2}{3}\left\{\frac{1}{3-m} - \frac{1}{m-2}\right\}^{-1}\left\{1 + \frac{1}{1-p}\right\} = 1 \tag{34}$$

$$m + p = 3 \tag{35}$$

The former equation was already indicated in [8], but the author was not aware of the latter one when [8] was published. The derivation of equation (35) is given in Appendix A. From equations (34) and (35) m and p are theoretically determined as

$$\left.\begin{aligned} m &= (1 + \sqrt{19})/2 = 2.679 \\ p &= (5 - \sqrt{19})/2 = 0.321 \end{aligned}\right\} \tag{36}$$

LeFevre and Rose [3] adopted empirically a value of $m = 3 - 1/3$ for their time-averaged drop-size distribution, which value gives a very good approximation to the theoretical value in equation (36).

Suppose that a pair of $n^*(\xi, \tau)$ and $a^*(\xi, \tau)$ is the solution of the basic equations (16) and (17) for a set of values of the basic parameters: ξ_1, ξ_{cri}, $\xi_{\min}$ and ξ_D. Here we consider the period before the occurrence of drop departure. Then, the last term on the right-hand side of equation (16) vanishes, and the upper bound of integrations in equations (16, 18) and (19), $\xi = 1$, can effectively be extended to infinity. Under these conditions, it is easy to prove that a pair of

$$n(\xi, \tau) = \frac{1}{k^3} n^*\left(\frac{\xi}{k}, \frac{\tau}{k^2}\right) \tag{37}$$

and

$$a(\xi, \tau) = \frac{1}{k} a^*\left(\frac{\xi}{k}, \frac{\tau}{k^2}\right) \tag{38}$$

becomes the solution of the basic equations for the case where all the four basic parameters are multiplied by a factor of k. In this case, if the basic parameters in the form in expression (28) are considered, only ξ_1 is multiplied by k while the other three: ξ_{cri}/ξ_1, $\xi_{\min}/\xi_{\mathrm{cri}}$ and $\xi_D/\xi_{\min}$, remain unchanged. Transformation in equation (38) is demonstrated by broken lines in Fig. 1, which assume $\xi_1 = 7.24 \times 10^{-4}$, $\xi_{\mathrm{cri}}/\xi_1 = 0.233$, $\xi_{\min}/\xi_{\mathrm{cri}} = 1.2$ and $\xi_D/\xi_{\min} = 2.1$. Namely, broken lines before $\tau = 4.67 \times 10^{-4}$, after which drop departure begins shortly, prove to be obtained by the parallel displacement of the solid lines in the direction of a straight line: $a = 1/\xi$.

Now, we consider the so-called steady dropwise condensation on a vertical surface and compare the two cases having respectively the same values of the basic parameters as the cases plotted in Fig. 1. As explained previously, the Nusselt number of dropwise condensation is theoretically calculated from the right-hand side of equation (26). Here, sweeping period τ_0 and instantaneous volume of condensate at time τ_0 in the process of transient dropwise condensation, $v(\tau_0)$, are both determined by the phenomena in the transient dropwise condensation at a fairly developed stage. In this respect we become aware that between the two cases plotted in Fig. 1 the phenomena concerned: growth of dominating drops near to the departing size, beginning of drop departure, breakdown of the universal distribution for large drop range and development of the terminal stationary distribution, proceed entirely the same in the dimensionless space if the dimensionless time scale is modified by a constant factor corresponding to the vertical spacing between the two sets of curves in a large drop range in Fig. 1. Consequently, theoretical Nusselt number is different between the two cases by this modification factor of time, which is easily calculated from the slope of the growth rate curve in the equilibrium region of small drops. We have thus accomplished our purpose of determining the effect of ξ_1 on Nu under constant values of ξ_{cri}/ξ_1, $\xi_{\min}/\xi_{\mathrm{cri}}$ and $\xi_D/\xi_{\min}$. As a result, expression (28) becomes

$$\mathrm{Nu} = \xi_1^{-(1-p)} F_1(\xi_{\mathrm{cri}}/\xi_1, \xi_{\min}/\xi_{\mathrm{cri}}, \xi_D/\xi_{\min}) \tag{39}$$

for

$$\xi_1, \xi_{\mathrm{cri}} \ll 1 \tag{40}$$

Condition (40) is necessary in order that the equilibrium region of small drops should have developed appreciably before drop departure begins.

Tanasawa, et al. [29] have recently measured the dependence of the heat-transfer coefficient on the departing drop size, using steam at atmospheric pressure. Both the steam flow and the centrifugal force were employed to prompt drop departure. Their experimental results were well correlated by

$$h = 2.4 \times 10^5 (2R_{\max})^{-0.31} \tag{41}$$

where h is in W/m^{2}K and $R_{\max}$ is in mm. In the present theoretical treatment, the parameters $\xi_{\min}/\xi_{\mathrm{cri}}$ and $\xi_D/\xi_{\min}$ are considered to characterize the nucleation of primary drops. Then we should be justified in assuming that these two parameters were invariables in the experiment of Tanasawa, et al. Further in their experiment not only the characteristic drop size r_1 from equations (6) and (8) was constant but also the thermodynamic critical radius r_{cri} from equation (10) was varied slightly. Under these conditions equation (39) with the aid of equation (36) predicts the relation:

$$h \propto R_{\max}^{-0.321}$$

which is in very good accord with equation (41).

Effect of ξ_{cri}/ξ_1. Fig. 2 presents comparison of the profiles of drop growth rate during the transient dropwise condensation which were calculated for various values of ξ_{cri}/ξ_1 satisfying condition (40), under a constant value of $\xi_1 = 1.0 \times 10^{-4}$. In this place again, conditions (29) were assumed concerning the nucleation of primary drops. Solid lines in Fig. 2 represent profiles of drop growth rate a just before the beginning of drop departure, exclusive of the size range of dominating drops. In the same manner as the difference of Nu between the two cases in Fig. 1 has been discussed, the theoretical Nusselt numbers for respective conditions in Fig. 2 can be readily evaluated by comparing the values of a with that of the solid line in Fig. 1, at a common ξ belonging in the equilibrium region of small drops (say at $\xi = 1.0 \times 10^{-2}$ for cases $\xi_{\mathrm{cri}}/\xi_1 \leqq 1$). The dependence of Nu on ξ_{cri}/ξ_1 has been thus determined and is shown by straight lines in Fig. 4, which gives Nu against ξ_1 with ξ_{cri}/ξ_1 as a parameter.

In this place the resultant expression of Nu for the case where $\xi_{\mathrm{cri}}/\xi_1 = 0$ becomes

$$\mathrm{Nu} = 5.64\xi_1^{-0.7} \tag{42}$$

From condition (40), this expression is valid for

$$\xi_1 \ll 1 \tag{43}$$

The exponent -0.7 in expression (42) is slightly different from its theoretical value $-(1-p)$ from equations (36) and (39). This is due to the fact that the substantial growth rate e can not completely be neglected in comparison with the apparent growth rate a in the actual equilibrium region of small drops, whereas e has been neglected as compared with a in deriving equation (34). Physically, the present

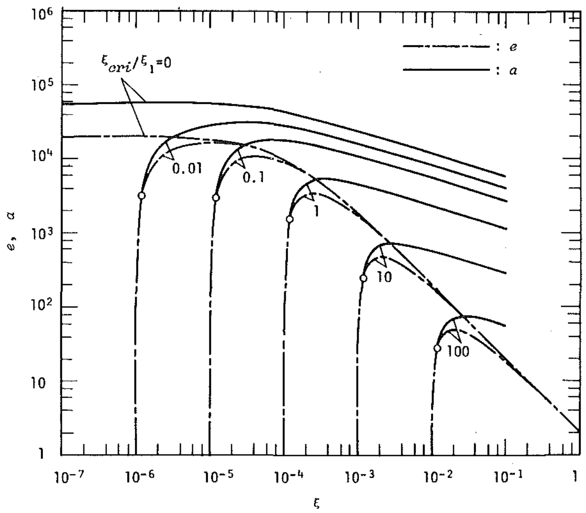

Fig. 2 Profiles of drop growth rate just before the beginning of drop departure, exclusive of the size range of dominating drops, calculated for various ξ_{cri}/ξ_1 under a constant $\xi_1 = 1.0 \times 10^{-4}$

case of $\xi_{cri}/\xi_1 = 0$ means the limit of ξ_{cri}/ξ_1 going to zero with ξ_1, ξ_{min}/ξ_{cri} and ξ_D/ξ_{min} unaltered. In this limit, the size range of existing drops extends to zero radius and there appears a wide region of $\xi \ll \xi_1$ ($= 1.0 \times 10^{-4}$ for the case of Fig. 2) where the substantial growth rate e in equation (21) is kept nearly constant as $e \fallingdotseq 2/\xi_1 = e_0$. It can be proved that in this constant-e region there develops another *equilibrium regime of small drops* than the one expressed by equations (30, 31) and (36) and that the following relations hold under the new regime (a proof is given in Appendix B).

$$m = (1 + \sqrt{97})/4 = 2.712 \tag{44}$$

$$a/e_0 = (7 + \sqrt{97})/6 = 2.808 \tag{45}$$

The relation (45) is ascertained for the case of Fig. 2, that is, a becomes flat for $\xi < 1.0 \times 10^{-6}$ amounting to $2.808 \times (2/10^{-4})$ at $\xi = 1.0 \times 10^{-7}$. In the limit of $\xi_{cri}/\xi_1 \rightarrow 0$, the space left between drops of over ξ_1 in size is completely covered by drops belonging in this new equilibrium regime of small drops. Thus a significant implication of equation (42) is that it gives the theoretical upper limit of Nu under a given ξ_1. Since we used equation (21) in the numerical calculations, equation (42) as well as the other theoretical results in Fig. 4 are applicable to the case of hemispherical drops. When the contact angle θ is different from $\pi/2$, the numerical constants such as 5.64 in equation (42) would be slightly changed according to the departure of θ from $\pi/2$.

Effect of ξ_{min}/ξ_{cri} and ξ_D/ξ_{min}. Investigation was performed into the influence of the last two parameters in expression (39), ξ_{min}/ξ_{cri} and ξ_D/ξ_{min}, which are concerned with the nucleation of primary drops. We chose three values of ξ_{cri}/ξ_1 and $\xi_1 = 1.0 \times 10^{-4}$. Four sets of values of ξ_{min}/ξ_{cir} and ξ_D/ξ_{min} were assumed, as indicated in the legend of Fig. 3. Predicted profiles of the drop growth rate just before the occurrence of drop departure are plotted and compared in Fig. 3. Here curves signed with 2 represent the same that are plotted in Fig. 2. In a range of parameter $\xi_{cri}/\xi_1 \geqq 1$, appreciable differences appear between the predicted curves according to the assumption of nucleation. In a range of $\xi_{cri}/\xi_1 < 1$, however, under which actual values of the condensing substances listed in Table 1 fall, predicted profiles in the equilibrium region of small drops come close together despite the variety of the nucleation conditions. In the limit of ξ_{cri}/ξ_1 going to zero, we have equation (42) irrespective of the nucleation conditions, as is expected from what was explained previously.

In the Case Where $\xi_1 \gg 1$. Suppose the case where ξ_1 is far larger than unity. Mercury at low pressures comes under this case. Then the heat transfer through a single drop is entirely controlled by the interfacial heat-transfer coefficient h_i in equation (6), and the substantial growth rate becomes constant, namely $e = 2/\xi_1 =$ const for the case of hemispherical geometry. For a general contact angle θ, since an area of the liquid-vapor interface of each individual drop is larger than its base area by a factor of $2(1 + \cos\theta)^{-1}$, the total area of the liquid-vapor interface is increased from the area of the condenser surface by this same factor, in the limit of complete coverage of the condenser surface by drops. Therefore, as heat transfer takes place at the liquid-vapor interface at a uniform heat flux of $h_i \Delta T$, the heat-transfer coefficient for dropwise condensation which is based on the condenser surface area becomes $2(1 + \cos\theta)^{-1} h_i$. In conclusion we find the following expression of the Nusselt number in the limit of ξ_{cri}/ξ_1 going to zero, with the aid of equations (8, 22) and (27).

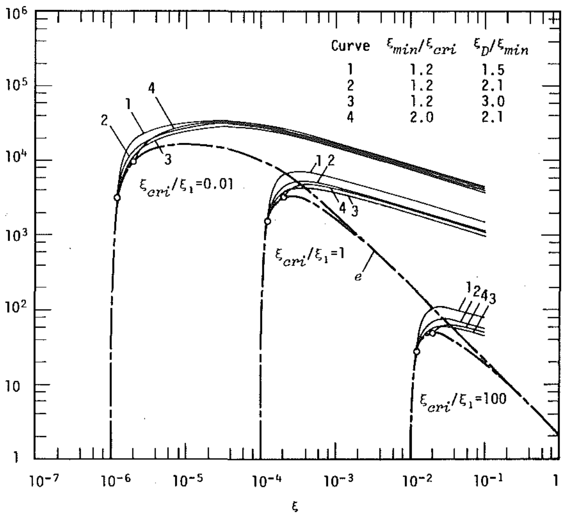

Fig. 3 Dependence of the drop growth rate profile on the difference in nucleation conditions, calculated for $\xi_{cri}/\xi_1 = 0.01$, 1 and 100 under $\xi_1 = 1.0 \times 10^{-4}$

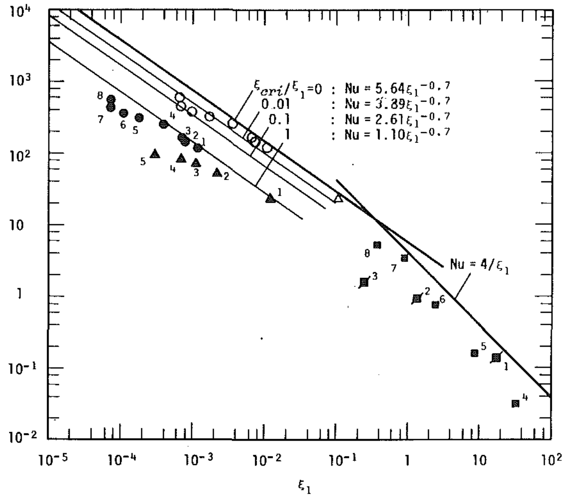

Fig. 4 Comparison between the theoretical and experimental Nusselt numbers; $\alpha = 1.0$ and $\alpha = 0.2$ were respectively assumed for solid and open symbols in the data reduction

$$\text{Nu} = 4(1 + \cos\theta)^{-1}\xi_1^{-1} \tag{46}$$

for

$$\xi_1 \gg 1 \tag{47}$$

Equations (42) and (46) are valid under the respective conditions (43) and (47) in the strict sense that they give the Nusselt number in the limit of ξ_{cri}/ξ_1 going to zero. At the same time they have another extensive meaning that they provide an upper bound that Nu can not go beyond. In the latter sense both equations are applicable without restrictions concerning ξ_1. Then, in Fig. 4, straight lines representing equations (42) and (46) (assuming $\theta = \pi/2$) are drawn beyond the limits of the respective conditions (43) and (47).

Comparison with Available Experimental Data and Discussion

The experimental data listed in Table 1 are plotted in Fig. 4 by solid symbols. As to mercury, while there are some differences between the data of two experimenters, data points are distributed on an average parallel to the line representing equation (46), and are lower than the prediction by a factor of about two. Experimental Nusselt numbers of water as well as ones of ethylene glycol at low pressures are smaller than the predicted Nusselt numbers by a factor of four or five even if the effect of ξ_{cri}/ξ_1 is taken into account. Further the deviation of the experimental points of ethylene glycol increases with increasing vapor pressure.

In the foregoing theoretical treatment an extreme case where the thermal conductivity of the condensing surface is infinitely high has been implicitly assumed by taking ΔT in equation (13) as a constant independent of the drop size r as well as the locality on the condensing surface. In case of an actual condenser material with a finite thermal conductivity, Mikic [11] has suggested an existence of an additional thermal resistance caused by the constriction of the heat flow lines near the condensing surface due to the presence of inactive surface area covered by big drops. Hannemann and Mikic have recently put forward a theory [30] for the constriction resistance which indicates the dependence of the effective heat-transfer coefficient for dropwise condensation on the thermal conductivity of the condenser material. In the light of their theory, the experimental system of water cited in Table 1 is almost free from the constriction resistance, since its maximum contribution to the total thermal resistance, occurring at the highest vapor pressure, is estimated at about five percent. The condensing surfaces for ethylene glycol and mercury in Table 1 are made of thin layers of ptfe and stainless steel on copper substrates, respectively. Hannemann [31] very recently developed the following estimate for the effect of condensing surface thickness δ on the constriction conductance h_c.

$$\frac{h_c R_{\max}}{\lambda_m} = 11.2(\lambda_m/\lambda_l)^{-0.07}[\tanh(4\delta/R_{\max})]^{-1}$$

where λ_m is the thermal conductivity of the condensing surface. Using this estimate, the constriction conductances of the surfaces in Table 1 are evaluated as $h_c = 7 \times 10^4$ and 1.2×10^6 W/m^{2}K for ethylene glycol and mercury, respectively. The experimental heat-transfer coefficients h in Table 1 are to be influenced by the constriction conductance through the relation $h = (h_d{}^{-1} + h_c{}^{-1})^{-1}$ where h_d is the heat-transfer coefficient in the absence of constriction effect. Then, as for mercury, the constriction resistance seems to have an appreciable effect only at the highest pressure in Table 1. On the other hand, experimental heat-transfer coefficients for ethylene glycol seem to be considerably affected by the constriction resistance, especially at higher pressures. This may probably be concerned with the trend of the data points to deviate downward with increased pressure in Fig. 4.

In the present paper the nucleation site density has been assumed to be infinitely high. It must also be remembered that in the reduction of the data listed in Table 1 the condensation coefficient α appearing in the interfacial heat-transfer coefficient h_i in equation (6) was taken as unity. However, this is not theoretically necessary, but the condensation coefficient could be less than unity. Then we find that good agreements between the predictions and the experiments are obtainable if we assume that $\alpha = 0.2$ for water as well as ethylene glycol at low pressures and that $\alpha = 0.6$ for mercury. It will be easily understood from equations (6, 8) and (22) that, when $\alpha = 0.2$, ξ_1 is multiplied by a factor of 9 as compared with the values in Table 1. Open symbols in Fig. 4 represent the so-reduced data for water and for ethylene glycol at the lowest pressure.

We could alternatively assume that $\alpha = 1.0$ and seek an appropriate value of the nucleation site density to make the calculated heat-transfer coefficient agree with the experimental one. In this case D in condition (5) is considered to represent the mean spacing between the nearest neighboring sites. Then, as for water, we become aware of the unreasonable fact that the so-estimated nucleation site density decreases with decreasing the saturation temperature, with the mean spacing between sites amounting to as large as 6 μm at $T_s = 304$ K [32], nevertheless the size of the thermodynamic critical drop is of an order of a hundredth of micron and is almost independent of the saturation temperature. Thus, although there remains the possibility that the nucleation sites are so scattered, the present author is inclined to think that a more physically possible explanation of the experimentally observed behaviors of the heat-transfer coefficient is given by assuming that the condensation coefficient is less than unity.

Conclusion

Phenomena of heat transfer in dropwise condensation are characterized by four basic parameters: ξ_1, ξ_{cri}, $\xi_{\min}$ and ξ_D. The Nusselt number of dropwise condensation which is defined by equation (27) can be expressed in terms of the foregoing parameters as equation (39). This equation satisfactorily predicts the experimentally observed dependence of the heat-transfer coefficient on the departing drop size. In the limit of complete coverage of the surface by drops, the Nusselt number is expressed by equations (42) and (46) which are valid under conditions (43) and (47), respectively. At the same time equations (42) and (46) give a theoretical upper bound of the Nusselt number for any given ξ_1. From comparison between the predicted and experimental Nusselt numbers we are incited to estimate the condensation coefficient of water as well as that of ethylene glycol at around 0.2, on the assumption that the primary drop can nucleate almost everywhere on the condensing surface. If the condensation coefficient should be unity, it must instead be admitted that nucleation sites are fairly scattered.

Acknowledgment

This work was supported by the Ministry of Education of the Japanese Government through a Grant in Aid for Scientific Reaearch, Project No. 246077.

References

1 Umur, A., and Griffith, P., "Mechanism of Dropwise Condensation," ASME Journal of Heat Transfer, Vol. 87, 1965, pp. 275–282.

2 McCormick, J. L., and Westwater, J. W., "Nucleation Sites for Dropwise Condensation," *Chemical Engineering Science,* Vol. 20, 1965, pp. 1021–1036.

3 LeFevre, E. J., and Rose, J. W., "A Theory of Heat Transfer by Dropwise Condensation," *Proceedings of the 3rd International Heat Transfer Conference,* Chicago, Vol. 2, 1966, pp. 362–375.

4 Rose, J. W., and Glicksman, L. R., "Dropwise Condensation—The Distribution of Drop Sizes," *International Journal of Heat and Mass Transfer,* Vol. 16, 1973, pp. 411–425.

5 Gose, E. E., Mucciardi, A. N., and Baer, E., "Model for Dropwise Condensation on Randomly Distributed Sites," *International Journal of Heat and Mass Transfer,* Vol. 10, 1967, pp. 15–22.

6 Tanasawa, I., and Tachibana, F., "A Synthesis of the Total Process of Dropwise Condensation Using the Method of Computer Simulation" *Proceedings of the 4th International Heat Transfer Confernece,* Paris, Vol. 6, Paper No. Cs1.3, 1970.

7 Glicksman, L. R., and Hunt, A. W. Jr., "Numerical Simulation of Dropwise Condensation," *International Journal of Heat and Mass Transfer,* Vol. 15, 1972, pp. 2251–2269.

8 Tanaka, H., "A Theoretical Study of Dropwise Condensation," ASME Journal of Heat Transfer, Vol. 97, 1975, pp. 72–78.

9 Tanaka, H., "Measurements of Drop-Size Distributions During Transient Dropwise Condensation," ASME Journal of Heat Transfer, Vol. 97, 1975, pp. 341–346.

10 Nabavian, K., and Bromley, L. A., "Condensation Coefficient of Water," *Chemical Engineering Science,* Vol. 18, 1963, pp. 651–660.

11 Mikic, B. B., "On Mechanism of Dropwise Condensation," *International Journal of Heat and Mass Transfer,* Vol. 12, 1969, pp. 1311–1323.

12 Tanner, D. W., Pope, D., Potter, C. J., and West, D., "Heat Transfer in Dropwise Condensation—Part 2 Surface Chemistry," *International Journal of Heat and Mass Transfer,* Vol. 8, 1965, pp. 427–436.

13 LeFevre, E. J., and Rose, J. W., "An Experimental Study of Heat Transfer by Dropwise Condensation," *International Journal of Heat and Mass Transfer,* Vol. 8, 1965, pp. 1117–1133.

14 Citakoglu, E., and Rose, J. W., "Dropwise Condensation—Some Factors Influencing the Validity of Heat-Transfer Measurements," *International Journal of Heat and Mass Transfer,* Vol. 11, 1968, pp. 523–537.

15 Tanner, D. W., Pope, D., Potter, C. J., and West, D., "Heat Transfer in Dropwise Condensation at Low Steam Pressures in the Absence and Presence of Non-Condensable Gas," *International Journal of Heat and Mass Transfer,* Vol. 11, 1968, pp. 181–190.

16 Wilmshurst, R., and Rose, J. W., "Dropwise Condensation—Further Heat-Transfer Measurements," *Proceedings of the 4th International Heat Transfer Conference,* Paris, Vol. 6, Paper No. Cs1.4, 1970.

17 Graham, C., and Griffith, P., "Drop Size Distributions and Heat Transfer in Dropwise Condensation" *International Journal of Heat and Mass Transfer,* Vol. 16, 1973, pp. 337–346.

18 Wilmshurst, R., and Rose, J. W., "Dropwise and Filmwise Condensation of Aniline, Ethanediol and Nitrobenzene," *Proceedings of the 5th International Heat Transfer Conference,* Tokyo, Vol. 3, Paper No. Cs2.4, 1974, pp. 269–273.

19 Ivanovskii, M. N., Subbotin, V. I., and Milovanov, Yu. V., "Heat Transfer with Dropwise Condensation of Mercury Vapor," *Teploenergetika,* Vol. 14, No. 6, 1967, pp. 81–86.

20 Necmi, S., and Rose, J. W., "Heat-Transfer Measurements During Dropwise Condensation of Mercury," *International Journal of Heat and Mass Transfer,* Vol. 20, 1977, pp. 877–881.

21 Gallaugher, A. F., and Hibbert, H., "Studies on Reactions Relating to Carbohydrates and Polysaccharides, LIV The Surface Tension Constants of the Polyethylene Glycols and Their Derivatives; LV Vapor Pressures of the Polyethylene Glycols and Their Derivatives," *Journal of the American Chemical Society,* Vol. 59, 1937, pp. 2514–2525.

22 Tanasawa, I., and Ochiai, J., "Experimental Study on Dropwise Condensation," *Bulletin of the Japan Society of Mechanical Engineers,* Vol. 16, 1973, pp. 1184–1197.

23 Peterson, A. C., and Westwater, J. W., "Dropwise Condensation of Ethylene glycol," *Chemical Engineering Progress Symposium Series,* Vol. 62, No. 64, 1966, pp. 135–142.

24 Wilcox, S. J., and Rohsenow, W. M., "Film Condensation of Potassium Using Copper Condensing Block for Precise Wall-Temperature Measurement," ASME JOURNAL OF HEAT TRANSFER, Vol. 92, 1970, pp. 359–371.

25 Narusawa, U., and Springer, G. S., "Measurement of the Condensation Coefficient of Mercury by a Molecular Beam Method," ASME JOURNAL OF HEAT TRANSFER, Vol. 97, 1975, pp. 83–87.

26 Mills, A. F., and Seban, R. A., "The Condensation Coefficient of Water," *International Journal of Heat and Mass Transfer,* Vol. 10, 1967, pp. 1815–1827.

27 Bonacci, J. C., Myers, A. L., Nongbri, G., and Eagleton, L. C., "The Evaporation and Condensation Coefficient of Water, Ice and Carbon Tetrachloride," *Chemical Engineering Science,* Vol. 31, 1976, pp. 609–617.

28 Necmi, S., and Rose, J. W., "Film Condensation of Mercury," *International Journal of Heat and Mass Transfer,* Vol. 19, 1976, pp. 1245–1256.

29 Tanasawa, I., Ochiai, J., Utaka, Y., and En-ya, S., "Experimental Study on Dropwise Condensation—Effect of Departing Drop Size," *Transactions of the Japan Society of Mechanical Engineers,* Vol. 42, 1976, pp. 2846–2853.

30 Hannemann, R. J., and Mikic, B. B., "An Analysis of the Effect of Surface Thermal Conductivity on the Rate of Heat Transfer in Dropwise Condensation," *International Journal of Heat and Mass Transfer,* Vol. 19, 1976, pp. 1299–1307.

31 Hannemann, R. J., "Condensing Surface Thickness Effects in Dropwise Condensation," *International Journal of Heat and Mass Transfer,* Vol. 21, 1978, pp. 65–66.

32 Glicksman, L., Graham, C., Griffith, P., and Hunt, A., Letter to the Editor, *International Journal of Heat and Mass Transfer,* Vol. 16, 1973, p. 1822.

33 Griffith, P., and Lee, M. S., "The Effect of Surface Thermal Properties and Finish on Dropwise Condensation," *International Journal of Heat and Mass Transfer,* Vol. 10, 1967, pp. 697–707.

Appendix A

Suppose that the equilibrium region of small drops extends over an interval $[\xi', \xi'']$. Assuming expressions (30–32) in this region and choosing a size ξ such that $\xi' < \xi \ll \xi''$, almost the same argument as is given in Appendix B of [8] leads to the following expression for the effective distribution density of drops with the size ξ which is based on the area of the space that is left unoccupied by drops greater than ξ.

$$\phi(\xi; n)n(\xi) = \left\{\pi\left(\frac{1}{3-m} - \frac{1}{m-2}\right)\right\}^{-1}\xi^{-3} \tag{A1}$$

Then the second term on the right-hand side of equation (16) can be reduced for $\xi' < \xi \ll \xi''$ as

$$\begin{aligned}&\int_{\xi}^{1} 2\pi\eta\{a(\xi) + a(\eta)\}\phi(\xi; n)n(\xi)n(\eta)d\eta \\ &= \left\{\pi\left(\frac{1}{3-m} - \frac{1}{m-2}\right)\right\}^{-1}\xi^{-3}\int_{\xi}^{\xi''} 2\pi\eta\{B\xi^{-p} + B\eta^{-p}\}A\eta^{-m}d\eta \\ &= 2\left\{\frac{1}{3-m} - \frac{1}{m-2}\right\}^{-1}\left\{\frac{1}{m-2} + \frac{1}{m+p-2}\right\}AB\xi^{-(m+p+1)}\end{aligned}$$

Here, the integration from ξ'' to 1 has been neglected in deriving the first equality. It has also been presumed in deriving the second equality that $m - 2 > 0$ and $m + p - 2 > 0$. The first term on the right-hand side of equation (16) becomes

$$-\frac{\partial na}{\partial \xi} = (m + p)AB\xi^{-(m+p+1)}$$

On the other hand, the left-hand side of equation (16) as well as the last term on the right-hand side vary with ξ^{-m} and their magnitudes are surpassed by the first two terms on the right-hand side as ξ becomes small. Furthermore, the last term on the right-hand side vanishes until the outbreak of drop departure. Thus the first two terms on the right-hand side dominate in equation (16) for $\xi' < \xi \ll \xi''$ and they are in keeping with each other. Therefore we have

$$(m + p) = 2\left\{\frac{1}{3-m} - \frac{1}{m-2}\right\}^{-1}\left\{\frac{1}{m-2} + \frac{1}{m+p-2}\right\} \tag{A2}$$

If the equilibrium region of small drops is sufficiently wide, equations (34) (valid for $\xi' \ll \xi < \xi''$) and (A2) which correspond to the basic equations (17) and (16), respectively, hold between m and p. Here it is easy to show that equation (35) provides a sufficient condition for simultaneous satisfaction of equations (34) and (A2).

Here will be given another exploratory derivation of equation (35). Instantaneous volume of condensate per unit condensing area is proportional to $\hat{\xi}$ which is a kind of characteristic dimension of drop-size distribution. Resultant rate of condensation per unit area is thus expressed by a constant times $\partial\hat{\xi}/\partial\tau$. On the other hand, the integrated rate of direct condensation on drops is in proportion to the distribution density of small drops, which is now proved from equations (31) and (33) to be in proportion to $\hat{\xi}^{m-3}$ (including the submicroscopic drop range belonging to the steady distribution for microscopic drops). Thus we have

$$\frac{\partial\hat{\xi}}{\partial\tau} = C\hat{\xi}^{m-3}$$

Integrating this under the condition that $\hat{\xi} = 0$ at $\tau = 0$ results in

$$\hat{\xi} = C'\tau^{1/(4-m)}$$

In the meantime, it has been shown in Appendix C of [8] that the characteristic dimension of the universal distribution for large drop range grows with $\tau^{1/(p+1)}$. Therefore we obtain

$$\frac{1}{4-m} = \frac{1}{p+1}$$

Appendix B

Suppose the case where $e = e_0 =$ const. In the limit of complete coverage of the surface by drops, vapor condenses on the condenser surface at a constant rate, as was explained concerning equation (46). Then, a mean thickness of condensate on the surface grows linearly with time τ. On the other hand, from Appendix C of [8], the characteristic dimension of the universal distribution for large drop range has to grow with $\tau^{1/(p+1)}$. Therefore we have

$$p = 0$$

It follows from expression (30) that

$$a = \text{const} = a_0$$

in the equilibrium region of small drops. Then, the basic equation (16) is reduced, in the same manner as equation (A2) was derived, as

$$m = 2\left\{\frac{1}{3-m} - \frac{1}{m-2}\right\}^{-1}\frac{2}{m-2} \tag{A3}$$

From this equation the value of m is determined as in equation (44). Further, the basic equation (17) becomes in place of equation (34) as

$$\frac{2}{3}\left\{\frac{1}{3-m} - \frac{1}{m-2}\right\}^{-1} \times 2 = 1 - \frac{e_0}{a_0} \tag{A4}$$

Substituting for m from equation (44) into this equation yields the ratio a_0/e_0 as in equation (45).

V. Betta
Full Professor.

P. Mazzei
Assistant Professor.

V. Naso
Assistant Professor.

R. Vanoli
Assistant Professor.

Istituto di Fisica Tecnica,
Facoltà di Ingegneria dell'Università,
Piazzale Tecchio,
80125 Napoli, Italy

Further Contributions to the Study of the Leidenfrost Phenomenon

Experimental values of both the minimum wall temperatures for spheroidal state and the total vaporization times of water, n-octane and carbon tetrachloride drops are presented. A novel apparatus was used and tests were run in a wall temperature range scarcely investigated by other authors. Vaporization times are compared with correlations accounting for the diffusive evaporation and these are suggested to be applied in ranges different from those recommended by the authors.

Introduction

On the basis of the theoretical and experimental studies performed up to nearly ten years ago, one would expect to have a fairly good knowledge of the Leidenfrost phenomenon for liquid drops on a surface. Experimental values were in fair agreement with the theoretical correlations for the shape and the total vaporization time of the drops. A new interest in Leidenfrost phenomenon has recently arisen in the field of nuclear reactor safety, both in emergency shutdown operations and in the interaction between the molten nuclear fuel and the coolant [1-3]. It is therefore worth looking at the proposed models and correlations more critically and verifying their reliability and applicability in a broader range of the variables.

In this paper results from tests on water, carbon tetrachloride and n-octane drops run through a novel apparatus are presented. With this experimental technique, spheroidal state was maintained at wall temperatures considerably lower than those of other authors. Results strengthen the difference between the lowest wall temperature and the Leidenfrost temperature. The former is not a thermodynamic property of the fluid: under certain metastable experimental conditions it can be lower than the saturation temperature, its theoretical limit being the wet bulb temperature of the ambient surrounding the drop [4, 5]. The latter is the minimum temperature allowing Leidenfrost phenomenon in stable conditions and can be theoretically correlated to the thermodynamic properties of the liquid and the solid [6, 7].

Diffusion from the side and the top of the drop affects total vaporization times in nonsaturated air. As the diffusive contribution to the vaporization is greater at low wall temperatures, the applicability of the correlations from the literature has been checked.

Experimental procedure

The experimental apparatus is sketched in Fig. 1. Drops fall on the upper flat surface of a parallelepipedic copper rod made in two formats (700 × 60 × 50 mm and 700 × 100 × 10 mm). Copper was chosen because of its thermal diffusivity. The second rod was chosen smaller to reduce the starting up period before steady-state was reached. To keep drops running in its central region, the upper surface is slightly concave, nearly 400 mm radius of curvature. Both the side and the lower surfaces were carefully insulated. The rod was heated at one end by an electric resistance element connected to a Variac and cooled at the other end by either water or low boiling fluids. In the experiments maximum and minimum wall temperatures were 350 and 60°C, respectively. Surface temperatures were measured by eight 24 gauge Chromel-Alumel thermocouples inserted in the vertical midplane of the rod, at a depth of 1 mm and 100 mm spaced. The whole apparatus could be rapidly and accurately sloped up to 10 deg on the horizontal by an eccentric and some micrometer screws.

Before each run of tests the surface was smoothed with rubbing paper and then polished with gasoline. In the first series of runs the droplets were produced with a liquid jacketed thermostatic deliverer. It delivered drops at a preset temperature between the ambient and the saturation temperature of the test liquid, by assuming it to be equal to the temperature of the liquid boiling in the jacket, which was easily measured. Since tests with water [9] showed that both the minimum wall temperature was independent on the initial drop temperature and the total vaporization time was little affected by it, in the subsequent series of runs the smaller water drops and all the octane and tetrachloride drops were produced at ambient temperature by a microliter syringe which can deliver drops of volume continuously varying in the range 1 ÷ 20 μl. The mean quadratic error of the arithmetic mean was always less than ±2 percent.

The test liquids were:

- deionized water, electric resistivity in the range $8 \cdot 10^2 \div 16 \cdot 10^2$ Ωm;
- n-octane, boiling point 124 ± 1°C;
- carbon tetrachloride, boiling point 76 ± 1°C.

The needle tip of the deliverer was about 5 mm above the hottest region of the surface. While laying down the liquid droplets, the rod was kept horizontal to get those stability conditions of the drop which make the film boiling easier. Run was discarded when the drops either shattered hitting the surface or wandered and picked up dirt during the evaporation. The vaporization times for wall temperatures sufficiently higher than the saturation temperature of the test liquid were determined by keeping the drops in the hottest area of the rod. This was not possible when the wall temperatures were close to the saturation temperature since disturbances did not succeed in dying out when the surface temperature was too low. In this case the upper part of the wall was kept hot enough to permit an easy placing of the drops and then, by suitably varying the slope of the rod by the eccentric, the liquid was run towards the cooler part of the rod and stopped upon the section at the desired temperature. It took no longer than 10 s to lay down and set up the drops; this was the case of the biggest liquid drop (0.0943 cm^3) at the minimum wall temperature (130°C), whose vaporization time is nearly 360 s.

The minimum wall temperatures were evaluated moving the drops slowly down the surface and marking the section where the drop collapsed; its wall temperature was assumed to be the lowest one which would support a drop in the spheroidal state. The rolling velocity of the drops was uncontrolled since we observed from our experiments [10] that it had no effect on the minimum temperature; however this was to be expected as the vapor below the liquid flows at a velocity of some ms^{-1} while the velocity of the drops was always of some cms^{-1}. The initial volumes of water, octane and carbon tet-

---

Contributed by the Heat Transfer Division for publication in the JOURNAL OF HEAT TRANSFER. Manuscript received by the Heat Transfer Division June 21, 1978.

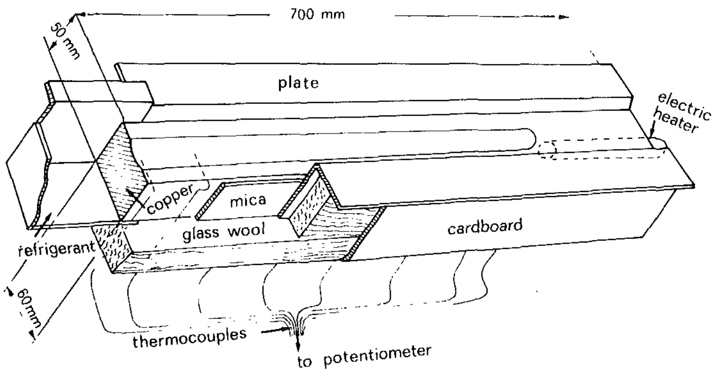

Fig. 1 Sketch of the experimental apparatus

rachloride drops were respectively 0.0149, 0.0090 and 0.0050 cm^3. Only one value was used for each test fluid since we ascertained experimentally [10] that it had no effect on the minimum wall temperatures for the very small drops of our tests whereas for large droplets the lowest wall temperature depends on the drop volume. One hundred tests were performed for each fluid; the uncertainty of the test was ±1°C.

The total vaporization times were computed after the first liquid drop hit the wall; each vaporization time is the average of ten tests. The mean quadratic error of the arithmetic mean was always less than ±3 percent.

Care was taken to minimize air currents in the laboratory. During the tests dry and wet bulb temperatures were 25 ± 1 and 18 ± 1°C, respectively.

Experimental Results

Minimum wall temperatures are shown in Figs. 2–4. They are 109 ± 3°C for water, 159 ± 3°C for octane, 117 ± 4°C for carbon tetrachloride.

Total vaporization times for various initial volumes of the drops, as a function of the wall temperature, are shown in Figs. 5–7 for water, octane and carbon tetrachloride. The curves were obtained using the standard technique of a least-squares method to fit a second-order polynomial.

Discussion of Results

The minimum wall temperatures from our experiments are remarkably lower than those obtained in systematic studies by other authors. Furthermore under any conditions different from those previously described—for instance when water drops vaporized in a nearly saturated atmosphere—water was supported in spheroidal state by wall temperatures lower than saturation temperature. This finding, observed and interpreted by other authors as well [4, 5], confirms that the lowest wall temperature, under the same conditions of the hot wall, is strongly dependent on the experimental technique. Therefore minimum wall temperatures determined by different techniques must be considered the lower theoretical limit of the surface temperature which would support a drop in spheroidal state. The actual lower limit is higher and the uncertainty in its evaluation raises some difficulties in predicting the heat flux whenever the Leidenfrost phenomenon is present either in normal or in emergency conditions. Hence one of the limits to the use of film boiling. The total vaporization times for water (Fig. 5) are in a range of wall temperatures scarcely studied; other authors have generally made their experiments with water at wall temperatures not lower than 300°C. Comparison at T_w = 300°C between data from Fig. 5 and from [11, 12] shows deviations within ±10 percent. A similar agreement also exists between the data from Figs. 6 and 7 and those reported by the same authors. This good agreement among data for very different liquids confirms the validity of our experimental technique for the evaluation of total vaporization times.

Vaporization times shown in Figs. 5–7 were evaluated in nonsaturated air. They are lower than those in saturated air, due to the diffusion from the side and the top of the drop. The less ΔT and V are, the higher the diffusive contribution that can be evaluated, according to Schoessow and Baumeister [13], by the dimensionless number

$$N_{Dc} = N^*/V^{*1/4} \tag{1}$$

which is the ratio between the vapor flow rates from the drop by diffusion and by film boiling.

When diffusion is not the prevailing phenomenon, that is for $N_{Dc} < 2$ [15], the theory of Baumeister and Schoessow [14], briefly presented in Appendix, can be applied. In the range of the dimensionless volumes $0.8 < V^* \leq 155$ they recommended the dimensionless cor-

Nomenclature

A_d = area of drop in which diffusion occurs
A_{fb} = area of drop in which film boiling occurs
c_p = specific heat at constant pressure of vapor
D = diffusion coefficient
g = acceleration of gravity
G_r = dimensionless parameter, $\rho_v(\rho_\ell - \rho_v)gL^3/\mu^2$
h_r = radiative heat transfer coefficient
h_r^* = dimensionless radiative heat transfer coefficient defined by equation (A4)
H = dimensionless parameter, $\lambda/c_p\Delta T$
H^* = dimensionless parameter, $\lambda^*/c_p\Delta T$
k = thermal conductivity of vapor
L = characteristic length, $[\sigma/g(\rho_\ell - \rho_v)]^{1/2}$
M = molecular mass
N^* = dimensionless diffusion parameter defined by equation (A3)
N_{DC} = dimensionless parameter defined by equation (1)
N_{Pr} = Prandtl number, $c_p\mu/k$
N_{Sc} = modified Schmidt number, $\mu/D(Mp_s/RT_s)$
p = pressure
r_0 = droplet radius
R = gas constant
t = vaporization time of the drop
t^* = dimensionless vaporization time defined by equation (A2)
T = temperature
V = drop volume
V^* = dimensionless drop volume defined by equation (A1)
V^+ = dimensionless drop pseudo volume defined by equations (A5), (A6) and (A7)
X = dimensionless parameter, $k\Delta T/\rho_v D\lambda$
Y = dimensionless parameter, $0.0265(t/r_0)(gD)^{1/3}(\rho_\ell/\rho_v)^{-0.407}(c_p\mu/k)^{0.874}(\mu/\rho_v D)^{-0.714}$
$\Delta T = T_w - T_s$
λ = latent heat of vaporization
λ^* = modified latent heat of vaporization, $\lambda(1 + 7c_p\Delta T/20\lambda)^{-3}$
μ = viscosity of vapor
ρ = density
σ = surface tension

Subscripts

ℓ = liquid
s = evaluated at saturation conditions
v = vapor
w = wall

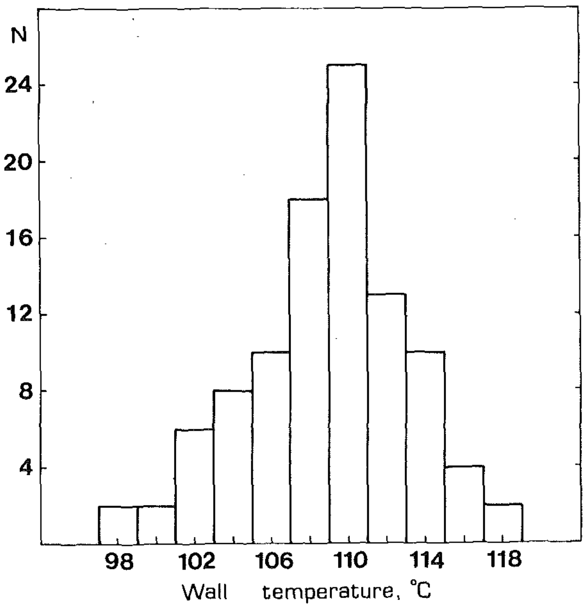

Fig. 2 Water minimum wall temperature distribution

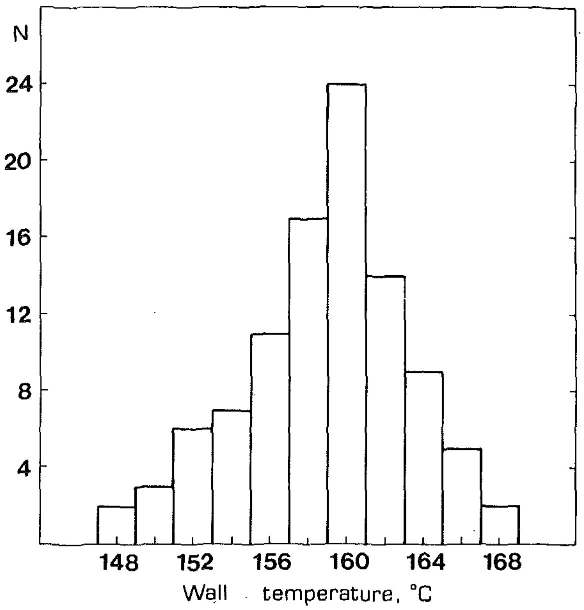

Fig. 3 Octane minimum wall temperature distribution

relation

$$t^* = 2.23\ V^{+1/3} - 0.97 \tag{2}$$

The same authors verified equation (2) only for $V^* > 9$ and then suggested, for $V^* < 0.8$, the numerical correlation by Gottfried, et al. [11]. This is based on a model different from that of Baumeister and Schoessow in the two assumptions:

- spherical drop;
- radiative heat transfer also from the top of the drop with constant emittance (0.96) of the liquid.

The authors determined by a theoretical analysis the variables affecting the total vaporization time and combined them into dimensionless groups. Finally they correlated experimental data by the equation:

$$t(g/r_0)^{1/2} = 37.8\ (k\Delta T/\rho_v D\lambda)^{-0.735}(\rho_\ell/\rho_v)^{0.407} \times (\mu c_p/k)^{-0.874}(\mu/\rho_v D)^{0.174}[D/(g r_0^3)^{1/2}]^{-1/3} \tag{3}$$

for $0.10 < k\Delta T/\rho_v D\lambda < 5.0$ and $300 < \rho_\ell/\rho_v < 4000$.

In Figs. 8 and 9 data for water and carbon tetrachloride from Figs. 5 and 7 have been compared with equations (2) and (3). Data for n-octane have not been taken into account since they would exhibit an anomalous behavior, probably due to thermal cracking [11]. The best agreement is with the theory of Gottfried for $V^* < 3$ and with the theory of Baumeister and Schoessow for $V^* > 3$.

Fig. 8 shows deviations less than ±15 percent for values of the abscissa greater than 0.03 whereas at lower values experimental data are not satisfactorily correlated by the theory. Anyway the range of applicability of this theory seems to be larger than that suggested by the authors on the basis of their experiments ($X > 0.10$). In Fig. 6 deviations between experimental data and theory are always less than ±15 percent.

Contrary to the suggestion of Baumeister and Schoessow, data for $V^* < 3$ disagree with their theory. However it should be noted that they show no experimental data in this range of V^* and simply modify by N^* the former theory presented in [8]. Vice versa, carbon tetrachloride data for $V^* = 2.9$ are in good agreement with both the theories.

Appendix

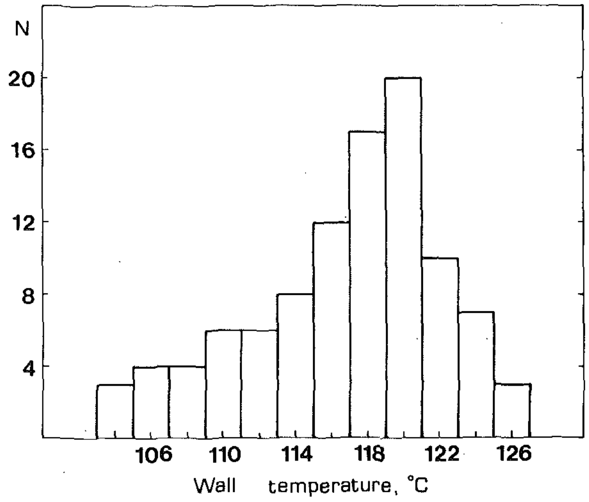

Fig. 4 Carbon tetrachloride minimum wall temperature distribution

Baumeister and Schoessow [14] apply the equations of continuity, momentum and energy to a drop in film boiling with diffusive and radiative contributions, modifying a previous theory of Baumeister, et al. [8]. A closed form solution for the total vaporization times can be obtained with these assumptions:

- disk shaped drop;
- heat transfer to the drop by conduction across the vapor film in creeping laminar flow and by radiation to the bottom of the drop;
- evaporation by diffusive vaporization from the top of the drop and by film boiling from the bottom;
- geometric parameters of the drop correlated by three simple power laws in definite ranges of volumes.

Through the definition of the basic dimensionless quantities:

$$V^* = V/[\sigma/(\rho_\ell - \rho_v)g]^{3/2} \tag{A1}$$

$$t^* = t/\lambda\rho_\ell[\mu L^5/k^3\lambda^* g(\rho_\ell - \rho_v)\rho_v\Delta T^3]^{1/4} \tag{A2}$$

$$N^* = 1.47(A_d/A_{fb})(H/N_{Sc})(N^3{}_{Pr}/G_r H^*)^{1/4} \tag{A3}$$

$$h^* = h_r/[k^3\lambda^*(\rho_\ell - \rho_v)\rho_v g/\Delta T\mu L]^{1/4} \tag{A4}$$

the authors correlate the dimensionless vaporization time, t^*, to a dimensionless pseudo volume V^+:
for $V^* \leq 0.8$

$$V^+ = (V^{*5/12} - 0.624\,N^* V^{*1/6} - 0.142 h_r^* V^{*1/2})^{12/5} \tag{A5}$$

$$t^* = 1.205\ V^{+5/12}$$

for $0.8 < V^* \leq 155$

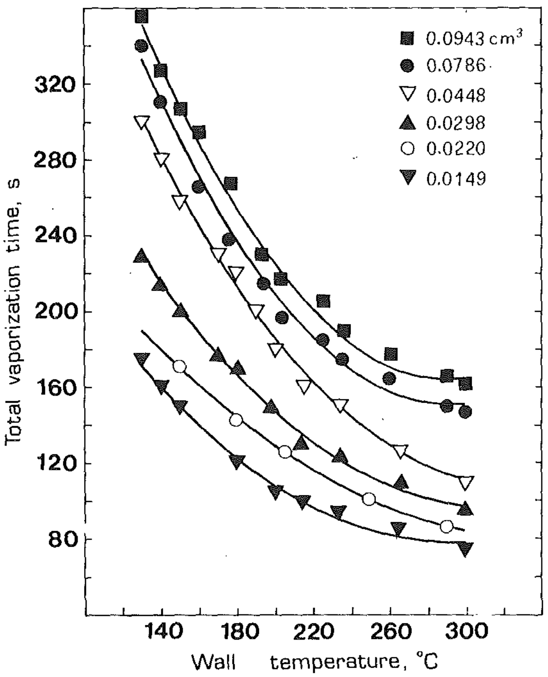

Fig. 5 Total vaporization time for water drops as a function of the wall temperature for various initial volumes

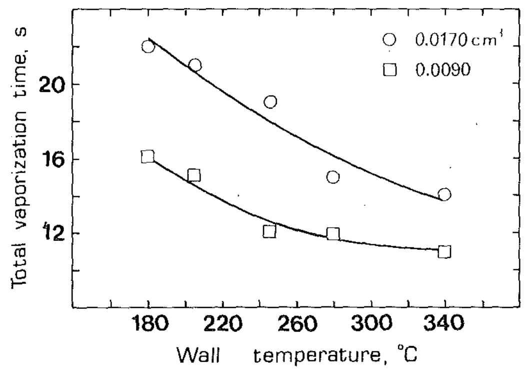

Fig. 6 Total vaporization time for octane drops as a function of the wall temperature for various initial volumes

$$V^+ = (V^{*1/3} - 1.345\,N^* V^{*1/12} + 0.995\,N^* - 0.465\,h_r^* V^{*1/2} + 0.345\,h_r^*)^3$$

$$t^* = 2.23\,V^{+1/3} - 0.97 \qquad \text{(A6)}$$

for $155 < V^*$

$$V^+ = [V^{*1/4} + 0.0625\,N^* \ln (V^*/155) + 2.29\,h_r^* V^{*1/2} - 0.524\,N^* - 32.3\,h_r^*]^4$$

$$t^* = 4.52\,V^{+1/4} - 5 \qquad \text{(A7)}$$

When diffusion and radiation are negligible ($N^* \rightarrow 0$ and $h_r{}^* \rightarrow 0$), the pseudo volume becomes equal to the actual volume V^* and equations (A5, A6) and (A7) become equal to those derived in [8].

Acknowledgment

This research was sponsored by a contract from the Consiglio Nazionale delle Ricerche.

References

1 Witte, L. C. and Cox, J. E., "Thermal Explosion Hazards," *Advances in Nuclear Science and Technology*, Academic Press, New York, Vol. 7, 1973, pp. 329–364.

2 Zyszkowski, W., "On the Transplosion Phenomenon and the Leidenfrost Temperature for the Molten Copper-Water Thermal Interaction," *International Journal of Heat and Mass Transfer*, Vol. 19, 1976, pp. 625–633.

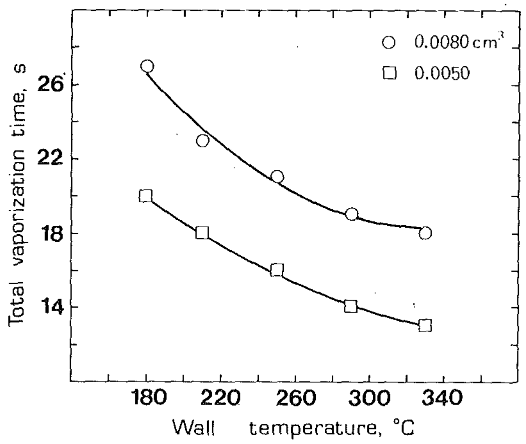

Fig. 7 Total vaporization time for carbon tetrachloride as a function of the wall temperature for various initial volumes

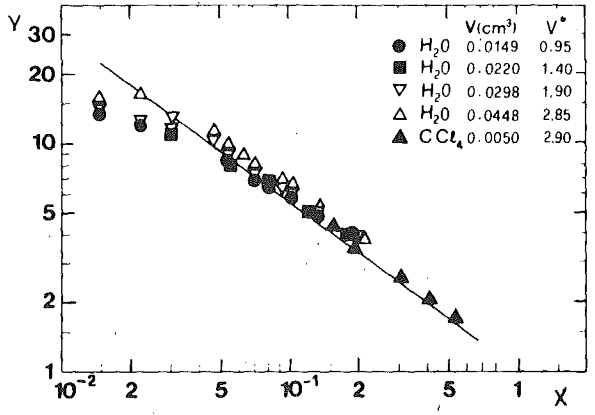

Fig. 8 Comparison of experimental data with the theory of Gottfried, et al. [8]

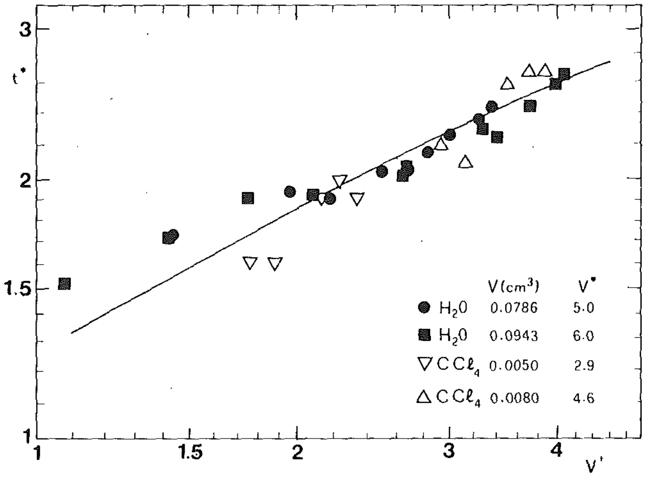

Fig. 9 Comparison of experimental data with the theory of Baumeister and Schoessow [5]

3 Hall, W. B., "Heat Transfer Problems in Nuclear Reactor Safety," *Heat and Fluid Flow*, Vol. 6, 1976, pp. 69–78.

4 Baumeister, K. J., Hendricks, R. C. and Hamill, T. D., "Metastable Leidenfrost States," NASA TN D-3226, 1966.

5 Wachters, L. H. J., Bonne, H. and Van Nouhuis, H. J., "The Heat Transfer from a Hot Horizontal Plate to Sessile Water Drops in the Spheroidal State," *Chem. Eng. Science*, Vol. 21, 1966, pp. 923–936.

6 Hsu, Y. Y., "A Review on Film Boiling," NASA TM X-52837, 1970.

7 Baumeister, K. J. and Simon, F. F. "Leidenfrost Temperature—Its Correlation for Liquid Metals, Cryogens, Hydrocarbons and Water," ASME JOURNAL OF HEAT TRANSFER, Vol. 95, 1973, pp. 166–173.

8 Baumeister, K. J., Hamill, T. D. and Schoessow, G. J., "A Generalized Correlation of Vaporization Times of Drops in Film Boiling on a Flat Plate," NASA TM X-52177, 1966.

9 Betta, V. and Naso, V., "Fenomeno di Leidenfrost: tempi di vaporizzazione e minima temperatura di esistenza," *Il Calore*, No. 4, 1972, pp. 1–5.

10 Betta, V., "Indagine sperimentale sulla temperatura di Leidenfrost," presented at XXIV Congresso ATI, Bari, 1969, also published in *Ricerche di Termotecnica*, Vol. 20, 1971, pp. 24–29.

11 Gottfried, B. S., Lee, C. J. and Bell, K. J., "The Leidenfrost Phenomenon: Film Boiling of Liquid Droplets on a Flat Plate," *International Journal of Heat and Mass Transfer*, Vol. 9, 1976, pp. 1167–1186.

12 Patel, B. M. and Bell, K. J., "The Leidenfrost Phenomenon for Extended Liquid Masses," *Chem. Eng. Progr. Symp. Ser.*, Vol. 62, No. 64, 1966, pp. 62–71.

13 Schoessow, G. J. and Baumeister, K. J., "Mass Diffusivity Effects on Droplets in Film Boiling," AIChE Symp. Ser., Vol. 68, No. 118, 1972, pp. 156–161.

14 Baumeister, K. J. and Schoessow, G. J., "Diffusive and Radiative Effects on Vaporization Times of Drops in Film Boiling," AIChE Symp. Ser., Vol. 69, No. 131, 1973, pp. 10–17.

15 Baumeister, K. J., Schoessow, G. J. and Chmielewski, C. E., "Film Boiling of Mercury Droplets," *The Canadian Journal of Chemical Engineering*, Vol. 55, 1977, pp. 521–526.

Homogeneous Vapor Nucleation and Superheat Limits of Liquid Mixtures[1]

E. L. Pinnes[2]
W. K. Mueller
Department of Mechanical and Aerospace Engineering,
Polytechnic Institute of New York,
Brooklyn, NY 11201

Two features distinguish vapor nucleation in multicomponent liquids from the single component case. Both result from the unequal volatilities of the species. One is that the vapor phase may contain several components; the other is that nucleus formation alters the composition of the nearby liquid. These two features are incorporated into the classical theory of homogeneous nucleation to yield a general theory applicable to multicomponent liquids. The theory is applied to binary hydrocarbon mixtures by using an equation of state extrapolated into the metastable region. Superheat limits thus calculated are compared with published experimental results.

Introduction

Homogeneous nucleation, the spontaneous formation of vapor within the body of a metastable liquid, plays a fundamental role in the physics of phase transitions. It has also been specified as the mechanism of vapor explosions that follow intimate contact of a hot with a cold liquid.

The classical theory of homogeneous nucleation in pure liquids was established decades ago by Becker, Doering, Volmer, Frenkel, and Zeldovich. Random thermal agitation on the molecular scale causes microscopic vapor embryos to appear. A certain size embryo can exist in unstable equilibrium with the surrounding liquid. An embryo of this size is known as a nucleus. If random processes cause a nucleus to grow slightly larger than the equilibrium size, the transition from liquid to vapor continues very rapidly (often accompanied by a shock wave).

The onset of homogeneous nucleation is determined by the rate of appearance of nuclei per unit volume, J, as determined from the classical rate equation $J = B \exp(-W/kT)$, where B is a pre-exponential factor, k is Boltzmann's constant, and T is the absolute temperature. The energy of formation, W, is related to the surface tension, σ, at the vapor-liquid interface and the pressure difference between the nucleus and the surrounding liquid by $W = 16\pi\sigma^3/3(P^V - P^L)^2$. This energy is the barrier which must be overcome for vaporization to proceed. The fundamental problem in analyzing the nucleation process is to obtain a thermodynamic description of a nucleus, by solving the conditions of thermal, mechanical, and chemical equilibrium between the vapor and its surrounding liquid. With this description both W and J may be computed.

When nucleation occurs in a multicomponent liquid, there are two effects which are not present in pure liquids. Both effects are the result of differing volatility of the species. First, the nucleus is, in general, a mixture of chemical species with a composition different from the composition of the liquid surrounding it. Therefore the conditions of phase equilibrium must be extended to include each component. Second, the nucleus formation may alter the composition of the liquid in its immediate vicinity. This occurs because volatile components are preferentially vaporized, and because the mobility of molecules in the liquid phase is limited (in contrast with the case of condensation of a metastable vapor, wherein the molecules of the parent phase are highly mobile).

The purpose of the present paper is to extend the classical theory of homogeneous nucleation to include both these effects.

Review of Literature

Among the first work on homogeneous nucleation in multicomponent systems is that of Reiss, which dealt with condensation of a liquid nucleus in a supersaturated vapor [1, 2]. Reiss focused on the composition dependence of embryo growth. He derived an expression for B applicable to binary systems, but in experimental work found that the effect of B on predicted metastable limits was small.

Ward, et al. [3] considered nucleation in liquids containing dissolved gases. Noting that the calculated metastable limit is sensitive to W but insensitive to B, their approach was to focus attention on the vapor nucleus state, and to compute the effect that the dissolved gas had on the nucleus pressure, and hence on W and J. They neglected the effect of local liquid phase compositional changes near the nucleus. This proved controversial, as seen in the published discussion, wherein several individuals claimed that diffusion in the liquid is so slow that the gas could hardly enter into the nucleus at all! Further theoretical and experimental papers regarding liquids with dissolved gases have been presented by Forest and Ward [4–5] and Mori, et al. [6]. Later, Hijikata, et al. [7] used a novel experimental technique to verify that in some cases the rate of diffusion of gas molecules governs the vapor nucleation process.

The theory of Blander, et al. [8–11] considered the limiting case when only one component is volatile in a binary mixture. They assumed the growth of such a nucleus was governed by diffusion of the volatile constituent into the nucleus, and that its effect on J was to replace B by $B' = B/(1 + \delta_D)$. Although they recognize the importance of diffusion control on the *rate* of nucleus formation, they completely ignore its effect on the nucleus *state*. Thus W is assumed to be unaffected. As has been seen J is sensitive to W but insensitive to B; hence their correction term has negligible effect on predicted metastable limits.

Mou and Lovett [12], in a study of the nucleation of the separation of a mixture of liquids, observe that when a nucleus is formed in finite time, an inhomogeneity in the bulk phase around it is inevitable. A layer around the nucleus is partially depleted of the species that preferentially diffuse into the nucleus, and beyond a certain cutoff radius, the bulk phase is unaffected.

Physical Process of Vapor Embryo Formation

The first appearance of vapor molecules in a metastable liquid is the result of thermal fluctuations in the liquid phase. Vapor embryos form, grow, or collapse by a random series of single-molecule condensations and vaporizations [13].

The kinetics of embryo growth will be treated by considering the condensation and vaporization processes at the phase interface as independent of each other. Ideal behavior will be used to estimate rates. For condensation, assume that each vapor molecule that strikes the liquid will condense, so that

$$\dot{c}_i'' = P_i{}^V (2\pi k T m_i)^{-1/2} \tag{1}$$

where $\dot{c}_i''$ is the number rate of molecules condensing per unit area, $P_i{}^V$ is the partial pressure of i in the vapor phase, and m_i is the mass of a single molecule. The rate of liquid molecules vaporizing into the embryo is governed by the fugacity of each component in the liquid phase:

$$\dot{v}_i'' = f_i{}^L (2\pi k T m_i)^{-1/2} \tag{2}$$

---

[1] Taken from a dissertation submitted in partial fulfillment of the requirements for the Ph.D at Polytechnic Institute of New York.

[2] Now at Bell Telephone Laboratories, Whippany, New Jersey 07981.

Contributed by the Heat Transfer Division for publication in the JOURNAL OF HEAT TRANSFER. Manuscript received by the Heat Transfer Division January 19, 1979.

where $\dot{v}_i''$ is the number rate per unit area of single-molecule vaporization events of component i and f_i^L is the fugacity. For the nucleus, when $\dot{v}_i'' = \dot{c}_i''$ and a dynamic equilibrium exists, equations (1) and (2) gives

$$f_i^L = P_{ie}^V \tag{3}$$

where the subscript e denotes equilibrium conditions. The partial pressures can be written as $P_i^V = y_iP^V$ and $P_{ie}^V = y_{ie}P_e^V$, where y is mole fraction, and then (1–3) are combined to yield:

$$\frac{\dot{v}_i''}{\dot{c}_i''} = \frac{y_{ie}P_e^V}{y_iP^V} \tag{4}$$

It is apparent that condensation will be more rapid for the species that are over-represented in the vapor phase ($y_i > y_{ie}$). For species that are instantaneously under-represented ($y_i < y_{ie}$), condensation slows down relative to vaporization. The conditions $\Sigma_{i=1}^k y_i = \Sigma_{i=1}^k y_{ie} = 1$ require that if $y_i > y_{ie}$ for one or more components, then $y_i < y_{ie}$ for at least one other one. The result of these physical processes is that the composition always tends toward $y_i = y_{ie}$. Growth of an embryo whose composition is different from the equilibrium composition is much less likely than growth of one with the equilibrium composition. The same conclusion was reached by different means by Reiss [1] for homogeneous condensation and by Moore [14] for heterogeneous nucleation. The important new feature in the present treatment is that a local change in liquid composition (and corresponding change in f_i^L) causes a change in y_{ie}. The physical effect is that the growing embryo always tends toward equilibrium with the *adjacent* liquid. Liquid-phase depletion of the volatile species in the neighborhood of the embryo modifies the equilibrium conditions the nucleus must attain.

Local Liquid Phase Compositional Changes in the Neighborhood of a Nucleus

At this point an approximate model will be developed for estimating the local liquid-phase composition changes caused by vapor nucleus formation. Because of the random nature of nucleus formation, and the microscopically small scale of the process, the macroscopic diffusion equation is unsuitable for analysis of this phenomenon. In the subnuclear size range, vapor growth opposes chemical potential gradients, and a Fickian type analysis indicates that embryos re-condense, which in fact most will do. For analyzing those which do reach the nucleus state, an approximate analysis will be used here.

The molecules which form the nucleus are not drawn uniformly from throughout the bulk of the liquid. Because of the limited mobility in the liquid phase, all of the n_N molecules which actually form the nucleus must have been in that neighborhood during the period of time the nucleus is forming. This will be modeled by assuming that there is a "pool" of liquid molecules from which the vapor molecules came.

A means of estimating the size of the pool is based on the "net time of formation," t_f. It is a concept that arises in the following manner: Consider a vapor embryo located in a liquid. Vaporization of a molecule alters the local mole fractions of all constituents in the nearby liquid, and initiates diffusion within the liquid phase. Condensation of a molecule of the same species returns the mole fractions to their original values, and initiates the reverse diffusion. The net effect of the two processes is nil, except for a disturbance of spherical symmetry. If a larger number of events is considered, it can be expected that on the average, deviations from spherical symmetry will be cancelled out. It is justifiable to say that molecules condensing cancel out all relevant effects caused by the same number having vaporized at some previous time. The only *net* diffusion takes place during the time periods corresponding to the n_N unbalanced vaporizations. The time taken to accomplish the n_N vaporizations necessary for the formation of the nucleus is defined as the "net time of formation," and symbolized by t_f. Each nucleus will have the same t_f, whether its formation is a result of n_N consecutive vaporizations with no intervening condensations, or a result of a "random walk" of one million steps (the latter being more likely!).

An estimate for t_f has been derived by Pinnes and Mueller [15] from equation (2) by considering the vaporization rate across the interface of the growing embryo. Its value is

$$t_f = \frac{3n_N(2\pi kTm_{\max})^{1/2}}{4\pi r^2P^V} \tag{5}$$

where $m_{\max}$ is the molecular mass of the heaviest component, excluding nonvolatile ones. (Since all further discussion applies to the nucleus only, the subscript e will not be repeated each time.)

The pool of molecules includes all within the nucleus, the one-molecule thick interfacial liquid layer, and those molecules in the surrounding liquid spherical annulus which are near enough to have been "in communication" with the developing nucleus. Denoting the mean velocity of molecules by V_m, then the boundary of the pool extends V_mt_f beyond the interfacial layer. The composition of the liquid within the outer boundary is modeled as uniformly modified by the unequal vaporization of the k species; the liquid outside this boundary is unaffected.

An expression for the mean velocity is given by Reiss [16] as

$$V_m = 6D/d \tag{6}$$

where D is the diffusivity, and d is the average molecular spacing.

The number of molecules in the nucleus is

$$n_N = (4\pi/3)r^3(\rho^VN_0/M^V) \tag{7}$$

and the total number of molecules in the pool is

$$n_T = n_N + (4\pi/3)[(r + d + V_mt_f)^3 - r^3](\rho^LN_0/M^L) \tag{8}$$

where ρ is the density, N_0 is Avogadro's constant, and M is the molar mass.

Of the n_T molecules, x_in_T are of species i. The number of i molecules vaporized is y_in_N, leaving $x_in_T - y_in_N$ in the liquid phase. The total number of molecules remaining in the liquid phase is $n_T - n_N$.

Nomenclature

B = pre-exponential factor in rate equation
$\dot{c}''$ = rate of condensation, molecules per time per area
D = diffusivity
d = average intermolecular spacing
f = fugacity
J = rate of appearance of nuclei per time per volume
k = Boltzmann's constant; number of components
M = molecular weight
m = mass of molecule
N_0 = Avogadro's constant
n_N = number of molecules in nucleus
n_T = number of molecules from which nucleus is drawn
P = pressure
Pc = parachor
r = radius
s = ratio $n_N/(n_T - n_N)$
T = temperature
T_{su} = superheat limit
t_f = net time of formation
$\dot{v}''$ = rate of vaporization, molecules per time per area
V_m = mean drift velocity of molecules in liquid phase
W = energy of formation of nucleus
x = liquid-phase mole fraction
y = vapor-phase mole fraction
μ = chemical potential
ρ = density
σ = surface tension

Subscripts

i = component
e = nucleus vapor properties (unstable equilibrium)
m = modified liquid properties in neighborhood of nucleus

Superscripts

L = liquid phase
V = vapor phase

Therefore the liquid near the nucleus has *modified* mole fractions, x_{im}, whose values are

$$x_{im} = \frac{x_i n_T - y_i n_N}{n_T - n_N}$$
$$= x_i + \frac{n_N(x_i - y_i)}{n_T - n_N} = x_i + s(x_i - y_i) \qquad (9)$$

Under the special condition $y_i = x_i$ for all i, $x_{im} = x_i$, since the liquid mole fractions change only as a result of unequal volatilities of the components. The ratio $n_N/(n_T - n_N)$, which is the ratio of vaporized to unvaporized molecules in the pool, is given the symbol s.

Equilibrium Conditions of a Nucleus in a Multi-Component Liquid

What are the physical consequences of this compositional modification? A nucleus will be surrounded not by liquid of the bulk composition, but by the remainder (unvaporized molecules) of its pool. In general, the properties of the nearby liquid will have been changed from their bulk values. The extent to which they do so cannot be determined a priori, so they are considered as modifications of the bulk values, and denoted by the subscript m. It has been shown above that x_i is replaced by a modified value x_{im}. Because chemical potential depends on mole fraction, it too must be replaced by the modified values $\mu_{im}{}^L$, $i = 1, \ldots k$.

It is important to note that there is interdependence between the kinetics and thermodynamics of the nucleus formation process. Consider the problem of finding the state of a nucleus in a metastable liquid of temperature T^L, pressure P^L, and mole fractions x_i, $i = 1, \ldots k$. The nucleus must be in unstable equilibrium with the adjacent liquid, while the composition of the adjacent liquid must be consistent with that nucleus having formed. The conditions that must be satisfied simultaneously are

$$T^V = T^L \qquad (10)$$

$$P^V = P^L + 2\sigma/r \qquad (11)$$

$$\mu_i{}^V(y_i) = \mu_{im}{}^L(x_{im}) \qquad i = 1, \ldots k \qquad (12)$$

$$x_{im} = x_i + s(x_i - y_i) \qquad i = 1, \ldots k \qquad (13)$$

To obtain a solution, one needs thermodynamic information for P and μ, and for the surface tension. Equation (13) cannot be decoupled, because s depends on n_N and n_T, which are related to r and P^V through equation (5). Therefore an iterative solution is required.

Superheat Limits of Binary Hydrocarbon Mixtures

To apply the theory to real liquids, it is necessary to be able to evaluate thermodynamic properties of both phases. The Benedict-Webb-Rubin equation of state is used for this purpose. It provides algebraic relations for pressure and chemical potential of both phases. The eight empirical coefficients for each compound were obtained from recent studies by Bishnoi, et al. [17]. They were extended to mixtures by applying the algebraic weighting formulas known as the B-W-R mixing rules [18].

An algebraic expression is also needed for the surface tension at the interface between a multicomponent liquid and its vapor. The usual method of basing the mixture surface tension on the surface tension of the pure constituents cannot be used, because we are frequently concerned with a mixture whose temperature exceeds the cirtical point of one constituent. The parachor equation does not have this drawback. This equation, originally developed by Bachinskii [19] and Macleod [20] and later extended to mixtures by Weinaug and Katz [21] related the surface tension directly to the density and composition of the adjacent liquid and vapor phases by use of the parachor, Pc:

$$\sigma^{1/4} = \frac{\rho^L}{M^L} \sum_{i=1}^{k} [(Pc)_i x_i] - \frac{\rho^V}{M^V} \sum_{i=1}^{k} [(Pc)_i y_i] \qquad (14)$$

Substituting the B-W-R and parachor equations into (10–12), and using (5–8) for s in (13), yields a complete set of equations for nucleus equilibrium conditions. Once the nucleus state is known, one can compute $W = 16\pi\sigma^3/3(P^V - P^L)^2$, and $J = B \exp(-W/kT)$. A numerical method for the solution has been presented by Pinnes [22].

The value of J which defines the superheat limit, T_{su}, is not a precise number. But $J = 10^{10}$ nuclei/(m^3·s) is typical of published experimental results, which are mostly obtained by the "buoyant drop" method. Using Skripov's value of $B = 7 \times 10^{36}\, m^{-3} s^{-1}$ [23] with this value of J, T_{su} is the temperature at which the Gibbs number, $Gb = W/kT$, has a value of 61.8.

Since the liquid is in a metastable state, its properties lie along one branch of the S-curve of the P-v-T relation. This amounts to an extrapolation procedure, since the curve is empirically based on stable states only. Since experimental studies by Skripov, et al. [23–24] have shown that no abrupt changes in P-v-T behavior take place at the boundary between stable and metastable regions, such an extrapolation is reasonable, but of course its accuracy cannot be guaranteed in advance. For this reason, an indirect test of the procedure was made by calculating the superheat limits of ten pure alkanes.

Results are presented in Table 1. Experimental values are taken from the compilation of Blander and Katz [9] and are shown for comparison. The discrepancy between the calculated and experimental values was large only for ethane. (This is probably due to the B-W-R coefficients, which for ethane were optimized on a temperature range that lies above the temperature used in the calculation.) For the other eight compounds, the discrepancy had a maximum of 3.7°C, an average magnitude of 1.5°C, and an algebraic average of −0.4°C. The small value of algebraic average indicates that the errors in the present method are not appreciably systematic.

Proceeding to alkane mixtures, results for two binary systems of components of similar volatility are presented: propane/isobutane and propane/n-butane. Plots of the superheat limit at normal atmospheric pressure are shown as functions of composition in Fig. 1. Each curve is based on calculations at mole fraction multiples of 0.1. A linear correction is applied to correct for the discrepancies encountered in Table 1, i.e., to remove the pure-component error from the mixture calculations.

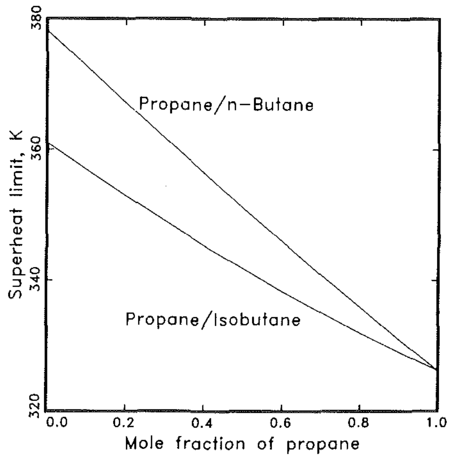

Fig. 1 **Calculated superheat limit at 101 kPa versus composition for the mixtures propane/normal butane and propane/isobutane**

Table 1 Superheat limits of pure alkane hydrocarbons at 101 kPa.

Compound	Calculated Superheat Limit, K	Experimental Superheat Limit, K [9]	Difference
Methane	167.5	—	—
Ethane	263.1	269.2	−6.1
Propane	324.7	326.2	−1.5
Normal Butane	377.7	378.2	−0.5
Isobutane	359.0	361.0	−2.0
Normal Pentane	422.2	421.0	+1.2
Isopentane	408.5	412.2	−3.7
Normal Hexane	459.0	457.2	+1.8
Normal Heptane	488.4	487.2	+1.2
Normal Octane	513.0	513.0	0.0

Experimental data for these systems were obtained by Blander, et al. [9, 25]. In each case, the superheat limit was essentially linear between the endpoints, with an approximate tolerance of ±1°C.

Systems of similar volatility are, in a sense, transitional because they exhibit some of the features of multicomponent mixtures but suppress others. Specifically, the effect of local liquid-phase concentration changes is negligible, as can be seen from equation (9). If each $y_i \approx x_i$, then $x_{im} \approx x_i$, and the liquid in the vicinity of the nucleus is close to the bulk composition. To observe the effect of local composition changes, we now consider systems with a greater difference in volatility. The systems ethane/propane, ethane/n-butane and methane/n-butane are chosen.

The superheat limit at atmospheric pressure is plotted in Figs. 2 and 3. Two curves are shown for each system. The solid curve is the calculated mixture superheat limit. The dashed curve is the superheat limit that would be calculated by neglecting the depletion effect, i.e., by using $s = 0$ in each case. The difference between the two curves has a maximum somewhere near midrange, and vanishes at each endpoint. For ethane/propane, the difference has a maximum of 1.3°C, for ethane/n-butane its maximum is 4.6°C, and for methane/n-butane it is 21.7°C. The magnitude of this difference is a function of the relative volatility of the components. In equation (9), the physical value of s for these systems is always of the order of 0.1, so the degree of local liquid modification depends mainly upon the difference between y_i and x_i.

Published experimental data by Porteous and Blander are available for two of the systems and are shown in Fig. 2 [25]. The experimental superheat limit for each composition tested actually consisted of a range, which is shown as a vertical bar. The observed scatter was severe in some cases; at 35 percent ethane/65 percent n-butane the observed superheat limit spanned a full 15°C! Porteous and Blander offer three candidate explanations for this large scatter. One is that the superheat limit is less sharply defined for mixtures. This would occur if $-(\partial Gb/\partial T)_{x,p^L}$ were much lower for mixtures than for pure liquids, for then the transition region in which J changes from a negligible value to its limiting value would comprise a broader range of temperatures. They were unable to confirm or disprove this hypothesis; however the present quantitative method provides a means of doing so. For the two systems in question, we have calculated $\partial Gb/\partial T$ over the whole range of composition and plotted the results in Fig. 4. In each case there is a slight depression in the mid-range of curve. However, the extent of the depression is nowhere near the value that would be needed to support the first hypothesis of Porteous and Blander, which would require that the derivative be 10 percent of what it is. Their other two hypotheses concern a possible change in composition of the test liquid.

Conclusion

Two features distinguish vapor nucleation in multicomponent liquids from the single component case. One is that the vapor phase is a mixture. The other is that nucleus formation alters the composition of the nearby liquid. These phenomena affect both the rate of vapor embryo growth, and the ultimate nucleus state. Both phenomena have been incorporated into the classical theory of homogeneous nucleation. Analytical results for superheat limits have been compared to published experimental data for hydrocarbon mixtures. Although no disagreements between theory and experiment have been found, the limited quantity of data does not permit a conclusive evaluation to be made.

The model herein presented for nucleus growth and local composition modification is apparently general for multi-component liquids. However, the calculation procedure is not. Because of the physical input required, namely a "mixable" equation of state and surface tension correlation, it is limited to alkane hydrocarbons.

References

1 Reiss, H., *J. Chem. Phys.*, Vol. 18, 1950, pp. 840–848.

2 Reiss, H. and L. Friedman, *J. Chem. Phys.*, Vol. 19, 1951, pp. 253–254.

3 Ward, C. A., A. Balakrishnan, and F. C. Hooper, *Jnl. Basic Engg.*, 92D,

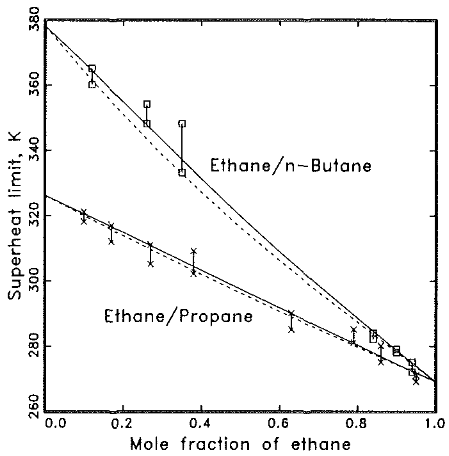

Fig. 2 **Superheat limit at 101 kPa versus composition for the mixtures ethane/normal butane and ethane/propane: Solid curves are complete calculation; *dashed curves are calculated by neglecting the effect of the modified* liquid composition in the neighborhood of the nucleus; experimental data from [9] and [25]**

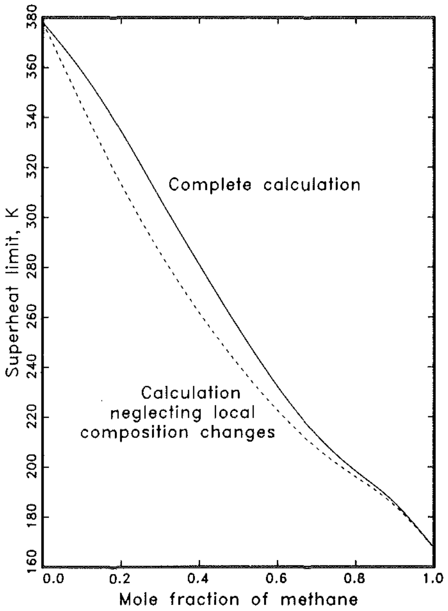

Fig. 3 **Superheat limit at 101 kPa versus composition for methane/n-butane**

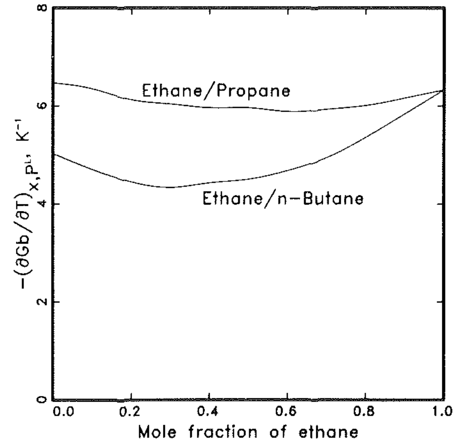

Fig. 4 **Calculated derivative of Gibbs number evaluated at the superheat limit, showing relatively weak functional dependence on mixture composition**

1970, pp. 695–704, (includes published discussion).
4 Forest, T. W. and C. A. Ward, *J. Chem. Phys.*, Vol. 66, 1977, pp. 2322–2330.
5 Forest, T. W. and C. A. Ward, *J. Chem. Phys.*, Vol. 69, 1978, pp. 2221–2230.
6 Mori, Y., K. Hijikata, and T. Nagatani, *Int. Jnl. Ht. Mass Transfer,* Vol. 19, 1976, pp. 1153–1159.
7 Hijikata, K., Y. Mori, and T. Nagatani, ASME JOURNAL OF HEAT TRANSFER, Vol. 100, 1978, pp. 460–465.
8 Blander, M., D. Hengstenberg, and J. L. Katz, *J. Physical Chemistry,* Vol. 75, 1971, pp. 3613–3619.
9 Blander, M. and J. L. Katz, *AIChE Jnl.,* Vol. 21, 1975, pp. 833–848.
10 Eberhart, J. G., W. Kremsner, and M. Blander, *Jnl. of Colloid and Interface Science,* Vol. 50, 1975, pp. 369–378.
11 Katz, J. L. and M. Blander, *Jnl. of Colloid and Interface Science,* Vol. 42, 1973, pp. 496–502.
12 Mou, C. Y. and R. Lovett, *J. Chem. Phys.*, Vol. 62, 1975, pp. 3298–3309.
13 Frenkel, J., *Kinetic Theory of Liquids,* Dover, New York, 1955.
14 Moore, G. R., *AIChE Jnl.,* Vol. 5, 1959, pp. 458–466.
15 Pinnes, E. L. and W. K. Mueller, "Homogeneous Nucleation in Multi-Component Liquid Mixtures," 1977 National Heat Transfer Conference.
16 Reiss, H., *J. Chem. Phys.*, Vol. 18, 1950, pp. 996–997.
17 Bishnoi, P. R., R. D. Miranda, and D. B. Robinson, *Hydrocarbon Processing,* Vol. 53, No. 11, 1974, pp. 197–201.
18 Benedict, M., G. B. Webb, and L. C. Rubin, *J. Chem. Phys.,* Part I: Vol. 8, 1940, pp. 334–345; Part II: Vol. 10, 1942, pp. 747–758.
19 Bachinskii, A. I., *Izv. Fiz. Instituta pri Moskovskom nauchnom Institute,* Vol. 11, 1922, p. 60.
20 Macleod, D. B., *Trans. Faraday Soc.,* Vol. 19, 1923, pp. 38–42.
21 Weinaug, C. F. and D. L. Katz, *Ind. Eng. Chem.,* Vol. 35, 1943, pp. 239–246.
22 Pinnes, E. L., "Spontaneous Nucleation in Multicomponent Liquids," Ph.D Thesis, Polytechnic Institute of New York, 1977.
23 Skripov, V. P. *Metastable Liquids,* Wiley, New York, 1974.
24 Skripov, V. P. et al., "Superheated Liquids: Thermophysical Properties, Homogeneous Nucleation and Explosive Boiling-Up," 1977 National Heat Transfer Conference.
25 Porteous, W. M. and M. Blander, *AIChE Jnl.,* Vol. 21, 1975, pp. 560–566.

A. R. Barber
K. E. Kneidel
Babcock and Wilcox Co.,
Senior Research
Engineers,
Research and Development Division,
Alliance, OH

C. S. Fitzgerald
Babcock and Wilcox Co.,
Research Specialist,
Research and Development Division,
Lynchburg, VA

L. C. Lynnworth
Head of Ultrasonics Department,
Parametrics, Inc.,
Waltham, MA

Ultrasonic Temperature Profiling System for Detecting Critical Heat Flux in Non-Uniformly Heated Tube Bundles

A new ultrasonic instrumentation system was developed and applied to the problem of detecting critical heat flux (CHF) in experiments that simulate a nuclear reactor fuel assembly. This instrumentation system used the principles of ultrasonic thermometry to detect and locate CHF in a tube bundle with non-uniform axial heat generation. The technique consists of measuring the time between pairs of ultrasonic echoes that reflect from a sequence of evenly spaced discontinuities along a sensor. Each measurement of time is directly related to the temperature of a specific segment of a sensor. The system was designed to handle many 16-zone sensors at a high rate of data acquisition so that CHF could be rapidly detected and accurately located. This paper includes a description of the sensor and the signal processing techniques as well as examples of the system's response to CHF.

Introduction

The maximum power output of a nuclear reactor core is limited by critical heat flux (CHF). These limits are defined through experiments that use electrically heated tube bundles to model the reactor fuel assembly. The most difficult of these CHF tests requires simulation of the non-uniform axial heat generation that is typical of a fuel assembly. The difficulty lies in the detection of CHF. The tube bundles must be equipped with instrumentation that not only detects CHF quickly enough to protect the bundle from overheating but also indicates the CHF location.

Generally, CHF is detected by monitoring the inside temperature of the bundle tubes. A sudden rise in that temperature corresponds to a change in the boiling mechanism around the outside of the tube. Liquid, which was prevalent around the tube surface prior to the CHF condition, is now replaced by a vapor film that dramatically reduces the heat transfer coefficient. Since the heat generation remains constant, the reduced heat transfer coefficient causes a rise in the tube temperature. The monitoring device senses the temperature rise, identifies the CHF event, and records its location. Note, it is not important to monitor the absolute tube temperature accurately; only *significant changes* in temperature are important. After the event is identified, the heat flux (power) to the tube bundle is reduced until a safe temperature is re-established. Rapid identification of CHF and immediate reaction to it are critical. If power is not reduced quickly after CHF occurs, tube failure may result. Therefore, from a testing viewpoint *every* CHF must be detected as rapidly as possible.

The critical heat flux event occurs at the most severe combination of thermohydraulic conditions and bundle heat flux. In bundles where the heat flux is axially uniform, this combination always occurs near the outlet end of the heated length. Since the possible CHF locations are few, the CHF detection system usually consists of a relatively small number of thermocouples attached to the inside of the tubes at the expected CHF locations. Properly designed, this system will provide satisfactory detection of CHF.

However, the location of CHF is not as predictable in a tube bundle that has non-uniform axial heat generation. Critical heat flux can theoretically occur anywhere from the location of the peak in the heat generation profile to the outlet end of the heated length.

Most experimenters install as many judiciously placed thermocouples as possible in this type of bundle. However, the small inside tube diameter that is typical of these tests severely limits the number of thermocouples that can be used. This limitation increases the risk of bundle damage if an undetected CHF should occur between thermocouple locations. It also increases the uncertainty in the axial measurement of the CHF location. The latter is important in the application of CHF data to reactor design. The lack of precise information on the location of CHF raises the uncertainty of the local thermohydraulic conditions at which CHF occurred. Because of this increased uncertainty the reactor designer must be overly conservative when predicting the reactor thermal limits.

It was judged that a more reliable and accurate technique was needed for detecting and locating CHF. The literature was reviewed to determine possible candidates. Adnams, et al. [1], has developed several sensor designs for detecting dryout. However, design difficulties due to our small tube size, the slow thermal response to our expected CHF conditions, and the handling characteristics of the electrical bridge networks made these techniques unattractive. A radiation style surface thermocouple was designed and proof tested but again the required small size became an overwhelming limitation that led to handling and manufacturing problems. Hewitt [2] discusses other techniques with potential application to detecting CHF, but none could provide a satisfactory combination of complete protection and accurate definition of the CHF location inside small bundle tubes.

Because of the shortcomings of these other techniques, a new ultrasonic instrumentation system with transient temperature profiling capabilities was developed and applied to the problem. The objective of this paper is to describe that system. Included is a description of the basic technique, the sensor, and the signal processing equipment. Examples of the system response to critical heat flux are also shown.

The Basic Technique

The technique used for detecting CHF in tube bundles with non-uniform axial heat generation was *ultrasonic thermometry.* The concept is based on the single zone thin-wire work of Bell [3], as extended to multiple zones by Lynnworth, et al. [4–6]. The following brief description shows how this technique was applied to detecting CHF in electrically heated tube bundles.

In any medium (solid, liquid, gas, or plasma) sound propagation is a function of temperature, T. In most solids the speed of sound decreases as temperature increases, primarily because of the reduced modulus of elasticity at the higher temperatures. In a straight, solid, homogeneous, isotropic, elastic waveguide with small cross-sectional

---

Contributed by the Heat Transfer Division for publication in the JOURNAL OF HEAT TRANSFER. Manuscript received by the Heat Transfer Division February 5, 1979.

dimensions compared to wavelength λ, the extensional wave velocity, v, is given by

$$v = \sqrt{E/\rho}$$

where E and ρ are known functions of temperature. Fig. 1 shows examples of the dependence of the velocity of sound upon temperature for several metals [7].

To determine the temperature of a segment of an ultrasonic waveguide, one can measure either the resonant frequency of the segment, or the transit time. The resonant frequency is proportional to velocity; the transit time, t, is inversely proportional to velocity, but nearly proportional to temperature. The latter is preferred for this application [4–6]. Therefore, accurate measurements of transit time allow the waveguide material to be used as a thermometer.

Now consider the acoustic reflection characteristics of the waveguide shown schematically in Fig. 2. When an ultrasonic wave travels along the waveguide, some of its energy is reflected and some is transmitted at each of the discontinuities. The resulting sequence of reflected echoes can be used to determine the average temperature of each zone between discontinuities by measuring the time between each pair of echoes. Therefore, a single sensor with $n + 1$ discontinuities placed inside a tube will provide n readings of tube temperature over whatever tube length is desired. Some limitations to this technique are the strength of the ultrasonic pulse, the acoustic impedance of the sensor, attenuation, spurious echoes due to waveguide non-uniformity or undesired mechanical contacts, and the minimum distance between discontinuities required to obtain separable and distinct echoes.

The effects of secondary echo reflections (reverberations) are also important and are controlled by the size ("strength") of the discontinuities. The strength of the discontinuities can be quantified using the sound pressure reflection coefficient, R. This is the ratio of reflected sound pressure to incident sound pressure at any discontinuity, which is equivalent to the square root of the ratio of reflected energy to incident energy at any discontinuity. Theoretically [4–6], R for each discontinuity must be small, less than or equal to 0.1, so that reverberations in any zone will not significantly interfere with echoes from succeeding zones. On the other hand, if R is too small, the signal-to-noise ratio will be inadequate. Therefore, an $R \approx 0.1$ was generally used to maximize the signal-to-noise ratio without creating excessive reverberations.

In the laboratory, probes have been built with as many as 22 zones [8]; and 32 zones are probably achievable. However, for this work a goal of 16 zones was judged practical. It can be shown that, if the sound pressure coefficient is 0.1 at each discontinuity of a 16-zone sensor, the amplitude of the seventeenth echo will be 1.5 dB smaller than the amplitude of the first echo. Attenuation at actual test temperatures also reduces the amplitude of the later echoes. To compensate for these effects, the discontinuity width was increased logarithmically from ~4 to ~8 mm down the sensor length. This provided larger sound pressure reflection coefficients for the latter attenuated echoes.

A satisfactory CHF detection system that is based on ultrasonic thermometry must be capable of sequentially pulsing a large number of sensors and processing the echoes into transit times. The system must process these signals rapidly to protect the tube bundle from overheating. The output must also be recorded in a convenient, usable form for experimental control and on-line data reduction.

The processing time was limited by the round-trip time required for the ultrasonic pulse in a sensor. The technique used for processing the echoes into transit times was blended with the echo reception so that each echo was processed as it was received. In this way each sensor output was processed in slightly more than the round-trip time.

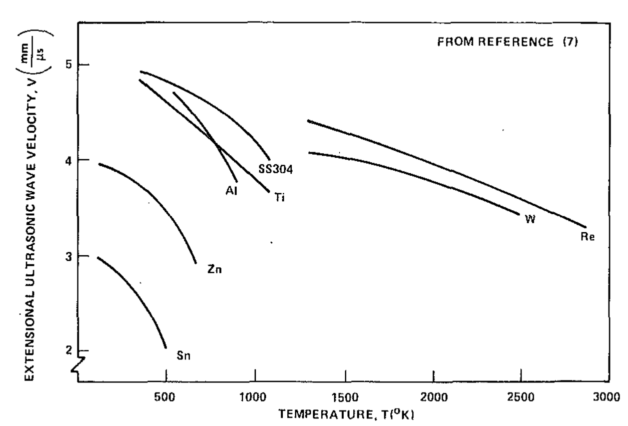

Fig. 1 Extensional ultrasonic wave velocity as a function of temperature for several metals

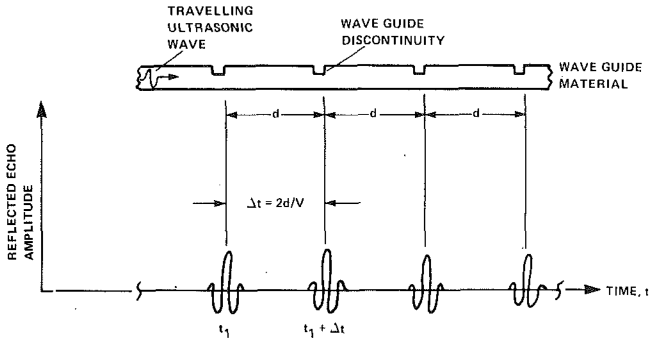

Fig. 2 Acoustic reflection characteristics of a waveguide material

Data access for the output devices was also synchronized with the echo stream so that the transit times were accessible whenever the echoes were not being processed.

To handle the volume of processed transit times from many 16-zone sensors, a minicomputer was needed. The time required for data transfer to the computer was minimized by using direct memory access (DMA) transfer. The computer was programmed to recognize and identify a CHF event, reduce power, and provide both on- and off-line data output.

Resulting Ultrasonic System

Discussion of the final ultrasonic system design for CHF detection can be divided into three main parts: sensor design, signal processing, and data acquisition.

Sensor Design. Fig. 3 provides a schematic of the final sensor and pictures of the key components. The magnetostrictive *transducer* was made of Remendur,[1] 1.6 mm in diameter by 20 mm in length, that was magnetically biased and used to launch the ultrasonic signals in the sensor. The transducer was energized ultrasonically by an electrically isolated solenoid pulsing *coil.* The coil also received the reflected echo sequence from the sensor discontinuities. The transducer and coil were physically located outside the bundle, and a *lead wire* that was silver brazed to the transducer carried the ultrasonic signals to and from the *CHF detection region* down inside the bundle tubes.

The detection region consists of 16 measurement *zones,* each 114 mm long, covering 1.83 meters of the non-uniform heater tube length.

---

[1] Trade name for a 48 percent Co, 4 percent Va, 0.4 percent Mn, balance Fe alloy.

Nomenclature

A = cross-sectional area, mm^2
d = distance between discontinuities, mm
E = Young's modulus, Pa
n = number of zones
R = sound pressure reflection coefficient
T = temperature, °C
t = transit time, s
v = extensional ultrasonic wave velocity, mm/μs
Z = acoustic impedance
Δt = differential transit time = $2d/v$, s
λ = wavelength, mm
ρ = density, kg/m^3
1,2, . . . , 16,17 = identifiers of sensor discontinuities and resulting echoes

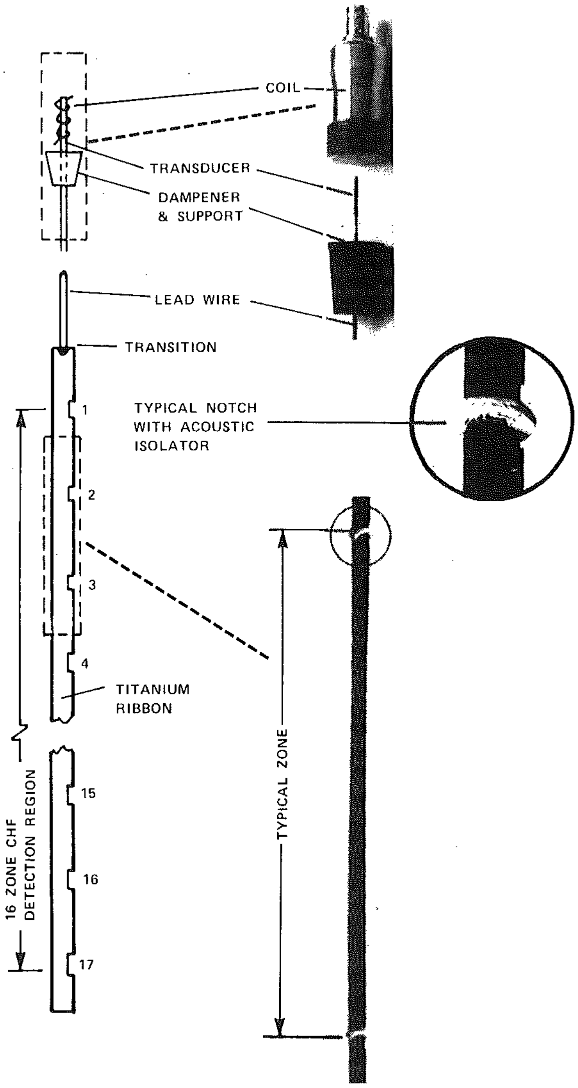

Fig. 3 Schematic of sensor design with pictures of key components

These zones encompassed the full length over which CHF could occur. Each zone was defined by *notches* in the sensor with sound pressure reflection coefficients of approximately 0.1. One sensor was positioned in each of 25 tubes after the bundle was assembled and installed in the test facility.

Traditionally, unwanted acoustic echoes from spurious sensor contacts with the surroundings are minimized by using a waveguide of high acoustic impedance, $Z = \rho v A$, where A = cross-sectional area. But high impedance results in a slow thermal response, which is unacceptable. This apparent dilemma has been resolved by departing from the conventional circular waveguide sensor and using a ribbon design. The ribbon cross section has a high surface-to-volume ratio which improves the thermal response. To provide acoustic as well as electrical isolation, *fibrous washers* were placed at selected notch locations.

The sensor was thermally coupled to the tube by radiation heat transfer. The thermal response was maximized by applying high emittance coatings to the sensor and the inner surface of the tubes. The most significant time delay in the entire system is the thermal response of the sensor. When given a theoretical step change in tube temperature, the sensor radiation time constant was on the order of one second.

Titanium ribbon (3.2 mm × 0.25 mm) was selected for the sensor material. The small cross-sectional dimensions were required because of the minimum tube inside diameter of 4.6 mm. The use of titanium ribbon provided two advantages: the sensitivity of velocity of sound to temperature is greater at the desired operating temperature than in most alternative materials (see Fig. 1), and its thermal mass is relatively low. Both improve the sensor's response to CHF.

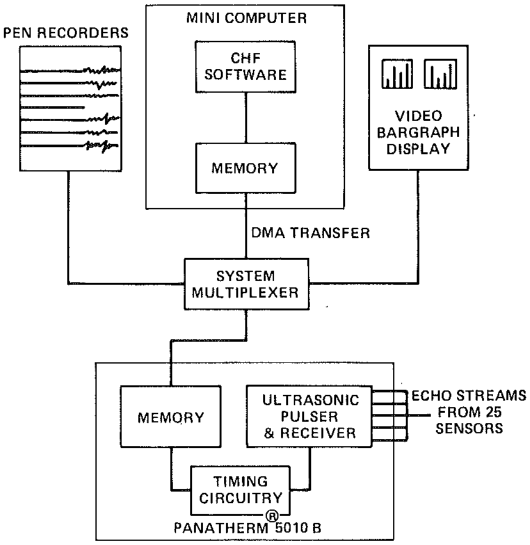

Fig. 4 Signal processing equipment

Signal Processing. The major components of the signal processing system are shown in Fig. 4.

The Panatherm 5010B was developed jointly by Parametrics and The Babcock & Wilcox Company (B&W) especially for this application. It sequentially pulsed the 25 sensors in 2 to 3 ms intervals. This was slightly longer than the round-trip time for an ultrasonic pulse in a sensor. After pulsing a sensor, the Panatherm received the returning echo sequence and determined the time interval between each echo pair. A typical echo stream from a sensor is shown in Fig. 5.

The echo detection scheme is shown in Fig. 6. Each echo is detected by a circuit which *arms* as the echo exceeds an amplitude *threshold* and defines the echo at the next point in time that the wave *crosses zero.*

The transit time between echo pairs is approximately 50 μs. Minor variations in this time depend on the operating temperature of the test facility and the waveform variations from zone-to-zone and from sensor-to-sensor. To eliminate background noise and spurious echoes, the time between echoes was divided into a fixed "blank" time interval and a variable time interval that was measured with a 20 MHz clock. A signal from the blank interval circuitry disabled the echo detection circuit mentioned above until just prior to the next expected echo. The clock was started at the end of the blank and stopped at the next zero cross. The clock counts for a zone were stored in the Panatherm memory and the blanking/counting sequence was repeated until all 16 echo pairs had been processed. The next sensor was pulsed just after the last echo had been received and processed.

The transit time from the initial pulsing of the sensor to the first echo was approximately 1 ms. The echo detection circuitry was again disabled by a blank time interval from the moment the transducer was pulsed until just prior to the first echo. In this way, lead wire noise and reflections from the lead wire/ribbon transition were disregarded.

The frequency of the variable time interval clock determines the temperature resolution of the system. With the titanium sensor and a 20 MHz clock, a 2°C change in zone temperature changes the measured transit time by one clock count (50 ns). A change of five clock counts was used to clearly distinguish between CHF indications and any system background noise.

The multiplexer in Fig. 4 was designed by B&W to read the Panatherm memory and provide convenient output. Selected signals for loop operation were formatted by the multiplexer and transmitted to pen recorders and video displays. All zones (25 sensors × 16 zones/sensor = 400 zones) were sent through the multiplexer to a minicomputer for on-line data acquisition. The multiplexer was synchronized with the Panatherm so that data could be accessed

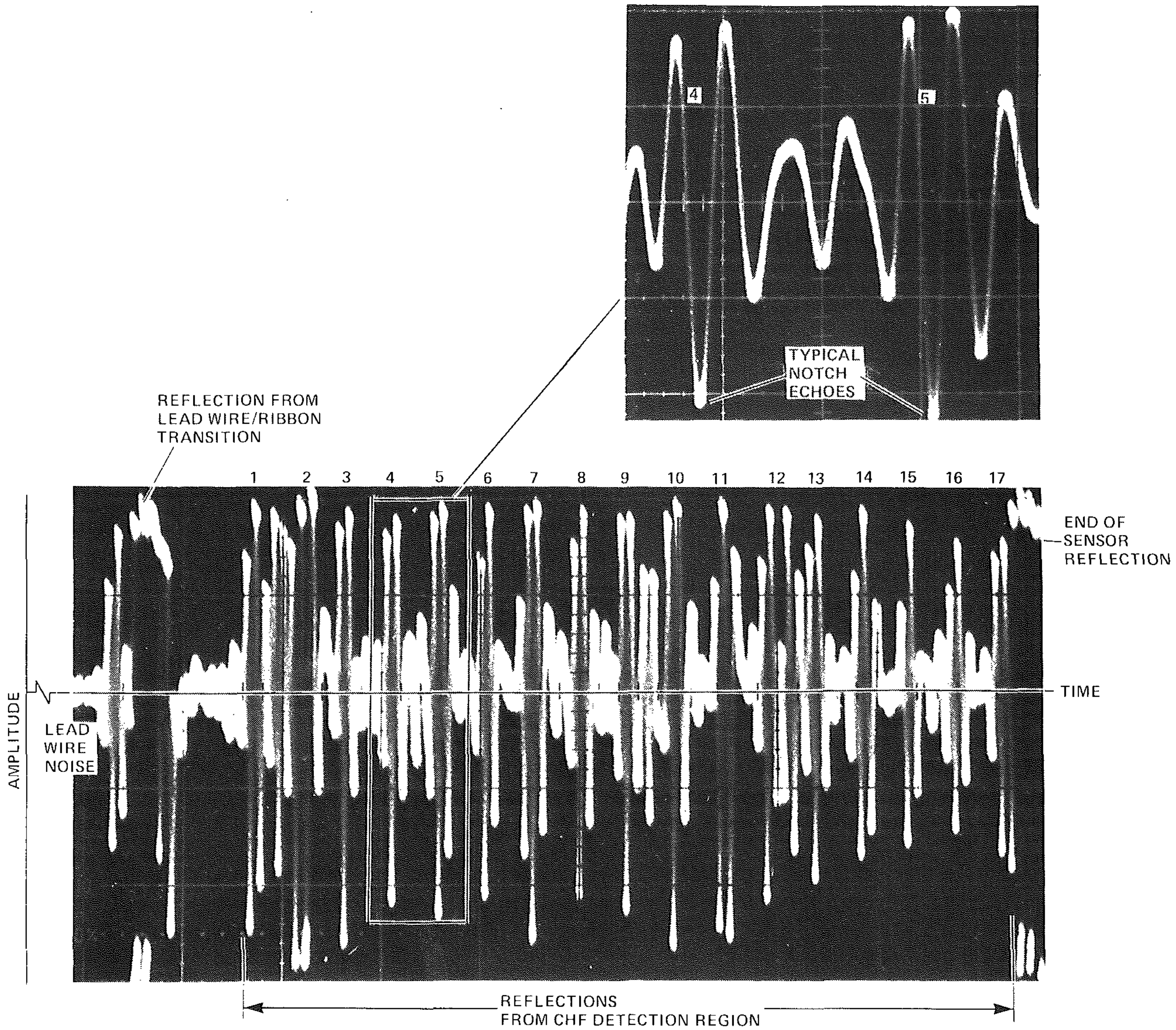

Fig. 5 A typical sensor echo stream

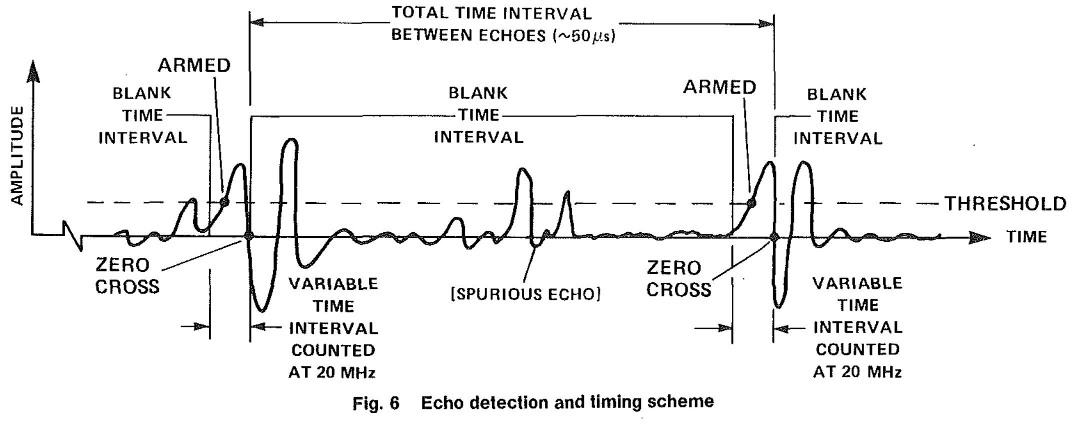

Fig. 6 Echo detection and timing scheme

during the blank time intervals. This helped to minimize the response time of the signal processing system. The multiplexer also had several features for checking and debugging the Panatherm data prior to system output.

Data Acquisition. On-line data acquisition was controlled by a minicomputer system dedicated to the B&W 10 megawatt heat transfer facility on which the actual tests were performed. The computer received a complete updated bundle scan (400 zones) on demand from the multiplexer at a rate of about 10 complete scans (4000 zones) per second. The computer was programmed to cross check the data and recognize a CHF event.

The data acquisition procedure was as follows:

1 A steady-state condition (an array of 400 transit times) was established at a safe power level below CHF.
2 As power was increased, the steady-state condition was subtracted from each bundle scan and the difference in counts (i.e., temperature change) was compared with a maximum allowable limit set by the experimenter. When this limit was reached, the

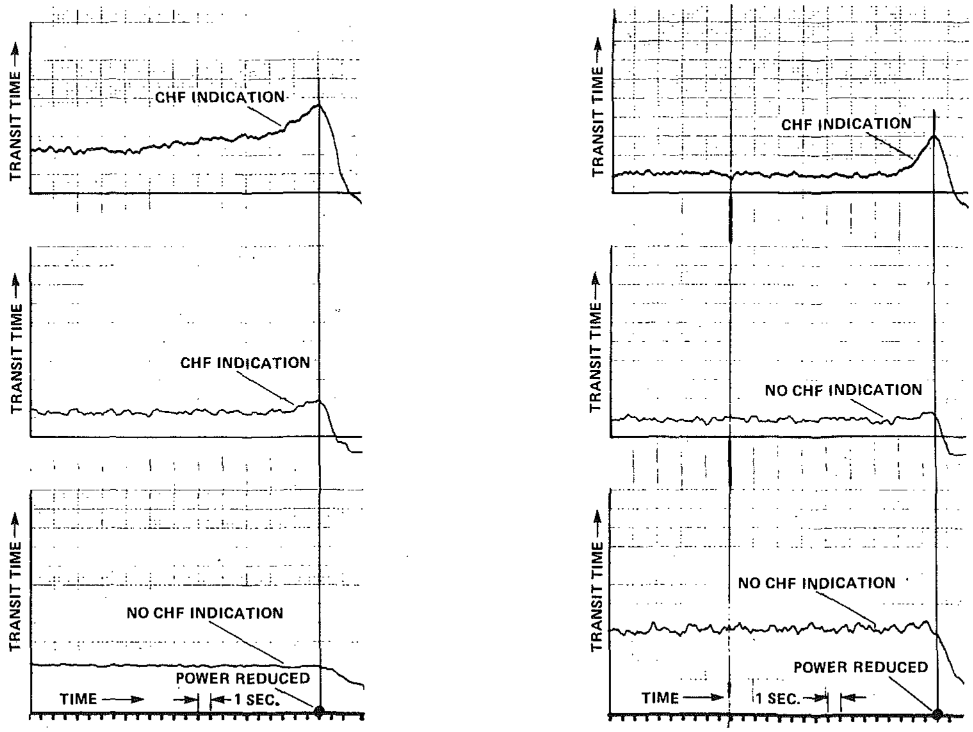

EXAMPLE 1

EXAMPLE 2

Fig. 7 Examples of pen recorder responses, showing zones with and without CHF indications

computer immediately reduced power to the tube bundle.

3 Any zone(s) revealing a significant change from the steady-state condition were output as the primary event indicators.

4 Pen recorder and video bar graph displays were also used to provide operator indications and control, and as fail-safe devices in case of computer failure or shutdown.

Two examples of CHF indications on the pen recorders are shown in Fig. 7. Both examples show a zone where a definite change in temperature (transit time) identified a CHF condition and a zone where no indication was observed. The data from all 400 zones at the time CHF was indicated were retained for post-test examination so that CHF indications that did not exceed the allowable limit (like the second trace in example 1) could be analyzed.

Ultrasonic System Advantages

This ultrasonic profiling technique has several advantages over other available approaches. The first and most obvious is that a single sensor of relatively simple construction provides continuous and complete spatial protection of each tube surface against overheating due to critical heat flux.

The ultrasonic technique also provides better overall axial resolution of the location of the CHF event than conventional thermocouples. When thermocouples are used, a CHF must either occur at, or spread to, a thermocouple location. If design limitations preclude adequate thermocouple coverage, or if a thermocouple fails because of age or handling, then tube damage may result. An example of a thermocouple detection system used for this type of testing is given in [9]. Comparing the referenced thermocouple system with the present ultrasonic system confirms the advantages discussed above. Even though the tubes were relatively large (13 mm OD versus 10 mm OD), the limitation to the number of thermocouples that could be installed forced the experimenters to leave some possible CHF areas uninstrumented. Also, the required distances between thermocouples often resulted in larger uncertainty in the axial location of the CHF.

The single-unit construction and ease of handling make the ultrasonic sensor convenient to install and use. Both [1] and [9] describe systems that require relatively complex assembles and installation techniques. This results in intricate and time consuming efforts that can lead to other failure modes, especially when every tube in a multi-tube bundle must be similarly treated.

The use of radiation heat transfer as the thermal coupling mechanism also simplifies installation. The ultrasonic sensors are lowered into place after the bundle has been assembled and installed in the test facility. Total sensor installation time requires only a few hours. Should failure occur, all key components are easily accessible. A sensor can be withdrawn from the bundle and a replacement installed with little difficulty. If an energizing coil fails, it too can be replaced in a matter of minutes since it is located outside the bundle. Another advantage is that, unlike thermocouples, all components of this system including sensors are reusable.

Test Results And Conclusions

This multi-zoned, ultrasonic profiling technique was initially proof-tested in an experiment that compared ultrasonic thermometry data with thermocouple data. In a bundle experiment an ultrasonic thermometer and a thermocouple were installed in the same tube. CHF was coincidentally measured 47 times by both the thermocouple and the ultrasonic thermometer, thus verifying the technique. The final ultrasonic system was used exclusively in the first full-length, non-uniformly heated bundle tested at B&W in 1977 and 1978. More than 150 CHF data points were taken over a wide range of pressurized water reactor (PWR) operating conditions. The power levels at which CHF occurred compare well with expectations. Because of the improved axial resolution of the instrumentation, the uncertainty in the location of the CHF event was generally reduced to ±57mm. This resulted in a reduced uncertainty in the local thermohydraulic properties at the location of CHF and therefore led to a better understanding of the critical heat flux phenomenon.

Post-test bundle inspection revealed that the heated tubes were satisfactorily protected from overheating, and the sensors showed no indications of wear or damage. Because the sensors were reusable, they were later installed in subsequent bundle tests.

From the above results it is concluded that the ultrasonic transient temperature profiling system reliably detects CHF in non-uniformly heated bundles. The system is easy to use, simple to install, and provides a significant savings in CHF test bundle design and construction. The speed of the system (4000 zones per second) provides a transient picture of the tube bundle reaction to critical heat flux as witnessed in Fig. 7. Development of the system provides a significant advance in the art of ultrasonic thermometry and critical heat flux experimentation.

References

1 Adnams, D. J., Salt, K. J., and Wintle, C. A., "The Development of Instruments for the Detection of Dryout in Uniform and Non-uniform Axially Heated Rod Clusters," AEEW-R574, 1972.

2 Hewitt, G. F., Lovegrove, P. C., "Experimental Methods In Two-Phase Flow Studies," Research Project 446-1, Final Report, NP118, prepared for EPRI, March 1976.

3 Bell, J. F. W., *Phil. Mag.*, Vol. 2, No. 8, 1957, p. 1113.

4 Lynnworth, L. C., and Patch, D. R., "New Sensors for Ultrasound: Measuring Temperature Profiles," *Materials Research and Standards*, Vol. 10, No. 8, Aug. 1970, Cover, pp. 6–11, 40.

5 Lynnworth, L. C., Patch, D. R., Carnevale, E. H., U. S. Patent No. 3,636,754, Jan. 25, 1972.

6 Lynnworth, L. C., and Carnevale, E. H., in: H. H. Plumb (ed), *Temperature—Its Measurement and Control in Science and Industry,* ISA, 1972, pp. 715–732.

7 Lynnworth, L. C., and Carnevale, E. H., NASA CR-72339, Aug. 1967.

8 Lynnworth, L. C., *Wear,* Vol. 41, 1977, pp. 195–199.

9 Rosal, E. R., Cermak, J. O., et al. "High Pressure Rod Bundle DNB Data With Axially Non-Uniform Heat Flux" *Nuclear Engineering and Design,* Vol. 31, 1974, pp. 1–20.

Turbulence Modeling of Axial Flow in a Bare Rod Bundle

J. G. Bartzis
N. E. Todreas
Department of Nuclear Engineering,
Massachusetts Institute of Technology,
Cambridge, MA 02139

Temperature distribution within the rod bundle of a nuclear reactor is of major importance in nuclear reactor design. However temperature information presupposes knowledge of the hydrodynamic behavior of the coolant which is the most difficult part of the problem due to the complexity of the turbulence phenomena. In the present work a two equation turbulence model—a strong candidate for analyzing actual three dimensional turbulent flows—has been used to predict fully developed flow of infinite bare rod bundle of various aspect ratios (P/D). The model has been modified to take into account anisotropic effects of eddy viscosity. Secondary flow calculations have been also performed although the model seems to be too rough to predict the secondary flow correctly. Heat transfer calculations have been performed to confirm the importance of anisotropic viscosity in temperature predictions. Experimental measurements of the distribution of axial velocity, turbulent axial velocity, turbulent kinetic energy and radial Reynolds stresses were performed in the developing and fully developed regions. A two channel Laser Doppler Anemometer working in the reference mode with forward scattering was used to perform the measurements in a simulated interior subchannel of a triangular rod array with P/D = 1.124. Comparisons between the analytical results and the results of this experiment as well as other experimental data in rod bundle arrays available in the literature are presented. The predictions are in good agreement with the results for high Reynolds numbers.

1 Introduction

The prediction of fuel pin clad temperatures is important to the safe and economic operation of nuclear reactor cores. Circumferential clad variations increase hot spot allowances and can lead to rod bowing. For a medium-sized sodium cooled reactor, a 5°F decrease in maximum cladding temperature corresponds to an allowable burnup increase of ~2500 MWd/MT [25]. Comparable temperature consequences on rod bowing have not yet been thoroughly assessed. While these reactors use wire wrap or grid spacers, investigation of spacerless arrays provides an applicable bound for sufficiently widely-spaced grids. However, temperature information presupposes knowledge of the hydrodynamic behavior of the coolant which requires analysis of the turbulence phenomena.

In the present work fully developed flow is studied in an infinite triangular array of bare rods (see Fig. 1) which is an ideal geometry associated with reactor fuel bundles. Preliminary temperature calculations have also been performed to study the effect of eddy viscosity anisotropy.

This study has been performed using the eddy viscosity concept and specifically the turbulent equation model approach [7]. Such an approach seems best since it directly utilizes turbulent quantities which are the natural parameters describing the turbulence phenomena. Moreover, the method is general and relatively simple. The parameters of turbulent kinetic energy dissipation that have been selected represent the most advanced and widely used approach for turbulence equation modeling within the eddy viscosity concept. Such an approach has been successfully used in a wide variety of problems in fluid mechanics.

For the specific case of the bare rod bundle, the previous work of Carajilescov and Todreas [1] incorporated two major simplifications—eddy viscosity isotropy and the utilization of turbulent kinetic energy only. However the approximation of isotropy is not consistent with recent experimental evidence. In fact, the present analysis will show that anisotropic eddy viscosity and a two equation turbulence formulation considerably affects the prediction of flow and heat in rod bundles. The importance of anisotropic viscosity in fluid flow and heat transfer calculations in a rod bundle has been confirmed by other investigators [4, 5].

2 Turbulence Modeling Approach

2.1 Reynolds Stresses. The Reynolds Shear Stresses, based on the eddy viscosity approach are given in Table 1. For $\nu_{rz}{}^T$, the approximation used successfully in one-dimensional flow [6, 7] has been adopted in the present work, i.e.,

$$\nu_{rz}{}^T = c_\mu \frac{k^2}{\epsilon} \tag{1}$$

For $\nu_{r\theta}{}^T$ which is useful only for secondary flow studies, we take $\nu_{r\theta}{}^T \approx \nu_{rz}{}^T$ on the grounds that v_θ fluctuations are expected to have a length scale comparable to the length scale of v_z fluctuations. On the other hand its effect on secondary flow is minor compared with the normal stress effect [8].

For $\nu_{\theta z}{}^T$, the following relation is used,

$$\nu_{\theta z}{}^T = \nu_{rz}{}^T/\psi_m \tag{2}$$

where ψ_m, the ratio of eddy viscosities, takes into consideration the eddy viscosity anisotropy. By virtue of the approximation

$$\psi_m = \frac{\nu_{rz}{}^T}{\nu_{\theta z}{}^T} \approx \frac{U_r \ell_r}{U_\theta \ell_\theta} \tag{3}$$

and the Prandtl hypothesis [9] ($U_r \sim U_\theta \sim k^{1/2}$), equation (3) reduces to

$$\psi_m \approx \ell_r/\ell_\theta. \tag{4}$$

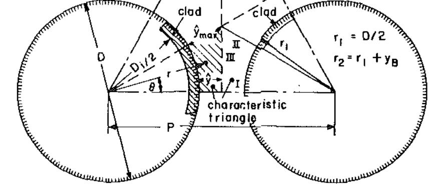

Fig. 1 Infinite triangular array

Contributed by the Heat Transfer Division and presented at the 18th AIChE/ASME Heat Transfer Conference, San Diego, California, Aug. 6–8, 1979. Manuscript received by the Heat Transfer Division October 19, 1978. Paper No. 79-HT-38.

Table 1 Differential equations and boundary conditions for k and ϵ

(A) The Differential Equations

General Forms: $\nabla \phi V + \nabla T_\phi = S_\phi$

	T_ϕ			
ϕ	$T_{\phi r}$	$T_{\phi\theta}$	S_ϕ	Remarks
	eff	eff		Reynolds Stresses
k	$-\dfrac{\nu_{rz}}{\sigma\kappa}\dfrac{\partial k}{\partial r}$	$-\dfrac{\nu_{\theta z}}{\sigma\kappa}\dfrac{\partial k}{r\partial\theta}$	$\nu_{rz}{}^T\left(\dfrac{\partial v_z}{\partial r}\right)^2 + \nu_{z\theta}{}^T\left(\dfrac{\partial v_z}{r\partial\theta}\right)^2 - \epsilon$	$\overline{v_r'v_z'} = -\nu_{rz}{}^T\dfrac{\partial v_z}{\partial r}$
ϵ	$-\dfrac{\nu_{rz}{}^{\text{eff}}}{\sigma_\epsilon}\dfrac{\partial\epsilon}{\partial r}$	$\dfrac{\nu_{z\theta}{}^{\text{eff}}}{\sigma_\epsilon}\dfrac{\partial\epsilon}{r\partial\theta}$	$c_{\epsilon 1}\dfrac{\epsilon}{k}\left[\nu_{rz}{}^T\left(\dfrac{\partial v_z}{\partial r}\right)^2 + \nu_{z\theta}{}^T\left(\dfrac{\partial v_z}{r\partial\theta}\right)^2\right]$	$\overline{v_z'v_\theta'} = -\nu_{z\theta}{}^T\dfrac{\partial v_z}{r\partial\theta}$
			$-c_{\epsilon 2}\dfrac{\epsilon^2}{k}$	$\overline{v_r'v_\theta'} = -\nu_{\theta r}{}^T\left[r\dfrac{\partial}{\partial r}\left(\dfrac{v_\theta}{r}\right) + \dfrac{1}{r}\dfrac{\partial v_r}{\partial\theta}\right]$

(B) Boundary Conditions

	Boundaries			Near Wall Region
ϕ	I	II	III	$y_B{}^+ = 30$
k	$\dfrac{\partial k}{r\partial\theta} = 0$	$\dfrac{\partial k}{r\partial\theta} = 0$	$\dfrac{\partial k}{\partial r} = \dfrac{\partial k}{r\partial\theta}tg\theta$	$k = \dfrac{(\overline{v_r'v_z'})}{\sqrt{c\mu}}\ y = y_B$
ϵ	$\dfrac{\partial\epsilon}{r\partial\theta} = 0$	$\dfrac{\partial\epsilon}{r\partial\theta} = 0$	$\dfrac{\partial\epsilon}{\partial r} = \dfrac{\partial\epsilon}{r\partial\theta}tg\theta$	$\epsilon = \dfrac{u^*}{ky}(-\overline{v_r'v_z'})_{y=y_B}$

2.1.1 Length Scales. It is evident that the use of equation (4), requires some knowledge of the ratio ℓ_r/ℓ_θ.

For the length scales the following relations are postulated

$$\left(\frac{1}{\ell_r}\right)^\alpha = \left(k\frac{dv_z/dr}{u^*}\right)^\alpha + \left(\frac{1}{c_L\hat{L}_r}\right)^\alpha \tag{5}$$

and

$$\ell_\theta = c_L\hat{L}_\theta. \tag{6}$$

Equation (6) is obtained assuming that a relation similar to equation (5) is valid for expressing ℓ_θ in which dv_z/dr is replaced by $dv_z/rd\theta$ and $\hat{L}_r$ is replaced by $\hat{L}_\theta$ and the velocity gradient term is neglected compared with the asymptotic effect term $(1/c_L\hat{L}_\theta)^\alpha$.

The rational for equation (5) is that it is a continuous length relation which reduces to the proper limits

$$\ell_r \approx y \quad \text{for} \quad 30 < y^+ \ll y_0{}^+ \tag{7}$$

and in the asymptotic region (the center region) i.e.,

$$\ell_r \approx c_L\hat{L}_r \text{ for } y \sim y_0. \tag{8}$$

The physical meaning of above relations is that length scale structure in fully developed flow depends primarily on the geometrical configuration of the test section. They can be called asymptotic lengths or "eigenlengths" of the test section. These asymptotic lengths are disturbed in presence of the shear to a degree that close to the wall the shear effect becomes dominant. The factor α defines the width of the transition region.

Another characteristic of the above length scales relations is they are directly related to the shear instead of the distance from the wall. Therefore it is expected to be a better formula for length scales where the logarithmic law is not valid. For example, in the laminar sublayer equation (5) yields

$$\ell_r \sim \nu/u^* \quad \text{for} \quad 0 \le u^+ < 5$$

which is the proper length scale whereas the common relation $\ell_r = y$ yields $\ell_r = 0$ at the wall.

To utilize equations (5) and (6), the parameters introduced need to be estimated.

The parameters c_L and $\hat{L}_r$ are obtained by examining the "asymptotic" length $\ell_r \approx c_L\hat{L}_r$ in the central region of a simple geometry such as parallel planes and/or a circular tube. The obvious approximation in this case is

$$\hat{L}_r = y_0. \tag{9}$$

Now y_0 and hence $\hat{L}_r$ is estimated from the simple relations

$$\nu_{rz}{}^T \approx 0.2\,k^{1/2}\ell_r \tag{10a}$$

$$\nu_{rz}{}^T \approx 0.07\,u^*y_0 \tag{10b}$$

$$k^{1/2} \approx 0.9\,u^* \tag{10c}$$

Nomenclature

c_L, c_μ = constants (equations (1, 5))
D = rod diameter
D_H = hydraulic diameter of the infinite array
D_i = clad inner diameter
k = turbulent kinetic energy
ℓ_r, ℓ_θ = length scales of the eddies
$\hat{L}_r, \hat{L}_\theta$ = asymptotic length scales
P = pitch
T_c = coolant temperature
T_{co} = outside clad temperature
$\overline{T}_{co}$ = average outside clad temperature
U_r, U_θ = effective velocities of the eddies
u_b = bulk velocity of the infinite array
u_0 = maximum channel velocity
u_{0L} = maximum channel velocity at position L
u^* = local friction velocity
$\overline{u}^*$ = average friction velocity
v_r, v_θ, v_z = radial, tangential and axial velocity
y = radial distance from the wall
y^+ = dimensionless radial distance, $y^+ = \dfrac{yu^*}{\nu}$
$\hat{y}$ = radial distance between the wall and zero shear stress line (Fig. 1)
y_B = distance of the first calculational node from the wall
$2y_0$ = diameter of the pipe or the distance between parallel plates
α = constant (equation (5))
ϵ = energy dissipation
θ = angle
κ = von Karman constant
λ_c = coolant heat conductivity
ν = viscous kinematic viscosity
$\nu_{\alpha\beta}{}^T$ = turbulent viscosity corresponding to shear stress $\overline{v_\alpha'v_\beta'}$
$\sigma_k, \sigma_\epsilon$ = diffusion Constants for k and ϵ
$(\tau_w/\rho)_{\text{avg}}$ = average wall shear stress
ψ = eddy viscosity ratio

and it is found that $c_L = 0.4$. The obvious approximation for the rod bundle is to take $c_L = 0.4$ and $\hat{L}_r = \hat{y}$. With respect to the parameter $\hat{L}_\theta$, the following possible approaches have been tested.

(1) Isotropy of eddy viscosity along the zero stress line, which obviously yields

$$\hat{L}_\theta = \hat{L}_r = \hat{y} \tag{11}$$

(2) Isotropy of the eddy viscosity at $\hat{y}_{\max}$ ($\hat{y}$ at 30 deg) which yields:

$$\hat{L}_\theta = \hat{L}_r(\theta = 30 \text{ deg}) = \hat{y}_{\max} \tag{12}$$

$$\hat{L}_r = \hat{y}.$$

In Fig. 2 the quantity v_z/u_0 is plotted versus $y/\hat{y}$ at $\theta = 0$ deg. The fitting of data by taking $\hat{L}_\theta = \hat{y}_{\max}$ considerably improves the data prediction and therefore is adopted in the present analysis.

It must be pointed out that experimental data obtained by Rehme [3] in a side subchannel of a rod bundle indicate isotropic eddy viscosity in the region which is consistent with case (2). Ramm and Johannsen [4] working with an approach based on Buleev's theoretical model [11] have also tested isotropy along the zero shear stress line versus the eddy viscosities. Although the length scales used in [4] have similar physical meaning to the present length scales, they are defined differently due to the different approach. Therefore their length scale ratio is not equal to the eddy viscosity ratio of the present approach. The above authors have chosen a calculation method similar to case (1) on the ground that it gives more conservative heat transfer results with their model.

Finally with respect to the parameter α, the nature of equation (5) suggests that the value of ψ_m should not change significantly for large α changes. Therefore the exact value of α is relatively unimportant. In the present approach α is taken equal to 10.

2.2 Normal Stresses. For the normal stresses, i.e., $\overline{v_r'^2}$ and $\overline{v_\theta'^2}$ which are mainly responsible for the secondary flow [8], two options have been introduced in the present work. The reasons for selecting two options is primarily for comparison and secondly because both options have been used for prediction of the secondary flow in square ducts.

First option: The normal stress relations are based on Launder and Ying's [12] model, adopted by Carajilescov and Todreas [1]. After the necessary manipulations [14] the following expressions are obtained.

$$\overline{v_r'^2} = \frac{2}{3}(1 - 1/c_1)k + \frac{2(9c_2+6)}{33c_1}\frac{k}{\epsilon}\left(\nu_{rz}{}^T\left(\frac{\partial v_z}{\partial r}\right)^2 + \psi_{\theta z}{}^T\left(\frac{\partial v_z}{r\partial\theta}\right)^2\right) - \frac{2(9c_2+6)}{11c_1}\frac{k}{\epsilon}\nu_{rz}{}^T\left(\frac{\partial v_z}{\partial r}\right)^2 \tag{13}$$

$$\overline{v_\theta'^2} = \frac{2}{3}(1 - 1/c_1)k + \frac{2(9c_2+6)}{33c_1}\frac{k}{\epsilon}\left(\nu_{rz}{}^T\left(\frac{\partial v_z}{\partial r}\right)^2 + \nu_{\theta z}{}^T\left(\frac{\partial v_z}{\partial r}\right)^2\right) - \frac{2(8c_2-2)}{11c_1}\frac{k}{\epsilon}\nu_{\theta z}{}^T\left(\frac{\partial v_z}{r\partial\theta}\right)^2 \tag{14}$$

The constant c_1, c_2 have to be found by experiment. Launder, et al. [13] suggest $c_1 = 1.5$ and $c_2 = 0.4$.

Second option: Normal stresses are given by the relations proposed by Bobkov, et al. [10].

$$(\overline{v_r'^2})^{1/2} = A_r v_z(1 - u_b/u_0)\exp\left(-B_r(1 - y/\hat{y})\right). \tag{15}$$

$$(\overline{v'^2})^{1/2} = A_\theta v_z(1 - u_b/u_0)\exp\left(-B_\theta(1 - y/\hat{y})\right). \tag{16}$$

where the A's and B's are constants with values

$$A_r = 0.4, \quad A_\theta = 0.6, \quad B_r = 0.48 \quad \text{and} \quad B_\theta = 1.17.$$

The above relations are valid for closed ducts of different shapes and we assume that they are approximately valid for rod bundles.

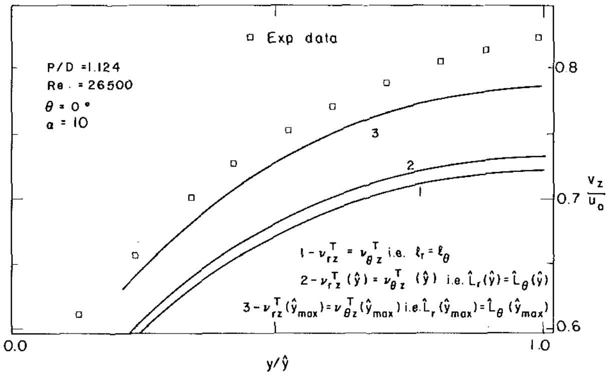

Fig. 2 Eddy viscosity comparisons

3 Governing Equations and Boundary Conditions

The momentum equations describing the fully developed flow in the cooling region of Fig. 1 after the approximation of Section 2.2 are used to calculate the velocity field. However, the introduction of the parameters k and ϵ generate a need for conservation equations for these quantities. Following the general approach adopted in [1] and [7] the differential equations for k and ϵ for the present problem can be put in the form [14]

$$\nabla\phi V + \nabla T_\phi = S_\phi$$

$$\nabla = (\partial/\partial r, \partial/r\partial\theta) \tag{17}$$

$$V = (v_r, v_\theta),\ T_\phi = (T_{\phi r}, T_{\phi\theta})$$

where ϕ stands for k and ϵ. The expressions for the parameters T_ϕ and S_ϕ are given in Table 1. It is noted that the momentum equations for v_r, rv_θ and v_z can be put also in the form of equation (17) [14].

The equations are to be solved within the characteristic triangle of the infinite rod bundle as shown in Fig. 1. The secondary flow quantities (i.e., v_r, v_θ) will be solved in the whole flow area of the characteristic triangle, whereas the v_z momentum and the k, ϵ transport equations will be solved only in the outer region of the flow (i.e., $y_B{}^+ \geq 30$).

The exclusion of the wall region is made for the following reasons:

(1) The sharp ingredients of the hydrodynamic quantities within the wall region require a relatively high number of points to describe the hydrodynamic field sufficiently well.

(2) The strongly anisotropic turbulent kinetic equation makes a turbulent model based on Pradntl's hypothesis questionable. On the other hand, the prescription for the quantities themselves within the wall region is not too difficult because the main parameters are the wall shear stress, the distance from the wall and the fluid viscosity.

The approach of excluding the wall region from the domain of solution has been used by several authors (see e.g., [12] and [13] and in the efforts preceding this work at M.I.T. [1]).

The boundary conditions for k and ϵ are shown in Table 1.

4 Numerical Solution

The solution of the problem is obtained by solving equation (17) together with the momentum and continuity equations. Following the procedure given in [14] which is based on the TEACH code [16], we obtain a set of elliptic finite difference equations the solution of which has been based on two options.

(1) The iteration technique proposed in the TEACH code [16] which consists in the present case of solving by matrix inversion [22] along radial lines and iterating along the peripheral ones.

(2) The point successive relaxation technique [19]. In both techniques an under relaxation factor is introduced to enhance stability [19].

Present experience has shown that:

(1) Line Iteration with under relaxation factor equal to 1 converges faster than successive relaxation as expected.

(2) Line Iteration with an under relaxation factor of order 0.7 or below, however converges slower than successive relaxation.

In the present analysis for the cases without secondary flow the Line Iteration technique was adopted whereas for the problems with secondary flow, the Point Iteration technique was adopted. In all cases the underrelaxation factor is taken equal to one.

5 Experimental Approach

The experimental effort consisted of measuring axial velocity, shear, and normal stresses at Re = 9000, 26,500 and 65,000. The measurements were performed using the two-channel Laser Doppler Velocimeter working in a Reference Beam Model used by Chen [23] and water as a working fluid. Due to low signal to noise ratio of the lateral velocity signal in the laterial direction it was impossible to make any meaningful measurements on secondary flow [14, 24]. The layout of the instruments is shown in Fig. 3. The test section in [1] (P/D = 1.124) was elongated to permit measurements up to L/D_H = 113 instead of only L/D_H = 77, the previous limit. Some flow development was observed between L/D_H = 77 and 113 although the difference was within the experimental error as Fig. 4 illustrates.

6 Results

6.1 Prediction Procedure. Turbulence models are not tools for understanding the turbulence phenomena which are complicated but are engineering methods for predicting useful hydrodynamic quantities. Therefore one has to examine their merits and drawbacks from this point of view.

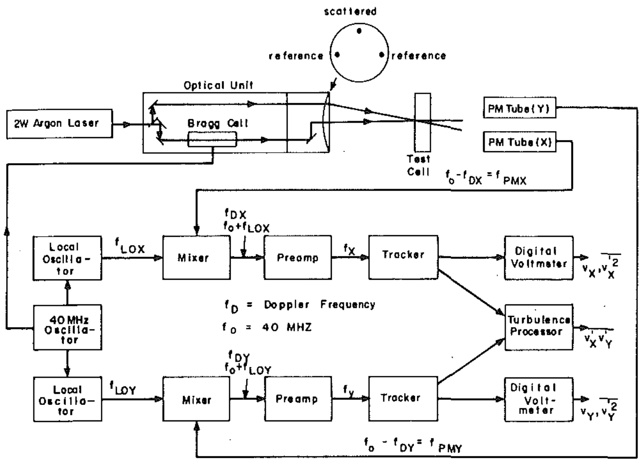

Fig. 3 Layout of instruments (taken from [23])

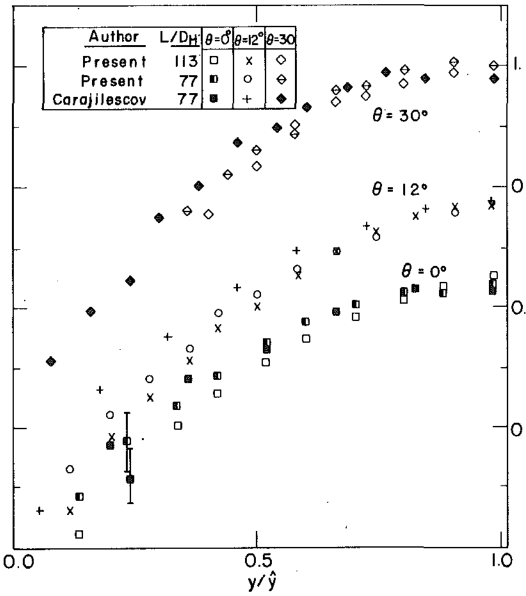

Fig. 4 Flow developments

The most attractive features of turbulence models are:

(1) The ability to use turbulence parameters (e.g., turbulent kinetic energy dissipation in this particular case) as part of the model.

(2) Their relative simplicity and flexibility to handle complicated problems since the predictions are based on adjustable constants.

Such an approach of course has some disadvantages.

(1) In reality for any given problem of nonhomogeneous turbulence, the constants are not constants but parameters changing with position and flow characteristics. The selection of the constants is made by best fit to data.

(2) The constants are not universal but depend in general on the problem under consideration.

(3) There is a relatively high number of constants so that more than one set of constants fit the data of any particular problem. For example for the geometry of this study it is shown in [14] that nearly identical results were obtained using the constants of Launder, et al. [7] and Hoffman [6]. The existence of several sets of constants fitting the data has the following pitfall. One can come out with a particular set of constants that only adequately fits his experimental configuration.

Taking into consideration the above remarks one has to follow a general and systematic way of selecting the model constants to come out with a general model. In the present work the following guidelines have been adopted.

(1) Since constants cannot be universal, there is a need to define the family of problems for which a particular set of constants can give satisfactory results. We will accept the Launder, et al. [7] constants on the ground that probably they are the most extensively tested.

Parenthetically it is noted that more systematic work is needed by analyzing a number of simple geometries at various Reynolds numbers and by identifying if possible all sets of constants applying to a particular case.

(2) Following the discussion in Section 1 which indicated the shortcomings of the isotropic eddy viscosity model, the anisotropic eddy viscosity model discussed previously will be used.

(3) The geometric peculiarities of the rod bundles will be reflected in the eddy viscosity model, e.g., the constant c_L in equations (5) and (6) can be expressed as a function of P/D ratio.

6.2 Secondary Flow. For the secondary flow calculations a 30 × 16 grid has been used. The geometrical characteristics of the test section have been used with an input average wall shear stress $(\tau_w/\rho)_{avg} = 4 \times 10^{-3}\ m^2/s^2$ (Re ≈ 26,000). For normal stresses the models mentioned in Section 2.2 are used, i.e.,

(1) Launder and Ying model as expressed by equations (13) and (14),

(2) Bobkov, et al. model as expressed by equations (15) and (16).

In Fig. 5 the velocity v_θ at $y = y_B$ is plotted for the above two cases which shows that case (1) gives a three loop system and case (2) a two loop system. The latter is in agreement with predictions in [1].

Fig. 5 shows clearly the significance of the normal shear stress

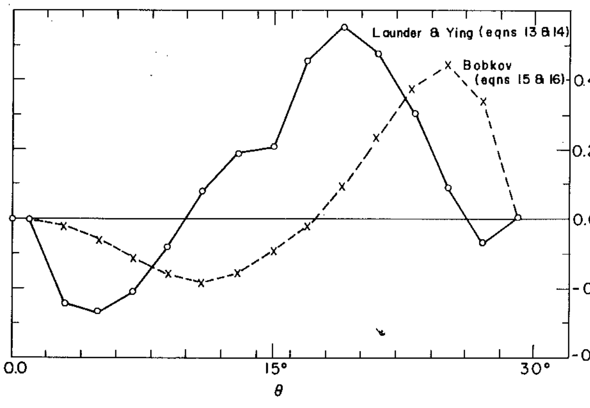

Fig. 5 Prediction of v_θ velocity at $y = y_B$

modeling in prediction of secondary flow independent of how well the rest of modeling has been done. However both predictions have in common a negative loop close to the vicinity of $\theta = 0$ deg which is weaker than the positive one at larger θ.

The 30 × 16 grid used for the present calculations is rather inadequate due to the existence of sharp v_θ gradients especially at $\theta = 30$ deg and at the wall. However increase of grid mesh points requires more computer storage and exceedingly high computer cost. The solutions presented here already required 4000 iterations and 90 minutes of computer time on an IBM 360/65. The small magnitude of the calculated secondary flow can be affected by computer round-off error although both cases were run with double precision. From the above calculations on secondary flow, we can draw the following conclusions.

(1) The calculations are indicative of the small magnitude of secondary flow, i.e., below 1 percent of the axial velocity.

(2) Taken into consideration the small size of the secondary flow and the sensitivity of the results on normal stress modeling, it is evident that quantitative secondary flow predictions need accurate enough turbulence modeling. The above turbulence models as well as other turbulent models which cannot predict the axial velocity with an error better than the secondary flow magnitude cannot qualify as models for calculating the secondary flow.

In spite of above negative conclusions, the question still remains: Is the secondary flow, at least as predicted by the two-equation turbulence model important in prediction of other hydrodynamic quantities, especially the mean velocity? Or at least how important is secondary flow compared with anisotropic eddy viscosity? These questions are answered in Fig. 6 which shows v_z/u_0 along the $\theta = 0$ radial line and demonstrates that the anisotropy is much more significant than the secondary flow effect. Under these circumstances, further investigation of secondary flow for this geometry has been deferred. Such a decision has also been prompted by the high computer cost due to the very low convergence rate. All subsequent data predictions are made with secondary flow suppressed. It should be recalled that a secondary flow search was conducted in this test section and it was concluded that such flows were less than 0.67 percent of the bulk axial velocity at a Reynolds number of 2.7×10^4 [1].

6.3 **Data Predictions.** The present model has been tested against the fully developed data of this study ($P/D = 1.124$, Re = 65,000, 26,500 and 9000) and with mean axial velocity data of Eifler [18] ($P/D = 1.08$, Re = 52,400), Trupp [17] ($P/D = 1.35$, Re = 60,000) and Kjellstrom [20] ($P/D = 1.217$, Re = 149,000).

The above data are representative of a variety of P/D ratios (1.08–1.35) and Reynolds numbers (9000–150,000). Figs. 7 and 8 shows mean axial velocity, radial Reynolds stress and turbulent kinetic energy predictions compared to the experimental results for Re = 65,000 of this study.

Figs. 9 and 10 show mean velocity predictions compared to the data of the present study for Re = 26,500 and 9000, Eifler's data, Trupp's data and Kjellstrom's data. The data of these other investigators were normalized by either u_0 or u_b depending on their availability. The predictions are independent of the normalization constant. Comparison between predictions and experimental data suggest that for $P/D \leq 1.20$ a value for c_L around 0.4 is appropriate whereas for $P/D > 1.20$, c_L has to be increased.

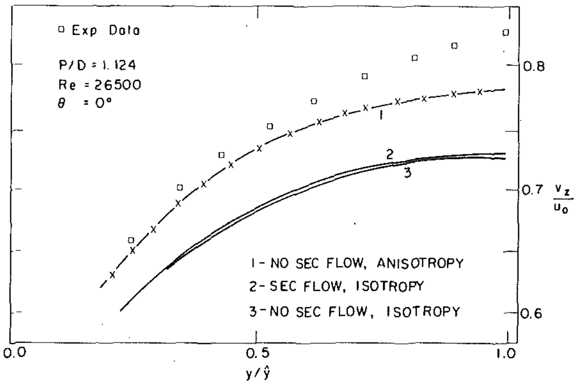

Fig. 6 Anisotrophy versus secondary flow

A relation for c_L satisfactorily fitting the above data ($P/D \geq 1.08$) is

$$c_L = 1.62 \exp(-17 (P/D - 1)) + 0.4$$

All data predictions were made with the above relation.

Although $c_L = 0.4$ gives less accurate results, it gives more conservative heat transfer results as shown in Fig. 11. The calculated c_L values from equation (18) are not in disagreement with the experimental data obtained by Rehme [3] in a side subchannel with $P/D = 1.07$ which suggest an eddy viscosity along the zero shear stress line of

$$v_{rz}{}^T = (0.10 - 0.16)u^*\hat{y} \tag{18}$$

Using above the expression and standard relations for simple geometries, we find

$$c_L = 0.55 \text{ to } 0.9$$

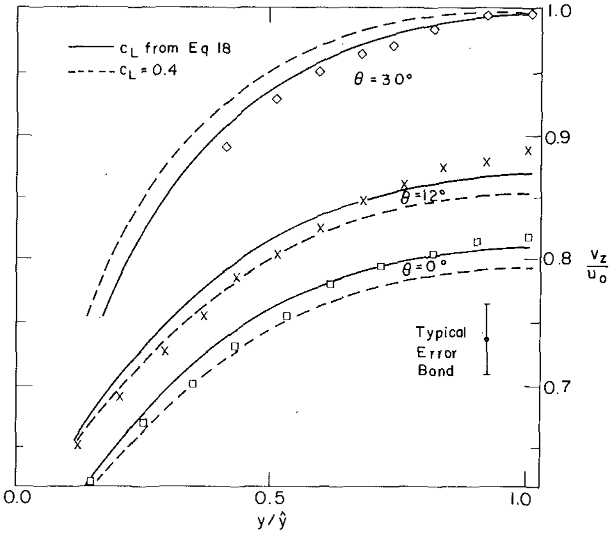

Fig. 7 Axial velocity prediction (Re = 65,000)

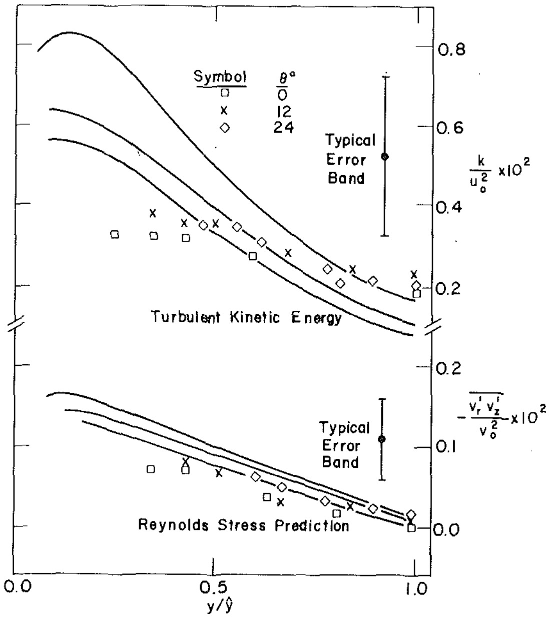

Fig. 8 Turbulent kinetic energy and shear stress prediction (Re = 65,000)

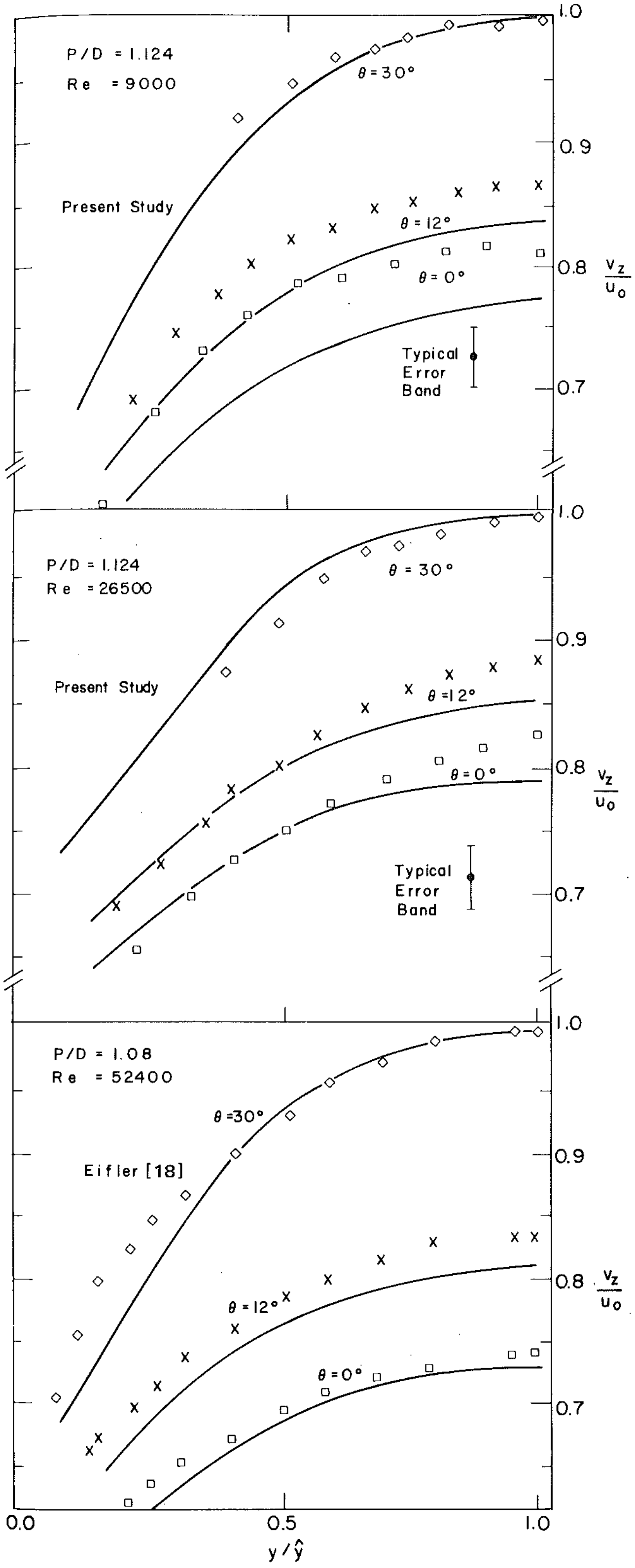

Fig. 9 Axial velocity prediction

The degree of success of the analytic predictions is a function of the Reynolds number range.

(1) *High Reynolds Number Predictions* (*Re* > *26,500*). The mean axial velocity and the wall shear stress distribution predictions are relatively good. The predictions for $\overline{v_r'v_z'}$ and k are good although more accurate measurements are needed for more definite conclusions.

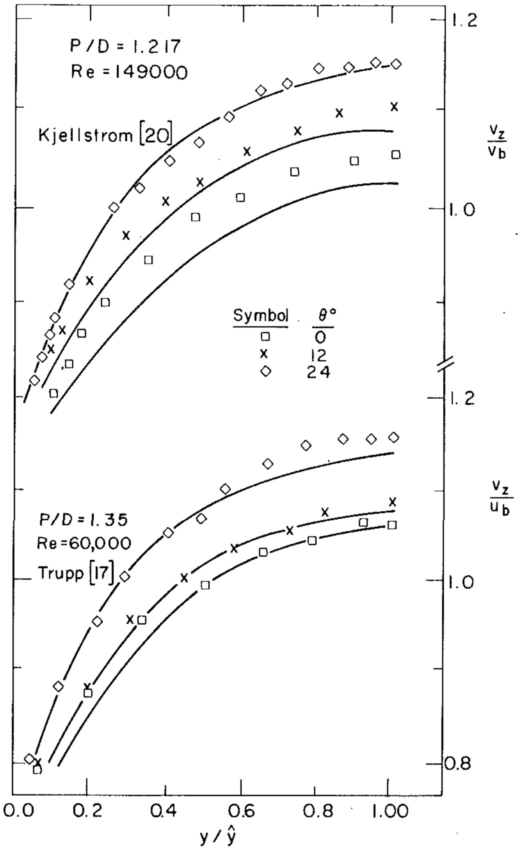

Fig. 10 Axial velocity predictions

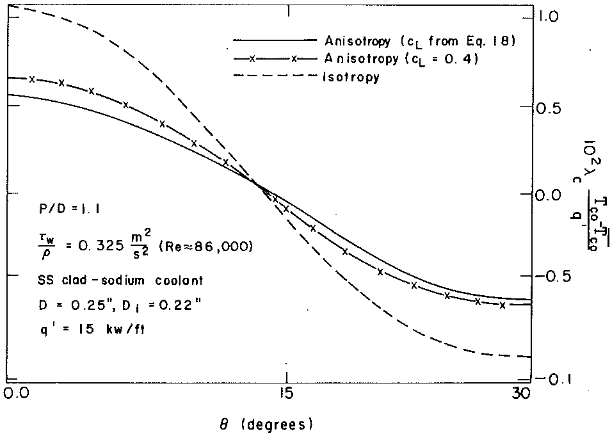

Fig. 11 Outside clad temperature difference

(2) *Low Reynolds Number Predictions* (*Re* = *9000*). The predictions are not as satisfactory as at High Reynolds Numbers as Fig. 9 shows. The present predictions for Re = 9,000 support the approach of modifying the two-equation turbulence model to take into account Low Reynolds Number Effects already initiated by other investigators [21].

6.4 Heat Transfer Calculations. Two region (clad + coolant) heat transfer calculations have been performed to examine the effect of anisotropic viscosity as introduced in the present work versus isotropic viscosity working with the two-equation turbulence model.

The calculations have been performed for a stainless steel clad fuel pin operating at 15 kw/ft in flowing sodium. All material properties were taken at 1000°F. A ratio of heat diffusivity to eddy viscosity equal to one for both radial and tangential directions was used.

In Fig. 11, the nondimensional temperature is plotted versus angular position. Fig. 11 shows the strong effect of anisotropic eddy viscosity where the value of $T_{co}^{\max} - \overline{T}_{co}$ shows a difference almost 2 to 1 or for the example chosen, 14 versus 7°F.

The importance of anisotropic model of eddy viscosity for heat transfer calculations as demonstrated earlier by other investigators [4, 5], is again clearly shown. The only clad temperature experimental results [26] are at different Peclet numbers for larger spacings and pins near the bundle periphery, factors which lead to opposing effects, so that comparisons with our predictions is not possible More accurate temperature predictions would have to be based on a model for the directional eddy diffusivity of heat which included the effects of turbulent structure, a task not addressed in this paper.

7 Conclusions

(1) The two-equation turbulence model as presently formulated is a satisfactory engineering tool for predicting useful hydrodynamic quantities (i.e., mean axial velocity, Reynolds stresses, shear stress) in a rod bundle at high Reynolds numbers (presently, it has been tested satisfactorily with Reynolds numbers above 26,500). The model does not seem to be a sufficient tool for predicting secondary flows in rod bundles.

(2) The model has been used to successfully predict the data obtained in this study and published rod bundle data (principally axial velocity) above Re = 26,500 utilizing one consistent set of constants for one-dimensional flow from the literature.

(3) Secondary flow calculations with the above model indicate secondary flow effects on the axial velocity distribution to be minor compared with eddy viscosity anisotropy effects.

(4) The introduction of eddy viscosity anisotropy through length scale ratios, while keeping the model simple, also make the model inherently extendable to three dimensions. (One can follow the same logic and introduce a length scale 1_z similar to 1_θ for axial diffusion.)

(5) The strong effect of the anisotropy in eddy viscosity on heat transfer calculations shown by other investigators is also confirmed in the present work.

Acknowledgments

This research was concluded as part of Contract E(11-1)-2245 sponsored by ERDA. The authors gratefully acknowledge this support.

References

1 Carajilescov, P. and Todreas, N. E., "Experimental and Analytical Study of Axial Turbulent Flows in an Interior Subchannel of Bare Rod Bundle," ASME, JOURNAL OF HEAT TRANSFER, Vol. 98, pp. 262–268.

2 Nijsing, R., Eifler, W., Delfau, B., "Laterial Turbulent Diffusion for Longitudinal Flow in a Rectangular Channel," *Nuclear Engineering and Design,* Vol. 32, pp. 221–238.

3 Rehme, K., "Anisotropic Eddy Viscosities in the Turbulent Flow through a Rod Bundle," *Symposium on Turbulent Shear Flows,* University Park, PA, 1977.

4 Ramm, H., and Johannsen, K., "A Phenomenological Turbulence Model and its Application to Heat Transport in Infinite Rod Arrays with Axial Turbulent Flow," ASME, JOURNAL OF HEAT TRANSFER, 1975, pp. 231–237.

5 Nijsing, R., and Eifler, W., "Temperature Fields in Liquid Metal Cooled Rod Assemblies," *Progress in Heat and Mass Transfer,* 1973.

6 Hoffman, G. H., "Improved Form of Low Reynolds Number k-ϵ Model," *The Physics of Fluids,* Vol. 18, No. 3, 1975.

7 Launder, B. E., "Progress in theModeling of Turbulent Transport," Short Course at the Pennsylvania State University, 1975.

8 Brundrett, E., and Baines, W. D., "The Production and Diffusion of Vorticity in Duct Flow," *Journal of Fluid Mechanics,* Vol. 19, 1964, pp. 375–394.

9 Prandtl, L., "Uber ein neus formelsystem für die augsgebildete Turbulenz," *Ludwig Prandtl Gesammete Abhandlungen,* Springer, Verlag, 1945, pp. 874–887.

10 Bobkov, V. P., Ibragimov, M. Ch., Savelev, G. I., "Correction of Experimental Data on the Pulsation Velocity Intensity for Turbulent Fluid Flow in Channels of Different Form," *Izv AN SSR Mekhanica Zhidosti i Gaza,* Vol. 3, No. 3, 1968, (English Translation pp. 111–113).

11 Buleev, N. I., "Theoretical Model for Turbulent Transfer in 3-Dimensional Flows," Paper No. 329 presented at the Third UN Int. Conference on Peaceful Uses of Atomic Energy, Geneva, 1964.

12 Launder, B. E., and Ying, "Prediction of Flow and Heat Transfer in Ducts of Square Cross Section," *The Institution of Mech. Engineering Proc.,* Vol. 187, 37/73, 1972, pp. 455–461.

13 Launder, B. E., Reece, G. J., and Rodi, W., "Progress in the Development of Reynolds Stress Turbulence Closure," *Journal of Fluid Mechanics,* 1975.

14 Bartzis, J. G., "Hydrodynamic Behavior of a Bare Rod Bundle," Ph.D. Thesis, MIT, Dept. of Nuclear Engineering, 1977.

15 Naot, D., Shavit, A., and Wolfshtein, M., "Numerical Calculations of Reynolds Stresses in a Square Duct with Secondary Flow," *Warme Stoffubertragung,* Vol. 7, 1975, pp. 151–161.

16 Gosman, A. D., "Listing of the TEACH-T Computer Program and Sample Output," The Pennsylvania State University, Aug. 1975.

17 Trupp, A. C., and Azad, R. S., "The Structure of Turbulent Flow in Triangular Array Rod Bundles," Dept. of Mech. Eng., University of Manitoba, Winnepeg, Canada, 1973.

18 Eifler, W., "Über die turbulente Geschwindigkeitsverteilung und Wandreibung in Strömungskanälen verschiedener Querschuitte," Doctoral Thesis, T.H. Darmstadt, 1968.

19 Gosman, A. D., Pun, W. M., Runchal, A. K., Spalding, D. B., and Wolfshtein, M., *Heat and Mass Transfer in Recirculating Flows,* Academic Press, London, 1969.

20 Kjellstrom, B., "Studies of Turbulent Flow Parallel to a Rod Bundle of Triangular Array," Report AE-RV-196, AB Atomenergi, Sweden, 1971.

21 Jones, W. P., and Launder, B. E., "The Calculation of Low-Reynolds Phenomena with 2-Equation Model of Turbulence," *International Journal of Heat and Mass Transfer,* Vol. 16, 1973, pp. 1119–1130.

22 Issacson, E., and Keller, H. B., *Analysis of Numerical Methods,* J. Wiley and Sons, 1966.

23 Chen, Y. B., "Coolant Mixing in the LMFBR Outlet Plenum," Ph.D. Thesis, Dept. of Nuclear Eng., MIT, 1977.

24 Bartzis, J. G. and Todreas, N. E., "Turbulent Measurements in a Triangular Array of Bare Rod Bundles," to be published.

25 Carrelli, M. and Willis, J., "An Analytical Method to Accurately Predict LMFBR Core Flow Distribution," *Transactions American Nuclear Society,* Vol. 32, pp. 575–576, 1979.

26 Möller, R. and Tschöke, H., "Experimental Determination of Temperature Fields in Sodium Cooled Pin Bundle," Presented at Nucl. Conf. 1976 in Düsseldorf, Germany. Translated by L. Wolf, MIT.

G. R. Knowles
E. M. Sparrow

Department of Mechanical Engineering,
University of Minnesota,
Minneapolis, Minn. 55455

Local and Average Heat Transfer Characteristics for Turbulent Airflow in an Asymmetrically Heated Tube

Turbulent airflow experiments were performed with a specially fabricated test section tube which facilitated nonuniform heat transfer around the tube circumference. Heating was accomplished by passing electric current axially through half the tube wall (subtending a 180 deg arc), while the other half of the wall was not directly heated. Measurements were made both in the thermal entrance region and the fully developed region, and the Reynolds number was varied from about 4400 to 64,000. The results of the experiments underscored the strong interaction between circumferential tube-wall conduction and fluid convection when a gas flowing in a tube is heated nonuniformly around its circumference. The effects of the wall conduction were shown to be significant at low Reynolds numbers but diminished as the Reynolds number increased. Owing to the circumferential nonuniformities, the thermal development was much slower than that for a uniformly heated pipe flow. By use of a suitably defined circumferential average heat transfer coefficient, the present fully developed results agreed well with a literature correlation for uniformly heated flows. At any cross section, the local coefficients varied around the tube circumference, with the smallest value at the mid-point of the heated arc. Buoyancy effects at low Reynolds numbers were investigated and found to be undetectably small.

Introduction

The tubes of heat exchange devices are commonly subjected to circumferential variations of heat flux. Such variations may be encountered for boiler, condenser, and heat exchanger tubes as well as for tubular absorbers of solar energy in flat plate and linear concentrating collectors. The fluid flowing in such tubes is subjected to circumferentially nonuniform thermal boundary conditions, so that the convective heat transfer processes may differ from those in conventional uniformly heated tubes.

The net effect of imposed circumferential variations depends on both convective transport in the flowing fluid and heat conduction in the tube wall. For a given variation of heat flux on the outside surface of the tube, the relative strengths of these processes determines the extent of the circumferential variations at the tube bore. This is because heat flowing from the outside of the tube into the fluid will, necessarily, follow the path of least resistance. Thus, for example, if the heat transfer coefficient for the tube flow is relatively small (i.e., high convective resistance), the heat will find the circumferential path within the tube wall to be an attractive option. This diminishes the magnitude of the circumferential variations at the bore. On the other hand, if the heat transfer coefficient is very high, the heat moves more or less radially across the thickness of the wall, thereby preserving at the bore the externally applied circumferential variation.

Since the heat transfer coefficients for gas flows are typically lower than those for liquid flows, it can be expected that wall conduction effects will play a greater role in gas-carrying tubes than in liquid-carrying tubes. In addition, since the heat transfer coefficient increases with the Reynolds number, the importance of the wall effects should be accentuated at lower Reynolds numbers.

Experiments concerned with turbulent pipe flows which are nonuniformly heated around their circumferences are described in [1, 2] and [3, 4] with air and water as working fluids, respectively. In [1], the nonuniform heating was accomplished by passing an electric current through the tube wall, the thickness of which varied around the circumference. The overall circumferential heat flux variation obtained by this technique was limited to a factor of two, and the varying thickness affected the circumferential conduction of heat in the wall. Heat transfer coefficients were not reported in [2], and the heated length was only three diameters. The experiments of [3] were performed with a sparsely instrumented test section, with corresponding uncertainties in the results. In [4], a nonuniformly heated test section was fabricated by slitting a tube longitudinally and then reassembling the two halves, using an epoxy adhesive at the cut edges to bond the halves and electrically isolate them from each other. Heating was accomplished by the passage of electric current axially through one of the halves of the reconstituted tube. Since [4] bears a filial relationship to the present investigation, it will be referred to from time to time throughout the paper.

In the present paper, experiments are reported on turbulent airflow in a circular tube subject to circumferentially nonuniform heating. One of the aims of the study was to employ larger heat flux variations than those of [1] and to extend the Reynolds number range to lower values in order to explore possible effects of natural convection. In addition, the present experiments avoided the nonuniform circumferential conduction path of [1] (associated with the varying tube wall thickness used there).

A second major aim of the work was to identify the influence of working fluid on the effects caused by nonuniform heating. As noted earlier, differences between liquid and gas flows are to be expected on the basis of sharp differences between the magnitudes of the respective heat transfer coefficients. To enable meaningful comparisons to be made, the test section for the present airflow experiments was fabricated in a manner identical to that for the water experiments of [4], with the respective tubes for the two experiments being cut from the same length of tubing. This insured that the circumferential conductance for the two cases would be the same, while the heat transfer coefficients differed by a factor of 50 or more (at the same Reynolds number). The difference in buoyancy effects for the two working fluids was also explored.

Heating was accomplished by passing electric current through half of the tube wall (subtending a 180 deg arc), while the other portion of the wall was unheated. The outer surface of the wall was heavily instrumented with thermocouples deployed both along the length and around the circumference. During the course of the experiments, the Reynolds number was varied from about 4000 to 64,000. The test section was horizontal throughout the experiments, but the heated half was alternately positioned in the upper and lower portions of the cross section to study possible natural convection effects.

Results are presented for both the thermal entrance region and the downstream region where thermally developed conditions were approached. The thermal development is illustrated graphically by both axial and circumferential tube-wall temperature distributions. These

---

Contributed by the Heat Transfer Division for publication in the JOURNAL OF HEAT TRANSFER. Manuscript received by the Heat Transfer Division December 15, 1978.

temperature distributions also reveal the effects of heat conduction within the wall of the tube. Another view of the thermal development is provided by axial distributions of the circumferential average Nusselt number, and the fully developed values are compared with literature correlations for uniformly heated flows. Circumferential distributions of the Nusselt number at downstream stations are compared with each other at various Reynolds numbers and, to explore buoyancy effects, at different positionings of the heated arc. Finally, the predictive procedure of [5] is employed to calculate Nusselt numbers as a function of angular position, and these results are brought together with the experimental data.

The Experiments

The experiments were performed in an open-loop flow circuit to which air was supplied from a central dryer-equipped compressor. Air taken from the building supply line was passed through a fine-tuned precision pressure regulator which ensured steady flow and then passed successively through a control valve, filter, and metering orifice. From the orifice, the air was ducted to the hydrodynamic development section—an 80 diameters long circular tube whose downstream end mated with the heated test section. The development and test sections were horizontal, colinear, and shared a common internal diameter. After traversing the length of the test section, the air passed through a mixing chamber and then was exhausted outside of the building. Schematic diagrams of the flow circuit and the test section are presented in Figs. 2.1–2.3 of [6].

The test section was a specially fabricated tube which enabled the flowing fluid to be heated only over part of its circumference. The fabrication procedure involved a substantial amount of development work, and only the highlights will be described here. To initiate the fabrication, a thin-wall stainless steel tube was internally honed to a high degree of smoothness and then cut longitudinally into two portions. The circumference of one portion subtended an arc of 180 deg, whereas the circumference of the other portion subtended a 150 deg arc—the other 30 deg having been removed in the cutting process. Then, with a high-strength electrically nonconducting epoxy as the adhesive, the two parts of the tube were reassembled around a teflon-coated circular rod which served as a mandril and also as a heat source for the curing of the epoxy. Upon extraction of the rod, the tube bore was lightly honed to remove any epoxy that was not flush with the wall, with the result that the presence of the epoxy seams could not be detected by feel.

During the fabrication operations, numerous difficulties were encountered which are described elsewhere [6, 7], along with the tooling and special fixtures that were employed. The development of the fabrication procedure represents a common ground between the present research and [4, 7]. In addition, the stainless steel tubes for the respective test sections were cut from a common length of tubing, with that for the present experiments being substantially longer to accommodate the expected longer thermal development for air compared with water. Aside from this, the two pieces of research are completely independent.

The reconstituted test section tube had an internal diameter of 30.8 mm (1.21 in.) and a mean wall thickness of 0.820 mm (0.0323 in.). Prior to the reassembly of the tube, the local wall thickness had been measured at all locations at which tube surface temperatures were to be determined, and this information was subsequently employed as input to the data reduction. It was found that the local thicknesses differed by as much as ±5 percent from the mean. The length of the tube was about 60 diameters.

Once the test section tube had been fabricated, the internal diameter of the hydrodynamic development tube was carefully matched with that of the test section. This was accomplished by a reaming operation which enlarged the bore diameter of the PVC entrance tube to the desired size. The reamed PVC surface was comparable in smoothness to the honed surface of the bore of the test section.

The electrical isolation of the two longitudinal portions of the test section tube from each other enabled one portion to be heated by internal ohmic dissipation while the other portion was free of electric currents. The 180 deg portion was selected as the heated part, and bus bars were attached at its upstream and downstream ends. Owing to the relatively low resistance of the test section tube (0.034 ohms), it was necessary to design the bus bars for currents up to 75 amps. Furthermore, the bars were designed to avoid extraneous heat conduction, both with respect to radial heat losses and to the circumferential temperature distribution in the tube wall.

In order not to obliterate circumferential variations which would otherwise exist, a conventional continuous-ring bus bar was not used. Rather, an arrangement consisting of 15 individual copper bars, deployed radially in a fan-like pattern, was employed (see Figs. 2.4 and 2.5 of [6]). To more accurately define the axial location at the start of heating, each bar was tapered to reduce the axial extent of its contact with the tube. The outer end of each bar was connected by wires to a terminal block, and an axuiliary heater at the terminal block was used to minimize extraneous heat loss along the wires.

Temperatures were measured on the outer surface of the test section tube by calibrated 30-gage copper and constantan thermocouple wire. The junctions were spot welded to the tube wall. All told, twenty axial stations were instrumented with a total of 192 thermocouples. The number of thermocouples circumferentially deployed at each station ranged from 4 to 20—with 14 being the most common number. The tube wall temperatures, as well as the other measured temperatures (fluid bulk, bus bars, etc.), were read by a digital datalogger that was coupled to a teletype-writer which produced a listing and a punched tape record of the data.

Fluid bulk temperatures were measured at the inlet to the hydrodynamic development tube and in the mixing chamber downstream of the test section. For measuring the rate of air flow through the system, either of two calibrated sharp-edged orifices were employed, depending on the Reynolds number range.

The apparatus was heavily insulated to minimize heat losses (or gains). The hydrodynamic development section, the test section, and the downstream mixing chamber were housed in an enclosure made of 5 cm (2 in.) thick styrofoam (two thicknesses of the styrofoam were

Nomenclature

c_p = specific heat at constant pressure
D = test section inside diameter
g = acceleration of gravity
h = local heat transfer coefficient, equation (1)
$\bar{h}$ = circumferential average heat transfer coefficient, equation (6)
k = thermal conductivity of air
k_w = thermal conductivity of tube wall
$\dot{m}$ = mass flow rate
Nu = local Nusselt number, hD/k
$\overline{\mathrm{Nu}}$ = circumferential average Nusselt number for heated surface, $\bar{h}D/k$
Pr = Prandtl number
Q_{cond} = circumferential conduction out of heated arc
Q_{conv} = convective heat transfer
q = local convective heat flux
$\bar{q}$ = average convective heat flux for heated arc
$\bar{\bar{q}}$ = mean heat flux to fluid
q_L = losses to the surroundings
q_{Le} = conduction losses from edges of heated section
Ra* = modified Rayleigh number, equation (13)
Re = Reynolds number, $4\dot{m}/\mu\pi D$
R_i = inner radius of tube
R_m = mean radius of tube
T_b = bulk temperature
T_{b0} = inlet bulk temperature
T_w = local wall temperature
$\bar{T}_w$ = average wall temperature for heated arc
t = local wall thickness
$\bar{t}$ = average wall thickness for heated section
x = axial coordinate measured from onset of heating
β = thermal expansion coefficient
θ = angular coordinate
μ = viscosity
ν = kinematic viscosity

used for the lid of the enclosure). The enclosure created a cavity with a 15 × 10 cm (4 × 6 in.) cross section, and the apparatus was positioned centrally in the cavity cross section. Once the apparatus was in place, the cavity was filled with silica aerogel, a fine powder with a thermal conductivity less than that of air. As a further precaution against extraneous heat losses, the test section was not supported at any point along its length; rather, it was suspended from its ends. The piping upstream of the hydrodynamic development tube was wrapped with fiberglass insulation.

Further information about the apparatus and the operating procedure are available in [6].

Data Reduction

As a first step in processing the data, estimates were made of the radial temperature variations across the thickness of the heated wall of the test section tube. At the intermediate heating rates, the temperature differences between the inner and outer surface of the tube were about 0.01°C, and at the maximum heating power there was a 0.03°C temperature difference. These differences are sufficiently small so that no further account need be taken of radial variations, and the measured outside wall temperatures can be used as inside wall temperatures in the evaluation of the heat transfer coefficient.

Two types of heat transfer coefficients for the heated wall were evaluated from the data. The first is the local heat transfer coefficient $h(x, \theta)$ at x, θ, where x is the axial coordinate and θ is the angular coordinate. The other is the circumferential average coefficient $\overline{h}(x)$ corresponding to an axial station x. Attention will first be given to the procedure used for determining $h(x,\theta)$, and subsequently to $\overline{h}(x)$.

The defining equation for $h(x,\theta)$ is

$$h(x,\theta) = \frac{q(x,\theta)}{T_w(x,\theta) - T_b(x)} \tag{1}$$

in which $q(x,\theta)$ and $T_w(x,\theta)$ are the local convective heat flux and local inside wall temperature respectively; $T_b(x)$ is the bulk temperature at x. Whereas $T_w(x,\theta)$ is obtained by direct measurement (as explained in a preceding paragraph), both $q(x,\theta)$ and $T_b(x)$ are computed quantities—using the data as input.

To determine $q(x,\theta)$, an energy balance is written for a control volume of dimensions t by $R_m d\theta$ by dx which spans the thickness t of the tube wall and subtends an arc $R_m d\theta$ (R_m = mean radius of tube wall). The use of such a wall-spanning element is permissible because of the extremely small radial temperature changes (relative to the circumferential changes). For the energy balance, the relevant terms include: (a) $q(x, \theta)$, (b) the ohmic dissipation, (c) the net circumferential heat flow, and (d) the heat loss from the outside surface of the tube. Mathematically, the balance can be written as

$$q(x, \theta) = (R_m t/R_i)P''' + \frac{k_w}{R_i}\frac{\partial}{\partial\theta}\left[\frac{t}{R_m}\frac{\partial T_w}{\partial\theta}\right] - q_L(x, \theta) \tag{2}$$

In this equation, P''' is the volumetric heating rate (derived in [6]), R_i is the inner radius of the tube wall, and R_m is the mean radius equal to $(R_i + t/2)$. The last term, $q_L(x, \theta)$, is the heat loss (per unit inside surface area) out through the insulation and into the air surrounding the apparatus. It is based on the series resistances of the two insulation layers and the external natural convection and radiation, together with the temperature difference $T_w(x, \theta) - T_\infty$, where T_∞ is the ambient temperature.

In evaluating equation (2), special consideration had to be given to the circumferential conduction term because of the required θ-derivatives of the measured wall thickness t and measured wall temperature T_w. The variation of the wall thickness was not a smooth function, which precluded its description by a simple algebraic expression.[1] As a consequence, a finite-difference representation was used for the outer derivative of the circumferential conduction term. If j denotes the point x, θ_j and $(j + 1)$, $(j - 1)$, respectively, denote the adjacent points, then the conduction term was written as

$$(k_w/R_i)[(t_{j+1} - t_{j-1})/2R_m\Delta\theta](\partial T_w/\partial\theta)_j + (k_w/R_iR_m)t_j(\partial^2 T_w/\partial\theta^2)_j \tag{3}$$

where $\Delta\theta$ is the angular separation of the points.

The measured circumferential temperature distributions on the heated wall were generally quite smooth, aside from a slight scatter caused by the variations in wall thickness. It was found that these distributions could be well represented by a second-degree polynomial

$$T_w = a_0 + a_1\theta + a_2\theta^2 \tag{4}$$

where the a's were determined from a least-squares fit. The derivatives appearing in (3) were evaluated by differentiating the polynomial representation (4).

With $q(x, \theta)$ determined, the only other ingredient needed for the calculation of $h(x, \theta)$ from equation (1) is the local bulk temperature $T_b(x)$. In terms of the inlet bulk temperature T_{b0} and the net convective heat flux $q_{\text{net}}(x)$ at any axial station x, $T_b(x)$ can be written as

$$T_b(x) = T_{b0} + (\pi D/\dot{m}c_p)\int_{-\ell}^{x} q_{\text{net}}(x)dx \tag{5}$$

Since T_{b0} is measured at the inlet of the hydrodynamic development tube where $x = -\ell$, the range of the integration is extended over the length of the development tube as well as into the heated test section. The convective flux $q_{\text{net}}(x)$ is the net of the local ohmic heating (equal to zero in the development tube) and the losses.

Attention may now be turned to the circumferential average heat transfer coefficient for the heated portion of the tube at a given axial station x. This quantity, denoted by $\overline{h}(x)$, is defined by

$$\overline{h}(x) = \frac{\overline{q}(x)}{\overline{T}_w(x) - T_b(x)} \tag{6}$$

where both $\overline{q}(x)$ and $\overline{T}_w(x)$ are averaged over the 180-degree heated segment. The expression used to determine $\overline{q}(x)$ is

$$\overline{q}(x) = (R_m\overline{t}/R_i)P''' - q_L(x) - q_{Le}(x) \tag{7}$$

All terms in equation (7) have been written per unit inside area of the heated portion of the tube. The first term on the right is the ohmic dissipation based on the average wall thickness $\overline{t}$ at axial station x. The quantity $q_L(x)$ is the heat loss out through the insulation into the surrounding ambient. It was evaluated in a manner identical to that used for $q_L(x, \theta)$ in equation (2), except that now the thermal potential is $\overline{T}_w(x) - T_\infty$ rather than $T_w(x, \theta) - T_\infty$.

The last term, $q_{Le}(x)$, takes account of heat losses from the edges of the heated arc into the epoxy seams which bond the tube together. If $\theta = 0$ deg denotes the midpoint of the heated arc, then the respective edges are at $\theta = \pm\pi/2$, and

$$q_{Le}(x) = (k_w/\pi R_iR_m)(|t\partial T_w/\partial\theta|_{\pi/2} + |t\partial T_w/\partial\theta|_{-\pi/2}) \tag{8}$$

The derivatives appearing in equation (8) were evaluated by means of the fitted polynomials (4).

The average wall temperature $\overline{T}_w(x)$ appearing in equation (6) was obtained from

$$\overline{T}_w(x) = (1/\pi)\int_{-\pi/2}^{\pi/2} T_w(x, \theta)d\theta \tag{9}$$

while the bulk temperature is from equation (5). With these inputs, $\overline{h}(x)$ was evaluated from equation (6).

The heat transfer coefficients $h(x, \theta)$ and $\overline{h}(x)$ will be represented in dimensionless form via the following Nusselt numbers

$$\text{Nu}(x, \theta) = h(x, \theta)D/k, \quad \overline{\text{Nu}}(x) = \overline{h}(x)D/k \tag{10}$$

where k denotes the thermal conductivity of air at the local bulk temperature. The data runs are parameterized by the Reynolds number, which was evaluated from

$$\text{Re} = 4\dot{m}/\mu\pi D \tag{11}$$

Here, μ is the air viscosity at the mean bulk temperature.

---

[1] A complex expression could have been employed, but it would have yielded unrealistic θ-derivatives.

Property variations do not play a major role in the experimental results. The inlet-to-exit bulk temperature rise was typically about 5°C (~10°F), and the wall-to-bulk temperature differences near the downstream end of the tube were in the same range. The Prandtl number for all cases was about 0.7.

Results and Discussion

Temperature Distributions. For the most part, the results will be presented in dimensionless form. However, to provide a feeling for the actual temperature levels and differences that were involved in the experiments, a representative set of axial temperature distributions along the tube wall will be presented on a dimensional basis. In Fig. 1, the wall temperature (in °C) at various fixed values of the angular coordinate θ are plotted as a function of the axial position x (expressed in terms of the diameter, D). The figure corresponds to a Reynolds number of 15,000 and to a power input of 41.6W. Curves have been passed through the experimental data to provide continuity. The curves that are situated in the upper part of the figure are for angular positions on the heated portion of the tube, while those in the lower part of the figure are for the unheated portion. The lowest curve depicts the bulk temperature distribution.

For purposes of orientation, it may be noted that $\theta = 0$ deg denotes the circumferential mid-point of the heated portion of the tube, while $\theta = 180$ deg is at the mid-point of the unheated portion. The plotted data at 40, 60, 80, 120, and 140 deg represent respective averages of temperature measurements at $\pm 40, \ldots, \pm 140$ deg. Available data at $\theta = \pm 20$ deg are not shown in the figure because of its proximity to $\theta = 0$ deg data and, similarly, data at ± 160 deg are omitted from the figure to avoid confusion with the 180 deg data.

The axial temperature distributions on the heated portion of the tube are generally similar in form to that for a uniformly heated tube. There is a rapid initial rise of the temperature just downstream of the onset of heating and a more gradual rise thereafter. Aside from local perturbations, the distribution curves at the various angular positions are approximately parallel to each other and to the bulk temperature line, but not precisely parallel. This observation suggests that thermally developed conditions have not quite been attained, a conclusion which is reinforced by the behavior of the temperature distributions on the unheated portion of the tube. Those distributions also have not attained precise parallelism with each other and with the bulk.

Inspection of graphs similar to Fig. 1 for other cases (available in [6]) shows that the thermal development is more rapid at lower Reynolds numbers and slower at higher Reynolds numbers. As will be further documented shortly, thermal development lengths for the present partial heating condition are substantially longer than the 8–10 diameters for conventional uniformly heated turbulent airflows.

Further study of Fig. 1 shows that at any axial station, the highest temperature on the heated arc occurs at the mid-point (i.e., at $\theta = 0$ deg), and that the temperatures are lower at circumferential locations nearer the unheated portion (i.e., at larger θ values). This finding is consistent with the fact that heat entering the flow at circumferential positions near the mid-point must travel along a relatively long transverse path before reaching the relatively cool bulk flow. On the other hand, heat entering the flow at larger θ values traverses shorter paths with smaller thermal resistance. Thus, the circumferential temperature variation on the heated arc is caused by phenomena which occur in the flowing fluid and does not result from circumferential conduction in the tube wall. Indeed, as will soon be demonstrated, the circumferential conduction works to diminish these temperature variations.

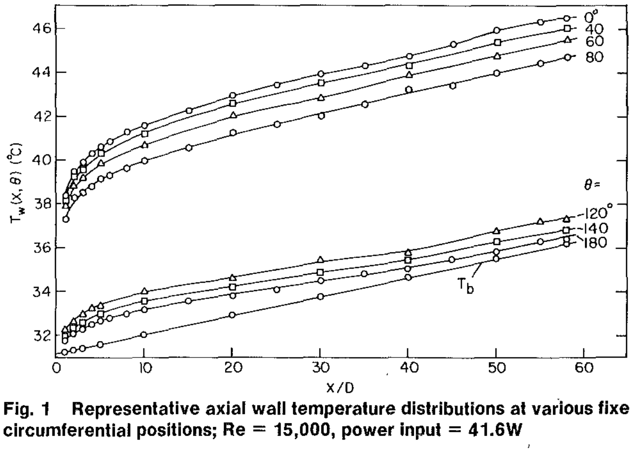

Fig. 1 Representative axial wall temperature distributions at various fixed circumferential positions; Re = 15,000, power input = 41.6W

It may also be observed that the temperatures on the unheated wall exceed the bulk temperature. Thus, there is heat transfer from this wall to the fluid. This heat is supplied to the wall by circumferential conduction from the heated wall—through the epoxy seams which bond the two walls. Therefore, although the so-called unheated wall does not receive heat directly by ohmic dissipation, it is heated indirectly by circumferential conduction. The amount of heat conducted into the unheated wall will be quantified after further evidence of its effect is presented. It should be noted, however, that the angular distribution of this heat around the unheated wall is not known with any degree of certainty and, therefore, no inferences should be drawn from Fig. 1 about heat transfer coefficients on that wall.

The wall temperature results will now be presented from an altogether different viewpoint and, in addition, a dimensionless temperature parameter

$$(T_w - T_{b0})/(\bar{\bar{q}} R_i/k) \tag{12}$$

is used. In this expression, $\bar{\bar{q}}$ is the mean heat flux to the fluid (power input minus losses, per unit inside surface area of the heated wall). Since T_w is the only variable in this grouping, it truly reflects the temperature distribution.

The circumferential temperature distributions at a succession of axial stations are plotted in Figs. 2, 3, and 4, for Re = 4360, 15,000, and 64,000, respectively. The plotted distributions at each station encompass both the heated portion $-90 \text{ deg} \leq \theta \leq 90$ deg and the unheated portion $105 \text{ deg} \leq \theta \leq 255$ deg. Curves based on least-squares second degree polynomials have been passed through the data to provide continuity, and dashed lines were used to interconnect the data for the heated and unheated portions of the tube at a given axial station. Results are presented at axial stations ranging from x/D = 1 to 58.

Inspection of the figures confirms that the highest wall temperature in each cross section is at the mid-point of the heated arc, and the lowest wall temperature is at the mid-point of the unheated arc. On both the heated and unheated walls, the circumferential temperature distributions vary smoothly and continuously. The distributions for the successive stations lie one above the other, as is consistent with the heat addition to the fluid.

The main message of these figures is revealed when comparisons are made among the successive figures. First, it may be observed that whereas at low Reynolds numbers the temperatures on the unheated wall are moderately lower than those on the heated wall, the differences between the unheated and heated walls are very large at high Reynolds numbers. Second, upon taking note of the ordinate scales, it can be seen that the circumferential temperature variations on the heated wall are least at the lowest Reynolds number and increase as the Reynolds number increases. These two observations point up the role of the circumferential conduction in the tube wall and demonstrate how this conduction effect is reduced as the Reynolds number increases.

The conduction tends to promote circumferential temperature uniformity, whereas convection causes circumferential nonuniformities. At low Reynolds numbers, convection is relatively weak, and the conduction has a relatively free hand to do its work. On the other hand, at high Reynolds numbers, the relatively large convective heat transfer coefficients relegate the conduction to a secondary role.

The just-discussed changing role of wall conduction also explains the diminution of data scatter in the heated-wall temperature distributions with decreasing Reynolds number. Because of local variations in the tube wall thickness, there is a corresponding local nonuniformity of the ohmic dissipation. When wall conduction plays an important role (low Reynolds numbers), this nonuniformity is

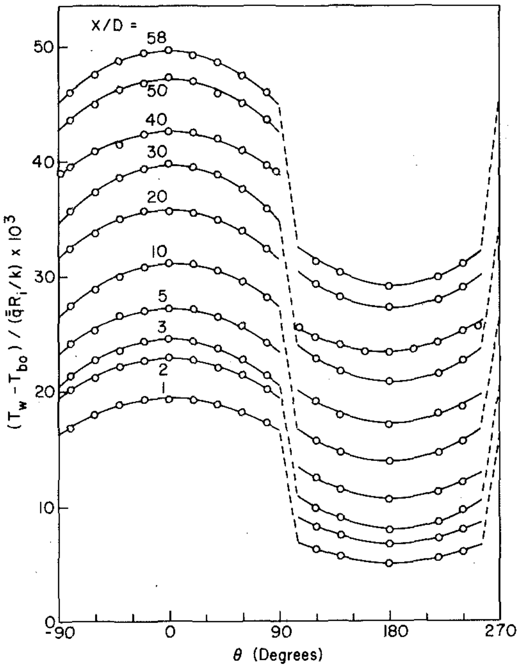

Fig. 2 Circumferential wall temperature distributions at a succession of axial stations; Re = 4360

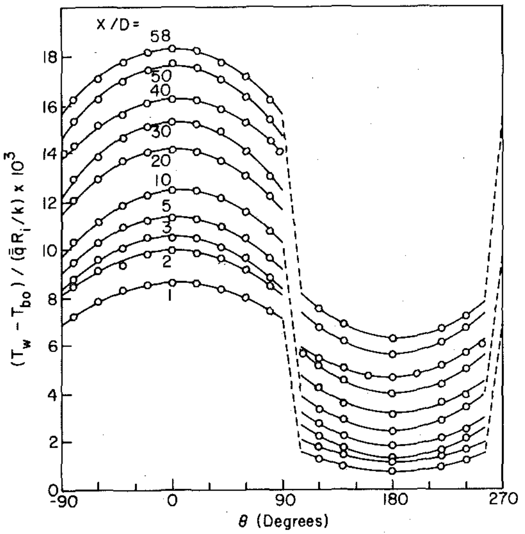

Fig. 3 Circumferential wall temperature distributions at a succession of axial stations; Re = 15,000

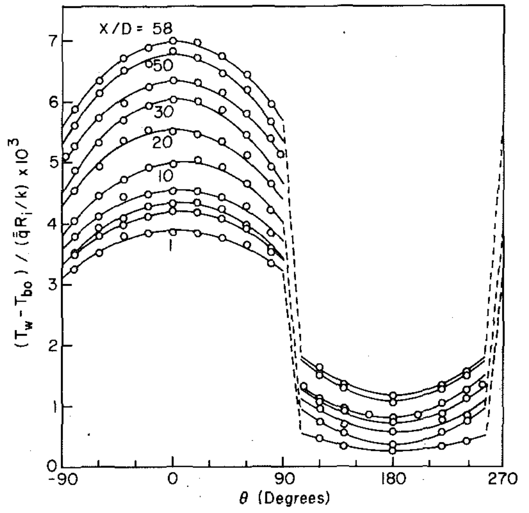

Fig. 4 Circumferential wall temperature distributions at a succession of axial stations; Re = 64,000

smoothed and there is a minimal effect on the tube wall temperatures. However, when the conduction is secondary, the smoothing does not occur and data scatter is in evidence.

To quantify the conduction effect, the circumferential heat flow Q_{cond} conducted out of the edges of the heated part of the tube into the epoxy seams has been evaluated by θ-differentiation of the fitted polynomial (4) at $\theta = \pm 90$ deg. Q_{cond} is compared to the convective heat transfer Q_{conv} in Table 1. These ratios apply to the downstream portion of the tube, $x/D \geq 30$. The table shows that $Q_{\text{cond}}/Q_{\text{conv}}$ decreases from 0.36 to 0.11 as Re ranges from 4360 to 64,000. To the best knowledge of the authors, this is the first such quantification of the circumferential conduction effect.

Circumferential Average Nusselt Numbers. Another view of the thermal development is provided by the axial distribution of the circumferential average Nusselt number $\overline{\text{Nu}}(x)$, which was evaluated from equations (6) and (10). The heat transfer coefficient embedded in this Nusselt number is based on the average heat flux and average wall temperature along the 180 deg heated arc at a given axial station. The $\overline{\text{Nu}}(x)$ results are plotted in Fig. 5 as a function of the dimensionless axial coordinate x/D for Reynolds numbers ranging from 4360 to 64,000. Curves have been faired through the data to provide continuity.

As expected, for any given Reynolds number, the Nusselt number attains a relatively high value just downstream of the onset of heating and then decreases monotonically with increasing downstream distance. Within the scatter of the data, it appears that thermal development is achieved at the lower Reynolds numbers but that the development lengths for the higher Reynolds numbers exceed the 60-diam length of the test section. To provide perspective for this finding, it may be noted that the thermal development length for turbulent airflow (Re > ~10,000) in a circular tube is about 10 diameters (based on five percent approach to the fully developed Nu), when the flow is hydrodynamically developed upstream of the onset of heating. For the present experiments, for Re = 8700 and 15,000, the thermal development lengths, based on the aforementioned five percent approach, are about 27 and 31 diameters, respectively. At the higher Reynolds numbers, the development lengths cannot be estimated with certainty from the available data, but they are, at least, in the range of 40 to 50 diameters. These findings clearly establish that the circumferential nonuniformities elongate the thermal development.

It may be observed that the $\overline{\text{Nu}}(x)$ data points at $x/D = 40$ generally lie above the faired curves. In addition, as seen in Figs. 2, 3, and 4, the heated-wall circumferential temperature distributions at that station lie lower than would logically be expected. The $x/D = 40$ station is more heavily thermocoupled than any other station and, to facilitate installation of the additional thermocouples at $\theta = \pm 90$ deg, some of the epoxy which backs the bonding seams was removed. It is not believed that these factors explain the inconsistent data at $x/D = 40$, and a satisfactory explanation remains to be found. The somewhat

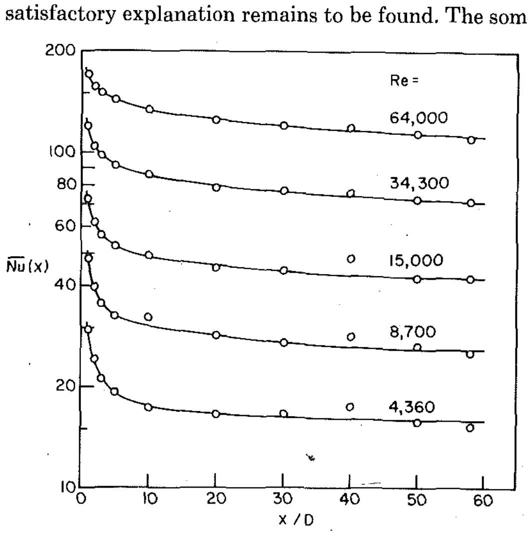

Fig. 5 Axial distributions of the circumferential average Nusselt number

low $\overline{\mathrm{Nu}}(x)$ data at $x/D = 58$ is, in all likelihood, due to the proximity of the bus bars.

It is interesting to compare the fully developed and nearly fully developed values of $\overline{\mathrm{Nu}}(x)$ with available correlations for conventional uniformly heated tubes. For the comparison, the venerable Dittus-Boelter equation and the newer, more accurate Petukhov-Popov equation [8] are used, both being applicable for Re $\geq$ 10,000. The comparison is shown in Fig. 6, where the Nusselt number is plotted as a function of the Reynolds number. For the present experiments, data points are shown for x/D = 30 and 50, by circular and square symbols respectively. Some of the data are flagged to indicate that the heated surface was situated in the bottom part of the cross section; the unflagged symbols correspond to top heating. Straight lines representing least-squares fits have been respectively passed through the data for x/D = 30 and 50.

There are two features of Fig. 6 that are worthy of note. The first is the close agreement between the Petukhov-Popov correlation and the present data. Thus, when a properly defined average heat transfer coefficient is used, i.e., equation (6), the conventional correlation for a uniformly heated tube is applicable to a non-uniformly heated tube. The second observation in Fig. 6 relates to the deviations between the data for x/D = 30 and 50. These deviations tend to vanish at small Reynolds numbers and are about five percent at Re = 64,000. This finding affirms the earlier conclusion about the elongation of the thermal development length with increasing Reynolds number.

Circumferential Nusselt Number Distributions. Local Nusselt numbers $\mathrm{Nu}(x, \theta)$, evaluated from equations (1) and (10), have been ratioed with the corresponding circumferential average value $\overline{\mathrm{Nu}}(x)$ and plotted in Figs. 7 and 8 as a function of the circumferential coordinate θ on the heated arc. Fig. 7 conveys results for Re = 4360 and 64,000, the highest and lowest Reynolds numbers investigated, while Fig. 8 is for an intermediate Reynolds number, Re = 15,000. In addition to the Nusselt number ratio, Fig. 8 shows heat flux distributions $q(x, \theta)/\bar{q}(x)$ on the heated arc; these distributions also apply to the other Reynolds numbers. Data for x/D = 30 and 50 are plotted in both figures.

In general, all of the Nusselt number distributions display a common shape, with the smallest value at the mid-point of the heated wall and the largest values at the extremities. This behavior is consonant with the earlier discussion of the temperature distributions, where note was taken of the greater thermal resistance encountered by heat entering the flow at circumferential positions near the mid-point.

By further observation of Figs. 7 and 8, it is seen that the circumferential variations of the Nusselt number grow larger as the Reynolds number increases. This behavior is due entirely to the effect of circumferential conduction in the tube wall. At low Reynolds numbers, Table 1 shows that an appreciable amount of heat is conducted from the electrically heated portion of the tube into the electrically unheated portion. Consequently, under these conditions, the heating of the fluid tends toward (but does not attain) circumferential uniformity, with an attendant tendency of the Nusselt number distribution toward uniformity. At higher Reynolds numbers, the circumferential conduction into the unheated portion of the wall diminishes (Table 1), so that the overall nonuniformity of the convective heat flux is heightened (i.e., there is very little convective heating at the unheated wall). With the heightened nonuniformity of the convective heating, the Nusselt number variation increases.

The aforementioned tendency toward greater nonuniformity of $\mathrm{Nu}(x, \theta)$ with increasing Reynolds number is, in a sense, opposite to that encountered in the water flow experiments of [4]. There, the greatest circumferential variations of $\mathrm{Nu}(x, \theta)$ for buoyancy-unaffected flow occurred at the lowest Reynolds number of the experiments (~3000). The variations decreased as the Reynolds number was increased up to a certain value (5000 to 10,000, depending on the Prandtl number) and, thereafter, the extent of the variation remained unchanged with further increases in Reynolds number.

Table 1 Heat transferred by tube-wall circumferential conduction

Re	4360	8700	15,000	34,000	64,000
$Q_{\mathrm{cond}}/Q_{\mathrm{conv}}$	0.36	0.29	0.23	0.16	0.11

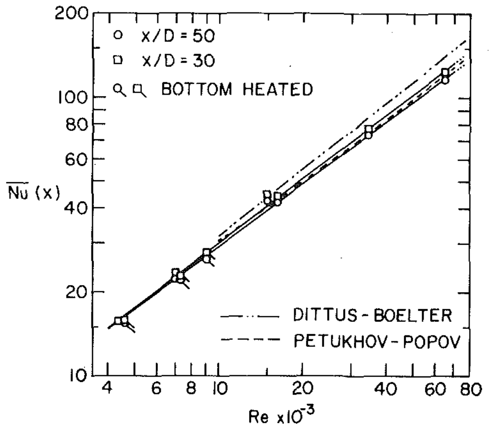

Fig. 6 Fully developed and nearly fully developed circumferential average Nusselt numbers

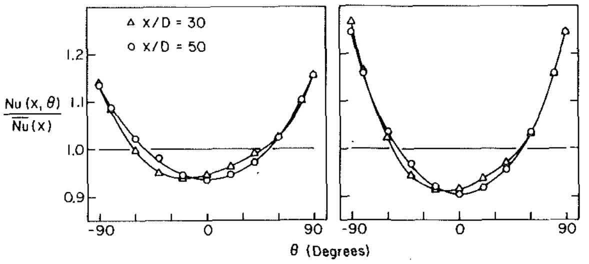

Fig. 7 Circumferential Nusselt number distributions at x/D = 30 and 50; Re = 4360 (left-hand graph) and 64,000 (right-hand graph)

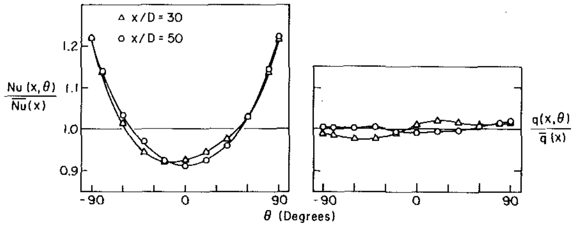

Fig. 8 Circumferential Nusselt number and heat flux distributions at x/D = 30 and 50; Re = 15,000

The trendwise differences between the present results and those of [4] are readily rationalized. As already noted, the present trend with Reynolds number is due to circumferential conduction in the tube wall. On the other hand, the circumferential conduction played no role in the experiments of [4] since the heat transfer coefficients encountered there are at least 50 times as large as those of the present experiments. Rather, the changes which resulted from increases in Reynolds number were caused by heightened circumferential transport via eddy diffusion in the fluid.

There is, therefore, no contradiction between the present results and those of [4]; rather, different transport mechanisms were operative in the two cases.

As a final matter with regard to these figures, attention may be turned to the distributions of heat flux on the heated portion of the tube wall as portrayed in Fig. 8. The distributions are seen to be within −3 to +2½ percent of being precisely uniform. The nonuniformity that is in evidence is due to local variations of the wall thickness. The thickness variations are somewhat different at each axial station, and this is reflected by the differences in the circumferential distributions of both $q(x, \theta)$ and $\mathrm{Nu}(x, \theta)$.

Buoyancy Effects. The major role played by buoyancy in the water experiments of [4] at low and intermediate Reynolds numbers prompted a careful examination of possible buoyancy effects in the present experiments. In this connection, the modified Rayleigh number

$$\mathrm{Ra}^* = (g\beta\bar{q}(x)R_i{}^4/k\nu^2)\mathrm{Pr} \qquad (13)$$

was evaluated (properties at the local bulk temperature) and found to be in the range of 2 to 5 × 10^4 for the low Reynolds number experiments. On the other hand, the Ra* values of [4] were 100 to 1000 times greater than those encountered here.

The presence or absence of buoyancy was assessed by comparing results from data runs in which the heated arc was at the top of the cross section with those from data runs in which the heated arc was at the bottom of the cross section. A graphical comparison for the lowest Reynolds number investigated (Re ~ 4500), the case most susceptible to buoyancy effects, is presented in Fig. 9. In this figure, $\mathrm{Nu}(x, \theta)/\overline{\mathrm{Nu}}(x)$ is plotted as a function of θ on the heated arc at $x/D = 50$. The data for bottom heating are designated by square symbols, while those for top heating are designated by circles. The two sets of data are seen to be coincident, affirming the absence of buoyancy effects. This finding was not unexpected because of the low value of the Rayleigh number.

Comparison of Nu(x, θ) Data with Predictions. In [5], a procedure was evolved for predicting the circumferential variation of the Nusselt number for thermally developed turbulent pipe flow subjected to a circumferentially nonuniform wall temperature. The application of that procedure to the conditions of the present experiments is rather lengthy and is described in detail in [6]. Only a brief recounting can be given here due to journal space limitations.

To use the method, the measured circumferential wall temperature distribution (over the entire 360 deg arc) has to be fit with a Fourier series. Then, the Fourier coefficients are used in conjunction with tabulated influence coefficients to compute $q(x, \theta)$ and $\mathrm{Nu}(x, \theta)$. One of the limitations of the method is that only six influence coefficients are available at each Reynolds and Prandtl number, so that the Fourier series has to be truncated after six terms. As shown in [6], a six-term series gives a somewhat wavy representation when applied to temperature distributions such as those of Figs. 2 to 4 and is especially inaccurate near the extremities of the heated arc. Another limitation is that the available influence coefficients, which are tabulated in [5] for five Reynolds numbers in the range from 10^4 to 10^6, do not pertain to any of the Reynolds numbers of the present research. It was, therefore, necessary to obtain the needed influence coefficients by interpolation.

A comparison of predicted and measured circumferential distributions of $\mathrm{Nu}(x, \theta)/\overline{\mathrm{Nu}}(x)$ is made in Fig. 10 for Re = 15,000 and 64,000 (left and right-hand graphs, respectively). The data correspond to $x/D = 50$, while the predictions are for any x/D in the thermally developed regime. The agreement between the data and the predictions is very good for Re = 15,000, but at 64,000 there is only fair agreement. Two factors can be cited that might contribute to this outcome. First, the $x/D = 50$ results for Re = 15,000 are essentially fully developed, as called for by the predictive method, while for Re = 64,000 thermal development is still in progress at $x/D = 50$. Second, the circumferential temperature nonuniformities are greater at Re = 64,000 than at Re = 15,000 (as can be seen by comparing Figs. 3 and 4), thereby providing a more demanding test of the predictive method.

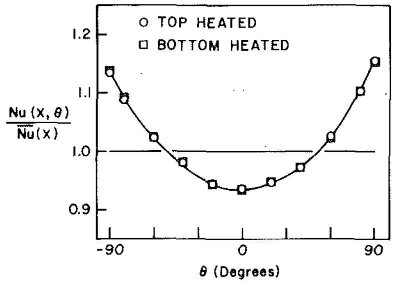

Fig. 9 Comparison of circumferential Nusselt number distributions for top and bottom heating at $x/D = 50$ and Re ~ 4500; Ra* ~ 2.5 × 10^4

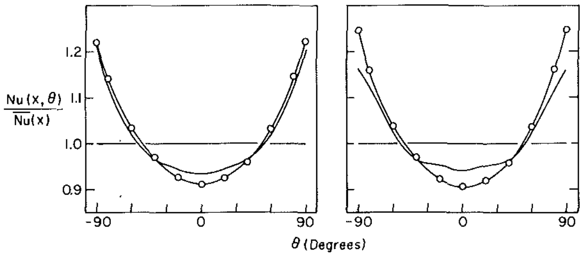

Fig. 10 Comparison of predicted with measured circumferential Nusselt number distributions for Re = 15,000 (left-hand graph) and 64,000 (right-hand graph). The data are at $x/D = 50$

It can be concluded that the predictive method is generally satisfactory, but that there are reservations with regard to the number of available influence coefficients and to the capability of the method to deal with relatively large circumferential variations.

Concluding Remarks

The results of the present experiments have underscored the strong interaction between circumferential tube-wall conduction and fluid convection when a gas flowing in a tube is heated nonuniformly around its circumference. The influence of the conduction is large at low Reynolds numbers, since the convection coefficients are relatively small. At higher Reynolds numbers, convection is enhanced and the conduction plays a lesser role. When operating conditions (i.e., low Reynolds numbers) permit wall conduction to work effectively, it tends to diminish circumferential nonuniformities. For the heating pattern of the present experiments (direct heating of a 180 deg portion of the tube wall), the resulting circumferential variations of the tube wall temperature and of the local Nusselt number increase with increasing Reynolds number.

For liquid flows (e.g., water flow as studied in [4]), the situation is altogether different since the wall conduction is rendered ineffective by the relatively large convective coefficients.

The nonuniform circumferential heating is found to substantially increase the length required to attain thermal development compared with that for conventional uniformly heated gas flows. The fully developed and nearly fully developed values of the circumferential average Nusselt number agreed very well with the Petukhov-Popov correlation for uniformly heated tube flows. This useful finding demonstrates that the conventional correlation for uniform heating can be applied to circumferentially nonuniform heating provided that a suitably defined average coefficient is employed.

At any cross section, the smallest value of the local Nusselt number occurs at the mid-point of the heated portion of the wall. The circumferential variation of the Nusselt number was predicted reasonably well by applying the method of [5].

Possible buoyancy effects at low Reynolds numbers were examined by means of experiments in which the heated portion of the tube was first situated in the upper portion of the cross section and then in the lower portion of the cross section. The results from the two sets of experiments were coincident, thereby affirming the absence of any significant buoyancy.

References

1 Black, A. W. and Sparrow, E. M., "Experiments on Turbulent Heat Transfer in a Tube with Circumferentially Varying Thermal Boundary Conditions," ASME JOURNAL OF HEAT TRANSFER, Vol. 89, 1967, pp. 258–268.

2 Quarmby, A. and Quirk, R., "Measurements of the Radial and Tangential Eddy Diffusivities of Heat and Mass in Turbulent Flow in a Plain Tube," *International Journal of Heat and Mass Transfer,* Vol. 15, 1972, pp. 2309–2327.

3 Chan, A. L., Baughn, J. W., and Hoffman, M. A., "Nonuniform Circumferential Heat Flux Experiments in a Circular Tube," ASME Paper No. 75-WA/HT-52.

4 Schmidt, R. R. and Sparrow, E. M., "Turbulent Flow of Water in a Tube with Circumferentially Nonuniform Heating, With and Without Buoyancy," ASME JOURNAL OF HEAT TRANSFER, Vol. 100, 1978, pp. 403–409.

5 Gärtner, D., Johannsen, K., and Ramm, H., "Turbulent Heat Transfer in a Circular Tube with Circumferentially Varying Thermal Boundary Conditions," *International Journal of Heat and Mass Transfer,* Vol. 17, 1974, pp. 1003–1018.

6 Knowles, G. R., "Local and Average Heat Transfer Characteristics for Turbulent Airflow in an Asymmetrically Heated Tube," Ph.D. Thesis, Department of Mechanical Engineering, University of Minnesota, Minneapolis, Minn., 1978.

7 Schmidt, R. R., "Experiments on Buoyancy-Affected and Buoyancy-Unaffected Turbulent Heat Transfer for Water in a Tube with Circumferentially Nonuniform Heating," Ph.D. Thesis, Department of Mechanical Engineering, University of Minnesota, Minneapolis, Minn., 1977.

8 Petukhov, B. S., "Heat Transfer and Friction in Turbulent Pipe Flow with Variable Physical Properties," *Advances in Heat Transfer,* Vol. 6, Academic Press, 1972, pp. 503–564.

M. M. Hasan
Research Assistant.

R. Eichhorn
Dean of Engineering,
Fellow, ASME

Department of Mechanical Engineering,
University of Kentucky,
Lexington, KY 40506

Local Nonsimilarity Solution of Free Convection Flow and Heat Transfer from an Inclined Isothermal Plate

The effect of the angle of inclination on free convection flow and heat transfer from an isothermal surface is analyzed by the local nonsimilarity method of solution. An inclination parameter ξ as obtained from the analysis is $\tan\gamma/4\ (Gr_x/4)^{1/4}$, where γ is the angle of inclination measured from the vertical and Gr_x is the local Grashof number, based on the component of the gravity vector along the surface. Numerical solutions of the equations are obtained for Prandtl numbers of 0.1, 0.7, 6 and 275. Results show an appreciable effect of ξ on the velocity field, and practically none on the temperature field, except for very large angles of inclination from the vertical or for very small values of the Prandtl number. In the limiting case of very large Prandtl number, ξ has no effect either on the velocity or the temperature field.

Introduction

The mechanism of free convection from vertical surfaces has been studied extensively both analytically and experimentally. For inclined surfaces, however, there has been relatively more experimental work than analysis. For an inclined surface the buoyancy force causing motion has a component in both the tangential and normal directions. This causes a pressure gradient across the boundary layer and leads to a theoretical analysis more complicated than that for vertical surfaces.

Experimental investigations on free convection from inclined surfaces has been reported by several authors [1-4]. All these works led to the conclusion that in the laminar region the heat transfer coefficient for the inclined plate can be correlated by the usual vertical plate formulas, if the gravity component parallel to the inclined surface is used in the Grashof number.

Kierkus [5], obtained a perturbation solution for the inclined isothermal plate free convection problem. His first order perturbation solution shows that the effect of angle of inclination on the temperature field is hardly noticeable but that the velocity field is profoundly affected by inclination. More recently Riley [6] has noted that the leading term of the solution outside the boundary layer given in [5] is incompatible with the primary boundary layer. Riley corrected the solution for the velocity field by reference to the work of Clarke [7]. He concluded that perturbation terms had no effect on the heat transfer up to, but not including terms of relative order of $\mathrm{Gr}_x^{-1/2}$. Fussey and Warneford [8] used an integral method to obtain a solution for an upward facing uniform heat flux plate. Recently, Emery, et al. [9] carried out experiments on free convection heat transfer to Newtonian and non-Newtonian high Prandtl number fluids from vertical and inclined uniform heat flux surfaces. They concluded that the thermal boundary layer was not influenced by inclination. Of course, they did find a considerable effect of inclination on the velocity field.

The purpose of this paper is to present a detailed theoretical analysis of the laminar free convection flow and heat transfer from an inclined isothermal surface. A specific study of the velocity and temperature fields, especially on both sides of the inclined surface is made by using the local non-similarity method [10], since this problem does not admit similarity solutions. A wide range of Prandtl number is considered. Theoretical local heat transfer coefficients and local shear stress coefficients, velocity and temperature profiles for different values of ξ, the parameter characterizing the inclination, are given for Prandtl numbers of 0.1, 0.7, 6 and 275.

Analysis

The physical model and the coordinate system are shown in Fig. 1. They are so chosen such that x represents the distance along the plate from its leading edge and y represents the distance normal to the surface. For a heated surface facing upward, y is taken as positive in the upward direction and for a heated surface facing downward, y is taken as positive in the downward direction. The angle of inclination γ (positive in both cases) is measured from the vertical.

In the analysis, the fluid properties are assumed to be constant except that density variations are considered to the extent that they contribute to the buoyancy forces. The following are the governing equations for the problem under consideration.

$$\frac{\partial u}{\partial x} + \frac{\partial v}{\partial y} = 0 \tag{1}$$

$$u\frac{\partial^2 u}{\partial x\partial y} + v\frac{\partial^2 u}{\partial y^2} = \nu\frac{\partial^3 u}{\partial y^3} + (g\cos\gamma)\beta\frac{\partial\theta}{\partial y} - R(g\sin\gamma)\beta\frac{\partial\theta}{\partial x} \tag{2}$$

$$u\frac{\partial\theta}{\partial x} + v\frac{\partial\theta}{\partial y} = \alpha\frac{\partial^2\theta}{\partial y^2} \tag{3}$$

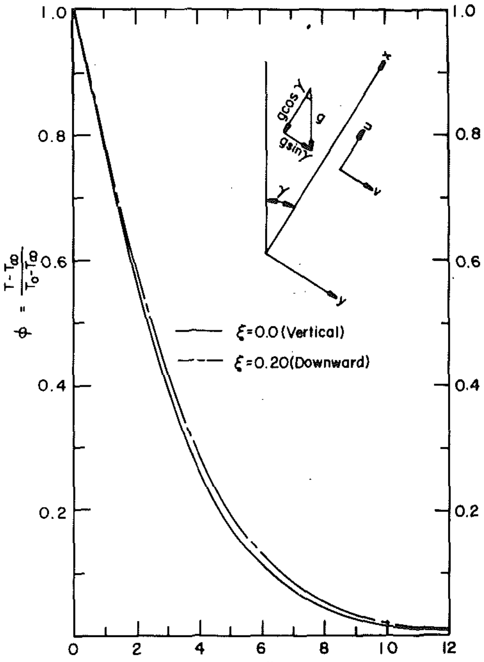

Fig. 1 Dimensionless temperature profiles for natural convection to an inclined plate; Pr-0.1. Inset: the coordinate system

---

Contributed by the Heat Transfer Division for publication in the JOURNAL OF HEAT TRANSFER. Manuscript received by the Heat Transfer Division September 5, 1978.

where u and v are the axial and normal velocity components, θ is the local temperature difference $T - T_\infty$. Equation (2) is obtained by eliminating the pressure terms in the x and y direction momentum equations and neglecting terms of the order of δ^2. The third term on the right hand side of equation (2) is due to the pressure gradient across the boundary layer. In equation (2) R is +1 and −1 for the heated surface facing upward and downward, respectively. The boundary conditions for equations (1–3) are

$$u = v = 0, \quad \theta = \theta_0 \quad \text{at } y = 0 \tag{4}$$

$$u = \frac{\partial u}{\partial y} = \theta = 0 \quad \text{as } y \to \infty$$

The following substitutions are used to transform the (x, y) coordinates to dimensionless $(\xi(x), \eta(x, y))$ form:

$$\eta = Cyx^{(m-1)/4}, \quad \xi = \xi(x) \tag{5}$$

The coordinate $\xi(x)$ is so chosen that x does not appear explicitly in either the transformed equations or the transformed boundary conditions. In addition, a reduced stream function $f(\xi, \eta)$ and a dimensionless temperature function ϕ are defined, respectively, as

$$f(\xi, \eta) = \frac{1}{4\nu C}\psi(x, y)x^{-(m+3)/4}$$

$$\phi(\xi, \eta) = \frac{T - T_\infty}{T_0 - T_\infty} = \frac{\theta}{\theta_0} = \frac{\theta}{Nx^m} \tag{6}$$

where

$$C = \left[\frac{(g \cos \gamma)\beta N}{4\nu^2}\right]^{1/4} \text{ and } \theta_0 = Nx^m \tag{7}$$

Introducing equations (5) to (7) into equation (2) and integrating the transformed equation once with respect to η, we obtain

$$\begin{aligned} f''' + (m + 3)ff'' - 2(m + 1)f'^2 + \phi[1 - (m - 1)R\eta\xi] \\ - (m + 3)\xi(f''f_\xi - f'f'_\xi) - (3m + 1)R\xi\left[\int_0^\eta \phi d\eta - \int_0^\infty \phi d\eta\right] \\ + (m + 3)R\xi^2\left[\int_0^\eta \phi_\xi d\eta - \int_0^\infty \phi_\xi d\eta\right] = 0 \end{aligned} \tag{8}$$

Similarly, equation (3) transforms to

$$\phi'' + \Pr[(m + 3)f\phi' - 4mf'\phi] = (m + 3)\Pr\xi(\phi'f_\xi - f'\phi_\xi) \tag{9}$$

And the transformed boundary conditions are

$$f(\xi, 0) = f'(\xi, 0) = 0, \phi(\xi, 0) = 1, f'(\xi, \infty) = \phi(\xi, \infty) = 0 \tag{10}$$

In the foregoing equations, primes denote partial differentiation with respect to η, Pr is the Prandtl number and ξ is

$$\xi = \tan\gamma/4Cx^{(m+3)/4} \tag{11}$$

Equations (8–11) show that this problem does not permit a similarity solution for physically meaningful values of the exponent m.

Table 1 Solution limits

	$R = +1$ Upward facing Surface	$R = -1$ Downward facing Surface
Pr	ξ	ξ
0.1	0.08*	0.20*
0.7	0.22*	0.45*
6	0.45*	0.5
275	1	1

* The convergence criterion could not be satisfied for values of ξ greater than this.

Uniform wall temperature equations are deduced from equations (8) and (9) by setting m equal to zero, and the parameter ξ reduces to

$$\xi = \tan\gamma/4(\mathrm{Gr}_x/4)^{1/4}, \text{ where } \mathrm{Gr}_x = (g \cos\gamma)\beta\theta_0 x^3/\nu^2 \tag{12}$$

The parameter, ξ, characterizes inclination and the distance along the plate from the leading edge. If the inclination γ is zero, we obtain $\xi = 0$ and equations (8) and (9) reduce to the similarity equations for a vertical plate. Alternatively, if Gr_x is very large and the inclination does not approach 90 deg, ξ also approaches zero. In this case we get a solution for an equivalent vertical plate, in which the gravity component parallel to the inclined plate is used in the definition of the Grashof number. For a nonzero value of ξ, a similarity solution cannot be obtained. Therefore, the above equations are solved by using the local nonsimilarity method.

For the local nonsimilarity solution the transformed equations (8) and (9) are retained exactly. Additional sets of equations are obtained by differentiating equation (8) and (9) with respect to ξ and neglecting the terms containing $\partial^2 f/\partial^2\xi$ and $\partial^2\phi/\partial^2\xi$. The formulation of the systems of equations is given in [11]. A detailed description of the local non-similarity method of solution can be found in [10, 12]. The result for uniform wall temperature, $m = 0$, is

$$\begin{aligned} g''' + 3fg'' - f'g' + V(1 + R\xi\eta) + R\eta\phi \\ - 3\xi(gg'' - g'^2) - R\left[\int_0^\eta \phi d\eta - \int_0^\infty \phi d\eta\right] \\ + 5R\xi\left[\int_0^\eta V d\eta - \int_0^\infty V d\eta\right] = 0 \end{aligned} \tag{13}$$

and

$$V'' + 3\Pr(fV' + f'V) + 3\Pr\xi(g'V - gV') = 0 \tag{14}$$

where

$$g = \partial f/\partial\xi \text{ and } V = \partial\phi/\partial\xi \tag{15}$$

Nomenclature

C = dimensional constant defined by equation (7)
C_f = dimensionless local shear stress coefficient
f = dimensionless dependent variable defined by equation (6)
$f_1 = \mathrm{Pr}^{3/4}f$
g = acceleration of gravity, also $\partial f/\partial\xi$
g_1 = defined by equation (23)
Gr_x = local Grashof number based on x
h_x = local heat transfer coefficient based on x
k = thermal conductivity
m = exponent in equation (6)
N = dimensional constant in equation (6)
Nu_x = local Nusselt number
Pr = Prandtl number
R = +1 and −1, for upward and downward facing surfaces, respectively
T = static temperature
u = axial velocity component
v = normal velocity component
x = distance along the plate from the leading edge
y = distance normal to the plate
α = thermal diffusivity
β = coefficient of thermal expansion, $-1/\rho(\partial\rho/\partial T)_p$
γ = angle of inclination measured from the vertical
$\eta = Cyx^{(m-1)/4}$ dimensionless independent variable
$\lambda = \mathrm{Pr}^{1/4}\eta$
$\theta = T - T_\infty$
ν = kinematic viscosity
$\xi = \tan\gamma/4Cx^{(m+3)/4}$
ρ = fluid density
ϕ = dimensionless temperature
ψ = steam function
δ = boundary layer thickness

Subscripts

0 = wall conditions
∞ = ambient condition

Table 2 Local nonsimilarity solution: Pr = 0.1 and 0.7

	Pr = 0.1				Pr = 0.7			
	Upward Facing Surface		Downward Facing Surface		Upward Facing Surface		Downward Facing Surface	
ξ	$f''(\xi, 0)$	$-\phi'(\xi, 0)$	$f''(\xi, 0)$	$-\phi'(\xi, 0)$	$f''(\xi, 0)$	$-\phi'(\xi, 0)$	$f''(\xi, 0)$	$-\phi'(\xi, 0)$
0.00	0.85914	0.2304	0.85914	0.2304	0.67891	0.49951	0.67891	0.49951
0.05	1.08479	0.22875	0.67582	0.22965	0.74683	0.49924	0.61393	0.49928
0.10			0.50756	0.22755	0.81934	0.49831	0.55096	0.49866
0.15			0.34425	0.22428	0.89976	0.49633	0.48934	0.49768
0.20			0.17865	0.21969	0.99839	0.49203	0.42860	0.49633
0.30							0.30831	0.49285
0.40							0.18740	0.48798

Table 3 Local nonsimilarity solution: Pr = 6 and 275

	Pr = 6				Pr = 275			
	Upward Facing Surface		Downward Facing Surface		Upward Facing Surface		Downward Facing Surface	
ξ	$f''(\xi, 0)$	$-\phi'(\xi, 0)$	$f''(\xi, 0)$	$-\phi'(\xi, 0)$	$f''(\xi, 0)$	$-\phi'(\xi, 0)$	$f''(\xi, 0)$	$-\phi'(\xi, 0)$
0.0	0.46842	1.00740	0.46842	1.00740	0.19679	2.83580	0.19670	2.83580
0.1	0.50712	1.00721	0.42329	1.00723	0.20290	2.83580	0.19068	2.83580
0.2	0.55093	1.00663	0.38288	1.00677	0.20902	2.83578	0.18458	2.83578
0.3	0.59508	1.00555	0.34164	1.00602	0.21514	2.83574	0.17848	2.83574
0.4	0.64185	1.00378	0.30126	1.00501	0.22126	2.83571	0.17238	2.83571
0.6					0.23352	2.83559	0.16018	2.83559
1.0					0.25809	2.83521	0.13582	2.83523

The boundary conditions are

$$f(\xi, 0) = f'(\xi, 0) = g(\xi, 0) = g'(\xi, 0) = V(\xi, 0) = 0, \phi(\xi, 0) = 1$$

$$f'(\xi, \infty) = g'(\xi, \infty) = \phi(\xi, \infty) = V(\xi, \infty) = 0 \tag{16}$$

Equation (14) is a homogeneous equation linear in V with homogeneous boundary conditions. Therefore, the solution is trivial. This reduces the number of equations to be solved for an isothermal plate to three (equations (8, 9) and (13) with $V(\xi, \eta) = 0$). It is to be noted that $V(\xi, 0) = 0$ does not reduce the problem to local similarity because equations (8) and (9) still contain the term g and its derivatives. Equations (8, 9) and (13) with the boundary conditions (16) were solved for Pr = 0.1, 0.7, 6 and 275 using the successive approximation method [11, 13, 14].

Results and Discussion

For a fixed Prandtl number and R the solution of the local nonsimilarity equations did not converge beyond a certain value of ξ. The maximum value of ξ for which the solutions were obtained for a fixed Prandtl number is given in Table 1.

Numerical values of $f''(\xi, 0)$, and $\phi'(\xi, 0)$ for different values of ξ are listed in Tables 2 and 3. The dimensionless axial velocities are plotted in Figs. 2–5. The normal velocities for Prandtl numbers of 0.7 and 6 are plotted in Figs. 3 and 4, respectively. The temperature profiles for Pr = 0.1 are shown in Fig. 1. For higher values of the Prandtl number the temperature profiles for different values of ξ are the same as those of the vertical plate problem.

The plots of the velocity profiles and the temperature profiles, for different values of the parameter ξ, show that there is an appreciable effect of ξ on the velocity field, while the temperature field remains practically unaffected. For the upward facing surface, the axial velocity component, u, is higher than that of the equivalent vertical surface, while for the downward facing surface, it is lower. The values of the dimensionless heat transfer coefficients $\phi'(\xi, 0)$, in Tables 2 and 3 show that the effect of ξ on the heat transfer is nearly negligible.

To explain this somewhat surprising result, we go back to the transformed local non-similarity equations (equations (8, 9, 13) and (14)). We recognize that for the isothermal case the solution of V is zero. The substitution $F = f - \xi g$ then transforms equations (8, 9) and (14) to the following equations:

$$F''' + 3FF'' - 2F'^2 + \phi = \xi^2 g'^2 \tag{17}$$

$$\phi'' + 3\mathrm{Pr}F\phi' = 0 \tag{18}$$

$$g''' + 3Fg'' - F'g' + R\eta\phi + 2\xi g'^2 = R\left[\int_0^\eta \phi d\eta - \int_0^\infty \phi d\eta\right] \tag{19}$$

If the nonlinear terms in equation (14) (underlined terms) are neglected (as many authors using local nonsimilarity method have done), we find that equations (17) and (18) reduce to the same equations as those of the isothermal vertical plate, and have the same boundary conditions. Therefore, equation (17) with the right hand side deleted and equation (18) will give a unique solution of ϕ and F for any value of the parameter ξ. To get f from F, we need to solve equation (19) which depends on ξ. This explains why the temperature field remains unchanged, while the velocity fields are affected profoundly depending on the values of ξ and R. However, the present solution is obtained by retaining the nonlinear terms in the subsidiary equation (13). The results show that the effect of this term is nearly negligible, since the temperature field remains almost unaffected even if the non-linear terms are retained.

The axial velocity profiles for Pr = 0.1 and 0.7 (Figs. 2 and 3) for the case of a downward facing plate show a flow reversal in the outer portion of the boundary layer for large values of ξ. The magnitude of the effect increases and the region of reversed flow moves closer to the wall as ξ increases (x decreases or γ increases). Physically this means that the flow reversal occurs for a downward facing plate near the leading edge with a large angle of inclination.

Fig. 9 shows the boundary layer development on a downward facing heated plate. Coordinates $\xi^{-4/3}$ and $\eta\xi^{-1/3}$ are proportional to the length of the plate x and the normal distance from the plate y, respectively. The lines marked as $\eta = 4.5$ and 11.5 show the approximate thermal boundary layer thickness for Pr = 0.7 and 0.1, respectively. The dimensionless normal distance η from the plate to the horizontal surface is given by the relation

$$\eta = 1/4\xi \tag{20}$$

Therefore, a portion of the thermal boundary layer extends below the horizontal line through the leading edge. The flow reversal occurs in this portion of the boundary layer.

Whether the flow is toward the leading edge or away from it depends in part on the direction of the net bouyancy force. It also depends on the magnitude of shear and inertia effects. Equation (8) shows that the net bouyancy for the downward facing heated surface is $\phi(1 - \eta\xi) + \xi[\int_0^\eta \phi d\eta - \int_0^\infty \phi d\eta]$. Therefore, the net bouyancy force, depending on the value of ξ, starts with some positive value at

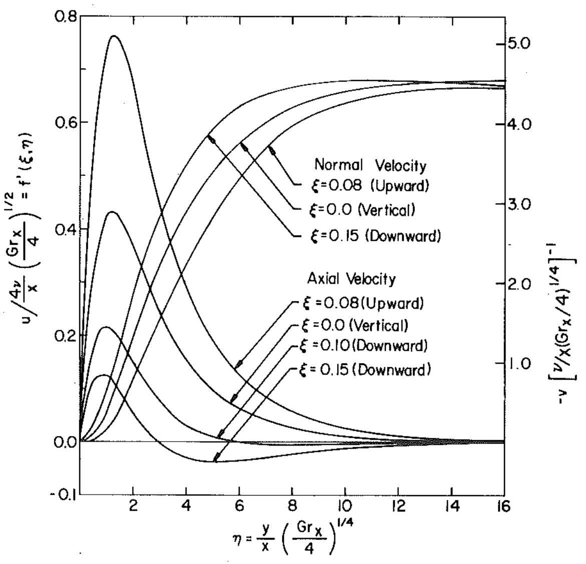

Fig. 2 Dimensionless axial and normal velocity profiles; Pr = 0.1

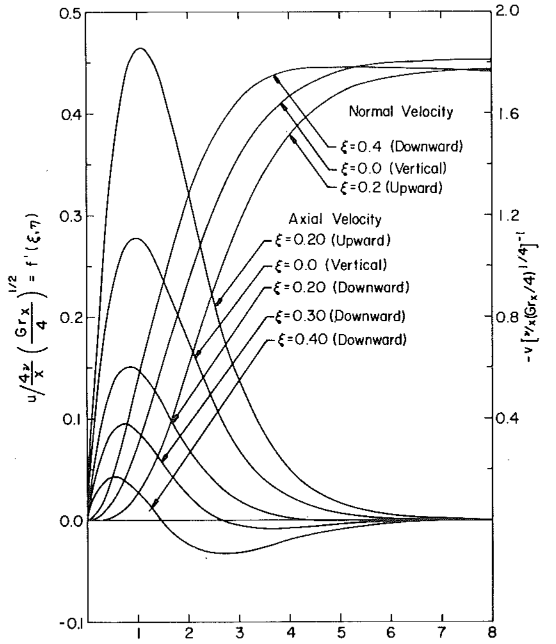

Fig. 3 Dimensionless axial and normal velocity profiles; Pr = 0.7

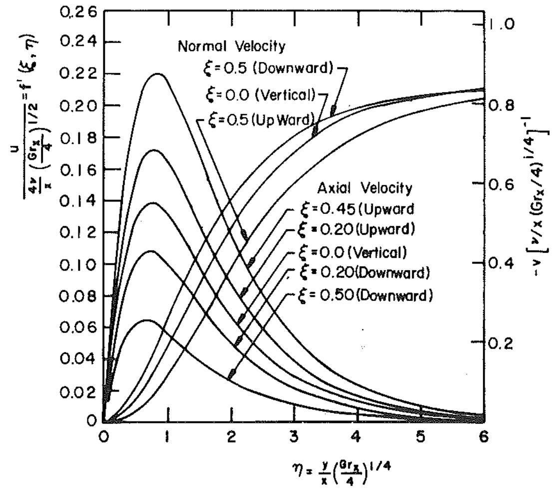

Fig. 4 Dimensionless axial and normal velocity profiles; Pr = 6.0

$\eta = 0$, then goes to zero at some value of η and thereafter is negative and finally goes to zero again as $\eta \rightarrow \infty$.

The dashed lines in Fig. 9 are the loci of zero axial velocity for Pr = 0.7 and 0.1 and the broken lines are the loci of zero net bouyancy force, which is determined by the set of values of ξ and η that satisfy the relation

$$\phi(1 - \eta\xi) + \xi\left[\int_0^\eta \phi d\eta - \int_0^\infty \phi d\eta\right] = 0 \tag{21}$$

The flow reversal occurs to the right of the dashed lines. The fact that the loci of zero axial velocity and zero net bouyancy force do not coincide shows that the flow is determined by the net effect of bouyancy, shear and inertia.

Comparison of Figs. 2–5 shows that the extent of the flow reversal region is strongly dependent on the Prandtl number. For Pr = 0.1, flow reversal is noticeable even for values of ξ less than 0.1. This is because the thermal boundary layer is much thicker for small than for large Prandtl numbers. For Pr = 275, there is no flow reversal even for values of ξ as large as unity. This result can be traced to the fact that the velocity profile is much thicker than the temperature profile and therefore, completely determines the flow field.

These results do not imply that heated fluid escapes around the leading edge. The equations we have solved are parabolic and are singular at $x = 0$ within the boundary layer approximation. The fluid that is moving toward the leading edge is turned on nearing the plate and is swept along the plate away from the leading edge.

The ratio of the local Nusselt number for an inclined plate to that of a vertical plate can be written as

$$\frac{Nu_x}{Nu_x\Big|_{\text{vertical}}(\cos\gamma)^{1/4}} = \frac{\phi'(\xi, 0)}{\phi'(0, 0)} \tag{22}$$

A plot of this ratio is presented in Fig. 7, which shows that the effect of the parameter ξ on the heat transfer coefficient is very small. Therefore, in the laminar region, the local Nusselt number for the inclined plate, either facing upward or downward, can be correlated by the usual vertical plate formulas, if the gravity component parallel to the inclined surface is used in Gr_x. This is not true for the limiting case of very large angles of inclination (very near to the horizontal) or for the case of an extremely low Prandtl number. Fig. 7 shows that for Pr = 0.1, the ratio $\phi'(\xi, 0)/\phi'(0, 0)$ varies from 1 to 0.97 for ($\xi = 0$ to 0.08) for an upward facing surface and from 1 to 0.95 (for $\xi = 0$ to 0.2) for a downward facing surface.

The wall shear stress coefficient $f''(\xi, 0)$ is profoundly affected by the parameter ξ. These variations for different values of Prandtl numbers are shown in Fig. 6.

The results show that the effect of the parameter ξ on the temperature and velocity fields decreases with the increasing Prandtl number. For the limiting case of very high Prandtl number (Pr → ∞), the parameter ξ will have no effect either on the temperature or the velocity field. To show this we start with equations (8, 9) and (13) and the transformations,

$$\lambda = Pr^{1/4}\eta, \quad f_1 = Pr^{3/4}f, \quad g_1 = Pr^{3/4}g \tag{23}$$

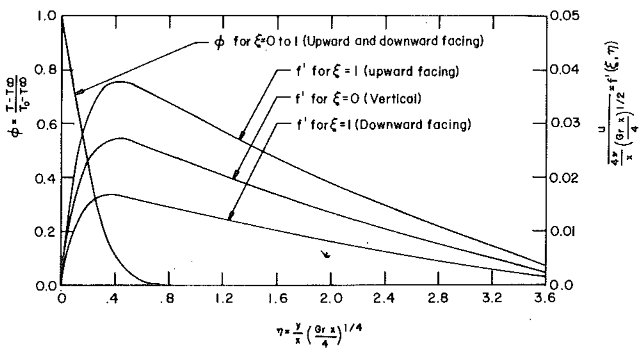

Fig. 5 Dimensionless temperature and axial velocity profiles; Pr = 275

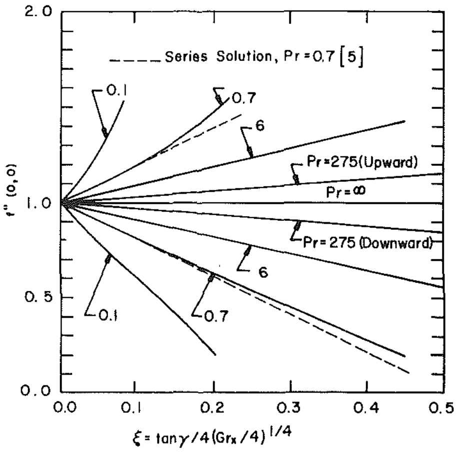

Fig. 6 Ratio of the dimensionless local wall friction coefficient for inclined plate to that of the equivalent vertical plate. Dashed lines are the results of series solution [5] for Pr = 0.7

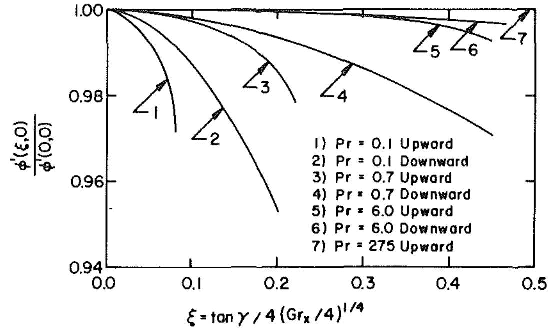

Fig. 7 Ratio of local Nu_x for the inclined plate to that of the equivalent vertical plate

and find that for Pr → ∞ equation (13) reduces to $g_1''' = 0$.

The boundary conditions are

$$g_1(\xi, 0) = g_1'(\xi, 0) = g_1'(\xi, \infty) = 0$$

This gives $g_1(\xi, \lambda) = 0$. Therefore, equations (8) and (9) reduce to

$$f_1''' + \phi = 0 \qquad (24)$$

$$\phi'' + 3f_1\phi' = 0 \qquad (25)$$

Equations (24) and (25) do not contain ξ, which shows that for Pr → ∞ the parameter will have no effect on the solution of either the velocity or temperature field. For this case the vertical plate solution will be applicable for both the temperature and velocity fields if the gravity component parallel to the inclined surface is used in Gr_x.

These findings are in agreement with all the previous experimental works referred to in the introduction. For example, Hassan and Mohammed [3] measured local heat transfer from an inclined isothermal plate in air. Their correlation of the local Nusselt number, $Nu_x = 0.348$ $(Gr_x \cdot \cos\gamma)^{1/4}$, is in good agreement with the vertical plate correlation for an inclination up to 75 deg (downward facing) and 60 deg for the upward facing surface. A comparison of this correlation and the data with the present solution is shown in Fig. 8. Some error was incurred by scaling numbers from the graph in [3], but this should be small in comparison with the 10 percent scatter of points as reported in [3]. Hassan and Mohammed found a higher value of Nu_x for angles of inclination greater than 60 degress for an upward facing surface. This increase in heat transfer is probably due to the transitional nature of the boundary layer.

It has been observed by many investigators that for the upward facing surface the critical value of Rayleigh number, Ra_x, for the onset of transitional flow is profoundly affected by inclination [15, 16]. So in these cases the assumption of a laminar boundary layer does not hold and the heat transfer coefficient cannot be obtained from the usual vertical plate correlation. Experimental results of Fujii and Imura [4] suggest that for the downward facing surface, the vertical plate formulas can be used for an angle of inclination up to 89 deg from the vertical.

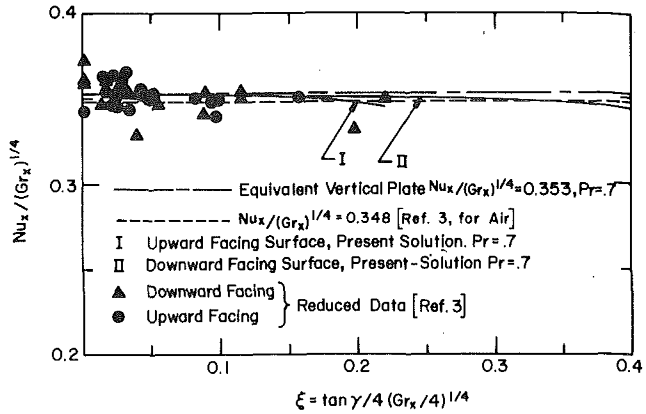

Fig. 8 Experimental heat transfer to inclined plate for air

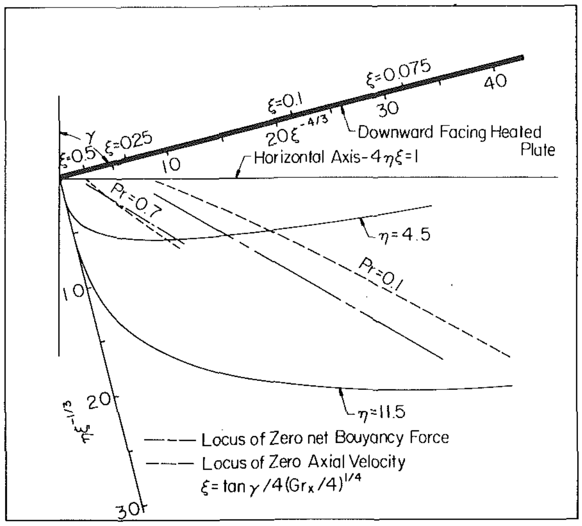

Fig. 9 Boundary layer development on a downward facing heated plate for Pr = 0.7 and 0.1. Flow reversal occurs to the right of the dashed line. Coordinates $\xi^{-4/3}$ and $\eta\xi^{-1/3}$ are proportional to x and y, respectively

Experiments by Emery, et al. [9] on constant heat flux upward and downward facing inclined surfaces using water-pluracol solutions with Prandtl numbers of 270 to 1020, show an insignificant effect of inclination on the temperature field, in contrast to a noticeable effect on the velocity field. Although the experiment was performed under conditions of constant heat flux, a comparison with Figs. 5 and 6 (which are for Pr = 275) of [9] with our Fig. 5 shows that the nature of the velocity and temperature profiles are in excellent agreement with the present solution.

Kierkus [5] obtained a series solution for the free convection flow and heat transfer from an inclined isothermal plate for Pr = 0.7. In the outer solution, he attempted to model the effect of a finite plate while retaining the solution for a semi-infinite plate in the inner region. Riley [6] noted this discrepancy and provided an asymptotic solution in an outer and an inner region for an infinite plate. His first order inner solution is the same as the solution given by Kierkus, if the series associated with the effect of a finite plate in the outer region is deleted from Kierkus' solution.

Both Kierkus and Riley expanded the flow variables in powers of $(Gr_x)^{-1/4}$. With this scheme, the angle of inclination γ appears explicitly in the transformed equations. Therefore, for a fixed Prandtl number the whole set of perturbation equations has to be solved for each angle of inclination. Kierkus provided solutions for Pr = 0.7 and angles of inclination $\gamma = 0, \pm 15, \pm 30, \pm 45$ and ± 60 deg. From his Table 1 we find that both his functions $p(0, \gamma)$ and $f''(0, \gamma)$ are linear in $\tan\gamma$. Neither Kierkus nor Riley seemed to be aware of that fact.

The formulas for $p(0, \gamma)$ and $f''(0, \gamma)$ are

$$p(0, \gamma) = 0.69977 \tan\gamma$$

where p is the dimensionless pressure difference between the local static pressure and the hydrostatic pressure at the remote medium, and

$$f''(0, \gamma) = 0.4431 + 0.7344 \tan\gamma \qquad (26)$$

The dimensionless shear stress coefficient for Pr = 0.7 can be written as

$$C_f = \frac{\tau_0}{2\rho \left(\frac{\nu}{x}\right)^2 \left(\frac{\mathrm{Gr}_x}{4}\right)^{3/4}} = 1.3578 + 1.28254\,(\mathrm{Gr}_x)^{-1/4} f''(0, \gamma) \qquad (27)$$

To compare the result of the series solution with the local nonsimilarity solution, we re-write the expression for C_f in terms of the parameter ξ. Thus we have

$$C_f = 1.3578 + 2.6641\xi + 0.5683(\mathrm{Gr}_x)^{-1/4} \qquad (28)$$

The last term of the above equation is due to the induced flow and is negligible for large Gr_x. From the local non-similarity solution on the other hand,

$$C_f = \frac{\tau_0}{2\rho \left(\frac{\nu}{x}\right)^2 \left(\frac{\mathrm{Gr}_x}{4}\right)^{3/4}} = 2f''(\xi, 0) \qquad (29)$$

A comparison of equations (28) and (29) is shown in Fig. 6. An important conclusion of this comparison is that the effect of inclination on the flow can be incorporated in the parameter ξ, and therefore one does not need to solve the whole set of equations for each angle of inclination. No effect on the temperature field is observed from the first order series solution. This is also in agreement with the local nonsimilarity solution.

Conclusions

The effect of angle of inclination on free convection flow from an isothermal flat plate has been analyzed by the local nonsimilarity method of solution. Numerical solutions of the governing differential equations, parameterized in ξ, have been obtained for Prandtl numbers of 0.1, 0.7, 6 and 275. The parameter ξ as obtained from the analysis of an isothermal inclined plate is $\tan\gamma/4(\mathrm{Gr}_x/4)^{1/4}$, which shows that the effect of inclination is incorporated in ξ.

Numerical results show that there is an appreciable effect of the parameter ξ (depending on Prandtl number) on the velocity field, while the temperature field remains practically unaffected. Some effects on the temperature field are noticeable for Pr = 0.1. Therefore, (if the Prandtl number is not too small, less than 0.1), in the laminar region, the local Nusselt number for the inclined plate either facing upward or downward can be correlated by the usual vertical plate relationships if the gravity component parallel to the inclined surface is used in the definition of Gr_x.

The dimensionless local wall friction coefficient $f''(\xi, 0)$ is profoundly affected by the parameter ξ. The friction coefficient for the upward facing inclined surface is higher than that of the equivalent vertical surface, while for the downward facing surface, it is lower.

It is shown that for the limiting case of very large Prandtl number the parameter ξ will have no effect either on the velocity field or the temperature field.

The results obtained by the local nonsimilarity method of solution are in good agreement with all the previous experimental and theoretical works.

Acknowledgments

The financial assistance provided by the National Science Foundation under Grant ENG 72-03904 is gratefully acknowledged. Computing time was furnished by the University of Kentucky.

References

1 Rich, B. R., "An Investigation of Heat Transfer from an Inclined Flat Plate in Free Convection," Trans. ASME, Vol. 75, 1953, pp. 489–499.

2 Vliet, G. C., "Natural Convection Local Heat Transfer on Constant Heat Flux Inclined Surface," ASME JOURNAL OF HEAT TRANSFER, Vol. 91, 1969, pp. 511–516.

3 Hassan, K. E. and Mohammed, S. A., "Natural Convection from Isothermal Flat Surfaces," *International Journal of Heat and Mass Transfer*, Vol. 13, 1970, pp. 1873–1886.

4 Fujii, T. and Imura, H., "Natural Convection Heat Transfer From a Plate with Arbitrary Inclination," *International Journal of Heat and Mass Transfer*, Vol. 15, 1972, pp. 755–767.

5 Kierkus, W. T., "An Analysis of Laminar Free Convection Flow and Heat Transfer About an Inclined Isothermal Plate," *International Journal of Heat and Mass Transfer*, Vol. 11, 1968, pp. 241–253.

6 Riley, N., "Notes on a Paper by Kierkus," *International Journal of Heat and Mass Transfer*, Vol. 18, 1975, pp. 991–993.

7 Clarke, J. R., "Transpiration and Natural Convection: The Vertical-Flat-Plate Problem," *Journal of Fluid Mechanics*, Vol. 57, 1973, pp. 45–61.

8 Fussey, D. E. and Warneford, I. P., "An Analysis of Laminar Free Convection From an Upward Facing Inclined Plate," *Letters in Heat and Mass Transfer*, Vol. 3, 1976, pp. 443–448.

9 Emery, A. F., Yang, A. and Wilson, J. R., "Free Convection Heat Transfer to Newtonian and Non-Newtonian High Prandtl Number Fluids From Vertical and Inclined Surface," 1976, ASME Paper No. 76-HT-46.

10 Sparrow, E. M., Quack, H. and Boerner, C. J., "Local Non-similarity Boundary Layer Solutions," *AIAA Journal*, Vol. 8, No. 11, 1970, pp. 1936–1942.

11 Hasan, M. M., "Local Non-similarity Solution of Free Convection Flow and Heat Transfer From an Inclined Isothermal Plate," M.S. Thesis, Mechanical Engineering, University of Kentucky, 1978.

12 Sparrow, E. M. and Yu, H. S., "Local Non-Similarity Thermal Boundary Layer Solutions," ASME JOURNAL OF HEAT TRANSFER, Vol. 93, 1971, pp. 328–334.

13 Eckert, E. R. G., Schneider, P. J., Hayday, A. A. and Larson, R. M., "Mass Transfer Cooling of a Laminar Boundary Layer Injection of a Light-Weight Foreign Gas," *Jet Propulsion*, Vol. 28, 1958, pp. 34–39.

14 Minkowycz, W. J. and Cheng, P., "Free Convection About a Vertical Cylinder Embedded in a Porous Medium," *International Journal of Heat and Mass Transfer*, Vol. 19, 1976, pp. 805–813.

15 Lloyd, J. R. and Sparrow, E. M., "On the Stability of Natural Convection Flow on Inclined Plates," *Journal of Fluid Mechanics*, Vol. 42(3), 1970, pp. 465–470.

16 Black, W. Z. and Norris, J. K., "The Thermal Structure of Free Convection Turbulence From Inclined Isothermal Surfaces and its Influence on Heat Transfer," *International Journal of Heat and Mass Transfer*, Vol. 18, 1975, pp. 43–50.

R. D. Flack
Assistant Professor.
Department of Mechanical and Aerospace Engineering,
University of Virginia,
Charlottesville, VA 22901
Assoc. Mem. ASME

T. T. Konopnicki
Engineer,
Texas Instruments, Inc.,
Dallas, TX
Assoc. Mem. ASME

J. H. Rooke
Graduate Research Assistant,
Department of Mechanical and Aerospace Engineering,
University of Virginia,
Charlottesville, VA 22901
Student Mem. ASME

The Measurement of Natural Convective Heat Transfer in Triangular Enclosures

Heat transfer rates were experimentally measured for laminar convection air flows in two-dimensional triangular enclosures with two side walls which were heated and cooled and an adiabatic bottom. Both local and overall heat transfer data were obtained by the use of a Wollaston prism schlieren interferometer. The angle between the two isothermal side walls was varied between 60 and 120 deg, which resulted in a variation in aspect ratio (enclosure height/base width) between 0.29 and 0.87, while the Grashof number was varied between 2.9 × 10^6 and 9.0 × 10^6. Results are compared to previously obtained isothermal inclined flat plate data and rectangular enclosure data. Present results agree with rectangular enclosure results. One deviation from local rectangular enclosure data was found in the apex regions of the triangular enclosures, where complex thermal and flow interactions occurred due to proximity of the two side walls.

Introduction

Natural convection has over the past decades been important in many engineering applications. In general free convection can be classified as either being internal (in enclosures) or external. Several geometries of internal flow have been previously examined. One geometry which has not been examined, however, is a triangular enclosure. In this paper, both local and overall free convective heat transfer in isosceles triangular enclosures are experimentally examined for three geometries. A Wollaston prism schlieren interferometer was utilized to obtain the data.

Previous to this time many investigators studied free convection in rectangular enclosures. Rectangular enclosures have been examined both theoretically and experimentally for wide ranges of Grashof numbers and aspect ratios [1–8]. Cylindrical and spherical enclosures are other geometries which have also been studied [9–10]. Triangular enclosures are a geometry which are often found in attic areas of domestic buildings, solar energy systems and sometimes in electronic consoles; but natural convection in such enclosures has not been previously studied. Previous to this time, if one were interested in predicting heat transfer rates due to natural convection in these geometries, one had to rely on data provided by tilted rectangular enclosures [11–12], or tilted isothermal flat plate data [13–14].

The aim of this paper is to present experimental laminar heat transfer data for isosceles air filled triangular enclosures with two isothermal sides and an insulated bottom. This geometry represents an attic enclosure with a solar collector (hot) on one surface and a cold condition on the second boundary. Differences are identified between the data presented herein and data previously available for rectangular enclosures and inclined plates. Both local and overall heat transfer rate data for Grashof numbers ranging from 2.9 × 10^6 to 9.0 × 10^6 are presented.

Apparatus

The air filled enclosure consisted of two constant temperature water tanks and one horizontal adiabatic bottom, as shown in Fig. 1(*a*). The face of each tank was polished aluminum (1.27 cm thick) and was 10.78 cm long (L) by 25.4 cm wide (Z). These plates formed the two inclined sides of the triangular enclosure. Six copper-constantan thermocouples were imbedded in the aluminum walls and were within 0.16 cm of the faces. The locations of the thermocouples are presented in Fig. 1(*b*). One tank was maintained at a constant hot temperature by an electrical heater coil and the temperature of the cold surface was maintained by an ice bath mixture in the second tank. The water in each bath was continually mixed by electrical stirrers, and the walls were uniform in temperature within 0.5°C.

The bottom surface of the enclosure was fabricated from a 2.54 cm thick Bakelite plate and was heavily insulated underneath with urethane foam. Aluminum templates on both ends of the test section were screwed into the two side tanks and bottom Bakelite plate for alignment. Adjustment of the apparatus to different geometries required only using different alignment holes in the templates. The end plates

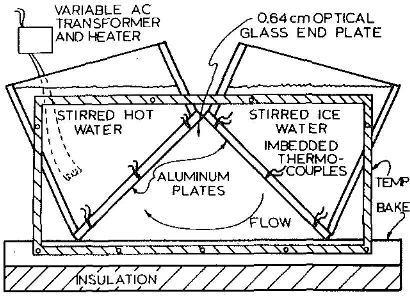

Fig. 1(*a*) Enclosure schematic

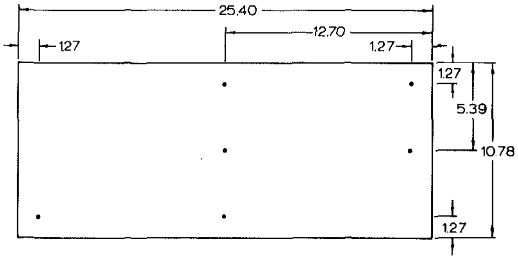

Fig. 1(*b*) Thermocouple locations

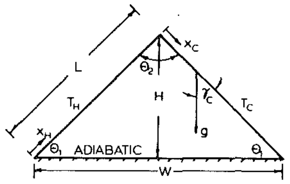

Fig. 1(*c*) Idealized enclosures

Fig. 1 Triangular enclosure schematic and idealized triangular enclosure

---

Contributed by the Heat Transfer Division and presented at the Winter Annual Meeting, December 10–15, 1978, San Francisco, California. Manuscript received by the Heat Transfer Division July 26, 1978. Paper No. 78-WA/HT-9.

Table 1 Values of W, H, θ_1 and θ_2 used

W(cm)	H(cm)	W/H	θ_1(deg)	θ_2(deg)
10.78	9.33	0.865	60	60
15.24	7.62	0.500	45	90
18.67	5.39	0.289	30	120

were made of 0.64 cm optical glass which was sealed onto the ends and held in place with silicon sealant/adhesive. Seams around the corners of the enclosures were also sealed on the exterior with this sealant.

Three geometries were examined and the idealized enclosure is presented in Fig. 1(c). The values of W, H, θ_1 and θ_2 which were used are listed in Table 1. One should note that the x direction is defined differently for the hot and cold walls due to the anticipated development of the flows.

A Wollaston prism schlieren interferometer similar to that used by Sernas, et al. [15] was utilized to make the heat transfer measurements. A diagram of the system is shown in Fig. 2. The light source was a 5mw HeNe Laser (λ = 6328Å). Two polarizers oriented at 90 deg to each other were used as well as two spherical mirrors with focal lengths (f) of 164.5cm and diameters of 20.3cm as shown. The Wollaston prism had a wedge angle (α) of 3 deg and indicies of refraction (n_e, n_0) of 1.55178 and 1.54272. Interferometric images of the enclosure were projected onto a large ground glass screen and photographed with a 35mm camera onto high resolution film.

Previous to the use of this interferometer for the triangular enclosures, the authors demonstrated the accuracy of the apparatus by measuring the natural convection heat transfer rates around a vertical isothermal flat plate. Results were within 5 percent of previous correlations, indicating the particular apparatus was capable of accurate measurements.

Experimental Procedure

Each geometric configuration was run at four different hot bath temperatures, and at least two different fringe orientations were used in the data analysis. Before each of these tests was run, however, the parallel reference fringes were recorded (i.e., both baths and bottom plate were at ambient conditions, see Fig. 3(a)). These fringes were necessary to analyze the shifted fringe data when one bath was heated and the other cooled (see Fig. 3(b)). The two reference fringe orientations which were used were horizontal and vertical. For all cases, the two sets of data agree within 5 percent.

The cold bath temperature was held constant at approximately 0°C, while for the hot bath, four temperatures were used: approximately 30, 50, 65, and 80°C. Photographs of the fringes were taken during transient periods. By the analysis and comparison of the transient patterns, it was found that waiting periods of more than one hour were necessary for steady-state conditions to be established.

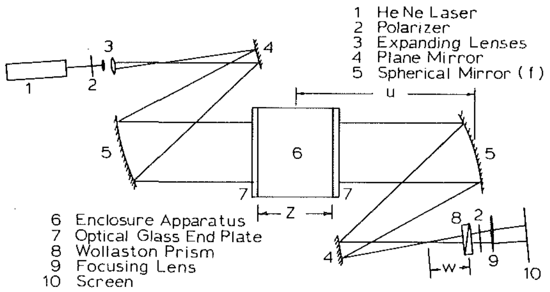

Fig. 2 Wollaston prism Schlieren interferometer

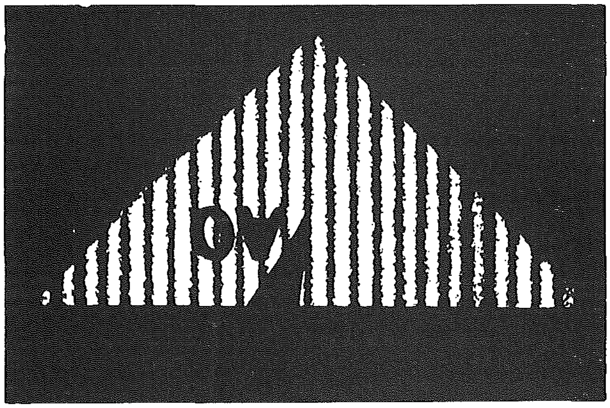

Fig. 3(a) Unshifted fringes

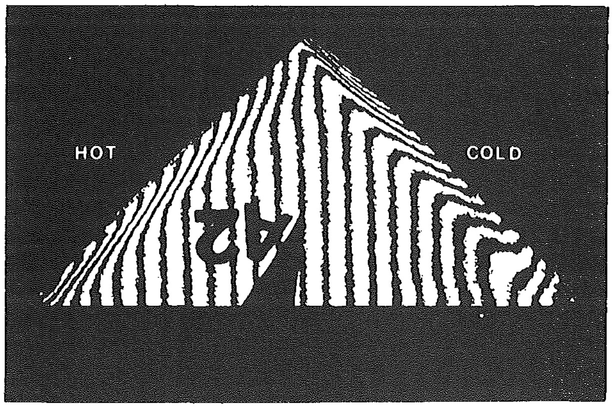

Fig. 3(b) Shifted fringes

Fig. 3 Photographs of interferograms for θ_2 = 90 deg

Nomenclature

f = focal length of spherical mirrors, see Fig. 2
g = acceleration due to gravity
Gr, $\overline{\text{Gr}}$ = local and overall Grashof numbers
$h, \bar{h}$ = local and average heat transfer coefficients
H = height of enclosure
K = Gladstone-Dale constant
k = thermal conductivity of air
L = length of side walls in enclosure
ℓ = horizontal direction, see Fig. 4
n_e, n_0 = extraordinary and ordinary indicies of refraction of Wollaston prism
Nu, $\overline{\text{Nu}}$ = local and overall Nusselt numbers
p = pressure in enclosure
Pr = Prandtl number
q = heat transfer (watts)
q'' = heat transfer per unit area (watts/m^2)
R = ideal gas constant
T = temperature
u = distance defined in Fig. 2
W = width of enclosure
w = distance defined in Fig. 2
x = direction tangent to direction of flow, see Fig. 1
y = direction normal to a surface
z = length of test section, see Fig. 2
α = wedge angle of Wollaston prism
β = volumetric coefficient of expansion
γ = angle between gravity vector and an inclined surface, see Fig. 1
$\Delta\ell$ = local distance between the sidewalls in the apex region
δ = angle between the reference interference fringes and y
ϵ = relative fringe shift
θ_1, θ_2 = angles in enclosure, see Fig. 1
λ = wavelength of light
ν = kinematic viscosity

Subscripts

C, H = refer to conditions at the cold and hot side walls
e = evaluated at edge of boundary layer, see Fig. 4
m = evaluated at the mean temperature, $T_m = (T_H + T_C)/2$
r = evaluated at the reference temperature, see equation (2)
s = evaluated at the surface temperature
1, 2 = refer to methods of correlating data, see equations (2–5)

To analyze the data recorded on film, an X-Y measuring microscope was used. The reference fringe interferogram was first analyzed to determine the exact fringe spacing and angles between the fringes and the various surfaces. A single reference fringe was also marked on this intergerogram and this fringe was observed and continuously remarked during any transient conditions (during temperature changes). Thus, by knowing the initial and final positions of one fringe, one could measure the relative motions of other fringes. The reference fringe was marked near the center of the enclosure where very little shifting of fringes occurred (pointer in Fig. 3).

Sernas, et al. [15] showed that the local temperature gradient was proportional to the relative fringe shift. Equations are also derived in this reference which allow the calculation of temperature gradient normal to a wall ($\partial T/\partial y$) and the heat transfer rate once the fringe shift is measured. For example, the thermal gradient evaluated at the surface is given by:

$$(\partial T/\partial y)_s = -(\lambda R {T_s}^2/p \sin \delta)[2KZ(n_e - n_0) \tan \alpha(f + w - wu/f)]^{-1}\epsilon \quad (1)$$

where R, K, p, δ, ϵ, w, and u are defined in the Nomenclature and Fig. 2.

Measurement error estimates are discussed in the Appendix. For local and average quantities the maximum errors are 6 and 8 percent, respectively. Also, at worst, 5 percent of the measured heat transfer was lost through the glass end plates. This loss is also discussed in the Appendix.

Analysis of Data

Two types of data are presented in this paper. First, local heat transfer data are presented for several configurations and Grashof numbers. These data are compared to theoretical results for inclined isothermal plates with a local Nusselt number versus local Grashof number plot. Second, the overall (or average) heat transfer data are compared to the rectangular enclosure data of Eckert and Carlson [1] and Sernas, et al. [7].

First, the local data are presented. To present results for rectangular enclosures in a form comparable to vertical plate data, Eckert and Carlson [1] utilized the temperature at the center plane to represent the temperature at "infinity" (the temperature at the edge of the boundary layer). For the present analysis a similar technique was used and the local heat transfer coefficient was calculated using the temperature at the edge of the boundary layer, T_e. This temperature was obtained by numerical integration of the experimental temperature gradient in the flow field. In the "core" of the enclosure a significant amount of stratification was found as will be discussed later. In this analysis, the edge of the boundary layer was determined where the temperature gradient in the horizontal direction, ($dT/d\ell$) was zero. A representation of the method of calculating $h(x)$ is presented in Fig. 4.

To account for temperature dependent properties, the suggestions by Sparrow and Gregg [16] were used to correlate the data. That is, a reference temperature at 38 percent of the fluid-wall temperature difference was used, and the volumetric coefficient of expansion was evaluated at T_e.

Also, for simple inclined heated surfaces, Kierkus [13] and Fujii and Imura [14] determined that by replacing the gravity term (g) in the Grashof number by $g \cos \gamma$ (which represents the gravity vector tangent to a wall), one obtains very good agreement with the vertical and the inclined surface. Therefore, for the present local data the correlating parameters which are used for each wall are:

$$\left.\begin{aligned} h_1 &= k_s(\partial T/\partial y)_s/(T_s - T_e) \\ \mathrm{Nu}_1 &= h_1 x/k_r \\ \mathrm{Gr}_1 &= g\beta \cos \gamma(T_s - T_e)x^3/{\nu_r}^2 \\ \beta &= 1/T_e \\ T_r &= T_s - 0.38(T_s - T_e) \end{aligned}\right\} \quad (2)$$

The present experimental data are, therefore, compared to the commonly accepted theoretical correlations for laminar free convection over an isothermal heated flat plate in an isothermal fluid [17, 18], which have been found to be accurate for inclined plates, regardless of γ, if the Grashof number is defined as above [13, 14]:

$$\mathrm{Nu} = F(\mathrm{Pr})(\mathrm{Gr})^{1/4} \quad (3)$$

where $F(\mathrm{Pr}) = 0.357$ for $\mathrm{Pr} = 0.72$.

Overall heat transfer data are presented and compared to large and small aspect rectangular enclosure data [1, 7]. The authors of these references used different correlating parameters to present their results. The overall temperature difference was used, $T_H - T_C$, and properties were evaluated at an average temperature, T_m. Therefore,

$$h_2 = k_s(\partial T/\partial y)_s/(T_H - T_C) \quad (4)$$

The average heat transfer coefficient was then correlated by:

$$\left.\begin{aligned} \overline{h_2} &= \int_0^1 h_2(x)d(x/L) \\ \overline{\mathrm{Nu}_2} &= \overline{h_2}L/k_m \\ \overline{\mathrm{Gr}_2} &= g\beta \cos \gamma(T_H - T_C)L^3/{\nu_m}^2 \\ \beta &= 1/T_m \\ T_m &= (T_H + T_C)/2 \end{aligned}\right\} \quad (5)$$

For the present study, the value of $\overline{\mathrm{Gr}_2}$ ranged from 2.9×10^6 to 9.0×10^6. By observing the interferograms during the test runs, one noted that the temperature gradient field at steady state was motionless. This indicates that for all of the data presented herein, the flow was steady and laminar since turbulent eddies would have resulted in fluctuating fringe patterns. This flow behavior agrees with that of Sernas, et al. [7] who measured laminar and steady flows up to Grashof numbers of 1.35×10^7.

Results and Discussion

Two types of measurements were made in this study as described above: local and average. Local results are presented to indicate the similarity of the data for different configurations and overall results are presented to provide engineering design guidelines.

Local Data. First, one typical set of dimensional data is presented ($\theta_2 = 90$ deg and $\overline{\mathrm{Gr}_2} = 5.60 \times 10^6$). This data set corresponds to the interferogram presented in Fig. 3(*b*). In Fig. 5 five isotherms are presented which were obtained by numerical integration of the temperature gradient data from the Wollaston prism interferometer. These isotherm data indicate that large thermal gradients occur near the surfaces and that in the central portion of the enclosure the air

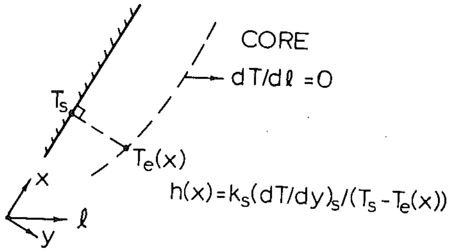

Fig. 4 Evaluation of local heat transfer coefficient

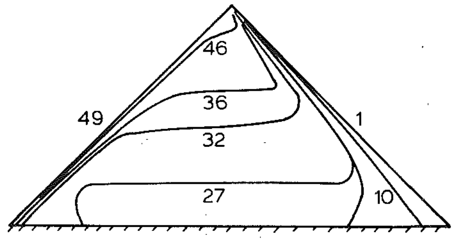

Fig. 5 Selected isotherms for $\theta_2 = 90$ deg and $\overline{\mathrm{Gr}_2} = 5.60 \times 10^6$ ($T_H = 49°\mathrm{C}$ and $T_C = 1°\mathrm{C}$, other temperatures in °C)

is stratified. Similarly, Eckert and Carlson [1], Briggs [8], and others found for rectangular enclosures that the gas was stratified in the central core for Grashof numbers ($\overline{Gr_2}$) larger than 10^5.

In Fig. 6 local heat transfer rate data are presented for both hot and cold walls. The integral of each curve represents the total heat transfer from each surface. As noted in Fig. 6 the difference between the total heat transfer from each surface is less than 4 percent which was typical of all data sets. One peculiarity of the results for this geometry is evidenced on this figure. For values of x_H/L near unity and x_C/L near zero large values of heat flux are seen. This is due to a highly conductive region near the top of the enclosure (due to the large temperature difference and small distance between the plates.) Also, near the top and for the same horizontal plane the values of q'' are approximately equal as denoted with +'s on Fig. 6 and are also approximately equal to the pure conduction heat flux calculated by $k_m(T_H - T_C)/\Delta\ell$, where $\Delta\ell$ is the distance between the surfaces at the particular value of x_C. Only very near the top does $q''_H = q''_C$, since this is the only region in which conduction dominates.

To present the nondimensionalized local results, the temperature at the edge of the boundary layer was determined for all geometries and Grashof numbers. These temperature data have been non-dimensionalized as done by Eckert and Carlson [1] and typical results are presented in Fig. 7. These nondimensionalized temperature profiles are relatively independent of θ_2 and $\overline{Gr_2}$. A least squares polynomial curve fit to these data yields:

$$(T_e - T_C)/(T_H - T_C) = 0.50\,(1 + (x_H/L)^2)$$
$$= 1 - (x_C/L) + 0.50\,(x_C/L)^2 \quad (6)$$

Local Nusselt number results for six typical hot and cold wall data sets are presented in Fig. 8. Also presented in Fig. 8 is the accepted correlation for inclined isothermal surfaces in isothermal fluids from equation (3). As can be seen, the data for the hot and cold walls follow separate curves. Near the "starting" corners and in the central portions of the surfaces, the data fall on straight line curves for both walls. For large values of x_H/L on the hot wall the value of Gr_l becomes small since the value of T_e approaches $T_s = T_H$ (Fig. 7). The region for which Gr_l decreases with increasing x_H/L will be defined as the apex region for the remainder of this paper. The apex represents where the influence of the cold wall becomes significant. This boundary causes the Gr_l versus x_H/L behavior to deviate from simple flat plat correlations and causes two-dimensionality of the flow field as evidenced by the velocity measurements in [19]. The location of the apex region has been determined to be located at values of $x_H/L = 0.76 \pm .02$ and greater. This value was determined for all three geometries and all values of $\overline{Gr_2}$.

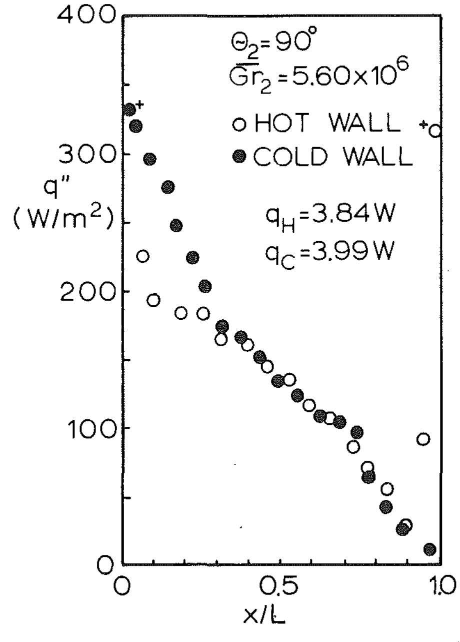

Fig. 6 **Local heat flux for hot and cold walls for θ_2 = 90 deg and $\overline{Gr_2}$ = 5.60 × 10^6**

Included in the apex region is a highly conductive region for values of x_H/L greater than approximately 0.90. In this region conduction dominates as indicated in Fig. 6. Thus, the apex region can be categorized into two subregions. For $0.76 < x_H/L < 0.90$ the flow is two-dimensional and both conduction and convection are important. For $x_H/L > 0.90$ very little flow exists and conduction is the most important heat transfer mechanism.

Also in Fig. 8 for the cold wall, values of Nu_l drop off with increasing Gr_l near the bottom (departing) corner due to the interference of the lower insulated boundary with the flow. In the apex region the values of Nu_l for the cold wall remain well behaved, since Nu_l is proportional to the product of the heat transfer coefficient, h_l, and x_C, which becomes small. The location of the departing region of the cold wall was found to be independent of $\overline{Gr_2}$ but a function of θ_2. A curve fit to the data indicates the departure region for the cold wall occurs for values of x_C/L greater than $0.59\,(\cos\theta_1)^{-0.36}$.

In Fig. 8 the hot wall data is seen to be significantly higher than for the simple isothermal plate correlations. Also, this data is seen to be slightly a function of θ_2 but not of $\overline{Gr_2}$. When the apex region is neglected, the local data represent curves given by:

$$Nu_l = C_1 Gr_l^{C_2} \quad (7)$$

where C_1 and C_2 are given in Table 2. Also in Table 2 are the coeffi-

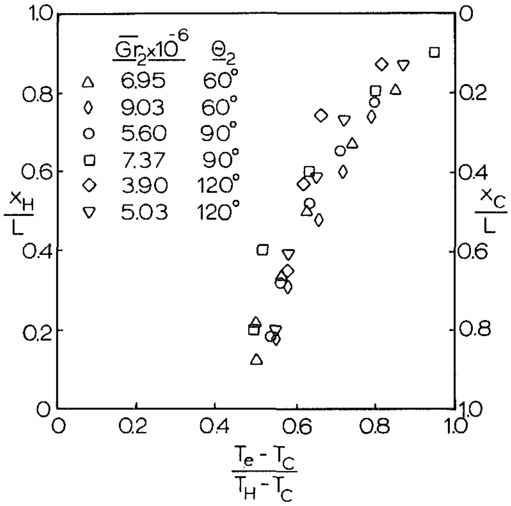

Fig. 7 **Nondimensionalized temperatures at the edge of the boundary layer**

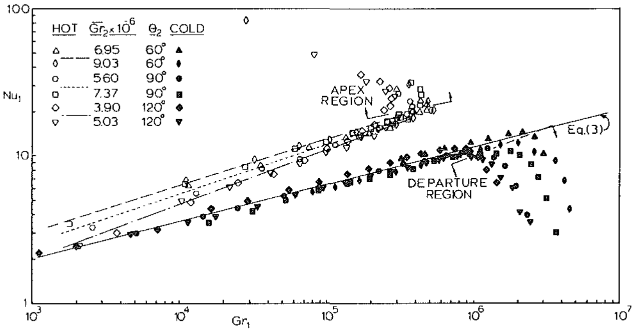

Fig. 8 **Local Nusselt numbers for both hot and cold walls**

Table 2 Least squares curve fit to hot wall data—equations (7) and (9)

θ_2	C_1	C_2	C_3
60	0.372	0.31	0.0921
90	0.239	0.34	0.0502
120	0.158	0.37	0.0284
Ref. [1]	0.231	0.30	0.119

cients which were determined by Eckert and Carlson [1] for the hot wall of a rectangular enclosure. Although exact agreement is not found, the results are in close agreement. In Fig. 8 one should realize that a large portion of the total heat transfer is occurring for Gr_1 greater than 10^5. Thus, only minor differences between the curves for $\theta_2 = 60, 90$ and 120 deg are observed for the central portion of the wall. Only near the starting corner (low Gr_1) and apex do significant differences occur.

Kierkus [13] theoretically and experimentally examined the temperature/heat transfer field and velocity field around vertical and inclined heated plates. He examined two types of inclined surfaces: facing up and down. His heated plate facing down corresponds to the heated wall of the triangular enclosure and his heated wall facing up corresponds to the cooled wall (facing down) in the triangular enclosure. In [13] (Fig. 9) Nu(hx/k) versus Gr($g\beta\Delta Tx^3/\nu^2$) is plotted for $\gamma = \pm 45$ and 0 deg. If one "corrects" his value of Gr by the factor cosγ, his experimental results for hot plate facing upward are nearly identical to those for a vertical plate for the range of Gr from 10^3 to 10^6. On the other hand the values of Nu for a hot plate facing downward are dependent on γ and are significantly higher than for a hot plate facing upward. Thus, the differences exhibited in Fig. 8 (or equation (7), Table 2 and equation (3)) between the hot and cold surfaces should not be surprising. Exactly the same trend is exhibited here as evidenced by Kierkus: the inclined hot walls yield larger values of Nu than do the inclined cold walls and are slightly dependent on γ and the inclined cold wall correlates well with vertical plate data.

Yang, et al. [20] theoretically investigated the effect of thermal stratification of the free stream medium on the heat transfer rates of vertical plates. By using the temperature profile given in Fig. 7 the results of reference [20] have been used to predict the dependence of Nu_2 on Gr_2. For hot isothermal wall cases in which the free stream temperature increases with x, the local nondimensionalized thermal gradient is larger than for cases with an isothermal free stream. For the particular stratification found here this nondimensional temperature gradient is approximately 0.80 as compared to 0.50 (isothermal free stream) as found in Fig. 3 of [20]. Thus, an increase in local heat transfer (and Nu_l) on the order of 60 percent should be expected due to the stratification in the core region. Experimentally, for values of $Gr_l = 10^5$ (center of the walls) the measured values of Nu_l were typically 70 percent higher than those obtained from the simple correlation (equation (3)). Thus, a second deviation of the data on the hot surface from equation (3) is attributed to the stratification in the core.

The cold wall data is relatively close to the curve generated by equation (3). The effect of stratification was again predicted using [20] and the temperature distribution in Fig. 7. For the cold wall, the increase in local heat transfer above the isothermal case was predicted to be only 5 to 10 percent. Thus, good agreement between the cold wall data and equation (3) should be expected.

Overall Data. The total or overall Nusselt numbers were also calculated for these data and these overall quantities are presented in Fig. 9. Previous to this time, triangular enclosures had not been studied. The most similar geometries were rectangular enclosures [1, 7]. Thus, they will be used for comparison here. The data of Sernas, et al. [7] are for aspect ratios less than unity, while the data of Eckert and Carlson [1] are for aspect ratios of 2.5 to 20.

As can be seen in Fig. 9 the present data are in qualitative agreement with previous data for rectangular enclosures. To correlate the hot wall data the curves representing the local Nusselt numbers and temperature differences (Figs. 6 and 7) have been used to calculate the total heat transfer along the walls. The total heat transfer is a combination of convection for values of x_H/L up to 0.76, and one-dimensional conduction, which has been used to approximate the heat transfer in the apex region ($0.76 \leq x_H/L \leq 1.0$). Thus, the total heat transfer is estimated as:

$$q = \int_0^{0.76} Lh(T_H - T_e)Zd(x_H/L) + \int_{0.76}^{1} Lk(T_H - T_C)Z/\Delta\ell d(x_H/L) \quad (8)$$

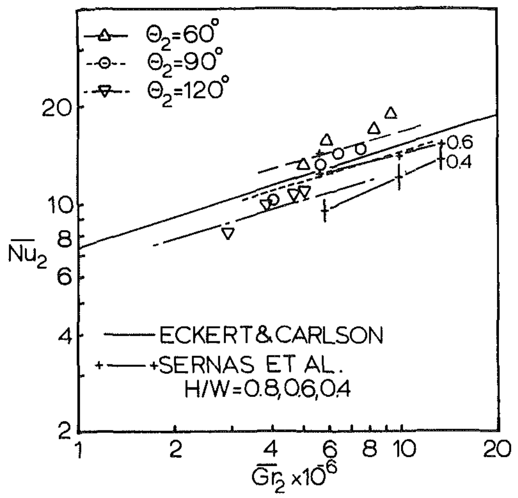

Fig. 9 **Overall Nusselt numbers as compared to rectangular enclosure data**

Recalling equations (6) and (7), the fact that $\Delta\ell = 2(L - x_H)\cos\theta_1$, and numerically integrating, equation (8) reduces to:

$$Nu_2 = C_3(\overline{Gr_2})^{C_2} + 1.589/\cos\theta_1 \quad (9)$$

where C_3 is a function of θ_2 and is defined in Table 2. Eckert and Carlson [1] also found a similar expression with the absence of the second (conduction) term. The constants of Eckert and Carlson are included in Table 2 and this curve is represented in Fig. 9. Also in Fig. 9 are the curves representing equation (9). The data points for each value of θ_2 are seen to be slightly higher than the curves representing equation (9). The main reason for this is that in the apex region, a combination of convection and conduction occurs. In equation (8) however, for values of x_H/L between 0.76 and 1.00 pure conduction was assumed. Thus, equation (9) should be expected to yield slightly low results.

The slopes of the present lines in Fig. 9 are 0.28, 0.29 and 0.29 for $\theta_2 = 60, 90$ and 120 deg and are very similar to the slope of Eckert and Carlson (0.30). The slopes differ somewhat from the data of Sernas, et al. [7] and this is attributed to two sources. First, and most important, Sernas' lines are drawn through the actual data points. The uncertainty reported by Sernas is plotted for $H/W = 0.4$. As one can see, the slope can change significantly depending how the lines are drawn through the uncertainties. Secondly, by observing their interferogram one can see a significant amount of heat transfer is occuring near the "insulated" boundaries, thus causing some concern as to the effectiveness of the channel.

As can be seen, the three curves, for different values of θ_2 in Fig. 9, are different by typically only 10 to 20 percent, while a 3:1 range of aspect ratios was studied. Gebhart [18] and others have noted for rectangular enclosures that when the boundary layer thickness is significantly thinner than the width of the enclosure, the local and overall Nusselt numbers do not depend strongly on the aspect ratio. As can be seen in Fig. 3(b), the boundary layer thickness is considerably thinner than the width except at the apex. Thus, for the geometry and range of Grashof numbers studied here, the effect of θ_2 (and aspect ratios) should not be large.

Conclusions

Experimental free convective heat transfer data were obtained for three isoceles triangular enclosures for which the overall Grashof number ($\overline{Gr_2}$) varied from 2.9×10^6 to 9.0×10^6, and θ_2 was varied from 60 to 120 deg. Such a class of enclosures has not been examined previously. Important conclusions from this study include: (1) The flow is always laminar and steady for this range of Grashof numbers. (2) The local Nusselt numbers are only slightly dependent on θ_2. (3) Local Nusselt numbers for the hot wall are larger than those for a simple isothermal plate in an isothermal medium due to the stratification in the central core and due to the inclination of the walls. Local

Nusselt numbers for the cold wall agree well with the isothermal case. These conclusions are consistent with simple inclined plate data. (4) Unlike rectangular enclosure data previously examined, for the hot surface, the value of Gr_1 increases and then decreases as x_H/L increases over 0.76. This effect is due to a complex thermal-flow interaction where the flow becomes two dimensional. For $0.76 \leq x_H/L \leq 0.90$ the heat transfer is a combination of convection and conduction. (5) Also unlike rectangular enclosure data previously examined for the hot surface the value of q''_H decreases and then increases as x_H/L increases over 0.90. This region is dominated by conduction. (6) For values of x_C/L near unity the values of Nu_1 decrease due to the flow interference at the insulated base of the enclosure, which causes a rapid growth of the boundary layer. (7) Overall Nusselt numbers are in approximate agreement with rectangular enclosure data and variations of only 10 to 20 percent are found due to the dependence on θ_2.

Acknowledgments

The authors gratefully acknowledge the support of the Department of Mechanical and Aerospace Engineering, University of Virginia, for the experimental apparatus.

References

1 Eckert, E. R. G., and Carlson, W. O., "Natural Convection in an Air Layer Enclosed Between Two Vertical Plates with Different Temperatures," *Int. J. Heat Mass Transfer,* Vol. 2, Nos. 1/2, March 1961, pp. 106–120.

2 MacGregor, R. K., and Emery, H. A., "Free Convection Through Vertical Plane Layers-Moderate and High Prandtl Number Fluids," ASME JOURNAL OF HEAT TRANSFER, Vol. 91, 1969, pp. 391–403.

3 Newell, M. E., and Schmidt, F. W., "Heat Transfer by Laminar Natural Convection Within Rectangular Enclosures," ASME JOURNAL OF HEAT TRANSFER, Vol. 92, No. 1, Feb. 1970, pp. 159–168.

4 Boyack, B. E., and Kearney, D. W., "Heat Transfer by Laminar Natural Convection in Low Aspect Ratio Cavities," ASME Paper No. 72-HT-52, presented at the AIChE-ASME Heat Transfer Conference, Denver, Colo., Aug. 1972.

5 Chu, H. H., Churchill, S. W., and Patterson, C. V. S., "The Effect of Heater Size Location, Aspect Ratio, and Boundary Conditions on Two Dimensional, Laminar, Natural Convection in Rectangular Channels," ASME JOURNAL OF HEAT TRANSFER, Vol. 98, No. 2, May 1976, pp. 194–201.

6 Tabarrok, B. and Lin, R. C., "Finite Element Analysis of Free Convection Flows," *Int. J. Heat Mass Transfer,* Vol. 20, No. 9, Sept. 1977, pp. 945–952.

7 Sernas, V., Fletcher, L. S., and Rago, C., "An Interferometric Study of Natural Convection in Rectangular Enclosure of Aspect Ratio Less Than One," ASME Paper No. 75-HT-63, Presented at the AIChE-ASME Heat Transfer Conference, San Francisco, CA., Aug. 1975.

8 Briggs, D. G., "Numerical Solutions of High Rayleigh Number Two-Dimensional Free Convection in Enclosures With An Aspect Ratio of One," *Proceedings of AICA International Symposium on Computer Methods for Partial Differential Equations,* Lehigh University, Bethlehem, Penn., June 1975.

9 Powe, R. E., Carley, C. T., and Bishop, E. H., "Free Convective Flow Patterns in Cylindrical Annuli," ASME JOURNAL OF HEAT TRANSFER, Vol. 91, No. 3, August 1969, pp. 310–314.

10 Yin, S. H., Powe, R. E., Scanlan, J. A., and Bishop, E. H., "Natural Convection Flow Patterns in Spherical Annuli," *Int. J. Heat Mass Transfer,* Vol. 16, No. 9, Sept. 1973, pp. 1785–1795.

11 Ozoe, H., Sayam, H., and Churchill, S. W., "Natural Convection in an Inclined Rectangular Channel at Various Aspect Ratios and Angles—Experimental Measurements," *Int. J. Heat Mass Transfer,* Vol. 18, No. 12, Dec., 1975, pp. 1425–1431.

12 Buchberg, H., Catton, I., and Edwards, D. K., "Natural Convection in Enclosed Spaces—A Review of Application to Solar Energy Collection," ASME JOURNAL OF HEAT TRANSFER, Vol. 98, No. 2, May 1976, pp. 182–188.

13 Kierkus, W. T., "An Analysis of Laminar Free Convection Flow and Heat Transfer About an Inclined Isothermal Plate," *Int. J. Heat Mass Transfer,* Vol. 11, No. 2, Feb. 1968, pp. 241–253.

14 Fujii, T., and Imura, H., "Natural Convection Heat Transfer from a Plate with Arbitrary Inclination," *Int. J. Heat Mass Transfer,* Vol. 15, No. 4, 1972, pp. 755–767.

15 Sernas, V., Fletcher, L. S., and Aung, W., "Heat Transfer Measurements with a Wollaston Prism Schlieren Interferometer," ASME Paper No. 72-HT-9, Presented at the AIChE-ASME Heat Transfer Conference, Denver, Colo., Aug. 1972.

16 Sparrow, E. M., and Gregg, J. L., "The Variable Fluid Property Problem in Free Convection," *Trans. ASME,* Vol. 80, 1958, pp. 879–886.

17 Ostrach, S., "An Analysis of Laminar Free Convection Flow and Heat Transfer About a Flat Plate Parallel to the Direction of Generating Force," NACA Report, 1111, 1953.

18 Gebhart, B., *Heat Transfer,* McGraw-Hill, New York, 1971.

19 Flack, R. D., and Witt, C. L., "Velocity Measurements in Two Natural Convection Air Flows Using a Laser Velocimeter," ASME JOURNAL OF HEAT TRANSFER, Vol. 101, No. 2, May 1979, pp. 256–260.

20 Yang, K. T., Novatny, J. L., and Cheng, Y. S., "Laminar Free Convection From a Nonisothermal Plate Immersed in a Temperature Stratified Medium," *Int. J. Heat Mass Transfer,* Vol. 15, No. 5, 1972, pp. 1097–1109.

21 Flack, R. D., "Shearing Interferometer Inaccuracies Due to a Misaligned Test Section," *Applied Optics,* Vol. 17, No. 18, 15 Sept. 1978, pp. 2873–2875.

APPENDIX

In this appendix an error analysis is performed. The most obvious inaccuracy is encountered when locating the center of a fringe using the X-Y measuring microscope. For typical fringe shifts ($\epsilon \simeq 2$) the inaccuracy is approximately 4 percent when fringes are not closely spaced, which is typical of this instrument [15]. However, at the apex of the triangles, accurately locating fringes becomes very difficult due to the small distances between fringes (approximately 10 to 20 percent of the heat transfer occurs here). In the apex region the fringe spacing was typically four times smaller than in the central portion of a surface, resulting in uncertainties of approximately 16 percent. Thus, when calculating the average quantities, errors are typically 6 percent ($0.04 \times 0.85 + 0.16 \times 0.15$) due to the limitations in fringe location. Also, when interpreting the interferograms, one has to use the parallel reference fringe interferogram. Thus, to measure a fringe shift one has to include the uncertainty of the position of the original reference fringes. The inaccuracy in measuring the reference fringes is the same as for moderately spaced fringes (4 percent). Next, errors resulting from using a finite number of elements for integration were encountered in determining the average (or overall) quantities. For most numerical integrations used herein 5 to 15 points were used. By using curve fitting techniques and by comparison of results using the trapezoidal rule and Simpson's rule, inaccuracies are estimated to be approximately 1 percent. Next, fringes can be modified by the boundary layer on the end plates [15]. Using the analysis of Sernas et al. [15] this error is estimated to be approximately 2 percent for typical fringe shifts. Lastly, errors can result from test section misalignment in the collimated beam and were estimated to be approximately 1 percent, both experimentally and analytically [21]. The measurement errors for the local (except in the apex region) and overall conditions are, therefore, estimated using the sum of the squares technique to be approximately 6 and 8 percent, respectively.

Since the glass end plates were not insulated, estimates of the heat losses through the ends were made to determine if they were significant. Two different methods were used to estimate the end losses. The first used the approximation of a uniform gas temperature on the inside of the chamber and a uniform glass temperature. The second accounted for stratification and non-uniform glass temperature.

For the first estimate, the air inside of the enclosure was estimated to be uniform at the mean temperature given by Fig. 7 at $x/L = 0.5$, and the glass temperature (T_g) was estimated to be at the arithmetic average of the inside and outside (room temperature) air. The local heat transfer coefficients for both the inside and outside were estimated using the simple flat plate correlation:

$$h = kF(\mathrm{Pr})(g\beta(T_g - T_\infty)/\nu^2)^{1/4}b^{-1/4} \tag{A1}$$

The total heat loss was then estimated by integrating over the triangular end area

$$q/(T_g - T_\infty) = \overline{hA} = \int h dA \tag{A2}$$

where $dA = 2/\tan\theta_1(H - b)db$, and b is the distance from the bottom of the enclosure. Or

$$\overline{hA} = 32/21kF(\mathrm{Pr})(g\beta(T_g - T_\infty)H^3/\nu^2)^{1/4}H/\tan\theta_1 \tag{A3}$$

Finally, by equating the heat flux on the inside and outside surfaces and by neglecting the thermal conductive resistance of the glass one obtains:

$$q_{\mathrm{total}} = (T_{\mathrm{in}} - T_{\mathrm{out}})/(1/\overline{hA}_{\mathrm{in}} + 1/\overline{hA}_{\mathrm{out}}) \tag{A4}$$

The second method is similar to the one above, but the simple vertical plate algebraic correlation was replaced by the graphical results from [20] for nonisothermal plates and surrounding medium. The glass plates were not assumed to be at a uniform temperature, but the local temperatures were found iteratively. Also, the local heat flux on the inside and outside surfaces of the glass were set equal.

Both methods yielded approximately the same results, and for all cases studied here, the total heat flux through both end plates was estimated to be less than 5 percent of the measured heat transfer from either side wall in the enclosure.

B. A. Meyer
Student Mem. ASME

J. W. Mitchell
Mem. ASME

M. M. El-Wakil
Mem. ASME

Mechanical Engineering Department,
The University of Wisconsin,
Madison, Wisc. 53706

Natural Convection Heat Transfer in Moderate Aspect Ratio Enclosures

Local and average heat transfer coefficients for natural convection between parallel plates separated by slats to create enclosures of moderate aspect ratio have been experimentally determined using an interferometric technique. The effects of Rayleigh number, tilt and slat angle, and aspect ratio on the Nusselt number have been determined. The Rayleigh number range tested was up to 7×10^4, and the aspect ratio (ratio of enclosure length to plate spacing) varied between 0.25 and 4. The angles of tilt of the enclosure with respect to the horizontal were 45, 60 and 90 deg. Slat angles of 45, 60, 90 and 135 deg were studied. The results obtained in a previous investigation [1] for aspect ratios of 9 to 36 are included to show continuity. The results indicate that the convective heat transfer is a strong function of the aspect ratio for aspect ratios less than 4. For aspect ratios in the range of 0.5 to 4, spacers between the plates increase, rather than decrease, natural convection heat transfer compared to that for long enclosures. Slat angles less than 90 deg (i.e., oriented downward) reduce convective heat transfer.

Introduction

The free convection heat loss across inclined layers is of interest in many engineering systems, and recently to designers of solar collectors. Reduction of heat loss from the absorber plate through the cover plates allows smaller collector areas to be used. The "slat enclosure," described in Fig. 1, is represented as an array of cells which are essentially contiguous enclosures each having a small aspect ratio.

Heat transfer results have been obtained by other experimenters for some moderate aspect ratio enclosures. Hollands [2] and Arnold, et al. [3, 4] have experimentally studied heat transfer for aspect ratios less than 0.25. Kee [5] determined the Rayleigh number effect at tilt angles of 0, 30 and 60 deg for aspect ratios of 1 and 2, and the angle effect at a particular Rayleigh number, but correlations were not given. His side walls were made of relatively high conductivity plastic, and as shown by Hollands [6], this has an effect on the heat transfer. Ozoe, et al. [7] has conducted experiments with liquids in enclosures of aspect ratios of 1 to 4 and tilt angles of 0 to 150 deg. The side walls were adiabatic both across the enclosure and between the cells. The experiments were compared to numerical studies. Koutsoheras [8] numerically evaluated the heat transfer in similar enclosures for the limiting cases of adiabatic and perfectly conducting side walls. Cane, et al. [9] have studied square honeycombs with aspect ratios in the range of 0.2 to 0.125.

The conclusions that can be drawn from these studies are that for aspect ratios less than 0.1, convection is suppressed for Rayleigh numbers up to 4×10^5 for a tilt angle of 60 deg [2]. As aspect ratio increases from a value of 0.1, convection heat transfer first increases, reaching a maximum at an aspect ratio of about 2, and then decreases as aspect ratio is further increased. The thermal boundary condition along the side walls affect the heat transfer, and an array of small enclosures separated by conducting walls has lower convective heat transfer than one with adiabatic side walls. For an aspect ratio of 0.25 there is little effect of horizontal aspect ratio (A_H) for ratios greater than unity [3, 4]. There are no studies reporting local heat transfer coefficients, and the influence of slat angle has not been studied.

In the present study, local values of the heat transfer coefficient along the heated plate were obtained using interferometric techniques. These local heat transfer coefficients were integrated over the surface to determine average values. The aspect ratio range studied was between 0.25 and 4 and the angle of inclination of the enclosure (θ) ranged from 45 deg with respect to the horizontal to the vertical. The Rayleigh number range studied was up to 7×10^4. Air is the medium in the enclosed space, and the results are limited to Prandtl numbers of about 0.7. Slat, or side wall, angles (ϕ) of 45, 60, 90 and 135 deg were studied. These parameters are defined in Fig. 1.

The results for flat plate enclosures with aspect ratios in the range of 9 to 36 have been previously determined and reported by Randall, et al., [1]. Since these results were obtained using the same test facility and data reduction methods as in the present study, they are included here to show continuity over the entire aspect ratio range of 0.25 to 36.

Test Procedure

The test model for the slat enclosure consisted of contiguous cells bounded on the top by an isothermal water cooled aluminum plate and on the bottom by an isothermal electrically heated aluminum plate. The plates are 25 cm long by 10.2 cm wide with emissivities of about 0.09. The plate spacing (L) was varied from 0.62 cm to 2.5 cm. The slat cell width (H) was varied from 0.62 cm to 5.0 cm to produce the various aspect ratios. The cell walls are made of white opaque paperboard 0.18 mm thick for all but one test run where an opaque polypropylene plastic spacer 0.58 mm thick was used. The ratio of the conductivity of the cell wall to that of air is 4.0 and 4.5, and the cell wall emissivity is 0.9 and 0.8, for the paperboard and plastic walls, respectively. The plate temperature variation is less than 0.5°C over the cold plate and 1.5°C over the hot plate at temperature differences

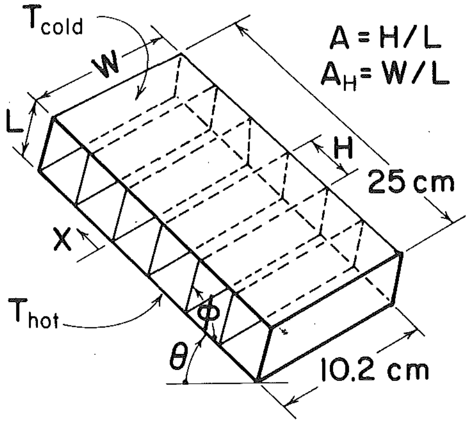

Fig. 1 Slat enclosure parameters

Contributed by the Heat Transfer Division for publication in the JOURNAL OF HEAT TRANSFER. Manuscript received by the Heat Transfer Division April 19, 1979.

up to 90°C. The mean temperature of the air varied from 35 to 55°C.

The temperature distribution in the enclosed air space was measured using a Mach-Zehnder interferometer. The fringe patterns are photographed and used to determine the temperature distribution within the test cell. Figs. 2–5 show interferograms typical of those obtained in this study. The dark and light lines are isotherms representing average temperatures in the direction of the light path.

Analysis of interferograms allows determination of the local tem-

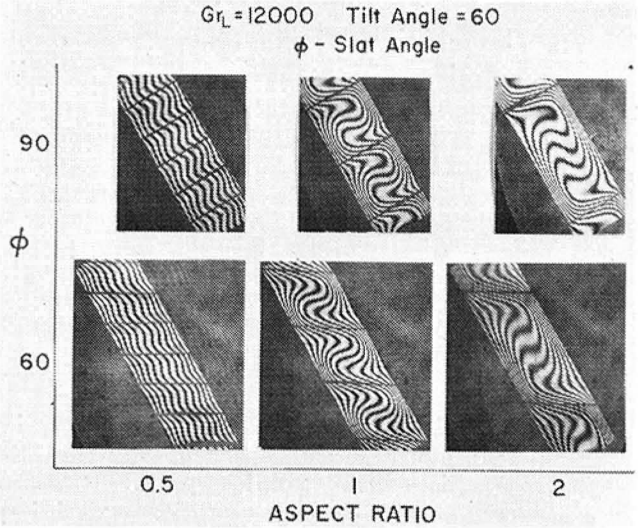

Fig. 2 Interferograms showing the effects of aspect ratio and slat angle

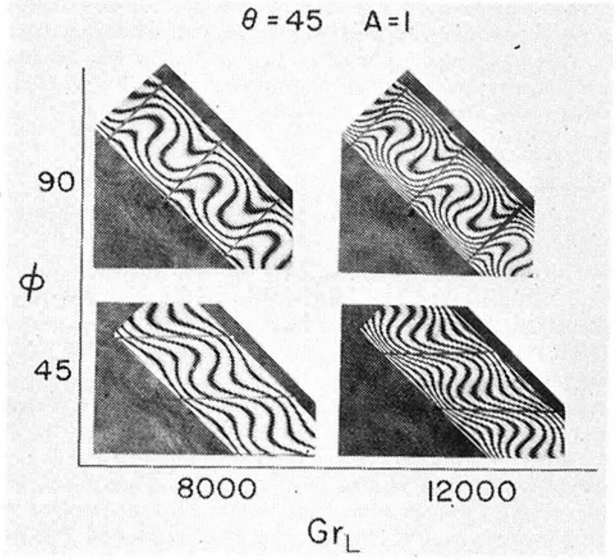

Fig. 3 Interferogram comparing $\phi = 90$ and 45 at $\theta = 45$

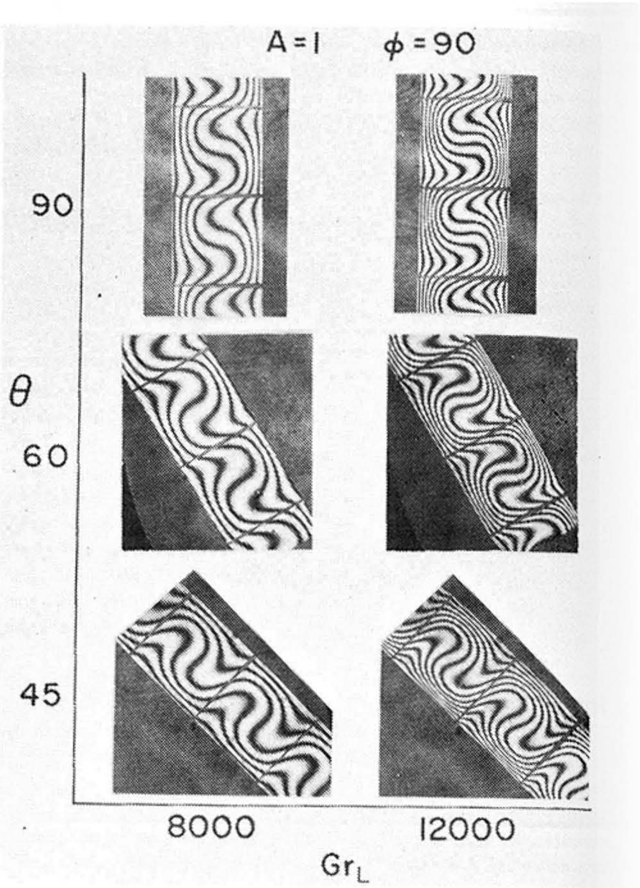

Fig. 4 Interferograms showing the effect of tilt angle (θ)

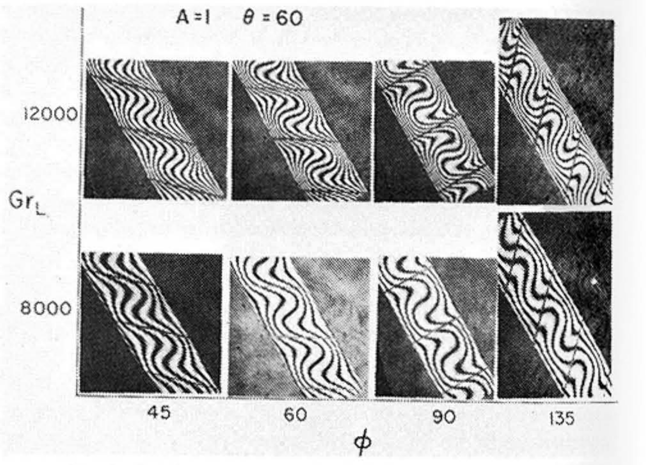

Fig. 5 Interferograms showing the effect of slat angle (ϕ)

Nomenclature

$A = H/L$ aspect ratio
$A_H = W/L$ horizontal aspect ratio
C_1, C_2 = constants in equation (3)
C_3 = constant in equation (4)
C = wall admittance group; $(k/kw)(L/(t/2))$
G = cell coupling group; $(k/kw)((t/2)/L)$
g = acceleration due to gravity
h = local heat transfer coefficient
$\bar{h}$ = average heat transfer coefficient
H = cell length
k = thermal conductivity of air; evaluated at mean temperature (k) or hot plate temperature (k_H)
k_w = thermal conductivity of spacers
L = plate spacing
N = radiation group; $4\sigma\, T_m{}^3L/k$
n = constant in equation (4)
t = thickness of spacers
T_C = cold plate temperature
T_H = hot plate temperature
T_m = mean absolute temperature
W = horizontal width
x = distance measured from the bottom of the cell
y = distance measured from hot plate
α = thermal diffusivity
β = coefficient of volumetric expansion
ν = kinematic viscosity
σ = Stefan-Boltzmann constant
θ = enclosure tilt angle from horizontal
ϕ = slat angle
$Gr_L = g\beta(T_H - T_C)L^3/\nu^2$ Grashof number based on L
$Nu_L = hL/k$ local Nusselt number based on L
$\overline{Nu}_L = \overline{hL}/k$ average Nusselt number based on L
$Ra_L = g\beta(T_H - T_C)L^3/\nu\alpha$; Rayleigh number based on L

peratures and therefore the temperature gradients at the wall. From these, the local heat transfer coefficients are obtained. The interferometer senses only density differences in the air, and thus does not yield information about radiation transport across the space. Radiation heat transfer influences convection heat transfer through its effect on the temperature distribution along the side walls. This distribution is experimentally determined to be close to linear for these tests. The heat transfer coefficient can be determined from the interferograms within ± 5 percent. The estimated experimental uncertainty of the Nusselt number is ±5 percent.

The local Nusselt number is based upon the plate spacing, L, and the total temperature difference, $T_H - T_C$. The Nusselt number is calculated from the nondimensional temperature gradient at the hot surface which is then multiplied by the ratio of the thermal conductivity evaluated at the surface temperature to that at the mean enclosure temperature

$$\mathrm{Nu}_L = \frac{hL}{k} = \left\{\frac{k_H}{k}\,\frac{\partial[(T - T_C)/(T_H - T_C)]}{\partial(y/L)}\right\}_{y=0} \qquad (1)$$

where k is evaluated at the mean temperature, $T_m = (T_H + T_C)/2$.

The average Nusselt number is found by numerically integrating the local values over the entire plate (cell) length (H)

$$\overline{Nu}_L = \frac{\bar{h}L}{k} = \frac{1}{H}\int_0^H \mathrm{Nu}_L\, dx \qquad (2)$$

The corresponding value of the Rayleigh number is based on properties evaluated at the mean temperature. The estimated experimental uncertainty of the Rayleigh number is ±3 percent.

Local Heat Transfer Results

Figs. 2–5 are interferograms for different aspect ratios, tilt angles, slat angles and Grashof (Rayleigh/Prandtl) numbers. The hot plate is the left-hand surface except when the tilt angle (θ) is 90 deg. The isotherms visually show how the heat flux varies with position along the plate. Close spacing of isotherms at the walls indicates high rates of heat transfer.

For example, in Fig. 2 for $\phi = 90$ and $A = 2$, the isotherms are closely spaced together near the surface at the lower left-hand corner of the cell, and further apart at the upper left-hand corner. The heat flux thus decreases along the surface from the lower to the upper corner. In Fig. 2 for ϕ of 90 and A of 2, there is a reversal in the temperature profile in the center of the enclosure.

The isotherms also suggest the convective flow patterns present. In Fig. 2, there is more convective motion as aspect ratio is increased from 0.5 to 2. At an aspect ratio of 0.5, there is little motion and the heat transfer is mainly by conduction. The effect of increased Grashof number, as shown in Figs. 3 and 4, is to increase convective motion. The effect of enclosure tilt angle is fairly small, as shown in Fig. 4 where the pattern of the isotherms is essentially the same at all angles. As the slat angle decreases, there is a suppression of convection. This is clearly seen in Fig. 5, where the motion decreases as ϕ decreases. The above observations based on flow visualization are confirmed by measurements of heat transfer as will be discussed later.

Fig. 6 shows the variation of the local Nusselt number with position for different aspect ratios. As can be seen, the local value is a strong function of aspect ratio and indicates enhanced convection at aspect ratios in the range of 1 to 2. As aspect ratio decreases from this range, convection is suppressed and the local value becomes more uniform and approaches unity. As aspect ratio increases beyond 2, the end effects occur over a smaller fraction of the area and Nusselt number again decreases.

Fig. 7 shows that changing the angle of inclination of the enclosure has little effect on the local, and hence the average, Nusselt number for an aspect ratio of 1. This result is typical of results at other Rayleigh numbers and slat angles for the aspect ratios of 1, 2, 3, and 4. As shown by Randall, et al., the effect of the angle of inclination on larger aspect ratio enclosures is more pronounced.

Fig. 8 shows the effect of the slat angle on the local Nusselt numbers at one condition. Decreasing slat angle shifts the positions of the

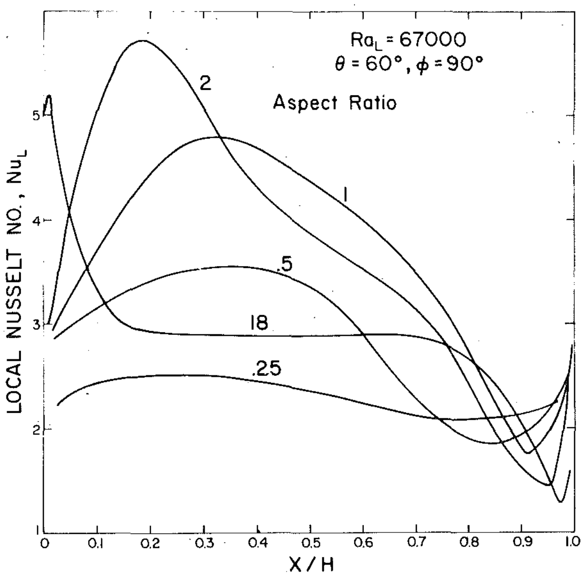

Fig. 6 Local Nusselt numbers along the plate surface for different aspect ratios

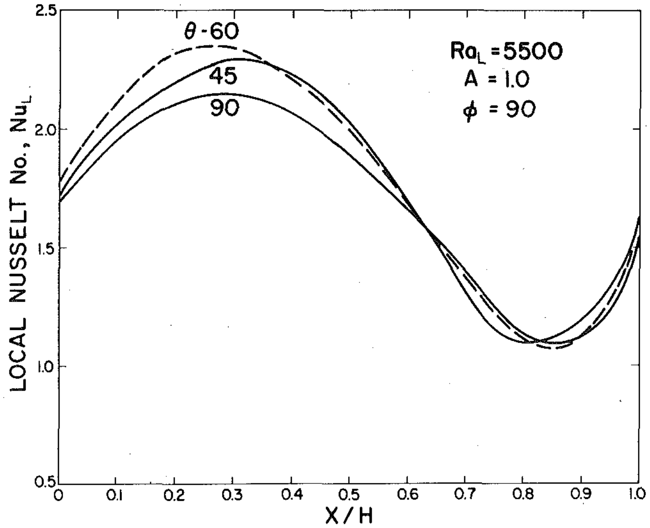

Fig. 7 Local Nusselt numbers along the plate surface for different tilt angles (θ)

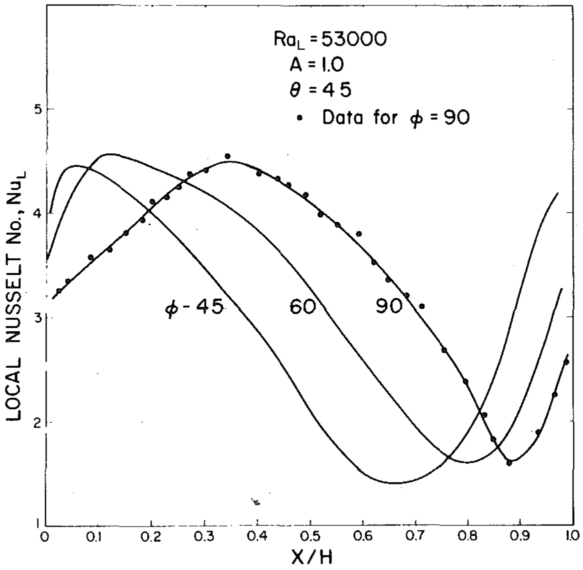

Fig. 8 Local Nusselt number along the plate surface for different slat angles (ϕ)

maximum and minimum coefficients to the left. The overall effect of this is to lower the average heat transfer coefficient.

Average Heat Transfer Results

The average heat transfer coefficients are determined through integration of the local Nusselt numbers over the plate surface. The effect of the aspect ratio on the average heat transfer is governed by the depth of penetration of the end disturbances in the starting and departure corners. For very large aspect ratios these disturbances occupy a relatively small portion of the total and therefore have little effect on the average values. As the aspect ratio is decreased, the end disturbances occupy a larger proportion of the total area and have a larger effect on the average values.

The average Nusselt number is plotted in Fig. 9 as a function of Rayleigh number for different aspect ratios, tilt angles, and slat angles. The effect of aspect ratio is demonstrated in Fig. 9(*a*) for a tilt angle of 60 degrees and a slat angle of 90 deg. As aspect ratio is increased from 0.25, the Nusselt number at a given Rayleigh number increases to a maximum at an aspect ratio of 2, and then decreases as aspect ratio is increased further. For aspect ratios of 0.5–4, the exponent on the Rayleigh number is constant.

The same trends as for a 60 deg tilt are seen in Fig. 9(*b*) for a 90 deg tilt. The effects of slat angle are shown in Fig. 9(*c*) and 9(*d*). Fig. 9(*c*) shows that at a slat angle of 60 deg the effect of aspect ratio is the same as for 90 deg. Fig. 9(*d*) shows that the effect of varying the slat angle at an aspect ratio of one is to change the exponent on the Rayleigh number. Decreasing the slat angle (slats oriented downward) reduces the Nusselt number. The plastic spacer produces a lower value of Nusselt number than the paperboard spacer as will be discussed later.

The average Nusselt number was correlated with Rayleigh number, aspect ratio, and tilt angle for a slat angle of 90 deg and the 0.18 mm thick paperboard wall material. The average value of Nusselt number is given by

$$\overline{\mathrm{Nu}}_L = C_1 C_2 \mathrm{Ra}_L{}^{0.28} \qquad (3)$$

This correlation is restricted to:

$$\mathrm{Ra}_L < 7 \times 10^4; \quad 0.5 \leqslant A \leqslant 36; \quad 4 \leqslant A_H \leqslant 16;$$
$$45 \text{ deg} \leqslant \theta \leqslant 90 \text{ deg}; \quad \phi = 90 \text{ deg}$$

The correlation presented by Randall, et al., [1] for $9 \leqslant A \leqslant 36$ has been modified by slightly changing the constant and exponent to fit the above form. The coefficients C_1 and C_2 include the effects of aspect ratio and tilt angle, respectively, and are given in graphical form in Figs. 10 and 11 and Table 1. The correlating equation and the empirically derived constants fit the present data over the aspect ratio range of 1 to 4 within ±4 percent provided that $\overline{\mathrm{Nu}}_L$ is greater than 1.2. For the aspect ratio of 0.5 the correlation fits the data within ±7 percent, and for the data of Randall, the fit is within ±8 percent. The conduction Nusselt number is unity.

For slat angles other than 90 deg it was found that a correlation of the following form fits the experimental data within ±5 percent provided $\overline{\mathrm{Nu}}_L$ is greater than 1.2.

$$\overline{\mathrm{Nu}}_L = C_3 \mathrm{Ra}_L{}^n \qquad (4)$$

This correlation is restricted to:

$$\mathrm{Ra}_L < 7 \times 10^4; \quad \text{and} \quad 4 \leqslant A_H \leqslant 16$$

The constants C_3 and n are tabulated in Table 2 for the tested combinations of tilt angles, slat angles and aspect ratios. The adequacy of equations (3) and (4) are demonstrated in Fig. 9, where the lines are the correlating equations.

The effect of aspect ratio on the average Nusselt number is shown

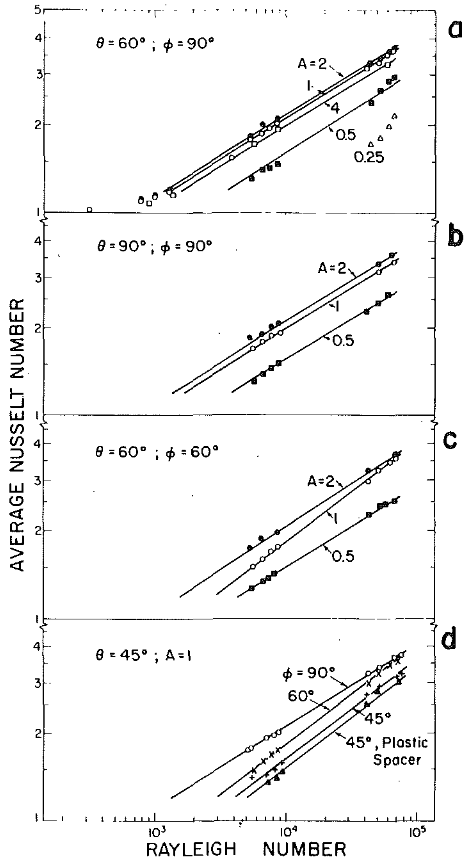

Fig. 9 Average Nusselt number as a function of Rayleigh number. (*a*) Aspect ratio effect at tilt angle of 60 deg. (*b*) Aspect ratio effect at tilt angle of 90 deg. (*c*) Aspect ratio effect at tilt angle of 60 deg and a slat angle of 60 deg. (*d*) Slat angle effect at a tilt angle of 45 deg and an aspect ratio of unity

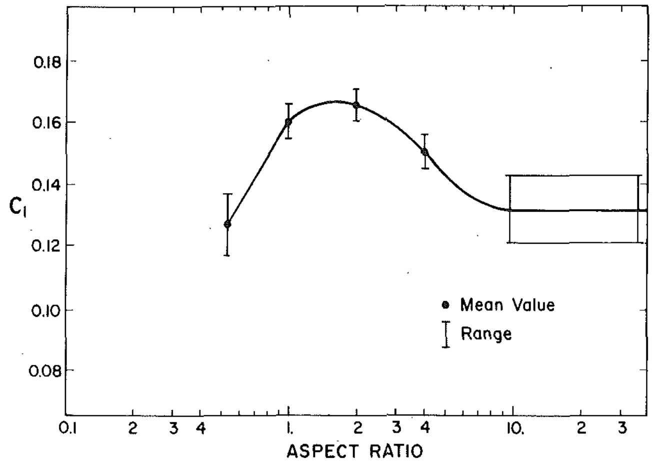

Fig. 10 Aspect ratio coefficient C_1; to be used in equation (3)

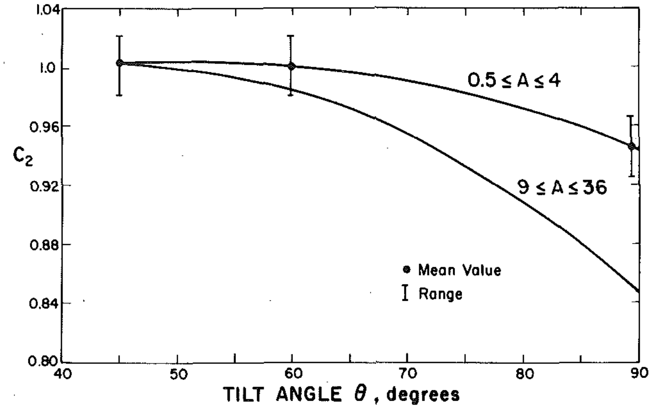

Fig. 11 Tilt angle coefficient C_2; to be used in equation (3)

Table 1 Constants for equation (3)

A	C_1
0.5	0.124
1	0.161
2	0.166
4	0.150

Table 2 Constants for equation (4)

θ, ϕ	A	C_3	n
60, 90	0.5	0.083	0.32
60, 60	0.5	0.113	0.28
60, 60	1	0.077	0.343
60, 60	2	0.137	0.295
45, 45	1	0.070	0.34
45, 45*	1	0.067	0.34

* spacer walls are plastic

Table 3 Parameter values

	C	G ($\times 10^3$)	N
Paperboard spacers	53 ± 15	1.3 ± 0.5	4.5 ± 2
Plastic spacers	15 ± 4	3.8 ± 1	4.5 ± 2
Perspex spacers (Kee, [5])	11	22	4.5

in Fig. 10 as a plot of the coefficient C_1 as a function of aspect ratio. There is a maximum value of the average Nusselt number between aspect ratios of 1 and 2. This maximum can be attributed to the end disturbances which encompass the entire cell at these ratios. As the aspect ratio is decreased below 1, the viscous effects on the cell wall begin to dominate and hence retard the fluid motion which reduces the convective heat transfer. At large aspect ratios, the flow becomes fully established in the center with a relatively less effect of the heat transfer in the end regions.

Reducing slat angle tends to decrease the average Nusselt number by suppressing convective currents. The magnitude of this effect can be significant. For example, at $A = 1$ and $\text{Ra}_L = 7 \times 10^3$ the average Nusselt numbers for $\phi = 60$ and 45 are lower by about 15 and 25 percent, respectively, than those at $\phi = 90$ deg.

The data from Kee [5] at an aspect ratio of 2 and an angle of 60 deg are consistently seven percent lower than those for the paperboard spacers. This is probably due to the difference in properties of the spacers. Hollands [6] and Cane, et al. [9] have shown that the thermal boundary conditions of the walls are determined by the parameters

$$C = \left(\frac{k}{k_w}\right)\left(\frac{L}{t/2}\right)$$

and

$$G = \left(\frac{k}{k_w}\right)\left(\frac{t/2}{L}\right) \tag{6}$$

and

$$N = \frac{4\sigma T_m{}^3 L}{k}$$

C is associated with the heat conducted along the spacers from the hot to cold plate, while G (denoted H in [9]) is associated with the heat conducted across the spacers and is related to the coupling of heat transfer between adjacent cells. N is a radiation group associated with radiation effects.

The values of C, G and N for this study are given in Table 3 in comparison to those for the experiments of Kee. The values for the plastic walls are closer to the values of Kee, and are more relevant for comparison. For an aspect ratio of 1, a tilt of 45 deg, and slat angle of 45 deg, the plastic walls reduce the heat transfer by about five percent from that of the paperboard walls (Table 2). Thus, if the effects of C and G are accounted for, the present data are in good agreement with Kee's. Additionally, the temperature distribution along the side walls was found to be closer to linear for the plastic spacers than for the paperboard spacers. This is in agreement with the values reported in Table 3. Finally, it should be noted that for square honeycombs with aspect ratios of 0.2 to 0.5, Cane, et al. [9] found no significant effect of C, H and N. However, the values of C in the present study are 0.05 to 0.25 times the value in that study and the values of G in the present study are 100 times larger. Ranges apparently exist over which these parameters may have some effect [8].

The present data agree within 15 percent of the correlations of Arnold et al. at an aspect ratio of 0.25. The results of Ozoe, et al. [7] are for insulated side walls, while in the present study heat is transferred along and across the spacer. The values for the adiabatic side walls are 5 to 35 percent higher depending on the aspect ratio and Rayleigh number. This effect is confirmed by the numerical work of Koutsoheras. The present results are representative of air filled enclosures with thin side walls.

Summary

An interferometric study was used to determine the local and average values of the Nusselt number in moderate aspect ratio enclosures. Investigation was made over enclosure tilt angles from 45 to 90 deg, aspect ratios from 0.25 to 36 and slat angles from 45 to 135 deg. The results show that aspect ratios between about 1 and 2 result in the highest heat transfer coefficients. Compared to large aspect ratio enclosures (greater than about 10), convection heat transfer is reduced only for slats placed so that the aspect ratio is less than 0.5. Geometries with slat angles oriented downward (less than 90 deg) are effective in reducing convective heat transfer.

Acknowledgments

The work reported in this paper was supported by the Department of Energy under contract E(11-1)-2941.

References

1 Randall, K. R., Mitchell, J. W. and El-Wakil, M. M., "Natural Convection Characteristics of Flat Plate Enclosures", ASME JOURNAL OF HEAT TRANSFER, Vol. 101, 1979, pp. 120–125.

2 Hollands, K. G. T., "Studies of Methods of Reducing Heat Losses from Flat-Plate Solar Collectors," ERDA Annual Progress Report, COO-2597-3, University of Waterloo, Waterloo, Ontario, Canada, 1977.

3 Arnold, J. N., Edwards, D. K. and Wu, P. S., "Effect of Cell Size on Natural Convection in High L/D Tilted Rectangular Cells Heated and Cooled on Opposite Faces," ASME Paper No. 78-WA/HT-5.

4 Arnold, J. N., Edwards, D. K. and Catton, I., "Effect of Tilt and Horizontal Aspect Ratio on Natural Convection in Rectangular Honeycomb Solar Collectors", ASME JOURNAL OF HEAT TRANSFER, Vol. 99, 1977, pp. 120–122.

5 Kee, Kay Hong, "An Experimental Study of Natural Convection in Rectangular Channels," MS Thesis, The University of Melbourne, March 1977.

6 Hollands, K. G. T., "Natural Convection in Horizontal Thin-Walled Honeycomb Panels," ASME JOURNAL OF HEAT TRANSFER, Vol. 95, 1973, pp. 439–444.

7 Ozoe, H., Yamamoto, K., Sayama, H. and Churchill, S. W., "Natural Circulation in an Inclined Rectangular Channel Heated on One Side and Cooled on the Other Side," *Int. Journal Heat of Mass Transfer,* Vol. 17, 1974, p. 1209.

8. Koutsoheras, W., "Natural Convection Phenomena in Inclined Cells with Finite Side Walls—a Numerical Solution," M. Eng. Sc. Thesis, The University of Melbourne, March 1976.

9. Cane, R. L., Hollands, K. G. T., Raithby, G. D. and Unny, T E., "Free Convection Heat Transfer Across Inclined Honeycomb Panels," ASME JOURNAL OF HEAT TRANSFER, Vol. 99, 1977, pp. 86–91.

C. T. Hsu
TRW/DSSG, One Space Park,
Redondo Beach, CA 90278

Ping Cheng
Department of Mechanical Engineering,
University of Hawaii, Honolulu, Hawaii 96822

Vortex Instability in Buoyancy-Induced Flow over Inclined Heated Surfaces in Porous Media

A linear stability analysis is performed for the study of the onset of vortex instability in free convective flow over an inclined heated surface in a porous medium. The undisturbed state is assumed to be the steady two-dimensional buoyancy-induced boundary layer flow which is characterized by a non-linear temperature profile. By a scaling argument, it is shown that the length scales of disturbances are smaller than those for the undisturbed boundary layer flow, thus, confirming the so-called "bottling effects" whereby the disturbances are confined within the boundary layer. By neglecting the lowest order terms in the three-dimensional disturbances equations, the simplified equations are solved based on the local similarity approximations, wherein the disturbances are assumed to have a weak dependence in the streamwise direction. The resulting eigenvalue problem is solved numerically. The critical parameter and the critical wave number of disturbances at the onset of vortex instability are computed for different prescribed wall temperature distribution of the inclined surface. It is found that the larger the inclination angle with respect to the vertical, the more susceptible is the flow for the vortex mode of disturbances; and in the limit of zero inclination angle (i.e., a vertical heated plate) the flow is stable for this form of disturbances.

Introduction

Much attention has been given to the vortex mode of instability in free convective flow over inclined heated surfaces in a viscous fluid during the last decade. The first experimental evidence of the longitudinal (or streamwise oriented) vortex exists in the buoyancy-induced flow over inclined heated surfaces was given by Sparrow and Husar [1]. Subsequent experimental investigations by Lloyd and Sparrow [2] clearly established that for inclined angles in excess of 17 deg relative to the vertical, the instability is characterized by longitudinal vortices. The occurrence of this form of instability is owing to the destabilizing effects of the component of buoyancy force normal to the inclined surface. These experimental observations have prompted a number of theoretical studies on the onset of longitudinal vortices in free convective flow about inclined surfaces. In particular, linear stability analyses on the vortex instability were performed by Haaland and Sparrow [3] and independently by Hwang and Cheng [4] who used an approach similar to that of Smith [5] for the analogous problem of Taylor-Goertler vortices along concave curved walls. In these analyses, a quasi-parallel flow model is assumed wherein the streamwise dependence of the basic flow is not neglected although the disturbances are assumed to be independent of the streamwise direction. It is further assumed that the disturbances at the onset of vortex instability are confined within the boundary layer of the basic flow. It is found in these analyses that the nature of the neutral stability curve changes drastically when the non-parallelism of the basic flow is taken into consideration. A similar analysis based on the quasi-parallel flow model for the investigation of vortex instability in free convection flow over inclined heated plates was given by Kahawita and Meroney [6]. In another paper both the wave and vortex modes of instability are considered by Iyer and Kelly [7] based on the parallel flow approximation where the x-derivatives of the basic flow and disturbances are neglected. In all of these works, neutral stability condition is obtained by setting both the temporal and spatial growth rates to zero.

Considerable attention has also been given to the related problem of wave instability in non-parallel boundary layer flow in the last decade. In the papers by Gaster [8], Eagles and Weissman [9], Saric and Nayfeh [10], and by Jaluria and Gebhart [11], the wave disturbances were assumed of the form

$$\Psi(x, y, t) = \hat{\Psi}(x, y) \exp \{i \int \alpha(x)\, dx - i\omega t\}, \tag{1}$$

where $\alpha(x) = \alpha_R(x) + i\alpha_i(x)$ (with α_R denoting wave number and $\alpha_i(x)$ the spatial growth rate) while ω is real and non-zero. ω is real implying the temporal growth rate is zero, and the non-zero value is required to assure the traveling wave characteristics. The effects of non-parallelism of boundary layer flows are taken into consideration by the x-dependence of $\hat{\Psi}(x, y)$ and $\alpha(x)$, both are weak functions of x. Gaster [8] as well as Eagles and Weissman [9] assumed that the onset of wave instability in the nonparallel boundary layer flow is marked when the amplitude of the disturbances does not change with x. Hence, a non-zero α_i is required to offset the increasing value of $\hat{\Psi}(x, y)$ at downstream (due to the developing boundary layer) in order to satisfy this neutral stability condition. This criterion, when applied to the amplitude of velocity or kinetic energy, would lead to different values of critical Reynolds number and different stability curves. To the lowest order, Gaster [8] shows that the more sophisticated neutral stability condition (for which the amplitude of disturbances no longer change with x) is equivalent to setting $\alpha_i = 0$, i.e., zero spatial growth rate. On the other hand, Jaluria and Gebhart [11] as well as Saric and Nayfeh [10] simply used $\alpha_i = 0$ as the condition for neutral stability. It appears therefore that $\alpha_i = 0$ is the neutral stability condition for wave instability in nonparallel boundary layer flows if only the lowest order approximation is carried out.

In this paper the problem of vortex instability in free convective flow in a porous medium adjacent to inclined heated surfaces is investigated. The approach adopted here is similar to a recent paper by Hsu, et al. [12] who performed a linear stability analysis for the problem of vortex instability in free convective flow in a porous medium adjacent to a heated horizontal surface. By a scaling argument, it is shown in this paper that the length scales of disturbances are smaller than those for the undisturbed boundary layer flow, thus, confirming the so-called bottling effects whereby the disturbances are confined within the boundary layer as proposed by Haaland and Sparrow [3]. The three-dimensional disturbance equations are considerably simplified by neglecting the lowest order terms. The amplitude of disturbances are assumed to be a weak function of the streamwise direction and the neutral stability condition is obtained by setting both the temporal and spatial growth rates to zero. The

---

Contributed by the Heat Transfer Division for publication in the JOURNAL OF HEAT TRANSFER. Manuscript received by The Heat Transfer Division August 18, 1978.

resulting equations for the amplitude of the disturbances are solved based on the local similarity approximation. This leads to an eigenvalue problem containing a single parameter in terms of the product of the inclination angle and the Rayleigh number. For this reason, separate computations for the critical parameter at different inclination angles is not necessary. The resulting linear eigenvalue problem was solved numerically on the basis of the fourth-order Runge-Kutta method incorporated with Kaplan filtering technique to maintain the linear independence of the eigen functions. As in the case of free convection over heated inclined surfaces in a viscous fluid, it is found that the larger the inclination angle with respect to the vertical, the more susceptible the flow is for the vortex type of disturbances; and in the limit of zero inclination angle, i.e., a vertical heated plate, the flow is stable for vortex mode of disturbances.

Linear Stability Analysis

Consider an inclined impermeable surface embedded in a porous medium as shown in Fig. 1, where the x- and z-coordinates are placed on the inclined surface (with an inclination angle α_0 with respect to the vertical) and the y-coordinate is perpendicular to the surface and pointing toward the porous medium. If the wall temperature is greater than the ambient temperature of the porous medium, a buoyancy-induced flow will be generated adjacent to the heated surface. The question whether the buoyancy-induced flow is stable or unstable to the vortex mode of disturbances will be the subject of investigation in this paper.

To perform a linear stability analysis, the variables in the flow and temperature fields will now be decomposed into basic undisturbed and infinitesimal disturbed quantities as

$$\begin{aligned} T(x, y, z, t) &= T_0(x, y) + T_1(x, y, z, t), \\ p(x, y, z, t) &= p_0(x, y) + p_1(x, y, z, t); \\ u(x, y, z, t) &= u_0(x, y) + u_1(x, y, z, t), \\ v(x, y, z, t) &= v_0(x, y) + v_1(x, y, z, t), \\ w(x, y, z, t) &= \qquad\qquad w_1(x, y, z, t), \end{aligned} \tag{2}$$

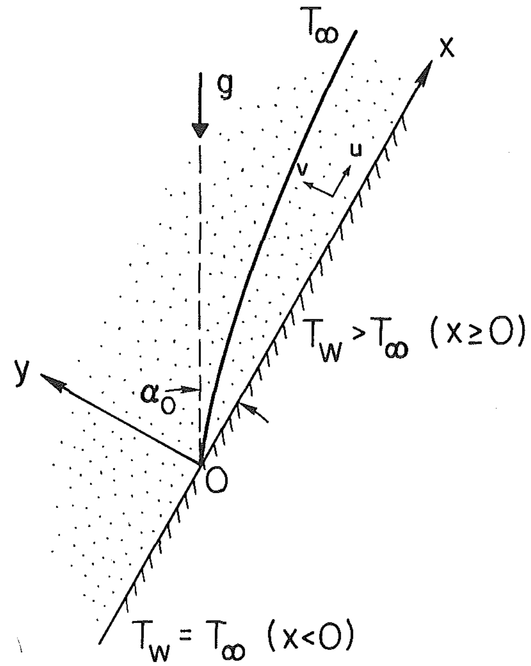

Fig. 1 Coordinate system for free convective flow in a porous medium adjacent to an inclined heated surface

where the three-dimensional disturbances are denoted by the subscript "1" and the two-dimensional basic undisturbed quantities are denoted by the subscript "0". The problem of the basic undisturbed buoyancy-induced flow in a porous medium adjacent to a vertical heated flat plate, with a power law variation of wall temperature i.e., $T_w = T_\infty + Ax^m$ (where A and m are constants), has been considered by Cheng and Minkowycz [13] based on boundary layer simplifications. The similarity solution obtained by Cheng and Minkowycz [13] is also applicable to the case of inclined surfaces if the gravitational acceleration g is replaced by $g \cos\alpha_0$, the streamwise component of gravity. It follows that the solution of undisturbed basic flow for the present problem is

$$\begin{aligned} T_0(x, y) &= T_\infty + Ax^m\, \theta_0(\eta), \\ \psi_0(x, y) &= \alpha\sqrt{\mathrm{Ra}_x} f_0(\eta), \\ \eta &= \sqrt{\mathrm{Ra}_x}\, y/x, \end{aligned} \tag{3a,b,c}$$

where $\mathrm{Ra}_x = K\beta(T_w - T_\infty)x\rho_\infty g \cos\alpha_0/\mu\alpha$ is the Rayleigh number

Nomenclature

a = dimensional spanwise wave number
A = constant in wall temperature relation
C = superposition constant
D = differentiation of the disturbed quantities with respect to η
f = dimensionless base state stream function
F = dimensionless disturbance stream function
G = dimensionless disturbance velocity in the x-direction
i = complex number
k = dimensionless wave number
K = Darcy permeability
m = exponent on wall temperature relation
p = pressure
P = dimensionless pressure
Ra_x = local Rayleigh number
Ra_l = Rayleigh number based on a characteristic length l
t = time
T = temperature
u = Darcy's velocity in x-direction
U = dimensionless Darcy's velocity in x-direction
v = Darcy's velocity in y-direction
V = dimensionless Darcy's velocity in y-direction
w = Darcy's velocity in z-direction
W = dimensionless Darcy's velocity in z-direction
x = dimensional coordinate in downstream direction
X = dimensionless coordinate in downstream direction
y = dimensional coordinate normal to bounding surface
Y = dimensionless coordinate normal to bounding surface
z = dimensional coordinate tangent to bounding surface
Z = dimensionless coordinates tangent to bounding surface
α = effective thermal diffusivity
$\alpha(x)$ = parameter defined by equation (1)
α_0 = inclination angle
β = coefficient of thermal expansion
Δ = quantity defined by equation (50)
λ = volumetric heat capacity of the fluid to that of the saturated porous medium
γ = quantity defined by equation (35)
μ = fluid viscosity
η = similarity variable
θ = dimensionless base state temperature
Θ = dimensionless disturbance temperature
Ψ = amplitude of disturbances defined in equation (1)
ψ = stream function
σ = temporal growth constant defined in equation (35)
ρ = fluid density
τ = dimensionless time
ω = frequency defined in equation (1)

Superscript

$\hat{}$ = amplitude function for disturbance
$*$ = critical values
$\tilde{}$ = dimensionless quantities

Subscripts

0 = basic undisturbed quantities
1 = disturbed quantities
∞ = condition away from the bounding surface
w = condition at the wall

based on the streamwise component of gravity; $\theta_0(\eta)$ and $f_0(\eta)$ are the dimensionless temperature and stream functions which are determined from

$$f_0'' - \theta_0' = 0, \tag{4}$$

$$\theta_0'' + \frac{m+1}{2} f_0 \theta_0' - m f_0' \theta_0 = 0, \tag{5}$$

subject to the boundary conditions

$$f_0(0) = 0, \quad \theta_0(0) = 1, \tag{6}$$

$$f_0'(\infty) = 0, \quad \theta_0(\infty) = 0, \tag{7}$$

where the primes on basic undisturbed quantities indicate derivatives with respect to η. The similarity solution given by equations (3–7) is obtained based on the following assumptions: (1) the Rayleigh number is large (so that boundary layer approximation can be applied), (2) the inclination angle α_0 is small (such that $\cos \alpha_0\, \partial T_0/\partial y \gg \sin \alpha_0\, \partial T_0/\partial x$) so that the normal component of the gravitational force can be neglected, (3) the Darcy law is applicable, and (4) the Boussinesq approximations can be invoked.

Substituting equations (2) into the governing equations for transient three-dimensional convective flow in a porous medium, subtracting the boundary layer equations for the basic undisturbed flow, and linearizing yields

$$\frac{\partial u_1}{\partial x} + \frac{\partial v_1}{\partial y} + \frac{\partial w_1}{\partial z} = 0, \tag{8}$$

$$\frac{\partial p_1}{\partial x} = -\frac{\mu u_1}{K} + \rho_\infty \beta g \cos \alpha_0 T_1, \tag{9}$$

$$\frac{\partial p_1}{\partial y} = -\frac{\mu v_1}{K} + \rho_\infty \beta g \sin \alpha_0 T_1, \tag{10}$$

$$\frac{\partial p_1}{\partial z} = -\frac{\mu w_1}{K}, \tag{11}$$

$$\alpha\left(\frac{\partial^2 T_1}{\partial x^2} + \frac{\partial^2 T_1}{\partial y^2} + \frac{\partial^2 T_1}{\partial z^2}\right) = \lambda \frac{\partial T_1}{\partial t} + u_0 \frac{\partial T_1}{\partial x} + v_0 \frac{\partial T_1}{\partial y} + u_1 \frac{\partial T_0}{\partial x} + v_1 \frac{\partial T_0}{\partial y}, \tag{12}$$

where the velocity components for the basic undisturbed flow are given by

$$u_0 = \frac{\alpha}{x} \mathrm{Ra}_x f_0'(\eta),$$

and (13)

$$v_0 = -\frac{\alpha}{2x} (\mathrm{Ra}_x)^{1/2} [(m+1) f_0 + (m-1)\eta f_0'],$$

which follows from equation (3*b*).

Next, we shall show that disturbances are confined within the boundary layer of the undisturbed flow—the so-called bottling effect proposed by Haaland and Sparrow [3]. For this purpose, we note that the disturbances may have length scales which are different from that of the basic flow. To explore this possibility, the disturbance equations will first be recasted into the length scales of the basic flow, i.e.,

$$X = x/l \quad \text{and} \quad Y = y/\epsilon l, \tag{14a,b}$$

where $\epsilon = (\mathrm{Ra}_l)^{-1/2}$ with Ra_l denoting the Rayleigh number based on the characteristic length l. Other basic flow quantities will be scaled as

$$U_0 = \frac{\epsilon^2 l u_0}{\alpha}, \quad V_0 = \frac{\epsilon l v_0}{\alpha} \quad \text{and} \quad \Theta_0 = \frac{T_0}{\Delta T_r}, \tag{15}$$

where ΔT_r is some characteristic temperature difference, so that U_0, V_0, and Θ_0 as well as their derivatives with respect to X and Y are 0(1) (see Cheng and Minkowycz, [13]). For vortex-roll disturbances, z and y are of the same scale, thus, according to equation (14*b*)

$$Z = z/\epsilon l. \tag{16}$$

The disturbance velocities v_1 and w_1 induced by T_1 have behavior similar to u_0 induced by T_0. The behavior of vortex rolls also suggests that the order of u_1 should not be greater than the orders of v_1 and w_1. Hence, if

$$\Theta_1 = \frac{T_1}{\Delta T_r}, \tag{17a}$$

we have

$$U_1 = \frac{\epsilon^2 l u_1}{\alpha}, \quad V_1 = \frac{\epsilon^2 l v_1}{\alpha}, \quad W_1 = \frac{\epsilon^2 l w_1}{\alpha}, \quad \text{and} \quad P_1 = \frac{\epsilon K p_1}{\mu \alpha}. \tag{17b}$$

The disturbance equations in terms of the new variables are

$$\epsilon \frac{\partial U_1}{\partial X} + \frac{\partial V_1}{\partial Y} + \frac{\partial W_1}{\partial Z} = 0, \tag{18}$$

$$\epsilon \frac{\partial P_1}{\partial X} = -U_1 + \Theta_1, \tag{19}$$

$$\frac{\partial P_1}{\partial Y} = -V_1 + \Theta_1 \tan \alpha_0, \tag{20}$$

$$\frac{\partial P_1}{\partial Z} = -W_1, \tag{21}$$

and

$$\epsilon^2 \frac{\partial^2 \Theta_1}{\partial X^2} + \left(\frac{\partial^2 \Theta_1}{\partial Y^2} + \frac{\partial^2 \Theta_1}{\partial Z^2}\right) = \frac{\partial \Theta_1}{\partial \tau} + U_0 \frac{\partial \Theta_1}{\partial X} + V_0 \frac{\partial \Theta_1}{\partial Y} + U_1 \frac{\partial \Theta_0}{\partial X} + \frac{V_1}{\epsilon} \frac{\partial \Theta_0}{\partial Y}, \tag{22}$$

where $\tau = \alpha t/\lambda l^2 \epsilon^2$. The first terms in equations (18, 19) and (22) are the smallest terms in their respective equations. Note that the last term $V_1/\epsilon/\partial\Theta_0/\partial Y$ in equation (22) is larger than other terms at least by $0(1/\epsilon)$. This means that (X, Y, Z) defined in equations (14) and (16) may not be the right length scale for the disturbances. From equation (22), Y and Z have to be rescaled to

$$\tilde{Y} = \epsilon^{-1/2} Y, \qquad \tilde{Z} = \epsilon^{-1/2} Z. \tag{23}$$

We also need to rescale X into

$$\tilde{X} = \epsilon^{-1/2} X, \tag{24}$$

to maintain the similarity characteristics between (y, z) and x. From equation (21) a proper scale for P_1 is

$$\tilde{P}_1 = \epsilon^{-1/2} P_1, \tag{25}$$

In terms of $(\tilde{X}, \tilde{Y}, \tilde{Z})$ and $\tilde{P}_1$, equations (18–22) become

$$\epsilon \frac{\partial U_1}{\partial \tilde{X}} + \frac{\partial V_1}{\partial \tilde{Y}} + \frac{\partial W_1}{\partial \tilde{Z}} = 0, \tag{26}$$

$$\epsilon \frac{\partial \tilde{P}_1}{\partial \tilde{X}} = -U_1 + \Theta_1, \tag{27}$$

$$\frac{\partial \tilde{P}_1}{\partial \tilde{Y}} = -V_1 + \Theta_1 \tan \alpha_0, \tag{28}$$

$$\frac{\partial \tilde{P}_1}{\partial \tilde{Z}} = -W_1, \tag{29}$$

and

$$\epsilon^2 \frac{\partial^2 \Theta_1}{\partial \tilde{X}^2} + \left(\frac{\partial^2 \Theta_1}{\partial \tilde{Y}^2} + \frac{\partial^2 \Theta_1}{\partial \tilde{Z}^2}\right) = \frac{\partial \Theta_1}{\partial \tilde{\tau}} + U_0 \epsilon^{1/2} \frac{\partial \Theta_1}{\partial \tilde{X}} + V_0 \epsilon^{1/2} \frac{\partial \Theta_1}{\partial \tilde{Y}} + \epsilon U_1 \frac{\partial \Theta_0}{\partial X} + V_1 \frac{\partial \Theta_0}{\partial Y}, \tag{30}$$

where $\tilde{\tau} = \tau/\epsilon$. Note that in equation (30) no rescaling for $\partial\Theta_0/\partial X$ and $\partial\Theta_0/\partial Y$ is required because these are the derivatives of the basic flow quantities which are already of 0(1).

We observe that (1) the rescaling of (X, Y, Z) into $(\tilde{X}, \tilde{Y}, \tilde{Z})$ suggests that the disturbances are confined in a length scale which is of $0(\epsilon^{1/2})$

smaller than the length scale of the basic flow for $\epsilon \ll 1$; this confirms the bottling effect of Haaland and Sparrow [3]. (2) When terms of $0(\epsilon^{1/2})$ and smaller are neglected in equations (26–30), the resulting equations do not contain any x-derivatives, which is the parallel-flow approximation. (3) The terms $\epsilon\, \partial U_1/\partial \tilde{X}$, $\epsilon\, \partial \tilde{P}_1/\partial \tilde{X}$, $\epsilon^2\, \partial^2\Theta_1/\partial \tilde{X}^2$ in equations (26, 27), and (30) are smaller than the rest of the terms in their respective equations. The omission of the lowest order terms in the disturbances equations are consistent with the level of approximation of the basic flow.

We now return our attention to the dimensional equations (8–12) with the first terms in equations (8, 9), and (12) neglected. If the first term in equation (8) is neglected, there exists a stream function ψ_1 for the secondary flow such that

$$v_1 = -\frac{\partial \psi_1}{\partial z} \quad \text{and} \quad w_1 = \frac{\partial \psi_1}{\partial y}. \tag{31}$$

To cast the disturbance equations (9–12) in the same level of approximation with the basic flow, we have

$$\frac{\mu u_1}{K} - \rho_\infty \beta g \cos \alpha_0\, T_1 = 0, \tag{32}$$

$$\frac{\mu}{K}\left(\frac{\partial^2 \psi_1}{\partial y^2} + \frac{\partial^2 \psi_1}{\partial z^2}\right) = -\rho_\infty \beta g \sin \alpha_0 \frac{\partial T_1}{\partial z}, \tag{33}$$

$$\alpha\left(\frac{\partial^2 T_1}{\partial y^2} + \frac{\partial^2 T_1}{\partial z^2}\right) = \lambda \frac{\partial T_1}{\partial t} + u_0 \frac{\partial T_1}{\partial x} + v_0 \frac{\partial T_1}{\partial y} + u_1 \frac{\partial T_0}{\partial x} - \frac{\partial \psi_1}{\partial z}\frac{\partial T_0}{\partial y}. \tag{34}$$

It is noted that all of the x-derivatives of disturbances, except the term $u_0\, \partial T_1/\partial x$, are neglected in equations (32–34).

For vortex instability, the three-dimensional disturbances are of the form

$$\begin{aligned} \psi_1(x, y, z, t) &= \hat{\psi}(x, y) \exp\,[iaz + \sigma t + \gamma(x)],\\ u_1(x, y, z, t) &= \hat{u}(x, y) \exp\,[iaz + \sigma t + \gamma(x)],\\ T_1(x, y, z, t) &= \hat{T}(x, y) \exp\,[iaz + \sigma t + \gamma(x)], \end{aligned} \tag{35}$$

where a is the spanwise periodic wave number, σ is the temporal growth factor while $\gamma(x) = \int \alpha_i(x)\, dx$ with $\alpha_i(x)$ denoting the spatial growth factor which is a weak function of x. It is worth noting that a, σ, and γ are all real for vortex disturbances. For the lowest order approximation, α_i can be considered as a constant [8] so that $\gamma(x) = \alpha_i x$. Note also that the amplitudes of the disturbance in equation (35) are functions of both x and y. Substituting equations (35) into equations (32–34) and setting both $\sigma = 0$ and $\alpha_i = 0$ for neutral stability yields

$$\hat{u} = \frac{K\rho_\infty g \cos \alpha_0}{\mu} \hat{T}, \tag{36}$$

$$\left[\frac{\partial^2 \hat{\psi}}{\partial y^2} - a^2 \hat{\psi}\right] = -\frac{iaK\rho_\infty \beta g \sin \alpha_0}{\mu} \hat{T}, \tag{37}$$

$$\alpha\left[\frac{\partial^2 \hat{T}}{\partial y^2} - a^2 \hat{T}\right] = u_0 \frac{\partial \hat{T}}{\partial x} + v_0 \frac{\partial \hat{T}}{\partial y} + \hat{u}\frac{\partial T_0}{\partial x} - ia\hat{\psi}\frac{\partial T_0}{\partial y}. \tag{38}$$

We now solve equations (36–38) by the local similarity method [14–16]. To this end, we let

$$\begin{aligned} \hat{\psi} &= i\alpha\sqrt{\mathrm{Ra}_x}\, F(\eta, X),\\ \hat{u} &= \frac{\alpha \mathrm{Ra}_x}{x} G(\eta, X),\\ \hat{T} &= Ax^m \Theta(\eta, X), \end{aligned} \tag{39}$$

where η is given by equation (3c). Substituting equations (39) into equations (36–38), we have

$$G = \Theta, \tag{40}$$

$$\left(\frac{\partial^2}{\partial \eta^2} - k^2\right) F = -k\Theta \tan \alpha_0, \tag{41}$$

$$\left(\frac{\partial^2}{\partial \eta^2} - k^2\right)\Theta - f_0' m\Theta + \frac{(m+1)f_0}{2}\frac{\partial \Theta}{\partial \eta} - \left(m\theta_0 + \frac{m-1}{2}\eta\, \theta_0'\right) G - k\sqrt{\mathrm{Ra}_x}\, \theta_0' F = f_0' X \frac{\partial \Theta}{\partial X}, \tag{42}$$

subject to boundary conditions

$$\Theta(0, X) = F(0, X) = 0, \tag{43}$$

$$\Theta(\infty, X) = F(\infty, X) = 0, \tag{44}$$

where $k \equiv ax/\sqrt{\mathrm{Ra}_x}$ is the dimensionless wave number. If the weak x-dependence is assumed such that $\partial/\partial X \ll \partial/\partial \eta$, the right hand side of equation (42) can be neglected. As a result, equations (40–44) contain X as a parameter. Similar approximations have been used in many problems in boundary layer flow, and the results are known as "local similarity" solutions [14–16]. The substitution of G and θ from equations (40) and (41) into equation (42) with the local similarity approximation yields

$$(D^2 - k^2)^2 F = mf_0'(D^2 - k^2)F - \frac{m+1}{2} f_0 D(D^2 - k^2)F + \left[m\theta_0 + \frac{m-1}{2}\eta\theta_0'\right](D^2 - k^2)F - \mathrm{Ra}_x{}^{1/2} \tan \alpha_0\, \theta_0'\, k^2 F, \tag{45}$$

where $D = d/d\eta$ is the differentiation of the disturbed quantities with respect to η and F can be considered as a function of η with X as a parameter.

The boundary conditions for equation (45) are

$$F(0) = D^2F(0) = 0, \tag{46}$$

$$F(\infty) = D^2F(\infty) = 0. \tag{47}$$

Equations (45–47) form an eigenvalue problem that will be solved numerically. It is important to note that Ra_x—the eigenvalue for equation (42), and $\tan \alpha_0$—the eigenvalue for equation (41), combine together into $\mathrm{Ra}_x \tan^2 \alpha_0$ in equation (45) as the eigenvalue of the problem. This has greatly simplified the numerical computations. This combination implies that different inclined angles α_0 and different distances x which result in the same eigenvalue $\mathrm{Ra}_x \tan^2 \alpha_0$ will trigger the vortex instability for buoyancy-induced flow in a porous medium adjacent to inclined heated surfaces.

Numerical Procedure

The eigensolutions to equations (45–47) were obtained numerically by means of the fourth-order Runge-Kutta integration procedure. The eigensolutions contain two modes: one is the nondiffusive mode which is regular and the other is the diffusive mode which increases very rapidly near the heated plate within a length scale of $0(\mathrm{Ra}_x \tan^2 \alpha_0)^{1/4}$. The diffusive mode is singular when the eigenvalue is large. These two modes resemble the inviscid and the viscous modes encountered in the hydrodynamic stability where the eigensolutions to the Orr-Summerfeld equation have to be found [17]. Special treatment for this type of problem is required to ensure the linear independence of the two modes obtained by numerical integration. In this paper, we have used the Kaplan filtering technique [18] in the routine of the integration.

The eigenvalue problem is best solved numerically by integrating equation (45) inward from $\eta \to \infty$ (the edge of the boundary layer of the basic flow) to $\eta = 0$ (at the wall). To start the numerical integration, the asymptotic behavior of $F(\eta)$ and its derivatives at $\eta \to \infty$ are needed. Because $\theta_0 \to 0$, $f_0 \to f_\infty$ (= const.), $\theta_0' \to 0$ and $f_0' \to 0$ at $\eta \to \infty$ from equations (4, 5), and (7), the asymptotic solution to equation (45) for $\eta \to \infty$ satisfying equation (47) is given by

$$F(\eta) = C_1\, e^{-a_1\eta} + C_2\, e^{-a_2\eta}, \tag{48}$$

where $a_1 = k$ and $a_2 = (m+1)f_\infty/4 + [(m+1/4)^2 f_\infty{}^2 + k^2]^{1/2}$. We shall designate $F_1(\eta)$ and $F_2(\eta)$, which satisfy $F_{1,2}(\eta) \to \exp\,[-a_{1,2}\eta]$ as $\eta \to \infty$, as the two linear independent eigen-functions for $F(\eta)$. Then we have for η in $[0, \infty]$

$$F(\eta) = C_1F_1(\eta) + C_2F_2(\eta), \tag{49}$$

where C_2 can be chosen arbitrary equal to one. Here, we identify $F_1(\eta)$ as the regular mode and $F_2(\eta)$ the singular mode. It is clear from equation (48) that $F(\eta)$ given by equation (49) satisfied the boundary condition at $\eta \to \infty$. The inner boundary condition equation (46) requires that

$$\Delta \equiv F_1(0)\, D^2F_2(0) - F_2(0)\, D^2F_1(0) = 0. \tag{50}$$

Condition (50) is in general not compatible unless $\mathrm{Ra}_x \tan^2 \alpha_0$ is the eigenvalue of the problem. The numerical procedure to determine the eigenvalue was performed as follows. For fixed values of m and k, the initial guess for $\mathrm{Ra}_x \tan^2 \alpha_0$ was made and the numerical solutions to $F_i(\eta)$, $i = 1, 2$, were found by integrating equation (45) from η_∞ to 0 with $e^{-a_1\eta}$ and its derivatives as the starting conditions for F_i, DF_i, D^2F_i and D^3F_i. Two paths of integration were required. The first path was performed to obtain $F_2(\eta)$ and the second path to obtain $F_1(\eta)$. The Kaplan filtering was applied during the second path of integration. The values $F_1(0)$, $F_2(0)$, $D^2F_1(0)$ and $D^2F_2(0)$ were obtained at the end of the two-path integration and hence the value of Δ was determined and tested against equation (50). This procedure was repeated until the adjustment of the value of $\mathrm{Ra}_x \tan^2 \alpha_0$ through the Newton-Ralphson method has resulted in $\Delta = 0$ to within the accuracy required.

Results and Discussion

Fig. 2 shows the neutral stability curves for the present problem where the eigenvalues $\mathrm{Ra}_x \tan^2 \alpha_0$ as a function of dimensionless wave number k are plotted. At a given value of m, the minimum value of $\mathrm{Ra}_x \tan^2 \alpha_0$ as shown in Fig. 2 is the critical parameter for the onset of vortex instability in free convective flow about inclined surfaces in a porous medium. The values of the critical parameter ($\mathrm{Ra}_x{}^* \tan^2 \alpha_0$) and the associated wave number (k^*) at selected values of m are also tabulated in Table 1 for future reference. It will be of interest to examine the special case of a vertical impermeable surface with $\alpha_0 = 0$. The finite value of $\mathrm{Ra}_x{}^* \tan^2 \alpha_0$ implies that the critical Rayleigh number $\mathrm{Ra}_x{}^* = K\rho_\infty g\beta(T_w - T_\infty)x/\mu\alpha$ for vortex instability in free convective flow about a vertical surface in a porous medium is infinite since both $\sin \alpha_0$ and $\tan \alpha_0$ approach zero as $\alpha_0 \to 0$. It follows therefore that vortex mode of instability will not manifest itself in free convective flow about a *vertical* surface in a porous medium. Table 1 also shows that the case of a step function increase in wall temperature ($m = 0$) is more susceptible to vortex instability than the case of constant heat flux ($m = 1/3$) since the critical parameter of the former case (having a value of 120.7) is less than that of the latter case (having a value of 195.1). Fig. 3 shows that the value of the critical parameter and critical wave number increases almost linearly with m. Fig. 4 is a plot showing the effect of inclination angle α_0 on the quantity $\mathrm{Ra}_x{}^* \tan \alpha_0$ from $\alpha_0 = 0$ (for a vertical surface) up to $\alpha_0 \simeq$ 65 deg for which the present analysis is valid. The quantity $\mathrm{Ra}_x{}^* \tan \alpha_0 = K\rho_\infty\beta\Delta T_r x^* g \sin \alpha_0/\mu\alpha$ is chosen for the ordinate since it is the critical Rayleigh number based on the buoyancy force normal to the inclined plate, and reduces to the usual definition of the critical Rayleigh number for the case of a horizontal plate when $\alpha_0 \to \pi/2$. The values of the critical Rayleigh number for vortex instability in free convection flow about a *horizontal* surface ($\alpha_0 = \pi/2$) in a porous medium have been obtained by Hsu, et al. [12] and are plotted as dashed line segments at the right hand margin (i.e., at $\alpha_0 = \pi/2$) of Fig. 4 for comparison. Fig. 5 shows the streamlines (solid lines) and isotherms (dashed lines) for the secondary flow ($m = 0$) at the onset of instability which show that the phase angle between streamlines and isotherms is $\pi/2$. The bottling effects of the disturbances at the onset of secondary flow is also apparent in this figure.

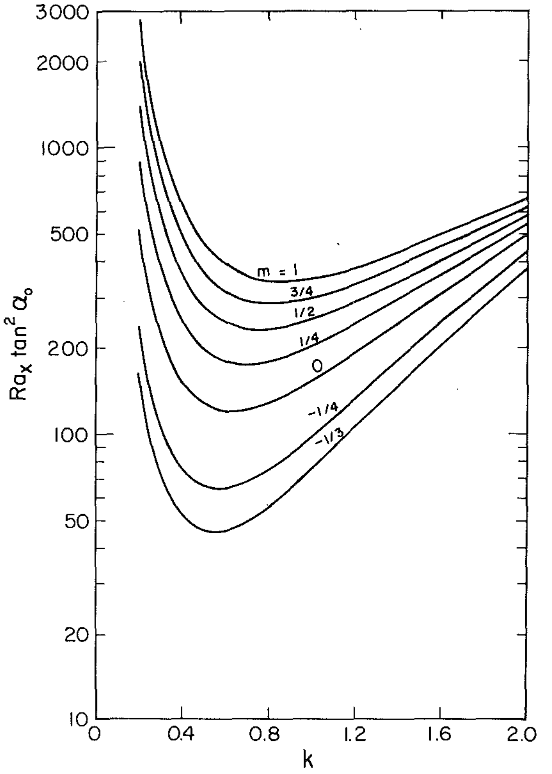

Fig. 2 Eigenvalues as a function of dimensionless spanwise wave number

Concluding Remarks

The conditions marking the onset of vortex instability in free convective flow in a porous medium adjacent to an inclined heated surface is studied in this paper. The analysis is based on the following assumptions: (1) The Darcy's law is applicable which is valid when the Reynolds number based on the pore diameter is less than one. (2) The undisturbed flow is the steady two-dimensional buoyancy-induced boundary layer flow for which similarity solution exists if the normal component of the buoyancy force is neglected. Thus, the

Table 1 Critical eigenvalues and critical wave numbers

m	$\mathrm{Ra}^* \tan^2\alpha_0$	k^*
−1/3	45.6	0.550
−1/4	64.7	0.570
0	120.7	0.636
1/4	176.5	0.698
1/3	195.1	0.717
1/2	232.2	0.758
3/4	287.9	0.814
1	343.7	0.865

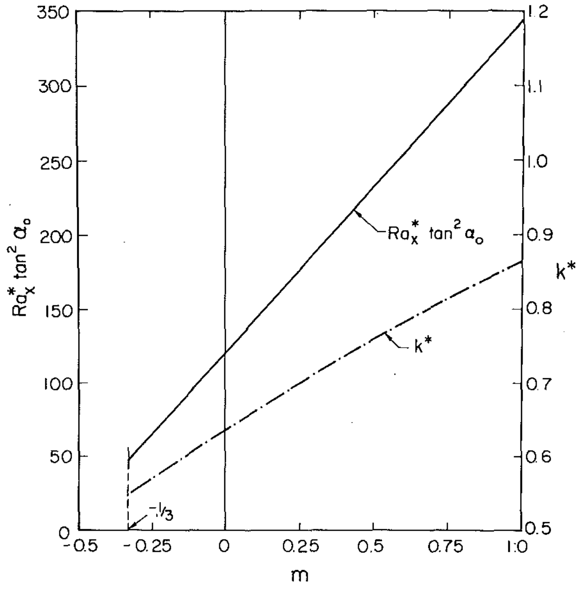

Fig. 3 The critical eigenvalues and the critical wave numbers as a function of m

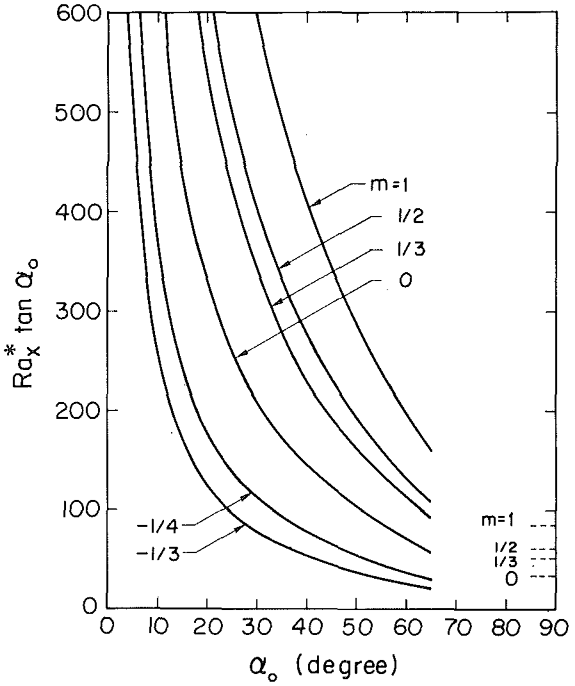

Fig. 4 Values of $Ra_x^* \tan\alpha_0$ as a function of inclination angle α_0 at selected values of m

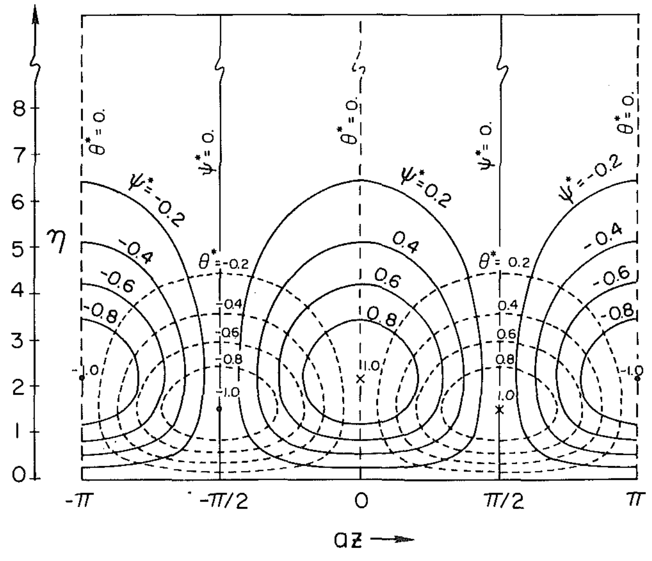

Fig. 5 Secondary flow streamlines (solid lines) and isotherms (dashed lines) at the onset of vortex instability

present analysis is not valid for large inclination angles with respect to vertical. (3) The disturbances are a weak function of the streamwise direction so that the local similarity concept is applicable.

By a scaling argument, it is shown in this paper that the length scales of disturbances are smaller than those for the undisturbed boundary layer flow, thus, confirming the so-called bottling effects proposed by Haaland and Sparrow [3]. It is found that the larger the inclination angle (with respect to the vertical), the more susceptible is the flow for the vortex mode of disturbances; and in the limit of zero inclination angle (i.e., a vertical heated plate) the flow is stable for this form of disturbances. Presumably, for small inclination angles the instability will be characterized by wave instability. This problem is currently under investigation by the authors.

Acknowledgments

This work was supported by the National Science Foundation through Grant No. ENG 77-27527. The authors wish to thank the reviewers for their valuable discussion which led to the considerable improvement in the paper.

References

1 Sparrow, E. M., and Husar, R. B., "Longitudinal Vortices in Natural Convection Flow on Inclined Plates," *J.F.M.*, Vol. 37, 1969, pp. 251–255.

2 Lloyd, J. R., and Sparrow, E. M., "On the Instability of Natural Convection Flow on Inclined Plates," *J.F.M.*, Vol. 42, 1970, pp. 465–470.

3 *Haaland, S. E., and Sparrow, E. M., "Vortex Instability of Natural* Convection Flow on Inclined Surfaces," ASME JOURNAL OF HEAT TRANSFER, Vol. 16, 1973, pp. 2355–2367.

4 Hwang, G. J., and Cheng, K. C., "Thermal Instability of Laminar Natural Convection Flow on Inclined Isothermal Plates," *The Canadian Journal of Chemical Engineering*, Vol. 51, 1973, pp. 659–666.

5 Smith, A. M. O., "On the Growth of Taylor-Goertler Vortices Along Highly Concave Walls," *Quarterly of Appl. Math.*, Vol. 13, 1955, pp. 233–262.

6 Kahawita, R. A., and Meroney, R. N., "The Vortex Mode of Instability in Natural Convection Flow Along Inclined Plates," *Int. J. Heat Mass Transfer*, Vol. 17, 1974, pp. 541–548.

7 Iyer, P. A., and Kelly, R. E., "The Stability of the Laminar Free Convection Flow Induced by a Heated Inclined Plate." *Int. J. Heat Mass Transfer*, Vol. 17, 1974, pp. 517–525.

8 Gaster, M., "On the Effects of Boundary-Layer Growth on Flow Stability," *J.F.M.*, Vol. 66, 1974, pp. 465–480.

9 Eagles, P. M., and Weissman, M. A., "On the Stability of Slowly Varying Flow: the Divergent Channel," *J.F.M.*, Vol. 69, 1975, pp. 241–262.

10 Saric, W. S., and Neyfeh, A. H., "Nonparallel Stability of Boundary-Layer Flows," *Phys. of Fluids*, Vol. 18, 1975, pp. 945–950.

11 Jaluria, Y., and Gebhart, B., "Stability and Transition of Buoyancy-Induced Flows in a Stratified Medium," *J.F.M.*, Vol. 66, 1974, pp. 593–612.

12 Hsu, C. T., Cheng, P. and Homsy, G. M., "Instability of Free Convection Flow over a Horizontal Impermeable Surface in a Porous Medium," *Int. J. Heat Mass Transfer*, Vol. 20, 1978.

13 Cheng, P., and Minkowycz, W. J., "Free Convection About a Vertical Flat Plate Embedded in a Porous Meidum with Application to Heat Transfer from a Dike," *J.G.R.*, Vol. 82, pp. 2040–2044.

14 Moore, F. K., *Theory of Laminar Flows*, Princeton University Press, 1964, pp. 486–490.

15 Sparrow, E. M., and Yu, H. S., "Local Non-Similarity Thermal Boundary Layer Solutions," ASME JOURNAL OF HEAT TRANSFER, Vol. 93, 1971, pp. 328–334.

16 Sparrow, E. M., Quack, H. and Boerner, C. J., "Local Nonsimilarity Boundary Layer Solutions," *AIAA J.*, Vol. 8, 1970, pp. 1936–1942.

17 Betchov, R. and W. O. Criminale, *Stability of Parallel Flows*, Academic Press, New York, 1967.

18 *R. E. Kaplan, "The Stability of Laminar Incompressible Boundary Layers in the Presence of Complaint Boundaries,"* M.I.T. Aero-Elastic and Structures Research Laboratory, ASRL-TR 116-1, 1964.

A. Yücel
Graduate Student

Y. Bayazitoğlu
Assistant Professor
of Mechanical Engineering

Mechanical Engineering Department,
Rice University,
Houston, TX 77001

Onset of Convection in Fluid Layers with Non-uniform Volumetric Energy Sources

The thermal stability of a fluid layer with non-uniform distribution of the volumetric energy sources is studied. The conditions leading to the onset of convective motions in the fluid are determined analytically by linear stability theory. The system considered consists of a fluid layer of infinite horizontal extent which is confined between two rigid parallel boundaries and subjected to general convective boundary conditions. The fluid is heated internally by way of absorption of the external radiation penetrating in the fluid body. The effects of the stabilizing and destabilizing temperature differences at the boundaries and the properties of the bounding surfaces are investigated. Optically thicker layers are found to be more stable.

1 Introduction and Literature Survey

The density of most fluids decreases with increasing temperature. In the presence of an adverse temperature field, potentially unstable situations may arise in which denser fluid lies above less dense fluid. Such an unstable density stratification, which might be created by heating a quiescent fluid from below or internally, can produce thermal convection.

In the present study the thermal stability of a horizontal layer of fluid with nonuniform volumetric energy sources is studied. The heat generation is by way of absorption of incident radiation penetrating in the fluid. The resulting heat source functions are essentially exponential and increase monotonically from the lower to the upper boundary. They may range from a uniform distribution to an impulse function at the upper boundary, depending on the optical thickness of the layer. The horizontal boundaries are rigid and subject to convective boundary conditions characterized by the respective Biot numbers. The various parameters that govern the stability problem may be grouped into two nondimensional numbers: the internal Rayleigh number, defined as

$$\mathrm{R}_I = \frac{g\beta I_{st} d^4}{\alpha \nu k} \tag{1}$$

and the external Rayleigh number, defined as

$$\mathrm{R}_E = \frac{g\beta(T_{\infty 1} - T_{\infty 2})d^3}{\alpha \nu} \tag{2}$$

The purpose of this study is to predict the critical values of R_I and R_E that mark the onset of convection in the fluid layer and to demonstrate the effects of the optical thickness of the layer, the Biot numbers and the surface properties of the boundaries.

The problem of the stability of a horizontal fluid layer with internal heat generation has received considerable attention owing to the importance of convection in the earth's mantle and for problems of astrophysical interest as well as for nuclear reactor design and safety problems. A survey of the literature indicates that studies dealing explicitly with non-uniform heat generation have not been reported. A general analysis considering arbitrary distributions of the heat source and/or temperature is not feasible unless these originate from a physical problem. The difficulty lies in defining the appropriate Rayleigh numbers and parameters as has been encountered in [1] and [2]. Whitehead and Chen [1] have studied a family of conduction temperature profiles, some of which resemble those considered in this study. Much consideration has been given to convection generated by uniform volumetric energy sources. Sparrow, et al. [2] have studied the effect on the instability of a fluid layer arising from nonlinear temperature profiles due to internal heating. Catton and Suo-Anttila [3] and Suo-Anttila and Catton [4] have reported numerical results for heat transfer in a layer with uniform heat generation. Kulacki and Goldstein [5] have applied the linear and energy theory stability criteria and presented a rigorous treatment of the problem for various hydrodynamic and thermal boundary conditions. Finite amplitude (nonlinear) effects are considered by Roberts [6], Watson [7], Peckover and Hutchinson [8], Tveitereid and Palm [9], Clever [10] and Tveitereid [11]. Much experimental work has been reported in the literature [12–16]. The stability of a fluid in an internally heated porous medium [17, 18] and the stability of radiating fluid layers [19–21] have also been studied.

2 Analysis

The schematic diagram of the system considered is shown in Fig. 1. The model consists of a fluid layer ($0 \le z^* \le d$) of infinite horizontal extent. It is bounded by two rigid planes and coupled thermally at the lower and upper boundaries to constant temperature environments at $T_{\infty 1}$ and $T_{\infty 2}$, respectively. The conductance at the boundaries are given in dimensionless form by the corresponding Biot numbers. The Boussinesq approximation is invoked; i.e., the fluid properties are assumed to be constant except for the density which appears in the body force term of the momentum equation.

The nondimensionalized governing equations are

$$\nabla \cdot \mathbf{U} = 0 \tag{3a}$$

$$\frac{\partial \mathbf{U}}{\partial t} + \frac{1}{\mathrm{Pr}}\mathbf{U} \cdot \nabla \mathbf{U} = -\nabla p + f i_z + \nabla^2 \mathbf{U} \tag{3b}$$

$$\mathrm{Pr} \cdot \frac{\partial T}{\partial t} + \mathbf{U} \cdot \nabla T = \nabla^2 T + q \tag{3c}$$

where

$$f = -[1 - \beta(T^* - T_0^*)]gd^3/\alpha\nu \tag{4}$$

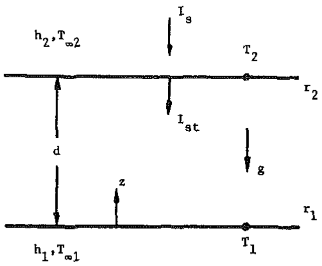

Fig. 1 Schematic illustration of the system

Contributed by the Heat Transfer Division and presented at the 18th AIChE/ASME National Heat Transfer Conference, August 6–8, 1979, San Diego, California. Manuscript received by the Heat Transfer Conference May 10, 1979. Paper No. 79-HT-100.

$$q = gd^5\beta q^*/\alpha\nu k \tag{5}$$

with the boundary conditions

$$\mathbf{U} = 0, \quad \frac{\partial T}{\partial z} = \mathrm{Bi}_1(T - T_{\infty 1}) \quad \text{at} \quad z = 0 \tag{6a}$$

$$\mathbf{U} = 0, \quad -\frac{\partial T}{\partial z} = \mathrm{Bi}_2(T - T_{\infty 2}) \quad \text{at} \quad z = 1 \tag{6b}$$

where the length, velocity, pressure and temperature are measured in units of d, α/d, $\rho_0\alpha\nu/d^2$ and $\alpha\nu/g\beta d^3$, respectively.

The volumetric rate of heat generated refers to that of the incident radiation being absorbed in the fluid body. The intensity of the radiation penetrating in the fluid layer and being reflected at the boundaries is

$$I(z^*) = I_{st}\frac{r_1e^{-Kd}e^{-Kz^*} - e^{-K(d-z^*)}}{1 - r_1r_2e^{-2Kd}}, \; z^* = zd \tag{7a}$$

$$I_{st} = I_s \cdot t_{\text{eff}} \tag{7b}$$

where I_{st} is the intensity of the transmitted part of external radiation of intensity I_s, normally incident on the top surface and t_{eff} is the effective transmissivity of the upper boundary. The fluid layer is assumed to be an absorbing and nonscattering medium. Emission is assumed to be negligible. The rate of heat generation in the fluid by way of absorption is

$$q^*(z^*) = -\frac{dI}{dz^*} \tag{8}$$

$$q^*(z^*) = I_{st}\frac{K(e^{Kz^*} + r_1e^{-Kz^*})}{e^{Kd} - r_1r_2e^{-Kd}} \tag{9a}$$

or in dimensionless form

$$q = \mathrm{R}_I\frac{\tau(e^{\tau z} + r_1e^{-\tau z})}{e^{\tau} - r_1r_2e^{-\tau}} \tag{9b}$$

where q is related to q^* by equation (5).

With the heat generation given by equation (9b), the steady-state conduction temperature distribution is

$$T^0 = c_1(e^{\tau z} + r_1e^{-\tau z}) + c_2z + c_3 \tag{10}$$

where superscript 0 is used to denote the undisturbed state. The coefficients c_1, c_2 and c_3 are given by

$$c_1 = -\frac{\mathrm{R}_I}{\tau(e^{\tau} - r_1r_2e^{-\tau})} \tag{11a}$$

$$c_2 = -\{\mathrm{R}_E + c_1\tau[(e^{\tau} - r_1e^{-\tau})/\mathrm{Bi}_2 + (1 - r_1)/\mathrm{Bi}_1 + (e^{\tau} + r_1e^{-\tau} - 1 - r_1)/\tau]\}/A \tag{11b}$$

$$c_3 = c_1[\tau(1 - r_1)/\mathrm{Bi}_1 - (1 + r_1)] + c_2/\mathrm{Bi}_1 \tag{11c}$$

where

$$A = 1/\mathrm{Bi}_1 + 1/\mathrm{Bi}_2 + 1 \tag{12}$$

Linear stability analysis assumes that the field variables undergo infinitesimal disturbances and investigates the reaction of the system to these small perturbations. The equations governing the z-component of the velocity and the temperature perturbations are [22]

$$\left(\frac{\partial}{\partial t} - \nabla^2\right)\nabla^2 w' = \nabla_1{}^2T' \tag{13}$$

$$\left(\mathrm{Pr}\cdot\frac{\partial}{\partial t} - \nabla^2\right)T = -\frac{dT^0}{dz}\cdot w' \tag{14}$$

writing

$$\nabla_1{}^2 = \frac{\partial^2}{\partial x^2} + \frac{\partial^2}{\partial y^2} \tag{15}$$

The stability of a system can be assessed by investigating its reaction to all possible disturbances. Since there are no lateral boundaries on the system, an arbitrary though infinitesimal disturbance can be expressed in terms of horizontal waves of the form

$$f'(x, y, z, t) = F(z, t)\cdot\exp\left[i(a_xx + a_yy) + \sigma t\right] \tag{16}$$

$$F = w \text{ or } \theta$$

where $a = (a_x{}^2 + a_y{}^2)^{1/2}$ is the horizontal wave number and

$$\sigma = \sigma_r + i\sigma_i \tag{17}$$

The solution of the stability problem requires the specification of the states characterized by the real part of σ being zero. Although the principle of exchange of stabilities cannot be shown to hold for this problem, we will assume it to be valid; i.e., the transition from stability to instability occurs through a stationary marginal state, $\sigma_i = 0$ accordingly. Equations (13, 14, 16) and (17) are combined to obtain the equations governing the marginal state:

$$(D^2 - a^2)^2\,W = a^2\theta \tag{18a}$$

$$(D^2 - a^2)\theta = \frac{dT^0}{dz}\cdot W \tag{18b}$$

with the boundary conditions

$$W = DW = 0, \quad D\theta = \mathrm{Bi}_1\theta \quad \text{at} \quad z = 0 \tag{19a}$$

$$W = DW = 0, \quad -D\theta = \mathrm{Bi}_2\theta \quad \text{at} \quad z = 1 \tag{19b}$$

To solve the stability problem, $\theta(z)$ is represented in a series of orthogonal functions that satisfy the boundary conditions (19a) and (19b) [23],

$$\theta(z) = \sum_{n=1}^{\infty} A_n\phi_n(z) \tag{20}$$

where

Nomenclature

a = horizontal wavenumber
Bi = Biot number, hd/k
d = thickness of the fluid layer
g = gravitational acceleration
G = the ratio $\mathrm{Bi}_2/\mathrm{Bi}_1$
i_z = unit vector in vertical (z) direction
I_s = intensity of radiation incident on the top surface
I_{st} = intensity of the incident radiation transmitted into the fluid
k = thermal conductivity
K = extinction coefficient
p = pressure
Pr = Prandtl number, ν/α
q = rate of heat generation
r = reflectivity of the boundary
R_E = external Rayleigh number, $g\beta(T_{\infty 1} - T_{\infty 2})d^3/\alpha\nu$
R_I = internal Rayleigh number, $g\beta I_{st}d^4/\alpha\nu k$
t = time
t_{eff} = effective transmittance of the upper boundary
T = temperature
$\mathbf{U}$ = velocity field
u, v, w = x, y, z components of the velocity
W = component of w' which is a function of z only
x, y, z = Cartesian coordinates
α = thermal diffusivitiy
β = thermal expansion coefficient
θ = component of T' which is a function of z only
ν = kinematic viscosity
ρ = density
σ = growth rate
τ = optical thickness, Kd

Subscripts

0 = reference state
1 = lower boundary
2 = upper boundary
∞ = ambient
c = critical

Superscripts

0 = undisturbed state
1 = perturbed state
* = dimensional quantity
′ = perturbation quantity

$$\phi_n = b_n \cos b_n z + \mathrm{Bi}_1 \sin b_n z \tag{21}$$

and the b_n's are the positive roots of

$$\tan b = \frac{b(\mathrm{Bi}_1 + \mathrm{Bi}_2)}{b^2 - \mathrm{Bi}_1 \cdot \mathrm{Bi}_2} \tag{22}$$

The functions $\phi_n(z)$ are orthogonal as

$$\int_0^1 \phi_n(z)\phi_m(z)dz = \delta_{mn}N_n \tag{23}$$

where δ_{mn} is the Kronecker delta and N_n is given by

$$N_n = \frac{1}{2}\left[\mathrm{Bi}_1 + (b_n{}^2 + \mathrm{Bi}_1{}^2)\left(1 + \frac{\mathrm{Bi}_2}{b_n{}^2 + \mathrm{Bi}_2{}^2}\right)\right] \tag{24}$$

Introducing (20) into (18*a*), W_n can be determined under the boundary conditions (19*a*) and (19*b*). The solutions are

$$W_n = B_n \cosh az + C_n \sinh az + D_n z \cosh az + E_n z \sinh az + \frac{1}{\gamma_n{}^2}\phi_n(z) \tag{25}$$

where $W(z) = a^2 \sum_{n=1}^{\infty} A_n W_n$

$$B_n = -b_n/\gamma_n{}^2 \tag{26a}$$

$$C_n = \{[(1 - \mathrm{Bi}_1)\,\mathrm{sinha} + a \cosh a]\cos b_n + [(b_n + \mathrm{Bi}_1/b_n)\sinh a + a\,\mathrm{Bi}_1 \cosh a/b_n]\sin b_n - a(1 + \mathrm{Bi}_1) - \cosh a \sinh a\} \cdot \frac{B_n}{\sinh^2 a - a^2} \tag{26b}$$

$$D_n = \mathrm{Bi}_1 B_n - C_n \tag{26c}$$

$$E_n = \left\{(\cos b_n + \frac{\mathrm{Bi}_1}{b_n}\sin b_n - \cosh a)B_n - C_n \sinh a - D_n \cosh a\right\} \cdot \frac{1}{\sinh a} \tag{26d}$$

$$\gamma_n = b_n{}^2 + a^2 \tag{26e}$$

Introducing θ and W constructed in this manner into equation (18*b*) and using the orthogonality property for $\phi(z)$ given by equation (23), one obtains

$$\sum_{n=1}^{\infty} A_n\{-\gamma_n \delta_{mn} N_n - a^2 \mathrm{R}_I[m/n]\} = 0, \quad m = 1, 2, \ldots \tag{27}$$

where

$$[m/n] = \int_0^1 \frac{dT^0}{dz} W_n(z)\phi_m(z)dz \tag{28}$$

The integral term $[m/n]$, defined by equation (28) is integrated exactly.

Equation (27) represents a linear homogenous system which has a nontrivial solution if and only if the infinite order determinant of (27) vanishes. Thus

$$\| - \gamma_n N_n \delta_{mn} - a^2 \mathrm{R}_I[m/n]\| = 0 \tag{29}$$

is a characteristic equation for R_I. For a given choice of the system parameters, there is a minimum value of R_I with respect to a that causes the determinant to be zero. Below this value a solution to the disturbance equations cannot be found; i.e., the quiescent state is stable. Therefore, this minimum internal Rayleigh number corresponds to the onset of convection and is referred to as the critical internal Rayleigh number.

3 Discussion of Results

In this section the variations in the critical internal Rayleigh number with respect to the optical thickness of the fluid layer are presented. The effects of the thermal conductance at the boundaries, stabilizing and destabilizing differences of the ambient temperatures and the surface properties (reflectivities) of the boundaries on the critical internal Rayleigh number are discussed.

In Fig. 2 the critical values of the internal Rayleigh number, R_{Ic} are presented as a function of the optical thickness τ for various values of the Biot number Bi when $G = \mathrm{Bi}_1/\mathrm{Bi}_2 = 1$. Results are restricted to the case $r_1 = 0$ and $T_{\infty 1} = T_{\infty 2}$, i.e., $\mathrm{R}_E = 0$. R_{Ic} are observed at first to decrease and then to increase with τ. As Bi decreases, R_{Ic} are monotonically decreasing for small values of τ while they are monotonically increasing for large values of τ. The effects on R_{Ic} of varying τ and Bi can be explained by referring to the heat source distributions and the conduction temperature profiles.

Fig. 3 shows the heat source distributions for various values of τ when $r_1 = 0$. The heat source function given by equation (9) increases monotonically for $z \geq 0$ (exponentially for $r_1 = 0$). The corresponding conduction temperature profiles are plotted in Fig. 4. The temperature of the lower boundary, T_1, is taken as a reference and its magnitude is indicated on the figure. A potentially unstable layer is observed to overlie a layer with a stabilizing temperature gradient. Basically the profiles are not symmetric with respect to the midplane as in the case of a uniform heat source distribution. Maximum fluid temperature (minimum density for a normal fluid) occurs above the midplane resulting in a relatively thinner layer of denser fluid. For $\tau \ll 1$ the heat source distributions are almost uniform and the corresponding conduction temperature profiles are very close to parabolic in shape (Fig. 4(*a*)). Using equation (9*a*) the magnitude of the heat source can be approximated as

$$q^*(z^*) \approx q^* = \frac{I_{st}}{d} \cdot \frac{1 + r_1}{1 - r_1 r_2}\tau, \quad 0 < z^* < d \quad \text{and} \quad \tau \ll 1 \tag{30}$$

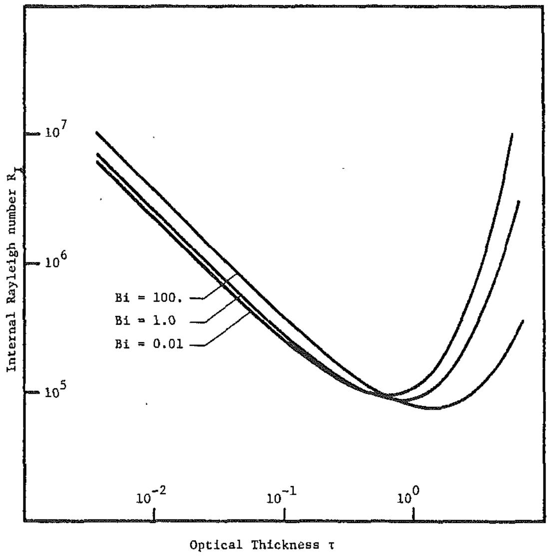

Fig. 2 Critical internal Rayleigh numbers versus optical thickness for various values of the Biot number [$\mathrm{Bi}_1 = \mathrm{Bi}_2 = \mathrm{Bi}(G = 1)$, $r_1 = 0$, $\mathrm{R}_E = 0$]

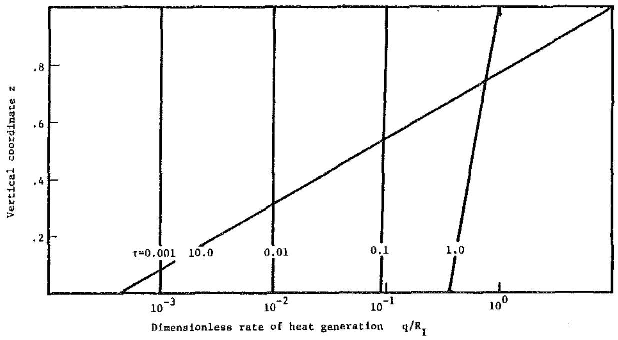

Fig. 3 Nondimensional heat source distributions with respect to the vertical coordinate for various values of the optical thickness $\tau(r_1 = 0)$

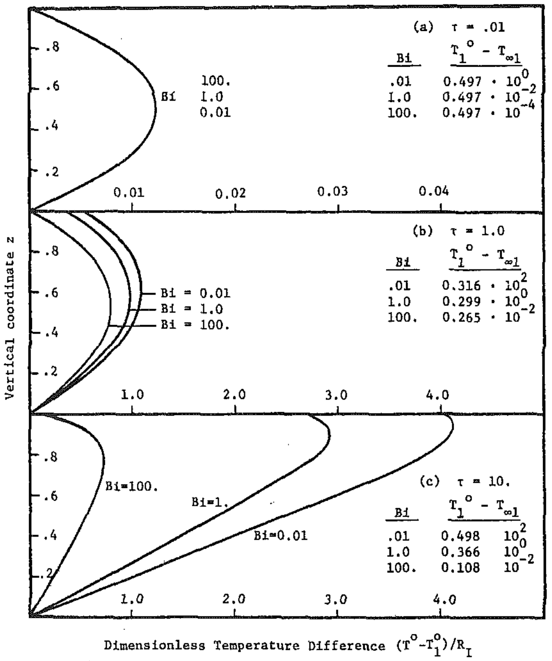

Fig. 4 Conduction temperature profiles with reference to the lower boundary temperature for various values of Bi and τ(G = 1, r_1 = 0, R_E = 0)

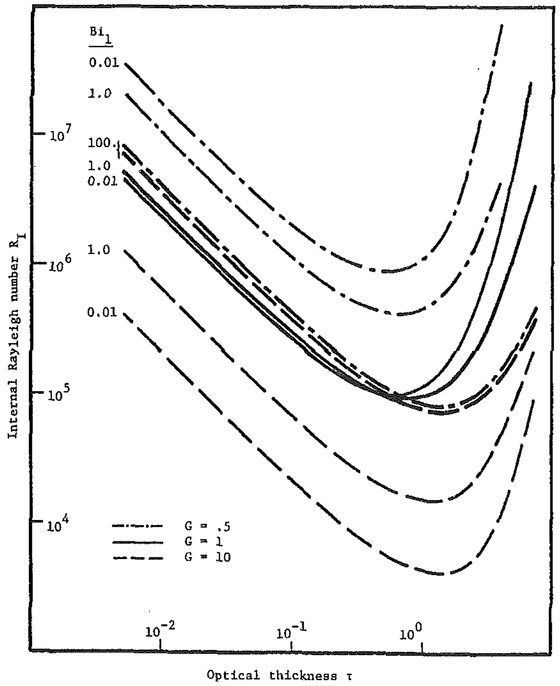

Fig. 5 R_I versus τ for asymmetric convective boundary conditions (r_1 = 0, R_E = 0)

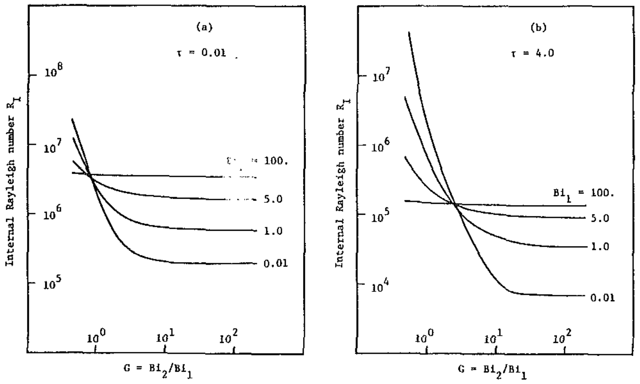

Fig. 6(a) τ = 0.01 (r_1 = 0, R_E =0) Fig. 6(b) τ = 4.0(r_1 = 0, R_E = 0)

Fig. 6 Internal Rayleigh number versus G = $\mathrm{Bi}_1/\mathrm{Bi}_2$ for optical thickness values

Thus an increase in τ directly increases the magnitudes of the heat source and the temperature levels. Recalling the definition of R_I it follows that R_{Ic} varies linearly with $1/\tau$ as

$$\mathrm{R}_{Ic} = \overline{\mathrm{R}}_{Ic}\frac{1 - r_1 r_2}{1 + r_1}\cdot\frac{1}{\tau} \qquad (31)$$

where $\overline{\mathrm{R}}_{Ic}$ is the critical value of the internal Rayleigh number in the case of uniform heat sources and defined as

$$\overline{\mathrm{R}}_{Ic} = \frac{g\beta q^* d^5}{\alpha\nu k} = 37328 \qquad (32)$$

The variation given by equation (31) corresponds to the left ends of the curves in Fig. 2. The same trend continues to hold for moderately small values of τ since there is very little deviation from a uniform distribution. As τ is increased further, the magnitude of the heat source begins to decrease starting from the lower boundary. However, its magnitude at the upper boundary continues to increase. Physically, this corresponds to the situation in which the penetrating radiation energy is absorbed mainly in the top strata. The conduction temperature profiles are skewed as a result of this antisymmetric internal heating of the fluid (Fig. 4(b, c)). The position of the maximum fluid temperature is moved closer to the upper boundary, concentrating the denser fluid in a smaller region. Therefore the degree of stability of the system is increased. In the limit as $\tau \to \infty$ the heat source function approaches an impulse function at the upper boundary. A stabilizing temperature distribution occurs throughout the layer and the system becomes stable.

R_{Ic} are observed to decrease with decreasing Biot number for small values of τ. Boundaries of fixed temperature ($\mathrm{Bi} \to \infty$) yield the highest critical value of the internal Rayleigh number. The most unstable situation corresponds to fixed heat fluxes (Bi = 0) at the boundaries (The variations in R_{Ic} for Bi = 100 and Bi = 0.01 given in Fig. 2 are almost identical to those for $\mathrm{Bi} \to \infty$ and Bi = 0 respectively). The trend that R_{Ic} decreases as Bi decreases has been demonstrated in [5] for the case of uniform heat sources. The predicted values of R_{Ic} for $\tau \ll 1$ have been found to agree well with the results of [5]. In the case of a uniform distribution of the heat sources it may be argued that surfaces of fixed temperature require the temperature perturbations to vanish at these surfaces. However, for finite Biot numbers the perturbations are allowed to fluctuate at the boundaries as implied by the boundary conditions given by equations (19a) and (19b). Therefore, fixing the boundary temperatures damps the temperature perturbations more than the case of convective boundary conditions. For large values of τ it is observed that the reverse trend holds: R_{Ic} decreases with increasing Bi. A stabilizing temperature difference at the boundaries ($T_1 < T_2$) forms in this case as opposed to the mere translation of the temperature profiles with Bi for $\tau \ll 1$. The magnitude of this temperature difference increases with decreasing Bi. Thus convective boundary conditions result in a region of stable equilibrium, relatively thicker and with a higher stabilizing temperature difference than does the fixed temperature boundary condition (Fig. 4(c)). Although fixing the boundary temperature provides a stronger constraint against the perturbation of the temperature profile, an antisymmetric internal heating of the fluid counteracts and may overcome this effect.

The results presented above are restricted to symmetric convective boundary conditions. An additional asymmetry is superimposed on the conduction temperature profile when $G \neq 1$. Convective boundary conditions tend to form at the boundaries stabilizing temperature differences ($T_1 < T_2$) for $G < 1$ and destabilizing temperature differences ($T_1 > T_2$) for $G > 1$. Therefore R_{Ic} are higher for $G < 1$ and lower for $G > 1$ than their values for $G \doteq 1$ (Fig. 5).

Figs. 6(a) and 6(b) show the variations in R_{Ic} with G at fixed values of Bi_1 for two optical thickness values, τ = 0.01 and τ = 4. These two values represent two distinct cases characteristic of the behavior of

R_{Ic} with respect to Bi_1 and display the various effects involved. Since $\tau \ll 1$ corresponds to uniform heat generation, the results of [5] apply as well to the present study for optically thin layers. In general, at any fixed value of Bi_1, R_{Ic} decreases monotonically with increasing G and attains its value in the limit as $G \rightarrow \infty$ at about $G = 10$ (Fig. 6(a)). The case $G < 1$ which is not given full consideration in [5] is noteworthy. It is observed that the stabilizing effect of the fixed temperature boundary condition is opposed by the formation of stabilizing temperature differences at the boundaries due to convective boundary conditions. The magnitude of the temperature difference increases with decreasing Bi_1 (G fixed) and with decreasing G (Bi_1 fixed). Therefore surfaces of prescribed heat flux become stabilizing relative to surfaces of fixed temperature. For large values of $\tau[\tau > 0(1)]$ the stabilizing effect of convective boundary conditions will be strengthened by the similar tendency of τ (discussed above for $G = 1$) when $G < 1$. Therefore R_{Ic} are higher for smaller Bi_1. The effect of convective boundary conditions to form, in the case $G > 1$, destabilizing temperature differences at the boundaries is opposed by the aforementioned stabilizing effect of τ. The dominance of the former effect is delayed to a higher $G > 1$ by the opposing action of the latter.

Next, the effects of stabilizing ($T_{\infty 1} < T_{\infty 2}$) and destabilizing ($T_{\infty 1} > T_{\infty 2}$) ambient temperature differences are considered for fixed boundary temperatures, that is, $Bi_1 = Bi_2 \rightarrow \infty$ and $T_1 \rightarrow T_{\infty 1}$, $T_2 \rightarrow T_{\infty 2}$. Critical internal Rayleigh numbers versus external Rayleigh numbers are plotted for various values of τ in Fig. 7. The neutral stability curves for $\tau \ll 1$ can be regarded as scaled forms of those for the case of uniform heat generation which are also presented in the figure. At a fixed value of τ, when $R_E < 0$ and there is little heat generation, a stable equilibrium exists. Increase in the radiation intensity above a certain magnitude will yield temperatures within the fluid higher than that of the upper boundary. This results in a situation in which denser fluid overlies less dense fluid and unstable conditions are established. The degree of stability of the system increases with increasing R_E. Therefore higher radiation intensities are required for instability to manifest itself. This is demonstrated by the monotonically increasing curves (dashed lines) in Fig. 7. In the case of a destabilizing temperature difference ($R_E > 0$) at the boundaries, R_{Ic} varies in the same manner for $R_E \leq 1707.76$.[1] The degree of stability is lower since there is basically an unstable condition. The interesting feature of the neutral stability curves in Fig. 7 is the existence of stable regions for values of R_E higher than 1707.76. This can be explained by a geometrical argument similar to the one carried out above. The fluid layer can be roughly divided into two regions by the position of the maximum deviation of the conduction temperature distribution from a hypothetical linear profile. As a result of the heat source distributions considered herein, the lower layer is relatively thicker and has a less, if any, adverse temperature gradient. Thus the stability of the system is governed mainly by the conditions in the lower layer. The rate of heat generation within the fluid is negligible for small values of the radiation intensity. Given $R_E > 1707.76$ at a fixed τ, the fluid layer will be unstable when R_I is small as there will be practically no deviation in the conduction temperature distribution from the linear profile. The temperature increases throughout the fluid with increase in the radiation intensity and the dominating lower layer is gradually stabilized. At a certain value of R_I stable conditions prevail. As the radiation intensity is increased further, more and more adverse temperature gradients develop in the upper layer which begin to influence the stability of the system. Eventually unstable conditions will be established that will lead to fluid motion. Stable regions are hardly visible for $\tau < 1$. The lower layer tends to occupy the whole region with increasing τ. With enlarged regions of stable equilibrium the system can tolerate higher destabilizing temperature differences at the boundaries.

The effect of reflectivities of the boundaries for the isothermal case is shown in Fig. 8. The most stable situation is when $r_1 = 0$. In this case all the radiation incident on the lower surface is absorbed and none is reflected. This minimizes the rate of heat generation, resulting in a higher degree of stability. The case of mirror boundaries ($r_1 = r_2 = 1$) corresponds to the most unstable situation. The radiation is totally reflected by both surfaces and absorbed wholly within the fluid. An approximately uniform distribution of the heat sources of magnitude $q = I_{st}/d$—the limit value as $\tau \rightarrow 0$, given by equation (9b)—is obtained up to values of τ of order 10^{-1}. Consequently, within this range, R_{Ic} differs very little from the value of 37328 it attains in the limit as $\tau \rightarrow 0$. The variations in R_{Ic} with τ for all the other possible combinations of r_1 and r_2 lie between these two limiting curves. As was previously pointed out, the heat source distributions are almost uniform and the reflectivities of the bounding surfaces determine by equation (31) the limiting values of R_{Ic} for $\tau \ll 1$. The neutral stability curves are observed to coincide for large values of τ. Since most of the radiation is absorbed in the upper strata and a very small fraction of it reaches the lower surface, the reflectivities of the boundaries do not play a significant role in the stability of optically thick layers.

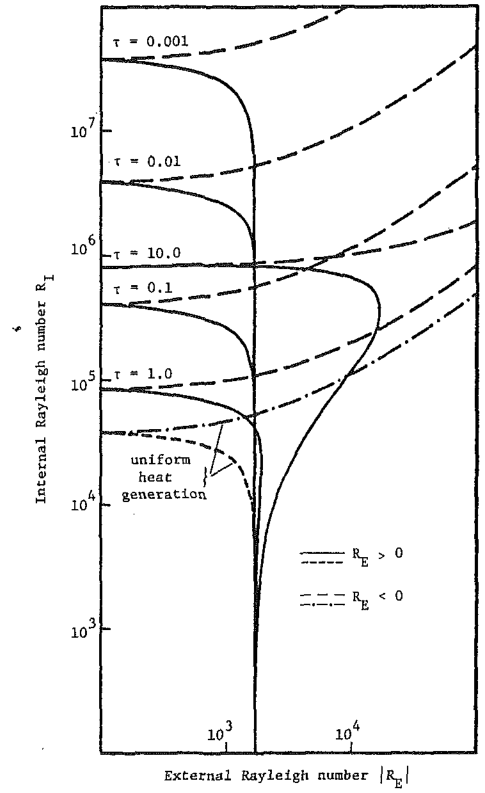

Fig. 7 R_I versus R_E for both stabilizing ($R_E < 0$) and destabilizing ($R_E > 0$) temperature differences at the boundaries for various values of the optical thickness $\tau(Bi_1 = Bi_2 \rightarrow \infty, r_1 = 0)$

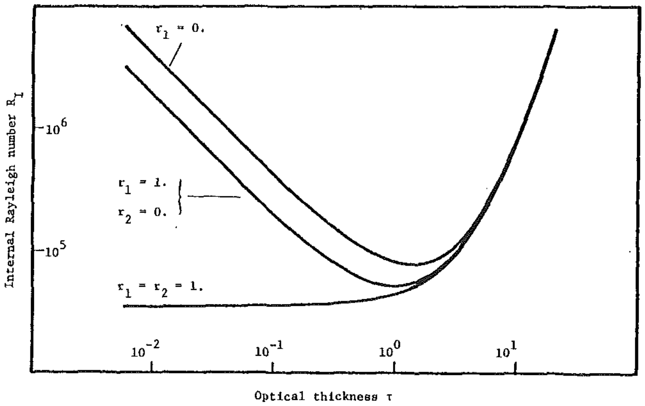

Fig. 8 Critical internal Rayleigh numbers versus optical thickness for various values of the reflectivities of the bounding surfaces ($Bi_1 = Bi_2 \rightarrow \infty$, $R_E = 0$)

---

[1] $R_E = 1707.76$ is the critical external Rayleigh number when there is no heat generation (Bénard problem) [20].

4 Conclusions

Linear stability theory has been used to determine the conditions for the onset of convective motion in a horizontal fluid layer with nonuniform heat generation. Internal heating of the fluid by way of absorption of external radiation has been considered. The heat generation is approximately uniform for optically thin layers. The predicted values of the critical internal Rayleigh number in the limit of uniform heat generation are in agreement with earlier studies. With increasing optical thickness the radiation is absorbed mainly in the top strata. This produces higher temperatures near the upper boundary and thus stabilizes the system. Optically thicker layers $[\tau \geq 0(1)]$ are therefore more stable. The reflectivities of the bounding surfaces are not of major importance because of this substantial attenuation of the radiation in the top strata.

The relative values of Bi_1 and Bi_2 which stand for the conductances at the lower and upper boundaries respectively are determining factors on the stability of the fluid layer. Stabilizing temperature differences are formed at the boundaries when $G = \mathrm{Bi}_2/\mathrm{Bi}_1 < 1$, while the situation is reverse when $G > 1$. The degree of stability of the system decreases with increasing G. All of the aforementioned effects are strengthened with decreasing Biot numbers. Although boundaries of fixed temperature are basically stabilizing, convective boundary conditions may yield higher Rayleigh numbers depending on the values of G and the optical thickness τ.

Acknowledgment

This work was supported in part through the National Science Foundation Grant ENG77-04122.

References

1 Whitehead, J. A. and Chen, M. M., "Thermal Instability and Convection of a Thin Fluid Layer Bounded by a Stratified Region," *Journal of Fluid Mechanics*, Vol. 40, 1970, pp. 549–576.

2 Sparrow, E. M., Goldstein, R. J. and Jonsson, V. K., "Thermal Instability in a Horizontal Layer: Effect of Boundary Conditions and Non-Linear Temperature Profile," *Journal of Fluid Mechanics*, Vol. 18, 1964, pp. 513–528.

3 Catton, I. and Suo-Anttila, A. J., "Heat Transfer from a Volumetrically Heated Horizontal Layer," *Proceedings of the Fifth International Heat Transfer Conference*, Vol. III, 1974, pp. 69–73.

4 Suo-Anttila, A. J. and Catton, I., "The Effect of a Stabilizing Temperature Gradient on Heat Transfer from a Molten Fuel Layer with Volumetric Heating," ASME JOURNAL OF HEAT TRANSFER, Vol. 97, 1975, pp. 544–548.

5 Kulacki, F. A. and Goldstein, R. J., "Hydrodynamic Instability in Fluid Layers with Uniform Volumetric Energy Sources," *Applied Scientific Research*, Vol. 31, 1975, pp. 81–109.

6 Roberts, P. H., "Convection in Horizontal Layers with Internal Heat Generation Theory," *Journal of Fluid Mechanics*, Vol. 30, 1967, pp. 33–49.

7 Watson, P. M., "Classical Cellular Convection with a Spatial Heat Source," *Journal of Fluid Mechanics*, Vol. 32, 1968, pp. 399–411.

8 Peckover, R. S. and Hutchinson, I. H., "Convective Rolls Driven by Internal Heat Sources," *The Physics of Fluids*, Vol. 17, 1974, pp. 1369–1371.

9 Tveitereid, M. and Palm, E., "Convection Due To Internal Heat Sources," *Journal of Fluid Mechanics*, Vol. 76, 1976, pp. 481–499.

10 Clever, R. M., "Heat Transfer and Stability Properties of Convective Rolls in an Internally Heated Fluid Layer," *Journal of Applied Mathematics and Physics*, Vol. 28, 1977, pp. 585–597.

11 Tveitereid, M., "Thermal Convection in a Horizontal Fluid Layer with Internal Heat Sources," *Int. Journal Heat Mass Transfer*, Vol. 21, 1978, pp. 335–339.

12 Tritton, D. J. and Zarraga, M. N., "Convection in Horizontal Layers with Internal Heat Generation Experiments," *Journal of Fluid Mechanics*, Vol. 30, 1967, pp. 21–31.

13 Schwiderski, E. W. and Schwab, H. J. A., "Convection Experiments with Electrolytically Heated Fluid Layers," *Journal of Fluid Mechanics*, Vol. 48, 1971, pp. 703–719.

14 Kulacki, F. A. and Goldstein, R. J., "Thermal Convection in a Horizontal Fluid Layer with Uniform Volumetric Energy Sources," *Journal of Fluid Mechanics*, Vol. 55, 1976, pp. 271–287.

15 Kulacki, F. A. and Nagle, M. E., "Thermal Convection in a Horizontal Layer with Volumetric Energy Sources," ASME JOURNAL OF HEAT TRANSFER, Vol. 97, 1975, pp. 204–211.

16 Suo-Anttila, A. J. and Catton, I., "An Experimental Study of a Horizontal Layer of Fluid with Volumetric Heating and Unequal Surface Temperatures," *AIChE Symposium Series*, No. 164, Vol. 73, 1976, pp. 72–77.

17 Kulacki, F. A. and Ramchandani, R., "Hydrodynamic Instability in a Porous Layer Saturated with a Heat Generating Fluid," *Wärme-und Stoffübertragung*, Vol. 8, 1975, pp. 179–185.

18 Gasser, R. D. and Kazimi, M. S., "Onset of Convection in a Porous Medium with Internal Heat Generation," ASME JOURNAL OF HEAT TRANSFER, Vol. 98, 1976, pp. 49–54.

19 Spiegel, E. A., "Convective Instability of a Radiating Fluid Layer," *Astrophysical Journal*, Vol. 132, 1960, pp. 716–728.

20 Arpaci, V. S. and Gözüm, D., "Thermal Stability of Radiating Fluids: The Bénard Problem," *The Physics of Fluid*, Vol. 16, 1973, pp. 581–588.

21 Arpaci, V. S. and Bayazitoğlu, Y., "Thermal Stability of Radiating Fluids: Asymmetric Slot Problem," *The Physics of Fluids*, Vol. 16, 1973, pp. 689–593.

22. Chandrasekhar, S., *Hydrodynamic and Hydromagnetic Stability*, Oxford University Press, Oxford, 1961, p. 18.

23 Hassab, M. A. and Özisik, M. N., "Stability of a Layer of Fluid Subjected to Convective Boundary Conditions," *Int. J. Heat Mass Transfer*, Vol. 21, 1978, pp. 1264–1266.

24 Pellew, A. and Southwell, R. V., "On Convective Motion in a Fluid Layer Heated from Below," *Proceedings, Royal Society of London*, Series A. Vol. 176, 1940, pp. 312–343.

P. S. Damerell[1]
MPR Associates, Inc.
Washington, D. C.

R. J. Schoenhals
Professor of
Mechanical Engineering,
Purdue University,
West Lafayette, Ind.,
Mem. ASME

Flow in a Toroidal Thermosyphon with Angular Displacement of Heated and Cooled Sections

A toroidal thermosyphon consisting of a fluid-filled torus located in a vertical plane was studied analytically and experimentally. Good agreement was obtained between analytical predictions and measurements for large values of the angular displacement of the heated and cooled sections. For smaller angular displacements, the analytical predictions of steady state flow rates were found to exceed the corresponding experimentally observed values. The discrepancies were attributed to a reverse flow phenomenon. Some analytically predicted flows were not physically achievable. In these situations the flow would either reach a steady condition in the opposite direction, or it would oscillate indefinitely.

Introduction

This paper is concerned with the buoyancy-driven flow of a single phase fluid inside a torus located in a vertical plane. Such a device is referred to as a toroidal thermosyphon (Fig. 1). Various types of thermosyphons are used for cooling purposes in industrial processes. A major advantage of these devices is that efficient heat removal is achieved by a flowing fluid without the need for a pump. Flow in a toroidal thermosyphon is driven by buoyancy forces created by heating and cooling of the internal fluid. The motion of the fluid is opposed by frictional shear forces between the fluid and the wall of the torus. For fixed heat addition and heat removal conditions, the steady-state flow rate in the thermosyphon is the value for which buoyancy and frictional forces are balanced. The circulatory flow is enhanced by larger heat addition rates because the fluid density differences within the thermosyphon are increased. Also, as the heat addition section is moved toward the bottom of the thermosyphon and the heat removal section toward the top, the flow rate increases. This behavior is contrary to the concept that a closed loop thermosyphon should be heated and cooled along its sides, with the fluid rising through the heated side and falling through the cooled side, as suggested by some other investigators of the problem [2–4]. The determination of flow rate when the heat source is at the bottom and the heat sink at the top is shown in [5–7].

The purpose of the present study was to investigate the variation in steady flow rate with angular displacement of the heated and cooled sections for a thermosyphon of simple well-defined geometry. A toroidal geometry heated over one-half its area and cooled over the remaining half was selected. Straightforward, one-dimensional models were developed to predict the variation of flow rate with angular displacement and these predictions were compared with experimental results. The effects of fluid properties, system dimensions and heat transfer rate on flow rate have been thoroughly discussed in previous literature [5–8] and were not specifically investigated in this study.

It has been shown analytically [5–7] and confirmed experimentally [5] that steady flow is not achievable in a closed loop thermosyphon for a certain range of heat input. In these cases unstable flow occurs and the flow rate oscillates with increasing amplitude until it eventually reverses direction, whereupon oscillations initiate in the new flow direction. Prediction and observation of this behavior have been previously performed only for a thermosyphon which was heated from directly below and cooled from directly above. At the outset of this investigation it was expected that this unstable flow behavior would also occur when the positions of the heated and cooled sections were altered. Results from an experimental study of this topic are also included in this paper.

Analysis

The analysis which follows predicts the steady flow velocity for a toroidal thermosyphon which is heated continuously over one-half its area and cooled continuously over the remaining half. Some portions of the analysis are condensed for conciseness. Complete details are contained in [1]. Although both steady and unsteady flow were encountered in the experimental portion of this work, only a steady flow analysis is presented herein. An analysis which predicts unsteady flow conditions is presented in [5]. The thermosyphon considered in the analysis is shown in Fig. 1. The analysis assumes steady laminar flow, and assumes the Boussinesq approximation is valid. Density is assumed to be a linear function of temperature, which varies only with θ. Axial conduction and viscous dissipation are neglected and viscosity, specific heat and thermal conductivity are assumed to be constant. Also, the effect of curvature on the flow is neglected. An investigation of the validity of this assumption carried out utilizing [9] showed that the effect of curvature would be expected to influence the prediction of flow rate by only ten to fifteen percent for the thermosyphon considered in the experimental portion of this study. Using an incre-

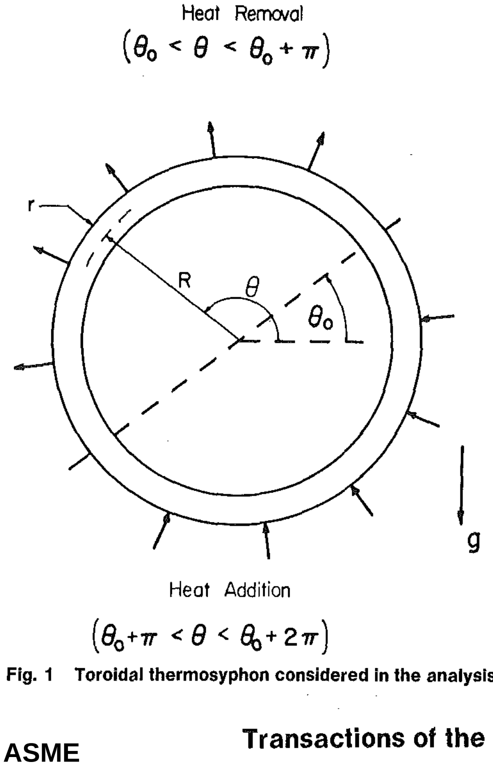

Fig. 1 Toroidal thermosyphon considered in the analysis

---

[1] This research was conducted while the first author was an NSF Graduate Fellow at Purdue University. Further details concerning this work are contained in an M.S.M.E. thesis [1].

Contributed by the Heat Transfer Division and presented at the AIAA/ASME Thermophysics and Heat Transfer Conference, Palo Alto, Calif., May 24–26, 1978. Manuscript received by the Heat Transfer Division July 28, 1979. Paper No. 78-HT-44.

mental control volume approach which assumes flow to be in the direction of increasing θ, the θ-direction momentum equation is written as

$$\tau_w(2\pi rR)d\theta + \rho g \cos\theta(\pi r^2 R)d\theta + \frac{dP}{d\theta}(\pi r^2)d\theta = 0 \qquad (1)$$

which represents a balance of shear, body and pressure forces. When equation (1) is integrated from 0 to 2π, the integral of the pressure force term vanishes because pressure is a continuous function of θ. In integral form, equation (1) appears as

$$\frac{2}{rg}\int_0^{2\pi} \tau_w d\theta = -\int_0^{2\pi} \rho \cos\theta d\theta \qquad (2)$$

Under the assumptions stated above, equation (2) is rewritten as

$$\frac{\pi f V^2}{2rg\beta} = \int_0^{2\pi} T\cos\theta d\theta \qquad (3)$$

where T is the mixed mean temperature at a particular cross-section, V is the average fluid velocity, and the definition $\tau_w = f\rho V^2/8$ has been utilized. To solve equation (3) for V, the variation of T with respect to θ must be determined. This relationship is found from the energy equation, which is written as

$$\frac{dT}{d\theta} = \frac{2q_L''(\theta)R}{\rho_0 VrC} \qquad (4)$$

where $q_L''(\theta)$ is the local wall heat flux at a given θ location. It is helpful at this point to consider two special cases for the function $q_L''(\theta)$.

1 $q_L''(\theta) = q'' =$ constant (constant wall flux heat addition or heat removal).

2 $q_L''(\theta) = h(T_w - T)$, where the heat transfer coefficient h and the wall temperature T_w are both considered constant.

For case 1 (constant wall flux) the temperature distribution obtained from the energy equation is a linear function of θ. For case 2 the temperature distribution is exponential with respect to θ when h and T_w are constant.

Two different toroidal thermosyphons are now considered. In the first one, constant flux heat addition occurs over one-half the torus ($\theta_0 + \pi < \theta < \theta_0 + 2\pi$), and constant flux heat removal occurs over the remaining half ($\theta_0 < \theta < \theta_0 + \pi$). In the second thermosyphon, constant flux heat addition occurs over one-half the torus ($\theta_0 + \pi < \theta < \theta_0 + 2\pi$), and constant wall temperature heat removal occurs over the remaining half ($\theta_0 < \theta < \theta_0 + \pi$). It will be shown that the simpler analysis of the first thermosyphon (which is not physically practical) is under many conditions an accurate approximation to the second thermosyphon (which is physically practical).

Thermosyphon with Constant Flux Heating and Cooling. In this analysis $q_L''(\theta) = q''$ for $\theta_0 + \pi < \theta < \theta_0 + 2\pi$, and $q_L''(\theta) = -q''$ for $\theta_0 < \theta < \theta_0 + \pi$. By substituting these expressions into the energy equation, a solution for the temperature distribution is obtained. Utilizing continuity boundary conditions, the result is

$$T(\theta) = T(\theta_0) - \frac{2q''R}{\rho_0 VrC}(\theta - \theta_0) \quad (\theta_0 < \theta < \theta_0 + \pi) \qquad (5)$$

$$T(\theta) = T(\theta_0) - \frac{2q''R}{\rho_0 VrC}(2\pi + \theta_0 - \theta) \quad (\theta_0 + \pi < \theta < \theta_0 + 2\pi) \qquad (6)$$

Insertion of equations (5) and (6) into equation (3) and simplifying leads to

$$V^3 = \frac{16q''g\beta R}{\rho_0 C f \pi}\cos\theta_0 \qquad (7)$$

Based on laminar flow, $f = 64/\mathrm{Re}$, and equation (7) becomes

$$V^* = (\cos\theta_0)^{1/2} \qquad (8)$$

where $V^* = V(2\pi\mu C/q''g\beta Rr)^{1/2}$, a dimensionless flow velocity.

The result expressed in equation (8) is shown graphically in Fig. 2. In the derivation of the momentum and energy equations it was assumed that flow was in the direction of increasing θ. Therefore, positive values of V^* represent counterclockwise flow and negative values represent clockwise flow. For a given θ_0, there are two analytically predicted steady flow velocities; they are equal in magnitude but one is in the counterclockwise direction and the other is in the clockwise direction.

Thermosyphon with Constant Flux Heating and Constant Wall Temperature Cooling. In this analysis $q_L''(\theta) = q''$ for $\theta_0 + \pi < \theta < \theta_0 + 2\pi$ and $q_L''(\theta) = h(T_w - T)$ for $\theta_0 < \theta < \theta_0 + \pi$, where h and T_w are considered constant. Using a procedure similar to the analysis shown above, it may be shown that

$$V^3 = (16q''g\beta R/f\rho_0 C\pi)[\cos\theta_0 + (hR/\rho_0 VrC)\sin\theta_0] \qquad (9)$$

Based on the assumption of fully developed laminar flow, the expressions $f = 64/\mathrm{Re}$ and $h = 1.83k/r$ are substituted into equation (9). Although it was expected that the average value of h would be greater due to entrance effects, the fully developed value was adequate since the flow rate was found to be somewhat insensitive to moderate variations in the value of h. When these substitutions are made, equation (9) becomes

$$V^3 = (q''g\beta Rr/2\pi\mu C)[V\cos\theta_0 + (1.83kR/\rho_0 r^2 C)\sin\theta_0] \qquad (10)$$

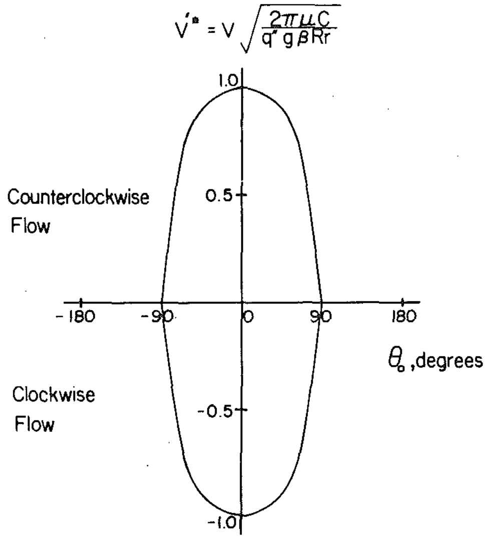

Fig. 2 Flow velocity for a thermosyphon with constant flux heating and cooling

Nomenclature

B = dimensionless quantity, equation (11)
C = specific heat
f = friction factor (Darcy)
g = acceleration due to gravity
h = heat transfer coefficient
k = thermal conductivity
$\dot{m}$ = mass flow rate
P = pressure
q'' = heat flux (constant)
q_L'' = local heat flux
R = major radius of torus
r = minor radius of torus
Re = Reynolds number
T = temperature
T_w = wall temperature
V = flow velocity
V^* = dimensionless flow velocity
α = arbitrary angle
β = thermal expansion coefficient
μ = dynamic viscosity
ρ = density
ρ_0 = density at reference temperature
θ = angular coordinate
θ_0 = angular displacement of heated and cooled sections
τ_w = wall shear stress

which can also be written as

$$(V^*)^3 - (V^*)\cos\theta_0 - (B)\sin\theta_0 = 0 \qquad (11)$$

where $V^* = V(2\pi\mu C/q''g\beta Rr)^{1/2}$ and

$$B = (1.83k/\rho_0 r^2)(2\pi\mu R/q''g\beta Cr)^{1/2} = \frac{hRr}{\rho_0(V/V^*)r^2C}$$

The second expression for B is seen to be a parameter indicating the number of transfer units (NTU) of the thermosyphon heat exchanger (i.e., NTU = $(h)\ x\ (\text{Area})/(\dot{m})\ x\ (C)$). According to equation (11), *the variation of the dimensionless flow velocity V^* as a function* of θ_0 will depend on the value of B, and hence will depend on the NTU of the thermosyphon. This dependence is shown in Fig. 3, where V^* is plotted versus θ_0 for several different values of B. These values of B are indicative of the range obtained in the experimental portion of this study.

By observing the thermosyphon from its back side, it is easily seen that clockwise flow for $\theta_0 = \alpha$ is physically identical to counterclockwise flow for $\theta_0 = -\alpha$, where α is any arbitrary angle. Thus, the curves in the first and third quadrants in Fig. 3 are identical, as are the curves in the second and fourth quadrants. The same statement applies to Fig. 2. In the neighborhood of maximum flow velocity between $\theta_0 = -60$ deg and +60 deg the curve given in Fig. 2 is essentially identical to that in Fig. 3. Hence, the constant flux model provides a simpler, though highly accurate, approximation to the thermosyphon with constant wall temperature cooling in this range. It is important to note that this conclusion applies only within the range of the values of B indicated in Fig. 3. As θ_0 is increased to 90 deg the curve of Fig. 2 approaches zero velocity, whereas the curves in Fig. 3 do not reach the axis until $\theta_0 = 180$ deg. Experimental observations confirmed that steady flow does exist in the range from $\theta_0 = 90$ to 180 deg. It is clear that the simpler constant flux model cannot be used as an approximation for operating conditions in this range. The reason that flows cannot exist beyond 90 deg in Fig. 2 is that the constant flux *assumption results in a linear temperature distribution for which no* solutions to equation (3) can be obtained when $\theta_0 > 90$ deg. This restriction to a linear temperature distribution is obviously not physically realistic for the low flows observed between 90 and 180 deg. However, the nonlinear temperature distribution permitted by the constant wall temperature assumption results in predicted flows in the region from 90 to 180 deg (Fig. 3). Moreover, the agreement between the two models for θ_0 less than 60 deg indicates that in this range the linear temperature distribution accurately approximates the temperature distribution in the constant wall temperature section.

The analysis performed here is only for the particular case in which the loop is heated over one half and cooled over the other half. However, the same technique could readily be used to analyze other heating and cooling distributions if analytical predictions for these cases are desired.

Experimental Apparatus

A schematic diagram of the experimental apparatus is shown in Fig. 4. The thermosyphon was fabricated from a Pyrex glass torus with a major radius of 0.38 m and a minor radius of 0.015 m. It was filled with distilled water. Heating elements were wound evenly around one-half of the torus, a close approximation to constant wall heat flux. Power was supplied to the heater through a variable transformer. A wattmeter in the heater circuit measured the power input to the system. Power input values ranged from zero to 1500 watts for the experiments, which corresponded to a heat flux range of zero to 13,300 watts/m². The heated portion of the torus was wrapped on the outside with insulation to minimize heat losses.

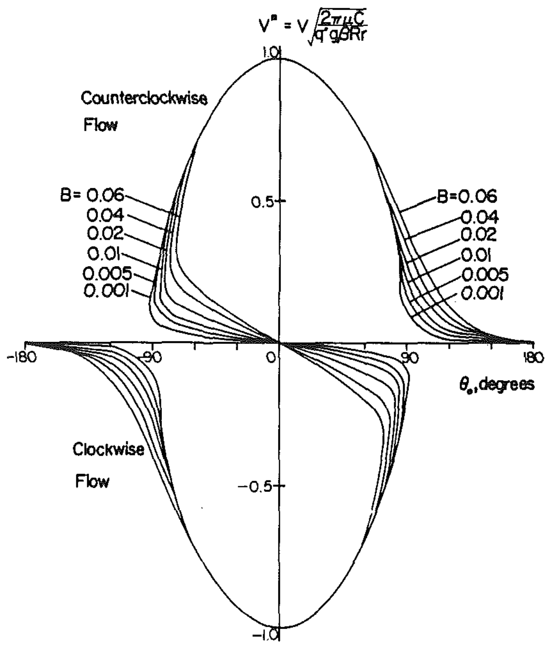

Fig. 3 Flow velocity for a thermosyphon with constant flux heating and constant wall temperature cooling

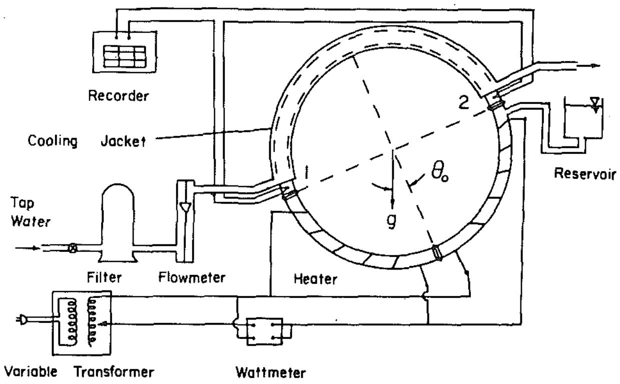

Fig. 4 Schematic diagram of experimental apparatus

Heat was removed by an annular cooling jacket which surrounded the remaining half of the torus. Filtered tap water was used as the coolant. The tap water flow rate was metered, and temperatures at both the inlet and outlet of the cooling jacket were measured. From these measurements, it was possible to compare the input power with the energy removed by the coolant and thereby obtain an estimate of the energy losses from the system. In the majority of the test runs these losses were a small percentage of the input heating rate, usually less than 10 percent. Since the temperature of the tap water was very close to ambient room temperature, insulation around the cooling jacket was not required. This arrangement also allowed visualization of the flow in the cooled section.

By insuring that the flow rate of cooling water was much greater than the flow rate of the water inside the thermosyphon, a close approximation to constant wall temperature cooling was provided. Under these conditions the temperature change experienced by the coolant in passing through the jacket (usually much less than 1°C) was much smaller than the temperature change experienced by the internal fluid as it passed through this section (usually several degrees Celsius).

Two Chromel-Alumel thermocouples were installed inside the thermosyphon to measure the temperature difference between the locations just upstream and downstream of the heated section. With this measured temperature difference, the measured power input and the known specific heat of the internal fluid, the flow rate for the thermosyphon was calculated from an energy balance for each test run in which the flow was steady. When the flow was not steady, the sign of the temperature difference indicated the flow direction, as confirmed by visual observation.

Measurements of heat input and temperature difference were made with precision instruments and were believed to be adequately accurate (within ±5 percent). The greatest possible source of error in the calculation of flow rate was the assumption that the measured temperature difference represented the actual difference in mixed mean temperature between the two points in the flow. An exact determination of the magnitude of this error was not performed. However, this error was believed to be minimized by placing the thermocouples at a radial location corresponding to the location of the mixed mean temperature for a fully developed laminar profile.

To provide angular displacement of the heated and cooled sections, the entire apparatus was mounted on a pivot at the center of the torus which allowed rotation in the vertical plane. Angular displacement was measured by suspending a plumb bob and measuring the angle between the plumb line and a fixed line on the apparatus. The reference geometry (zero displacement) was the configuration in which heating occurred from directly below and cooling from directly above.

Observed Flow Behavior

For each experiment the heat input, cooling water flow rate and angular displacement of the heated and cooled sections were adjusted to prescribed values. The system was then allowed to operate under these fixed conditions for a sufficient time period to allow transient effects to die out. In some cases a steady flow would then be established. In other instances, though, the flow would not achieve a steady value but would oscillate indefinitely. These oscillations continually amplified until the flow eventually reversed direction, whereupon amplifying oscillations occurred in the new flow direction. This behavior was not unexpected. Unstable flow in a toroidal thermosyphon had been previously observed and described by Creveling, et al. [5]. However, these previous observations had been made only for a thermosyphon heated from directly below and cooled from directly above, and the extent of this behavior when the heat addition and heat removal sections are displaced from this geometry was not known. Therefore, an experimental study of the stability behavior under the displaced condition ($\theta_0 \neq 0$) was performed as a part of the present investigation. The results are shown in Fig. 5, which contains a map of the experimentally observed stability behavior as a function of the input heat flux, q'', and the displacement angle of the heat transfer sections, θ_0. Two distinct regions of behavior are identified. For operating points located in the central enclosed region in Fig. 5, the flow oscillated indefinitely and never achieved a steady value. This region extended between values of θ_0 of −6 and +6 deg. For each value of θ_0 in this range there was an associated range of input heat flux for which unstable flow was observed.

For operating points outside the unstable flow region identified in Fig. 5, steady flow was observed when sufficient time was allowed for transient effects to die out. Except for the case of $\theta_0 = 0$, each stable condition yielded steady flow in one direction only. For each case in which θ_0 was greater than zero, the resulting steady flow was observed to occur in the counterclockwise direction. Similarly, for each case in which θ_0 was less than zero, the resulting steady flow was observed to occur in the clockwise direction. On an intuitive basis this behavior is not surprising. Even though flow in the opposite direction is somewhat plausible in light of the analysis just presented, steady flow in that direction was not observed. On the other hand, for θ_0 equal to zero, it was observed that the resulting steady flow could occur in either direction.

Comparison of Steady Flow Results with Analytical Predictions

As explained in the previous section, counterclockwise steady flow was found to be physically unachievable for $\theta_0 < 0$, and similarly clockwise steady flow was found to be physically unachievable for $\theta_0 > 0$. Therefore, experimental confirmation of the analytically predicted steady flow behavior in the second and fourth quadrants of Fig. 3 was not possible. Also, since the behavior in quadrant 3 is identical to that in quadrant 1, as previously discussed, it is only necessary to consider the first quadrant in comparing the observed and predicted flow velocities.

Fig. 6 shows a comparison of the experimentally observed steady flow velocities with the analytically predicted values in the first quadrant. Note that the analytically predicted results are represented by two curves. Both curves correspond to equation (11), which was derived assuming laminar flow, but one curve is for a value of B equal to 0.004 and the other is for a value of B equal to 0.021. These are the minimum and maximum values of B calculated for the experiments. Hence, the two curves define a narrow envelope in which the experimental data should ideally lie. For $\theta_0 < 60$ deg and for $\theta_0 > 140$ deg the curves essentially coincide.

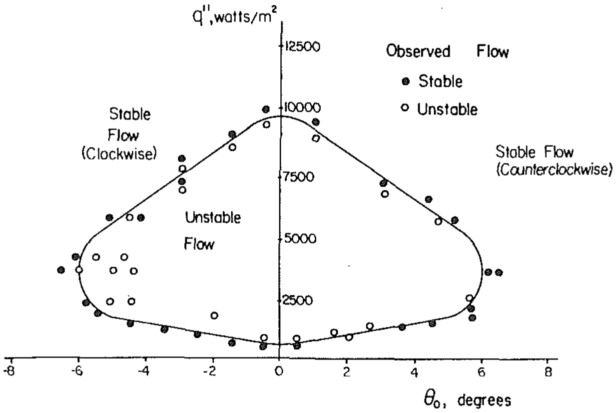

Fig. 5 Stability behavior of the experimentally observed flow

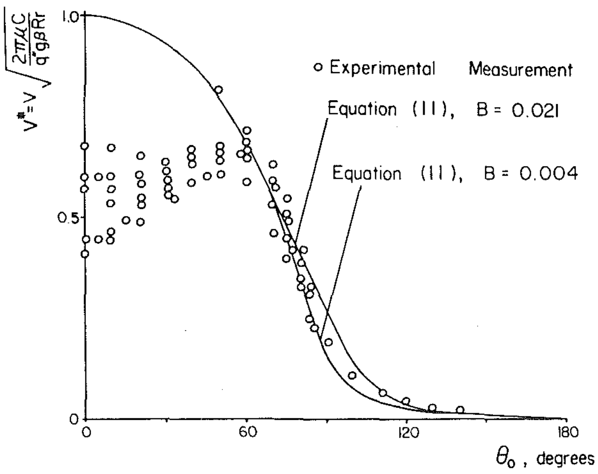

Fig. 6 Comparison of observed and predicted flow velocities

Trends in the experimental results are similar to analytical predictions, but the values of observed flow velocity are less than the corresponding analytically predicted values in the range of θ_0 between 0 and 60 deg. Between 60 and 140 deg the agreement between experiment and analysis is quite favorable. Experimental results were not obtainable for θ_0 greater than 140 deg because of potential overheating damage to the glass thermosyphon as a result of the very low flow rates in this range.

The experimentally measured values plotted in Fig. 6 cover a range of Reynolds number from 100 to 4000. Although this range nominally indicates cases of both laminar and turbulent flow, it was found that the data were most simply and effectively reduced when the laminar correlation for friction factor was used. (Recall that the dimensionless quantity V^* was derived employing the friction factor for fully developed laminar flow in a tube.) When a turbulent flow friction factor was used for those data points with Re values exceeding 2300, slight improvement in the comparison could be obtained, but considerable scatter of those points was observed. Therefore, it was deemed appropriate to plot all the data for the complete range of Re in a single representation for comparison with a single analytical model (Fig. 6).

One observation which seemed to explain the discrepancy between observed and predicted values of flow velocity was the presence of velocity profiles with reverse flow features in certain sections of the thermosyphon. These features were noted by inserting very small

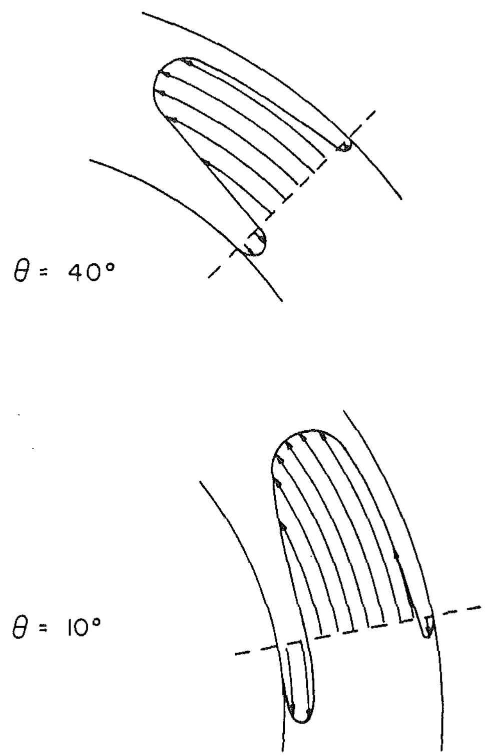

Fig. 7 Qualitatively observed velocity profiles with $\theta_0 = 0$ deg

plastic beads in the fluid and observing the flow patterns in the transparent cooled section. Fig. 7 shows two examples of the flow patterns observed in the thermosyphon. These profiles are qualitative representations based on visual observation only. Fig. 7 shows estimated profiles at the locations $\theta = 40$ deg and $\theta = 10$ deg, with θ_0 equal to zero (heating from directly below and cooling from directly above). Profiles of this type were observed over the range of θ-values from 0 to 60 deg. The reverse flow feature of this profile is apparently due to rapid cooling of the fluid near the wall of the torus. It is reasonable to expect that frictional losses associated with flow patterns like the ones shown in Fig. 7 would be greater than for fully developed laminar flow in a tube at a given Reynolds number. Thus, it is highly plausible that the presence of such flow patterns accounts for the observed velocities being somewhat lower than the corresponding predicted values. It was also observed that the magnitude of the reverse flows was greatest when θ_0 was equal to zero. Angular displacement of the heated and cooled sections from this geometry resulted in a diminishing of intensity of the reverse flow features, and a reduction of the range of θ-values in which these patterns were observed. For $\theta_0 > 60$ deg, reverse flow was not observed at all. This trend in the reverse flow parallels the discrepancy between the observed and predicted flow velocities shown in Fig. 6. It can be seen that the discrepancy between observed and predicted flow velocity is a maximum at θ_0 equal to zero, when reverse flow effects were greatest. The discrepancy diminishes as θ_0 approaches 60 deg, as did the observed reverse flow phenomena. For $\theta_0 > 60$ deg, where reverse flow was not observed, there is close agreement between observed and predicted flow velocities.

The observation of similar velocity profiles and overprediction of observed flow rates has also been noted by previous investigators. Hamilton, et al. [2] report both of these findings for flow in a thermal convection "harp," which consisted of a glass tube formed into a parallelogram with heating along one vertical leg and cooling along the other. Davies, et al. [3] report that the friction factor for flow in a rotating thermosyphon was significantly greater than for conventional flow in a tube. Creveling, et al. [5] also report similar reverse flow phenomena in a toroidal thermosyphon heated from below, and over-prediction of observed flow rates when standard correlations for friction factor were used. On the other hand, Lapin [8] conducted research using a rectangular thermosyphon heated along its bottom half and cooled along its upper half, but did not mention any observation of reverse flow. Also, it was reported that standard friction factor correlations for flow in a tube gave reasonably accurate predictions of the flow rate for this system. This result would not be expected based on the results of the present study.

Summary

1 The analysis predicts maximum flow rate in a toroidal thermosyphon when heating occurs from directly below and cooling from directly above (Figs. 2 and 3). This result is contrary to the suggestions of several previous reports in the literature.

2 Steady-state flow rate predictions based on the standard friction factor correlation for fully developed laminar flow exceed the corresponding experimentally observed values when the displacement angle of the heat transfer sections is between 0 and 60 deg (Fig. 6). A reverse flow phenomenon, as evidenced by visual observation, is apparently responsible for the overprediction of observed flow rates (Fig. 7). This effect was observed to be strongest when θ_0 was equal to zero, and was observed to subside to negligible significance as θ_0 approached 60 deg.

3 Steady-state flow rate predictions based on the standard friction factor correlation for fully developed laminar flow were found to be reasonably accurate when the displacement angle of the heat transfer sections was between 60 and 140 deg (Fig. 6).

4 Some analytically predicted steady flows were not physically achievable, apparently corresponding to unstable states of the system.

(*a*) For some operating conditions steady flow was never achieved experimentally. In these cases the flow oscillated indefinitely (Fig. 5).

(*b*) For some operating conditions more than one steady flow velocity was analytically predicted (Fig. 3). However, only one of these flow conditions was found to be physically achievable, that condition corresponding to flow in the direction of displacement of the heat transfer sections (Fig. 5). Flow in the opposite direction, although analytically predicted, was not observed experimentally. With $\theta_0 = 0$, however, steady flow in either direction was observed to occur within the stable ranges of heat flux shown in Fig. 5.

Acknowledgments

Support of the National Science Foundation through a graduate fellowship is gratefully acknowledged.

References

1 Damerell, P. S., "Flow in a Toroidal Thermosyphon with Angular Displacement of the Heated and Cooled Sections," M.S.M.E. Thesis, Purdue University, 1977.

2 Hamilton, D. C., Lynch, F. E. and Palmer, L. D., "The Nature of the Flow of Ordinary Fluids in a Thermal Convection Harp," Oak Ridge National Laboratory, ORNL-1624, 1954.

3 Davies, T. H. and Morris, W. D., "Heat Transfer Characteristics of a Closed Loop Rotating Thermosyphon," *Proceedings of the International Heat Transfer Conference*, 3rd, Chicago, Vol. 2, 1966, pp. 172–181.

4 Japikse, D., "Advances in Thermosyphon Technology," *Advances in Heat Transfer*, Vol. 9, Academic Press, New York, 1973, pp. 1–111.

5 Creveling, H. F., dePaz, J. F., Baladi, J. Y., and Schoenhals, R. J., "Stability Characteristics of a Single-Phase Free Convection Loop," *Journal of Fluid Mechanics*, Vol. 67, Part I, 1975, pp. 65–84.

6 Keller, J. B., "Periodic Oscillations in a Model of Thermal Convection," *Journal of Fluid Mechanics*, Vol. 26, 1966, pp. 599–606.

7 Welander, P., "On the Oscillatory Instability of a Differentially Heated Fluid Loop," *Journal of Fluid Mechanics*, Vol. 29, Part I, 1967, pp. 17–30.

8 Lapin, Y. D., "Heat Transfer in Communicating Channels Under Conditions of Free Convection," *Thermal Engineering* (USSR), 16(9), 1969, pp. 94–97.

9 "Flow of Fluids through Valves, Fittings and Pipe," Technical Paper No. 410, Crane Co., Chicago, 1957.

K. E. Torrance

Sibley School of Mechanical and Aerospace Engineering,
Cornell University, Ithaca, N.Y. 14853

Open-Loop Thermosyphons with Geological Applications

Natural convection flows in open-loop thermosyphons are examined. The thermosyphons are embedded in an impermeable medium which is heated uniformly from below. The thermosyphon loops charge and discharge fluid at a horizontal boundary of the medium. The impermeable medium is of high thermal conductivity and the temperature of both the medium and the thermosyphon walls increases linearly with depth. Analytical and numerical solutions are presented for a range of thermosyphon geometries. Critical Rayleigh numbers for the onset of motion are determined. A maximum exit temperature is found for elliptical-open-loop thermosyphons. Higher exit temperatures require long residence times at depth. Results are applicable to the cooling of porous materials and to hydrothermal circulations in the oceanic and continental crusts.

Introduction

Natural convection flows in thermosyphons have long been attractive for technological applications. Indeed, many types of thermosyphons are possible (see the review by Japikse [1]). We are here concerned with a type known as an open-loop thermosyphon. In such a device, fluid is pumped from one reservoir to another simply by heating or cooling the duct which connects the reservoirs. The resulting buoyancy forces which arise in a gravitational field are used to pump the fluid. In this paper, we will consider ducts of simple geometry which interconnect two reservoirs which are at nearly the same elevation. The duct wall temperature will be a prescribed function of position.

The motivation for the present study was to develop an understanding of thermosyphons in the earth's crust. Such thermosyphons may result from the flow of groundwater through a connected sequence of fractures or through permeable layers in folded sedimentary formations. In all cases, water at depth is heated by the surrounding impermeable rocks. These rocks are, in turn, heated by conduction from magmatic intrusions at greater depth or by the local geothermal flux from the mantle. Since our motivation is geophysical, we will develop our model in terms of groundwater ducts (aquifers) and surrounding country rock. The model and the results, however, are applicable to a wide range of engineering geometries.

Hydrothermal circulations in the earth's crust have been observed as surface thermal springs on the continents [2] and, recently, as warm-water vents on the ocean floor [3, 4]. Models for crustal circulations are of two types. One type pictures the crust as a saturated porous layer which is heated from below, and in which finite amplitude cellular convection occurs [5, 6]. Such models have been applied to both continental [7] and oceanic [8–10] regions.

The second model for crustal circulations pictures the flows as occurring in open-loop thermosyphons. These are often called aquifer models. However, relatively few such models have appeared. Those that have were approximate [11, 12] or were concerned with aquifer startup [13]. Engineering models of open-loop thermosyphons include those summarized in [1], as well as more specific studies [14, 15]. None of these studies have addressed geometries or heating conditions appropriate for crustal aquifers. Recent work on recirculating (closed-loop) thermosyphons has revealed the presence of flow oscillations in both single-phase [16, 17] and boiling systems [18]. We will here consider single-phase (open-loop) systems where observations have not revealed any systematic oscillations. As a result, a steady flow model will be applicable.

The following sections outline a one-dimensional model for natural convection flows in aquifers of simple geometry. A very general formulation is adopted so as to include a wide class of flow regimes. Results from the idealized model reveal the existence of a critical Rayleigh number and a maximum exit temperature for flow in an aquifer. Additional results, such as temperature distributions and graphical solutions of the momentum balance, are presented for a range of aquifer geometries. In the application section, the model is used to interpret data from a thermal spring in Virginia.

Formulation of the Problem

Geometry and Basic Equations. Consider the thermosyphon sketched in Fig. 1. As previously mentioned, we will develop the problem in terms of underground aquifers, and will equivalently refer to the duct as either an aquifer or a thermosyphon in what follows. In Fig. 1, the centerline of the underground aquifer describes an ellipse with principal radii of a and b. As shown, b is also the maximum depth of the aquifer. Along the length of the aquifer, both cross-sectional area, A, and perimeter, P, are constant, but otherwise arbitrary. The underground aquifer is water filled and may be viewed either as an open duct (such as a large fracture) or as a duct filled with a porous, permeable medium. Fluid motion is described in the former case by conventional friction factor-pressure drop relations, and in the latter case by Darcy's law. Although the geometry of Fig. 1 is idealized, it is representative of folded sedimentary formations (known as synclines) with associated warm springs.

The aquifer is assumed to be embedded in impermeable country rock. The region is heated uniformly from below so that a constant temperature gradient $(dT/dz)_\infty$, known as the ambient geothermal gradient, exists far from the aquifer. We will later assume that this gradient applies right up to the aquifer. The surface temperature is the annual mean surface temperature T_0.

In general, one end of the aquifer may be elevated a distance h, thus providing a topographic drive. Water flowing through the aquifer is heated by the geothermal gradient. Consequently, water in the ascending leg is warmer than water in the descending leg. The result is a net buoyant head which may provide a thermosyphon flow in the absence of a topographic drive ($h = 0$) or may augment any existing topographic drive.

The coordinate system is as shown in Fig. 1, with the z-axis aligned

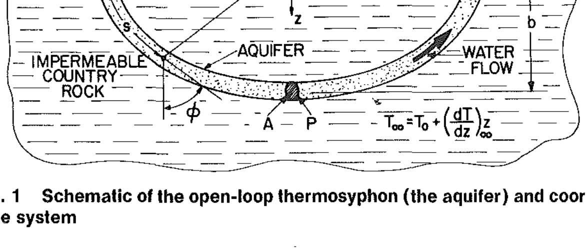

Fig. 1 Schematic of the open-loop thermosyphon (the aquifer) and coordinate system

---

Contributed by the Heat Transfer Division and presented at the 18th AIChE/ASME National Heat Transfer Conference, San Diego, California, August 6–8, 1979. Revised manuscript received by the Heat Transfer Division, March 16, 1979. Paper No. 79-HT-64.

with the gravity vector. Linear and angular coordinates s and σ are used to denote position along the aquifer. Flow may occur in either direction within the aquifer. For convenience, we will take the flow direction to be as shown. The local angle between the fluid velocity and gravity vectors is denoted by ϕ.

We assume that a fully developed flow exists within the aquifer. The area-averaged force balance for the aquifer requires that

$$\rho_f g h - \rho_f g \beta_f c \int_0^L (T_b - T_0) \cos\phi \, ds = \frac{f}{8} \rho_f \overline{u}^2 \frac{P}{A} L \tag{1}$$

where ρ_f is the density of the water at the surface temperature T_0, g is the acceleration of gravity, β_f is the thermal expansion coefficient of water (assumed constant), c is a profile dependent constant to be explained later, L is the length of the aquifer, $T_b(s)$ is the bulk temperature of the water at any point along the aquifer, f is the friction factor, and $\overline{u}$ is the mean flow velocity (a constant). The first term on the left is the topographic head, the second is the net buoyant head due to thermal expansion of the water, and the term on the right is the frictional head due to fluid flow. The sum of topographic and buoyant heads equals the head drop due to friction.

The isothermal compressibility of water has been neglected in writing equation (1). In addition, the coefficient c serves to relate the bulk temperature T_b (which characterizes convective energy flow) to the area-average temperature (which characterizes buoyancy). The coefficient depends upon the shapes of the velocity and temperature profiles. For slug flow and for turbulent duct flow, $c \simeq 1$; for Poiseuille flow, $c = 0.73$. In view of the approximate nature of the present analysis, it will be reasonable in many applications to set $c = 1$.

Water in the aquifer picks up or loses heat to the surrounding country rock. A heat balance applied to the duct requires that

$$\rho_f c_{pf} A \overline{u} \frac{dT_b}{ds} = -h_c P (T_b - \overline{T}_w) \tag{2}$$

where c_{pf} is the specific heat of water, h_c is the local heat transfer coefficient between the fluid and the duct wall, and $\overline{T}_w(s)$ is the mean wall temperature at any station along the duct. Clearly, $\overline{T}_w$ appears as a forcing function in the heat balance. Axial conduction and viscous dissipation effects have been neglected in equation (2).

Heat conduction in the country rock is governed by Laplace's equation. In general, this must be solved simultaneously with equation (2) in order to find the temperatures of both water and rock. However, an important simplification arises when the country rock temperature approaches the ambient geothermal gradient. For this case, the aquifer wall temperature is given by

$$\overline{T}_w(s) = T_\infty(z) = T_0 + \left(\frac{dT}{dz}\right)_\infty z \tag{3}$$

where z is the vertical depth to the aquifer centerline. Equation (3) assumes that the surrounding medium has a high thermal conductivity, λ_r. Strictly speaking, equation (3) is valid whenever λ_r is large compared to the convective conductance within the aquifer (i.e., $\lambda_r / h_c P$ large).

Dimensionless Variables. Appropriate scaling quantities may be found by reference to Fig. 1. We select for a length scale the aquifer depth, b, and for a temperature scale the temperature difference between the bottom of the aquifer and the surface, $\Delta T \equiv (dT/dz)_\infty b$. When cast in dimensionless form, the governing equations (1–3) become

$$H - \int_0^{L/b} \theta_b \cos\phi \, d(s/b) = M \cdot N \tag{4}$$

$$\frac{d\theta_b}{d(s/b)} = -\frac{1}{N} (\theta_b - \overline{\theta}_w) \tag{5}$$

$$\overline{\theta}_w = (z/b) \tag{6}$$

where θ is a dimensionless temperature defined by $\theta \equiv (T - T_0)/\Delta T$, and three dimensionless groups appear

$$H = \frac{h}{\beta_f c \Delta T b}, \; M \cdot N = \frac{f}{8} \frac{P}{A} \frac{\overline{u}^2 L}{g \beta_f c \Delta T b}, \; N = \frac{A}{P} \frac{\rho_f c_{pf} \overline{u}}{h_c b} \tag{7}$$

The groups H and $M \cdot N$, respectively, represent the topographic head and the frictional resistance, both scaled relative to the buoyant drive. The parameter N is a ratio of heat transfer processes within the aquifer (convective heat capacity to convective conductance).[1]

Although the parameters H, M, and N are compactly stated in equations (7), it is often convenient when considering applications to express M and N in an alternate form. The alternate form helps to isolate the appearance of the mean velocity, $\overline{u}$, and is

$$M = 2f \frac{L}{b} \frac{\mathrm{ReNu}}{\mathrm{Ra}}, \; N = \frac{1}{4} \frac{d_h}{b} \frac{\lambda_f}{\lambda_m} \frac{\mathrm{RePr}}{\mathrm{Nu}} \tag{8}$$

where

$$\mathrm{Re} = \frac{\overline{u} d_h}{\nu_f}, \; \mathrm{Nu} = \frac{h_c d_h}{\lambda_m}, \; \mathrm{Ra} = \frac{g \beta_f c (dT/dz)_\infty d_h{}^4}{\nu_f \lambda_m / \rho_f c_{pf}}, \; \mathrm{Pr} = \frac{\nu_f}{\alpha_f} \tag{9}$$

are identified as Reynolds, Nusselt, Rayleigh and Prandtl numbers based on hydraulic diameter, defined here as $d_h = 4A/P$. Other parameters are the kinematic viscosity, ν_f, thermal conductivity, λ_f, and thermal diffusivity, α_f, of the fluid. For cases involving flow through a porous aquifer, the conductivity λ_m of the fluid-saturated porous medium appears. For other cases, set $\lambda_f = \lambda_m$.

The governing equations (4–6) will now be specialized to the elliptical geometry shown in Fig. 1. Recall that on an ellipse, $x = -a \cos\sigma$, $z = b \sin\sigma$, and $d(s/b) = ((a/b)^2 \sin^2\sigma + \cos^2\sigma)^{1/2} d\sigma$. Thus, after combining, the governing equations become

$$H - \int_0^\pi \theta_b \cos\sigma d\sigma = M \cdot N \tag{10}$$

$$\frac{d\theta_b}{d\sigma} = -\frac{1}{N} (\theta_b - \sin\sigma)((a/b)^2 \sin^2\sigma + \cos^2\sigma)^{1/2} \tag{11}$$

Solution of this pair of equations will in general lead to elliptic integrals. The problem formulation thus becomes equations (10) and (11), with H, M, and N defined by (7) or, alternatively, by (7) and (8). The parameters H, M, and N, together with the aquifer aspect ratio, a/b, and the inlet water temperature, θ_{bi}, represent the five basic parameters which appear in the present problem.

Discussion of Parameters. The basic features of aquifer flows are conveniently illustrated in the results section in terms of the generalized parameters H, M, and N. This approach also allows some very general results to be deduced. However, it is important to note that the aforementioned three parameters are not independent. Indeed, one of them represents a dependent, or derived, variable. Any two of the parameters may be prescribed independently; the third must be found by using the force balance (10) and the energy equation (11).

The foregoing fact was employed in obtaining the solutions presented in the present paper. For convenience, H was treated as the dependent variable. With aquifer geometry, θ_{bi}, M, and N prescribed independently, the energy equation (11) was integrated to obtain $\theta_b(s)$. Subsequently, the buoyancy integral in the force balance (10) was evaluated, and combined with the product $M \cdot N$ to obtain the unknown H. When the resulting solutions are graphed (as in Figs. 3(c) and 4(c)), it is possible to find any one of the parameters H, M, or N when the other two are given.

Generally, and in most practical applications, either the topographic head, h, or the mean velocity, $\overline{u}$, will appear as the physical quantity which is to be found from the solution. All other quantities, such as aquifer geometry, θ_{bi}, and those remaining in (7), are presumed known. Finding the topographic head as an unknown is then relatively straightforward, since h appears only in the parameter H. Nevertheless, knowledge of the friction factor, f, and the heat transfer coefficient, h_c, is required. If available, together with $\overline{u}$, the procedure outlined in the preceding paragraph may be used to find h.

On the other hand, finding the mean velocity as an unknown is somewhat more complex, since $\overline{u}$ appears in the parameters M and N both explicitly and implicitly. If functional relationships for f and

---

[1] N is not to be confused with the number of heat exchanger transfer units NTU, to which it is related by $N = (L/b)/\mathrm{NTU}$ (see [19]).

h_c in terms of $\bar{u}$ are available, and if aquifer geometry, θ_{bi}, and all other quantities in (7) are known, the problem then reduces to that of finding $\bar{u}$. In this case, it will usually be advantageous to convert to the formulation of M and N given by (8), where $\bar{u}$ is replaced by a Reynolds number. Equations (8) thus provide a pair of equations for M and N in terms of Re. These equations must be solved simultaneously with (10) and (11) to find Re. For the general case just described, some type of iteration is usually required.

For special cases, it is possible to simplify the governing equations in order to solve directly for the unknown Reynolds number. An example is the closed toroidal thermosyphon considered by Creveling, et al. [17]. Heating conditions were sufficiently simple (uniform heat flux, q, on lower half of loop, constant wall temperature on upper half) that the energy equation (11) could be directly integrated, and an asymptotically-valid estimate for the buoyancy integral in (10) constructed. By considering a closed loop ($H = 0$) and a friction-factor relation of the form $f = m/\text{Re}^n$ (where m and n are empirical constants), the force balance (10) was used (with the definitions of M and N given by (8)) to obtain [17]

$$\text{Re}^{3-n} = \frac{16}{m\pi}\frac{\text{Ra}'}{\text{Pr}^2}\frac{b}{d_h} \qquad (12)$$

In this expression, b represents the major radius of the torous. The Rayleigh number Ra′ differs algebraically from (9) in that the term $(dT/dz)_\infty$ is replaced by q/λ_f. Clearly, (12) serves to relate Re to other parameters.

Explicit expressions similar to (12) do not arise in the present study for physically-interesting ranges of Re. However, there are occasions when an additional, independent constraint on the energy equation may be used to determine Re. For example, the discharge temperature from an aquifer may be known. (We shall consider an application in a later section which falls in this category.) With inlet and discharge temperatures prescribed, the energy equation (11) may be integrated to find appropriate values for N. The second equation in (8) then allows Re to be determined, provided other quantities and a functional relationship for Nu are known. With N known, the force balance (10) allows the required heads to be found.

The previous paragraphs describe procedures for extracting specific values of topographic head or mean fluid velocity from the generalized parameters H, M, and N. The next section considers results obtained in terms of the generalized parameters.

Results

Solutions have been obtained for a wide range of aquifer geometries and for a wide range of the generalized parameters H, M, and N which appear in the governing equations. The geometries considered are sketched in Fig. 2. Detailed flow and temperature data are first presented for aspect ratios of $a/b = 0$, 1 and 4, as shown in Fig. 2(a). The solutions are then extended to other aspect ratios, and to aquifers with a horizontal underground section as shown in Figs. 2(b) and 2(c). To simplify all graphic results, we assume that water enters an aquifer at the mean ground temperature, i.e., $\theta_{bi} = 0$.

The Semicircle, $a/b = 1$. Consider first an aquifer whose centerline describes a semicircle (i.e., $a/b = 1$ in Fig. 2(a)). This geometry illustrates flow features shared by all other aspect ratios.

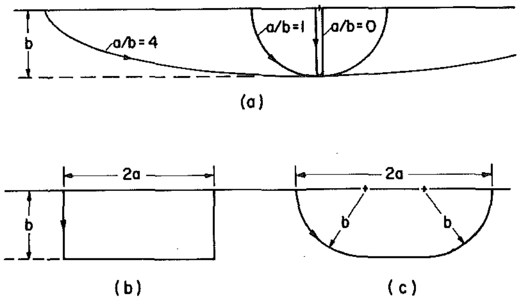

Fig. 2 Thermosyphon geometries considered

For the semicircle, the wall temperature varies as $\bar{\theta}_w = \sin\sigma$. Integration of equation (11) yields

$$\theta_b = \left\{\theta_{bi} + \frac{N}{1+N^2}\right\} e^{-(s/b)/N} + \frac{N}{1+N^2}\left\{\frac{1}{N}\sin\frac{s}{b} - \cos\frac{s}{b}\right\} \qquad (13)$$

where the angular coordinate has been replaced by $\sigma = s/b$. The bulk temperature from this equation is graphed in Fig. 3(a) for several values of N. The curve for $N = 0$ also represents the wall temperature profile. The abscissa is $s/\pi b$, which varies from 0 at the inlet to 1 at the outlet. The aquifer length is $L = \pi b$.

The curve parameter N in Fig. 3(a) is proportional to the flow rate in the aquifer. For small values of N ($N < 0.1$) the fluid tends to equilibrate to the wall temperature. Fluid enters at the surface temperature, $\theta_{bi} = 0$, and is discharged at very nearly this temperature. For larger values of N, convective transport becomes important and the fluid temperature departs from the wall temperature profile. At large values of N (say $N \geq 100$), when the fluid residence time is too short for appreciable warming to occur, the flow process is essentially isothermal.

As the flow rate is increased from $N = 0$ to 100 in Fig. 3(a), the fluid exit temperature at $s/\pi b = 1$ at first increases and then decreases. The resulting exit temperature, θ_{be}, is shown in Fig. 3(b). A maximum is apparent at $N = 1.196$. This is the highest exit temperature that may be achieved by water flowing through the aquifer, and corresponds to 52.8 percent of the rock temperature at the bottom of the aquifer. This result is independent of the detailed nature of the flow within the aquifer. For all aquifers, we will henceforth denote the maximum exit temperature and the corresponding value of N by $\theta^*{}_{be}$ and N^*.

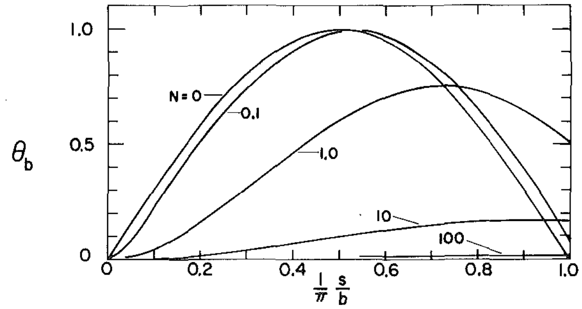

Fig. 3(a) Fluid bulk temperature profiles along the length of the thermosyphon

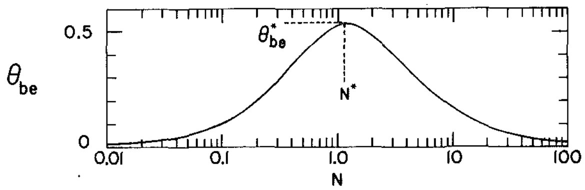

Fig. 3(b) Exit bulk temperature versus N

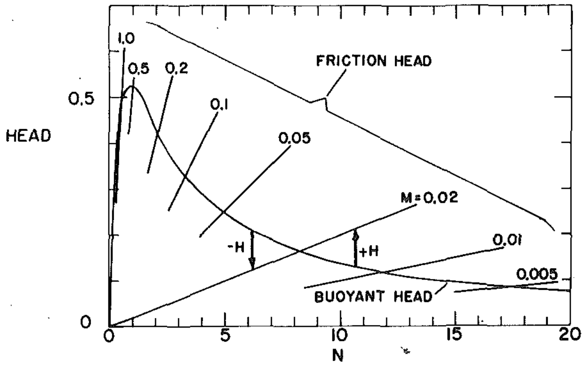

Fig. 3(c) The buoyant head and the friction head versus N

Fig. 3 Results for thermosyphons with aspect ratio $a/b = 1$. H, M and N are given by equations (7) and (8)

With θ_b given by equation (13), the force balance on the aquifer may be integrated to obtain

$$H - \frac{N}{1+N^2}\left[\left(\theta_{bi} + \frac{N}{1+N^2}\right)(e^{-\pi/N}+1) - \frac{\pi}{2}\right] = M\cdot N \qquad (14)$$

The various terms in this equation are shown graphically in Fig. 3(*c*). The curve peaking at $N = 0.92$ is the buoyant head (the second term in the equation). To this is added the topographic head, H. The sum of H and the buoyant head is, of course, the friction head, $M\cdot N$. The friction head is, in turn, represented by a family of straight lines of slope M emanating from the origin. The intersection of a friction line, such as $M = 0.02$, with the buoyant head represents a solution for H_* = 0. Values of N to the right or left of the intersection correspond to solutions with positive or negative topographic heads, as shown. For example, to the right of an intersection the topographic head supplements the buoyant head in order to overcome friction. Clearly, Fig. 3(*c*) provides a functional relationship between H, M, and N. Given two of the parameters, the third may be found from the figure.

The curve parameter M in Fig. 3(*c*) is essentially the ratio of the frictional resistance to the buoyant drive. As M is decreased for a given topographic head (say $H = 0$), the solution intersection moves to larger flow rates, N. On the other hand, increasing M (i.e., increasing friction or reducing buoyancy) leads to lower flow rates.

It is important to observe that an upper limit on the allowable range of M occurs for the case of zero topographic drive ($H = 0$). Above this limit, frictional forces suppress natural convection and flows do not exist. The upper limit occurs when the friction line is just tangent to the buoyant head curve at the origin in Fig. 3(*c*). The tangency condition is found by differentiation of equation (14) and yields the upper bound of

$$M \leq M_{\text{crit}} = \pi/2 \qquad (15)$$

This upper bound may be converted into a critical Rayleigh number for the onset of convection by using equations (8)

$$\text{Ra}_{\text{crit}} = 2f\frac{L}{b}\frac{\text{ReNu}}{M_{\text{crit}}} \qquad (16)$$

Clearly, natural convection flows can exist when Ra > Ra_{crit}, and are damped by friction when Ra < Ra_{crit}.

Note that a critical Rayleigh number does not appear when a finite topographic head exists (i.e., $H \neq 0$). Instead, flows may occur in either direction depending upon the sign of H. For $H > 0$ in Fig. 3(*c*), solutions are possible for all positive values of M. For $H < 0$ (negative topographic drive), solutions are possible for positive values of M only up to an upper limit. At that time, the flow reverses direction from that shown in Fig. 1.

The upper bound in (15) is independent of the particular flow regime within the aquifer. When converted to a Rayleigh number in (16), it becomes necessary to define the flow regime, and thus the friction and heat transfer characteristics in the aquifer. In general, flows near the onset of motion will be laminar. Accordingly, for an aquifer in the form of a smooth-walled circular duct, we may use expressions of the form $f = 64/\text{Re}$ and $\text{Nu} = 48/11$ [20]. Equation (16) thus becomes

$$\text{Ra}_{\text{crit}} = 558.5\frac{L}{b}\frac{1}{M_{\text{crit}}} \qquad (17)$$

and the dependence on Re cancels out. The value of Ra_{crit} for a semicircular aquifer with $L/b = \pi$ is 1117.1.

Influence of Aspect Ratio *a*/*b*. Results for aquifers with aspect ratios of $a/b = 0$ and 4 are shown by dashed and solid lines, respectively, in Fig. 4. The organization of this figure is similar to Fig. 3 of the previous section. Bulk temperature profiles are shown in Fig. 4(*a*), exit temperatures in 4(*b*), and buoyant, friction, and topographic heads in 4(*c*). The abscissa in Fig. 4(*a*) is s/L, where the aquifer length L is $2b$ for $a/b = 0$ and $8.58b$ for $a/b = 4$. All of the trends and observations discussed in the previous section also apply to Fig. 4. We thus need address only the influence of aspect ratio in this section.

The aspect ratios of 0 and 4 approximate the mathematical limits of very narrow, and of very wide, ellipses (see Fig. 2(*a*)). As such, their associated wall temperature profiles (labeled $N = 0$ in Fig. 4(*a*)) represent lower and upper bounds. For $a/b = 0$, the wall temperature varies linearly with depth, whereas for $a/b = 4$ the wall temperature is essentially a semicircle centered at $\theta_b = 0$, $s/L = 0.5$. Indeed, the asymptotic wall temperature profile as $a/b \to \infty$ is a semicircle. Of course, the case $a/b = 0$ is a drastic idealization since heat conduction through the country rock between the vertical legs would compromise the thermal performance of the aquifer.

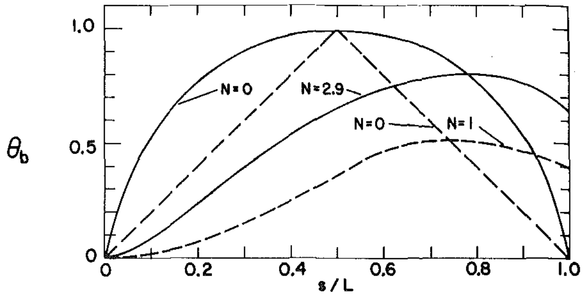

Fig. 4(*a*) Fluid bulk temperatures along the thermosyphon

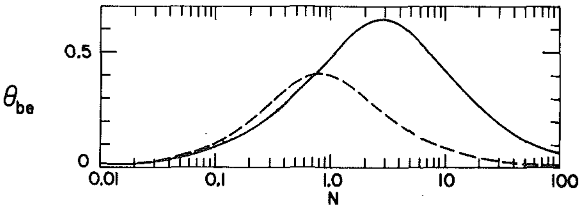

Fig. 4(*b*) Exit bulk temperatures

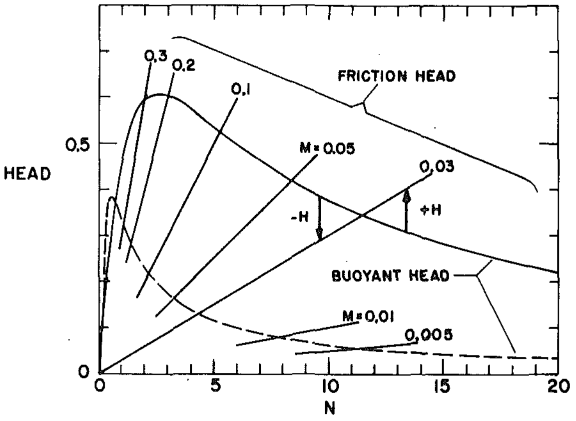

Fig. 4(*c*) Buoyant and friction heads

Fig. 4 Results for thermosyphons with aspect ratios of $a/b = 0$ (dashed lines) and $a/b = 4$ (solid curves)

For the case $a/b = 0$, the fluid energy equation (11) may be integrated to yield

$$\theta_b = (\theta_{bi} + N)e^{-(s/b)/N} + \left(\frac{s}{b} - N\right) \text{ for } 0 \leq \frac{s}{b} \leq 1 \qquad (18a)$$

$$\theta_b = (\theta_{bi} + N)e^{-(s/b)/N} - 2Ne^{-(s/b-1)/N} - \left(\frac{s}{b} - N - 2\right) \qquad (18b)$$

$$\text{for } 1 \leq \frac{s}{b} \leq 2$$

The dashed lines in Figs. 4(*a*) and 4(*b*) are based on the foregoing equations. The force balance may also be integrated to obtain

$$H - N[(\theta_{bi} + N)e^{-2/N} - 2(\theta_{bi} + 2N)e^{-1/N} + \theta_{bi} + 3N - 2] = M\cdot N \qquad (19)$$

The second term on the left is the buoyant head, which is shown by the dashed line in Fig. 4(*c*). The term on the right is the friction head, which is shown by a family of straight lines.

For the case $a/b = 4$, numerical solutions of the governing equations were obtained. Second order correct finite differences were used for equation (11), whereas trapezoidal rule integration was used for equation (10). The resulting temperature profiles and buoyant heads are shown with solid lines in Fig. 4. Numerical solutions were also obtained for other aspect ratios to be discussed later. In all cases, sufficient mesh points were used to assure an accuracy of 0.1 percent.

Comparison of the two aspect ratios shown in Fig. 4 reveals that generally higher exit temperatures are achieved for $a/b = 4$. This is apparent from the bell-shaped exit temperature variations in Fig. 4(*b*), where the peak occurs at a larger flow rate for $a/b = 4$. The bulk temperature profiles shown in Fig. 4(*a*) at $N = 1$ ($a/b = 0$) and $N = 2.9$ ($a/b = 4$) are essentially those which yield the maximum exit temperatures for these aspect ratios. The profile for $N = 2.9$ ($a/b = 4$) is within 0.03 ordinate units of the bulk temperature profiles which yield the maximum exit temperatures for all aspect ratios larger than 4. Consistent with the higher exit temperatures, the buoyant heads shown in Fig. 4(*c*) are larger for $a/b = 4$ than for $a/b = 0$. This implies that for a given value of N, a larger frictional resistance may be sustained for $a/b = 4$.

The influence of aspect ratio is displayed in yet another way in Fig. 5. This figure illustrates the maximum exit temperature from an aquifer, θ^*_{be}, the corresponding flow rate, N^*, and the parameter M_{crit}. The abscissa is the aspect ratio a/b. Asymptotes are shown by dashed lines. Clearly, the maximum exit temperature ranges from 0.407 for $a/b = 0$ to 0.688 for a/b large. The case $a/b = 4$ is seen to yield exit temperatures which are very close to the maximum achievable exit temperatures. Values of the parameter M_{crit} are useful for estimating critical Rayleigh numbers from (16) or (17). It is of interest to note that the exit temperature variations for all aspect ratios follow bell-shaped curves as in Figs. 3(*b*) and 4(*b*). When suitably normalized to the value and location of the peak (i.e., θ^*_{be} and N^*), the curves are quite similar in shape. The buoyant head distributions (Figs. 3(*c*) and 4(*c*)) may also be scaled to a roughly similar form by normalizing the head and N by θ^*_{be} and N^*.

Influence of a Horizontal Underground Section. Results in the previous section clearly establish that the fluid exit temperature from elliptical aquifers is limited to 0.688 of the country rock temperature at the bottom of the aquifer. However, some warm springs exceed this limit, particularly those where fluid ascends rapidly after a long residence time at depth.

It is thus reasonable to extend the present analytical model to the geometries shown in Figs. 2(*b*) and 2(*c*). In these sketches, a horizontal, underground section has been added between the ascending and descending legs. A split vertical pipe aquifer is shown in Fig. 2(*b*), and a split semicircular aquifer in Fig. 2(*c*). These two geometries admit of analytical solutions. However, in the interests of brevity the analytical solutions will not be presented. It is sufficient to note that the bulk temperatures in the descending legs are given by equations (18*a*) and (13), respectively, and that the bulk temperature varies exponentially along the horizontal, underground section according to

$$\frac{\theta_b - 1}{\theta_b' - 1} = e^{-(s'/b)/N} \qquad (20)$$

where θ_b' is the temperature at the start of the horizontal section, and s' is the distance along the section [19].

For long residence times in the horizontal section, the fluid temperature given by equation (20) equilibrates to the local rock temperature. Flow in the ascending leg will then start with $\theta_b = 1$. The resulting fluid bulk temperatures are shown in Figs. 6(*a*) and 6(*b*), where s'' is the distance measured along the ascending leg. The curves for $N = 0$ also represent the wall temperature profiles. Clearly, the exit temperatures approach unity as N is increased in both aquifers. Exit bulk temperatures are also shown in Fig. 6(*c*) for the split pipes, the split semicircle, and a split 4:1 ellipse. In all cases, the exit temperatures approach unity as N is increased. This is in contrast to the bell-shaped curves in Figs. 3(*b*) and 4(*b*). It is thus possible to achieve high exit temperatures when a horizontal section is added at the bottom of an aquifer.

Application

The aquifer model will now be applied to the Virginia thermal springs region of the Appalachian Mountains of the Southeastern United States. The underlying terrain is folded with many synclines and antisynclines, and with embedded permeable layers which can act as aquifers. As a result of erosion, many of the permeable beds are now exposed at the rising, or antisynclinal points. There are no known magmatic intrusions nearby and a normal geothermal gradient exists.

The Virginia warm springs have been cataloged by Reeves [21] who provides information on the outlet temperatures, flow rates, and structural geology. His structural cross-sections show several synclines with embedded permeable layers and associated warm springs which closely resemble Fig. 1 of this paper. Reeves notes that the local

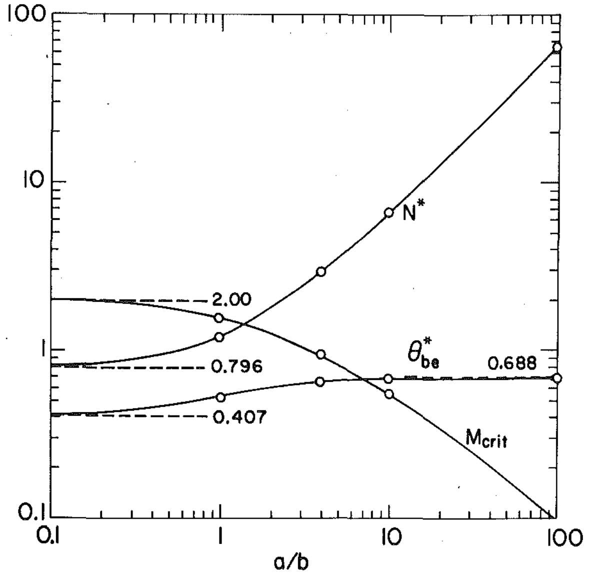

Fig. 5 The maximum exit temperature, θ^*_{be}, the corresponding flow rate, N^*, and the maximum value of the parameter M, M_{crit}, versus aspect ratio

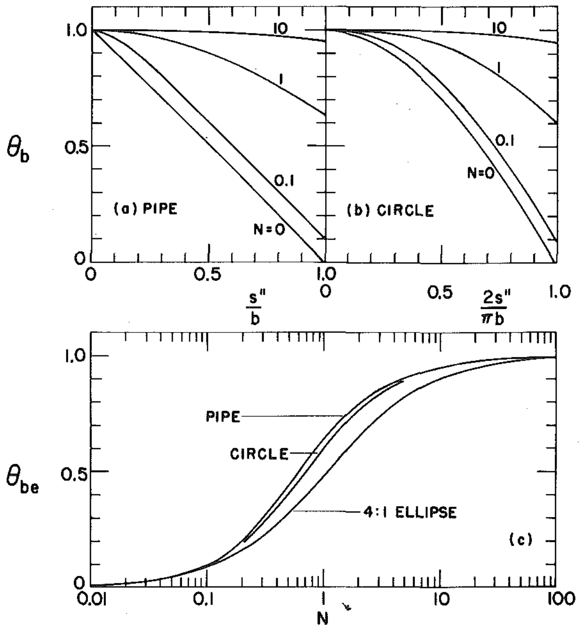

Fig. 6 Results for the ascending leg of a thermosyphon which starts with fluid at $\theta_b = 1$. (*a*) Bulk temperature profiles for the thermosyphon in Fig. 2(*b*); (*b*) Bulk temperature profiles for the thermosyphon in Fig. 2(*c*); (*c*) Exit temperatures versus N for three split thermosyphons

scarcity of vertical thrust faults has left many of the permeable beds uninterrupted, and this undoubtedly accounts for the large number of warm springs. Reeves attributes the warm springs to a topographic head difference between inlet and outlet. However, his cross sections suggest that this head is very small.

We would like now to examine whether buoyant drive is a reasonable explanation for the warm springs. We will select a spring for which a structural profile is available: the Bolar Spring near Bolar, Virginia. This spring has a high flow rate (0.16 m^3/s or 2500 gal/min) and a high exit temperature (20°C) for the region, and should provide a test of the buoyant drive mechanism. The aquifer depth b is 1.67 km, the mean surface temperature T_0 is 10°C, and the geothermal gradient $(dT/dz)_\infty$ is 30°C/km

Consistent with the structural profile of the Bolar Spring, the aquifer is modeled as a thin permeable layer of thickness d whose transect is as shown in Fig. 1. The aquifer width normal to the figure is denoted by ℓ. The cross-sectional area and flow perimeter are thus $A = d \cdot \ell$ and $P = 2d + 2\ell$. The friction factor for a permeable layer may be reformulated in terms of Darcy's law [22] to yield

$$f = 8\frac{\nu_f}{k}\frac{A}{P}\frac{1}{\overline{u}} \tag{21}$$

A permeability, k, of 5×10^{-9} m^2 is assumed. This value is appropriate for the fractured layers described by Reeves [21] assuming a 1 percent porosity and mean crack openings of 2.5 mm. For comparison, limestone and sandstone are relatively impermeable with permeabilities of about 10^{-17} m^2 and 10^{-16} m^2, respectively. The heat transfer coefficient may be estimated assuming slug flow in the aquifer and a prescribed heat flux at the aquifer-country rock boundary [20]. The appropriate estimate for channel flow is

$$\mathrm{Nu} = \frac{h_c d_h}{\lambda_m} = 4 \tag{22}$$

where the aquifer thermal conductivity is taken to be that of a water-saturated limestone layer, $\lambda_m = 2.3$ W/m K. All fluid properties appearing in the governing equations are evaluated at a mean temperature of 35°C.

With the physical data and aquifer model just stated, we may now proceed to find three parameters which remain unspecified. These are the mean velocity $\overline{u}$ in the aquifer and the flow cross sectional dimensions d by ℓ. We will take the aquifer aspect ratio a/b to be unity, and will obtain a graphical solution from Fig. 3. The solution proceeds as follows. With the dimensionless outlet temperature of $\theta_{be} = 0.2$ known, Fig. 3(b) yields the upper and lower branch solutions of $N = 0.2$ and $N = 8$. Moving to Fig. 3(c) (or to equation (14)) with these values, we find corresponding values for the buoyant head to be 0.26 and 0.16. If we then neglect the topographic head (i.e., take $H = 0$), the buoyant head equals the friction head, $M \cdot N$. Thus, the implied values of slope of the friction line are $M = 1.3$ and 0.02. Both of these values are below the upper bound at this aspect ratio (equation (15)). With $M \cdot N$ known, the middle equation of (7) and equation (21) may be combined to find $\overline{u}$. The implied mean velocities are $\overline{u} = 5.2 \times 10^{-5}$ m/s and 3.2×10^{-5} m/s. We next combine the last equation in (7) with (22), assume the aquifer is thin compared with its width ($d < \ell$), and find the aquifer thickness corresponding to the two branch solutions to be $d = 3.8$ m and 30 m. With $\overline{u}$ found and the total flow rate known, the continuity equation may be used to find the implied aquifer widths ℓ of 815 m and 164 m.

Clearly both branch solutions appear realistic. They yield similar mean velocities since the $M \cdot N$ products for the two solutions are similar. They thus differ only in the dimensions d and ℓ of the cross-sectional area for flow. The permeable aquifer which supplies Bolar Spring has a thickness d of about 30 m. The width ℓ is determined by the distance between thermal springs, which in this region is about 1.2 km. We thus conclude that the upper branch solution is the appropriate one, and that a purely buoyant drive is sufficient to pump the observed spring discharge.

We may also note that the proposed aquifer model assumes a large thermal conductivity for the surrounding country rock. When heat transfer to the aquifer is limited by heat conduction in the surrounding rock, the thermal output of the warm spring will be reduced. The net effect will be to require a greater flow area within the aquifer to produce the observed volume flow rate. We see that additional flow width is possible near the upper branch solution.

We also observe that 20 percent of the warm springs in the Virginia thermal region have higher outlet temperatures (T_{be} of 35–40°C) than Bolar Spring. However, their flow rates are generally less than half of that at Bolar. Since the maximum depth of all springs in the region is probably about 1.67 km [21], dimensionless exit temperatures of θ_{be} between 0.5 and 0.6 are implied. Clearly, from Fig. 5, such exit temperatures would require any elliptical aquifer to be performing at conditions near to those for the peak exit temperature. It is unlikely that solutions near the peak should occur very often. Another explanation is therefore required. The structural geology suggests that several of the warmer springs look more like the sketch in Fig. 2(c) than those in Fig. 2(a). When longer residence times at depth b in the aquifer exist, the solutions in Fig. 6 may be used as upper bounds on the exit temperatures. Clearly, from Fig. 6(c), exit temperatures of 0.5 to 0.6 or more may be achieved for flow rates N which are not substantially different from the $N = 8$ upper branch solution for Bolar Spring. The aquifer model displayed in Fig. 6 is thus required in order to explain the higher exit temperatures.

Conclusions

An open-loop thermosyphon model has been outlined. Solutions for the flow rate and exit temperature are given for elliptical thermosyphons in Figs. 3–5. The formulation shows that unique values exist for the maximum exit temperature and for the critical Rayleigh number at the onset of convection. These results are applicable to a broad class of thermosyphon flows. The maximum possible exit temperature is found to be 0.688 of the temperature at the bottom of an elliptical thermosyphon. Higher exit temperatures require long residence times at or near the maximum depth of the syphon.

The predictions of the model are in reasonable accord with exit temperatures and flow rates observed for warm springs in the Virginia thermal springs region. Although the qualitative features of the model appear dynamically correct, further refinements are needed to allow for heat conduction effects in the country rock surrounding an aquifer.

Acknowledgments

This research has been supported by the Division of Engineering of the National Science Foundation under Grant ENG 76-11821 and by the Earth Sciences Section of the National Science Foundation under Grant EAR 76-82556.

References

1 Japikse, D., "Advances in Thermosyphon Technology," in *Advances in Heat Transfer,* edited by Irvine, T. F., Jr. and Hartnett, J. P., Vol. 9, Academic Press, New York, 1973, pp. 1–111.

2 Waring, G. A., "Thermal Springs of the United States and Other Countries of the World—a Summary," *U. S. Geological Survey, Prof. Paper 492,* 1965.

3 Crane, K. and Normark, W. R., "Hydrothermal Activity and Crestal Structure of the East Pacific Rise at 21°N," *J. Geophys. Res.*, Vol. 82, 1977, pp. 5336–5348.

4 Corliss, J. B., Dymond, J., Gordon, L. I., Edmond, J. M., von Herzen, R. P., Ballard, R. D., Green, K., Williams, D., Bainbridge, A., Crane, K., and van Andel, T. H., "Submarine Thermal Springs on the Galápagos Rift," *Science,* Vol. 203, 1979, pp. 1073–1083.

5 Donaldson, I. G., "Temperature Gradients in the Upper Layers of the Earth's Crust Due to Convective Water Flows," *J. Geophys. Res.*, Vol. 67, 1962, pp. 3449–3459.

6 Elder, J. W., "Steady Free Convection in a Porous Medium Heated from Below," *J. Fluid Mech.*, Vol. 27, 1967, pp. 29–48.

7 Turcotte, D. L., Ribando, R. J. and Torrance, K. E., "Numerical Calculations of Two-Temperature Thermal Convection in a Permeable Layer with Application to the Steamboat Springs Thermal System, Nevada," in *The Earth's Crust,* edited by Hancock, J. G., Monograph 20, American Geophysical Union, Washington, D. C., 1977, pp. 722–736.

8 Lister, C. R. B., "On the Thermal Balance of a Mid-Ocean Ridge," *Geophys. J. Roy. Astron. Soc.*, Vol. 26, 1972, pp. 515–535.

9 Wolery, T. J. and Sleep, N. H., "Hydrothermal Circulation and Geochemical Flux at Mid-Ocean Ridges," *J. Geol.*, Vol. 84, 1976, pp. 249–275.

10 Ribando, R. J., Torrance, K. E. and Turcotte, D. L., "Numerical Models

for Hydrothermal Circulation in the Oceanic Crust," *J. Geophys. Res.*, Vol. 81, 1976, pp. 3007–3012.

11 Donaldson, I. G., "The Simulation of Geothermal Systems with a Simple Convective Model," in *U.N. Symp. on the Development and Utilization of Geothermal Resources, Pisa*, Vol. 2, Pt. 1, 1970, pp. 649–654.

12 Bodvarsson, G. and Lowell, R. P., "Ocean-Floor Heat Flow and the Circulation of Interstitial Waters," *J. Geophys. Res.*, Vol. 77, 1972, pp. 4472–4475.

13 Lowell, R. P., "Circulation in Fractures, Hot Springs and Convective Heat Transport on Mid-Ocean Ridge Crests," *Geophys. J. Roy. Astron. Soc.*, Vol. 40, 1975, pp. 351–365.

14 Boy-Marcotte, J. L., Chevalier, P., and Jannot, M., "Study of Temperature Gradients Due to Gas Thermosyphons Induced Within the Phenix Nuclear Reactor," in *Heat Transfer and Turbulent Buoyant Convection*, edited by Spalding, D. B. and Afgan, N., Vol. II, Hemisphere-McGraw-Hill, New York, 1977, pp. 555–565.

15 Lapin, Y. D., "Heat Transfer in Communicating Channels Under Conditions of Free Convection," *Thermal Engineering*, Vol. 16, 1969, pp. 94–97.

16 Damerell, P. S. and Schoenhals, R. J., "Flow in a Toroidal Thermosyphon with Angular Displacement of Heated and Cooled Sections," ASME Paper 78-HT-44, 1978.

17 Creveling, H. F., dePaz, J. F., Baladi, J. Y., and Schoenhals, R. J., "Stability Characteristics of a Single-Phase Free Convection Loop," *J. Fluid Mech.*, Vol. 67, 1975, pp. 65–84.

18 Chexal, V. K. and Bergles, A. E., "Two-Phase Instabilities in a Low Pressure Natural Circulation Loop," *AIChE Symp. Series*, Vol. 69, No. 131, 1974, pp. 37–45.

19 Kreith, F., *Principles of Heat Transfer*, Third Edition, Intext, New York, 1973, pp. 563–565.

20 Eckert, E. R. G. and Drake, R. M., Jr., *Analysis of Heat and Mass Transfer*, McGraw-Hill, New York, 1972, pp. 331, 340 and 442.

21 Reeves, F., "Thermal Springs of Virginia," *Bull. 36*, Virginia Geological Survey, Charlottesville, 1932, 56 p.

22 Bear, J., *Dynamics of Fluids in Porous Media*, American Elsevier, New York, 1972, p. 164.

R. Greif
Department of Mechanical Engineering,
University of California,
Berkeley, CA 94720

Y. Zvirin
Faculty of Mechanical Engineering,
Technion-Israel Institute of Technology,
Haifa, Israel

A. Mertol
Department of Mechanical Engineering,
University of California,
Berkeley, CA 94720

The Transient and Stability Behavior of a Natural Convection Loop

A study has been made of the transient flow and energy transfer in a natural convection loop. In particular, a toroidal thermosyphon has been considered with orientation in a vertical plane that is heated over the lower half and cooled in the upper half. The basic conservation equations have been solved and the velocity and temperature distributions have been obtained which elucidate the phenomena in natural convection loops. The results include stable, as well as unstable configurations.

Introduction

Natural convection loops (thermosyphons), created by heating fluids from below and cooling them from above, appear in geophysical phenomena as well as in such practical engineering systems as solar heaters. Some of the previous studies on natural circulation loops were concerned with the stability of the steady-state motion, including the early analyses of Keller [1] and Welander [2], which were applicable to a point heat source, point heat sink loop with two vertical branches. The work of Creveling, et al. [3] and Damerell and Schoenhals [4] considered a toroidal loop and demonstrated, experimentally and theoretically, the presence and importance of instabilities. Zvirin, Shitzer and Grossman [5] and Zvirin, et al. [6] studied the stability characteristics of the common thermosyphonic solar water heater and showed that this system can become unstable at high energy utilizations. Jasinsky and Buckley [7] investigated a thermic diode solar heater where the solar collector and the storage tank are incorporated into the same unit. Zvirin [8] studied the effects of dissipation on the steady state and stability of thermosyphons.

Studies of the transient behavior of loops have been carried out by Ong [9] and by Zvirin and Greif [10]. Both studies utilized approximate methods and did not emphasize stability characteristics. Welander [2] presented some results for numerical calculations of transients in the point heat source, point heat sink loop. The results show the correct stability characteristics although there is little information provided concerning the numerical procedures. In this work, a toroidal loop is considered that is oriented in a vertical plane and is heated over the lower half and cooled on the upper half (cf. Fig. 1). This system is referred to as a toroidal thermosyphon. The basic conservation equations which describe the transient flow and energy transfer in the loop are solved and the velocity and temperature distributions are obtained. The results include stable as well as unstable configurations.

Analysis

The analysis which follows is for the determination of the transient velocity and temperature profiles in a toroidal thermosyphon. The loop is heated continuously by a constant heat flux q over the bottom half of its area and is cooled continuously over the top half (cf. Fig. 1). For the cooled region, a constant wall temperature, T_w, and a constant heat transfer coefficient, h, are taken. The conservation equations are applied to a cylindrical control volume that is of diameter $2r$ and of length $Rd\theta$. Variations in the radial direction are not considered so that the temperature and velocity are values that are averaged over the cross section and the only space coordinate, θ, runs along the loop (cf. [3]). Axial conduction and viscous dissipation are neglected along with effects of curvature. The flow is taken to be laminar and the fluid properties are considered to be constant except for the evaluation of the density in producing buoyancy. For this term only, the density is assumed to vary linearly with temperature.

From the equation of continuity for one-dimensional incompressible flow, we have that the velocity is a function of time only:

$$v = v(t) \tag{1}$$

The momentum equation in the θ direction is given by

$$\rho\pi r^2 Rd\theta\frac{dv}{dt} = -\pi r^2 d\theta\frac{dp}{d\theta} - \rho g\pi r^2 Rd\theta\cos\theta - \tau_w 2\pi rRd\theta \tag{2}$$

Integrating this equation around the loop and using the relation $\rho = \rho_w[1 - \beta(T - T_w)]$ in the body force term in equation (2) yields

$$\rho_w\frac{dv}{dt} = \frac{g\rho_w\beta}{2\pi}\int_0^{2\pi}(T - T_w)\cos\theta\, d\theta - \frac{2\tau_w}{r} \tag{3}$$

To solve for the velocity from equation (3) it is necessary to obtain the temperature variation, $T(\theta, t)$. The energy equations for the heated lower and cooled upper regions are given by

$$\rho_w c\left(\frac{\partial T}{\partial t} + \frac{v}{R}\frac{\partial T}{\partial\theta}\right) = \begin{cases} -\dfrac{2h}{r}(T - T_w),\ 0 < \theta < \pi & (4a) \\ \dfrac{2}{r}q,\ \pi < \theta < 2\pi & (4b) \end{cases}$$

Note that the solution for the velocity and the temperature must be obtained by solving equations (3) and (4) simultaneously.

The governing equations are made dimensionless according to the following definitions:

$$\phi = \frac{T - T_w}{q/h},\ w = \frac{v}{V},\ \tau = \frac{t}{2\pi R/V} \tag{5}$$

where V is the characteristic velocity defined by Creveling, et al. [3]:

$$V = \left(\frac{g\beta Rrq}{2\pi c\mu}\right)^{1/2} \tag{6}$$

The wall shear stress in equation (3) is expressed as $\tau_w = {}^1\!/_2 f\rho_w v^2$ where the friction coefficient for laminar flow is given by $f = 16/\mathrm{Re}$ with $\mathrm{Re} = \rho_w v 2r/\mu$.

The dimensionless forms of equations (3) and (4) then become

$$\frac{dw}{d\tau} + \Gamma w = \frac{\pi\Gamma}{4D}\int_0^{2\pi}\phi\cos\theta d\theta \tag{7}$$

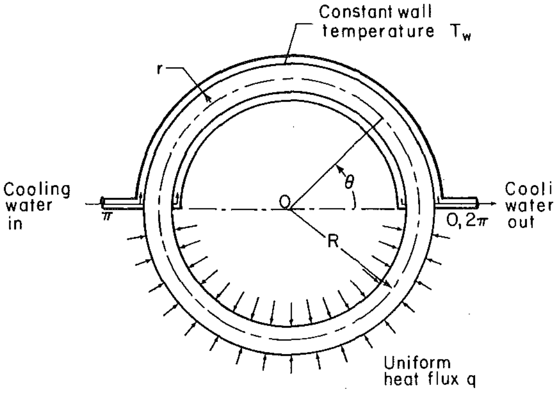

Fig. 1 The circular, toroidal natural circulation loop

Contributed by the Heat Transfer Division for publication in the JOURNAL OF HEAT TRANSFER. Manuscript received by the Heat Transfer Division January 31, 1979.

and

$$\frac{\partial\phi}{\partial\tau} + 2\pi w\frac{\partial\phi}{\partial\theta} = \begin{cases} -2D\phi, 0 < \theta < \pi & (8a) \\ 2D, \pi < \theta < 2\pi & (8b) \end{cases}$$

where the parameters D and Γ are defined by

$$D = \frac{2\pi Rh}{\rho_w crV}, \Gamma = \frac{16\pi\mu R}{\rho_w r^2 V} \quad (9)$$

Γ is related to the parameter E of Creveling, et al. [3] according to $\Gamma = 32\pi/E$.

Steady-State Solution

The steady-state temperature profile is obtained by solving equations (8a) and (8b) with $\partial\phi/\partial\tau = 0$, subject to the condition that the temperature is continuous at $\theta = 0, 2\pi$ and at $\theta = \pi^-, \pi^+$, so that $\phi(0) = \phi(2\pi)$ and $\phi(\pi^-) = \phi(\pi^+)$. The results are (cf. [3]):

$$\phi(\theta) = \phi_{ss} = \begin{cases} \dfrac{D}{w_{ss}}\dfrac{e^{-(D\theta/w_{ss}\pi)}}{1 - e^{-(D/w_{ss})}}, 0 \leqslant \theta \leqslant \pi & (10a) \\ \dfrac{D}{w_{ss}}\left[\dfrac{\theta}{\pi} + \dfrac{2e^{-(D/w_{ss})} - 1}{1 - e^{-(D/w_{ss})}}\right], \pi \leqslant \theta \leqslant 2\pi & (10b) \end{cases}$$

where ϕ_{ss} and w_{ss} denote the steady-state values of the temperature and the velocity, respectively. Substituting equations (10a) and (10b) into the momentum equation (7), with $dw/d\tau = 0$ yields:

$$w_{ss}{}^2 = \frac{1}{2} + \frac{(D/w_{ss})[1 + e^{-(D/w_{ss})}]}{4[1 + (D/\pi w_{ss})^2][1 - e^{-(D/w_{ss})}]} \quad (11)$$

Note that the steady-state values of the velocity depend only on D and the temperature on D and θ. The values are tabulated in Table 1. For small values of D, $w_{ss} = v_{ss}/V \approx 1$.

Method of Solution

The governing equations, equations (7, 8a) and (8b) have been solved numerically using a finite difference method to calculate the spatial and temporal variation of the temperature and the temporal variation of the velocity. The backward difference formula was used in the spatial derivatives and the forward difference formula was used in the temporal derivatives. The integral in equation (7) was evaluated by using the trapezoidal rule. The equations solved are given by

$$w_{n+1} = w_n(1 - \Gamma\Delta\tau) + \frac{\pi}{4}\frac{\Gamma}{D}\left\{\frac{1}{2}\phi_{0,n+1}\cos(0) + \sum_{i=1}^{M-1}\phi_{i,n+1}\cos(i\Delta\theta) + \frac{1}{2}\phi_{M,n+1}\cos(M\Delta\theta)\right\}\Delta\theta\Delta\tau \quad (12)$$

$$\phi_{i,n+1} = \phi_{i,n}\left(1 - 2D\Delta\tau - 2\pi w_n\frac{\Delta\tau}{\Delta\theta}\right) + 2\pi w_n\phi_{i-1,n}\frac{\Delta\tau}{\Delta\theta}, 0 \leqslant \theta \leqslant \pi \quad (13)$$

$$\phi_{i,n+1} = \phi_{i,n}\left(1 - 2\pi w_n\frac{\Delta\tau}{\Delta\theta}\right) + 2\pi w_n\phi_{i-1,n}\frac{\Delta\tau}{\Delta\theta} + 2D\Delta\tau, \pi \leqslant \theta \leqslant 2\pi \quad (14)$$

where $\theta = i\Delta\theta$, $2\pi = M\Delta\theta$ and $\tau = n\Delta\tau$. The initial conditions are specified and the boundary conditions are given by

$$\phi(0, \tau) = \phi(2\pi, \tau), \phi(\pi^-, \tau) = \phi(\pi^+, \tau) \quad (15)$$

Table 1 Steady-state velocities and temperatures

		$\phi_{ss}(\theta)$				
D	w_{ss}	$\theta = 0, 2\pi$	$\theta = \pi/2$	$\theta = \pi$	$\theta = 3\pi/2$	$\phi_{ss}(0) - \phi_{ss}(\pi)$
0.01	1.000	1.005	1.000	0.995	1.000	0.010
0.1	1.000	1.051	1.000	0.951	1.000	0.100
1.0	0.996	1.585	0.959	0.580	1.083	1.005
2.5	0.974	2.780	0.770	0.214	1.497	2.566
10.0	0.832	12.019	0.030	0.000	6.010	12.019

The time and space increments were chosen so as to satisfy the stability criteria of the numerical procedure and are given by:

$$1 - \Gamma\Delta\tau \geqslant 0 \quad (16a)$$

$$1 - 2D\Delta\tau - 2\pi w_n\frac{\Delta\tau}{\Delta\theta} \geqslant 0 \quad (16b)$$

$$1 - 2\pi w_n\frac{\Delta\tau}{\Delta\theta} \geqslant 0 \quad (16c)$$

A time increment of 0.01 was used and a space increment of $\Delta\theta$ equal to $2\pi/60$ or $2\pi/80$ was chosen depending on the particular parameter being considered.

Results and Discussion

Calculations were begun at time $\tau = 0$ for a specified velocity in the counter-clockwise direction, and a specified initial temperature distribution, in conjunction with constant heating over the lower half of the loop, $\pi \leqslant \theta \leqslant 2\pi$. As the fluid emerges at $\theta = 2\pi$ (or $\theta = 0$) from the heated region, it cools by convection to the cold wall which is maintained at a constant temperature over the range $0 \leqslant \theta \leqslant \pi$. Note that the cold fluid entering at $\theta = \pi$ is heated in the lower region. Typical results for the temperature for values of $\Gamma = 1$, $D = 2.5$, an initial temperature profile $\phi_i = 0$ and an initial valocity $w_i = 1.5$, are shown in Fig. 2. The corresponding variation of the velocity is shown in Fig. 3 along with results for other values of the initial velocity.

In Fig. 2, it is seen that for small times there is a thermal penetration depth in the cooled region ($0 \leqslant \theta \leqslant \pi$) beyond which there is no heating effect. Similarly, for small times, there is a thermal penetration depth in the heated region ($\pi \leqslant \theta \leqslant 2\pi$) beyond which there is no cooling effect—resulting from the incoming fluid at $\theta = \pi$. Indeed, this follows directly from a formal solution to equations (8a) and (8b) for small times. This was carried out (cf. Appendix) and good agreement was obtained between the results obtained from a formal solution to equations (8a) and (8b) and those obtained from equations (13) and (14).

Results for larger times, as well as for small times, for the case $\Gamma = 1$, $D = 2.5$, $\phi_i = 0$ and $w_i = 1.5$ are also shown in Fig. 2 for the temperature. Calculations were also carried out over a range of values of the initial velocity and the results are shown in Figs. 4(a) and 4(b) for the temperature and in Fig. 3 for the velocity. It is seen that for all the cases considered, the initial temporal variation of the velocity is de-

Nomenclature

c = specific heat
D = dimensionless parameter, equation (9)
E = dimensionless parameter, equal to $32\pi/\Gamma$
f = friction coefficient = $2\tau_w/\rho_w v^2$
g = acceleration of gravity
h = heat-transfer coefficient per unit of length
M = total number of grids
p = pressure
q = heat flux
R = radius of the circular loop, Fig. 1
Re = Reynolds number
r = radius of the toroid, Fig. 1
T = temperature
t = time
V = characteristic velocity, equation (6)
v = velocity of the fluid
w = dimensionless velocity, equation (5)
β = thermal expansion coefficient
Γ = dimensionless parameter, equation (9)
θ = space coordinate, Fig. 1
θ_p = thermal penetration depth
ϕ = dimensionless temperature, equation (5)
μ = absolute viscosity
ρ_w = reference density
τ = dimensionless time, equation (5)
τ_w = shear stress

Subscripts

0 = location at $\theta = 0$
i = initial value, space step in the finite difference equations
M = location at $\theta = 2\pi$
n = time step in the finite difference equations
ss = steady state
w = wall

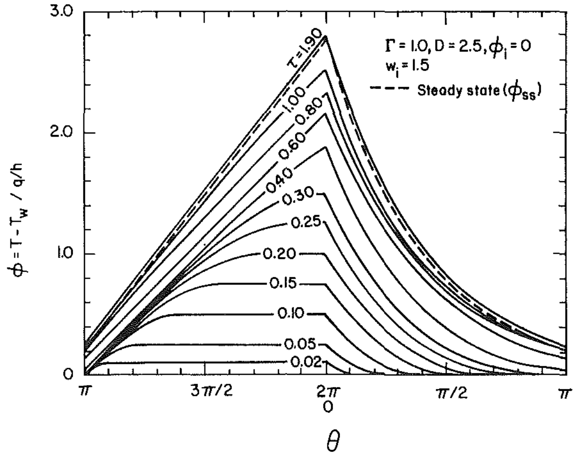

Fig. 2 Temperature distribution at different times for stable condition

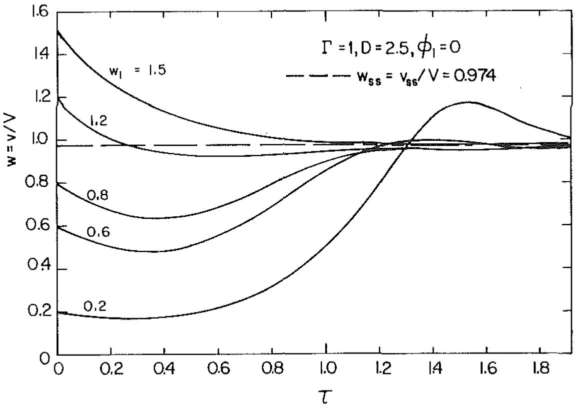

Fig. 3 Velocity variation for different initial velocities for stable condition

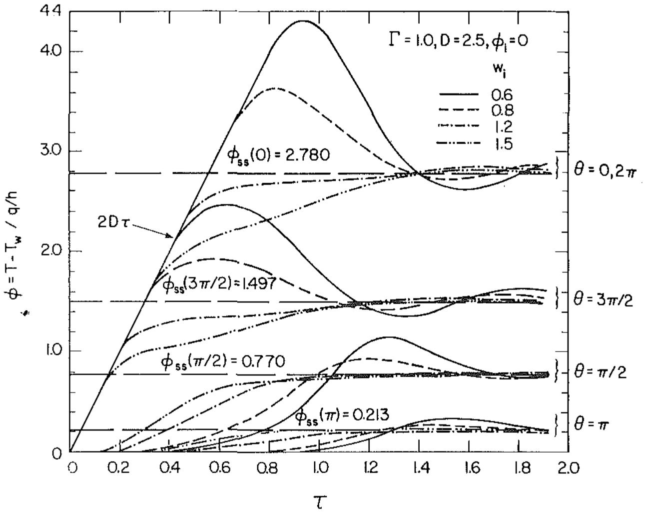

Fig. 4(*a*) Temperature variation for different initial velocities for stable condition

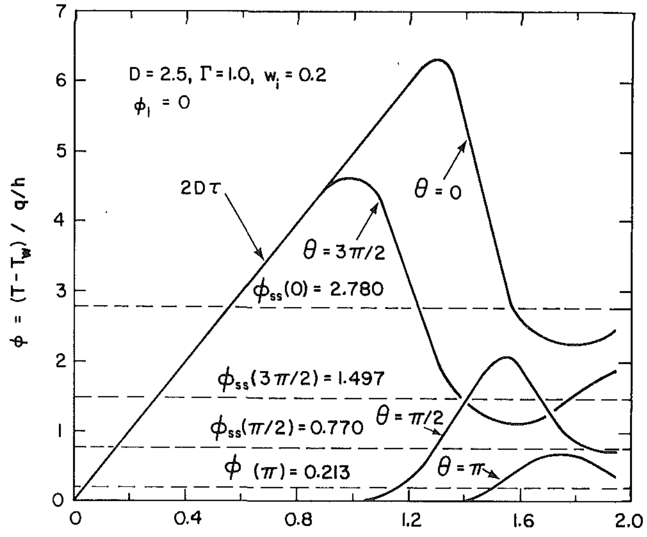

Fig. 4(*b*) Temperature variations for a small initial velocity (w_i = 0.2) for stable condition

creasing. For values of $w_i/w_{ss} < 1$ this causes, for small times, an increasing disparity between the instantaneous value w/w_{ss} and the steady-state value $w/w_{ss} = 1$. The velocity then increases and for cases with small w_i there is substantial overshooting of the steady-state value, that is $w/w_{ss} > 1$. This in turn is accompanied by a large overshoot in the temperature, that is, $\phi/\phi_{ss} > 1$ as is shown at four locations in Fig. 4(*a*) (cf. $w_i = 0.6$ case) and Fig. 4(*b*). Obviously, when the velocity decreases the heat source becomes "more effective" in heating the fluid. The temperature overshoot is very large for the small values of w_i (cf. Fig. 4(*b*) and note the scale). The overshoots in velocity and temperature are not in phase. The temperatures and velocities oscillate about the steady state values with decreasing amplitude.

Another interesting result is the appearance of a "kink" in the temperature versus time profiles for large values of w_i, (cf. Fig. 4). This is due to the arrival of the thermal signals which cause, in the heated region, a drop in the rate at which the temperature rises. At a later time[1] this rate is increased due to the arrival now of warmer fluid that had been heated and is now at the particular location being considered. A similar discussion holds for the cooled region.

The above results are characteristic of flows which approach the steady state values and are designated as stable flows. As mentioned earlier, the steady-state motion and the stability characteristics of the toroidal loop have been studied experimentally and theoretically by Creveling, et al. [3]. They obtained and used the following results for the friction factor, *f*, for steady laminar and turbulent flows:

$$f = \frac{a}{\mathrm{Re}^b}\begin{cases}\text{laminar flow: } a = 151, b = 1.17\\ \text{turbulent flow: } a = 0.88, b = 0.45\end{cases} \tag{17}$$

However, in a recent study with the same system, Damerell and Schoenhals [4] used the fully developed laminar result *f* = 64/Re (16/Re in our notation) to analyze the flow. The present study is for laminar flow and the friction factor was taken to be 16/Re in determining the dynamic behavior of the loop.[2] Results have been reported [1–3, 8] for unstable cases where the flow and temperature oscillate with increasing amplitude as well as for neutrally stable cases where the magnitude of the oscillations about the steady-state value remain constant. Creveling, et al. [3] and Zvirin [8] analyzed the stability of the toroidal loop by superposing small disturbances upon the steady state conditions and solving for the resulting flow. They obtained marginal or neutral stability curves using linearized stability analysis where the friction factor *f* in [3] was based on their experimental results as given in equation (17) while the relation *f* = 16/Re was used in [8]. These two neutral stability curves are presented in Fig. 5. Note that points to the right of the specific neutral stability curve are stable, points to the left are unstable.

Calculations were carried out in the present work based on the finite difference equations using the steady-state temperature distributions and small perturbations from the steady-state values of the velocity as the initial conditions with *f* = 16/Re. Results from these calculations are in agreement with the linearized stability analysis as shown in Fig. 5 by the stable and unstable points denoted by *S* and *U*, respectively.

---

[1] Half a cycle at $\theta = \pi +$, three-fourths of a cycle at $\theta = 3\pi/2$, full cycle at $\theta = 2\pi -$.

[2] It is noted that there are apparently no data reported for the friction factor during the transient period.

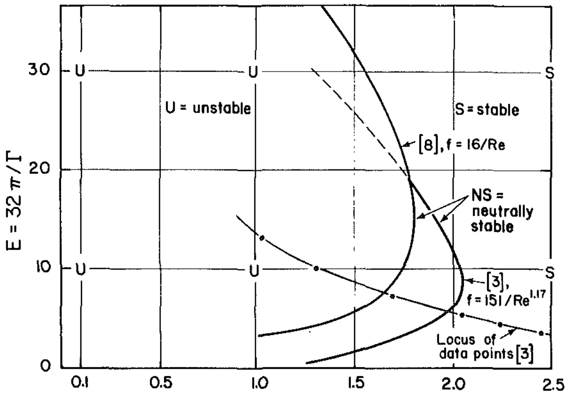

Fig. 5 Stability map for laminar flow

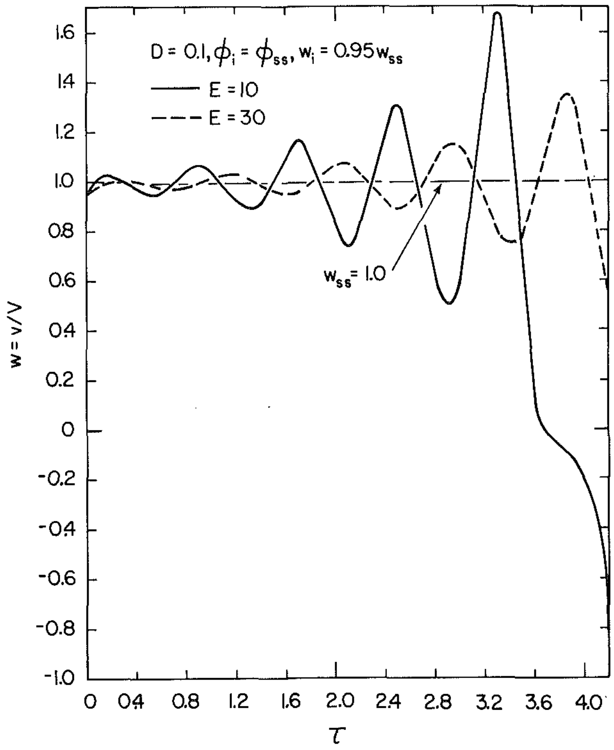

Fig. 6 Velocity variation for unstable condition

Unstable points far from the neutral stability curve exhibit the anomalous condition of a "pocket" of fluid in the cooled region at $\theta = 0+$ being at a higher temperature than the fluid in the heated section; a corresponding cold pocket exists in the heated region at $\theta = \pi+$. This then leads to the oscillations of increasing amplitude which characterize the unstable condition. Welander [2] and Creveling, et al. [3] postulated that a hotter-than-normal pocket at $\theta = 0+$ would proceed more rapidly than is usual (due to the increased buoyancy) through the cooled section so that, by the time the pocket re-entered the heated section at $\theta = \pi+$, it would be at a temperature that is higher than normal. In this region, the pocket would then have a decreased buoyancy which would cause a movement that is slower than usual. Thus, when it finally emerged from the heated section at $\theta = 0+$, it would be even hotter than before, would move still more rapidly through the cooled section, and the process would be repeated again. A similar description holds for a cold pocket that originates in the entrance to the heated region. This discussion is in accord with the calculated build-up of oscillations as shown in Figs. 6 and 7. Note that the results show that the period of the oscillations is approximately equal to the time required for an element of fluid to circulate once around the loop, $\Delta\tau \sim 1$ for $w_{ss} \sim 1$ (see equation (5)), which is in accord with the observations of Creveling, et al. [3].

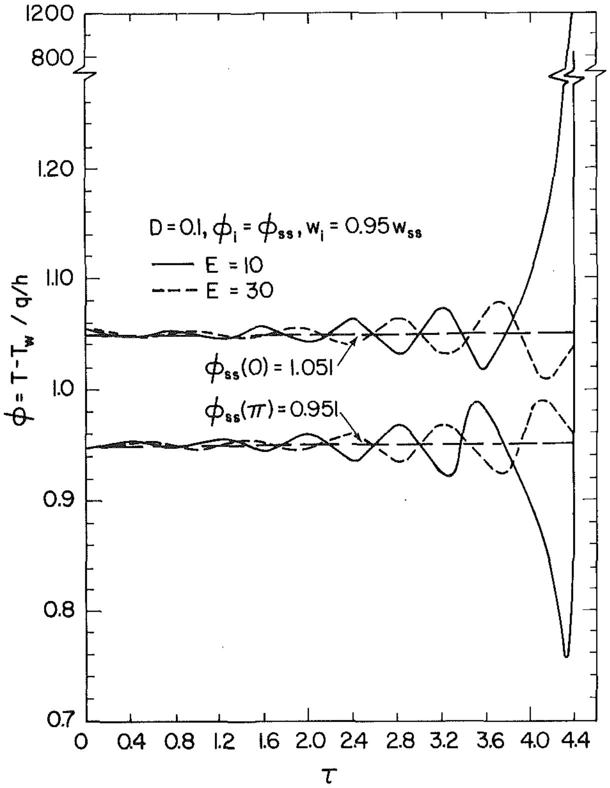

Fig. 7 Temperature variation for unstable condition

For all the unstable cases, the temperature difference, $\phi(0, \tau) - \phi(\pi, \tau)$, becomes negative, giving the anomalous result that the fluid leaving the heated region is cooler than the fluid entering the heated region. Ultimately, there would be a flow reversal, but the flow direction and heating effect (as manifested by the cited temperature difference) would not necessarily be in phase.

Calculations were also carried out in the region close to the neutral stability curve in Fig. 5. In this region, the magnitude of the oscillations about the steady state value remain constant, which is consistent with the linearized analysis, and typical results are shown in Figs. 8 and 9.

The locus of experimental points for stable and unstable flows from Creveling, et al. [3] is shown on Fig. 5. It is noted that stable experimental points begin on this curve for values of D larger than 2.5 (not shown). The disagreement between the data and the theoretical neutral stability curves [3, 8] based on the two friction factors is significant but not surprising in view of the complexity of the problem [3]. Further work is clearly called for which would include such effects as velocity and temperature variations in the radial direction, heat conduction in the axial direction and experimental determination of the friction factor during the transient period.

Appendix

Solution for Small Time and Determination of the Thermal Penetration Depth

It is possible to obtain a formal solution of the energy equation (8) for small times and this will yield the "thermal penetration depth." From the theory of characteristics for $2\pi \int_0^\tau w(\bar{\tau})d\bar{\tau} < \pi$, the temperature is given by:

$$\phi(\theta, \tau) = \left\{ \begin{array}{l} 0 \text{ for } \theta \geq \theta_p \\ e^{-2D\tau} fcn_I \left[2\pi \int_0^\tau w(\bar{\tau}) d\bar{\tau} - \theta \right] \text{ for } \theta < \theta_p \end{array} \right\} \quad \text{for } 0 \leq \theta \leq \pi \quad \text{(A1)}$$

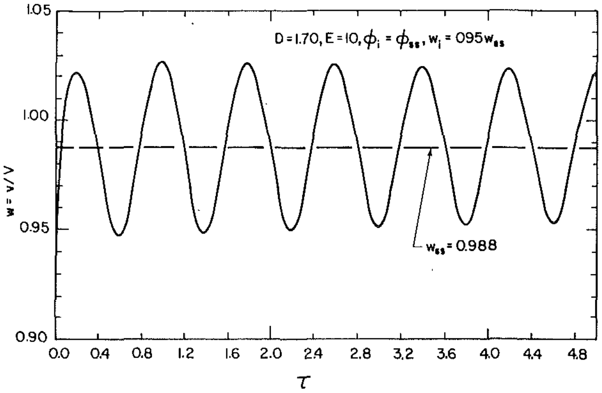

Fig. 8 Velocity variation for neutrally stable condition

and

$$\phi(\theta,\tau)=\begin{Bmatrix} 2D\tau \text{ for } \theta-\pi \geqslant \theta_p \\ 2D\tau - fcn_{II}\left[2\pi\int_0^\tau w(\bar{\tau})d\bar{\tau}-(\theta-\pi)\right] \text{ for } \theta-\pi<\theta_p \end{Bmatrix}$$

$$\text{for } \pi \leqslant \theta \leqslant 2\pi \quad \text{(A2)}$$

where θ_p, the thermal penetration depth or thermal signal, is equal to $2\pi\int_0^\tau w(\bar{\tau})d\bar{\tau}$. In the upper (cooled) region for $2\pi\int_0^\tau w(\bar{\tau})d\bar{\tau} \leq \theta \leq \pi$ it is seen (equation (A1) and Fig. 2) that $\phi = 0$; in the lower (heated) region for $2\pi\int_0^\tau w(\bar{\tau})d\bar{\tau} \leqslant \theta - \pi \leqslant \pi$ it is seen (equation (A2) and Fig. 2) that $\phi = 2D\tau$, which is the effect of the heating with a constant heat flux.

It should be noted that the functions in equations (A1) and (A2) may be obtained by using the conditions that are valid for small time, namely $\phi(0,\tau) = 2D\tau$ and $\phi(\pi,\tau) = 0$ so that

$$fcn_I\left[2\pi\int_0^\tau w(\bar{\tau})d\bar{\tau}\right] = 2D\tau e^{2D\tau} \quad \text{(A3)}$$

and

$$fcn_{II}\left[2\pi\int_0^\tau w(\bar{\tau})d\bar{\tau}\right] = 2D\tau \quad \text{(A4)}$$

Note, however, that the velocity variation $w(\tau)$ is unknown a priori and must be obtained along with the temperature variation. A consistency check on the calculated results for the temperature was made by substituting the results for the velocity obtained from the finite difference calculations (cf. Fig. 3) for small times into equations (A1–A4). Good agreement was obtained between the temperatures thus obtained and the solution of the finite difference equations (13, 14).

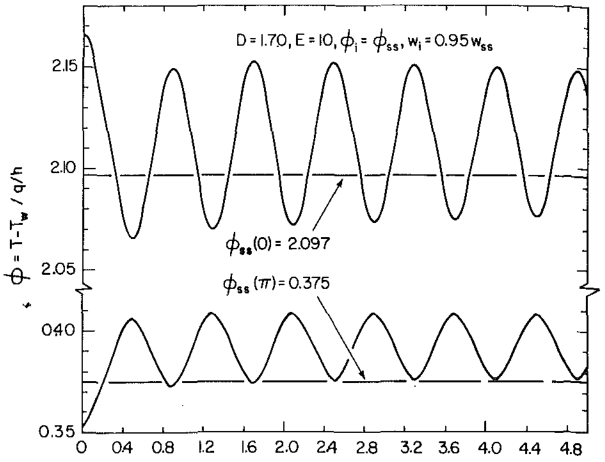

Fig. 9 Temperature variation for neutrally stable condition

References

1 Keller, J. B., "Periodic Oscillations in a Model of Thermal Convection," *J. Fluid Mech.*, Vol. 26, 1966, pp. 599–606.

2 Welander, P., "On the Oscillatory Instability of a Differentially Heated Fluid Loop," *J. Fluid Mech.*, Vol. 29, 1967, pp. 17–30.

3 Creveling, H. F., De Paz, J. F., Baladi, J. Y., and Schoenhals, R. J., "Stability Characteristics of a Single-Phase Free Convection Loop," *J. Fluid Mech.*, Vol. 67, 1975, pp. 65–84.

4 Damerell, P. S., and Schoenhals, R. J., "Flow in a Toroidal Thermosyphon with Angular Displacement of Heated and Cooled Sections," AIAA-ASME Thermophysics and Heat Transfer Conference, Palo Alto, CA., Paper No. 78-HT-44, May 24–26, 1978.

5 Zvirin, Y., Shitzer, A., and Grossman, G., "The Natural Circulation Solar Heater-Models with Linear and Nonlinear Temperature Distributions," *Int. J. Heat Mass Transfer*, Vol. 20, 1977, pp. 997–999.

6 Zvirin, Y., Shitzer, A., and Bartal-Bornstein, A., "On the Stability of the Natural Circulation Solar Heater," in *Proceedings of the 6th International Heat Transfer Conference*, Toronto, Canada, Vol. II, 1978, pp. 141–145.

7 Jasinsky, T., and Buckley, S., "Thermosyphon Analysis of a Thermic Diode Solar Heating System," ASME Paper No. 77-WA/Sol-9, 1977.

8 Zvirin, Y., "The Effect of Dissipation on Free Convection Loops," *Int. J. Heat Mass Transfer*, accepted for publication, 1979.

9 Ong, K. S., "A Finite Difference Method to Evaluate the Thermal Performance of a Solar Water Heater," *Solar Energy*, Vol. 16, 1974, pp. 137–147.

10 Zvirin, Y., and Greif, R., "Transient Behavior of Natural Circulation Loops: Two Vertical Branches with Point Heat Source and Sink," *Int. J. Heat Mass Transfer*, Vol. 22, 1979, pp. 499–504.

Analysis of Diffuse-Specular Axisymmetric Surfaces with Application to Parabolic Reflectors

J. R. Mahan
Assoc. Mem. ASME

J. B. Kingsolver
Student Mem., ASME

D. T. Mears
Assoc. Mem., ASME

Mechanical Engineering Department,
Virginia Polytechnic Institute and State University,
Blacksburg, VA 24061

Presented is an exact numerical technique for radiative analysis of diffusely emitting axisymmetric enclosures, passages, and cavities having both diffuse and specular components of reflectivity. The specular components of the required exchange factors are synthesized by chaining together partial exchange factors, defined as the fraction of diffusely distributed radiation leaving one surface and arriving at another after one intervening specular reflection with a reflectivity of unity. The technique is employed to predict the temperature distributions on parabolic reflectors in radiative equilibrium with sources located at their foci. It is demonstrated that, at least for this important geometry, an accurate representation of the exchange factors can be obtained by considering only low order chains.

Introduction

It was not until 1961 that Eckert and Sparrow [1] presented a systematic method for calculating radiant interchange among surfaces having specular components of reflection. It was in this landmark paper that the concept of an angle factor which includes the effects of intervening specular reflections was first introduced. This "exchange factor" was shown to be expressible in terms of the image of the diffuse source surface as viewed by the receiving surface through the intervening array of specular surfaces. Applications and extensions of this idea were presented by several investigators over the next five years: notably, Sparrow, et al. [2], Perlmutter and Siegel [3], Bobco [4], Lin and Sparrow [5], and Hering [6]. By the mid-1960's the exchange factor had found its way into textbooks on heat transfer, of which [7–10] are contemporary editions, and is now a standard tool of radiative analysis.

In [5] Lin and Sparrow describe a general analytical approach for obtaining the exchange factors between ring elements of a surface of revolution. They demonstrate that exact analytical expressions can be obtained for these exchange factors in the cases of cylindrical and conical cavities. In principle their approach should yield the exchange factors for all cases of concave surfaces of revolution having uniform reflectivities. However, it is doubtful that solutions actually could be obtained in most cases without resorting to numerical techniques. Skeptics of this assertion are directed to [5] in which Lin and Sparrow outline in some detail the analysis leading to the exchange factors for the relatively "simple" cylindrical and conical geometries.

The authors of the present paper were unsuccessful in applying the approach of Lin and Sparrow to the important and interesting problem of parabolic reflectors. An "exact" numerical approach to problems of the more general type resulted from that failure. It should be noted that the approach of Lin and Sparrow is itself adaptable to numerical implementation along the lines followed in the present paper. However, their approach has one minor but inherent limitation that made the search for an alternative attractive; their formulation is applicable only in those cases where the specular component of reflectivity is uniform along the surface. The alternative approach offered here permits variation of the specular component of reflectivity from ring element to ring element such as might occur if the surface optical properties were temperature dependent or if nonuniform layers of dust or oxidation were present.

As a demonstration of its utility, the numerical technique is employed to predict the temperature distribution along the surface of a parabolic reflector in radiative equilibrium with a point source of radiant energy located at its focus. The numerous practical applications of this and related problems include space telescopes, radiometers, and other optical systems. Parabolic reflectors have always been important components in the lighting industry and more recently they have begun to assume a prominent role as focusing elements for solar energy concentration, both within the Earth's atmosphere and in outer space.

General Exchange Factor Formulation

Consider the surface of revolution formed by rotating the curve $y = f(x)$ about the x-axis over the interval $a \le x \le b$, Fig. 1. If $d^2y/dx^2 \le 0$ on the interval $[a, b]$, the surface forms a cavity whose walls are everywhere locally concave. In a cavity of this general form there is no opportunity for "shadowing"; all points on the interior surface can view all other points directly. The analysis which follows applies only to surfaces of this general form.

In keeping with the idea that variations of local temperature, heat flux, and surface optical properties can occur only in the axial direction and in anticipation of an eventual finite surface net exchange formulation, the surface of revolution in Fig. 1 is divided into n ring-shaped elements of finite axial length. The number of divisions actually used in a given analysis would depend on the trade-off of desired accuracy and resolution against available computing resources. There is no particular requirement that the divisions be of equal axial length; indeed, in some cases it might be advantageous to provide more divisions in a region where greater resolution is required.

Each finite ring element can be further subdivided into infinitesimal area elements,

$$dA = r d\theta ds. \tag{1}$$

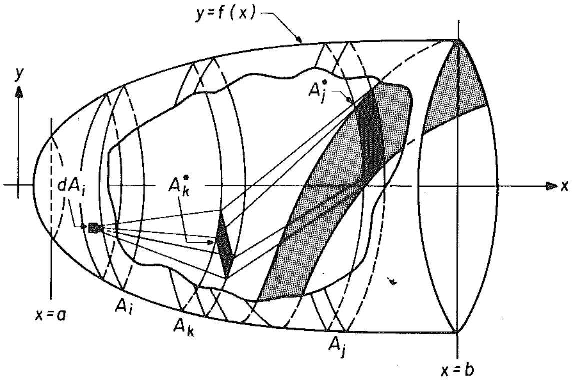

Fig. 1 Axisymmetric surface of revolution

Contributed by the Heat Transfer Division and presented at the 18th AIChE/ASME National Heat Transfer Conference, August 6–8, San Diego, California, of THE AMERICAN SOCIETY OF MECHANICAL ENGINEERS. Manuscript received by the Heat Transfer Division April 16, 1979. Paper No. 79-HT-22.

Let dA_i be such an area element on finite ring element i and let a beam of radiant energy whose source is on dA_i sweep over ring element k, which has a specular component of reflectivity. The resulting pattern of specularly reflected radiation from ring k incident on the interior surface would be somewhat as indicated by the irregularly shaped lightly shaded area in Fig. 1. We define the differential partial exchange factor $dP_{dA_i(dA_k)-dA_j}$ as the fraction of diffusely distributed energy leaving dA_i and arriving at dA_j after one intervening specular reflection in dA_k with $\rho_k{}^s = 1.0$. It is clear from application of this definition to the geometry of Fig. 1 that

$$dP_{dA_i(dA_k)-dA_j} = dF_{dA_i-dA_k}, \tag{2}$$

with the restriction that dA_k lie in the darkly shaded area $A_k{}^*$.

The partial exchange factor from A_i to A_j with one intervening specular reflection in A_k may then be determined by integration. First, the left-hand side of equation (2) is integrated over $A_j{}^*$ and, correspondingly, the right-hand side is integrated over $A_k{}^*$, yielding

$$P_{dA_i(A_k)-A_j} = \int_{A_k{}^*} dF_{dA_i-dA_k}. \tag{3}$$

Equation (3) is then multiplied through by dA_i and reciprocity invoked for the left-hand side, whence

$$A_j dP_{A_j-dA_i(A_k)} = dA_i \int_{A_k{}^*} dF_{dA_i-dA_k}. \tag{4}$$

Upon integration over all of ring i and application of reciprocity to the left-hand side, there results after rearrangement

$$P_{A_i(A_k)-A_j} = \frac{1}{A_i} \int_{A_i} \int_{A_k{}^*} dF_{dA_i-dA_k} dA_i. \tag{5}$$

In principle equation (5) with the appropriate expression for the diffuse angle factor from dA_i to dA_k can be used to compute the partial exchange factors for all combinations of rings i, k, and j once the limits on the double integration over $A_k{}^*$ have been suitably defined. For some geometries it may be possible to carry out the indicated integrations analytically; however, this generally will not be the case for an arbitrary surface of revolution. In cases where analytical evaluation of the integrals is prohibitively difficult, exact integrations can be carried out numerically to a degree of accuracy limited only by available computing resources.

Once the partial exchange factors $P_{i(k)-j}$ have been obtained, calculation of the exchange factors E_{i-j}, defined as the fraction of diffusely distributed radiant energy leaving A_i and arriving at A_j directly and by all possible intervening specular reflections, is nothing more than a monumental bookkeeping task well suited to the special capabilities of a modern high speed digital computer.

The theoretically correct continuation would be to identify all possible chains of partial exchange factors which begin on ring i and end on ring j. Such a chain of order m would have a "value"

$$\begin{aligned} V_{i-j}^{(m)} = {} & [\rho_{k1}^s P_{i(k_1)-k_2}][\rho_{k2}^s P_{k_1(k_2)-k_3}] \ldots \\ & [\rho_{km-1}^s P_{k_{m-2}(k_{m-1})-k_m}][\rho_{km}^s P_{k_{m-1}(k_m)-j}]. \end{aligned} \tag{6}$$

In general there will be several, perhaps many, chains of a given order linking rings i and j. The specular component of the exchange factor E_{i-j} is then the sum of the values of all such chains of all orders which link rings i and j. The justification for this assertion is that any receiving ring "sees" an apparent diffuse source when it looks into another ring (or itself) having a specular component of reflectivity. This apparent diffuse source is a composite of all diffuse image sources which chain into the receiving ring from the mirror ring.

The number of possible chains linking ring i with ring j can become unmanageably large as the total number of surface elements increases. This is because both the order of the highest order chain and the number of chains of a given order increase with n. Fortunately, the more links involved in a given chain the less significant will be its contribution to the value of E_{i-j}. This is true because the value of an mth-order chain is of the order $(\bar{\rho}^s\bar{P})^m$, where the mean value of the specular component of reflectivity $\bar{\rho}^s$ and the mean value of the partial exchange factors within the chain $\bar{P}$ are both fractions. Thus a conservative estimate of the relative values of chains of different order may be obtained by considering the maximum possible values of $\bar{\rho}^s$ and $\bar{P}$. Of course the maximum possible value of $\bar{\rho}^s$ is unity and the maximum value of $\bar{P}$ is limited to $1/n$ by application of the mean value theorem to equation (5). Then, for example, if third-order chains are considered in an axisymmetric enclosure which is divided into ten rings, the contribution to the specular component of E_{i-j} of a typical third-order chain will be less than one percent of the contribution of a typical first-order chain.

The approximately reciprocal relationship between $\bar{P}$ and n tends to offset the need for considering increasingly higher order chains as n increases. Indeed, experience applying the technique to the analysis of parabolic reflectors has shown that only chains of relatively low order actually need be considered to obtain an accurate representation of E_{i-j}. Note that the technique is exact in the sense that

$$\lim_{m \to n} [E_{i-j}^{(m)} - E_{i-j}] = 0, \tag{7}$$

where $E_{i-j}^{(m)}$ is the mth-order approximation of the exchange factor E_{i-j}.

The procedure for obtaining the exchange factors is as follows. First, the axisymmetric enclosure is divided into n ring elements, each of which is further subdivided into a two-dimensional array of area elements in anticipation of a numerical integration scheme. Then the numerical implementation of equation (5) is

Nomenclature

A = surface area (m^2)
a, b = limits of interval on x over which $y = f(x)$ obtains (m)
E = exchange factor (−)
F = diffuse angle factor (−)
f_{ik} = defined by equation (18)
i, j, k = unit vectors along x, y, and z axes of a Cartesian coordinate system (−)
ℓ = distance between points on surface elements (m)
N = number of increments in numerical integration scheme (−)
n = number of finite ring elements (−)
n = unit normal vector to a surface (−)
P = partial exchange factor (−)
p = distance from vertex to focus of a parabola (m)
q = radiosity (diffusely emitted + diffusely reflected flux, W/m^2)
r = radial coordinate in a cylindrical coordinate system (m)
s = distance measured along a surface of revolution (m)
T = temperature (K)
u = unit vector (−)
V = "value" of a chain of partial exchange factors, defined by equation (6)
x, y, z = Cartesian coordinates (m)
β = angle between surface unit normal vector and line connecting surface elements (r)
Γ_{ik} = defined by equation (19)
δ_{ik} = Kronecker delta, defined by equation (31)
ϵ = emissivity (−)
η = dimensionless axial coordinate, $\eta \equiv x/p$ (−)
θ = circumferential coordinate in a cylindrical coordinate system (r)
Λ_i = defined by equation (17)
ρ = reflectivity (−)
σ = Stefan-Boltzmann constant, 5.6693 × 10^{-8} W/m^{2}K^4
χ_{ij} = defined by equation (30)

Subscripts

I, O = interior and exterior of reflector
i, j, k, l, m = various surface ring elements
max = maximum value
s = heat source at focus of paraboloid

Superscripts

d = diffuse
(m) = order of approximation
s = specular
* = refers to intersection of specular reflection pattern and a surface ring element
— = overbar refers to the mean value

$$P_{i(k)-j} = \frac{2\pi}{A_i} \sum_{N_{xi}} \sum_{N_{\theta k}^*} \sum_{N_{xk}^*} \frac{\cos\beta_i \cos\beta_k}{\pi(\ell_{ik})^2} r_i r_k \Delta\theta_k \Delta s_k \Delta s_i. \tag{8}$$

Note that it is not necessary to sum over θ_i because of symmetry.

Before equation (8) can be used to evaluate the partial exchange factors, the quantities β_i, β_k, ℓ_{ik}, r_i, and r_k must be expressed in terms of θ_k, s_k, and s_i, and the limits on the summation over the irregularly shaped area A_k^* must be defined. The former task is approached in the usual manner; that is, $\cos\beta_i$, $\cos\beta_k$, and ℓ_{ik} are expressed in terms of the unit normal vectors at (r_i, θ_i, x_i) and (r_k, θ_k, x_k) and the vector from (r_i, θ_i, x_i) to (r_k, θ_k, x_k). The unit normal vectors are given by

$$\mathbf{n} = -\nabla S/|\nabla S|, \tag{9}$$

where $S = S(r, \theta, x)$ is the equation of the surface of revolution. Note that for such an axisymmetric surface $r = r(x \text{ only})$ and

$$(\Delta s)^2 \approx (\Delta x)^2 + (\Delta r)^2. \tag{10}$$

Therefore r and s can be eliminated from equation (8) in favor of x. The vector $\boldsymbol{\ell}_{ik}$ is given by

$$\boldsymbol{\ell}_{ik} = (x_k - x_i)\mathbf{i} + (r_k \cos\theta_k - r_i \cos\theta_i)\mathbf{j} + (r_k \sin\theta_k - r_i \sin\theta_i)\mathbf{k}. \tag{11}$$

Then we have

$$\cos\beta_i = \mathbf{n}_i \cdot \boldsymbol{\ell}_{ik}/\ell_{ik}$$

and (12)

$$\cos\beta_k = -\mathbf{n}_k \cdot \boldsymbol{\ell}_{ik}/\ell_{ik}.$$

Upon introduction of the above expressions into equation (8), calculation of the partial exchange factors involves only summations over x_i, x_k, and θ_k of terms which are explicitly functions of these variables only. Note that because of symmetry any value of θ_i can be selected without changing the value of $P_{i(k)-j}$.

The need for advance knowledge of the limits on the integration over A_k^* can be eliminated by judicious selection of the numerical scheme for evaluating equation (8). For each discrete value of x_i on ring i, x_k is allowed to range over its discrete values on ring k. Similarly, for each combination of values of x_i and x_k, θ_k is allowed to assume all of its discrete values on ring k. For each combination of x_i, x_k, and θ_k the axial location is determined of the point on the surface S which intercepts a beam originating at (x_i, θ_i) and reflected from (x_k, θ_k), as described below. If the axial location of this point is within the range of x which defines ring j, the corresponding value of the integrand of equation (8) is identified as an element of $P_{i(k)-j}$. When every combination of x_i, x_k, and θ_k has been considered in this way, all of the partial exchange factors have been obtained. In practice only values of θ_k in the range $0 \le \theta_k \le \pi$ need be considered because of symmetry. The total number of calculations required to obtain the partial exchange factors is $(N_{x_i})(N_{x_k})(N_{\theta_k})/2$.

The most straightforward way of determining the point where a reflected beam will strike the surface begins by identifying the component of the unit vector in the direction of $\boldsymbol{\ell}_{ik}$ which is parallel to $\mathbf{n}_k$. Then the unit vector in the direction of $\boldsymbol{\ell}_{kj}$ is given by

$$\mathbf{u}_{kj} = \mathbf{u}_{ik} - 2(\mathbf{u}_{ik} \cdot \mathbf{n}_k)\mathbf{n}_k; \tag{13}$$

that is, it is the sum of the unit vector in the direction of $\boldsymbol{\ell}_{ik}$ and twice the component of that unit vector which is parallel to $\mathbf{n}_k$. The coordinates of the point on ring j where the beam strikes are then given by

$$x_j = x_k + (\mathbf{u}_{kj} \cdot \mathbf{i})\ell_{kj},$$

$$y_j = y_k + (\mathbf{u}_{kj} \cdot \mathbf{j})\ell_{kj}, \tag{14}$$

and

$$z_j = z_k + (\mathbf{u}_{kj} \cdot \mathbf{k})\ell_{kj}.$$

These represent three equations in four unknowns: x_j, y_j, z_j, and ℓ_{kj}. The fourth equation required to find x_j is the equation of the surface, $S = S(x, y, z)$.

In the case of an open-ended cavity or passage many of the reflected beams will leave the enclosure without striking the surface. The values of the integrand of equation (8) corresponding to these beams should also be recorded as elements of a fictitious partial exchange factor $P_{i(k)-n+1}$. Then as a diagnostic routine the summation

$$\sum_{j=1}^{n+1} P_{i(k)-j}$$

can be computed and compared with F_{i-k}, which can always be determined exactly for enclosures of the type being considered and is needed anyway because it is a component of the exchange factor E_{i-k}. Of course, F_{i-k} should be equal to the above summation if no mistakes have been made.

Once the partial exchange factors have been computed and tabulated, the exchange factors can be obtained by adding to the value of the diffuse angle factor F_{i-j} the values of all the chains connecting ring i with ring j. As stated previously it is usually neither possible nor necessary to include all of the chains connecting ring i with ring j in this calculation. The highest order family of chains which actually must be considered in a given problem will depend on the nature of the enclosure, the value of the specular component of reflectivity, and the accuracy required. In general the decision on the order of the highest order chain will also be influenced by available computing resources.

Application to Parabolic Reflectors

We now consider cavities whose bounding surfaces are described by the relation

$$4px = y^2 + z^2, \tag{15}$$

which we recognize as the equation of a paraboloid whose focus is located at $x = p$. If such a surface is truncated at some axial location $x = x_{\max}$ there results a parabolic reflector. The exact thermal analysis of diffuse-specular parabolic reflectors has eluded investigators in the past mostly because of mathematical complexities associated with existing methods.

Under the change of variable $\eta = x/p$ all paraboloids of the same relative axial length $\eta_{\max}$ are similar. Thus because the partial exchange factor is itself a dimensionless quantity some economy of effort can be gained by nondimensionalizing the version of equation (8) which applies to the problem at hand. When this is done there results

$$P_{i(k)-j} = \Lambda_i \sum_{N_{xi}} \sum_{N_{xk}^*} \sum_{N_{\theta k}^*} f_{ik}, \tag{16}$$

where

$$\Lambda_i = 3\eta_{\max}^2[(1 + \eta_{i2})^{3/2} - (1 + \eta_{i1})^{3/2}]^{-1}/8nN_xN_\theta \tag{17}$$

and

$$f_{ik} = [1 + (\eta_k - \eta_i)^2/4\Gamma_{ik}]^{-2}. \tag{18}$$

In writing equations (17) and (18) the arbitrary angular position on ring i, θ_i, has been set equal to zero for convenience and it has been assumed that $N_{x_i} = N_{x_k} = N_x$. The quantity Γ_{ik} is defined

$$\Gamma_{ik} = \eta_i + \eta_k - 2\sqrt{\eta_i\eta_k}\cos\theta_k. \tag{19}$$

Equations (16–19) follow directly from equations (8–12) and equation (15). It is possible that the triple integral implied by equation (16) can be evaluated analytically, perhaps by recasting it in contour integral form, but all attempts by the authors to accomplish this were defeated. Solution of the diffuse-specular parabolic reflector problem using the numerical technique developed above thus serves to illustrate the technique while providing valuable information on the influence of specularity on the thermal behavior of such reflectors.

Values of f_{ik} and Λ_i and the corresponding values of η_j are computed within three nested calculation loops, where η_j is given by

$$\eta_j = \eta_k + [\mathbf{u}_{kj}]_x(\ell_{kj}/p). \tag{20}$$

The quantity ℓ_{kj}/p in equation (20) is given by

$$\ell_{kj}/p = \frac{4[\mathbf{u}_{kj}]_x - 4\sqrt{\eta_k}([\mathbf{u}_{kj}]_y \cos\theta_k + [\mathbf{u}_{kj}]_z \sin\theta_k)}{1 - [\mathbf{u}_{kj}]_x{}^2}, \quad (21)$$

where

$$[\mathbf{u}_{kj}]_x = [(1+\eta_k)(\eta_k - \eta_i) + 2\Gamma_{ik}]/(1+\eta_k)[(\eta_k-\eta_i)^2 + 4\Gamma_{ik}], \quad (22)$$

$$[\mathbf{u}_{kj}]_y = 2[(1+\eta_k)(\sqrt{\eta_k}\cos\theta_k - \sqrt{\eta_i}) - \Gamma_{ik}\sqrt{\eta_k}\cos\theta_k]/(1+\eta_k)[(\eta_k-\eta_i)^2 + 4\Gamma_{ik}], \quad (23)$$

and

$$[\mathbf{u}_{kj}]_z = 2[(1+\eta_k)\sqrt{\eta_k}\sin\theta_k - \Gamma_{ik}\sqrt{\eta_k}\sin\theta_k]/(1+\eta_k)[(\eta_k-\eta_i)^2 + 4\Gamma_{ik}]. \quad (24)$$

The quantity $\Lambda_i f_{ik}$ obtained in each calculation is added to one of $n \times n \times n = n^3$ accumulating sums depending on the value of η_j. When $nN_xN_\theta/2$ such calculations have been performed these n^3 sums are each multiplied by two (because of symmetry) after which they contain the n^3 values of $P_{i(k)-j}$. Equations (20–24) follow directly from equations (14) and (15).

An array of partial exchange factors $[P_{i(k)-j}]$ must be created for each length reflector to be studied and for each value of n. For the present study two different lenths, $\eta_{\max} = 6.25$ and $\eta_{\max} = 12.5$, were considered. For each length the reflector was divided first into $n = 10$ and then $n = 20$ equal length ring elements in order to insure that the solutions were independent of n for sufficiently large values of n. This proved to be the case. Calculation of the partial exchange factors is by far the most expensive component of a thermal analysis based on this technique. For example, generation of these factors for the case of $\eta_{\max} = 6.25$ with $n = 10$ requires nearly twenty-five minutes of central processing unit (CPU) time on an IBM 370 computer, and the case of $\eta_{\max} = 12.5$ with $n = 20$ requires about eight times this amount of CPU time. For that reason the thermal analysis is broken up into three passes through the computer. In the first pass the partial exchange factors are computed. These can be stored and used to generate arrays of exchange factors for a range of values of the specular component of reflectivity, as described below.

The arrays of exchange factors $[E_{i-j}]$ are created by adding together the values of chains of partial exchange factors defined by equation (6) and then adding these sums to the corresponding values of the diffuse angle factors F_{i-j}. The diffuse angle factor between any two ring elements of a concave surface of revolution can be defined in terms of the angle factors between parallel disks using angle factor algebra. Angle factors determined in this way are exact and can be compared with the summation of the partial exchange factors as a check of the accuracy of the latter. When this is done in the present analysis using ten axial divisions and 100 circumferential divisions of each ring element, F_{i-k} agrees with

$$\sum_{j=1}^{n+1} P_{i(k)-j}$$

to four significant figures.

The array of partial exchange factors and the corresponding array of diffuse angle factors are combined into an array of exchange factors $[E_{i-j}]$ corresponding to each value of the specular component of the reflectivity to be considered. This is done in the second pass through the computer. In the present analysis three values of the specular component of reflectivity are considered: $\rho^s = 0$, $\rho^s = 0.6$, and $\rho^s = 0.9$. Although variation of ρ^s with η could have been considered, this was not done in the present example. Note that the case $\rho^s = 0$ corresponds to a diffuse reflector so that $[E_{i-j}] = [F_{i-j}]$ in this case.

Calculation of the exchange factors is performed in a program which reads in the values of the partial exchange factors, the diffuse angle factors, and the specular component of reflectivity corresponding to a given case. The subroutine of that program which computes the values of all the members of a family of chains of order m must have m nested calculation loops. Then as might be anticipated, the amount of CPU time required to compute an array of mth-order exchange factors grows geometrically with the order m. For example, the CPU times required for the case of $\eta_{\max} = 6.25$ with $n = 20$ and $\rho^s = 0.9$ are approximately 12, 15, 90, and 1846 s corresponding respectively to $m = 1, 2, 3$, and 4. Fortunately, the point of diminishing returns on the computer resources invested is reached very rapidly as the order m increases because values of E_{i-j} tend to converge rapidly with order. In this example first-order values of the specular component of the exchange factor typically account for about 97 percent of the effect of specular reflections. Thus, if only first-order exchange factors had been used the error would have been only about 1.5 per cent because the specular component of the exchange factor in this particular configuration represents about one-half the total value of the exchange factor. Virtually no improvement is obtained by using fourth-order exchange factors instead of third-order factors; the difference appears only in the sixth significant figure in this case.

The actual thermal analysis occurs in a third pass through the computer and is performed by a program which reads in the array of exchange factors $[E_{i-j}]$ corresponding to the length of the parabolic reflector, the number of axial divisions, and the value of the specular component of reflectivity. The program also requires as inputs the values of the other quantities which describe the thermal environment of the reflector, such as the diffuse component of reflectivity of the interior surface, the emissivity of the exterior surface, the relative size and equivalent blackbody temperature of the source located at the focus, and the equivalent blackbody temperature of the surroundings.

In the present analysis the surfaces are assumed to be gray and the surroundings are assumed to be very cold compared to the equilibrium temperatures on the reflector. Also, the diameter of the point source is arbitrarily fixed at 20 percent of the distance from the origin to the source to insure that, while of practical size, the source does not intercept a significant amount of radiation from the reflector surface elements. These restrictions reduce the number of parameters of the study without seriously compromising its value. Thus the reflector is always in thermal equilibrium with a point source at its focus whose equivalent blackbody temperature is given by

$$T_s = [Q_s/\sigma\epsilon_s A_s]^{1/4}. \quad (25)$$

Consideration is given to exterior surface emissivities ranging from zero (corresponding to an insulated reflector) to unity, source equivalent temperatures ranging from 500 to 5000 K, and two values of interior emissivity, $\epsilon_I = 0.05$ and 0.10.

A net exchange formulation is used to compute the equilibrium temperature distribution on the reflector. This is an exact formulation in the same sense that the technqiue used to generate the exchange factors is exact; that is

$$\lim_{n\to\infty} [T^{(n)} - T] = 0, \quad (26)$$

where $T^{(n)}$ is the approximation for the local temperature T based on n rings. As in the case of the exchange factors, experience has shown that an arbitrarily good approximation of the temperature distribution on the reflector can be obtained using only a modest number of rings. The temperature of ring i for the case of radiative equilibrium (no conduction, convection, or unsteady effects) is approximated as

$$\sigma T_i{}^4 = \left(\frac{\epsilon_I}{\epsilon_0 + \epsilon_I}\right)\left(\sum_{j=1}^{n} q_j E_{i-j} + q_s F_{i-s}\right). \quad (27)$$

This equation follows from an energy balance on ring i and is an approximation only in the sense that the reflector is divided into a finite number of rings.

Equation (27) represents n equations in $2n$ unknowns, where the unknowns are the n temperatures T_i and the n radiosities q_j. Another n equations can be written based on the definition of radiosity as the sum of the diffusely emitted and reflected radiation,

$$q_i = \epsilon_I \sigma T_i{}^4 + \rho^d\left(\sum_{j=1}^{n} q_j E_{i-j} + q_s F_{i-s}\right). \quad (28)$$

Note that the radiosity appears in two different locations in equation (28), on the left-hand side and under the summation. The equation can be solved explicitly for q_i, yielding

$$q_i = \sum_{j=1}^{n} [\chi_{ij}]^{-1}(\sigma T_j{}^4 + \rho^d q_s F_{i-s}/\epsilon_I), \tag{29}$$

where

$$[\chi_{ij}] = (\delta_{ij} - \rho^d E_{i-j})/\epsilon_I, \tag{30}$$

and where δ_{ij} is the Kronecker delta,

$$\delta_{ij} = \begin{cases} 0, & i \neq j \\ 1, & i = j \end{cases}. \tag{31}$$

The diffuse angle factor from ring i to the source, F_{i-s}, is given by reciprocity,

$$F_{i-s} = A_s F_{s-i}/A_i, \tag{32}$$

where F_{s-i} is the difference between the solid angles subtended at the focus by the two disks which form ring i by their intersection with the reflector.

Solution of equations (27) and (29) for the temperature distribution on the reflector is accomplished by first guessing the temperature distribution and then iterating back and forth between the two sets of equations until a convergent distribution is obtained. The temperature distributions converge rather rapidly, with little change after ten to fifteen iterations; however, to be safe twenty iterations were used in every case. Typical CPU times for solution of equations (27) and (29) for the temperature distribution were about 15 s.

Results

Typical results of the analysis appear in Fig. 2 for parabolic reflectors of relative length $\eta = 6.25$ (a and b) and 12.5 (c and d). The curves do not extend to $\eta = 0$ or to the openings of the reflectors because they have been plotted to the centers of the rings used (ten in this case). In cases such as the parabolic reflectors considered here where the function $y = f(x)$ used to generate the surface has a continuous slope through $y = 0$, it may be possible to place a node at $\eta = 0$. However, this is unnecessary in practice because a node can be placed arbitrarily close to either end of a cavity, passage, or enclosure being analyzed simply by using a finer mesh of rings there.

The similarity among the various temperature distributions in Fig. 2 is striking, suggesting the possibility of a correlation. Indeed, a successful correlation would lend credence to the results and by implication to the technique used to obtain them. After trying and rejecting several candidate correlation schemes, the following was found to work quite well.

The variation with degree of specularity correlates nicely when the abscissa is multiplied by

$$e^{\rho^s/(\rho^s + \rho^d)},$$

as does the variation with $\eta_{\max}$ when the abscissa is multiplied by

$$e^{\eta/\eta_{max}}.$$

The former correlation was arrived at more or less intuitively. However, in the latter case it was reasoned that adding additional length to a long reflector would have less effect than adding the same additional length to a short reflector, a line of reasoning which leads to an exponential function.

The variation with T_s was found to correlate when the ordinate is divided by T_s, and the variations with interior and exterior emissivity were found to correlate when the ordinate is multiplied by

$$[(\epsilon_I + \epsilon_0)/\epsilon_I]^{1/4}.$$

These correlations were arrived at by considering a radiative energy balance on ring i,

$$(\epsilon_I + \epsilon_0)A_i\sigma T_i{}^4 = \epsilon_I A_i \sigma T_s{}^4 f(\eta_i), \tag{33}$$

or

$$(T_i/T_s)[(\epsilon_I + \epsilon_0)/\epsilon_I]^{1/4} = f(\eta_i). \tag{34}$$

The correlated temperature distributions for a large sampling of the results obtained in this study are shown in Fig. 3. All of the results shown in Fig. 3 correspond to cases for which $n = 20$ and $m = 4$. The equation for the line passing through the correlated results is

$$T^* \equiv \frac{T}{T_s}\left(\frac{\epsilon_I + \epsilon_0}{\epsilon_I}\right)^{1/4} = 0.177 - 0.066 \log_{10}(\eta^*), \tag{35}$$

where

$$\eta^* \equiv \eta e^{\eta/\eta_{max}} e^{\rho^s/(\rho^s+\rho^d)}. \tag{36}$$

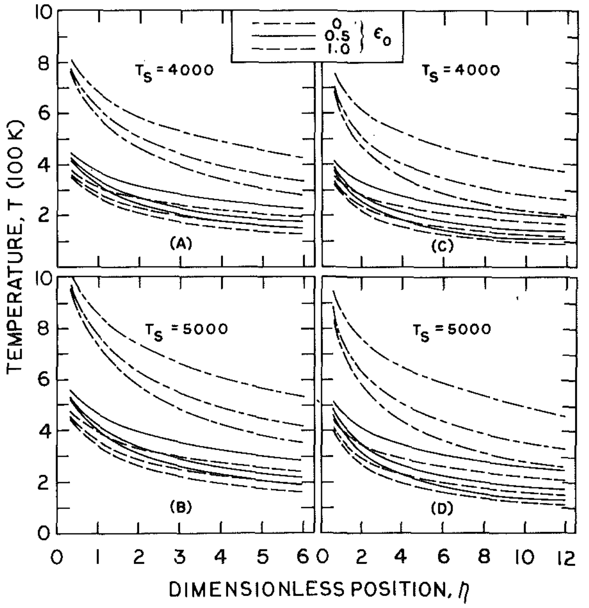

Fig. 2 Typical temperature distributions for $\epsilon_I = 0.05$ (In each three curve grouping, the top curve corresponds to $\rho^s/(\rho^s + \rho^d) = 0$; middle curve, = 0.63; bottom curve, = 0.95.)

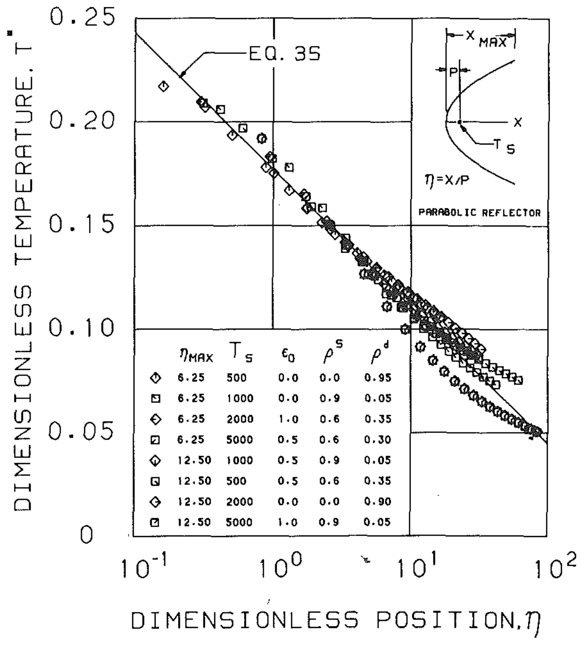

Fig. 3 Correlated temperature distributions

Conclusions

An exact numerical technique has been developed for performing a radiative analysis of diffuse-specular gray enclosures, passages, and cavities defined by concave surfaces of revolution. The exchange factors required are defined in terms of the corresponding diffuse angle factors and partial exchange factors which may be chained together to account for the specular component. The technique is applied to the analysis of parabolic reflectors and then shown to give accurate results for the exchange factors even though only low order approximations for the specular components are considered. Temperature distributions obtained from the analysis are correlated for a wide range of values of the optical properties and geometrical and environmental conditions. The resulting correlation lends valuable insight into the behavior of real parabolic reflectors.

Acknowledgment

The authors owe a debt of gratitude to Bea Mahan for her technical assistance in the data processing phase of this work.

References

1 Eckert, E. R. G., and Sparrow, E. M., "Radiation Heat Exchange Between Surfaces with Specular Reflection," *International Journal of Heat and Mass Transfer,* Vol. 3, 1961, pp. 42–54.

2 Sparrow, E. M., Eckert, E. R. G., and Jonsson, V. K., "An Enclosure Theory for Radiative Exchange Between Specularly and Diffusely Reflecting Surfaces," ASME JOURNAL OF HEAT TRANSFER, Vol. 84, 1962, pp. 294–300.

3 Perlmutter, M., and Siegel, R., "Effect of Specularly-Reflecting Gray Surfaces on Thermal Radiation Through a Tube and From its Heated Wall," ASME JOURNAL OF HEAT TRANSFER, Vol. 85, 1963, pp. 55–62.

4 Bobco, R. P., "Radiation Heat Transfer in Semigray Enclosures with Specularly and Diffusely Reflecting Surfaces," ASME JOURNAL OF HEAT TRANSFER, Vol. 86, 1964, pp. 123–130.

5 Lin, S. H., and Sparrow, E. M., "Radiant Interchange Among Curved Specularly Reflecting Surfaces—Application to Cylindrical and Conical Cavities," ASME JOURNAL OF HEAT TRANSFER, Vol. 87, 1965, pp. 299–307.

6 Hering, R. G., "Radiative Heat Exchange Between Conducting Plates with Specular Reflection," ASME JOURNAL OF HEAT TRANSFER, Vol. 88, 1966, pp. 29–36.

7 Sparrow, E. M., and Cess, R. D., *Radiation Heat Transfer, Augmented Edition,* McGraw-Hill, New York, 1978.

8 Siegel, R., and Howell, J. R., *Thermal Radiation Heat Transfer,* McGraw-Hill, New York, 1972.

9 Holman, J. P., *Heat Transfer,* 4th Edition, McGraw-Hill, New York, 1976.

10 Özişik, M. Necati, *Radiative Transfer,* John Wiley & Sons, 1973.

An Iterative Solution for Anisotropic Radiative Transfer in a Slab

W. H. Sutton
M. N. Özişik
Mechanical and Aerospace Engineering Department,
North Carolina State University,
Raleigh, N. C. 27650

An iterative method is applied to solve the integral form of the equation of radiative transfer for the cases of isotropic scattering, highly forward, and backward anisotropic scattering in plane-parallel slab with reflecting boundaries. Calculations are performed for the values of single scattering albedo from $\omega = 0.7$ to 1.0 where the convergence was previously reported to be poor. It is found that the convergence is significantly improved for most cases if the P-1 approximation of the spherical harmonics method is used for the initial guess. Results are presented for the hemispherical reflectivity and transmissivity of the slab over a wide range of parameters.

Introduction

The exact solution of the equation of radiative transfer for isotropic and anisotropic scattering is of interest in many engineering applications. The exact methods of solution developed by Chandrasekhar [1] and Case [2] are generally suitable for solving problems in plane-parallel geometry with isotropic and linearly isotropic scattering [3–7]. Therefore, numerical approaches are generally applied to solve radiation problems involving higher order anisotropic scattering. The Gaussian quadrature method has been applied [8, 9] to transform the equation of radiative transfer into a set of coupled ordinary differential equations. Computer programs using the Monte Carlo methods have been developed to solve the transport equation in the field of neutron transport theory. The one-dimensional equation of radiative transfer for plane-parallel medium can be transformed into an integral equation for the source function [10] and the resulting equation can be solved by iteration. Once the source function is known, the quantities of practical interest, such as the net radiative heat flux anywhere in the medium, the transmissivity and reflectivity of the medium are readily determined. Recent analytical studies on the convergence of iterative schemes [11–12] for the equation of radiative transfer show that the convergence can be very slow for the values of single scattering albedo ω, close to unity. A numerical solution of a radiation problem in a plane-parallel slab for isotropic scattering using an iterative scheme [13] showed that the convergence was indeed very slow for the range $0.7 < \omega < 1$. The purpose of this investigation is to demonstrate that, if a suitable initial guess can be made, the convergence of the solution can be significantly improved. Then, the iterative technique can provide a straightforward approach for the solution of radiation problems involving anisotropy with sufficiently high accuracy and reasonable computer time.

Analysis

The problem of radiative transfer for an absorbing, emitting, anisotropically scattering plane-parallel, gray slab, allowing for both diffuse and specular reflection components at the boundaries is taken as

$$\mu \frac{\partial I(\tau, \mu)}{\partial \tau} + I(\tau, \mu) = (1 - \omega) I_b(T) + \frac{\omega}{2} \int_{-1}^{1} p(\mu, \mu') I(\tau, \mu') d\mu',$$

$$\text{in } 0 \le \tau \le \tau_0, -1 \le \mu \le 1 \qquad (1a)$$

and subject to the boundary conditions

$$I(0, \mu) = \epsilon_1 I_b(T_1) + \rho_1^s I(0, -\mu) + 2\rho_1^d \int_0^1 I(0, -\mu') \mu' d\mu',$$

$$\text{at } \tau = 0, 0 < \mu \le 1 \qquad (1b)$$

$$I(\tau_0, -\mu) = \epsilon_2 I_b(T_2) + \rho_2^s I(\tau_0, \mu) + 2\rho_2^d \int_0^1 I(\tau_0, \mu') \mu' d\mu',$$

$$\text{at } \tau = \tau_0, 0 < \mu \le 1 \qquad (1c)$$

where the phase function $p(\mu, \mu')$ is given by

$$p(\mu, \mu') = \sum_{n=0}^{N} A_n P_n(\mu) P_n(\mu'), \text{ with } A_0 = 1 \qquad (2)$$

and $P_n(\mu)$ being the Legendre polynomial of order n.

We now define the source function, $S(\tau, \mu)$, as

$$S(\tau, \mu) \equiv (1 - \omega) I_b(T) + \frac{\omega}{2} \int_{-1}^{1} p(\mu, \mu') I(\tau, \mu') d\mu' \qquad (3)$$

Then the radiative heat transfer problem given above by equations (1) and (2) can be transformed into a single integral equation for the source function $S(\tau, \mu)$ as described in [10] by utilizing the results given by equations (8–103, 8–113) and (8–120) of this reference. Once the source function $S(\tau, \mu)$ is determined from the solution of such an integral equation, the net radiative heat flux, $q^r(\tau)$, anywhere in the medium is calculated according to its definition ([10], equation (8–81)).

In many engineering applications the hemispherical reflectivity and the transmissivity of the slab are of interest. For example, for the special case of transparent boundary at $\tau = 0$, the emission term $a_1 \equiv \epsilon_1 I_b(T_1)$ can represent an external isotropic radiation incident on the slab at the boundary $\tau = 0$. If we further assume that the emission of radiation from both the medium itself and the boundary surface at $\tau = \tau_0$ is negligible in comparison to the external irradiation $a_1 \equiv \epsilon_1 I_b(T_1)$, then the transmissivity, Γ, of the slab is determined from

$$\Gamma = \frac{q^r(\tau_0)}{\pi a_1} \qquad (4)$$

and the hemispherical reflectivity R is determined from

$$R = \frac{2\pi \int_0^1 I(0, -\mu') \mu' d\mu'}{\pi a_1} \qquad (5)$$

where the quantity $I(0, -\mu')$ is the exit distribution at the boundary $\tau = 0$ and is different from the incoming radiation intensity $I(0, \mu)$. The net radiative heat flux $q^r(\tau_0)$ is determined from its definition as discussed above.

Results

The integral equation for the source function was solved by iteration. Each of the integrals involving τ and μ variables was represented by a ten point Gaussian quadrature. The coefficients for the phase function $p(\mu, \mu')$ were obtained from the tables of angular distribution given in [10]. Fig. 1 illustrates the phase diagrams for the two cases of anisotropic scattering considered in the present study. The phase diagram shown in Fig. 1(a) represents a highly forward scattering situation, characterized by $n = 1.2$ and $x = 10$, where n is the real refractive index of the medium and $x = \pi D/\lambda$ is the size parameter; eleven terms are taken in the phase function. The diagram in Fig. 1(b) represents a backward scattering situation characterized by $n = \infty$ and $x = 1$, in which seven terms are taken in the phase function.

Contributed by the Heat Transfer Division for Publication in the JOURNAL OF HEAT TRANSFER. Manuscript received by the Heat Transfer Division March 26, 1979.

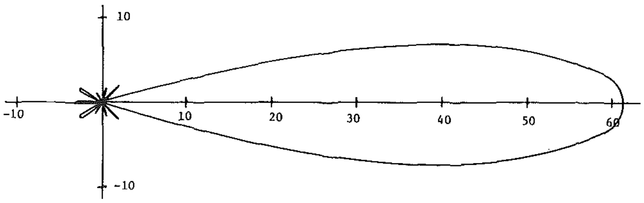

Fig. 1(*a*) Highly forward scattering (n = 1.2, x = 10)

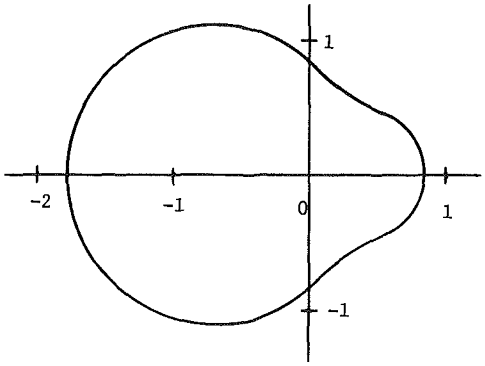

Fig. 1(*b*) Backward scattering (n = x = 1)

Fig. 1 Scattering phase diagram

Two different approaches used for starting the iterations included:

1 The source function was taken as zero (i.e., $S = 0$),

2 The P-1 approximation of the spherical harmonics method was used to calculate the starting value of $S(\tau, \mu)$ in the integral equation. The P-1 equation and the Marshak boundary condition scheme used in the analysis were the same as those described in [10].

To perform the numerical calculations, the optical thickness τ_0 of the slab is divided into ten subregions, x_i, i = 1 to 10, on the basis of Gaussian quadratures. The integrations are performed from $\tau = 0$ to $\tau = x_i$ and from $\tau = x_i$ to $\tau = \tau_0$, again by dividing each region into 10 quadrature points. The value of the source function $S(\tau, \mu)$ for each location not coinciding with the original quadrature points was determined by linear interpolation between two neighboring quadrature points. The $S(\tau, \mu)$ values determined in this manner were used as guess for the subsequent iteration. A ten point Gaussian quadrature was also used for the angular variable μ.

To check the effect of the increasing number of quadrature points on the accuracy of the results, sample calculations were performed by using 20, 40, and 80 quadrature points. The number of iterations needed for each of these cases did not significantly change from the ten point quadrature. The computer time needed significantly increased with increasing quadrature points, while the accuracy of the results did not significantly improve. The results obtained in this manner were sufficiently accurate for most practical purposes for the calculation of the integrated quantities such as the radiative heat flux and the hemispherical reflectivity and transmissivity of the slab. However, if directional quantities such as the angular distribution of radiation intensity are needed, it might be desirable to use a higher number of quadrature points.

The values of the parameters x, n or ω did not significantly effect the number of quadrature points to be used in the analysis. However, larger optical thickness, say, greater than about 5, would require the use of more quadrature points.

The convergence of the solution was slow as ω approached unity. It was proved mathematically [11, 12] that the solution of the integral equation of the type considered in the present analysis would be slow as ω approaches unity. The physical reasoning for this may be attributed to the fact that in the integral equation the contribution of the term due to the scattering from the medium becomes important as $\omega \rightarrow 1$. Similarly, as the optical thickness τ_0 of the medium increases, the contribution due to the scattering from the medium becomes important and the convergence of the solution becomes slow.

The calculations were performed for four values of the single scattering albedo, ω = 0.7, 0.8, 0.9 and 1.0, for which the convergence of the solutions were expected to be very slow. Two optical thicknesses studied included $\tau_0 = 2$ and 5.

The transmissivity and the hemispherical reflectivity of the slab were determined by assuming that the boundary surface at $\tau = 0$ was transparent and the slab was irradiated by an externally incident isotropic radiation. The emission from the medium and the boundary surface at $\tau = \tau_0$ was considered to be negligible in comparison to the strength of the externally incident radiation. Therefore, the transmissivity and the reflectivity could be determined according to their definitions given by equations (4) and (5). Both specular and diffuse reflection were considered for the boundary surface at $\tau = \tau_0$. All the calculations for the source function were iterated to a convergence criterion of 10^{-3} percent between two successive iterations.

Table 1 shows the hemispherical reflectivity and transmissivity of the slab for isotropic scattering, calculated with the above convergence criterion. Included in this table are the number of iterations needed for the source function calculations for the two different starting conditions discussed above. In order to check the accuracy of the iterative calculations, the exact solutions of the same problem available in the literature were also listed in this table. The iterative method yields results which are sufficiently accurate for most engineering applications. The number of iterations needed is significantly reduced for most cases if the results from the P-1 solution are used for starting the iterations.

Table 2 shows the results of a similar calculation for the case of highly forward scattering illustrated in the phase diagram shown in Fig. 1(a). The number of iterations needed to obtain these solutions are also given in this table for both starting conditions discussed above. As no exact solutions were available in the literature for the higher order anisotropic scattering cases considered here, P-11 calculations were performed by using the DLBVP subroutine from the IBM Scientific Subroutine Package to solve the resulting coupled ordinary differential equations. These solutions are expected to be sufficiently accurate, since high order P-N solutions can give good results for ω near unity and for large optical thicknesses. Iterative solutions give sufficiently accurate results, but the reduction in the number of iterations is not as significant for this case as for the isotropic scattering. The reason for this is the extremely forward nature of the anisotropy and the fact that the P-1 solution cannot accommodate the effects of extreme anisotropy.

Finally, Table 3 shows the results of calculations for the case of backward scattering according to the phase diagram shown in Fig.

Nomenclature

$I(\tau, \mu)$ = radiation intensity
$I_b(T)$ = black body radiation intensity
n = real refractive index
$p(\mu, \mu')$ = the phase function
$P_n(\mu)$ = the Legendre polynomial of order n
$q^r(\tau)$ = net radiative heat flux
R = hemispherical reflectivity defined by equation (5)
$S(\tau, \mu)$ = the source function
T = temperature
x = size parameter
ϵ = emissivity
Γ = transmissivity defined by equation (5)
ρ_i^s, ρ_i^d = specular and diffuse reflectivity coefficients respectively at the boundary surface, i, i = 1 or 2
μ = cosine of the angle between the direction of the radiation intensity and the positive τ axis
τ = optical variable
τ_0 = optical thickness of the slab
ω = single scattering albedo

Table 1 Hemispherical reflectivity and transmissivity for isotropic scattering

	Wall Reflectivity at τ_o			HEMISPHERICAL REFLECTIVITY*			TRANSMISSIVITY*		
τ_o	ρ^s	ρ^d	ω	Exact	Iterative with S=0	Iterative with P-1 Initial Guess	Exact	Iterative with S=0	Iterative with P-1 Initial Guess
2	0	0	0.7	0.2506	0.2517 (19)	0.2517 (16)	0.1551	0.1558 (19)	0.1558 (16)
2	0	0	0.8	0.3280	0.3294 (24)	0.3294 (19)	0.1973	0.1983 (24)	0.1983 (19)
2	0	0	0.9	0.4376	0.4386 (31)	0.4386 (23)	0.2656	0.2666 (31)	0.2666 (23)
2	0	0	1.0	0.6099	0.6098 (42)	0.6098 (13)	0.3901	0.3897 (42)	0.3898 (13)
2	0.5	0	0.7	0.2657	0.2669 (22)	0.2669 (17)	0.0880	0.0885 (22)	0.0885 (17)
2	0.5	0	0.8	0.3527	0.3543 (28)	0.3543 (21)	0.1172	0.1178 (28)	0.1178 (21)
2	0.5	0	0.9	0.4837	0.4854 (37)	0.4854 (27)	0.1689	0.1696 (37)	0.1696 (27)
2	0.5	0	1.0	--	0.7202 (55)	0.7202 (30)	--	0.2789 (55)	0.2789 (30)
2	0	1.0	0.7	0.2827	0.2842 (25)	0.2842 (19)	0.0	0.0	0.0
2	0	1.0	0.8	0.3859	0.3880 (33)	0.3880 (24)	0.0	0.0	0.0
2	0	1.0	0.9	0.5626	0.5652 (49)	0.5652 (33)	0.0	0.0	0.0
2	0	1.0	1.0	--	0.9991 (89)	0.9992 (22)	0.0	0.0	0.0
5	0	0	0.7	0.2565	0.2603 (29)	0.2603 (16)	0.0124	0.0133 (29)	0.0133 (16)
5	0	0	0.8	0.3417	0.3474 (39)	0.3474 (22)	0.0229	0.0247 (39)	0.0247 (22)
5	0	0	0.9	0.4763	0.4841 (58)	0.4841 (33)	0.0534	0.0571 (58)	0.0571 (33)
5	0	0	1.0	0.7923	0.7910 (116)	0.7910 (43)	0.2077	0.2062 (116)	0.2063 (43)
5	0.5	0	0.7	0.2566	0.2605 (30)	0.2605 (20)	0.0070	0.0076 (30)	0.0076 (20)
5	0.5	0	0.8	0.3420	0.3478 (42)	0.3478 (27)	0.0137	0.0148 (42)	0.0148 (27)
5	0.5	0	0.9	0.4783	0.4863 (64)	0.4863 (40)	0.0349	0.0374 (64)	0.0374 (40)
5	0.5	0	1.0	--	0.8264 (146)	0.8264 (66)	--	0.1696 (146)	0.1696 (66)
5	0	1.0	0.7	0.2567	0.2606 (32)	0.2606 (24)	0.0	0.0	0.0
5	0	1.0	0.8	0.3425	0.3484 (46)	0.3484 (33)	0.0	0.0	0.0
5	0	1.0	0.9	0.4818	0.4904 (79)	0.4904 (54)	0.0	0.0	0.0
5	0	1.0	1.0	--	0.9873 (151)	0.9946 (131)	0.0	0.0	0.0

*Exact results are obtained from C. C. Lii and M. N. Özisik [7] except the cases $\rho^s = \rho^d = 0$, $\omega = 1$ which are obtained from I. W. Busbridge and S. E. Orchard [15]. Quantities in paranthesis denote the number of iterations.

Table 2 Hemispherical reflectivity and transmissivity for anisotropic scattering with $n = 1.2$, $x = 10$ (i.e., highly forward scattering)

	Wall Reflectivity at τ_o			HEMISPHERICAL REFLECTIVITY*			TRANSMISSIVITY*		
τ_o	ρ^s	ρ^d	ω	P-Eleven	Iterative with S=0	Iterative with P-1 Initial Guess	P-Eleven	Iterative with S=0	Iterative with P-1 Initial Guess
2	0	0	0.7	0.0280	0.0290 (22)	0.0290 (20)	0.3487	0.3493 (22)	0.3493 (20)
2	0	0	0.8	0.0437	0.0446 (27)	0.0446 (23)	0.4621	0.4627 (27)	0.4627 (23)
2	0	0	0.9	0.0725	0.0733 (35)	0.0734 (28)	0.6229	0.6233 (35)	0.6233 (28)
2	0	0	1.0	0.1348	0.1350 (48)	0.1350 (26)	0.8651	0.8646 (48)	0.8646 (26)
2	0.5	0	0.7	0.0980	0.0992 (24)	0.0992 (19)	0.1760	0.1763 (24)	0.1763 (19)
2	0.5	0	0.8	0.1624	0.1636 (30)	0.1636 (24)	0.2348	0.2351 (30)	0.2351 (24)
2	0.5	0	0.9	0.2822	0.2832 (40)	0.2832 (33)	0.3209	0.3210 (40)	0.3210 (33)
2	0.5	0	1.0	0.5385	0.5379 (59)	0.5379 (49)	0.4615	0.4610 (59)	0.4610 (49)
2	0	1.0	0.7	0.1531	0.1546 (24)	0.1546 (21)	0.0	0.0	0.0
2	0	1.0	0.8	0.2671	0.2687 (30)	0.2687 (27)	0.0	0.0	0.0
2	0	1.0	0.9	0.4998	0.4926 (41)	0.4926 (34)	0.0	0.0	0.0
2	0	1.0	1.0	1.0000	0.9991 (61)	0.9992 (18)	0.0	0.0	0.0
5	0	0	0.7	0.0298	0.0311 (28)	0.0311 (26)	0.0896	0.0921 (28)	0.0921 (26)
5	0	0	0.8	0.0495	0.0512 (36)	0.0512 (32)	0.1697	0.1731 (36)	0.1731 (32)
5	0	0	0.9	0.0947	0.0969 (50)	0.0969 (43)	0.3375	0.3411 (50)	0.3411 (43)
5	0	0	1.0	0.2515	0.2504 (84)	0.2505 (43)	0.7485	0.7467 (84)	0.7467 (43)
5	0.5	0	0.7	0.0351	0.0367 (30)	0.0367 (28)	0.0452	0.0465 (30)	0.0465 (28)
5	0.5	0	0.8	0.0672	0.0695 (39)	0.0695 (37)	0.0863	0.0881 (39)	0.0881 (37)
5	0.5	0	0.9	0.1602	0.1634 (57)	0.1634 (52)	0.1753	0.1773 (57)	0.1773 (52)
5	0.5	0	1.0	0.5752	0.5715 (106)	0.5715 (90)	0.4248	0.4227 (106)	0.4227 (90)
5	0	1.0	0.7	0.0381	0.0399 (30)	0.0399 (29)	0.0	0.0	0.0
5	0	1.0	0.8	0.0798	0.0828 (41)	0.0828 (39)	0.0	0.0	0.0
5	0	1.0	0.9	0.2206	0.2257 (61)	0.2257 (57)	0.0	0.0	0.0
5	0	1.0	1.0	1.0000	0.9942 (124)	0.9944 (53)	0.0	0.0	0.0

*Quantities in paranthesis denote the number of iterations.

Table 3 Hemispherical reflectivity and transmissivity for anisotropic scattering with $n = \infty$, $x = 1$ (i.e., backward scattering)

	Wall Reflectivity at τ_o			HEMISPHERICAL REFLECTIVITY*			TRANSMISSIVITY*		
τ_o	ρ^s	ρ^d	ω	P-Eleven	Iterative with S=0	Iterative with P-1 Initial Guess	P-Eleven	Iterative with S=0	Iterative with P-1 Initial Guess
2	0	0	0.7	0.2787	0.2805 (20)	0.2805 (17)	0.1373	0.1380 (20)	0.1380 (17)
2	0	0	0.8	0.3594	0.3613 (25)	0.3613 (21)	0.1738	0.1748 (25)	0.1748 (21)
2	0	0	0.9	0.4716	0.4734 (33)	0.4734 (25)	0.2349	0.2359 (33)	0.2359 (25)
2	0	0	1.0	0.6486	0.6486 (45)	0.6486 (16)	0.3514	0.3510 (45)	0.3510 (16)
2	0.5	0	0.7	0.2909	0.2928 (22)	0.2928 (19)	0.0793	0.0797 (22)	0.0797 (19)
2	0.5	0	0.8	0.3791	0.3812 (28)	0.3812 (24)	0.1053	0.1060 (28)	0.1060 (24)
2	0.5	0	0.9	0.5090	0.5110 (39)	0.5110 (31)	0.1528	0.1535 (39)	0.1535 (31)
2	0.5	0	1.0	0.7411	0.7407 (58)	0.7408 (39)	0.2589	0.2584 (58)	0.2584 (39)
2	0	1.0	0.7	0.3049	0.3070 (25)	0.3070 (21)	0.0	0.0	0.0
2	0	1.0	0.8	0.4066	0.4091 (34)	0.4091 (28)	0.0	0.0	0.0
2	0	1.0	0.9	0.5760	0.5790 (51)	0.5790 (39)	0.0	0.0	0.0
2	0	1.0	1.0	1.0000	0.9991 (97)	0.9992 (24)	0.0	0.0	0.0
5	0	0	0.7	0.2841	0.2887 (30)	0.2887 (25)	0.0119	0.0102 (30)	0.0102 (25)
5	0	0	0.8	0.3717	0.3779 (40)	0.3779 (32)	0.0120	0.0191 (40)	0.0191 (32)
5	0	0	0.9	0.5060	0.5144 (61)	0.5144 (44)	0.0418	0.0453 (61)	0.0453 (44)
5	0	0	1.0	0.8190	0.8174 (126)	0.8175 (47)	0.1810	0.1797 (126)	0.1798 (47)
5	0.5	0	0.7	0.2842	0.2887 (31)	0.2887 (25)	0.0055	0.0059 (31)	0.0059 (25)
5	0.5	0	0.8	0.3718	0.3781 (43)	0.3781 (34)	0.0071	0.0117 (43)	0.0117 (34)
5	0.5	0	0.9	0.5072	0.5158 (67)	0.5158 (49)	0.0280	0.0303 (67)	0.0303 (49)
5	0.5	0	1.0	0.8471	0.8449 (151)	0.8450 (96)	0.1529	0.1511 (151)	0.1512 (96)
5	0	1.0	0.7	0.2845	0.2888 (33)	0.2888 (27)	0.0	0.0	0.0
5	0	1.0	0.8	0.3721	0.3784 (47)	0.3784 (37)	0.0	0.0	0.0
5	0	1.0	0.9	0.5096	0.5186 (81)	0.5186 (59)	0.0	0.0	0.0
5	0	1.0	1.0	1.0000	0.9847 (151)	0.9946 (148)	0.0	0.0	0.0

*Quantities in paranthesis denote the number of iterations.

1(*b*). Again P-11 solutions are included for the comparison of the results. In this case, there is significant improvement in the number of iterations required if the results from the P-1 solutions are used for starting the iterations.

The cases tested in this investigation for ω from 0.7 to 1.0 represent the situations for which the covergence was reported to be very slow. However, if a suitable starting value, such as those obtained from the P-1 solutions are used to start the iterations, the convergence is significantly improved. The computer time required to perform the iterative calculations with the IBM 370/165 computer was approximately one second per iteration. The convergence for the cases $\omega <$ 0.7 and smaller optical thicknesses was very rapid and computer time was much less.

In conclusion, the iterative technique using the proper initial guess can provide a straightforward approach for the solution of radiative heat transfer in an anisotropically scattering medium, since it is capable of handling a high degree of anisotropy and boundary reflection with no additional complications in the analysis.

Acknowledgment

This work was supported in part through National Science Foundation Grant No. ENG 77-12949.

References

1 Chandrasekhar, S., *Radiative Transfer*, Oxford University Press, London, 1950; also Dover Publications, New York, 1960.

2 Case, K. M. and Zweifel, P. F., *Linear Transport Theory*, Addison-Wesley Publishing, Reading, Mass., 1967.

3 Özişik, M. N. and Siewert, C. E., "On the Normal-Mode Expansion Technique for Radiative Transfer in a Scattering, Absorbing and Emitting Slab with Specularly Reflecting Boundaries," *Int. J. Heat Mass Transfer*, Vol. 12, 1969, pp. 611–620.

4 Beach, H. L., Özişik, M. N. and Siewert, C. E., "Radiative Transfer in Linear Anisotropic-Scattering, Conservative and Non-conservative Slabs with Reflective Boundaries," *Int. J. Heat Mass Transfer*, Vol. 14, 1971, pp. 1551–1565.

5 Simmons, G. M. and Ferziger, J. H., "Non-gray Radiative Heat Transfer Between Parallel Plates," *Int. J. Heat Mass Transfer*, Vol. 11, 1968, pp. 1611–1620.

6 Reith, Jr., R. J., Siewert, C. E. and Özişik, M. N., "Non-gray Radiative Heat Transfer in Conservative Plane Parallel Media with Reflecting Boundaries," *J. Quant. Spectry, Radiative Transfer*, Vol. 11, 1971, pp. 1441–1462.

7 Lii, C. C. and Özişik, M. N., "Hemispherical Reflectivity of an Absorbing, Emitting, Isotropically Scattering Slab with Reflecting Boundaries," *Int. J. Heat Mass Transfer*, Vol. 16, 1973, pp. 685–690.

8 Hsia, H. M. and Love, T. J., "Radiative Heat Transfer Between Parallel Plates Separated by a Non-isothermal Medium with Anisotropic Scattering," ASME JOURNAL OF HEAT TRANSFER, Vol. 89, Aug. 1967, pp. 197–203.

9 Love, T. J. and Grosh, R. J., "Heat Transfer in Absorbing, Emitting, and Scattering Media," ASME JOURNAL OF HEAT TRANSFER, Vol. 87, 1965, pp. 161–166.

10 Özişik, M. N., *Radiative Transfer*, Wiley-Interscience, New York, 1973.

11 Pao, C. V., "Method of Successive Approximations for Nonlinear Stationary Transport Equations," *SIAM J. Appl. Math.*, Vol. 27, 1974, pp. 83–91.

12 Pao, C. V., "An Iterative Method for Radiative Transfer in a Slab with Specularly Reflecting Boundary," *Appl. Math. and Computation*, Vol. 1, 1975, pp. 353–364.

13 Roux, J. A. and Smith, A. M., "Comparison of Three Techniques for Solving the Radiative Transport Equation," Arnold Engineering Dev. Center, AEDC-TR-73-200, Arnold Air Force Station, Tenn., January, 1974.

14. Chu, C. M., Clark, G. C., and Churchill, S. W., *Tables of Angular Distribution Coefficients for Light Scattered by Spheres*, Univ. of Michigan Press, Ann Arbor, Mich., 1957.

15 Busbridge, I. W. and Orchard, S. E., "Reflection and Transmission of Light by a Thick Atmosphere According to a Phase Function: 1 + x cos θ," *Astrophys. J.*, Vol. 149, 1967, pp. 655–664.

A. M. Cary, Jr.
Leader, Turbulence Modeling Group
Fluid Mechanics Branch

D. M. Bushnell
Head, Fluid Mechanics Branch
Mem. ASME

J. N. Hefner
Leader, Turbulent Drag Reduction and LFC
Fluid Mechanics Branch

High-Speed Aerodynamics Division,
NASA Langley Research Center,
Hampton, VA 23665

Predicted Effects of Tangential Slot Injection on Turbulent Boundary Layer Flow over a Wide Speed Range

Paper describes a numerical calculation method using eddy viscosity/mixing length concepts for tangential slot injection (wall-wake) flows; application of the method over a wide range of flow conditions indicates increased accuracy compared to previous work. Predictions from the numerical code were in good agreement with experiment (velocity profile, skin friction, and effectiveness data) for low and high speed flows. To achieve improved accuracy, improvements in the turbulence modeling, compared to previous research, were necessary for the imbedded shear layer region in the near field and for the wall region near shear layer impingement. Anomalous behavior was noted for far field experimental velocity profiles in low speed flow when the slot-to-free stream velocity ratio was near one.

Introduction

Mass injection into turbulent boundary layers by slots and holes has been extensively investigated in recent years because of the multiplicity of practical applications of this technique. Film cooling of turbine blades [1, 2] and engine components [3–6] allows an engine to operate more efficiently (at higher temperatures). If the operational surface temperature of high-speed flight vehicles is reduced, lighter and less expensive structural materials can be used [7]. Film cooling can be used to alleviate intense heating in regions of shock interactions or shear layer impingement as well as to reduce the extent of boundary layer separation [8]. Other applications for slot injection include inlet boundary layer control [9], aerodynamic windows for gas dynamic lasers [10], and reduction of skin friction drag [11].

The physical structure of the type of slot injection flow which is the subject of the present paper is illustrated in Fig. 1. Here, a two-dimensional slot flow is injected tangentially beneath an established turbulent boundary layer. At the end of the slot lip the slot and boundary layer flow begin to mix forming an embedded mixing region which grows in the downstream direction until eventually spanning the entire boundary layer. This type of injection is characterized by pure slot flow (channel-type flow), a two-stream mixing region, and a turbulent boundary layer flow existing simultaneously in the near slot region; this convoluted profile eventually relaxes to a full boundary-layer-like profile far downstream.

While much experimental information is now available on the effects of slot injection, analytical and empirical correlation methods have not as yet provided reliable predictive tools for use in systems analyses of slot injection schemes. A necessary ingredient to any systems analyses of the benefits of slot injection balanced against the systems penalties is a good, general purpose predictive technique. One of the major reasons that correlating data for slot injection flows is extremely difficult is the large number of variables which influence the downstream flow development; Fig. 1 illustrates a typical wall wake-type flow and some of the many variables which influence its development. Obviously, a prediction method should be quite comprehensive to include all the factors listed in Fig. 1.

A summary of available experimental data and analytical prediction methods for slot injection-type flows up to 1970 is presented by Goldstein [12]. Since that time several techniques have been developed which solve numerically the equations concerning the flow development downstream of slot injection [13–15]. Each of these prediction methods has advantages, depending on the particular equations solved and the turbulence modeling used. The method of reference [15] has been successful in predicting adiabatic wall effectiveness and skin friction data for high-speed flows [15–18] in the near slot region ($x/S < 10$) as well as far downstream. In addition, this method uses simple turbulence modeling (algebraic length scale/eddy viscosity) which is easily modified to account for new experimental evidence. In [17], however, it was shown that predicted velocity profiles from [15] were in poor agreement with experiment; further comparisons with experimental velocity and temperature profile data by the present authors (presented later) confirmed this disagreement and suggested that the turbulence modeling of [15] should be modified to better represent experimental evidence.

The purpose of this investigation is to examine the turbulence modeling in the method of [15], and using the more abundant experimental information now available, to define an improved turbulence model which will demonstrate prediction accuracy over a wide range of conditions from subsonic to hypersonic speeds. Results obtained using the improved turbulence model with the numerical method of [15] are compared to a representative sample of experimental data from subsonic to hypersonic speeds to illustrate the efficacy of the new modeling. Comparisons of results obtained with the old and new modeling as well as with other prediction methods are made.

Description of Numerical Method

The numerical method [15] used herein solves the partial-differential equations for the mean motion of a two-dimensional, compressible turbulent boundary layer with tangential injection by an implicit finite-difference procedure. The equations solved are those for the conservation of mass, momentum, and total enthalpy; in addition, a conservation of species equation is included with which the injected flow is treated as a trace species to delineate the extent of the mixing region and therefore provide appropriate scales and criteria for the turbulence modeling. Details of the numerical procedure and the computer program are given in [15] and [19]. The turbulence modeling is first order in that the Reynolds stress terms are modeled using conventional algebraic length scale/eddy viscosity concepts. The mixing lengths are scaled to reflect the physical location of interest; for the near slot region a channel flow mixing length scaled on S is appropriate, near walls the Prandtl slope is assumed, in the turbulent mixing region a length scale based on the width of the mixing region is assumed, and in the outer boundary layer flow the scale is the boundary layer thickness. The modeling scheme adopted here and in [15], conceptually allows calculations to be made in the near-slot flow field as well as downstream and, to first order, accounts for lip thickness effects. Current restrictions on the calculation method are:

Contributed by the Heat Transfer Division and presented at the Winter Annual Meeting, November 27–December 2, 1977 of THE AMERICAN SOCIETY OF MECHANICAL ENGINEERS. Manuscript received by the Heat Transfer Division December 15, 1978. Paper No. 77-WA/HT-29.

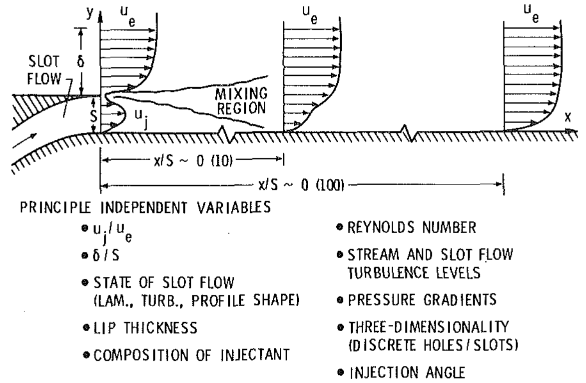

Fig. 1 Typical flow field and independent variables

(1) air-to-air injection, (2) constant normal pressure ($dp/dy = 0$ everywhere, no shocks), (3) thin slot lip (no extensive separation/recirculation), and (4) $u_j < u_e$. Effects induced by the interaction between the boundary displacement thickness and the external pressure field were included in the program in [16], and the effects of foreign gas injection were considered in [20].

Turbulence Modeling. A complete discussion of the philosophy and structure of turbulence modeling for slot flows is presented in [15] and [16]; the discussion here will consider the modifications made to the modeling of [15]. The turbulence modeling logic employed herein was guided to a large extent by the necessity to apply the present approach to high speed as well as low speed flows. The primary modifications made were in the mixing length distributions (see Fig. 1 of [15] for an illustration of the mixing length distribution used in [15]). The modified mixing length distribution is shown in Fig. 2 along with typical velocity and concentration profiles. Three zones are defined downstream of the slot and are discussed individually. Zone I is physically the near-slot region in which can be distinguished the pure injectant flow region, the embedded boundary layer-injectant mixed flow region and the pure boundary layer flow region. In Zone II the mixing region has engulfed the pure injectant flow such that only the mixed flow and pure boundary layer flow regions are distinguishable. In Zone III the mixed flow region is nearing the boundary layer edge, and the flow is considered fully mixed.

Zone I. Zone I, the initial mixing region, is the region for which

$$l_j \geq l_t < l_b$$

The coordinates for the y-location and magnitude of the mixing length at the pivot points 1–5 (see Fig. 2) are as follows:

Point	y	l
1	$a_jS/2K$	$a_jS/2$
2	$S(1 - a_j/2K)$	$a_jS/2$
3	$S - a_m\Delta N_{\mathrm{Sc},t}/K$	$a_m\Delta N_{\mathrm{Sc},t}$
4	$S + t + a_m\Delta N_{\mathrm{Sc},t}/K$	$a_m\Delta N_{\mathrm{Sc},t}$
5	$S + t + a_3(\delta - y_{S1})/K$	$a_3(\delta - y_{S1})$

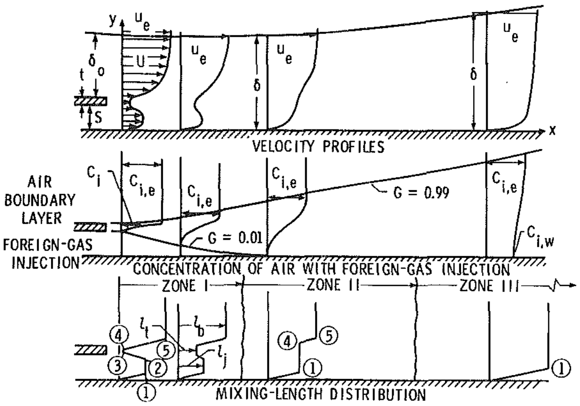

Fig. 2 Illustration of velocity, concentration, and mixing length profiles for a typical slot flow ($u_j/u_e < 1$)

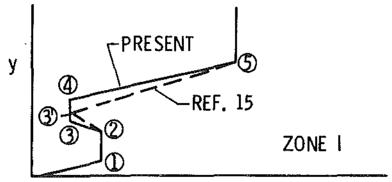

Sketch A

The physical significance of the constants a_j, a_m, a_3, and K are presented in [15], and here it suffices to note that the a constants are ratios of mixing length to width of various flow regions and K is the Prandtl constant. The particular values for these constants used herein will be discussed later. The parameter Δ is the normal extent or thickness of the embedded mixing region downstream of the slot lip, $\Delta = y_{S2} - y_{S1}$. Pivot points 3 and 4 (Sketch A) were used herein instead of pivot point 3′ in [15] in an effort to better represent the physical flow development; i.e., the extent of the mixing region downstream of the slot lip is allowed to determine the location of points 3 and 4 and the magnitude of the mixing length between 3 and 4 which corresponds to the results obtained in [21] for free shear layers (see Fig. 13 of [21]).

The values of mixing length through the boundary layer in Zone I are as follows:

From wall to point 1	$l = Ky$
From point 1 to point 2	$l = Sa_j/2$
From point 2 to point 3	$l = K(S - y)$
From point 3 to point 4	$l = a_m\Delta N_{\mathrm{Sc},t}$
From point 4 to point 5	$l = K(y - S - t)$
From point 5 to δ	$l = a_3(\delta - y_{S1})$

Zone II. Zone II is the region for which

$$l_j \leq l_t \leq l_b$$

Nomenclature

a_j, a_m, a_3 = ratios of mixing length to width of various flow regions
A = Van Driest's damping parameter, $A^+\nu(\tau_w/\rho_w)^{-1/2}$
A^+ = damping function
C_f = skin friction coefficient, $2\tau_w/\rho_e u_e^2$
C_i = mass concentration of species i, ρ_i/ρ
G = normalized concentration profile, $(C_i - C_{i,w})/(C_{i,e} - C_{i,w})$
K = constant in Prandtl's mixing length relation
l_b, l_j, l_t = mixing lengths of various flow regions, see Fig. 1
M = Mach number
N_{Sc} = Schmidt number
p = pressure
S = slot height, see Fig. 1
T = absolute temperature
t = thickness of slot lip, see Fig. 1
u = velocity in x-direction
x = boundary layer coordinate along the mainstream direction
y = boundary layer coordinate normal to the surface
y_{S1} = y-location where $G = 0.01$
y_{S2} = y-location where $G = 0.99$
Δ = normal extent of the mixing region, $y_{S2} - y_{S1}$
δ = boundary layer thickness evaluated where $u/u_e = 0.995$
ν = kinematic viscosity
ρ = density
τ = shear stress

Subscripts

e = edge of the boundary layer conditions
eq = equilibrium conditions
i = species
j = slot flow region
0 = initial condition or no-slot condition
T = total or stagnation conditions
t = turbulent
w = wall conditions

The coordinates for the pivot points are:

Point	y	l
1	$a_m \Delta N_{\mathrm{Sc},t}/K$	$a_m \Delta N_{\mathrm{Sc},t}$
4	$a_m \Delta N_{\mathrm{Sc},t}/K + S + t$	$a_m \Delta N_{\mathrm{Sc},t}$
5	$a_3(\delta - y_{S1})/K + S + t$	$a_3(\delta - y_{S1})$

In Zone II the mixing region originating at the slop lip is allowed to continue to propagate into the external boundary layer, but the mixing length distribution outside the mixing region is unchanged; this was true for [15] modeling only for $y \geq S + t + a_3\delta_0/K$. The basic assumption here is that the mixing region does not destroy the character of the external flow until mixing actually occurs in that region. The values for mixing lengths through the boundary layer in Zone II are as follows:

From wall to point 1	$l = Ky$
From point 1 to point 4	$l = a_m \Delta N_{\mathrm{Sc},t}$
From point 4 to point 5	$l = K(y - S - t)$
From point 5 to δ	$l = a_3(\delta - y_{S1})$

Zone III. It is assumed that the boundary layer has reached equilibrium in Zone III which occurs when

$$l_t > l_b$$

The coordinate of the pivot point is

Point	y	l
1	$a_3\delta/K$	$a_3\delta$

The values for mixing lengths are:

From wall to point 1	$l = Ky$
From point 1 to δ	$l = a_3\delta$

Modeling in Zone III is essentially unchanged from that used in [15].

Two additional changes were made in the turbulence modeling. The first redefines the minimum distance from the wall that y_{S1} can approach. The logic is that the lower edge of the mixing region should not extend into the logarithmic region of the wall boundary layer since the extent of the mixing region is used to define the turbulent scale. Therefore, when

$$a_m \Delta N_{\mathrm{Sc},t}/K < y_{S1}$$

a new y_{S1} was defined as

$$y_{S1} = a_m \Delta N_{\mathrm{Sc},t}/K = a_m(y_{S2} - y_{S1})N_{\mathrm{Sc},t}/K$$

which is the edge of the wall region where $l = Ky$ and $l = a_m \Delta N_{\mathrm{Sc},t}$ are equivalent. Under some conditions, this modification can be significant. The second change was made as a result of disagreement between predictions using the improved modeling and experimental wall skin friction data. Since the new modeling was effective for predicting velocity profiles (as shown later) and yet produced underpredictions of skin friction, a physical explanation for the increased experimental skin friction was sought. Two publications [22, 23], both of which made turbulence measurements downstream of slot injection, indicate that the turbulence level in the near-wall region increases sharply where the mixing zone nears the wall ($x/S \simeq 10$) and then relaxes downstream. It is reasonable to assume that this virulent turbulence would thin the viscous sublayer and result in increases in local wall shear. Accordingly, the Van Driest exponential damping function was empirically modified to reflect this sublayer thinning by making the wall damping region constant, A^+, a function of the rate of change of wall concentration. The rate of change of wall concentration reflects the arrival of the mixing region and increased turbulence at the wall by a sharp increase and subsequent relaxation downstream. The constant in the equation for A^+ was determined by comparison with experiment and then held fixed. The mixing length in the wall region for negligible pressure gradient, curvature, and mass transfer is given by

$$l = Ky\left[1 - \exp\left(-\frac{y}{A}\right)\right]$$

where

$$A = A^+\nu\left(\frac{\tau_w}{\rho_w}\right)^{-1/2}$$

and from experiment

$$A^+ = 26/[1 + 60(dC_w/d(x/S))]$$

This modification had no discernable effect on velocity profile predictions but significantly altered predictions of wall shear.

A comparison between the gross features of the mixing length modeling for [15] and the present modeling is given in Fig. 3. The largest differences are obvious in Zone I where the present modeling was not tied to the $G = 0.5$ location. The change in Zone II is less severe but significant. The Zone III modification is insignificant and both modeling schemes will asymptotically approach the same prediction.

The constants a_j, a_m, a_3, and K used in the turbulence modeling have not as yet been specified. Comparisons with experiment with only small pressure gradients indicates best agreement between prediction and data when $a_j = 0.14$, $a_m = 0.12$, and $K = 0.4$. The factor a_3 is the maximum value of l/δ for the outer boundary layer flow and is subject to various effects [24]. The values used herein were $a_3 = 0.09$ for flat plate type flows and $a_3 = 0.1$ for tunnel wall flows (see [24] for justification).

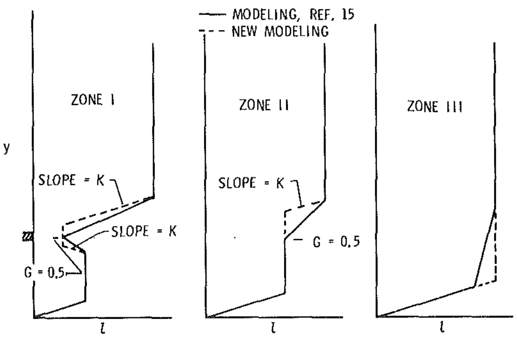

Fig. 3 Comparison of mixing length distributions used in [15] with the improved model

Comparisons with Experimental Data

The numerical method [15] using the turbulence modeling described in the previous section of this paper was used to predict velocity profile development, skin-friction, and effectiveness for several slot flow investigations available in the published literature as well as for unpublished data at Mach 6 obtained at NASA Langley Research Center. Comparisons of predictions with these data (covering subsonic to hypersonic speeds) are then used to assess the efficacy of the proposed new turbulence modeling. The data chosen for comparison represent two-dimensional or axisymmetric, tangential slot injection experiments with turbulent boundary layer flow.

For all experiments, measured initial velocity and temperature profiles at the slot exit location as well as measured inviscid flow conditions were used as input to the program. Obviously these initial conditions could have been predicted from state-of-the-art numerical methods, but since the present objective is to test the turbulence modeling the more accurate input was used. For several experiments small longitudinal pressure gradients were measured and were input into the numerical code. All test cases were for adiabatic wall (equilibrium) conditions downstream of the slot. For all calculations the molecular Prandtl number was assumed to be 0.7, $N_{\mathrm{Sc},t}$ was 1.0 and N_{Sc} was 0.8.

Low Speed Flow. Several comparisons of predictions with subsonic experimental data [23, 25, 26] are shown in Figs. 4–6. Predictions of velocity profile development for slot injection at Mach 0.12 and $u_j/u_e = 0.63$ (two-dimensional slot on a flat nozzle wall) are compared with prediction in Fig. 4(a) for distances up to 87 slot heights downstream of the slot exit. Numerical predictions obtained with the method of [15] using the improved as well as the original turbulence

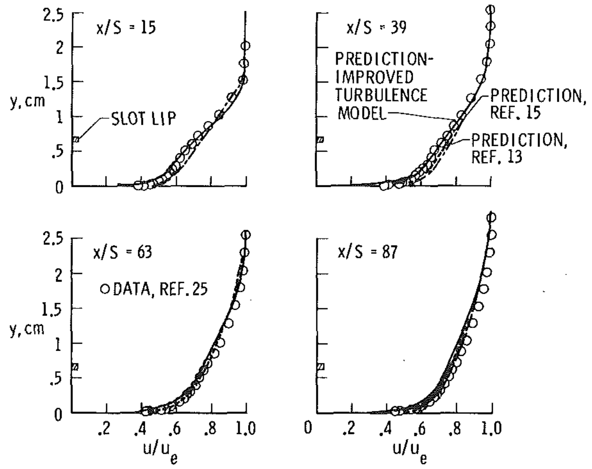

Fig. 4(*a*) Velocity profiles

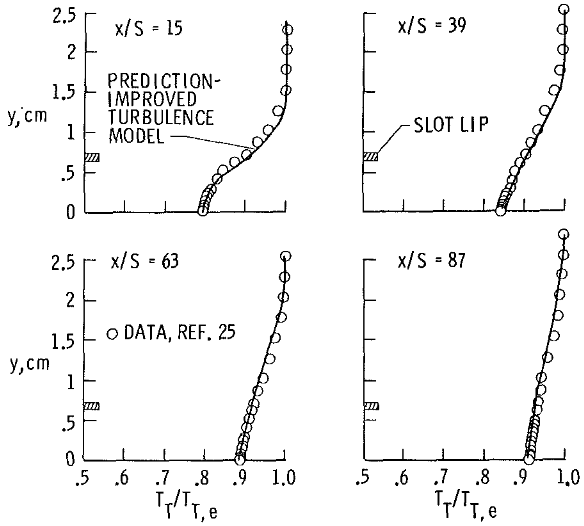

Fig. 4(*b*) Total temperature profiles

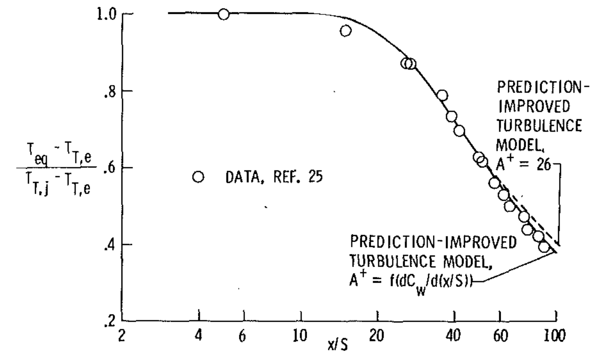

Fig. 4(*c*) Effectiveness

Fig. 4 Comparisons of predictions with experimental data from [25]. $u_j/u_e = 0.63$, $T_{T,j}/T_{T,e} = 0.79$, $M = 0.12$, $dp/dx \neq 0$

modeling are presented; in addition, predictions representative of the numerical method of [13] which essentially uses Zone III modeling throughout the flow field are included. Predictions using the improved modeling are superior in the region nearer the slot ($x/S \leq 39$), but no improvement is apparent for $x/S \geq 63$. There is a tendency toward underprediction of the velocity profiles far downstream of the slot in Fig. 4(*a*). This underprediction will again be apparent in a subsequent comparison in Fig. 5. Since the present numerical prediction procedure is expected to be most accurate far downstream of the slot where the mixed boundary layer is approaching "equilibrium," the underprediction cannot easily be attributed to a turbulence modeling error.

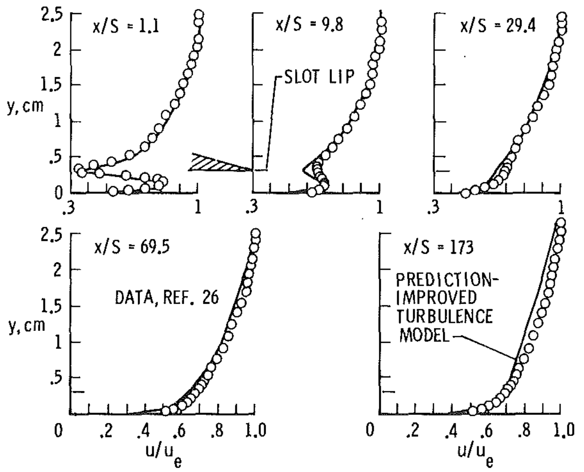

Fig. 5 Comparisons of predictions with experimental velocity profile data from [26]. $u_j/u_e = 0.82$, $T_{T,j}/T_{T,e} = 0.9$, $M = 0.08$, $dp/dx = 0$

The more likely explanation for the disagreement is the presence of some new physics, a possibility being that the slot lip is shedding Karman vortices which develop downstream and increase entrainment; thus, the resulting experimental velocity profiles would be more full than the prediction. Some justification for this explanation is presented in [27] where, for a subsonic mixing flow, it was shown that for u_j/u_e near one, Karman vortices were shed from the splitter plate; however, as u_j/u_e was reduced by reducing the "slot" velocity, the vortices did not form. This is consistent with the present results where some disagreement was noted for $u_j/u_e = 0.69$ (Fig. 4(*a*), $x/S = 87$), and even more disagreement for the data of [26] for which $u_j/u_e = 0.83$ (Fig. 5, $x/S = 173$). A more sophisticated prediction method than the present one would be necessary to include such phenomena as vortex formation effects on downstream flow characteristics.

Examples of prediction of temperature profiles [25] are shown in Fig. 4(*b*) for stations corresponding to the velocity data in Fig. 4(*a*). The agreement between prediction and data is satisfactory, and no unusual deviations occur at large x/S stations. Predictions are compared with the corresponding adiabatic wall effectiveness data [25] in Fig. 4(*c*). Here the effect of the Van Driest wall damping modification for low speed flow is illustrated and is seen to be small. The prediction using the modification is, however, slightly better at large x/S.

Predictions for experimental velocity profiles from [26] for a two-dimensional slot injecting along a flat surface at Mach 0.08 and $u_j/u_e = 0.83$ are shown in Fig. 5. Agreement between prediction and data is again good in the region $x/S \leq 30$ except in a small region centered around the height of the slot; this disagreement may be caused by the downslope at the top of the slot lip (see insert on Fig. 5) which was not accounted for in the code. As mentioned previously the experimental data are significantly underpredicted in the far field of the slot ($x/S = 173$), and this disagreement is probably caused by the presence of Karman vortices in the flow field.

Experimental skin friction data [23] downstream of tangential slot injection along an axisymmetric nozzle wall at Mach 0.8, $u_j/u_e = 0.4$ are shown in Fig. 6. These data were measured with floating element balances and are expected to be accurate. Predictions are shown using the improved turbulence model with and without the Van Driest damping parameter modification. It is clear that the damping modification is necessary to provide a good prediction of the wall shear downstream of slot injection; note that the prediction is good even in the near-slot region. The damping parameter modification has no discernable effect on velocity profile predictions.

High Speed Flow. Comparisons of predictions using the improved turbulence modeling with experimental data at Mach 3 [28] and 6 [18] are shown in Figs. 7 and 8. These data are for the case of approximately "matched" slot and free stream static pressures [17, 18] so that no strong shocks are present in the flow field and the slot flow is sonic.

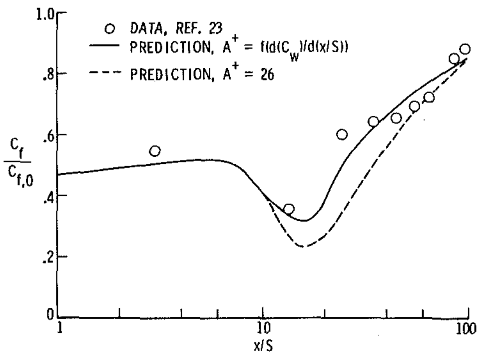

Fig. 6 Comparisons of predictions with skin friction data from [23]. $u_j/u_e = 0.4$, $T_{T,j}/T_{T,e} = 1.0$, $M = 0.8$, $dp/dx \neq 0$

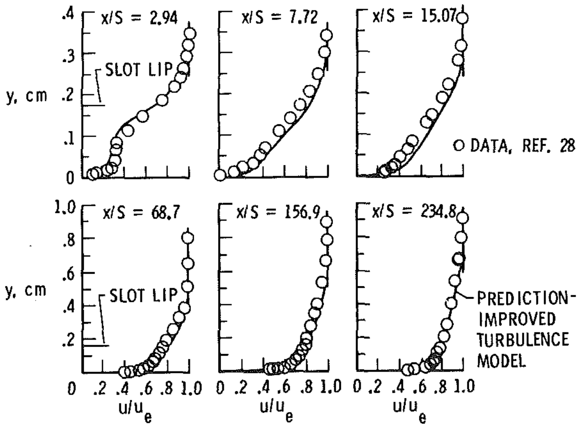

Fig. 7 Comparison of predictions with experimental velocity profile data from [28]. $u_j/u_e = 0.32$, $T_{T,j}/T_{T,e} = 0.93$, $M = 3$, $dp/dx \neq 0$

Comparisons of predictions with velocity profile data for supersonic flow (Mach 3, slight injection angle) for a two-dimensional slot injecting over a flat plate are shown in Fig. 7. The turbulence modeling constants are unchanged from the values used for low speed flows as discussed earlier. The agreement between prediction and data in Fig. 7 is reasonably good with some deviation obvious near the slot; this deviation probably results from the slight injection angle (15 deg to the mainstream flow) which was not accounted for in the prediction method. Agreement far downstream of the slot ($x/S > 6$) is good as would be expected for supersonic flow since Karman vortices are not present.

Comparisons of predictions with velocity profile data downstream of a two-dimensional slot injecting over a flat nozzle wall for Mach 6 flow are shown in Fig. 8(a). These data were obtained by the present authors in the Langley 20 in., Mach 6 Hypersonic Tunnel using the same apparatus as described in [18]. Included are predictions from [15] using the original turbulence modeling, from [13], which essentially uses Zone III modeling throughout the flow field, and from the method of [15] using the improved turbulence modeling. Here, the necessity for the improved modeling is apparent. The modified modeling provides a clearly superior prediction of the velocity profiles at both locations downstream of the slot.

Predictions for the effectiveness (equilibrium wall temperature) downstream of the slot for the same conditions as Fig. 8(a) are shown in Fig. 8(b). Predictions are shown using the improved turbulence modeling both with and without the Van Driest damping parameter modification (the same modification as was used for low speed flow). The prediction including the damping parameter modification is in good agreement with experiment except in the near-slot region where heat conduction into the slot injection manifold reduced the equilibrium wall temperature slightly [18].

Corresponding prediction of skin friction data for the same conditions as for Figs. 8(a) and 8(b) are shown in Fig. 8(c) for two different slot heights. The prediction using the improved turbulence modeling and the damping parameter modification again agrees well with the experimental data while there is obvious disagreement between data and the prediction using conventional near-wall modeling. It thus appears that this damping parameter modification is a necessary ingredient for predicting wall variables downstream of slot injection for high speed flows as well as for low speed flows.

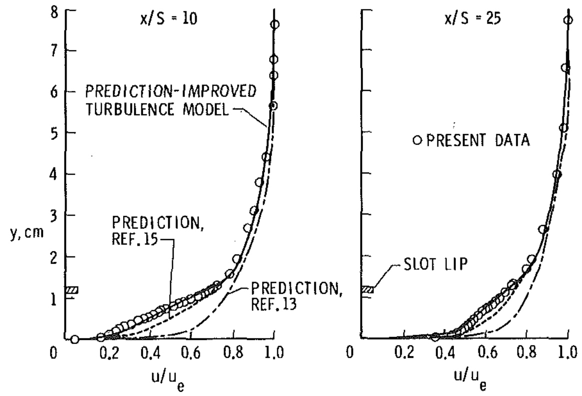

Fig. 8(a) Velocity profiles

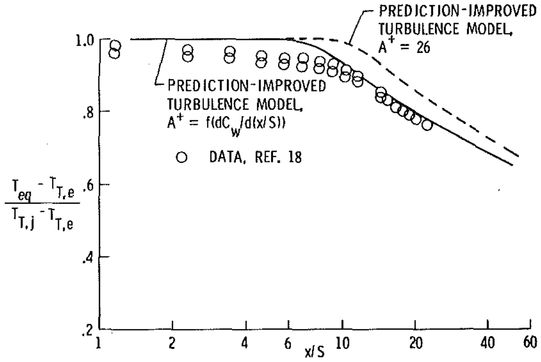

Fig. 8(b) Effectiveness

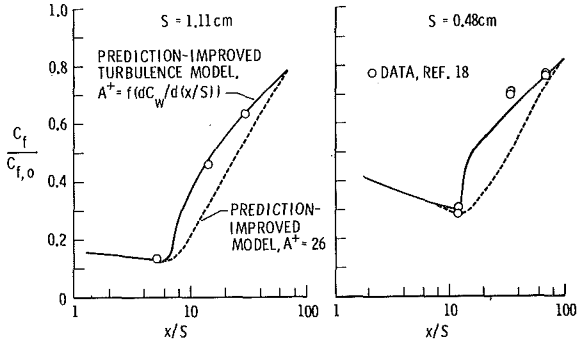

Fig. 8(c) Skin friction

Fig. 8 Comparison of predictions with experimental data from [18]. $u_j/u_e = 0.33$, $T_{T,j}/T_{T,e} = 0.63$, $M = 6$, $dp/dx \neq 0$.

Concluding Remarks

The turbulence modeling for a numerical turbulent boundary layer code used to predict tangential slot injection flows was modified to better represent the physical flow development downstream of the slot. The resulting predictions of the velocity and temperature flow field downstream of injection were in good agreement with experimental data from subsonic to hypersonic speeds. Predictions were valid for the near-slot region as well as for the far-field region except in subsonic flow with injection-to-free stream velocity ratios near 1.0; here, it is suggested that Karman vortices increase entrainment and accelerate mixing which causes underprediction of the far-field velocity profiles. Wall values of skin friction and adiabatic wall effectiveness were also well predicted over the speed range when an empirical modification of the Van Driest damping parameter was included. This modification was necessary because the slot/external flow mixing causes a high turbulence level to occur near the wall where the mixing region approaches the wall ($x/S \simeq 10$); the attendant sublayer thinning causes increases in wall shear which could only be accounted for with the present method by an empirical modification. The present method has not been verified for flows where $u_j/u_e > 1.0$ or for flows with large pressure gradients and should be used with caution for these cases.

References

1 Saarlas, M., "Film Cooling of Turbine Blades," International Symposium on Air Breathing Engines, 2nd, Sheffield, England, March 24–29, 1974, *Proceedings, London Royal Aeronautical Soc.*

2 Hippensteele, S. A., "Pressure-Loss and Flow Coefficients Inside a Chordwise-Finned, Impingement, Convection, and Film Air-Cooled Turbine Vane," NASA TM X-3028, April 1974.

3 Jubasz, A. J., and Marek, C. J., "Combustor Liner Film Cooling in the Presence of High Free-Stream Turbulence," NASA TN D-6360, July 1971.

4 Ledford, O. C., and Stollery, J. L., "Film Cooling of Hypersonic Inlets," 1st International Symposium on Air Breathing Engines, Marseille, France.

5 Tabakoff, W., and Ravuri, R., "Film Cooling Effectiveness for Combustion Chambers," AIAA Paper 75-162, presented at the AIAA 12th Aerospace Sciences Meeting, Pasadena, CA, Jan. 20–22, 1975.

6 Williams, J. J., and Giedt, W. H., "The Effect of Gaseous Film Cooling on the Recovery Temperature Distribution in Rocket Nozzles," ASME Paper No. 70-HT/SpT-42, presented at the Space Technology and Heat Transfer Conference, Los Angeles, CA, June 21–24, 1970.

7 Ferri, A., Fox, H., and Hoydysh, W., "Active Cooling of Hypersonic Airplanes," NASA CR-66930, Jan. 1970.

8 Peake, D. J., "Three-Dimensional Swept Shock/Turbulent Boundary-Layer Separations With Control by Air Injection," NRC No. 15579, Aeronautical Report LR-592, Ottawa, July 1976.

9 Ogarodinikov, D. A., Grin, V. T., and Zakharov, N. N., "Boundary Layer Control of Hypersonic Air Inlets," TT F-13,927, Oct. 1972, NASA.

10 Parmentier, E. M., "Supersonic Flow Aerodynamic Windows for High Power Lasers," AIAA Paper No. 72-710, June 1972.

11 Cary, A. M., Jr., Bushnell, D. M., and Hefner, J. N., "Slot Injection for Skin-Friction Drag Reduction," AGARD/VKI Special Course on "Concepts for Drag Reduction," von Karman Institute for Fluid Dynamics, March 28–April 1, 1977.

12 Goldstein, R. J., "Film Cooling," *Advances in Heat Transfer*, Vol. 7, Academic Press, New York-London, 1971, pp. 321–379.

13 Kacker, S. C., and Whitelaw, J., "Prediction of Wall-Jet and Wall-Wake Flows," *Journal of Mechanical Engineering Science*, Vol. 12, No. 6, 1970. pp. 404–420.

14 Kurkov, A. P., "Mixing of Supersonic Jets Including the Effects of Transverse Pressure Gradient Using Difference Methods," NASA TN D-6592, Dec. 1971.

15 Beckwith, I. E., and Bushnell, D. M., "Calculation by a Finite-Difference Method of Supersonic Turbulent Boundary Layers With Tangential Slot Injection," NASA TN D-6221, April 1971.

16 Miner, W. E., and Lewis, C. H., "A Finite-Difference Method for Predicting Supersonic Turbulent Boundary Layer Flows With Tangential Slot Injection," NASA CR-2124, Oct. 1972.

17 Hefner, J. N., Cary, A. M., Jr., and Bushnell, D. M., "Investigation of the Three-Dimensional Turbulent Flow Downstream of Swept Slot Injection in Hypersonic Flow," AIAA Paper No. 76-679. ASME Paper No. 74-HT-13, presented at AIAA/ASME 1974 Thermophysics and Heat Transfer Conference, Boston, MA, July 15–17, 1974.

18 Cary, A. M., Jr., and Hefner, J. N., "Film-Cooling Effectiveness and Skin Friction in Hypersonic Turbulent Flow," *AIAA Journal*, Vol. 10, No. 9, Sept. 1972, pp. 1188–1193.

19 Hixon, B. A., Beckwith, I. E., and Bushnell, D. M., "Computer Program for Compressible Laminar or Turbulent Nonsimilar Boundary Layers," NASA TM X-2140, April 1971.

20 Murray, A. L., and Lewis, C. H., "Supersonic Turbulent Boundary-Layer Flows With Mass Injection Through Slots and/or Porous Walls," NASA CR-2587, Sept. 1975.

21 Spencer, B. W., and Jones, B. G., "Statistical Investigation of Pressure and Velocity Fields in the Turbulent Two-Stream Mixing Layer," AIAA Paper No. 71-613, presented at the AIAA 4th Fluid and Plasma Dynamics Conference, Palo Alto, CA, June 21–23, 1971.

22 LaRue, J. C., and Libby, P. A., "Measurements in the Turbulent Boundary Layer With Slot Injection of Helium," *The Physics of Fluids*, Vol. 20, No. 2, Feb. 1977.

23 Zakkay, V., and Wang, C. R., "Skin Friction Reduction by Slot Injection at Mach 0.8," NASA CR-2694, July 1976.

24 Bushnell, D. M., Cary, A. M., Jr., and Holley, B. B., "Mixing Length in Low Reynolds Number Compressible Turbulent Boundary Layers," *AIAA Journal*, Vol. 13, No. 8, Aug. 1975, pp. 1119–1121.

25 Brown, G. L., "Gas Film Cooling Past a Non-Adiabatic Flat Plate," Ph.D. Dissertation, University of Idaho, April 1969.

26 Samuel, A. E., and Joubert, P. N., "Film Cooling of an Adiabatic Flat Plate in Zero Pressure Gradient in the Presence of a Hot Mainstream and Cold Tangential Secondary Injection," ASME JOURNAL OF HEAT TRANSFER, Aug. 1965, pp. 409–418.

27 Boldman, D. R., Brinich, P. F., and Goldstein, M. E., "Vortex Shedding from a Blunt Trailing Edge With Equal and Unequal External Mean Velocities," *Journal of Fluid Mechanics*, Vol. 75, June 1976, pp. 721–735.

28 Peterson, J. B., Jr., McRee, D. I., Adcock, J. B., and Braslow, A. L., "Further Investigation of Effect of Air Injection Through Slots and Porous Surfaces on Flat-Plate Turbulent Skin Friction at Mach 3," NASA TN D-3311, March 1966.

N. Nishikawa
Associate Professor.

H. Takase
Graduate Student.

Department of Mechanical Engineering,
Faculty of Engineering,
Chiba University,
Chiba, Japan

Effects of Particle-Size and Temperature Difference on Mist Flow over a Heated Circular Cylinder

An analytical study is performed to evaluate the surface heat flux and the boundary layer structure over an isothermally heated circular cylinder subjected to evaporating particle-vapor flow in forced convection. The governing equations are solved by the local nonsimilarity method and by the Goertler-type series solution. The applicability of both methods is supported by a comparison between the obtained results and with existing solutions for particle-free, single phase flow. Numerical results for the velocity, temperature, and particle size profiles are presented for single component steam-droplets mixture with oncoming velocity 5 m/s at the saturation temperature 100°C. For the number density 5 $\times$ 10^8 numbers/m^3 the droplet diameter at free stream is chosen as 10, 30, and 60 μm. For each cases, the wall-to-free stream temperature difference are chosen as 100, 200, and 350 K. Some results are also shown for cases where the free stream droplet diameter is 1, 3 or 5 μm for the fixed value of droplet number density equated 5 $\times$ 10^{11} m^{-3} and of the wall-to-free stream temperature difference as 100 K. The results show that the enhancement of heat transfer rate is comparatively small in cases where there is large temperature difference but distinctly large in cases involving large particles.

1 Introduction

Forced convection heat transfer to a gas-particle mixture around a body is of considerable interest in various technical applications. In general the presence of particles enhances the heat transfer coefficient, and evaluation of heat transfer and friction over the surface is important in the design of heat exchange equipment.

The problem of a gas-particle boundary layer in the presence of evaporation has been studied recently for the flat plate flow [1–3]. Though the many assumptions in these analyses make the situation uncommon for manufacturing engineers, the predictions are expected to provide important knowledge for relevant phenomena. The evaporating particle vapor flow around a circular cylinder has not yet been analyzed, and the behavior of enhancement in the heat transfer coefficient and the nonsimilarity of the boundary layer, accompanied by both free stream velocity variation and evaporation of particles, have not been considered.

Heat transfer by forced convection to a mixture of evaporating drops and vapor over an isothermally heated circular cylinder is investigated in the present paper. The following are expected to occur in the flow around the cylinder, partly in common with the facts in the flat plate problem in the previous analyses [1–3].

For the vapor-gas-droplets mixture over the flat plate Heyt and Larsen [2] confirmed that with increase of the mass fraction of droplets a larger magnitude is shown for the deviation of the temperature than for single phase flow and the vapor layer thickness becomes smaller. The recent paper dealing with the flat plate problem by Bhatti and Savery [4] should be noted as an example of analysis in which the relative motion of particle to gas-phase is considered in heat transfer study of a spray flow. By analogy to the case of flat plate flow with a small content of droplets, for the case of flow around the cylinder, the class of mist flow may be realized for surface temperature high enough that all liquid particles are evaporated before reaching the surface. In the present problem the vapor layer covers the cylinder surface instead of a liquid film such as in the problem studied by Goldstein, et al. [5]. Goldstein, et al. analyzed the flow structure inside the liquid film, determining the film surface conditions with the impinging droplet flux and the droplet trajectory until impinging. However after their analysis, the papers related to spray flow over objects have scarcely treated the particle trajectory. In this paper, after confirming the smallness of velocity slip between phases outside the boundary layer, the main droplets' contribution—which is taken into account—to the velocity field is the density variation due to vaporization.

As for momentum, in the previous study [2], for the case of flat plate immersed in a uniform stream, the vapor-droplet mixture behaves as a homogeneous fluid with properties dependent on the particle mass fraction. The previous studies have given the results for so small a liquid content that the velocity field varies slightly with variation in liquid content. For flow around a cylinder accompanied by nonuniform potential flow, the analysis has not yet been given for the various combinations of wall temperature and particle size for which the velocity field is considerably affected by the variation of mixture density.

Even if the liquid content is small, as for energy equation, the effect of the presence of particles on the temperature profile is greatly pronounced by the enthalpy of the evaporation; that is, at intermediate values of normal coordinate in the boundary layer the temperature shows a lower value than that obtained for single phase flow. The heat transferred from the wall is consumed not by remote vapor but by the mixture adjacent to the wall. According to the abovementioned mechanism, the thermal boundary layer is expected to become thinner than that for single phase flow and thus the wall temperature gradient may become larger. The deviation of the flow variables from those for single phase flow probably becomes considerable with increasing circumferential angle at which the influence of heat sink accumulates. We employ almost all assumptions used in the previous analyses [1, 2], replacing the assumptions of constant properties with the assumptions that the product of mixture density ρ and viscosity or the product of ρ and thermal conductivity are constant for variable mixture density. In addition to these the main additional assumptions considered here are the following. Firstly, the appearance of liquid film on the cylinder surface is negligible for a given large temperature difference between the surface and free stream. Secondly, the velocity relaxation of droplets is accomplished near the stagnation region because of short relaxation length for small particles concerned here. However, the temperature of the particles does not appreciably increase because of heat release by evaporation.

Contributed by the Heat Transfer Division for publication in the JOURNAL OF HEAT TRANSFER. Manuscript received by the Heat Transfer Division November 30, 1978.

The numerical methods in this paper are chosen as the local nonsimilarity method [6] and the Goertler-type expansion [7] for the following reasons. The present problem requires solutions for several unknowns and solutions at relatively large circumferential locations. Thus these methods in which the upstream solutions are not necessary are advantageous, since the economized grid configurations can be chosen in the region of interest. To the authors' knowledge, these methods have not yet been applied to evaporating particle-vapor flow around the cylinder, while for the flat plate configuration the relaxation processes such as slip of velocity or temperature between particles and gas, as well as evaporation [8] were analytically attempted by the local nonsimilarity method. However, the single phase flow around a cylinder is successfully investigated by these methods [6]. In the present problem a comparison between the results by the two methods is a proof of their applicability. Moreover, at the particle-free condition the dimensionless skin friction and stagnation Nusselt number agree well with the previous numerical results [6] and the analytic one [9], respectively.

2 Basic Equation

The present analysis is based on the following physical model. A compressible forced flow of a steam-droplets mixture exists over a heated circular cylinder with uniform surface temperature T_w as shown in Fig. 1. The free stream with the temperature T_e is assumed to be at the saturation state of steam, then the contained droplets and steam are in thermal equilibrium. Moreover we postulate the following assumptions. (1) The flow is steady and laminar. (2) The free stream velocity is not so large and both the viscous dissipation and the work done by pressure are negligible. The effects of pressure variation on steam density at the free stream and on the phase equilibrium at a droplet surface are negligible. (3) The temperature of the droplets is equal to the free stream temperature over the whole region concerned. The heat conduction to a droplet is proportional to the temperature difference between particle and vapor. The temperature of the vapor around a particle is chosen as the vapor temperature value obtained for the location of particle center instead of taking into account the vapor temperature variation along a particle surface. (4) The particle number density n is equal to its free-stream value in the whole flow field. Then particle size is zero but n not zero inside the vapor layer whose edge is illustrated as the broken line in Fig. 1. Particle shape is uniformly spherical, even when evaporating. (5) Relative motion between phases is negligible and the centrifugal force on particle is not considered. To avoid unnecessary complication we employ the same simplifying assumption as used by Simpson, et al. [1] except those for the transport properties or the density.

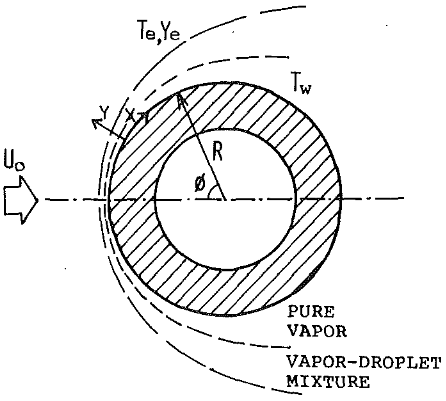

Fig. 1 Flow configuration

Under the boundary layer approximation the governing equations are written in terms of the coordinate system shown in Fig. 1 as

$$\frac{\partial(\rho u)}{\partial x} + \frac{\partial(\rho v)}{\partial y} = 0 \tag{1}$$

$$\rho u \frac{\partial u}{\partial x} + \rho v \frac{\partial u}{\partial y} = \frac{\partial}{\partial y}\left(\mu \frac{\partial u}{\partial y}\right) + \rho_e U \frac{\partial U}{\partial x} \tag{2}$$

$$\rho_v C_p \left(u \frac{\partial T}{\partial x} + v \frac{\partial T}{\partial y}\right) = \frac{\partial}{\partial y}\left(k \frac{\partial T}{\partial y}\right) - n\pi d Nu_p k_e (T - T_e) - w C_p (T - T_e) \tag{3}$$

$$\frac{\partial(\rho_p u)}{\partial x} + \frac{\partial(\rho_p v)}{\partial y} = -w \tag{4}$$

$$n\pi d Nu_p k_e (T - T_e) = w h_{fg} \tag{5}$$

where the properties, μ, k, Cp are pertinent to vapor. These conservation equations are the extended form of those in [3] applicable to the case of nonuniform free stream. For determination of densities,

$$P = \rho_v R T \tag{6}$$

$$\rho_p = \rho_L n d^3 \pi/6 \tag{7}$$

are employed.

Consideration is given here to the case of irrotational potential flow covering the boundary layer and to the conditions at free stream and at the cylinder surface for velocity, temperature, and particle cloud density

$$y \to \infty,\ u \to U = 2U_0 \sin(x/R),\ T \to T_e,\ \rho_p \to \rho_{pe}$$
$$y = 0,\ u = v = 0,\ T = T_w \tag{8}$$

Nomenclature

$A = T_e/(T_w - T_e)$
C_p = specific heat at constant pressure
C_d = drag coefficient for particle
d = particle diameter [micrometer]
E_i = dimensionless heat conduction rate between vapor and particle ($i = 0, 1, 2$)
f = dimensionless stream function
H = dimensionless latent heat
h = heat transfer coefficient
h_{fg} = latent heat of vaporization
k = thermal conductivity
n = particle number density (meter^{-3})
Nu = local Nusselt number
Nu_p = particle Nusselt-number; product of heat transfer coefficient between phases and the ratio d/k_e
p = pressure
Pr = Prandtl number
q_w = surface heat flux
R = cylinder radius
Re = Reynolds number, U_0R/ν_e
T = temperature
U = free stream velocity
U_0 = oncoming velocity
u = velocity component along cylinder surface
v = velocity component normal to surface
V = vector of particle velocity
V_s = vector of velocity slip between particle and vapor
t = dimensionless time appears only for confirmation of small velocity slip
w = vapor production rate
x = circumferential coordinate started at stagnation point
y = coordinate normal to surface
Y = particle mass fraction
η = boundary layer coordinate normal to surface
θ = dimensionless temperature, $(T - T_e)/(T_w - T_e)$
μ = absolute viscosity
ν_e = kinematic viscosity at free stream; $\mu_e/\rho_{\text{pure vapor}}$
ξ = transformed circumferential coordinate $= (1 - \cos\phi)/2$
ρ = density, ρ_L: specific density of liquid
ϕ = circumferential angle measured from forward stagnation point
ϕ_b = angle between particle incidence direction and tangent to surface
ϕ_c = circumferential angle for which particle trajectory is tangential to surface
ψ = stream function

Subscripts

e = free stream
p = particle cloud
v = vapor
w = surface
ξ = differentiation with respect to ξ

In terms of the varying free stream velocity U the following transformation of variables are introduced

$$\xi = \frac{1}{4R}\int_0^x \frac{U}{U_0}dx,\ \eta = \frac{U}{\sqrt{8R\rho_{ve}\mu_e U_0 \xi}}\int_0^y \rho dy \tag{9}$$

Here we introduce the stream function

$$\rho u = \frac{\partial\psi}{\partial y},\ \rho v = -\frac{\partial\psi}{\partial x} \tag{10}$$

and the dimensionless variables

$$f = \psi/\sqrt{8R\rho_{ve}\mu_e U_0\xi} \tag{11}$$

$$\theta = (T - T_e)/(T_w - T_e) \tag{12}$$

$$Y = \rho_p/\rho \tag{13}$$

For simplicity we introduce here the assumption $\rho\mu = \rho_e\mu_e$, $\rho k = \rho_e k_e$. These assumptions are expected to be appropriate for the steam-droplets mixture, because the value of properties μ, k increases as temperature increases, whereas mixture density accordingly decreases. The examination of these assumptions will be shown when we designate the sets of parameters for the results. By the use of these assumptions, the dimensionless variables, and the prime denoting the partial differentiation with respect to η, we rewrite the system of equations (1–8) as follows

$$f''' + ff'' + 2\xi\frac{U_\xi}{U}\left[\frac{\rho_e}{\rho} - (f')^2\right] = 2\xi(f'f_\xi' - f''f_\xi) \tag{14}$$

$$\frac{1}{\mathrm{P_r}}\theta'' + (1 - Y)f\theta' = 2\xi(1 - Y)(f'\theta_\xi - \theta' f_\xi) + \xi K\frac{d\rho_e}{d_e\rho}\frac{U_0^2}{U^2}\theta\left(1 + \frac{\theta}{H}\right) \tag{15}$$

$$fY' = 2\xi(f'Y_\xi - Y'f_\xi) + \xi K\frac{d}{d_e}\frac{\rho_e}{\rho}\frac{U_0^2}{U^2}\frac{\theta}{H} \tag{16}$$

where

$$K = 8\pi Nu_p n d_e^3(R/d_e)^2/(\mathrm{RePr}_e)(\rho_{ve}/\rho_e) \tag{17}$$

$$H = h_{fg}/C_p(T_w - T_e) \tag{18}$$

and where $\mathrm{Re} = U_0R/\nu_e$, $\Delta T = T_w - T_e$. The vapor density ratio is derived from equation (6) as

$$\frac{\rho_v}{\rho_{ve}} = \frac{A}{A + \theta} \tag{19}$$

where $A = T_e/\Delta T$. Thus these equations imply that the solution depends on the parameters n, d_e, R, H, Pr, A and the Reynolds number Re.

The boundary conditions expressed in the dimensionless form are

$$\eta = 0; f = f' = 0, \theta = 1 \quad \eta \to \infty; f' = 1, \theta = 0, Y = Y_e \tag{20}$$

3 Numerical Methods

3.1 Method 1. Local Nonsimilarity Solution. For the local nonsimilarity method we can postulate that the solutions are obtained independently of information from other streamwise locations. This technique is particularly useful for solving problems in which many unknowns appear and for which forward marching technique needs considerable computation procedure in knowing the solution at downstream locations. Moreover, in this method, manipulation to introduce a finite difference expression is not necessary and the derived ordinary differential equations can be directly integrated numerically.

If we can determine the $\partial/\partial\xi$'s at any location ξ without informations for other value of ξ, we can solve (14–16) locally-autonomously. With this in aim, Sparrow, et al. [6] introduced the equations for the streamwise derivatives by differentiating the original dimensionless equations with respect to the streamwise coordinate. In the present paper, we employ this method to gas-particle flow through the following procedure.

For later use we rewrite the value $2\xi U_\xi/U$, and $(U_0/U)^2$ appearing in the system of equations (14–16) by the use of the definition (9) and $U/U_0 = 2\sin(x/R)$ in the boundary condition (8)

$$2\xi\frac{U_\xi}{U} = \frac{1 - 2\xi}{1 - \xi} \tag{21}$$

$$\frac{U_0^2}{U^2} = \frac{1}{16\xi(1 - \xi)} \tag{22}$$

where the subscript ξ denotes the differentiation with respect to ξ. Taking partial derivatives of (14–16) and the boundary conditions with respect to ξ, and omitting the ξ-wise second order derivatives, results in the equations to be solved simultaneously with the original ones (14–20)

$$f_\xi''' + ff_\xi'' + f_\xi f'' = [\rho_e/\rho - (f')^2]/(1 - \xi)^2 - (1 - 2\xi) \times [(\rho_e/\rho)_\xi - 2f'f_\xi']/(1 - \xi) + 2[f'f_\xi' - f''f_\xi + \xi f_\xi'f_\xi' - \xi f_\xi''f_\xi] \tag{23}$$

$$\theta_\xi''/\mathrm{Pr} - Y_\xi f\theta' + (1 - Y)(f_\xi\theta' + f\theta_\xi') = 2(1 - Y - \xi Y_\xi)(f'\theta_\xi - \theta'f_\xi) + 2\xi(1 - Y)(f_\xi'\theta_\xi - \theta_\xi'f_\xi) + E_\xi(1 + \theta/H) + E\theta_\xi/H \tag{24}$$

$$fY_\xi' + f_\xi Y' = 2(f'Y_\xi - Y'f_\xi + \xi f_\xi'Y_\xi - \xi Y_\xi'f_\xi) + E_\xi/H \tag{25}$$

where

$$E = \frac{K}{16(1 - \xi)}\frac{d\rho_e}{d_e\rho}\theta \tag{26}$$

$$E_\xi = \frac{K}{16(1 - \xi)}\left[\left(\frac{d}{d_e}\right)_\xi\frac{\rho_e}{\rho}\theta + \frac{d}{d_e}\left(\frac{\rho_e}{\rho}\right)_\xi\theta + \frac{d}{d_e}\frac{\rho_e}{\rho}\theta_\xi - \frac{d}{d_e}\frac{\rho_e}{\rho}\frac{\theta}{(1 - \xi)}\right] \tag{27}$$

the boundary conditions for f_ξ, θ_ξ, and Y_ξ are

$$\eta = 0; f_\xi' = f_\xi = 0, \theta_\xi = 0$$

$$\eta \to \infty; f_\xi' = 0, \theta_\xi = 0, Y_\xi = 0 \tag{28}$$

The higher order subsidiary equations can be derived by differentiating equations (23–25) with respect to ξ, and so on. In this paper we treat the system of the differential equations derived so far, which is the so-called two equation model in the previous example of local nonsimilarity method, since in the above system of equations (14–28) the two equations are derived for each unknown f, θ, Y, respectively.

The numerical solutions of the system of equations were obtained by the Runge-Kutta-Gill scheme. To solve equations (14–28) we should employ the following procedure together with numerical integration. Here we note that the conditions for equations (16) and (25), respectively, for Y, and Y_ξ are given only at $\eta \to \infty$. Unfortunately there may be no technique to estimate the value of Y or its ξ-wise derivative at the wall or the particle vanishing point before calculation. Thus we integrate equations (16) and (25) from the assumed boundary layer edge $\eta = 5$ towards the wall. This procedure constructs the iterative scheme in which the thus evaluated or initially estimated profiles of Y are used as the coefficients in the integration of equation (14) and (15), starting at the wall. The integration recurrently started at $\eta = 5$ provides the re-evaluated profile of Y. In particular we can evaluate the distance between the particle vanishing point and the wall by means of this procedure. The location of particle vanishing point may not be known by the usual shooting method involving the integration from the wall to the boundary layer edge. By the aforementioned procedure we obtain the solution for the present problem without knowing the solution at upstream locations.

3.2 Method 2, Goertler-type Series Expansion. The dimensionless circumferential coordinate ξ introduced in equation (9) is $1/(4U_0R/\nu)$ of the coordinate variable used in the proposal of Goertler series expansion [7], and thus the expansion of the dependent variables with respect to ξ is temporarily named the Goertler-type expansion.

$$f = f_0 + f_1\xi + f_2\xi^2 \tag{29}$$

$$\theta = \theta_0 + \theta_1\xi + \theta_2\xi^2 \tag{30}$$

$$Y = Y_0 + Y_1\xi + Y_2\xi^2 \tag{31}$$

In deriving the expanded form of momentum equation (14), firstly we show the expanded form of equation (21) and that of mixture density ratio $\rho_e/\rho = (1 + \theta/A)/(1 - Y_e)\cdot(1 - Y)$.

$$2\xi\frac{U_\xi}{U} = 1 - \xi - \xi^2 \tag{32}$$

$$\frac{\rho_e}{\rho} = \left\{\left(1 + \frac{\theta_0}{A}\right)(1 - Y_0) + \left[(1 - Y_0)\frac{\theta_1}{A} - Y_1\left(1 + \frac{\theta_0}{A}\right)\right]\xi \right.$$
$$\left. + \left[(1 - Y_0)\frac{\theta_2}{A} - Y_2\left(1 + \frac{\theta_0}{A}\right) - Y_1\frac{\theta_1}{A}\right]\xi^2\right\}\Big/ m \tag{33}$$

where $m = 1 - Y_e$ denotes steam mass fraction in the free stream. Substituting equations (29–33) into equation (14) and equating the coefficients, we find that the equation for f_0 becomes

$$f_0''' + f_0f_0'' = (f_0')^2 - (1 - Y_0)(1 + \theta_0/A)/m \tag{34}$$

with

$$f_0 = f_0' = 0 \text{ for } \eta = 0, \text{ and } f_0' = 1 \text{ for } \eta \to \infty \tag{35}$$

The remaining two equations in the hierachy for which numerical solutions have been obtained are

$$f_1''' + 3f_0''f_1' + f_0'f_1'' = 4f_0'f_1' - (f_0')^2$$
$$+ [(1 + \theta_0/A)(1 - Y_0 + Y_1) - (1 - Y_0)\theta_1/A]/m \tag{36}$$

$$f_2''' + 5f_2f_0'' + f_0f_2'' = 6f_0'f_2' + 3(f_1')^2 - 2f_0'f_1' - 3f_1''f_1 - (f_0')^2$$
$$+ [1 - Y_0 - Y_1 + Y_2 + (1 - Y_0)(\theta_0 + \theta_1 - \theta_2)/A$$
$$+ (Y_2\theta_0 + Y_1\theta_1 - Y_1\theta_0)/A]/m \tag{37}$$

with $f_i = f_i' = 0$ $(i = 1, 2)$ for $\eta = 0$, and for $\eta \to \infty$ $f_i' = 0$ $(i = 1, 2)$

For the deduction of expanded form of the conservation equations (15, 16), the heat sink term is rewritten through the following manipulation. Since $d/d_e = (\rho_p/\rho_{pe})^{1/3}$ can be written as

$$\frac{d}{d_e} = \left(\frac{A}{\theta + A}\,\frac{Y}{Y_e}\,\frac{1 - Y_e}{1 - Y}\right)^{1/3} \tag{38}$$

Instead of the direct substitution of equations (30, 31) into this expression which yields a complicated form with the expanded form of θ, and Y in the denominator, we employ the following approximations

$$(1 + \theta/A)^{2/3} = 1 + 2\theta/3A,\ Y \ll 1 \tag{39}$$

Then by the use of equations (29–33) and (39) the group $d/d_e\cdot\rho_e/\rho$ can be written as

$$\frac{d}{d_e}\frac{\rho_e}{\rho} = \left(\frac{Y_0}{Y_e}\right)^{1/3}\left(1 + \xi\frac{Y_1}{Y_0} + \xi^2\frac{Y_2}{Y_0}\right)^{1/3}\frac{[1 + 2(\theta_0 + \xi\theta_1 + \xi^2\theta_2)/3A]}{(1 - Y_e)^{2/3}}$$

Moreover we introduce the approximate expression

$$\left(1 + \xi\frac{Y_1}{Y_0} + \xi^2\frac{Y_2}{Y_0}\right)^{1/3} = 1 + \xi\frac{Y_1}{3Y_0} + \xi^2\frac{Y_2}{3Y_0}$$

which is based on $(\xi Y_1 + \xi^2 Y_2)/Y_0 \ll 1$ and appropriate for the region except very near to the particle vanishing point. Finally we obtain

$$\frac{d}{d_e}\frac{\rho_e}{\rho} = \left[\frac{Y_0}{(1 - Y_e)^2Y_e}\right]^{1/3}\left\{1 + \frac{2\theta_0}{3A} + \left[\frac{2\theta_1}{A} + \frac{Y_1}{Y_0}\left(1 + \frac{2\theta_0}{3A}\right)\right]\frac{\xi}{3}\right.$$
$$\left. + \left[\frac{2\theta_2}{A} + \frac{Y_2}{Y_0}\left(1 + \frac{2\theta_0}{3A}\right) + \frac{Y_1\theta_1}{3AY_0}\right]\frac{\xi^2}{3}\right\} \tag{40}$$

By considering the expanded form of $1/(1 - \xi)$ in U_0^2/U^2 in equation (22), the following expression is obtained which accurately approximates the heat sink term at the region away from the vapor layer edge

$$K\frac{d}{d_e}\frac{\rho_e}{\rho}\frac{U_0^2}{U^2}\theta = C(E_0 + \xi E_1 + \xi E_2^2) \tag{41}$$

where

$$C = \frac{K}{16[Y_e(1 - Y_e)^2]^{1/3}} \tag{42}$$

$$E_0 = Y_0^{1/3}(\theta_0 + 2\theta_0^2/3A) \tag{43}$$

$$E_1 = Y_0^{1/3}(1 + 2\theta_0/3A)[\theta_1 + (1 + Y_1/3Y_0)\theta_0] + 2\theta_1\theta_0/3A \tag{44}$$

$$E_2 = Y_0^{1/3}(1 + 2\theta_0/3A)[(1 + Y_1/3Y_0 + Y_2/3Y_0)\theta_0$$
$$+ (1 + Y_1/3Y_0)\theta_1 + \theta_2]$$
$$+ 2/(3A)(\theta_1^2 + \theta_0\theta_1 + \theta_0^2) + Y_1/(9AY_0)\cdot\theta_0\theta_1 \tag{45}$$

The appropriate series solution for (15) is written as

$$\theta_0''/\mathrm{Pr} + (1 - Y_0)f_0\theta_0' = CE_0(1 + \theta_0/H) \tag{46}$$

$$\theta_1''/\mathrm{Pr} + (1 - Y_0)(f_0\theta_1' + 3f_1\theta_0' - 2f_0'\theta_1)$$
$$- Y_1f_0\theta_0' = C[(1 + \theta_0/H)E_1 + \theta_1E_0] \tag{47}$$

$$\theta_2''/\mathrm{Pr} + (1 - Y_0)(3f_1\theta_1' - 4f_0'\theta_2 - 2f_1'\theta_1 + 5f_2\theta_0' + f_0\theta_2')$$
$$+ Y_1(2f_0'\theta_1 - 3f_1\theta_0' - f_0\theta_1') + Y_2f_0\theta_0'$$
$$= C[(1 + \theta_0/H)E_2 + \theta_1/HE_1 + \theta_2/HE_0] \tag{48}$$

with

$$\theta_0 = 1,\ \theta_i = 0\ (i = 1, 2) \text{ for } \eta = 0$$
$$\theta_0 = \theta_1 = \theta_2 = 0 \text{ for } \eta \to \infty \tag{49}$$

The appropriate series solution for equation (16) is written as

$$f_0Y_0' = CE_0/H \tag{50}$$

$$f_0Y_1' = 2f_0'Y_1 - 3f_1Y_0' + CE_1/H \tag{51}$$

$$f_0Y_2' = 2f_0'Y_1 + 4f_0'Y_2 - 3f_1Y_1' - 5Y_0'f_2 + CE_2/H \tag{52}$$

with

$$Y_0 = Y_e,\ Y_i = 0\ (i = 1, 2) \text{ for } \eta \to \infty \tag{53}$$

The ordinary differential equations for f_i, θ_i, Y_i $(i = 0, 1, 2)$ given above are numerically integrated for each set of f_0, θ_0, Y_0 and f_1, θ_1, Y_1, and f_2, θ_2, Y_2 by the Runge-Kutta-Gill program. Y_i's are integrated from $\eta = 5$ towards the wall as we have seen in the integration of Y, and Y_ξ discussed in Section 3.1.

As for the actual computation employed in the local nonsimilarity method and in the Goertler-type series solutions we note here the following aspects. At first in the local nonsimilarity method six coupled equations (14–16, 23, 24) and (25) should be solved as nonlinear simultaneous equations for which computational data often show divergent behavior. Fortunately, in the cases treated here and to be illustrated in the following section, such couplings have mostly insignificant influence on the convergence of the solution, especially at the boundary layer edge. When we recall the simplicity in the reduction of the two equation model, the local nonsimilarity method is relatively easy to handle, for cases where the number of coupled equations is six or so.

Secondly, the procedure to obtain the universal function in the Goertler-type series solution is unexpectedly very hard to manage in some cases for which the solutions can be obtained without difficulty by the local nonsimilarity method. In such cases the first or second order solutions which have maximum at intermediate position inside the boundary layer are excessively sensitive to the wall value of f_i'', or θ_i'. Once the universal functions are obtained, the series solution, which is the result of the "three equation system" with zeroth, first and second order terms, may have accuracy comparable to the results obtained by the two equation model. The truncated terms are expected to be ineffective where the value of ξ is 0.5 at ϕ = 90 deg the downstream end of the flowfield concerned here. In the present calculations, or in general the drawback of the series solution method is that the solutions of universal functions, though they are not affected by higher order solutions, are not always obtained easily, while the local nonsimilarity method, in which equations for unknowns and their ξ-wise derivatives are coupled, gives the solutions at least at the region where the variables show moderate behavior.

In terms of a Nusselt number and local heat transfer coefficient

$$\mathrm{Nu} = hR/k_w \tag{54}$$

$$h = q_w/(T_w - T_e) \tag{55}$$

and from Fourier's law

$$q_w = -k_w(\partial T/\partial y)_{y=0} \tag{56}$$

in conjunction with $\mathrm{Re} = U_0R/\nu_e$ and $\xi = [1 - \cos(x/R)]/2$ from equation (9), it follows that

$$\frac{\mathrm{Nu}}{\mathrm{Re}^{1/2}} = -\theta'(\xi, 0)\frac{\rho_w}{\rho_{ve}}(1 + \cos(x/R))^{1/2} \tag{57}$$

While on the basis of the assumption $\rho\mu = \rho_e\mu_e$ the dimensionless skin friction can be expressed as

$$f''(\xi, 0) = \frac{2\mu_w}{\rho_e U^2}\left(\frac{\partial u}{\partial y}\right)_w [\mathrm{Re}(1 - \cos(x/R))]^{1/2} \tag{58}$$

4 Results and Discussion

Numerical computations were carried out on the steam and water-droplets mixture with fixed values of free stream temperature T_e = 100 °C, $\mathrm{Nu}_p = 2$, and oncoming velocity U_0 = 5m/s at atmospheric pressure. For the cylinder with radius R = 0.5m; i.e., Re = 1.14 × 10^5, free stream particle-number-density n was chosen as 5 × 10^8 and 10^9 numbers/m^3, which were selected together with particle diameter d_e, so that the distance between particles might not be less than $10d_e$ and simultaneously might not be larger than the boundary layer thickness in the flow specified so far. For $n = 5 \times 10^8\mathrm{m}^{-3}$, the computations were performed for the nine cases which consisted of the combination of three values of particle diameter such as d_e = 10, 30, 60 μm, and three levels of wall temperature such as ΔT = 100, 200, and 350 K. The role of large liquid content at $n = 10^9 m^{-3}$, d_e = 60 μm will be discussed. We will also discuss some results for flow at $n = 5 \times 10^{11} m^{-3}$, d_e = 1, 3, 5 μm around a relatively small cylinder of radius R = 0.05 m. The Prandtl number was chosen as 1.01 for $\Delta T \geq 200$ and as 1.03 for ΔT = 100 K to be fitted to the change of the average temperature $(T_w + T_e)/2$, considering that steam is superheated in the boundary layer. The deviation from the boundary condition in the results obtained by the above-mentioned methods is limited within 10^{-5} as a criterion of convergence.

The assumed property relations $\rho\mu = \rho_e\mu_e$, $\rho k = \rho_e k_e$ which have often been employed for analyses of compressible boundary layer were checked and can be justified for the conditions described as above for the following reasons. That is, for the range of temperature 380 < T < 740 K the property ratios $\rho\mu/\rho_e\mu_e = (1 - Y_e)/(1 - Y)\,(T/T_e)^{0.09}$, $\rho k/\rho_e k_e = (1 - Y_e)/(1 - Y)(T/T_e)^{0.15\sim0.18}$ can be introduced. The value $(1 - Y_e)/(1 - Y)$ is always unity at free stream, and for $n = 5 \times 10^8 m^{-3}$ takes 0.917 at the wall for d_e = 60 μm, while it deviates at most 1 percent from unity at the wall for $d_e \leqq 30$ μm. Thus $\rho\mu/\rho_e\mu_e$ and $\rho k/\rho_e k_e$ at the wall are respectively about 1.061 and 1.126 for the latter cases, whereas for the former case of d_e = 60 μm, where the liquid content is 8.302 percent, the values should be multiplied by 0.917. The results are closer values to unity. Thus the assumption that $\rho\mu = \rho_e\mu_e$, $\rho k = \rho_e k_e$ can be justified by these examples.

Moreover to examine the assumption of negligible velocity slip which should be employed carefully for a curved surface, we evaluated the droplet trajectory and magnitude of the velocity slip over the potential flow region around the circular cylinder of radius R = 0.5m. The estimation was performed by numerically integrating the equation of motion [5] $dV/dt = -3\,RC_d/4d(\rho_v/\rho_L)V_s|V_s|$, where V and V_s are, respectively, the dimensionless vector of droplet velocity and of relative velocity of droplet to gas phase referred to U_0. Here the drag coefficient of a droplet is expressed as $C_d = 24[1/\mathrm{Re}(R/d) + 0.0625 - 0.00035\mathrm{Re}(d/R)]$, and $\rho_L/\rho_v = 1602.7$. The integration with respect to time t was started from $3R$ upstream location of the cylinder center and the particle trajectory towards the cylinder was tracked. It should be noted that the values listed in Table 1 are applicable to various R, d, and Re which give the same values of $C_d(R/d)$ as in the present cases.

Table 1 Estimation of droplets' incidence angle and velocity slip

PARTICLE DIAMETR d_e μm	10	30	60	100
LOCATIONS WHERE (deg) ϕ_b=20	2.7	4.5	13.0	27.0
ϕ_b=0; ϕ_c =	9.3	20.0	31.7	43.6
CIRCUMFEREN-TIAL VELOCITY FOR ϕ_b=0				
DROPLET	.356	.655	.852	0.964
STEAM	.352	.684	1.051	1.378
LOCATION WHERE VELOCITY SLIP VANISHES, ϕ deg	11	22.3	33.7	52.6

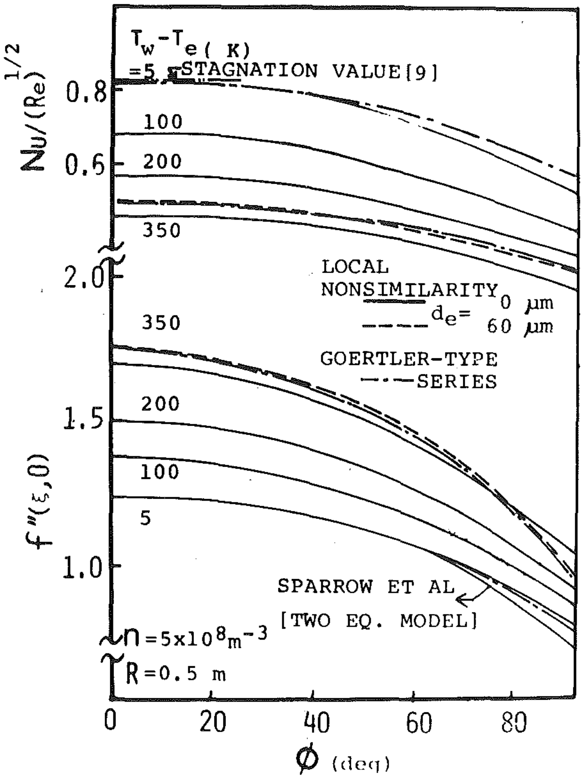

Fig. 2 Comparison of Nusselt number and dimensionless skin friction, $\xi = [1 - \cos\phi]/2$

In Table 1 we can observe the decrease of droplet incidence angle as farther away from the forward stagnation point as well as the fact that the trajectory is tangential to the cylinder surface at $\phi = \phi_c$. At $\phi > \phi_c$ the droplets may scarcely impinge on the cylinder. Also shown in Table 1 is the location where almost all particles are expected to have completed the velocity equilibration to gas phase. That is, the distance between the location and the position $\phi = \phi_c$ is equal to the relaxation length $4d/3C_d(\rho_L/\rho_v)|V_s|$ for $|V_s|$ the absolute value of velocity slip which is given from the third column of Table 1. When we consider that the estimation was for the cases where the decrease in particle size due to evaporation is neglected, the assumption of negligible velocity slip is considered tolerable except for d_e = 100 μm. Where d_e = 100 μm, the computation was performed for various cases, but they have been omitted here due to this and also to the fact that they contradict the increase of mixture volume as anticipated by the assumption of n = constant.

Table 2 Comparison of the results by local nonsimilarity method (two equation model) and Goertler-type series solution

d_e	$T_w - T_e$ (K)		$f''(\xi,0)$				Nu/(Re)$^{1/2}$			
		ϕ (deg)	20	40	60	80	20	40	60	80
10 μm	100	L-N	1.357	1.295	1.178	1.0014	0.6483	0.6143	0.5498	0.4651
		G-S	1.353	1.291	1.174	0.9987	0.6479	0.6096	0.5466	0.4623
	350	L-N	1.683	1.603	1.442	1.216	0.4414	0.4166	0.3740	0.3203
		G-S	1.681	1.597	1.436	1.195	0.4404	0.4136	0.3694	0.3104
60 μm	100	L-N	1.382	1.320	1.198	1.058	0.7271	0.6919	0.6338	0.5545
		G-S	1.381	1.319	1.197	1.012	0.7248	0.6897	0.6317	0.5521
	350	L-N	1.742	1.656	1.500	1.255	0.4825	0.4531	0.3978	0.3408
		G-S	1.740	1.648	1.479	1.222	0.4796	0.4539	0.4112	0.3534

$\xi = [1-\cos\phi]/2$. L-N ;Local Nonsimilarity Method(2EQ model),G-S;Goertler-type Series.

The check of the numerical scheme for the local nonsimilarity method, whose form applied here is the two equation model, can be verified in the following discussion. In Fig. 2 we first compare the results obtained by this method with those obtained by the Goertler-type series solution for cases where the presence of evaporating particles with heat sink is expected to have a significant role. Secondly we compare the results obtained by these methods with the existing available results for particle-free or incompressible condition. The values of the dimensionless skin friction $f''(\xi, 0)$ and the Nusselt number show small deviations between the results by the two methods employed here for the condition $T_w - T_e = 350$ K, $d_e = 60$ μm, $n = 5 \times 10^8 \text{m}^{-3}$, as can be seen in the Table 2. In general the deviations are large downstream but not more than 5 percent even at $\phi = 80$ deg. For cases of particle-free Fig. 2 shows that with a decrease of $T_w - T_e$, $f''(\xi, 0)$ and Nu/(Re)$^{1/2}$ asymptotically approach the respective results of the incompressible flow around a cylinder. That is, the deviation of $f''(\xi, 0)$ by the two methods for $T_w - T_e = 5$ K from the results for incompressible flow with two equation model by Sparrow, et al. [6] is within 2 percent at $\phi = 40$ deg and within 6 percent at $\phi = 80$ deg. Whereas the values of Nu/(Re)$^{1/2}$ for $\phi < 10$ deg are 0.8298 and 0.8294, respectively, by the local nonsimilarity method and by the Goertler-type series. Thus they are analogous to the result Nu/Re$^{1/2}$ = 0.831 which is evaluated from the tabulated value in Table 12.3 of *Boundary Layer Theory* [9]. Thus the capability of the method employed to predict the flow properties in the evaporating particle vapor flow around the cylinder is supported by these comparisons.

As regards the dependence of the solutions upon the particle radius, Table 2 implies that the dimensionless skin friction $f''(\xi, 0)$ maintains a slightly larger value as d_e increases, whereas the relative decrease rate versus ϕ is smaller for large d_e. That is, the value of $f''(\xi, 0)/f''(0, 0)$ at $\phi = 80$ deg ($\xi = 0.4128$) for $d_e = 60$ μm is about one percent larger than that for $d_e = 10$ μm for a fixed value of ΔT. As for the dependence upon temperature difference ΔT, the level of $f''(\xi, 0)$ becomes appreciably higher, as ΔT varies over a few hundreds degrees. However, the rate of decrease in $f''(\xi, 0)$ versus ϕ is also comparatively larger for larger ΔT.

Representative particle size profiles are presented in Fig. 3 for the largest and smallest temperature difference. Hereafter in this paper the results obtained by the local nonsimilarity methods are shown. For the case of large temperature difference or vice versa for the latent heat $h_{fg}/C_p\Delta T$, the particle size profiles locate at larger η and the vapor-layer thickness increases. Here we should note the comparison among the results for cases with $\Delta T = 100$ K and the same liquid content or $nd_e{}^3$ but with different n and d_e. That is, the real dimension of vapor layer thickness for $n = 5 \times 10^{11} m^{-3}$, $d_e = 1$ μm, R = 0.05m is about one third of that for $n = 5 \times 10^8 m^{-3}$, $d_e = 10$ μm, R = 0.5m, even though the ratio of the radius R is one tenth. The analogous comparison will be shown later. The relatively thick vapor layer surrounding the smaller cylinder is expected to simulate the situation in drying process or liquid extraction process.

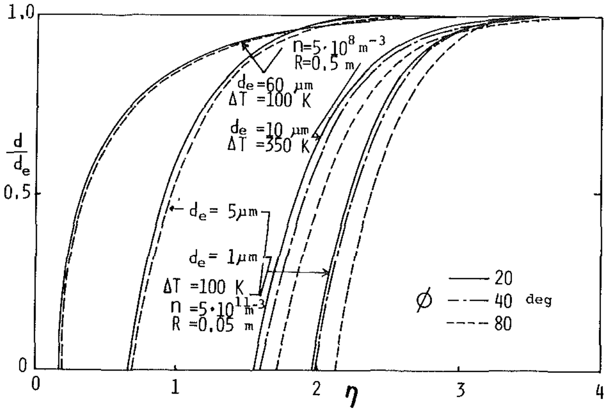

Fig. 3 Representative particle size profiles

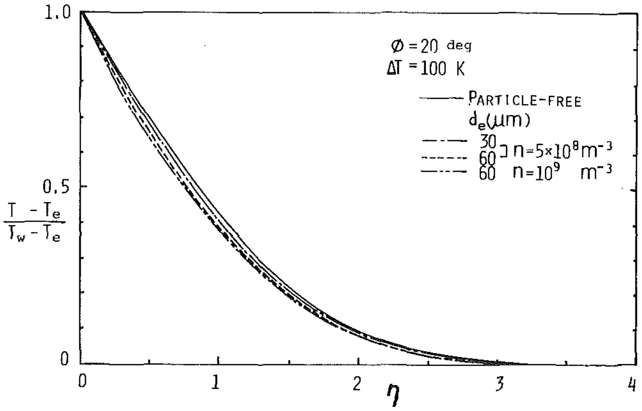

Fig. 4 Representative temperature profiles

Representative temperature profiles and $\theta'(\xi, 0)$ distribution along the surface are shown in Figs. 4 and 5, respectively. The temperature distribution which was obtained in actual computation, but is not illustrated here, should be considered located between the curve for the particle-free condition and that for $n = 10^9 m^{-3}$, $d_e = 60$ μm. The lower temperature for the flow in the presence of large particles can be attributed to the heat sink at droplet surfaces. In Fig. 5 the wall temperature-gradient $\theta'(\xi, 0)$ for large d_e shows a slower decrease with an increase of ϕ compared to those for smaller d_e. For a fixed value of d_e, $-\theta'(\xi, 0)$ for larger temperature difference has a larger decreasing rate and consequently becomes lower than $-\theta'(\xi,0)$ for smaller ΔT at a downstream region, especially for $d_e = 30, 60$ μm. It is expected that for the case of a liquid content larger than those treated in this paper the heat sink effect is predominant over the effect

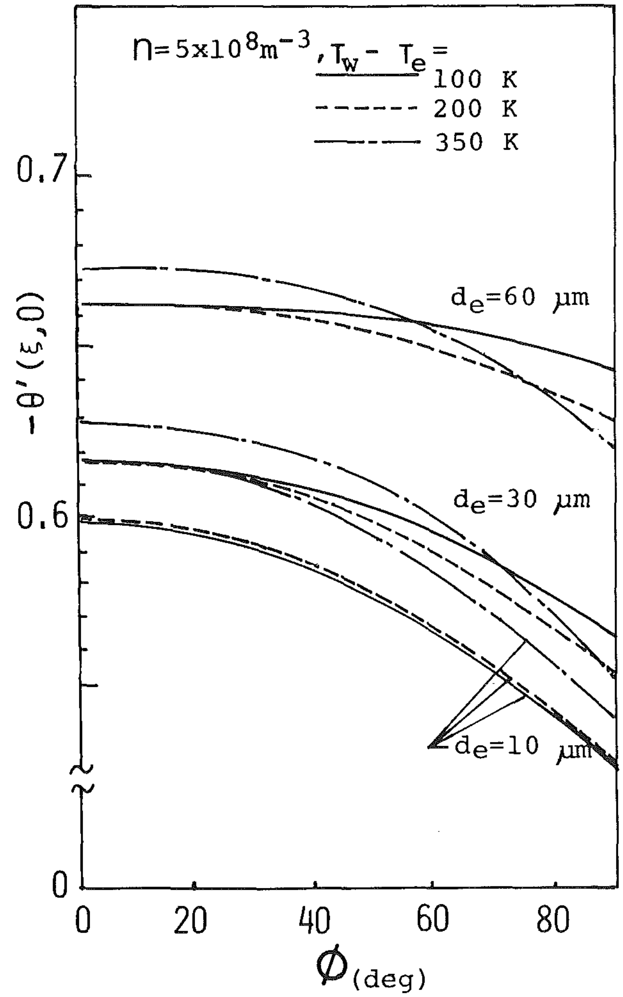

Fig. 5 Temperature gradient at the wall

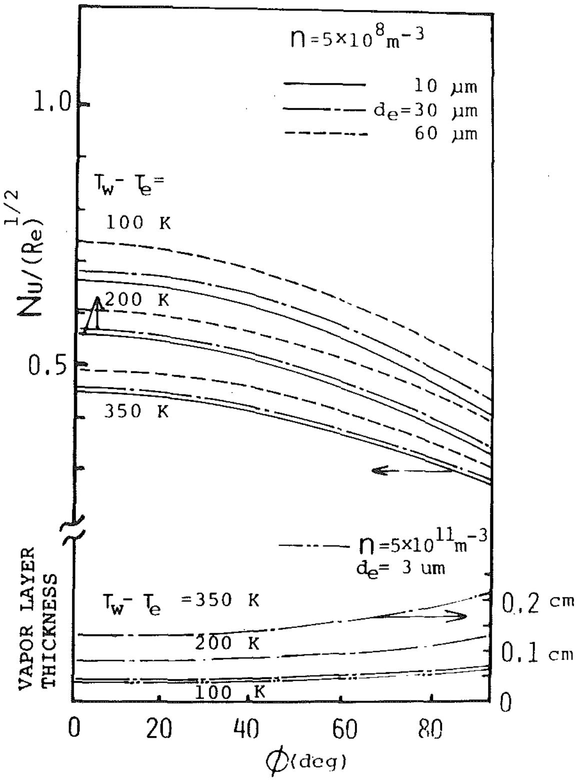

Fig. 6 Distribution of Nusselt number and vapor layer thickness

of the thickening of boundary layer on the temperature gradient $\theta'(\xi, 0)$ and the value of $-\theta'(\xi, 0)$ increases versus ϕ.

The distribution of $\mathrm{Nu/Re}^{1/2}$ at $n = 5 \times 10^8$ is summarized in Fig. 6 together with the distribution of vapor layer thickness along the surface. Inspection of this figure indicates that the curves for a temperature difference ΔT approach each other but, as d_e increases, each curve for a ΔT shifts to higher Nu values. Comparison of vapor layer thickness for $d_e = 3\ \mu\mathrm{m}$, $R = 0.05\mathrm{m}$ with that for $d_e = 30\ \mu\mathrm{m}$, $R = 0.5\mathrm{m}$, though the remaining parameters except number density are equated, qualitatively shows how the smaller particles easily evaporate. The fact that the curves for higher T_w show lower Nu values can be attributed to the contribution of the relatively smaller dimensionless latent heat H. That is, the inspection of vapor layer thickness together with the corresponding curves of $\mathrm{Nu/Re}^{1/2}$ at the same conditions respectively shows that with an increase of surface temperature or $T_w - T_e$ the vapor layer thickness becomes larger and simultaneously $\mathrm{Nu/Re}^{1/2}$ decreases, being affected by the vanishing of heat sink or of particles. Thus for a relatively small dimensionless latent heat H or large $T_w - T_e$ the droplets are easier to evaporate and their contribution to the enhancement in the heat transfer coefficient becomes smaller compared to those for the case of small $T_w - T_e$.

Conclusions

In this paper the effects of both the surface temperature and particle size on heat transfer in the forced convection evaporating droplets-steam flow over a cylinder are analyzed by means of the two types of locally independent solution methods; that is the local nonsimilarity method and the Gortler-type series expansion. The particle temperature is assumed to be equal to the free stream temperature in the whole field, and the evaporation rate can then be expressed in the form proportional to the temperature difference between particle and vapor. The particle-free result obtained by the local nonsimilarity method are compared with the previous result and with that by the Goertler-type series solution and show a reasonable agreement. As for the velocity field, an increase of skin friction due to density change is predicted. It is also found that the rate of surface heat transfer decreases with increasing surface temperature and increases with increasing particle size at free stream. The rate of decrease, as the circumferential angle increases, of surface temperature gradient shows larger value for higher wall temperature. These behaviors are attributable to the magnitude of heat sink by the particle which mostly become ineffective as thickening of vapor layer occurs.

References

1 Simpson, A. U., Timmerhaus, K. D., Kreith, F., and Jones, M. C., "Heat and Mass Transfer in Dispersed Two-Phase, Single Component Flow," *International Journal of Heat and Mass Transfer,* Vol. 12, 1969, pp. 1141–1155.

2 Heyt, J. W. and Larsen, P. S., "Heat Transfer to Binary Mist Flow," *International Journal of Heat Transfer,* Vol. 14, 1971, pp. 1395–1405.

3 Nishikawa, N. and Oguchi, H., "Local Nonsimilar Solutions for Subliming Particle-Vapor Boundary Layer Flow," ASME JOURNAL OF HEAT TRANSFER, Vol. 99, 1977, pp. 342–343.

4 Bhatti, M. S. and Savery, C. W., "Augmentation of Heat Transfer in a Laminar External Gas Boundary Layer by the Vaporization of Suspended Droplets," ASME JOURNAL OF HEAT TRANSFER, Vol. 97, 1975, pp. 179–184.

5 Goldstein, M. E., Yang, W. J., and Clark, J. A., "Momentum and Heat Transfer in Laminar Flow of Gas With Liquid-Droplets Suspension Over a Circular Cylinder," ASME JOURNAL OF HEAT TRANSFER, Vol. 89, 1967, pp. 185–194.

6 Sparrow, E. M., Quack, H., and Boerner, C. J., "Local Nonsimilarity Boundary-Layer Solutions," *AIAA Journal,* Vol. 8, 1970, pp. 1936–1942.

7 Goertler, H., "A New Series Solution for the Calculation of Steady Boundary Layer Flows," *Journal of Mathematics and Mechanics,* Vol. 6, 1957, pp. 1–66.

8 Nishikawa, N., and Takase, H., "An Analysis of Nonequilibrium Boundary Layer Containing Evaporable Particles," *Proc. of the 26th Japan Congress for Applied Mechanics,* 1978 (presented 1976, Nov.) pp. 431–443.

9 Schlichting, H., *Boundary-Layer Theory,* 6th ed., McGraw-Hill, New York, 1968, p. 291 or Squire, H. B., section of *Modern Developments in Fluid Dynamics,* ed. by Goldstein, S., Oxford, 1938, pp. 623–627.

Experimental Study of Evaporation and Breakdown of Thin Liquid Films Driven by Shear Stresses

E. Ihnatowicz
Lecturer.

S. Gumkowski
Lecturer.

J. Mikielewicz
Professor.

Institute for Fluid Flow Machinery,
Polish Academy of Sciences,
Gdańsk, Poland

An experimental investigation of a thin water film driven by steam, its evaporation and breakdown, was carried out. The shear stresses, the main factor influencing the film motion, were calculated as a function of the "blowing parameter." The influence of the blowing parameter on evaporation and breakdown of the film was investigated. The results obtained are in agreement with a theoretical analysis which included the effects of the evaporating mass stream and of small droplets within the vapor boundary layer.

Introduction

The question of evaporation and breakdown of a continuous liquid film driven by shear stresses flowing on a solid surface is important in a number of practical applications. It arises in the operation of large steam turbines, particularly in the last few stages. The structure of the droplet stream leaving the liquid phase and impinging on the rotor blades depends to a large extent on the flow regime of the liquid phase on the surface of the stator blades. Of no less interest is the reverse process of surface rewetting. Most investigations of film flow and evaporation are devoted to gravity driven films. Related literature is quoted in [1–3]. Film evaporation on internally heated turbine guide blade surfaces is of primary interest to the authors [4, 5]. The effectiveness of film evaporation depends to a large extent on the liquid phase flow structure, so that film breakdown and formation of rivulets were considered first [6]. When the amount of liquid is small—for instance, at near-complete evaporation—the structure of the liquid layer is discontinuous and rivulets form [7]. Generally in the literature rather thick films, driven by a moderate velocity gaseous phase, are considered. The thermal resistance of such films is much larger than that of the boundary layer. Heat transfer is then limited by the thermal resistance of the film. The films existing on guide blade surfaces are much thinner and are driven by a very fast gas flow. In this case the film thermal resistance is comparable to the boundary layer resistance. In addition, the film evaporation process occurs in the presence of a small amount of moisture contained in the form of small droplets in the working steam [8]. Some information on thin films driven by shear stresses is given. [9–12].

The stability of thin liquid layers is another essential element of the process and was the object of a number of theoretical investigations. In most of these small disturbances are applied to the fluid-gas interface. However, this kind of instability does not inevitably effect film breakdown. The small-disturbance theory does not take into account the contact angle an essential parameter of the breakdown process. Another approach to the problem has been put forward by Hartley and Murgatroyd [13]. Extensions of their theory, including not only hydrodynamic but also thermal effects exist in the literature. Still other approaches to the film breakdown problem have been proposed by Hobler [14] and Bankoff [15], and systematically extended by Mikielewicz and Moszynski [16, 17]. The set of equations developed by Mikielewicz and Moszynski allows one to predict the minimum thickness of the breaking down film as well as the radius of curvature of the rivulets and the distance between them. As was mentioned above, the contact angle is an essential parameter governing the breakdown process. Systematic investigations into this question are now under way at the Institute of Fluid-Flow Machines [18].

In this paper the breakdown theory has been tested against the experimental investigations in adiabatic as well as in nonadiabatic conditions. The main objective of the film breakdown investigations was to investigate a possible extension of the hydrodynamic breakdown theory to the nonadiabatic conditions.

Theory

The evaporation process occurs with a wall heat flux density q_w. The heat flux goes through the film of the thickness of δ_l and the boundary layer of the thickness of δ_v. Thus, the equivalent heat transfer coefficient for film h_ℓ and boundary layer h_v may be written as

$$h_e = \frac{1}{\dfrac{1}{h_l} + \dfrac{1}{h_v}} \tag{1}$$

The analyzed evaporation process is controlled by the thermal resistances of both the film and the boundary layer.

Thermal Resistance of the Liquid Film. Assuming laminar incompressible steady flow of a thin film with constant properties and neglecting inertia forces the momentum equation takes the form

$$g_x(\rho_l - \rho_v) - \frac{dp}{dx} + \mu_l \frac{d^2 u_l}{dy^2} = 0 \tag{2}$$

Introducing the shear stress

$$\tau = \mu_\ell \frac{du_l}{dy} \tag{3}$$

we obtain after an integration of equation (2) with the boundary conditions $y = \delta_l$, $\tau = \tau_i$ the shear stress distribution in a laminar film in the form

$$\tau = a(\delta_l - y) + \tau_i \tag{4}$$

where

$$a = g_x(\rho_\ell - \rho_v) - \frac{dp}{dx}$$

Substituting equation (3) into equation (4) and integrating the velocity distribution within the laminar film, with the boundary condition

$$y = 0 \qquad u_\ell = 0, \qquad \text{gives}$$

$$u_l = \frac{1}{\mu_l}\left[a\left(\delta_l y - \frac{y^2}{2}\right) + \tau_i y\right] \tag{5}$$

Equation (5) allows one to predict the film mass flow rate:

$$\dot{m}_l = \rho_l \int_0^{\delta_l} u_l dy = \frac{\rho_l}{\mu_l}\left[\frac{1}{3} a \delta_\ell^3 + \frac{\tau_i \delta_\ell^2}{2}\right] \tag{6}$$

The temperature distribution within the laminar film may be found from

$$q_w = -\lambda_l \frac{dt}{dy} \tag{7}$$

Contributed by the Heat Transfer Division and presented at the 98th Winter Annual Meeting, Atlanta, Georgia, Nov. 27–Dec. 2, 1977. Revised manuscript received by the Heat Transfer Division September 27, 1978. Paper No. 77-WA/HT-7.

Assuming q_w = const and after integration of equation (7), with the condition $y = 0\ t_\ell = t_w$ we have

$$t_l = -\frac{q_w}{\lambda_l} y + t_w \tag{8}$$

The heat transfer coefficient is then

$$h_l = \frac{q_w}{t_w - t_i} \tag{9}$$

The temperature of the film surface t_i may be higher than the saturation temperature t_s in view of the non-equilibrium nature of the two-phase flow. The authors' experimental results indicate that substancial liquid superheats may occur under forced convection conditions.

Substituting equation (8) into equation (9) the heat transfer coefficient formula takes the elementary form

$$h_l = \frac{\lambda_l}{\delta_l} \tag{10}$$

Thermal Resistance of the Boundary Layer. There exist a number of theories of the boundary layer with transverse blowing [19, 20]. The theory proposed here is expected to give a simple formulation including the effect of evaporating droplets and to provide a basis for evaluating the experimental results. One-dimensional vapor flow within the boundary layer is governed by the following equations:

$$\frac{d(\rho_v v_v)}{dy} = 0 \tag{11}$$

$$\rho_v v_v \frac{du_v}{dy} = \mu_v \frac{d^2 u_v}{dy^2} \tag{12}$$

$$\rho_v v_v \frac{di_v}{dy} = \frac{\lambda_v}{c_{pv}} \frac{d{i_v}^2}{dy^2} - q_v \tag{13}$$

Integration with the boundary conditions:

$$y = 0;\ u_{iv} = 0;\ i_v = i_{iv}; \qquad \text{due to } u_{v\infty} \gg u_l$$

$$y = \delta_v;\ u_v = u_{v\infty};\ i_v = i_{v\infty};$$

yields

$$\frac{u_v}{u_{v\infty}} = \frac{\exp\left(\frac{j_{iv}\delta_v}{\mu_v} \cdot \frac{y}{\delta_v}\right) - 1}{\exp\left(\frac{j_{iv}\delta_v}{\mu_v}\right) - 1} \tag{14}$$

$$\frac{i_{iv} - i_v}{i_{iv} - i_{v\infty}} = \frac{(B+1)\left(\exp A \frac{y}{\delta_v} - 1\right)}{\exp A - 1} - B\frac{y}{\delta_v} \tag{15}$$

where

$$A = \frac{c_{pv} j_{iv} \delta_v}{\lambda_v} = \frac{j_{iv}\delta_v}{\mu_v} \cdot \mathrm{Pr}_v$$

$$B = \frac{-q_v \delta_v}{j_{iv}(i_{iv} - i_{v\infty})}$$

$$j_{iv} = \rho_v \cdot v_v$$

Employing equations (14, 15) and introducing the blowing parameter

$$b = \frac{j_{iv}\delta_v}{\mu_v} = \frac{j_{iv}}{u_{v\infty}\rho_v F_a} \tag{16}$$

one obtains

$$\frac{F_n}{F_a} = \frac{b}{\exp b - 1} \tag{17}$$

and

$$\frac{h_v}{h_a} = \frac{b\mathrm{Pr}_v}{\exp(b\mathrm{Pr}_v) - 1} - \left[\frac{q_v\delta_v}{q_{ia}}\right]\left[\frac{1}{\exp(b\mathrm{Pr}_v) - 1} - \frac{1}{b\mathrm{Pr}_v}\right]$$
$$= f_1(b\mathrm{Pr}_v) + Zf_2(b\mathrm{Pr}_v) \tag{18}$$

where

$$Z = \frac{-q_v\delta_v}{q_{ia}}$$

Equations (17) and (18) were obtained for a laminar vapor flow. Their validity may be extended to a turbulent boundary layer if the influence of mass blowing is assumed significant only within the laminar sublayer. Dependence of equations (17) and (18) on the parameter b is identical only if $q_v = 0$ and $\mathrm{Pr}_v = 1$. This suggests that the analogy between heat and momentum transfer in the presence of transverse blowing exists only when the energy generation rate (heat sinks) may be neglected and the Prandtl number is nearly one. The function $f_2(b\mathrm{Pr}_v)$ is always negative and increasing. This means that the existence of a heat sink—q_v, due to droplet evaporation in the boundary layer, intensifies heat transfer in comparison with a boundary layer without evaporating droplets.

Equations (17) and (18) were verified experimentally at constant Pr_v. It is reasonable to assume, that the evaporation from the film is

Nomenclature

a = defined by equation (4)
A, B = defined by equation (15)
b = blowing parameter
c = mass concentration of droplets within boundary layer
c_p = specific heat at constant pressure
d = diameter
D = deposition mass flux
e = energy per unit length
f = function defined by equation (18)
F = friction factor; also area
g = gravitational acceleration
h = heat transfer coefficient
i = enthalpy
Δi = latent heat of vaporization
j = mass flow rate per unit volume defined by equation (15)
k = mass transfer coefficient
l = linear dimension
m = mass
$\dot{m}$ = mass flow rate
p = pressure
q = heat flux
q_v = energy generation rate per unit volume
r = radius
t = temperature
Δt = temperature difference
u, v = velocities
x = coordinate, also quality
y = coordinate
Z = defined by equation (18)
Pr = Prandtl number
Re = Reynolds number
δ = film thickness
Δ = difference
Θ_0 = contact angle
λ = thermal conductivity
μ = dynamic viscosity
ρ = density
σ = surface tension
τ = time; also shear stress

Subscripts

a = adiabatic wall conditions
b = film breakdown
d = dry surface
e = equivalent value
i = interface liquid-vapor
in = inlet
l = liquid; film
n = nonadiabatic conditions
out = outlet
r = rivulet
re = rewetting
s = saturation
t = total values; transmission
v = vapor; volume
w = wall
∞ = undisturbed flow
1 = annulus zone between film and surface of zero shear stress

Superscripts

$-$ = mean value
$+$ = dimensionless quantity

analogous to blowing through a porous wall. Introducing the velocity of the vapor evaporated from the film surface

$$v_v = \frac{q_w}{\Delta i \rho_v} \tag{19}$$

into equation (16) we obtain for the blowing parameter

$$b = \frac{q_w}{\Delta i \rho_v u_{v\infty} F_a} \tag{20}$$

a form convenient for experimental verification.

Film Breakdown. The Mikielewicz and Moszynski theory [16, 17] considers the following criteria for film breakdown: (1) mass flow rate in the film and the rivulets is equal, (2) total energy of film and rivulets is equal and (3) the newly formed rivulets are stable; i.e., their total energy exhibits a local minimum. The total mechanical energy of the film and rivulets consists of kinetic and surface energy the latter being a sum of the surface energy of every interface, i.e., solid-liquid, solid-vapor, liquid-vapor.

As a results was obtained the dimensionless thickness of the shear driven film at breakdown as a function of the contact angle Θ_0.

$$\delta_{lb}^{+} = \frac{\rho_l \tau_i^2 \delta_{lb}^3}{6\mu_l^2 \sigma} = \delta_{lb}^{+}(\Theta_0) \tag{21}$$

It follows from equation (21) that the limiting thickness is a function of physical parameters which may vary with temperature and of the shear stress on the interface. Under nonadiabatic conditions there exists a mass flux of evaporation transverse to the main flow. This mass flux exchanges momentum within the boundary layer and affects the shear stress distribution in it, as shown in the preceding section.

Assuming, that the heat flux influences the film breakdown phenomenon only through the shear stress modifications at the interface, it is possible to extend the adiabatic breakdown theory to nonadiabatic conditions. As a result one obtains

$$\frac{\delta_{lbn}}{\delta_{lba}} = \left(\frac{F_n}{F_a}\right)^{-2/3} \tag{22}$$

where the function of b occurring on the right-hand side may be based on existing theories of boundary layers with blowing or may be determined experimentally as was done in this paper.

Experimental Investigations

The experimental investigations of the thin film flow driven by steam, its evaporation and breakdown was carried out in an annular channel 652 mm long formed by two tubes 34 mm and 100 mm in diameter, respectively. The outer tube was made of glass to allow observation of the flow. The experimental apparatus was placed between the outlets of two steam turbines. Hence, the properties of the steam supplied to the apparatus were approximately the same as in the last stages of a turbine. In the present experiments the pressures were in the range from 6 to 18 kPa with corresponding saturation temperatures. The test section was arranged vertically with both steam and water flowing downwards. Fully developed thermal conditions were established in the test section due to the approximately 2 m long straight channel supplying steam. The film was introduced through a porous section of the surface of the inner heated copper tube, and steam was flowing in the annular channel. The film was heated by hot water flowing inside the copper tube. The test section is shown in Fig. 1.

The inner tube was equipped with thermocouples for wall temperature, heating water temperature and initial film temperature measurements. Water used to form the film was heated nearly to the saturation temperature and then was fed into test section. Water flowing as a thin film over the outer surface of the copper tube was partially evaporated and then passed back to the steam plant and the remainder was collected by a conical funnel.

Reduction of Data. The mass flow rate of water in the film was measured by a variable area flowmeter with a range from 5 to 60 liters per hour and an accuracy of ± 1 percent.

The Reynolds number was defined as

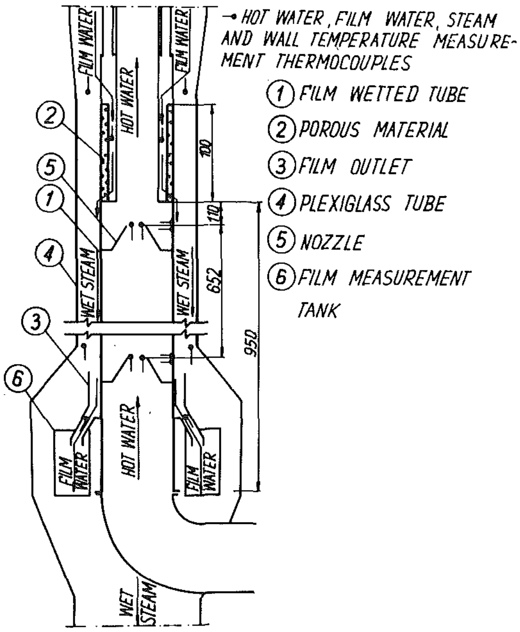

Fig. 1 Schematic arrangement of the test section; all dimensions in millimeters

$$\mathrm{Re}_l = \frac{\dot{m}_l}{\pi d_1 \mu_l} \tag{23}$$

The experiments were performed within the range of $\mathrm{Re}_l = 40 - 190$ assuring a laminar character for the film flow.

The heat flux to the film was determined from a heat balance on the heating water and ranged from 0 to 40 kW/m^2.

Based on the heat flux density q_w, total temperature difference $\Delta t_t = t_w - t_v$ and the predicted film thickness, the heat transfer coefficient were determined:—for the film

$$h_l = \frac{\lambda_l}{\delta_l} \tag{24}$$

—for the boundary layer

$$h_v = \frac{q_w}{\Delta t_t - q_w \dfrac{\delta_l}{\lambda_l}} \tag{25}$$

The film thickness was calculated from equation (6) and known film mass flow rate $\dot{m}_\ell$.

The shear stress was determined with the aid of a method developed by Hewitt and Lacey [21] and adopted to the present case. The method is based on the division of the channel into two regions. The boundaries of the regions are the wall (wet and dry, respectively) and the zero-shear-stress surface (maximum velocity surface). For these two regions conservation equations of mass and momentum have been written. Dry wall friction coefficient was assumed. The set of equations allow finding the shear stresses on the liquid-vapor interface.

Experimental Results. Some of the experimental data concerning the evaporation and breakdown process are shown in Figs. 2 and 3. The experiments were carried out under non-equilibrium conditions between the wet steam and the superheated liquid layer. An analysis of experimental accuracy shows the data have approximately ± 3.5, ± 13, ± 2.3, ± 25, and ± 10 percent of mean square relative sistematic error in heat flux, pressure gradient, film mass flow rate, interface shear stresses and film thickness, respectively. It was observed that, at near critical value of the film thickness, waves with initially sharp and afterwards smoother crests appeared on the film surface. As the film mass flow rate was decreased the film surface became even and later on the film broke forming one or two converging rivulets. The rewetting phenomenon occurred as the film mass flow rate increased. A distinctly thick liquid "belt" appeared around

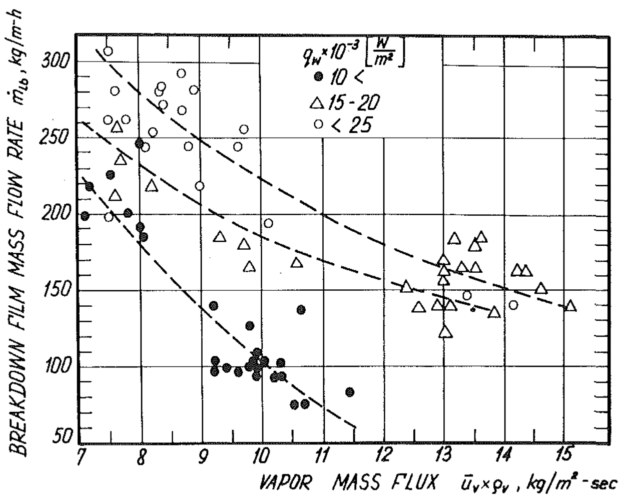

Fig. 2 Breakdown film mass flow rate per unit circumference $\dot{m}_{\ell b}$ versus steam mass flux $\rho_v \bar{u}_v$ and heat flux q_w

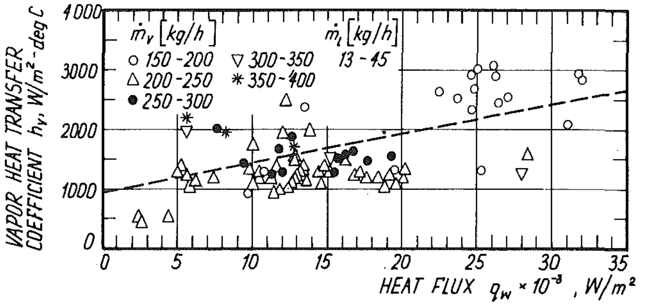

Fig. 3 Heat transfer coefficient h_v versus heat flux q_w for various mass flow rates of steam $\dot{m}_v$ and film $\dot{m}_\ell$

the dry spots, and afterwards overflowed the whole surface forming a continuous film again.

Analysis of Experimental Results

The following were determined experimentally under nonadiabatic conditions: friction factor at the interface, heat transfer coefficient for film and boundary layer and film thickness at the moment of breakdown and rewetting. The main parameter controlling the film flow, heat transfer and breakdown appears to be the shear stress at the liquid-gas interface. Under adiabatic wall conditions the interface friction factor is a function of film and vapor Reynolds number and is well correlated by the experimental formula

$$F_a = F_d\,(1 + 0.025\,\mathrm{Re}_\ell) \tag{26}$$

where

$$F_d = 0.0007 + 0.0625\,(\mathrm{Re}_{v1})^{-0.32}$$

is Koo's friction factor for dry wall as used in [21]. A comparison of the adiabatic film-gas interface friction factor with the results of Hewitt and Lacey [21] is shown in Fig. 4. The ratio of the nonadiabatic friction factor F_n to the adiabatic friction factor F_a, given by equation (26) is shown in Fig. 5 as a function of the blowing parameter b. The experimentally determined ratio F_n/F_a well correlated by

$$\frac{F_n}{F_a} \cong 1 - 1.1b^{0.6} \tag{27}$$

By virtue of the analogy between heat and momentum transfer the heat transfer coefficient without evaporation ($b = 0$) was determined by making use of the adiabatic friction factor:

$$h_a = \frac{2F_a \cdot \mathrm{Re}_{v1}}{d_{e1}}\,\lambda_v \cdot \mathrm{Pr}_v{}^{1/3} \tag{28}$$

The ratio of the heat transfer coefficient h_v predicted from equation (25) to the coefficient h_a from equation (28) is shown in Fig. 6.

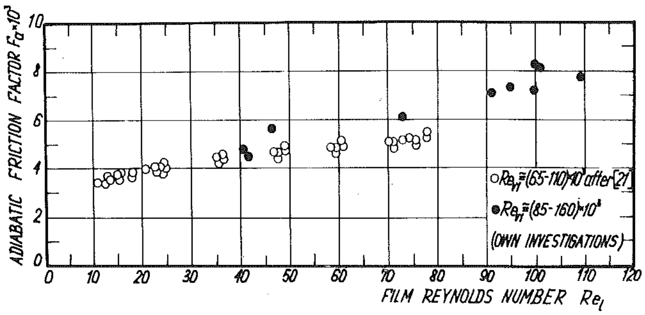

Fig. 4 Adiabatic friction factor F_a versus film Reynolds number Re_ℓ

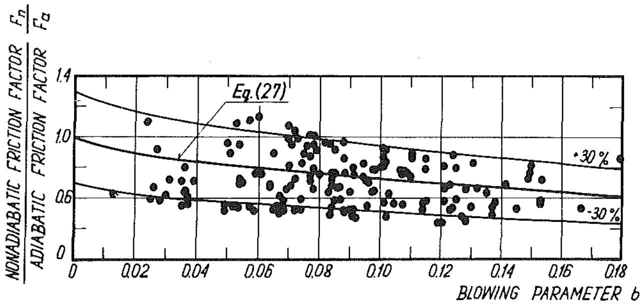

Fig. 5 Ratio F_n/F_a versus blowing parameter b

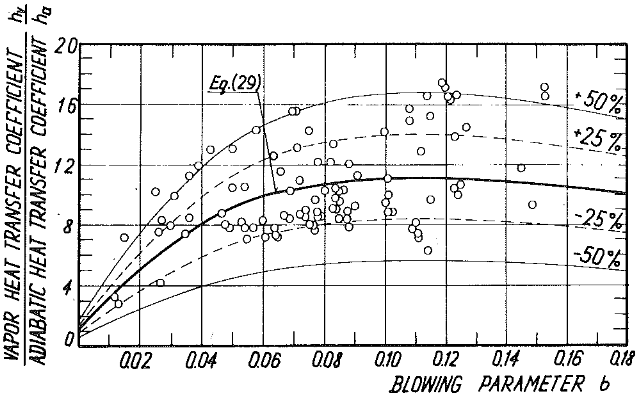

Fig. 6 Ratio h_v/h_a versus blowing parameter b

As discussed in the section on thermal resistance of the boundary layer, the variation of h_v/h_a with the blowing parameter b is not analogous to that of F_n/F_a because of the heat sinks within the boundary layer (evaporation of droplets). The ratio h_v/h_a may be approximated within the present range by formula

$$\frac{h_v}{h_a} = 1 + 248b\,\exp(-9b) \tag{29}$$

An approximate analysis of the droplet evaporation within the boundary layer is presented in the Appendix.

The dependence of the breakdown and rewetting film thickness on shear stress is shown in Fig. 7. The thickness of the rewetting film according to the experimental correlation

$$\delta_{lre} = \sqrt[3]{\frac{15\mu_l^2\sigma\delta_{lb}^{+}}{\rho_l\tau_i{}^{1.8}}} \tag{30}$$

corresponds to that, when the film rewets the entire surface after initial breakdown. It follows from Fig. 7, that the rewetting film thickness is larger than the breakdown thickness by an almost constant value. Fig. 8 shows the ratio of the non-adiabatic and adiabatic breakdown film thickness. The adiabatic breakdown film thickness was determined from theory Mikielewicz and Moszynski [16, 17] for the contact angle $\Theta_0 = 56$ deg, which was separately determined [18], for the same three-phase system and the same surface finish.

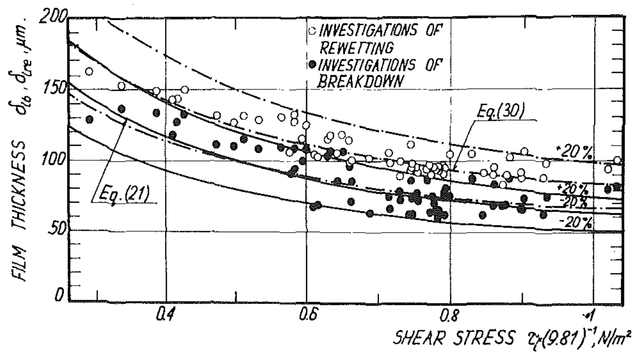

Fig. 7 Thickness of the breaking-down and rewetting films versus shear stress

Conclusions

There exist many theoretical and experimental investigations of the influence of transverse blowing on shear stress at the interface. Such work is usually concerned with the changes in shear stress on the solid-gas interface due to a transverse gas stream. Fig. 9 [20, 23] shows a comparison of gas transpiration with film evaporation.

The quantitative discrepancy of the shear stress variation with b in both processes seems to be due to the liquid film on the wall and to the fact that in transpiration gas enters the boundary layer through a finite number of orifices in the dry wall, whereas in the authors' investigations vapor entered the boundary layer uniformly along its entire surface. The variation of h_v/h_a with b is also qualitatively and quantitatively different when compared with transpiration. These differences are a consequence of the existence of the film and the presence of droplets in the boundary layer. Scatter within the experimental data reflects changes in output of turbines supplying the steam to the test apparatus resulting in fluctuations of the steam quality and generation of droplets of different diameter. It follows from the analysis, that the heat transfer coefficient h_v is sensitive to the droplet size and their concentration. Entrainment and deposition were also considered. Within the investigated range of parameters entrainment did not occur because the interface was stable. On the other hand, deposition contributed to the augmentation of the boundary layer heat transfer coefficient, as is shown in Appendix.

Acknowledgment

This work was supported in part by the National Science Foundation under Grant Nr OIP75-01317 through the joint U.S.—Polish "Marie Skłodowska-Curie" Research Fund.

The authors are grateful to Prof. J. R. Moszynski of the University of Delaware for fruitful discussions and suggestions and his help in preparing this paper.

References

1 Fulford, G. D., "The Flow of Liquid in Thin Films," *Advances in Chemical Engineering*, No. 5, Academic Press, New York and London, 1964, pp. 151–236.

2 Brauer, H., "Gas-Flüssigkeits-Strömungen in Rohren und Kolonnen," *Grundlagen der Chemischen Technik*, Vol. 5, Verlag Sauerländer, Aarau und Frankfurt am Main, 1971, pp. 673–765.

3 Vorontsov, Ye. G. and Yu. M. Tanayko, "Heat Transfer in Liquid Films," (in Russian), *Technica*, Kiev, 1972.

4 Szewalski, R., and B. Wieczorek, "A Stator Ring for Large Condensing Turbines," (in Polish), Patent No. 43 185 K 14 917, 1960. Patent owner: "Zamech" Mechanical Works, Elblag, Poland.

5 Ihnatowicz, E., "Experimental Investigations of the Evaporation of Thin Liquid Layers Driven by the Fast Flow of Vapor Phase," (in Polish), PhD Thesis, Institute of Fluid-Flow Machinery, Gdańsk, 1977.

6 Gumkowski, S., "Experimental Investigations of the Breakdown of Thin Liquid Layers Driven by the Fast Flow of Vapor Phase," (in Polish), PhD Thesis, Institute of Fluid-Flow Machinery, Gdańsk, 1977.

7 Mooré, M. J., and P. Sculpher, "Conditions Producing Concentrated Erosion in Large Steam Turbines," *Thermodynamics and Fluid Mechanics Convention*, 1970 Glasgow, Institution of Mechanical Engineers, I Bridcage Walk, Westminster, London, SW1.

8 Krzyżanowski, J., "Selected Problems of the Liquid Phase Motion in a Stage of a Condensing Turbine" (in Polish), PWN, Warszawa-Poznań, 1969.

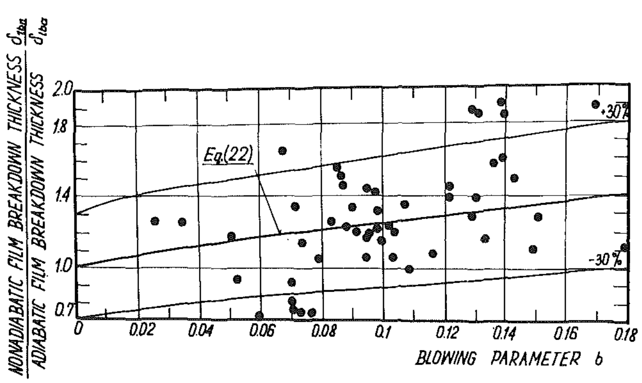

Fig. 8 Ratio $\delta_{\ell bn}/\delta_{\ell ba}$ versus blowing parameter b

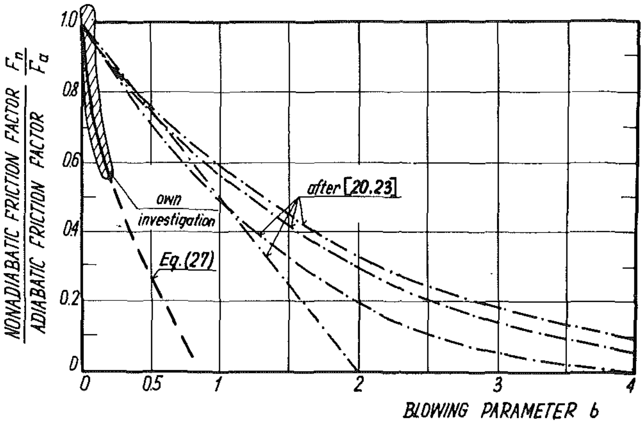

Fig. 9 Comparison of the shear stress distribution predicted after [20, 23] with own investigations

9 Tchernuhin, W. A., "Investigations of the Liquid Film Flow Interacting with an Unstabilized Gas Flow," (in Russian), *Izvestija Vyzshyh Utchebnych Zavedenij-Mashinostroenie*, No. 8, Moscow, 1962, pp. 149–155.

10 Tchernuhin, W. A., "Experimental Determination of the Liquid Film Thickness and the Entrainment Flux," (in Russian), *Izvestija Vyzshyh Utchebnyh Zavedenij-Mashinstroe-nie*, No. 4, Moscow, 1965, pp. 107–112.

11 Rekin, A. D., "Stability of the Liquid Film Flowing Over the Wall Under the Influence of the Turbulent Gas Flow," (in Russian), *Issledovanie Teplo-i Massoobmena v Technologitcheskih processah i apparatah, "Nauka i Technika,* Mińsk, 1966, pp. 275–280.

12 Doroshtchuk, W. E., "Heat Transfer Crisis in Flow Boiling of Water in Tubes," (in Russian), *Energia*, Moscow, 1970, pp. 16–22.

13 Hartley, D. F., and W. Murgatroyd, "Criteria for the Break-up of Thin Liquid Layers Flowing Isothermally Over Solid Surface," *Int. J. of Heat and Mass Transfer*, Vol. 7, No. 9, 1964, pp. 1003–1015.

14 Hobler, T., "Minimum Wetting of Surface," (in Polish), *Chemia Stosowana*, Vol. 2B, PWN Wrocław 1964, pp. 145–159.

15 Bankoff, S. G., "Minimum Thickness of Draining Liquid Film," *Int. J. of Heat and Mass Transfer*, Vol. 14, No. 12, 1971, pp. 2143–2146.

16 Mikielewicz, J., and J. Moszynski, "Breakdown of a Shear Driven Liquid Film," *Prace IMP PAN*, No. 66, PWN Warszawa-Poznań, 1975, pp. 3–11.

17 Mikielewicz, J., and J. Moszynski, "Minimum Thickness of a Liquid Film Flowing Vertically Down a Solid Surface," *Int. J. of Heat and Mass Transfer*, Vol. 19, No. 7, 1976, pp. 771–776.

18 Semiczek-Szulc, S., and J. Mikielewicz, "The Influence of Surface Roughness and the Presence of a Gaseous Medium on the Wettability of Metals," Seventh Symposium on Thermophysical Properties National Bureau of Standards—ASME Gaithersburg, Maryland, 1977.

19 Kutateladze, S. S., and A. J. Leontiev, "Heat and Mass Transfer and Friction in Turbulent Boundary Layer," (in Russian). *Energia*, Moscow, 1972.

20 Wallis, G. B., *One Dimensional Two-Phase Flow*, McGraw Hill, New York 1969, p. 168.

21 Hewitt, G. F., and P. M. C. Lacey, "The Breakdown of the Liquid Film in Annular Two-Phase Flow," Chemical Engineering Division, Atomic Energy Research Establishment-R 4303, Harwell, Berkshire, England, 1963.

22 Hewitt, G. F., and N. S. Hall-Taylor, *Annular Two-Phase Flow*, Chemical Engineering Division, A.E.R.E., Pergamon Press, Harwell, England, 1970, p. 163.

23 Mikielewicz, J., "Influence Transitions on the Magnitude of Shear Stress on the Interface," *Prace IMP PAN*, to be published, PWN, Warszawa-Poznań.

APPENDIX

Analysis of Droplet Evaporation Within the Boundary Layer

In the present case, when the liquid film is thin enough, entrainment does not occur. However, there may be deposition. Assuming, that all the droplets separated from the main flow along the test section are evaporated completely and remaining ones evaporate partially depending on the residence time, within the test section, the deposition mass flux may be determined from [22].

$$D = k \cdot c \tag{31}$$

The mass flow rate of the liquid partially evaporated within the test section is given by

$$\Delta \dot{m}_t = (\dot{m}_{in} - D \cdot F) - \dot{m}_{\text{out}} \tag{32}$$

where:

$$\dot{m}_{in} = \dot{m}_v\,(1 - x)$$

Assuming, that the mass of droplets is proportional to their volume and the number of droplets remains constant

$$\frac{\dot{m}_{\text{out}}}{(\dot{m}_{\text{in}} - D \cdot F)} = \left(\frac{r_{\text{out}}}{r_{\text{in}}}\right)^3 \tag{33}$$

and

$$\Delta \dot{m}_t = (\dot{m}_{\text{in}} - D \cdot F)\left[1 - \left(\frac{r_{\text{out}}}{r_{\text{in}}}\right)^3\right] \tag{34}$$

From equations (31) and (34) the mass flow rate of the liquid evaporated in the boundary layer is determined by

$$\Delta \dot{m} = D \cdot F + \Delta \dot{m}_t = \dot{m}_{in}\left[1 - \left(\frac{r_{\text{out}}}{r_{\text{in}}}\right)^3\right] + \mathrm{D} \cdot \mathrm{F}\left(\frac{r_{\text{out}}}{r_{\text{in}}}\right)^3 \tag{35}$$

The volumetric energy generation rate q_v for the boundary layer is given by

$$q_v \cong \frac{-\Delta \dot{m} \Delta i}{F \cdot \delta_v} \tag{36}$$

and is assumed to be constant. Substituting equation (35) into (36) and then into

$$Z = -\frac{\left\{\dot{m}_{\text{in}}\left[1 - \left(\frac{r_{\text{out}}}{r_{\text{in}}}\right)^3\right] + D \cdot F\left(\frac{r_{\text{out}}}{r_{\text{in}}}\right)^3\right\} \cdot \Delta i}{F \cdot q_{ia}} \tag{37}$$

Table 1 Experimental and theoretical values of h_v/h_a

	MEASUREMENTS							PREDICTIONS			
Point No.	t_s (°C)	Δt_v (°C)	$\dot{m}_v$ (kg/s)	$\bar{u}_v$ (m/s)	h_a (W/m²°C)	b (−)	h_v/h_a (−)	$\dot{m}_{in} \times 10^3$ (kg/s)	$D \times 10^4$ (kg/s)	Z (−)	h_v/h_a (−)
1	43.9	8.5	0.0491	113.5	167.8	0.108	15.6	1.475	1.39	−21.6	11.8
2	42.4	11.3	0.0458	114.1	171.2	0.153	16.5	1.375	1.30	−18.1	10.0
3	47.8	7.0	0.0561	108.6	170.4	0.066	11.5	1.694	1.58	−26.6	14.3
4	43.0	10.4	0.0503	121.6	129.6	0.061	7.2	1.51	1.44	−25.7	13.8
5	46.8	4.6	0.0643	130.5	154.1	0.030	8.0	1.93	1.86	−33.2	17.6
6	52.9	22.1	0.0878	132.6	203.3	0.114	6.2	2.63	2.55	−20.0	11.0

Because of the very small droplet size the ratio $r_{\text{out}}/r_{\text{in}}$ may be predicted by considering heat transfer between vapor and droplet in terms of heat conduction. After an evaporation time τ the droplet radius is changed in the ratio

$$\frac{r_{\text{out}}}{r_{\text{in}}} = \sqrt{1 - \frac{(t_v - t_s)\lambda_v}{\Delta i \cdot \rho_l \cdot r_{\text{in}}^2}\,\tau} \tag{38}$$

The evaporation time τ is given by

$$\tau = l/\bar{u}_v \tag{39}$$

From equations (39) and (38), taking, a mean value of $t_v - t_s = \overline{\Delta t_v}/2$ and substituting $q_{ia} = h_a \cdot \overline{\Delta t_v}$

$$Z = -\frac{\left\{\dot{m}_{\text{in}} - (\dot{m}_{\text{in}} - D \cdot F)\left[1 - \frac{\overline{\Delta t_v} \cdot \lambda_v \cdot \ell}{2 \Delta i \rho_l r_{\text{in}}^2 \bar{u}_v}\right]^{3/2}\right\} \Delta i}{F \cdot h_a \cdot \overline{\Delta t_v}} \tag{40}$$

Next we may compute h_v/h_a from equation (18). Some results of this calculation and their comparison with experiments are given in Table 1 under the following assumptions:

heat transfer area $- F = \pi \cdot d_1 \cdot \ell = \pi \times 0.034 \times 0.652$
$= 0.069643 m^2$

steam quality $-x = 0.97$

droplet radius $- r_{\text{in}} = 0.7 \times 10^{-6}$ m.

It follows from Table 1 that a very small number of small droplets in the vapor results in a significant increase of the heat transfer coefficient within the boundary layer.

A. Bejan
Assistant Professor,
Department of Mechanical Engineering,
University of Colorado,
Boulder, CO 80309
Assoc. Mem. ASME

A Study of Entropy Generation in Fundamental Convective Heat Transfer

The second law aspects of heat transfer by forced convection are illustrated in terms of four fundamental flow configurations: pipe flow, boundary layer over flat plate, single cylinder in cross-flow, flow in the entrance region of a flat rectangular duct. The interplay between irreversibility due to heat transfer along finite temperature gradients and, on the other hand, irreversibility due to viscous effects is analyzed in detail. The spatial distribution of irreversibility, entropy generation profiles *or* maps, *and those flow features acting as strong sources of irreversibility are presented. It is shown how the flow geometric parameters may be selected in order to minimize the irreversibility associated with a specific convective heat transfer process.*

Introduction

Our understanding of heat transfer processes is destined to play a significant role in the effort toward workable alternatives to the growing energy problem. In particular, the task of conserving useful energy rests heavily on our ability to produce thermodynamically efficient heat transfer processes and equipment for such processes. Consequently, in recent years we witnessed a growing interest in the thermodynamics of heat transfer and the thermodynamics of heat exchange equipment. This interest will continue to grow in the future.

Heat transfer processes are generally accompanied by thermodynamic irreversibility or entropy generation. The generation of entropy may be due to a variety of sources, primarily heat transfer down temperature gradients and, characteristic of convective heat transfer, viscous effects. There exists a direct proportionality between the irreversibility (entropy generation) of the process and the amount of useful work dissipated in the process [1–3]. This relationship implies that in cases where the heat transfer process is part of a power cycle, the process irreversibility causes a direct drop in the useful power output of the cycle. Conversely, should the heat transfer process be part of a refrigeration cycle, the process irreversibility leads to a direct increase in the mechanical power input to the cycle. Either way, the irreversibility brought by the heat transfer process amounts to a penalty in useful power.

With a better understanding of how entropy is being generated in heat transfer processes and engineering components for heat exchange it is possible to reduce the process irreversibility, thus registering savings in useful (available) power. With this objective in mind, Bejan showed how the entropy generation rate can systematically be reduced in simple components for heat exchange, namely, counterflow gas-to-gas heat exchangers [4], heat exchangers with prescribed heat flux distribution [5] and sensible heat units for energy storage [6].

The main objective of the present article is to analyze the mechanism of entropy generation in basic configurations encountered in convective heat transfer. Unlike the earlier papers which addressed the subject of irreversibility reduction in the design of engineering components for heat exchange [4–6], the present work is fundamental. In this article we seek to identify the origin of entropy production and its distribution through fluid flows most commonly found in convective heat transfer situations. In addition, we discuss the engineering implications of this study, specifically, the manner in which a basic flow geometry may be selected in order to minimize the rate of entropy generation associated with the convective heat transfer process.

A second objective of this study is to illustrate, in a very modest way, the place thermodynamics *duly* occupies in heat transfer. It is unfortunate that the link which exists between the two fields is not debated the way it should be, in view of its relevance to the energy conservation questions facing the engineering profession. By analyzing the irreversibility associated with heat transfer *we are not* including one additional effect in an already complex heat transfer model. On the contrary, through irreversibility we are bringing out that feature of heat transfer present even in the simplest possible heat transfer model.

Local Rate of Entropy Generation

Consider the two-dimensional infinitesimal fluid element *dxdy* shown schematically in Fig. 1. The fluid element is part of a considerably more complex convective heat transfer picture. However, for the scope of this presentation, we regard the element as an open thermodynamic system subjected to mass fluxes, energy transfer and entropy transfer interactions through a fixed control surface. The element size is small enough so that the thermodynamic state of the fluid inside the element may be regarded as uniform (independent of position). However, the thermodynamic state of the small fluid element may change with time.

For this study, we limit our attention to incompressible fluids without internal heat generation. In such cases, the expression for the volumetric rate of entropy generation reduces to [7]

$$S''' = \frac{k}{T^2}\left[\left(\frac{\partial\theta}{\partial x}\right)^2 + \left(\frac{\partial\theta}{\partial y}\right)^2\right] + \frac{\mu}{T}\left\{2\left[\left(\frac{\partial v_x}{\partial x}\right)^2 + \left(\frac{\partial v_y}{\partial y}\right)^2\right] + \left(\frac{\partial v_x}{\partial y} + \frac{\partial v_y}{\partial x}\right)^2\right\} \quad (1)$$

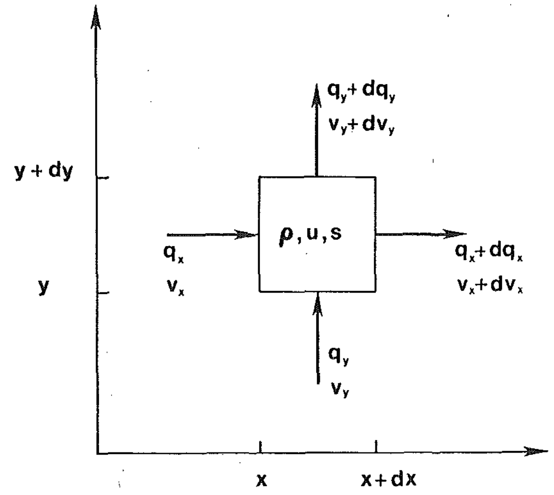

Fig. 1 Entropy generation analysis for an infinitesimal element *dxdy* in convective heat transfer

---

Contributed by the Heat Transfer Division for publication in the JOURNAL OF HEAT TRANSFER. Manuscript received by the Heat Transfer Division March 8, 1979.

As we might have expected, the irreversibility indicator S''' contains two additive parts, one due to conduction in the presence on non-zero temperature gradients, the other accounting for viscous dissipation of mechanical power throughout the flow. In the second term of equation (1), the factor in brackets represents the viscous dissipation function Φ for two-dimensional incompressible flow. The other symbols appearing in equation (1) have been defined in the Nomenclature.

The local entropy generation rate formula (1) can be derived in straightforward fashion by performing an entropy transfer accounting around the infinitesimally small element illustrated in Fig. 1. The entropy transfer to and from the $(dxdy)$ system is associated with heat transfer, q_x and q_y, as well as with mass fluxes, ρv_x and ρv_y. In the interest of brevity we do not show this derivation, urging the reader to consult any irreversible thermodynamics book for additional details. Alternate versions of formula (1) corresponding to coordinate systems other than the two-dimensional cartesian system of Fig. 1 may be found in [8].

Conductive Versus Viscous Effects. In many heat transfer problems it is often possible and convenient to neglect the viscous dissipation term $\mu\Phi$ in the equation for energy conservation.

$$\rho c_p\left(v_x\frac{\partial\theta}{\partial x} + v_y\frac{\partial\theta}{\partial y}\right) = k\left(\frac{\partial^2\theta}{\partial x^2} + \frac{\partial^2\theta}{\partial y^2}\right) + \mu\Phi. \tag{2}$$

This is particularly the case in heat transfer through gases at subsonic velocities. The dimensionless group which expresses the magnitude of the dissipation energy term relative to the conduction energy term in (2) is [9]

$$\text{Ec Pr} = \left(\frac{v^{*2}}{c_p\theta^*}\right)\left(\frac{\nu}{\alpha}\right) \tag{3}$$

where v^* and θ^* are the characteristic fluid velocity and temperature difference for the convective heat transfer problem. Thus, in many engineering problems, we find Ec Pr $\ll 1$.

Consider now the same question relative to expression (1). Under what conditions is the viscous dissipation contribution to S''' negligible? If we regard expression (1) as the sum $S''' = S'''_{\text{conductive}} + S'''_{\text{viscous}}$, then, in an order of magnitude sense,

$$0\left(\frac{S'''_{\text{viscous}}}{S'''_{\text{conductive}}}\right) = \frac{\text{Ec Pr}}{\tau}. \tag{4}$$

Here, $\tau = \theta^*/T^*$, where T^* is the absolute temperature characteristic to the problem at hand. The *dimensionless temperature difference,* τ, is always an important dimensionless parameter in second law analyses of heat transfer problems. With the exception of applications at cryogenic temperatures, the temperature difference number τ is generally much smaller than unity, $\tau \ll 1$.

It is now clear that the energy argument by which viscous dissipation is neglected in (2); i.e., Ec Pr $\ll 1$, has no bearing on the question of negligible viscous contribution to the local rate of irreversibility production. It is then possible to encounter situations where, although the energy equation can be simplified according to Ec Pr $\ll 1$, S''' is in fact dominated by viscous effects. This is the limit in which τ is very small, small enough so that Ec Pr/$\tau > 1$.

Below we examine a series of important convective heat transfer configurations in an effort to illustrate the coupling of viscous and conductive effects in the makeup of S'''. In the process we will study the spatial distribution of irreversibility, pointing out those flow features which act as concentrators (sources) of entropy generation S'''.

Forced Convection in a Round Tube

Laminar Flow. Consider the Poiseuille flow through a round tube with uniform heat flux q'' around its circumference (see insert in the left side of Fig. 2). The velocity and temperature profiles for this flow are particularly simple [8]:

$$v_x = v_{x,\max}\left[1 - \left(\frac{r}{r_0}\right)^2\right] \tag{5}$$

$$\theta = \frac{q''r_0}{k}\left[-4\frac{x}{x_0} - \left(\frac{r}{r_0}\right)^2 + \frac{1}{4}\left(\frac{r}{r_0}\right)^4\right] \tag{6}$$

with

$$v_{x,\max} = \frac{r_0^2}{4\mu}\left(-\frac{dP}{dx}\right), \quad \frac{x_0}{r_0} = \frac{r_0 v_{x,\max}}{\alpha} = \text{Pe}. \tag{7, 8}$$

The equation for S''' in the cylindrical geometry of Fig. 2 is [8]

$$S''' = \frac{k}{T^2}\left[\left(\frac{\partial\theta}{\partial x}\right)^2 + \left(\frac{\partial\theta}{\partial r}\right)^2\right] + \frac{\mu}{T}\left(\frac{\partial v_x}{\partial r}\right)^2 \tag{9}$$

which, in combination with relations (5–8), yields

$$S''' = \frac{q''^2}{kT^2}\left[(2R - R^3)^2 + \frac{16}{\text{Pe}^2}\right] + \frac{4\mu v^2_{x,\max}}{T r_0^2}R^2, \quad R = \frac{r}{r_0} \tag{10}$$

Equation (10) is the entropy generation profile in the pipe cross-section. Together with the velocity and temperature profiles, the entropy generation profile completes the thermodynamic description of the convective heat transfer phenomenon.

It is convenient to nondimensionalize expression (10) and define *the local entropy generation number* $N_{S'''}$

Nomenclature

a = half-thickness of flat duct, Fig. 5
B_0, B = duty parameters, equations (17) and (37)
c_p = specific heat at constant pressure
C_D = drag coefficient, equation (44)
$C_{f,x}$ = local skin friction coefficient, equation (34)
D = hydraulic diameter
Ec = Eckert number, equation (3)
f = function, equation (26); friction factor, equation (14)
F_D = drag force
h_x = local heat transfer coefficient
k = thermal conductivity
L_E = entrance region length
L_{FD} = length of irreversibility-equivalent fully-developed section, equation (58)
$\dot{m}$ = mass flow rate
$N_{S'''}$, $N_{S''}$, $N_{S'}$ = entropy generation number
Nu = Nusselt number
P = pressure
Pr = Prandtl number
q'', q', q = heat transfer interaction, $[W/m^2]$, $[W/m]$, $[W]$
r = radial position
r_0 = tube radius, Fig. 2
R = dimensionless radial position
Re = Reynolds number
s = specific entropy
S''', S'', S' = rate of entropy generation, $[W/m^3K]$, $[W/m^2K]$, $[W/mK]$
S''_{FD} = rate of entropy generation in the fully-developed region
t = time
T = absolute temperature
T_0 = reference temperature
u = specific internal energy
v_x, v_y = velocity components
V_0 = entrance velocity, Fig. 5
V_1 = centerline velocity, Fig. 5
V_1^* = dimensionless centerline velocity, equation (50)
x = horizontal coordinate
x^* = dimensionless coordinate, equation (51)
y = vertical coordinate
α = thermal diffusivity
δ = velocity boundary layer thickness
δ_T = thermal boundary layer thickness
ζ = dimensionless coordinate across flat duct
η = similarity variable in boundary layer flow over flat plate
θ = temperature difference, $T - T_0$
θ_∞ = extreme tremperature difference, $T_\infty - T_0$
μ = viscosity
ν = kinematic viscosity
ρ = fluid density
τ = ratio of characteristic temperature difference divided by the absolute temperature
τ_0 = wall shear stress, equation (34)
Φ = viscous dissipation function, equation (2)

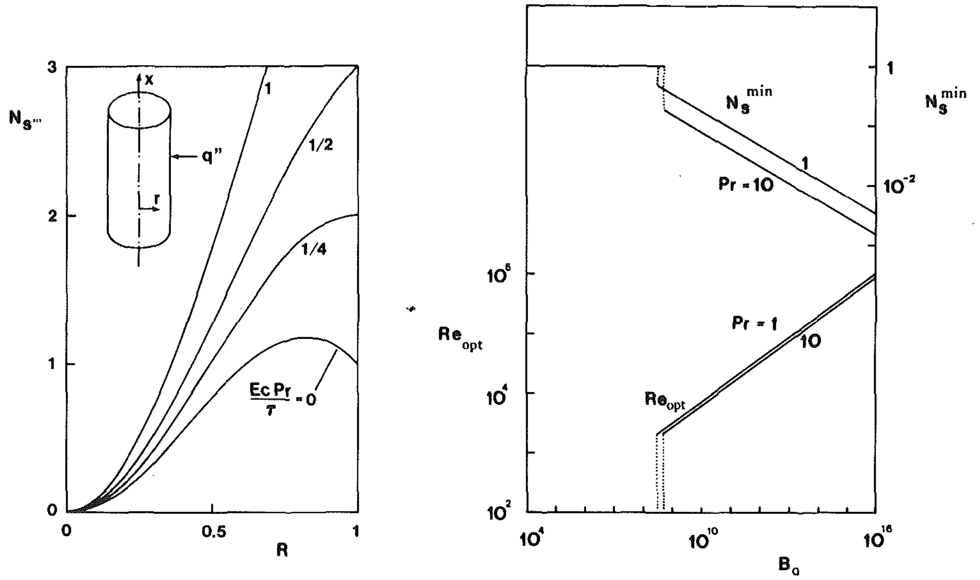

Fig. 2 Left: entropy generation profiles $N_{S'''}$ inside a smooth tube with constant wall heat flux in laminar flow. Right: optimum Reynolds number and corresponding minimum entropy generation number for forced convection heat transfer in a round tube

$$N_{S'''} = S''' \frac{kT_0^2}{q''^2} = (2R - R^3)^2 + \frac{16}{\mathrm{Pe}^2} + \frac{4\,\mathrm{Ec\,Pr}}{\tau} R^2. \qquad (11)$$

Here we made the assumption that the temperature variation over the pipe cross-section is negligible compared with the absolute temperature, hence $T \simeq T_0$ where T_0 is a characteristic (reference) absolute temperature. The irreversibility figure $N_{S'''}$ depends on radial position, on Pe and on the group Ec Pr/τ which, as discussed in the preceding section, determines the relative importance of viscous effects. The Peclet number Pe governs the importance of irreversibility associated with conduction in the axial direction. We see that for Pe < 4 the axial conduction contribution dominates the radial conduction effect.

The left side of Fig. 2 displays a family of entropy generation profiles in the pipe cross-section, for cases where the axial conduction effect is negligible (Pe ≫ 4). The value of Ec Pr/τ increases gradually to the point where viscous effects dominate $N_{S'''}$. In all cases, the pipe wall region acts as a strong concentrator of irreversibility. When Ec Pr/τ = 0, the maximum $N_{S'''}$ occurs inside the fluid at $R = (2/3)^{1/2}$, the same place where due to the wall curvature effect the maximum radial temperature gradient is located. As viscous effects take over, the point of highest $N_{S'''}$ migrates toward the wall and, for Ec Pr/τ > 1/4, it coincides with the wall.

The rate of entropy generation over the entire tube cross section is obtained by integrating expression (10),

$$S' = 2\pi\, r_0^2 \int_0^1 S''' R\, d\,R. \qquad (12)$$

Neglecting axial conduction, Pe ≫ 4, result (12) can be written as

$$S' = \frac{11}{48\pi}\frac{q'^2}{k\,T^2} + \frac{8}{\pi}\frac{\mu \dot m^2}{T \rho^2\, r_0^4}, \qquad (13)$$

Here $\dot m$ is the mass flow rate through the tube, while q' is the heat transfer rate per unit length, $2\pi r_0 q''$. Once more, the irreversibility production S' appears as the sum of two effects, heat transfer in the direction of a finite temperature gradient and fluid friction. It should be noted that the heat transfer contribution to S', the first term in equation (13), is fixed as soon as the heat transfer rate per unit length q' (the heat transfer duty of the tube) is specified. We return to this observation later in this section when we address the question of optimum tube radius for minimum irreversibility and fixed q'.

Turbulent Flow. Exact analytical solutions for the turbulent velocity and temperature fields in the tube cross-section are not available. Therefore, one cannot evaluate the rate of entropy generation at any point in the pipe cross-section, as done through equation (10) for laminar flow. However, one can still evaluate the rate of entropy generation averaged over the tube cross-section by using the integral result developed by Bejan [5] for irreversibility in a duct of arbitrary geometry.

Using the present notation for forced convection through a tube, the integral result is [5]

$$S' \frac{1}{\pi\, Nu\, k}\frac{q'^2}{T^2} + \frac{\dot m^3 f}{\rho^2 T\, r_0^5}, \qquad (14)$$

which shows how S' can be evaluated based on average heat transfer (Nu) and fluid friction (f) information. As one might expect, the laminar flow expression (13) is only a special case of the more general result (14) since, in laminar flow, Nu = 48/11 and $f = 8\,\pi\,\mu\, r_0/\dot m$. Unlike in laminar flow, the heat transfer contribution to S' is not necessarily constant when the heat transfer duty q' is specified.

Optimum Tube Radius for Minimum Irreversibility. In an application in which the heat transfer duty q' and the mass flow $\dot m$ are already specified, it is possible to select an optimum tube radius which insures the minimum rate of entropy generation in the heat transfer device. This design optimization procedure is described best by placing the irreversibility rate expression (14) in dimensionless form. We define *the entropy generation number N_S' as the ratio* $S'/S'_{\Delta T,\mathrm{laminar}}$ where S' is the actual entropy generation rate given by (14) and $S'_{\Delta T,\mathrm{laminar}}$ is the first term appearing in (13). We commented earlier that $S'_{\Delta T,\mathrm{laminar}}$ is constant when the heat transfer rate q' is specified, hence, $S'_{\Delta T,\mathrm{laminar}}$ assumes the role of *characteristic* rate of entropy generation in the system of interest.

The entropy generation number is therefore

$$N_S' = \frac{48}{11}\mathrm{Nu}^{-1} + \frac{3\pi^4}{22} f\,\mathrm{Re}^5 B_0^{-2}, \qquad (15)$$

showing that the duct irreversibility depends primarily on two dimensionless groups, the Reynolds number based on tube diameter Re and the "duty" parameter B_0,

$$\mathrm{Re} = \frac{2\dot m}{\rho \mu r_0}; \quad B_0 = q'\dot m \frac{\rho}{\mu^{5/2}(kT)^{1/2}}. \qquad (16, 17)$$

With q', $\dot m$ and working fluid specified, the task of finding the optimum radius for minimum S'' is equivalent to minimizing the N_S' expression (15) with respect to Re, subject to a specified constant B_0. This procedure is straightforward, therefore only the final results are given here.

For laminar flow, using $\mathrm{Nu} = 48/11$ and $f = 16/\mathrm{Re}$ in expression (15), the minimization procedure yields

$$\mathrm{Re}_{\mathrm{opt}} = 0; \quad N_{S'}{}^{\min} = 1 \tag{18, 19}$$

In engineering terms, this result implies that the selected tube radius r_0 must be large enough so that the rate of entropy generation is strongly dominated by the contribution due to heat transfer across a finite temperature difference. In other words, based on expression (15),

$$\frac{24\,\pi^4}{11}\,\mathrm{Re}^4\,B_0{}^{-2} \ll 1. \tag{20}$$

For turbulent flow, the $N_{S'}$ expression (15) has a unique minimum. Substituting $\mathrm{Nu} = 0.023\,\mathrm{Pr}^{0.4}\,\mathrm{Re}^{0.8}$ and $f = 0.046\,\mathrm{Re}^{-0.2}$ into (15) and differentiating with respect to Re yields

$$\mathrm{Re}_{\mathrm{opt}} = 2.023\,\mathrm{Pr}^{-0.071}\,B_0{}^{-0.358} \tag{21}$$

and

$$N_{S'}{}^{\min} = 126\,\mathrm{Pr}^{-0.343}\,B_0{}^{-0.286}. \tag{22}$$

Expressions (21, 22) have been summarized in the right hand side of Fig. 2 for two discrete values of Prandtl number. As the aggregate duty parameter B_0 increases, we see that the optimum tube radius decreases ($\mathrm{Re}_{\mathrm{opt}}$ increases) and the minimum entropy generation number $N_S{}^{\min}$ decreases also.

As a numerical example, consider the heat transfer to an air stream at atmospheric pressure and an average temperature of 1100 K. In order to use realistic values for q' and $\dot{m}$ in the B_0 formula (17), it is helpful to replace q' by $\dot{m}c_p(dT/dx)$. For a longitudinal temperature gradient of the order of 10 K/m, and for a mass flow of 100 Kg/hr, we obtain $B_0 = (2.6)\,10^{10}$ and, from (21), $\mathrm{Re}_{\mathrm{opt}} = (1.11)10^4$. Finally, expression (16) yields an optimum tube radius $r_{0,\mathrm{opt}} = 3.6$ cm. Calculations of this type are relevant to the optimum thermodynamic design of heat exchanger passages with prescribed heat transfer distribution. Examples of such heat exchangers are the core of a nuclear reactor and, from a recently expanding technology, a superconducting cable cooled with liquid helium by forced convection [10].

Boundary Layer Over Flat Plate

Laminar Flow over Isothermal Plate. Consider now the development of laminar momentum and thermal boundary layers along a flat plate. The situation is shown schematically in the horizontal plane of the isometric drawing of Fig. 3. At some distance from the solid wall the fluid velocity and temperature are uniform, $v_{x,\infty}$ and T_∞. The wall temperature is constant, T_0.

The study of the velocity and temperature fields in the vicinity of the plate constituted the subject of numerous investigations [11]. The purpose of this section is to examine the distribution of entropy generation in the boundary layer. For this we rely on solutions available in the literature for $v_x(x, y)$ and $\theta(x, y)$ in laminar flow.

The task of evaluating the entropy generation profile S''' is simplified greatly if we restrict the discussion to the case $\mathrm{Pr} = 1$ for which the Blasius-Pohlhausen solution [12] reduces to

$$\frac{\theta}{\theta_\infty} = \frac{v_x}{v_{x,\infty}} = \frac{df}{d\eta} \tag{23, 24}$$

The similarity variable η equals $y[v_{x,\infty}/(\nu x)]^{1/2}$, while $f(\eta)$ is the function tabulated by Howarth [13]. Combining now solution (23, 24) with the S''' expression (1) and neglecting the irreversibility terms associated with velocity and temperature gradients in x direction, we find

$$S''' = \frac{k\theta_\infty{}^2\,v_{x,\infty}}{T_0{}^2\nu x}\,(f'')^2 + \frac{\mu v_{x,\infty}{}^3}{T_0\,\nu x}\,(f'')^2 \tag{25}$$

The local entropy generation number is

$$N_{S'''} = \frac{S'''}{k}\left(\frac{\nu T_0}{\theta_\infty v_{x,\infty}}\right)^2 = \left(1 + \frac{\mathrm{Ec\,Pr}}{\tau}\right)\frac{(f'')^2}{\mathrm{Re}_x} \tag{26}$$

where Re_x is defined as $v_{x,\infty}x/\nu$.

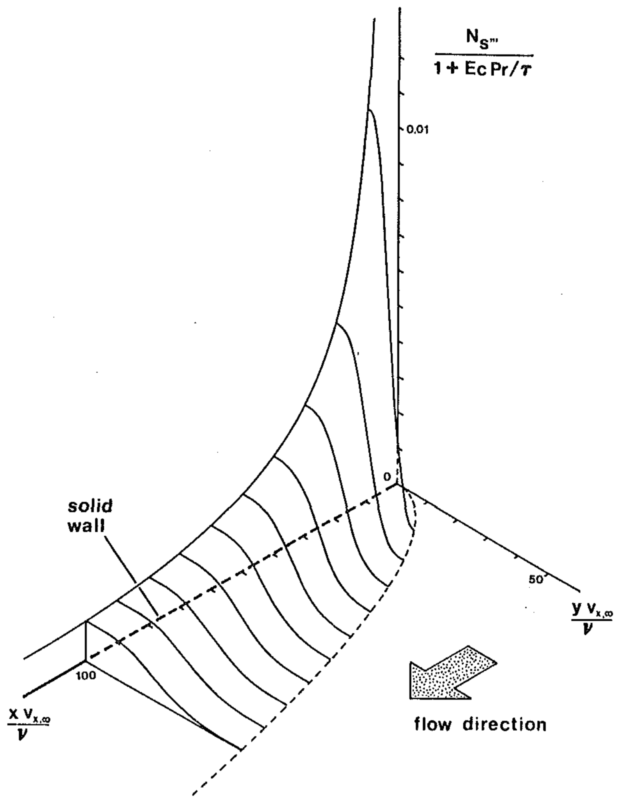

Fig. 3. Entropy generation surface for laminar boundary layer flow and heat transfer along a flat plate

The complex dependence of S''' on both x and y is shown in Fig. 3. The three-dimensional display was done in terms of $(x\,v_{x,\infty}/\nu)$ and $(y\,v_{x,\infty}/\nu)$ in the horizontal plane, and $N_{S'''}/(1 + \mathrm{Ec\,Pr}/\tau)$ in the vertical direction. It is evident that the irreversibility effects are limited to the boundary layer. Regarding the y dependence of $N_{S'''}$, the entropy generation rate is highest reaching a peak at the solid wall. The longitudinal variation of S''' is as $1/x$, indicating that like all gradients in this boundary layer solution S''' blows up at the origin. The viscous effect again scales up as $\mathrm{Ec\,Pr}/\tau$.

Integrating (25) across the boundary layer we can calculate the rate of entropy generation per unit area of flat plate,

$$S'' = \int_0^\infty S'''\,dy = 0.25\,\frac{k v_{x,\infty}\theta_\infty{}^2}{\nu T_0{}^2}\left(1 + \frac{\mathrm{Ec\,Pr}}{\tau}\right)\mathrm{Re}_x{}^{-1/2} \tag{27}$$

with the corresponding entropy generation number defined as

$$N_{S''} = S''\,\frac{\nu T_0{}^2}{k v_{x,\infty}\theta_\infty{}^2} = 0.25\left(1 + \frac{\mathrm{Ec\,Pr}}{\tau}\right)\mathrm{Re}_x{}^{-1/2}. \tag{28}$$

Finally, by analogy with the Nusselt number nomenclature for boundary layer heat transfer, we integrate (27) in the x direction to find the total rate of entropy generation produced by boundary layer flow and heat transfer over a length L

$$S' = \int_0^L S''\,dx = 0.50\,\frac{k\theta_\infty{}^2}{T_0{}^2}\left(1 + \frac{\mathrm{Ec\,Pr}}{\tau}\right)\mathrm{Re}_L{}^{1/2}, \tag{29}$$

where $\mathrm{Re}_L = v_{x,\infty}\,L/\nu$. The overall entropy generation number based on S' is

$$N_{S'} = S'\,\frac{T_0{}^2}{k\,\theta_\infty{}^2} = 0.50\left(1 + \frac{\mathrm{Ec\,Pr}}{\tau}\right)\mathrm{Re}_L{}^{1/2}. \tag{30}$$

It is worth mentioning that in general the Prandtl number will have an additional effect on the relative importance of viscous and conductive effects in the constitution of S''', S'' and S'. It is easy to show that when $\mathrm{Pr} \neq 1$ the viscous effects scale up as

$$\frac{\mathrm{Ec\,Pr}}{\tau}\left(\frac{\delta_T}{\delta}\right)^2 \approx \frac{\mathrm{Ec\,Pr}^{1/3}}{\tau} \tag{31}$$

where δ and δ_T are the velocity and temperature boundary layer thicknesses. In writing (31) we made use of the approximation $\delta/\delta_T \approx Pr^{1/3}$. The significance of (31) is that when the two thicknesses are not equal, the thinner layer exhibits larger gradients thereby enhancing its contribution to the total S''' figure. According to (31), viscous effects are more likely to play a role in low Prandtl number fluids where $\delta \ll \delta_T$.

Laminar and Turbulent Flow over Constant Heat Flux Plate. To study the generation of entropy in a turbulent boundary layer one has to rely on an integral method which takes into account the heat transfer and fluid friction characteristics of the flow in an overall manner, as Nusselt number and friction factor information. Consider, for example, a flat plate of negligible thickness suspended in a uniform flow field, parallel to the flow velocity $v_{x,\infty}$. The heat flux q'' over the plate surface is uniform. Consider also a control surface which surrounds the plate of finite length L at a large enough distance through portions of external flow in which the fluid motion is nearly uniform and the temperature nearly constant, T_∞. Regardless of whether the boundary layer is turbulent or laminar, the entropy generation rate in one half of the control volume (i.e., for one side of the plate) is given by

$$S' = \frac{q''^2}{T_\infty} \int_0^L \frac{dx}{h_x} + \frac{\rho\, v_{x,\infty}{}^3}{2\,T_\infty} \int_0^L C_{f,x} dx, \qquad (32)$$

where h_x and $C_{f,x}$ are the local heat transfer coefficient and skin friction coefficient,

$$h_x = \frac{q''}{T_0(x) - T_\infty}, \quad C_{f,x} = \frac{2\,\tau_0}{\rho v_{x,\infty}{}^2}. \qquad (33, 34)$$

In the above definitions $T_0(x)$ is the wall temperature, τ_0 the wall shear stress and q'' the uniform heat flux. Note that unlike equation (29) in the preceding sub-section where we considered the laminar boundary layer over an isothermal flat plate, the S' expression (32) refers to a uniform heat flux situation.

Expression (32) is the result of an entropy flux accounting around the control volume, analysis omitted here due to space limitations. Like all entropy generation results for forced convection heat transfer, S' consists of two additive parts, one due to heat transfer across the $[T_0(x) - T_\infty]$ temperature difference, the other being associated with the total friction drag force exerted by the fluid on the plate. Below, we use result (32) to determine the optimum plate length L which yields the minimum rate of entropy generation in a heat transfer application in which the uniform flow velocity $v_{x,\infty}$ and the total heat flux $q' = \int_0^L q''\, dx$ are specified. We do this by first substituting appropriate correlations for h_x and $C_{f,x}$ into expression (32) and solving the equation $\partial S'/\partial L = 0$.

Optimum Plate Length for Minimum Irreversibility. For laminar flow, the local skin friction coefficient is $C_{f,x} = 0.664\, \mathrm{Re}_x{}^{-1/2}$ while the local heat transfer coefficient is given by $h_x\, x/k = 0.332\, \mathrm{Pr}^{1/3}\, \mathrm{Re}_x{}^{1/2}$ [14]. Writing $q' = q''\, L$ for the total heat transfer rate from plate to fluid over the plate length L, the entropy generation number $N_{S'}$ becomes

$$N_{S'} = S' \frac{k\, T_\infty{}^2}{q'^2} = 2.008\, \mathrm{Pr}^{-1/3}\, \mathrm{Re}_L{}^{-1/2} + 0.664\, \mathrm{Re}_L{}^{1/2}\, B^{-2}. \quad (35)$$

Here, Re_L and B are the Reynolds number based on L and the "duty" parameter, respectively,

$$\mathrm{Re}_L = \frac{v_{x,\infty} L}{\nu}, \quad B = \frac{q'}{v_{x,\infty}(\mu k T)^{1/2}}. \qquad (36, 37)$$

The optimum plate length $\mathrm{Re}_{L,\mathrm{opt}}$ yielding the minimum rate of entropy generation at constant q' and $v_{x,\infty}$ is

$$\mathrm{Re}_{L,\mathrm{opt}} = 3.024\, \mathrm{Pr}^{-1/3}\, B^2, \quad N_{S'}^{\mathrm{min}} = 2.309\, \mathrm{Pr}^{-1/6}\, B^{-1} \quad (38, 39)$$

For turbulent flow we use a similar set of correlations for friction and heat transfer, $C_{f,x} = 0.0576\, \mathrm{Re}_x{}^{-1/5}$ and $h_x\, x/k = 0.0296\, \mathrm{Pr}^{1/3}\, \mathrm{Re}_x{}^{0.8}$ [15]. We also assume that the laminar layer which precedes the turbulent boundary layer is much shorter than the plate length L. Substituting these correlations into the entropy generation result (32) yields

$$N_{S'} = S' \frac{k\, T_\infty{}^2}{q'^2} = 28.15\, \mathrm{Pr}^{-1/3}\, \mathrm{Re}_L{}^{8/5} + 0.036\, \mathrm{Re}_L{}^{-8/5}\, B^{-2}, \quad (40)$$

$$\mathrm{Re}_{L,\mathrm{opt}} = 64.31\, \mathrm{Pr}^{-5/24}\, B^{5/4}, N_{S''}{}^{\mathrm{min}} = 2.013\, \mathrm{Pr}^{-1/6}\, B^{-1}. \quad (41, 42)$$

The optimum plate length and the resulting minimum entropy generation number prescribed by equations (38, 39) and (41, 42) are shown on the left side of Fig. 4. The discontinuity illustrated by dashed lines corresponds to the transition region, cases in which the laminar and turbulent portions of the boundary layer are of comparable lengths. The trends are similar to those presented in the right graph of Fig. 2: the higher the duty parameter B, the higher the op-

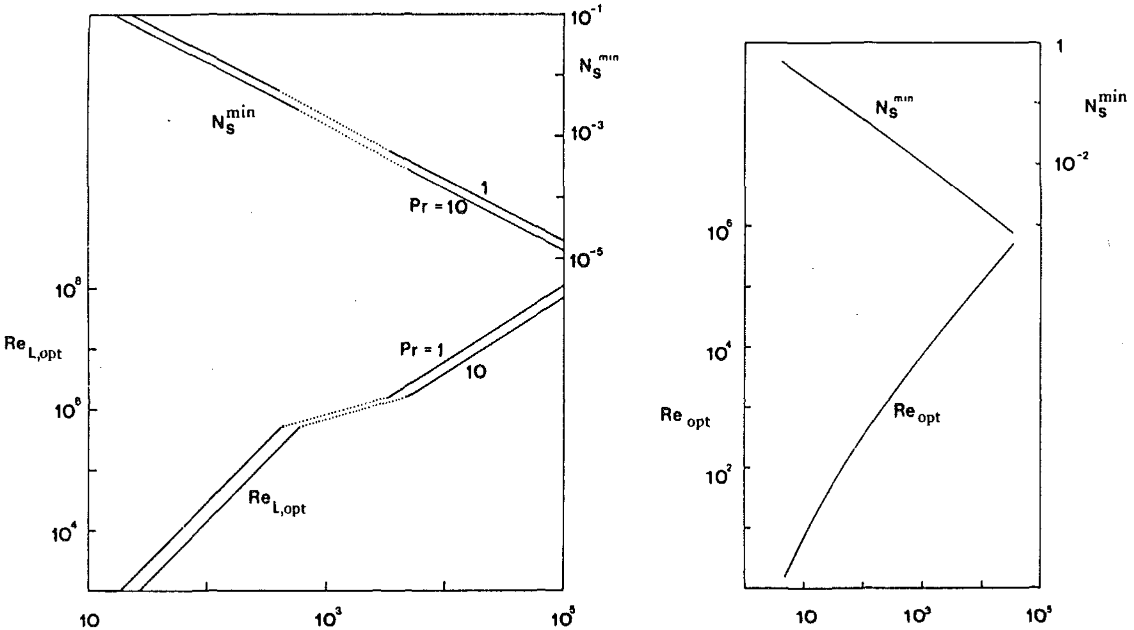

Fig. 4. Optimum Reynolds number and corresponding minimum entropy generation number. Left: boundary layer flow over a flat plate. Right: single cylinder in gaseous cross-flow

timum Reynolds number (plate length) and the lower the minimum entropy generation number. In other words, if the total heat transfer rate q' is constant and the flow velocity increases, the optimum plate length decreases and the minimum attainable entropy generation rate increases.

These conclusions are applicable to the optimization of local flow geometry in plate-fin surfaces for compact heat exchangers. The chief conclusion is that for a plate-fin with q' and $v_{x,\infty}$ fixed, there exists an optimum fin dimension in the flow direction which, if selected, yields the minimum rate of entropy generation.

Single Cylinder in Cross-Flow

The heat transfer between a cylindrical surface and a fluid flow normal to the cylinder axis is one of the most frequent heat transfer configurations encountered in actual engineering equipment for heat exchange processes. It is appropriate to examine here the thermodynamic irreversibility introduced by this configuration. Due to inherent similarities with the plate of finite length in parallel boundary layer flow, example concluded in the preceding section, the case of a single cylinder in cross-flow will be summarized very briefly and only the key analytical results will be given.

Consider a cylinder of diameter D with uniform surface heat flux q'' in a cross-flow of uniform velocity $v_{x,\infty}$ and temperature T_∞. An entropy generation analysis of the flow region affected by heat and momentum transfer from the cylinder yields the total entropy generation rate

$$S' = \frac{q''}{T_\infty^2} \oint [T(\ell) - T_\infty] d\ell + \frac{v_{x,\infty} F_D}{T_\infty} \qquad (43)$$

In this expression, ℓ is the curvilinear coordinate around the cylindrical surface and $T(\ell)$ is the local surface temperature. It is again assumed that the temperature differences are much smaller than characteristic absolute temperature of the medium $[T(\ell) - T_\infty] \ll T_\infty$. F_D is the force (drag) per unit length exerted by flow on cylinder, force calculated from drag coefficient experimental information, C_D,

$$C_D = \frac{F_D/D}{\rho\, v_{x,\infty}^2/2} \qquad (44)$$

Replacing the line integral in (43) with the average wall-fluid temperature difference times πD, and expressing the average temperature difference in terms of the average Nusselt number, $T(\ell)_{av} - T_\infty = q''\, D/(k\ \mathrm{Nu})$, yields,

$$S' = \frac{q'^2}{\pi\, k\, T_\infty^2} \frac{1}{\mathrm{Nu}} + \frac{1}{2} C_D\, \mathrm{Re}\, \frac{\mu\, v_{x,\infty}^2}{T_\infty} \qquad (45)$$

In writing (45), we used the drag coefficient to replace F_D in equation (43). We also wrote $q' = \pi D\, q''$ for the total heat transfer rate per unit length of cylinders. Finally, expression (45) is put in dimensionless form defining the entropy generation number

$$N_{S'} = S' \frac{k\, T_\infty^2}{q'^2} = \frac{1}{\pi\, \mathrm{Nu}} + \frac{1}{2} C_D\, \mathrm{Re}\, B^{-2} \qquad (46)$$

where B is a duty parameter which has the same form as in equation (37).

Optimum Cylinder Diameter for Minimum Irreversibility. As in the heat transfer configurations examined earlier, we can use the entropy generation number formula (46) to determine which flow geometry (cylinder diameter D) is best for minimizing the thermodynamic losses associated with the heat transfer process. For an application in which q', $v_{x,\infty}$ and the fluid are known, the optimization procedure amounts to minimizing expression (46) with respect to Re, subject to constant B. The results of this optimization procedure are shown as $\mathrm{Re}_{\mathrm{opt}}$ and $N_{S'}{}^{\mathrm{min}}$ on the right side of Fig. 4, a plot qualitatively similar to the left graph obtained for a flat plate. The right graph of Fig. 4 was constructed based on equation (46) coupled with Hilpert's average Nusselt number correlation for gas flow [16] and with Eisner's presentation of drag coefficient [17].

From a practical viewpoint, expression (46) and the optimum design summarized on the right side of Fig. 4. can be used to calculate and minimize the thermodynamic losses exhibited by engineering components which embody the simple heat transfer configuration considered in this section. These results can be applied not only to single cylinders in cross-flow, but also to arrays of cylinders (tube banks) spaced sufficiently far apart so that their mutual influence is not a major effect in the heat transfer and fluid friction characteristics of the arrangement. In the case of arrays of cylinders in cross-flow in which the spacing between neighboring cylinders plays an important role [18] it is possible to reconstruct the above analytical procedure based on heat transfer and fluid friction information for tube banks in cross-flow [19]. Further, one should be able to combine the external flow configuration (flow normal to tube banks) with the internal flow configuration studied in the first example of this paper (pipe flow) to establish the least irreversible combined geometry for two-fluid heat exchangers using one fluid in the tubes and the other normal to the tubes. The question of optimum pin-fin surface geometry can be

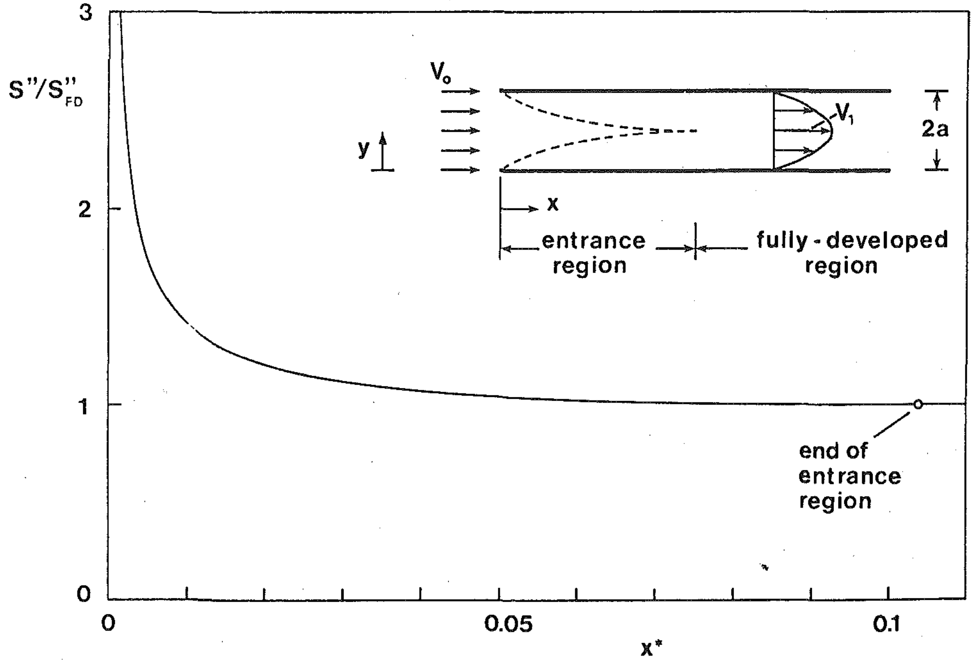

Fig. 5. Distribution of the entropy generation rate in the entrance region of a flat rectangular duct in laminar flow

addressed in a similar manner. For this one would have to use Nusselt number and friction factor data obtained specifically for pin-fin surfaces where, as shown recently by Sparrow and Ramsey [20], the pin-wall attachment makes the flow strongly three-dimensional, unlike the two-dimensional configuration considered in this section.

Laminar Forced Convection in the Entrance Region of a Flat Rectangular Duct

A frequent flow configuration which embodies the characteristics of the first two flow examples discussed here is sketched in the insert of Fig. 5. In the entrance region of a parallel-plate duct temperature and velocity boundary layers develop simultaneously along both walls, gradually filling the duct and leading to the well-known fully-developed laminar regime. There have been many studies of the heat transfer and velocity problems associated with this basic configuration, as indicated recently by Bhatti and Savery [21]. In this section we address the irreversibility problem, once again relying on published solutions for the temperature and velocity field in the duct.

Sparrow [22] analyzed the boundary layer development in the entrance region using the Karman-Pohlhausen integral technique. The Sparrow solution is unique, considering its simplicity versus the good agreement between its predictions and experimental findings. In what follows we use this solution in combination and the S''' formula (1) to illustrate the distribution of irreversibility in the channel.

The ultimate goal of the irreversibility analysis is to discover how the thermodynamic losses due to entrance effects compare with similar losses in the fully-developed section of the duct. In other words, what length of fully-developed flow is guilty of generating as much entropy as the entire entrance region? The answer to this question is simplified substantially if, in addition to using Sparrow's analytical solution, we focus on the $\tau \to 0$ limit in which the viscous effects totally dominate the rate of entropy generation in the channel (see the discussion following equation (4)). Consequently, to calculate S''' we need only the velocity solution which is (22)

$$v_x = V_0 V_1^* \, (2\zeta - \zeta^2) \tag{47}$$

with

$$\zeta = y/\delta, \quad \delta/a = 3(1 - V_1^{*-1}) \tag{48, 49}$$

$$V_1^* = V_1/V_0, \quad x^* = \frac{x\nu}{a^2 V_0} \tag{50, 51}$$

As shown on Fig. 5, V_0 is the uniform fluid velocity at $x = 0$, while V_1 and δ are the centerline velocity and boundary layer thickness, respectively. For the function $V_1^*\,(x^*)$, Sparrow reports a differential equation which, integrated, yields

$$x^* = \frac{3}{10}\left(9V_1^* - 2 - \frac{7}{V_1^*} - 16\,\ell\text{n}\, V_1^*\right) \tag{52}$$

The entrance region extends to $x^* = 0.1038$, corresponding to $V_1^* = 3/2$ as for plane Poiseuille flow.

Using equation (1) and leaving out the conductive contribution we obtain

$$S''' = \frac{4\mu\, V_0^2}{T\,\delta^2}\, V_1^{*2}\,(1 - \zeta)^2 \tag{53}$$

and, integrating across the duct,

$$S'' = 2\int_0^a S'''\, dy = \frac{8}{3}\,\frac{\mu\, V_0^2}{T\delta}\, V_1^{*2} \tag{54}$$

From (54) we find that in the fully-developed section of the duct (FD) the rate of entropy generation per unit area of duct wall is

$$S''_{FD} = 6\,\frac{\mu\, V_0^2}{Ta} \tag{55}$$

Fig. 5 shows the variation of S''/S''_{FD} with axial position along the duct. As expected, the irreversibility effects are most intense near $x = 0$. However, as x^* increases, S'' rapidly approaches the fully-developed entropy generation level S''_{FD} a good distance *before* the end of the entrance region, $x^* = 0.1038$.

The total irreversibility associated with entrance effects is estimated integrating expression (54) from $x^* = 0$ to $x^* = 0.1038$. The result of this operation is

$$S' = \frac{11}{15}\,\frac{\rho a\, V_0^3}{T} \tag{56}$$

where ρ is the fluid density. Similarly, the total rate of entropy generation over a fully-developed stretch of length L_{FD} is, from (55),

$$S'_{FD} = 6\,\frac{\mu\, V_0^2}{Ta}\, L_{FD}. \tag{57}$$

Comparing results (56) and (57), we conclude that the fully-developed equivalent of the entire entrance region is a fully-developed section of length L_{FD} given by

$$\frac{L_{FD}}{D} = \frac{11}{1440}\,\text{Re}_D = 0.00764\,\text{Re}_D. \tag{58}$$

where D is the hydraulic diameter $4a$, while $\text{Re}_D = V_0 D/\nu$. It is time now to compare the irreversibility-equivalent length L_{FD} with the physical extent of the entrance region, L_E. Setting $x^* = 0.1038$ and $x = L_E$ in expression (51) we find that familiar result

$$\frac{L_E}{D} = 0.00649\,\text{Re}_D. \tag{59}$$

Therefore, from (58, 59), the irreversibility contributed by the entrance region is roughly equal to (actually, only about 18 percent higher than) the irreversibility estimated assuming fully-developed flow over a duct length equal to the entrance length. This conclusion is important in practical irreversibility calculations, as it is considerably easier to treat the entire duct as in the fully-developed regime.

In a manner similar to the analysis presented in the previous three examples, future research should address the more general case when conductive effects are sizeable. For this extension of the present example, the Sparrow solution [22] will again be the place to start in view of its closed-form presentation of the mechanics of the flow. Overall, the entrance flow example is relevant to the engineering task of minimizing the thermodynamic irreversibility of strip fin heat exchanger surfaces where, to some extent, the strip fins act as a succession of entrance regions to flat ducts. In addition, the analysis developed in this section suggests simpler means of evaluating the entropy generation rate in the complicated entrance region flow, namely, by considering the fully-developed entropy generation rate (57) as a first approximation.

Concluding Remarks

We presented a study of four basic convective heat transfer phenomena from the unique point of view of entropy generation. We have seen what features of the flow act as concentrators of entropy generation. In the process we developed analytical means for estimating and minimizing the irreversibility associated with these heat transfer configurations. The analytical results presented in this article, together with similar results which must be derived for other pedestal-type convective heat transfer configurations, constitute the fundamental building blocks for calculating and minimizing the irreversibility production rate in heat transfer and thermal design calculations pertaining to energy conservation.

The important engineering conclusion to be drawn from this study is that, while seeking to minimize the destruction of available work in complex heat transfer equipment, it is necessary to start with optimizing the simplest, most elementary, design features such as the geometry of internal and external surfaces engaged in convective heat transfer.

Acknowledgment

This work was supported by the Office of Naval Research, Grant No. N00014-79-C-0006. The many comments received by this author from Mr. Keith Ellingsworth of the Power Program, Office of Naval Research, are gratefully acknowledged. In addition, this paper reflects a number of constructive suggestions offered by three anonymous reviewers of the original manuscript. This author feels indebted to these individuals as well as to Professor E. M. Sparrow whose comments provided a valuable stimulus for the present work.

This line of research is rooted into the author's studies at the Massachusetts Institute of Technology, where Professors E. G. Cravalho and J. L. Smith, Jr. have created a unique thermodynamics method [2]. During his postdoctoral years at the University of California, Berkeley, this author benefited from the advice of Professor C. L. Tien, who encouraged him to go public with his interest in the second law aspect of heat transfer and thermal design.

References

1 Keenan, J. H., *Thermodynamics*, Wiley, New York, 1941, Chapter XVII.

2 Cravalho, E. G. and Smith, J. L., Jr., *Thermodynamics—An Introduction*, Preliminary Edition, Holt, Rinehart and Winston, 1971, Chapter 8.

3 Van Wylen, G. J., and Sonntag, R. E., *Fundamentals of Classical Thermodynamics*, Wiley, New York, 1973, pp. 276, 277.

4 Bejan, A., "The Concept of Irreversibility in Heat Exchanger Design: Counterflow Heat Exchangers for Gas-to-Gas Applications," ASME JOURNAL OF HEAT TRANSFER, Vol. 99, No. 3, Aug. 1977, p. 374.

5 Bejan, A., "General Criterion for Rating Heat-Exchanger Performance," *Int. J. Heat Mass Transfer*, Vol. 21, 1978. p. 655.

6 Bejan, A., "Two Thermodynamic Optima in the Design of Sensible Heat Units for Energy Storage," ASME JOURNAL OF HEAT TRANSFER, Vol. 100, Nov. 1978, p. 708.

7 Kestin, J., *A Course in Thermodynamics*, Vol. II, Blaisdell, Waltham, Massachusetts, 1968, p. 433.

8 Bird, R. B., Stewart, W. E. and Lightfoot, E. N., *Transport Phenomena*, Wiley, New York, 1960.

9 Kestin, J. and Richardson, P. D., Heat Transfer Across Turbulent, Incompressible Boundary Layers, *Int. J. Heat Mass Transfer*, Vol. 6, 1963, p. 147.

10 Bejan, A. and Hoenig, M. O., "Method for Estimating the Refrigeration Costs of Supercritical Helium Cooled Cable Superconductors," *IEEE Transactions on Magnetics*, Vol. MAG-13, 1977, p. 686.

11 Schlichting, H., *Boundary Layer Theory*, 6th Edition, McGraw-Hill, New York, 1968.

12 Pohlhausen, E. Z., *Zeitschrift für angewandte Mathematik und Mechanik*, Vol. 1, 1921, p. 115.

13 Howarth, L., "On the Solution of the Laminar Boundary Layer Equations," *Proceedings of the Royal Society of London*, Series A. Vol. 164, 1938, p. 547.

14 Rohsenow, W. M. and Choi, H. Y., *Heat, Mass and Momentum Transfer*, Prentice-Hall, Englewood Cliffs, 1961, pp. 39, 148.

15 Rohsenow, W. M. and Choi, H. Y., *Op. Cit.*, pp. 76, 198.

16 Hilpert, R., "Wärmeabgabe von geheizten Drähten und Rohren im Luftstrom," *Forsch. Geb. Ingenieur.*, Vol. 4, 1933, p. 215.

17 Eisner, F., *3rd Int. Cong. App. Mech.*, Stockholm, 1930, also in Rohsenow, W. M. and Choi, H. Y., *Op. Cit.*, p. 79.

18 Zukauskas, A., "Heat Transfer from Tubes in Crossflow," *Advances in Heat Transfer*, Vol. 8, 1972, p. 93.

19 Kays, W. M. and London, A. L. *Compact Heat Exchangers*, McGraw-Hill, New York, 1964.

20 Sparrow, E. M. and Ramsey, J. W., "Heat Transfer and Pressure Drop for a Staggered Wall-Attached Array of Cylinders with Tip Clearance", *Int. J. Heat Mass Transfer*, Vol. 21, 1978, p. 1369.

21 Bhatti, M. S. and Savery, C. W., "Heat Transfer in the Entrance Region of a Straight Channel: Laminar Flow with Uniform Wall Temperature," ASME JOURNAL OF HEAT TRANSFER, Vol. 100, Aug. 1978, p. 539.

22 Sparrow, E. M., "Analysis of Laminar Forced Convection Heat Transfer in the Entrance Region of Flat Rectangular Ducts," NACA TN 3331, 1955.

F. E. Romie
Palos Verdes Estates, CA 90274

Periodic Thermal Storage: The Regenerator

The regenerator alternately stores and supplies heat to two gases which enter at different but constant temperatures and flow counter-currently and sequentially through the same flow passages for periods t_a and t_b. The periodic steady-state temperatures of the two gases and the regenerator solid are found as functions of time and position. The analysis is based on the use of polynomials of the position coordinate to represent the matrix temperature distributions at the beginning of each flow period. The subsequent gas and matrix temperatures are expressed in terms of functions which are readily evaluated by use of a computer. The initial, time average, and final temperatures of the gas leaving the regenerator are tabulated. Results for a single regenerator are applied to the rotating regenerator and to switched regenerators.

Introduction

The regenerator is distinguished from the usual heat exchanger by its thermal capacitance which alternately supplies and accepts heat from two fluids which enter at different but constant temperatures and flow countercurrently and sequentially through the same flow passages. During steady-state periodic operation the heat transferred from the hot fluid to the matrix composing the regenerator is equal to the heat transferred from the matrix to the cooler fluid. The heat transferred to the cooler fluid during its flow period is equal to the capacity rate times the time-integral, over the flow period, of the difference between the time varying exit fluid temperature and the constant entrance fluid temperature.

$$Q = (wc)_a \int_0^{t_a} (\tau_a'(t, 1) - \tau_a'(0))dt \tag{1}$$

This equation can be recast in the form

$$Q = (wct)_a \bar{\tau}_a (\tau_b'(1) - \tau_a'(0)) \tag{2}$$

in which $\tau_b'(1)$ is the constant entrance temperature of the hotter fluid and $\bar{\tau}_a$ is a temperature modulus.

$$\bar{\tau}_a = \frac{\bar{\tau}_a' - \tau_a'(0)}{\tau_b'(1) - \tau_a'(0)} \tag{3}$$

The time-average temperature of fluid "a" as it leaves the matrix is $\bar{\tau}_a'$. The temperature modulus $\bar{\tau}_a$ is entirely analogous to the thermal effectiveness defined for the usual steady flow exchanger.

The purpose of this paper is to present the operation of the regenerator in a manner suited for evaluating its use for thermal storage applications. Most of the publications on regenerator operation are directed to its use as a heat exchanger for which thermal storage, while inherent to its operation, is nevertheless incidental to the application. The governing equations and their solution are, of course, the same irrespective of the application and the difference is one of emphasis. An additional purpose is to present a new method of solution of the system equations.

Kays and London [1] summarize in tabular form the thermal effectiveness (i.e., $\bar{\tau}_a$) for rotating regenerators and also present a summary of the effect of axial conduction in the matrix. Their numerical results are based largely on papers by Lambertson [2], Bahnke and Howard [3] and Mondt [4], which, together, give a very complete description of the operation of rotating regenerators intended for use with the regenerative cycle gas turbine engine. (Results for rotating regenerators are readily translated for use with stationary regenerators as will be indicated.) A review of various approaches to the mathematical description of regenerator operation is given by Hausen [5] who also discusses the effects of transverse conduction in the matrix. A companion article by Willmott [6] reviews work on the regenerator problem since the advent of the digital computer.

Despite the simplicity of the differential equations their solution has proved to be challenging and most of the numerical results available in the literature are based on finite difference methods carried out, as with the present work, using a computer. In this paper the mathematical method uses the fact that if the response of a linear system is known for a given excitation then the integral of the response is the response to the integral of the excitation. For the matrix the integrations are carried out with respect to the axial coordinate, y, and the successive integrations start with the response to a step change in matrix temperature. The first integral gives the response to an initial linear (y) matrix temperature distribution, the second to an initial parabolic (y^2) distribution and so on. The responses are additive and hence the matrix response to an arbitrary initial polynomial temperature distribution is constructed. The polynomial coefficients are determined by imposing the requirement that the matrix temperature distribution at the end of a flow period equal the distribution of the beginning of the succeeding flow period.

The Differential Equations

The matrix is defined as follows:

1 The conductance, hA, for transfer of heat between the solid and fluid is uniform and constant throughout the matrix as are the thermal capacity, WC, of the matrix material and the capacity rate, wc, of the fluid. (The conductances and capacity rates for the two fluids and the two flow times will, in general, be different.)
2 There is no axial conduction of heat in the matrix material.
3 The thermal conductivity of the solid is infinite in the direction normal to flow.

With these definitions an energy balance on an elemental length of the matrix produces two equations applicable during the flow of fluid "a." (Similar equations are, of course, applicable during the flow of fluid "b.")

$$T - \tau = -\frac{\partial T}{\partial \theta} \tag{4}$$

$$T - \tau = \frac{\partial \tau}{\partial Z} + \frac{\rho c V}{WC}\frac{\partial \tau}{\partial \theta} \tag{5}$$

(See Nomenclature for definition of the symbols. The temperature moduli T and τ will henceforth be termed temperatures).

The factor of $\partial\tau/\partial\theta$ in equation (5) is the ratio of the thermal capacity of the fluid contained in the matrix (at any instant) to the thermal capacity of the matrix. If the fluid is a gas the ratio of these two capacities will be much less than unity and therefore the last term of equation (5) will be dropped. A corollary to the smallness of the capacity ratio is that a flow period will be many times the transit time of a particle of gas if the matrix temperature changes appreciably during the period.

Contributed by the Heat Transfer Division for publication in the JOURNAL OF HEAT TRANSFER. Manuscript received by the Heat Transfer Division, October 17, 1978.

Solution of the Equations

The gas "a" enters at zero temperature at $y = 0$ and the matrix temperature distribution at the beginning of the flow period is expressed as an mth degree polynomial of the axial coordinate y.

$$T_a(0, y) = \sum_{n=0}^{m} A_n y^n \tag{6}$$

For these two conditions the solution for the matrix temperature is expressible in the form,

$$T_a(\theta, y) = \sum_{n=0}^{m} A_n y^n H_n(\theta, yN_a) \tag{7}$$

and the gas temperature, from this equation and equation (4), is

$$\tau_a(\theta, y) = \sum_{n=0}^{m} A_n y^n \left(H_n(\theta, yN_a) + \frac{\partial H_n}{\partial \theta} \right) \tag{8}$$

The functions, H_n, are related by the recurrence equation

$$\frac{y^{n+1} H_{n+1}(\theta, yN)}{n+1} = \int_0^y \nu^n H_n(\theta, \nu N) d\nu \tag{9}$$

The first function, H_0, is the temperature response of a matrix initially at unity temperature to a gas entering at zero temperature. This response is well known [7, 8] and can be expressed in the form, ($Z = yN$)

$$H_0(\theta, Z) = 1 - \int_0^\theta e^{-(\nu+Z)} I_0(2\sqrt{\nu Z}) d\nu \tag{10}$$

For θ or Z or both greater than about eight a closed asymptotic form, given in terms of the complementary error function, is

$$H_0(\theta, Z) = \frac{1}{2} erfc \left(\theta^{1/2} - Z^{1/2} - \frac{1}{4(\theta Z)^{1/4}} \right) \tag{11}$$

This latter equation is difficult to integrate repeatedly in the manner indicated by equation (9). However for calculational purposes the functions H_n can be found by expressing the modified Bessel function of equation (10) in series form and carrying out the indicated integrations term by term. This procedure gives, after some manipulation,

$$\begin{aligned}
H_0(\theta, Z) &= e^{-(\theta+Z)} 0! \left\{ \frac{1}{0!} + \frac{Z}{1!}(1+\theta) + \frac{Z^2}{2!}\left(1 + \theta + \frac{\theta^2}{2!}\right) + \ldots \right\} \\
H_1(\theta, Z) &= e^{-(\theta+Z)} 1! \left\{ \frac{1}{1!} + \frac{Z}{2!}(2+\theta) + \frac{Z^2}{3!}\left(3 + 2\theta + \frac{\theta^2}{2!}\right) + \ldots \right\} \\
H_2(\theta, Z) &= e^{-(\theta+Z)} 2! \left\{ \frac{1}{2!} + \frac{Z}{3!}(3+\theta) + \frac{Z^2}{4!}\left(6 + 3\theta + \frac{\theta^2}{2!}\right) + \ldots \right\}
\end{aligned} \tag{12}$$

Series expressions for larger values of the index n can be found by extension upon noting that if $b_{n,p}$ is the polynomial in θ multiplying the pth power of Z in the expression for H_n then,

$$b_{n,p} = b_{n-1,p} + b_{n,p-1} \tag{13}$$

During the flow period of gas "b" the gas enters the matrix at $y = 1$ with a temperature of unity. The temperature of the matrix during the flow period "b" is therefore,

$$T_b(\theta, y) = 1 - \sum_{n=0}^{m} B_n (1-y)^n H_n(\theta, (1-y)N_b) \tag{14}$$

and the gas temperature is,

$$\tau_b(\theta, y) = 1 - \sum_{n=0}^{m} B_n (1-y)^n \left(H_n(\theta, (1-y)N_b) + \frac{\partial H_n}{\partial \theta} \right) \tag{15}$$

Evaluation of Constants

The matrix temperature distribution at the beginning of the "a" flow period is the distribution at the end of the "b" flow period,

$$T_a(0, y) = T_b(\theta_b, y) \tag{16}$$

Similarly, the temperature distribution at the end of the flow period "a" is the distribution at the beginning of the "b" period,

$$T_a(\theta_a, y) = T_b(0, y) \tag{17}$$

Steady-state periodic operation requires that these two temperature distributions not change from cycle to cycle.

Substituting equations (7) and (14) into the latter two equations produces the two equations used to find the values of the constants A_n and B_n.

$$\sum_{n=0}^{m} A_n y^n H_n(\theta_a, yN_a) + \sum_{n=0}^{m} B_n (1-y)^n = 1 \tag{18}$$

$$\sum_{n=0}^{m} A_n y^n + \sum_{n=0}^{m} B_n (1-y)^n H_n(\theta_b, (1-y)N_b) = 1 \tag{19}$$

For an mth degree polynomial the $2(m + 1)$ values of A_n and B_n are found by requiring that each of these two equations be satisfied at $(m + 1)$ points. The resultant $2(m + 1)$ equations are solved for the values of A_n and B_n. For the symmetrical case for which $N_a = N_b$ and $\theta_a = \theta_b$ the coefficients A_n and B_n are equal and the required number of simultaneous equations is halved.

Trial operation of the computer program showed that, with a given degree of the polynomial, improved accuracy is realized if the points, y_p, at which equations (18) and (19) are satisfied are more closely spaced near the ends of the matrix than in the central portion. The equation used for this purpose is,

$$y_p = \frac{1}{2}\left(1 - \cos \frac{\pi p}{m}\right), \quad (p = 0, 1, 2, \ldots m) \tag{20}$$

Capacitance Utilization

The heat transferred to gas "a" during its flow period must equal the change in internal energy of the matrix during the flow period.

$$(wct)_a(\bar{\tau}_a' - \tau_a'(0)) = WC \int_0^1 [T_a'(0, y) - T_b'(0, y)] dy \tag{21}$$

Nomenclature

A = heat transfer area of matrix
A_n = coefficient
B_n = coefficient
c = specific heat of gas
C = specific heat of matrix material
d = number of discharging regenerators
e = number of recharging regenerators
h = convective conductance per unit area
H_n = function, see equation (12)
K_n = function, see equation (A-2)
L = length of matrix
m = degree of polynominal
$N = hA/wc$
N_{tu} = see equation (26)
Q = heat transferred during flow period
R = see equation (23)
t = time
t_a = flow period for gas "a"
t_b = flow period for gas "b"
T' = matrix temperature
$T = (T' - \tau_a'(0))/(\tau_b'(1) - \tau_a'(0))$
U = see equation (22)
V = volume occupied by gas in matrix
w = mass rate of gas
W = mass of matrix
x = distance from matrix entrance (for "a" gas)
$y = x/L$
$Z = Ny$
α = angle, Fig. 3
$\theta_a = (hAt)_a/WC$
$\theta_b = (hAt)_b/WC$
$\theta = \theta_a t/t_a$ or $\theta_b t/t_b$ as appropriate
ρ = density of gas
τ' = gas temperature
$\tau_a'(0)$ = entrance temperature of gas "a"
$\tau_b'(1)$ = entrance temperature of gas "b"
$\bar{\tau}_a'$ = time average temperature of leaving gas "a"
$\tau = (\tau' - \tau_a'(0))/(\tau_b'(1) - \tau_a'(0))$
$\bar{\tau}_a = (\bar{\tau}_a' - \tau_a'(0)/(\tau_b'(1) - \tau_a'(0))$

Subscripts

a = refers to gas "a"
b = refers to gas "b"
m = refers to mixed gases
r = refers to rotating or switched regenerator

The maximum thermal energy the matrix can store between the inlet gas temperatures $\tau_b'(1)$ and $\tau_a'(0)$ is $WC(\tau_b'(1) - \tau_a'(0))$. Dividing equation (21) by this maximum storage capability and carrying out the integration gives the capacitance utilization, U.

$$U \equiv \frac{(wct)_a}{WC}\bar{\tau}_a = -1 + \sum_{n=0}^{m} \frac{A_n + B_n}{1+n} \tag{22}$$

For a given thermal storage per flow period the required capacitance (i.e., WC) of the matrix is inversely proportional to the capacitance utilization which cannot exceed unity.

Equation (22) is used to calculate the time-average temperature $\bar{\tau}_a$.

Storage Effectiveness

For many applications the ratio of the energy returned by the matrix, $(wct)_a(\bar{\tau}_a' - \tau_a'(0))$, to the energy made available by the hot gas, $(wct)_b(\tau_b'(1) - \tau_a'(0))$, is an important parameter. This ratio, which will be termed the storage effectiveness, R, is,

$$R = \frac{(wct)_a}{(wct)_b}\bar{\tau}_a \tag{23}$$

The maximum, $\tau_a(0, 1)$, time average, $\bar{\tau}_a$, and minimum, $\tau_a(\theta_a, 1)$, temperatures at which the gas is returned are tabulated in a following section.

Limiting Case

For short flow periods the change in matrix temperature during the course of a cycle is small relative to other temperature differences in the matrix. In the limit, as t_a and t_b go to zero, the matrix temperature becomes time invariant. For this limiting case the equations for the matrix temperature distribution and the gas temperature distributions are the same as those applying [1] to the usual steady flow counter flow heat exchanger provided that, in the latter case, $(wc)_a/(wc)_b$ is replaced by $(wct)_a/(wct)_b$. The time-average temperature of the gas leaving the regenerator for this limiting case is therefore,

$$\bar{\tau}_a = \frac{1 - \exp\left[N_{tu}\left(\frac{(wct)_a}{(wct)_b} - 1\right)\right]}{1 - \frac{(wct)_a}{(wct)_b}\exp\left[N_{tu}\left(\frac{(wct)_a}{(wct)_b} - 1\right)\right]} \tag{24}$$

When $(wct)_a/(wct)_b = 1$ this equation reduces to,

$$\bar{\tau}_a = \frac{N_{tu}}{N_{tu} + 1} \tag{25}$$

For the limiting case the temperatures are time invariant and therefore the maximum, time average, and minimum temperatures of the gas leaving the matrix are equal.

The parameter N_{tu} (number of transfer units) is defined by the equation,

$$N_{tu} = \left[\frac{1}{N_a} + \frac{(wct)_a}{(wct)_b}\frac{1}{N_b}\right]^{-1} \tag{26}$$

Either gas, irrespective of whether it is the hotter or colder, can be designated as the "a" gas without change in the equations presented. (The "b" gas is treated as the hotter to facilitate exposition). If the subscript "a" is assigned such that $(wct)_a/(wct)_b$ is not greater than unity then $\bar{\tau}_a$ is identifiable as the regenerator thermal effectiveness which will approach unity as N_{tu} increases provided that (see equation (22)) $(wct)_a/WC$ is not greater than unity.

Results of Calculation

The system parameters used in formulating the mathematical description of regenerator operation are θ_a, θ_b, N_a and N_b. The parameters selected to present the results of calculation are N_{tu}, $(wct)_a/(wct)_b$, $(wct)_a/WC$, and N_a/N_b. Either set of four parameters can be translated into the other. The selected set has the advantage that the first two parameters, with slight modification, are often used in the design of steady flow exchangers and the second and third occur naturally in expressions of operational parameters (see equations (22) and (23)). The fourth parameter, N_a/N_b, is equal to the ratio of the Stanton numbers for the two flows and, at least for turbulent flows, will often not depart greatly from unity.

Tables 1 to 4 give the maximum, $\tau_a(0, 1)$, time-average, $\bar{\tau}_a$, and minimum, $\tau_a(\theta_a, 1)$, temperature of gas "a" leaving the regenerator for selected values of N_{tu} and $(wct)_a/WC$. For Tables 1, 2 and 3 the value of $(wct)_a/(wct)_b$ is 1.0, 0.9 and 0.8, respectively, and the value of N_a/N_b is unity. It will be observed from equation (24) that the value of $\bar{\tau}_a$ is independent of N_a/N_b when $(wct)_a/WC$ is zero and therefore the effect, if any, of N_a/N_b on the tabulated values can be anticipated to increase with increasing values of $(wct)_a/WC$. Table 4 shows the effect of different values of N_a/N_b when $(wct)_a/WC$ and $(wct)_a/(wct)_b$ are both unity. For the conditions covered $\bar{\tau}_a$ is independent, to three decimal places, of the ratio N_a/N_b. (The maximum change in $\bar{\tau}_a$ for

Table 1 Matrix exit temperatures for gas "a": $(wct)_a/(wct)_b = 1$; $N_a/N_b = 1$

$(wct)_a/WC$	0	0.25	0.50	0.75	1.00	0	0.25	0.50	0.75	1.00
			$N_{tu} = 0.5$					$N_{tu} = 1.0$		
$\tau_a(0,1)$	0.333	0.360	0.385	0.410	0.434	0.500	0.553	0.602	0.648	0.689
$\bar{\tau}_a$	0.333	0.333	0.330	0.327	0.322	0.500	0.498	0.491	0.481	0.467
$\tau_a(\theta_a,1)$	0.333	0.307	0.281	0.255	0.230	0.500	0.445	0.391	0.337	0.286
			$N_{tu} = 2.0$					$N_{tu} = 4.0$		
	0.667	0.744	0.810	0.862	0.901	0.800	0.808	0.944	0.974	0.988
	0.667	0.662	0.649	0.628	0.601	0.800	0.794	0.776	0.748	0.709
	0.667	0.582	0.495	0.407	0.323	0.800	0.697	0.589	0.471	0.347
			$N_{tu} = 8.0$					$N_{tu} = 16.0$		
	0.889	0.971	0.994	0.999	1.000	0.941	0.997	1.000	1.000	1.000
	0.889	0.882	0.865	0.836	0.790	0.941	0.935	0.921	0.897	0.850
	0.899	0.782	0.674	0.536	0.364	0.941	0.844	0.747	0.603	0.375
			$N_{tu} = 32.0$					$N_{tu} = 64.0$		
	0.970	1.000	1.000	1.000	1.000	0.985	1.000	1.000	1.000	1.000
	0.970	0.965	0.956	0.938	0.893	0.985	0.982	0.976	0.964	0.924
	0.970	0.888	0.806	0.671	0.383	0.985	0.920	0.854	0.734	0.389

Table 2 Matrix exit temperatures for gas "a": $(wct)_a/(wct)_b = 0.9$; $N_a/N_b = 1.0$

$(wct)_a/WC$	0	0.25	0.50	0.75	1.00	0	0.25	0.50	0.75	1.00
	N_{tu} = 0.5					N_{tu} = 1.0				
$\tau_a(0,1)$	0.339	0.365	0.390	0.414	0.436	0.513	0.565	0.614	0.658	0.697
$\bar{\tau}_a$	0.339	0.338	0.336	0.332	0.327	0.513	0.510	0.503	0.491	0.476
$\tau_a(\theta_a,1)$	0.339	0.313	0.287	0.261	0.237	0.513	0.458	0.403	0.349	0.297
	N_{tu} = 2.0					N_{tu} = 4.0				
↓	0.689	0.764	0.826	0.874	0.909	0.831	0.908	0.955	0.979	0.991
	0.689	0.684	0.667	0.646	0.615	0.831	0.823	0.803	0.772	0.727
	0.689	0.605	0.517	0.427	0.340	0.831	0.735	0.627	0.503	0.371
	N_{tu} = 8.0					N_{tu} = 16.0				
	0.925	0.981	0.996	0.777	1.000	0.975	0.999	1.000	1.000	1.000
	0.925	0.917	0.898	0.865	0.811	0.975	0.970	0.956	0.929	0.871
	0.925	0.841	0.737	0.588	0.396	0.975	0.922	0.842	0.687	0.419
	N_{tu} = 32.0					N_{tu} = 64.0				
	0.996	1.000	1.000	1.000	1.000	1.000	1.000	1.000	1.000	1.000
	0.996	0.993	0.986	0.969	0.914	1.000	1.000	0.998	0.990	0.943
	0.996	0.976	0.930	0.799	0.440	1.000	0.998	0.984	0.907	0.460

Table 3 Matrix exit temperatures for gas "a": $(wct)_a/(wct)_b = 0.8$; $N_a/N_b = 1.0$

$(wct)_a/WC$	0	0.25	0.50	0.75	1.00	0	0.25	0.50	0.75	1.00
	N_{tu} = 0.5					N_{tu} = 1.0				
$\tau_a(0,1)$	0.345	0.370	0.394	0.417	0.439	0.525	0.577	0.625	0.667	0.703
$\bar{\tau}_a$	0.345	0.343	0.341	0.337	0.332	0.525	0.523	0.515	0.502	0.486
$\tau_a(\theta_a,1)$	0.345	0.319	0.293	0.268	0.243	0.525	0.471	0.416	0.361	0.308
	N_{tu} = 2.0					N_{tu} = 4.0				
↓	0.711	0.783	0.841	0.886	0.917	0.860	0.926	0.964	0.984	0.993
	0.711	0.705	0.689	0.663	0.629	0.860	0.852	0.829	0.793	0.742
	0.711	0.628	0.539	0.446	0.356	0.860	0.771	0.663	0.532	0.392
	N_{tu} = 8.0					N_{tu} = 16.0				
	0.952	0.988	0.998	1.000	1.000	0.992	1.000	1.000	1.000	1.000
	0.952	0.944	0.924	0.887	0.826	0.992	0.988	0.977	0.949	0.883
	0.952	0.888	0.790	0.631	0.423	0.992	0.966	0.906	0.747	0.449
	N_{tu} = 32.0					N_{tu} = 64.0				
	1.000	1.000	1.000	1.000	1.000	1.000	1.000	1.000	1.000	1.000
	1.000	0.999	0.997	0.983	0.922	1.000	1.000	1.000	0.997	0.947
	1.000	0.997	0.979	0.868	0.470	1.000	1.000	0.999	0.961	0.483

the conditions covered in Table 4 was four units in the fourth decimal place).

Fig. 1 shows, for an arbitrarily selected case, the matrix temperature distributions at the beginning and end of the flow periods. The ratio of the area between the two curves to the total area of the figure is the capacitance utilization, U (equation (22)). Fig. 2 shows temperature-time histories of fluid "a" leaving a matrix. The gas temperature for each curve of Fig. 2 starts at $\tau_a(0, 1)$ on the left ordinate and ends at $\tau_a(\theta_a, 1)$ on the right ordinate.

Comparison, where possible, between the values of $\bar{\tau}_a$ given in Tables 1–4 and the values of the thermal effectiveness tabulated in [1] shows complete agreement. Accuracy of the present work was investigated by determining the effect of the degree of the polynomial on the value computed for $\bar{\tau}_a$. For the parameters $N_{tu} = 4.0$, $(wct)_a/(wct)_b = 0.8$, $(wct)_a/WC = 1$, and $N_a/N_b = 1$ no change in the first four decimal places was found in $\bar{\tau}_a$ for m of four or greater and no change in the first eight decimal places for m of eight or greater. The computer is programmed to select the degree of the polynomial according to the equation,

$$m = 4 + INT\left(\frac{\pi}{2} N^{1/2}\right) \tag{27}$$

The value of N is the larger of N_a and N_b and for the preceding specific case $m = 8$. (INT = integer of).

Rotating Regenerator

Two or more regenerators are required to produce a steady (but varying temperature) flow of heated gas. A steady flow of constant temperature heated gas is produced by the rotating regenerator illustrated on Fig. 3.

Table 4 Matrix exit temperatures for gas "*a*": $(wct)_a/WC = 1.0$; $(wct)_a/(wct)_b = 1.0$

N_a/N_b	0.5	0.7	1.0	1.4	2.0	0.5	0.7	1.0	1.4	2.0
			$N_{tu} = 0.5$					$N_{tu} = 1.0$		
$\mathcal{T}_a(0,1)$	0.414	0.422	0.434	0.446	0.461	0.664	0.676	0.689	0.701	0.711
$\bar{\mathcal{T}}_a$	0.322	0.322	0.322	0.322	0.322	0.467	0.467	0.467	0.467	0.467
$\mathcal{T}_a(\theta_a,1)$	0.244	0.238	0.230	0.221	0.210	0.306	0.297	0.286	0.275	0.262
			$N_{tu} = 2.0$					$N_{tu} = 4.0$		
↓	0.890	0.896	0.901	0.903	0.904	0.987	0.988	0.988	0.988	0.988
	0.601	0.601	0.601	0.601	0.601	0.709	0.709	0.709	0.709	0.709
	0.346	0.336	0.323	0.311	0.297	0.371	0.360	0.347	0.334	0.320
			$N_{tu} = 8.0$					$N_{tu} = 16.0$		
	1.000	1.000	1.000	1.000	1.000	1.000	1.000	1.000	1.000	1.000
	0.790	0.790	0.790	0.790	0.790	0.850	0.850	0.850	0.850	0.850
	0.389	0.377	0.364	0.351	0.336	0.401	0.389	0.375	0.362	0.346
			$N_{tu} = 32.0$					$N_{tu} = 64.0$		
	1.000	1.000	1.000	1.000	1.000	1.000	1.000	1.000	1.000	1.000
	0.893	0.893	0.893	0.893	0.893	0.924	0.924	0.924	0.924	0.924
	0.409	0.397	0.383	0.370	0.355	0.415	0.403	0.389	0.375	0.360

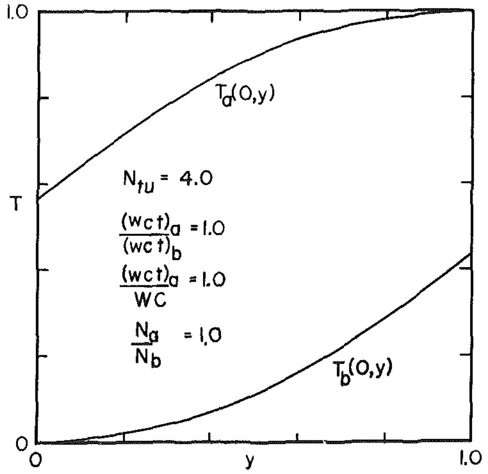

Fig. 1 Matrix temperature distributions at the beginning and end of the flow periods

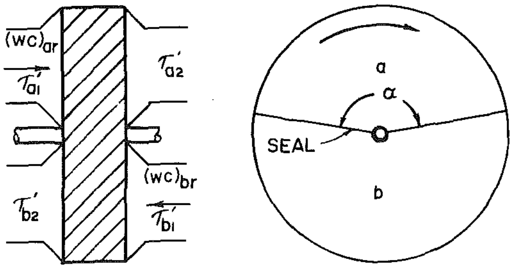

Fig. 3 Rotating regenerator

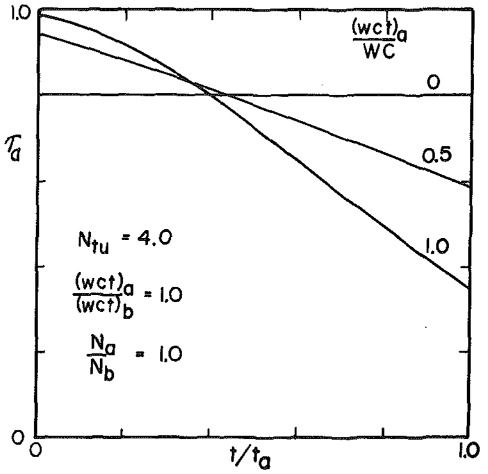

Fig. 2 Temperature-time history of gas leaving a matrix for different flow periods

Table 5 Correspondence of rotating and stationary regenerators

Rotating Regenerator (Fig. 3)	This Paper (Tables 1 to 4)
Interpret	as
N_{tur}	N_{tu}
$[(wc)_a/(wc)_b]_r$	$(wct)_a/(wct)_b$
$(wc)_{ar}t_r/(WC)_r$	$(wct)_a/WC$
N_a/N_b	N_a/N_b
$\dfrac{\mathcal{T}'_{a2} - \mathcal{T}'_{a1}}{\mathcal{T}'_{b1} - \mathcal{T}'_{a1}}$	$\bar{\mathcal{T}}_a$

Note: $\frac{1}{N_{tur}} = \frac{1}{N_a} + \left[\frac{(wc)_a}{(wc)_b}\right]_r \frac{1}{N_b}$

The preceding analysis and the results given in Tables 1–4 are directly applicable to the rotating regenerator through the use of Table 5 in which t_r is the time for a complete revolution and $(WC)_r$ is the total thermal capacity of the rotating regenerator.

Table 5 can be derived by following a small cross-section (i.e., a small regenerator) of the disk through a complete revolution and noting that the time-average temperature for the small cross-section as it passes through the angle α (Fig. 3) must be the steady mixed-mean temperature, τ_{a2}', because all small cross-sections undergo identical histories.

The extensive numerical results tabulated in [1–4] can be converted to the nomenclature used in this paper (and conversely) by interpreting $C_{\min}/C_{\max}$ as $(wct)_a/(wct)_b$, the reciprocal of $C_r/C_{\min}$ as $(wct)_a/WC$, $(hA)^*/(C_{\min}C_{\max})$ as N_a/N_b, N_{tu} as N_{tu}, and ϵ as $\bar{\tau}_a$. The conversion applies results for a rotating regenerator to a stationary regenerator (and conversely).

Regenerator Switching

As remarked above, two or more regenerators are required to provide a steady flow of heated gas. Let $d + e$ identical regenerators be valved such that, at any time, d regenerators are being discharged into a common duct and e regenerators are being recharged. If the discharge time of a regenerator is t_a then its recharge time, t_b, must be $t_a\, e/d$ if dead-time is to be precluded. At time intervals of t_a/d a discharged regenerator will be switched from discharge to recharge and simultaneously one recharged regenerator will be switched to discharge. The temperature, τ_{am}, of the mixed gases from the d discharging regenerators must therefore vary periodically with time with a period t_a/d. Energy conservation requires that the time-average temperature, $\bar{\tau}_{am}$, of the mixed gases be unchanged from the time-average temperature of the gas leaving one discharging regenerator ($\bar{\tau}_{am} = \bar{\tau}_a$).

If the temperature-time history of the gas leaving a discharging regenerator is given as $\tau_a(t/t_a)$ (see Fig. 2) then the temperature-time history of the mixed gases leaving the d discharging regenerators will be, using mixing laws,

$$\tau_{am}(t/t_a) = \frac{1}{d}\sum_{n=0}^{d-1}\tau_a\left(\frac{t}{t_a}+\frac{n}{d}\right), \left(0 \leqslant \frac{t}{t_a} \leqslant \frac{1}{d}\right) \tag{28}$$

The maximum temperature of the mixed gases occurs just after switching ($t/t_a = 0$) and the minimum temperature occurs just before switching ($t/t_a = 1/d$). Therefore the peak to trough amplitude of the periodically varying temperature of the mixed gases is, using equation (28),

$$AMP\ \tau_{am} = \frac{1}{d}\left(\tau_a(0) - \tau_a(1)\right) \tag{29}$$

The temperatures $\tau_a(0)$ and $\tau_a(1)$ are identifiable as $\tau_a(0, 1)$ and $\tau_a(\theta_a, 1)$ given in Tables 1–4.

Table 5 applies to regenerator switching by interpreting t_r as the sum of the discharge and recharge times for one regenerator ($t_r = t_a + t_b = t_a(1 + e/d)$), $(WC)_r$ as the total thermal capacity of the $d + e$ regenerators, $(wc)_{ar}$ as the total capacity rate through the d discharging regenerators and $(wc)_{br}$ as the total capacity rate through the e recharging regenerators. It is noted that the rotating regenerator can be regarded as an assembly of many small regenerators with switching provided by rotation past the seals.

Concluding Remarks

A new method of solution of the regenerator equations has been presented and the results of computer calculations given in a form suited for use in evaluating the regenerator for thermal storage applications. Interpretation of the results for switched and rotating regenerators has been indicated. The computation time on a high speed computer can be characterized as short. For example the CPU time to calculate the tabulated values for $N_{tu} = 4.0$, $(wct)_a/(wct)_b = 0.8$, $(wct)_a/WC = 1.0$ and $N_a/N_b = 1.25$ is about one-half second on a CDC 6000.

Acknowledgments

The author wishes to thank Nahum Gat who programmed the computer. Other friends at TRW Systems made the computer work possible.

References

1 Kays, W. M., and A. L. London, *Compact Heat Exchangers,* 2nd Edition, McGraw Hill, New York, 1964, pp. 44–49.

2 Lambertson, T. J., "Performance Factors of a Periodic-flow Heat Exchanger," Trans. ASME, Vol. 80, 1958, pp. 586–592.

3 Bahnke, G. D. and C. P. Howard, "The Effect of Longitudinal Heat Conduction in Periodic-flow Heat-Exchanger Performance," ASME *Journal of Engineering for Power,* Vol. 86, 1964, pp. 105–120.

4 Mondt, J. R., "Vehicular Gas Turbine Periodic-flow Heat Exchanger Solid and Fluid Temperature Distributions," ASME *Journal of Engineering for Power,* Vol. 86, 1964, pp. 121–126.

5 Hausen, H., "Survey of the Heat Transfer Theories in Regenerators," *Heat Exchangers: Design and Theory Sourcebook,* McGraw-Hill, New York, 1974, pp. 207–222.

6 Willmott, A. J., "Developments in Regenerator Theory Since the Advent of the Digital Computer," *Heat Exchangers: Design and Theory Sourcebook,* McGraw-Hill, New York, 1974, pp. 223–237.

7 Anzelius, A., "Über Erwärmung vermittels durchströmeder Medien," *Z. angew. Math. Mech.,* Vol. 6, 1926, pp. 291–294.

8 Schumann, T. E. W., "Heat Transfer: A Liquid Flowing through a Porous Prism," *Franklin Institute Journal,* Vol. 208, 1929, pp. 405–416.

APPENDIX

Gas Temperature Equations

Equation (12) shows that the functions H_n are the product of an exponential term and a series, f_n.

$$H_n = e^{-(\theta+Z)}f_n(\theta, Z) \tag{A1}$$

Therefore,

$$H_n + \frac{\partial H_n}{\partial \theta} = e^{-(\theta+Z)}\frac{\partial f_n}{\partial \theta} = K_n(\theta, Z) \tag{A2}$$

Series expressions for the functions K_n are readily found from equation (12). The gas temperature (equation (8)) is then expressible as,

$$\tau_a(\theta, y) = \sum_{n=0}^{m} A_n y^n K_n(\theta, yN_a) \tag{A3}$$

Similarly, equation (15) becomes,

$$\tau_b(\theta, y) = 1 - \sum_{n=0}^{m} B_n(1-y)^n K_n(\theta, (1-y)N_b) \tag{A4}$$

For θ or Z or both greater than about eight an asymptotic form for the temperature of a gas which enters, at zero temperature, a matrix initially at unity temperature is, (compare with equation (11)),

$$K_0(\theta, Z) = \frac{1}{2}\,erfc\left[\theta^{1/2} - Z^{1/2} + \frac{1}{4(\theta Z)^{1/4}}\right] \tag{A5}$$

journal of heat transfer

technical notes

This section contains shorter technical papers. These shorter papers will be subjected to the same review process as that for full papers.

Melting about a Horizontal Row of Heating Cylinders

J. W. Ramsey,[1] E. M. Sparrow,[1] and L. M. C. Varejao[1]

Introduction

Recent experimental studies of melting have revealed the dominant role played by natural convection [1–3]. These experiments were performed with either a horizontal or a vertical heating cylinder embedded in a solid phase-change medium. For the horizontal case, it was found that there was substantially more melting above the cylinder than below, indicating the presence of a plume of hot liquid rising from the top of the cylinder and passing upward through the melt layer. The measured heat transfer coefficients for melting varied with time but ultimately attained steady state values that are in close agreement with those for natural convection. The vertical cylinder studies revealed a melting pattern where the thickness of the melt layer increased along the height of the cylinder—also the result of natural convection.

The aforementioned studies dealt with melting about a single heating cylinder. On the other hand, in applications, an array of heating cylinders may be employed, and the present experiments were undertaken to obtain information about melting in such heating configurations. The experiments were performed with an array of parallel, equally spaced cylinders, all lying in a common horizontal plane. The phase-change medium used in the experiments was the eutectic mixture of sodium nitrate and sodium hydroxide, which has a melting temperature of 244°C (471°F).

Heating was accomplished by ohmic dissipation within the cylinders. Prior to the initiation of a data run, the solid phase-change material was brought to a temperature just below the melting point. Once heating was initiated, the power input was maintained constant, and the timewise variation of the surface temperature of each cylinder was recorded as melting progressed. These data enabled melting coefficients to be evaluated. In addition, with a view to determining the shape of the evolving melt region, temperature data were collected from a thermocouple grid deployed throughout the phase-change medium.

In the presentation of results, greater consideration will be given to comparisons between the melting coefficients for the multicylinder array and the single cylinder than to the actual magnitudes of the coefficients. This is because the measured coefficients are specific to the conditions of the experiments whereas the single-cylinder—multi-cylinder comparisons will, in all likelihood, have broader generality. The importance of such comparisons is underscored by the aforementioned close correlation between the single-cylinder melting coefficients and those for natural convection.

A complementary study of melting about an array of horizontal cylinders is reported in [4], where a cluster of three cylinders was employed to model staggered rows. In addition to geometrical differences, different phase-change media were used in the two studies, that of [4] being a paraffin with a melting temperature of 28.2°C (82.8°F). Although a detailed presentation of melting coefficients is made in [4], comparisons of single-cylinder and multi-cylinder results are not made.

Experimental Apparatus

The apparatus employed in the present multi-cylinder melting studies was an adaptation of that used for single cylinder melting experiments in [1]. Therefore, only a brief account of the apparatus need by given here. The phase-change medium and the heating cylinders were housed in a cubical test chamber made of mild steel, 33 cm (13 in.) on a side. The chamber was surrounded on all sides, on top, and on bottom by heating panels and insulation layers. Whereas the chamber and its contents were specifically constituted for the present studies, the heating panel—insulation arrangement was taken over directly from [1].

An array consisting of four parallel cylinders situated in a common horizontal plane was used in all of the experiments. Each cylinder was 1.9 cm (3/4 in.) in diameter and 25.4 cm (10 in.) in length. A three-diameter center-to-center distance between adjacent cylinders was selected on the basis of the melt layer shapes given in [1] for the single cylinder. The rationale for the selection was that there be ample time both for the development of separate melt zones about the individual cylinders and for the interaction of these melt zones as the solid boundaries between them are eaten away by the melting process. The cylinders were positioned so that their centers were about $6\frac{1}{4}$ cm ($2\frac{1}{2}$ in.) above the floor of the chamber.

The temperature of each cylinder was measured at a position midway along its length by six chromel-alumel thermocouples spot welded to the surface at 60 deg intervals around the circumference. For sensing the temperature field in the phase-change medium, an array of 82 thermocouples was stretched horizontally between a pair of parallel perforated plates, each situated adjacent to a side of the chamber. The thermocouples were threaded through the perforations and were held taut by springs situated outside the test chamber.

The electrical resistances of the heating elements encapsulated within the respective cylinders differed by less than one percent, and the wiring was arranged to provide, within this tolerance, identical heat inputs to all four cylinders. With a view to facilitating comparisons of results, the heating rates were selected to coincide closely with those used in the single cylinder experiments of [1].

Auxiliary devices were installed to neutralize potential problems associated with the density change which accompanies phase change. These devices, as well as the temperature reading and recording instrumentation and the control circuity for the heating panels, were the same as those employed in [1]; the experimental procedure used in the present experiments is similar to that described there.

---

[1] Department of Mechanical Engineering, University of Minnesota, Minneapolis, Minn. 55455.

Contributed by the Heat Transfer Division for publication in the JOURNAL OF HEAT TRANSFER. Manuscript received by the Heat Transfer Division March 29, 1979.

Results and Discussion

Instantaneous heat transfer coefficients were deduced from the measured temperatures and heating rates by evaluating the defining equation, $h = q/(T_w - T^*)$. In this equation, q is the rate of heat transfer per unit surface area of each cylinder, T_w is the circumferential average surface temperature, and T^* is the melting temperature. Coefficients were evaluated at a succession of times for all four of the heating cylinders, with prime attention focused on the two inner cylinders (i.e., those away from the side walls). At each instant of time at which data were available, the coefficients for the inner cylinders were averaged, and it is these averages that will be reported here.

The thus-determined melting coefficients are plotted in Fig. 1 as a function of time for three parametric values of the per-tube heating rate. In addition to the results for the multi-cylinder array (circular data symbols), the figure also shows the results for the single cylinder (square data symbols) taken from [1]. The abscissa portrays the time t in terms of the energy input qt for the period between $t = 0$ and $t = t$. The use of the qt time scale instead of t itself rationalizes the different heating powers and run times (longer run times at lower powers, shorter times at higher powers).

An overall examination of Fig. 1 reveals that for all the cases shown there, the melting coefficients for the multi-cylinder array and for the single cylinder are of comparable magnitude, although there are noteworthy differences in detail. Immediately following the initiation of heating, the melting coefficients are very high and decrease sharply with time—this is the heat conduction regime. The decrease is arrested by the onset of natural convection, so that the coefficients increase after having attained a minimum. Thereafter, natural convection is the dominant transport mechanism.

The single cylinder and multi-cylinder heat transfer coefficients are more or less identical during the initial stages of melting. After the attainment of the minimum, the coefficients for the multi-cylinder case increase and then reach a flat plateau (a kind of interim steady state) before beginning a slow decline. On the other hand, the single cylinder coefficients tend to increase more slowly subsequent to their minimum, but the increase is sustained and a steady value is ultimately attained (see also Fig. 2 of [1]). As can be seen in the figure, the data for the two heating arrangements cross.

The different behaviors of the single and multiple-cylinder results will be rationalized shortly, following the description of the evolution of the melt layer size and shape. However, of greater importance than these differences are the similarities among the results. From the standpoint of applications, the heat transfer coefficients for the horizontal multi-cylinder array can, as a first approximation, be regarded as being equal to those for the single horizontal cylinder. This finding affords a great simplification, especially since the single cylinder melting coefficients can be estimated from available correlations for natural convection [1].

Before leaving Fig. 1, mention may be made of a data run at a power level of 5.72kW/m^2 which is not shown in the figure. The heat transfer coefficients for that case did not reproduce all the trends in evidence in Fig. 1. In particular, at later times (i.e., well beyond that for the minimum point of h), the coefficients for both the multi-cylinder array and the single cylinder leveled off, the former lying about fifteen percent below the latter. Since the initial temperature of the solid (i.e., prior to the onset of heating) was not as close to the melting temperature in this run as in the others, it was repeated. Unfortunately, during the replicate run, a malfunction occurred in the control circuit for the heating panels, resulting in overheating and destruction of the apparatus.

As mentioned earlier, an array of thermocouples was deployed throughout the phase-change medium to detect the size and shape of the evolving melt zone. Owing to numerous expansions and contractions associated with temperature cycling and to loss of strength at higher temperatures, dimensional stability of the support structure was not maintained. This introduced some uncertainty into the locations of the thermocouples in the grid, with the result that only qualitative information could be inferred about the melt zone.

A schematic diagram showing the evolution of the melt zone is presented in Fig. 2, with representative solid-liquid interfaces labelled as A, B, C, D. Case A corresponds to pure conduction, while Case B depicts a situation where the melt layers for the individual cylinders are independent of each other. The shape of the melt zone shortly after the partitioning walls have been breached is pictured by Case C. At larger times, the upper branch of the melt line advances to positions well above the cylinders and becomes nearly horizontal (Case D).

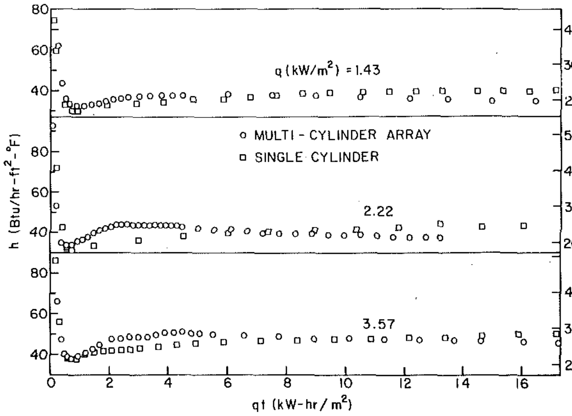

Fig. 1 Timewise distributions of the melting coefficients for single and multiple horizontal heating cylinders

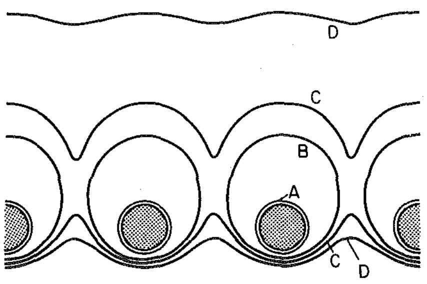

Fig. 2 Schematic description of the timewise evolution of the melt zone

This information can be employed in rationalizing the post-conduction trends evidenced by the multi-cylinder melting coefficients of Fig. 1. The relatively rapid rise subsequent to the minimum h may be ascribed to the more energetic natural convection motions which result from the decrease of the retarding friction forces as the partitioning walls are eaten away. At later times, the increasing separation distance between the cylinders and the upper phase boundary leads to a diminished recirculation [5] and a diminishing of the heat transfer coefficient.

Acknowledgment

This research was carried out under the auspices of the Department of Energy, contract DE-AS0279ER10343.A000.

References

1 Sparrow, E. M., Schmidt, R. R., and Ramsey, J. W., "Experiments on the Role of Natural Convection in the Melting of Solids," ASME JOURNAL OF HEAT TRANSFER, Vol. 100, 1978, pp. 11–16.

2 White, R. D., Bathelt, A. G., Leidenfrost, W., and Viskanta, R., "Study of Heat Transfer and Melting Front from a Cylinder Imbedded in a Phase Change Material," ASME paper No. 77-HT-42, 1977.

3 Ramsey, J. W. and Sparrow, E. M., "Melting and Natural Convection Due to a Vertical Embedded Heater," ASME JOURNAL OF HEAT TRANSFER, Vol. 100, 1978, pp. 368–370.

4 Bathelt, A. G., Viskanta, R., and Leidenfrost, W., "Latent Heat-of-Fusion Energy Storage: Experiments on Heat Transfer from Cylinders During Melting," ASME paper No. 78-HT-47, 1978.

5 Yaghoubi, M. A., and Incropera, F. P., "Natural Convection from a Heated Horizontal Cylinder Submerged in a Shallow Water Layer," Paper NC-15, *Proceedings, Sixth International Heat Transfer Conference,* Vol. 2, 1978, pp. 269–274.

Average Nusselt Numbers for External Flows

A. F. Mills[1]

Nomenclature

g = gravitational acceleration
h = heat transfer coefficient
k = thermal conductivity
L = plate length
Nu = Nusselt number
q = heat flux
Re = Reynolds number
Pr = Prandtl number
x = streamwise coordinate
Γ = mass flow per unit width
ν = kinematic viscosity

Subscripts

x = local
m = average
L = at location L
D = at location D

Local Nusselt numbers on a surface heated at uniform wall temperature (UWT) are lower than the corresponding values for a surface heated at uniform heat flux (UHF). *Appropriately averaged* Nusselt numbers are however less sensitive to wall boundary condition. The purpose of this note is to show that average Nusselt numbers for UWT and UHF are almost identical, a fact useful for engineering calculations, as well as for evaluation of reliability of experimental data.

As an example consider the forced convection laminar boundary layer on a flat plate, for which the local Nusselt numbers obtained analytically can be correlated as [1]

$$\mathrm{Nu}_x = \frac{h_x x}{k} = \frac{q_x x}{\Delta T k} = 0.332 \mathrm{Re}_x{}^{1/2} \mathrm{Pr}^{1/3} \quad \text{(UWT)} \tag{1a}$$

$$\mathrm{Nu}_x = \frac{h_x x}{k} = \frac{q x}{\Delta T_x k} = 0.453 \mathrm{Re}_x{}^{1/2} \mathrm{Pr}^{1/3} \quad \text{(UHF)} \tag{1b}$$

for $\mathrm{Pr} \geq 1$, showing a 36 percent higher value for UHF. The average Nusselt number corresponding to equation (1*a*) for UWT is obtained using

$$h_m = \frac{q_m}{\Delta T}; \; h_m = \frac{1}{L} \int_0^L h_x dx \tag{2a}$$

giving

$$\mathrm{Nu}_m = \frac{h_m L}{k} = 0.664 \mathrm{Re}_L{}^{1/2} \mathrm{Pr}^{1/3} \tag{2b}$$

For a nonisothermal surface an average heat transfer coefficient defined by equation (2*a*) is of little use. For UHF h_m is preferably defined in terms of ΔT_m as

$$h_m = \frac{q}{\Delta T_m}; \; \Delta T_m = \frac{1}{L} \int_0^L \Delta T_x dx \tag{3a}$$

a form which is particularly convenient when resistance thermometry is used to measure the average temperature of the nonisothermal wall. Combining equations (1*b*) and (3*a*) gives

$$\mathrm{Nu}_m = \frac{h_m L}{k} = 0.680 \mathrm{Re}_L{}^{1/2} \mathrm{Pr}^{1/3} \tag{3b}$$

showing that Nu_m for UHF is only 2.4 percent higher than for UWT.

A similar comparison can be made for the natural convection laminar boundary layer on a vertical wall. Using analytical results from [2] at Pr = 10, Nu_m for UHF is 1.5 percent higher than for UWT; in this case the difference between UWT and UHF values is slightly Prandtl number dependent. For the forced convection turbulent boundary layer on a flat plate Kays [1] gives results using the Boussinesq hypothesis and a 1/7 power law for eddy diffusivity and claims excellent agreement with experiment: the local Nusselt numbers of UHF are only 4 percent higher than for UWT, consistent with the concept that a turbulent boundary layer has a poorer memory than a laminar one. When the corresponding average Nusselt numbers are calculated they are equal (to the significant figures given). For the circular cylinder in cross-flow Krall [3] obtained finite difference numerical solutions at low Reynolds numbers. At Re = 100, Nu_m for UHF was 2.7 percent higher than for UWT, while at Re = 200 the discrepancy was 3.4 percent. If laminar film condensation on a vertical wall is analyzed following Nusselt by ignoring the inertia and convective terms in the momentum and energy equations, respectively, it is found that the average Nusselt numbers for UWT and UHF are identical [4], a result which might have been suspected owing to the absence of convection.

The near equality of average Nusselt numbers has obvious engineering utility when data are available for one of the boundary conditions and not the other. Another use is in the evaluation of the reliability of experimental data. For example, precise values of average heat transfer at UHF are required for cylinders in cross-flow in order to evaluate the performance of cylindrical hot film anemometers. Boulos and Pei [5] determined average heat transfer from cylinders in cross-flow for both UWT and UHF: although the same wind tunnel was used, the test cylinders were of differing construction. At Re = 3000, Nu_m for UHF was 27 percent higher than for UWT: given the above described behavior of Nu_m, the validity of the experimental result may be questionable. Krall and Eckert [6] measured average Nusselt numbers for an approximately UHF boundary condition and reported values 7 percent higher than those given by Morgan's correlation [7] which is for essentially UWT. Since this difference is more in line with theory it is suggested that these data are more reliable than that of Boulos and Pei. (However, the values of Nu_m reported in Krall's Ph.D. dissertation [3] should be ignored since the averages were calculated incorrectly therein.)

As a final example consider laminar film condensation on a horizontal cylinder, once again analyzed ignoring inertia and convective terms. With the definitions $\mathrm{Nu}_m = h_m(\nu^2/g)^{1/3}/k$ and $\mathrm{Re}_D = 4\Gamma_D/\mu$, the result for both UWT and UHF can be written as

$$\mathrm{Nu}_m = C \, \mathrm{Re}_D{}^{-1/3} \tag{4}$$

$$C_{\mathrm{UWT}} = \frac{8}{3\pi 3^{1/3}} \int_0^\pi \sin^{1/3} \theta d\theta; \; C_{\mathrm{UHF}} = \frac{\pi(8\pi/3)^{1/3}}{\int_0^\pi (\theta/\sin\theta)^{1/3} d\theta}$$

Using the numerical evaluation of $\int_0{}^\pi \sin^{1/3}\theta$ of Abramowitz [8], $C_{\mathrm{UWT}} = 1.523$, while Fugii, et al. [4] obtained $C_{\mathrm{UHF}} = 1.43$, which is 5.3 percent *lower* than the UWT value. Based on the vertical wall result it might be expected that C be identical for the two boundary conditions, and certainly a *lower* value for C_{UHF} is surprising. The integral $\int_0{}^\pi(\theta/\sin\theta)^{1/3}d\theta$ is improper and needs careful evaluation; however, a re-calculation showed that Fugii's result is essentially correct.

References

1 Kays, W. M., *Convective Heat and Mass Transfer*, McGraw-Hill, New York, 1966.

2 Gebhart, B., *Heat Transfer*, 2nd ed., McGraw-Hill, New York, 1971.

3 Krall, K. M., "Local Heat Transfer around a Transverse Cylinder in Slip Flow," Ph.D. Dissertation, University of Minnesota, 1969.

4 Fujii, T., Uehara, H., and Oda, K., "Filmwise Condensation on a Surface with Uniform Heat Flux and Body Force Convection," *Heat Transfer Res. Japan*, Vol. 1, No. 4, 1972, pp. 76–83.

5 Boulos, M. I., and Pei, D. C. T., "Dynamics of Heat Transfer from Cylinders in a Turbulent Air Stream," *Int. J. Heat Mass Transfer*, Vol. 17, 1974, pp. 767–783.

---

[1] Professor, School of Engineering and Applied Science, University of California, Los Angeles, CA Assoc. Mem. ASME

Contributed by the Heat Transfer Division for publication in the JOURNAL OF HEAT TRANSFER. Manuscript received by the Heat Transfer Division May 17, 1979.

6 Krall, K. M., and Eckert, E. R. G., "Local Heat Transfer around a Cylinder at Low Reynolds Number," ASME JOURNAL OF HEAT TRANSFER, Vol. 95, 1973, pp 273–275.

7 Morgan, V. T., "The Overall Convective Heat Transfer from Smooth Circular Cylinders," *Advances in Heat Transfer*, Vol. 11, ed. T. F. Irvine and J. P. Hartnett, Academic Press, 1975.

8 Abramowitz, M., "Tables of the Functions $\int_0^\phi \sin^{1/3} xdx$ and $\frac{4}{3} \sin^{-4/3} \phi \times \int_0^\phi \sin^{1/3} xdx$," *Journal of Research*, National Bureau of Standards, Vol. 47, 1951, pp. 288–290.

A Simple Differential Approximation for Radiative Transfer in Non-Gray Gases

M. F. Modest[1]

Nomenclature

$e_b, e_{b\lambda}$ = black-body emissive power, (per unit wavelength)

E_B = band integrated emissive power, $= 4 \sum_{i=1}^{N} e_{bi}$

$I_{0\lambda}$ = direction-integrated intensity

I_B = band-integrated intensity, $= \sum_{i=1}^{N} I_{0i}$

$\vec{n}$ = outward surface normal

$S(\vec{r})$ = source function

$\vec{q}$ = radiative heat flux

$\vec{q}_B$ = band integrated radiative flux, $= \sum_{i=1}^{N} \vec{q}_i$

T = temperature

$\kappa_\lambda, \bar{\kappa}$ = monochromatic and average absorption coefficient

ϵ = wall emissivity

λ = wavelength

$\Delta\lambda_i$ = band width of band "i"

τ = optical length, $= \int_0^x \bar{\kappa} dx$

Subscripts

B = integrated over all bands

Tr = transparent gas

$w, 1, 2$ = wall, wall 1, wall 2

λ = per unit wavelength

i = integrated over wavelengths of band "i" $= \int_{\Delta\lambda_i} (\quad) d\lambda$

Introduction

When calculations are performed to determine radiative heat transfer rates through participating media, it is commonly assumed that the media are gray absorbers and emitters. If the medium is an undissociated gas this assumption is very poor due to the vibration-rotation bands of the gas, resulting in large errors, in particular for optically thick situations, e.g., [1]. However, if the band structure is taken into account the mathematical complexity of the problem becomes formidable, e.g., [2]. Indeed, if multi-dimensional effects must be accounted for, the mathematical complexity may become prohibitive. The well-established differential approximation [3] provides an extremely simple tool to calculate even multi-dimensional effects if the medium is gray, or if the temperature distribution is known a priori. For the general non-gray case one may substitute Planck-mean and Rosseland-mean absorption coefficients into the respective parts of the differential approximation, as was done by Traugott [4], but this still neglects the important contribution from the optical windows present in a gas. The Rosseland approximation yields accurate results only if the system has an optically thick medium over all wavelengths, as shown by Simmons and Ferziger [5]. In the one-dimensional plane layer the optical windows may be accounted for in a simple fashion, as was done by Greif [1, 6], using the exponential kernel approximation. It is the purpose of this note to show that Greif's simple box-model approach can be incorporated into the differential approximation, yielding a multi-dimensional tool essentially as simple as the gray differential approximation.

Analysis

On a monochromatic basis, the differential approximation for a non-gray absorbing-emitting medium may be written as [3]:

$$\nabla \cdot \vec{q}_\lambda = \kappa_\lambda (4e_{b\lambda} - I_{0\lambda}), \tag{1}$$

$$\nabla I_{0\lambda} = -3\kappa_\lambda \vec{q}_\lambda, \tag{2}$$

with boundary conditions

$$2\vec{q}_w \cdot \vec{n}_w = \frac{\epsilon_w}{2 - \epsilon_w} [4e_{bw\lambda} - I_{0w\lambda}]. \tag{3}$$

Overall conservation of energy demands that

$$\nabla \cdot \vec{q} = \nabla \cdot \int_0^\infty \vec{q}_\lambda d\lambda = S(\vec{r}), \tag{4}$$

where the source function S connects radiation with conduction and convection, if present. The monochromatic absorption coefficient, with contributions from N vibration-rotation bands may be written as

$$\kappa_\lambda(\lambda) = \bar{\kappa} \sum_{i=1}^{N} f_i(\lambda), \tag{5}$$

where $\bar{\kappa}$ is some average absorption coefficient, and the $f_i(\lambda)$ are non-dimensional functions of wavelength and each is non-zero only over one relatively narrow band. We make now the mathematical assumption that

$$\int_0^\infty f_i(\lambda) e_{b\lambda} d\lambda \simeq \int_{\Delta\lambda_i} e_{b\lambda} d\lambda = e_{bi},$$

$$\int_0^\infty f_i(\lambda) \vec{q}_\lambda d\lambda \simeq \int_{\Delta\lambda_i} \vec{q}_\lambda d\lambda = \vec{q}_i,$$

$$\int_0^\infty f_i(\lambda) I_{0\lambda} d\lambda \cong \int_{\Delta\lambda_i} I_{0\lambda} d\lambda = I_{0i}; \; i = 1, N; \tag{6}$$

where $\Delta\lambda_i \equiv \int_0^\infty f_i(\lambda) d\lambda$ defines the width of the "i"-th band.

This approximation will be nearly always good for the first integral. Monochromatic flux and integrated intensity, however, depend strongly on monochromatic optical thickness. Their approximate expressions will certainly be accurate if the bands can be approximated by boxes of constant absorption coefficient $\bar{\kappa}$ and varying widths $\Delta\lambda_i$. Thus, integrating equation (1) over all bands and over all windows:

$$\nabla \cdot \vec{q}_B = \nabla \cdot \sum_{i=1}^{N} \vec{q}_i \simeq \bar{\kappa} \sum_{i=1}^{N} (4e_{bi} - I_{0i}) = \bar{\kappa}(E_B - I_B) \tag{7}$$

$$\nabla \cdot (\vec{q} - \vec{q}_B) = 0. \tag{8}$$

It follows then, from equations (4) and (8) that

$$\nabla \cdot \vec{q}_B = S(\vec{r}). \tag{9}$$

Also, integrating equations (2) and (3) over all bands yields

$$\nabla I_B \simeq -3\bar{\kappa} \vec{q}_B, \tag{10}$$

and

$$2\vec{q}_{Bw} \cdot \vec{n}_w = \frac{\epsilon_w}{2 - \epsilon_w} [E_{Bw} - I_{Bw}], \tag{11}$$

---

[1] Associate Professor of Mechanical Engineering, Rensselaer Polytechnic Institute, Troy, N. Y. 12181. Member ASME.

Contributed by the Heat Transfer Division for publication in the JOURNAL OF HEAT TRANSFER. Manuscript received by the Heat Transfer Division May 7, 1979.

6 Krall, K. M., and Eckert, E. R. G., "Local Heat Transfer around a Cylinder at Low Reynolds Number," ASME JOURNAL OF HEAT TRANSFER, Vol. 95, 1973, pp 273–275.

7 Morgan, V. T., "The Overall Convective Heat Transfer from Smooth Circular Cylinders," *Advances in Heat Transfer*, Vol. 11, ed. T. F. Irvine and J. P. Hartnett, Academic Press, 1975.

8 Abramowitz, M., "Tables of the Functions $\int_0^\phi \sin^{1/3} x dx$ and $\frac{4}{3} \sin^{-4/3} \phi \times \int_0^\phi \sin^{1/3} x dx$," *Journal of Research*, National Bureau of Standards, Vol. 47, 1951, pp. 288–290.

A Simple Differential Approximation for Radiative Transfer in Non-Gray Gases

M. F. Modest[1]

Nomenclature

$e_b, e_{b\lambda}$ = black-body emissive power, (per unit wavelength)

E_B = band integrated emissive power, $= 4 \sum_{i=1}^{N} e_{bi}$

$I_{0\lambda}$ = direction-integrated intensity

I_B = band-integrated intensity, $= \sum_{i=1}^{N} I_{0i}$

$\vec{n}$ = outward surface normal

$S(\vec{r})$ = source function

$\vec{q}$ = radiative heat flux

$\vec{q}_B$ = band integrated radiative flux, $= \sum_{i=1}^{N} \vec{q}_i$

T = temperature

$\kappa_\lambda, \bar{\kappa}$ = monochromatic and average absorption coefficient

ϵ = wall emissivity

λ = wavelength

$\Delta\lambda_i$ = band width of band "i"

τ = optical length, $= \int_0^x \bar{\kappa} dx$

Subscripts

B = integrated over all bands

Tr = transparent gas

w, 1, 2 = wall, wall 1, wall 2

λ = per unit wavelength

i = integrated over wavelengths of band "i" $= \int_{\Delta\lambda_i} (\quad) d\lambda$

Introduction

When calculations are performed to determine radiative heat transfer rates through participating media, it is commonly assumed that the media are gray absorbers and emitters. If the medium is an undissociated gas this assumption is very poor due to the vibration-rotation bands of the gas, resulting in large errors, in particular for optically thick situations, e.g., [1]. However, if the band structure is taken into account the mathematical complexity of the problem becomes formidable, e.g., [2]. Indeed, if multi-dimensional effects must be accounted for, the mathematical complexity may become prohibitive. The well-established differential approximation [3] provides an extremely simple tool to calculate even multi-dimensional effects if the medium is gray, or if the temperature distribution is known a priori. For the general non-gray case one may substitute Planck-mean and Rosseland-mean absorption coefficients into the respective parts of the differential approximation, as was done by Traugott [4], but this still neglects the important contribution from the optical windows present in a gas. The Rosseland approximation yields accurate results only if the system has an optically thick medium over all wavelengths, as shown by Simmons and Ferziger [5]. In the one-dimensional plane layer the optical windows may be accounted for in a simple fashion, as was done by Greif [1, 6], using the exponential kernel approximation. It is the purpose of this note to show that Greif's simple box-model approach can be incorporated into the differential approximation, yielding a multi-dimensional tool essentially as simple as the gray differential approximation.

Analysis

On a monochromatic basis, the differential approximation for a non-gray absorbing-emitting medium may be written as [3]:

$$\nabla \cdot \vec{q}_\lambda = \kappa_\lambda (4e_{b\lambda} - I_{0\lambda}), \tag{1}$$

$$\nabla I_{0\lambda} = -3\kappa_\lambda \vec{q}_\lambda, \tag{2}$$

with boundary conditions

$$2\vec{q}_w \cdot \vec{n}_w = \frac{\epsilon_w}{2 - \epsilon_w} [4e_{bw\lambda} - I_{0w\lambda}]. \tag{3}$$

Overall conservation of energy demands that

$$\nabla \cdot \vec{q} = \nabla \cdot \int_0^\infty \vec{q}_\lambda d\lambda = S(\vec{r}), \tag{4}$$

where the source function S connects radiation with conduction and convection, if present. The monochromatic absorption coefficient, with contributions from N vibration-rotation bands may be written as

$$\kappa_\lambda(\lambda) = \bar{\kappa} \sum_{i=1}^{N} f_i(\lambda), \tag{5}$$

where $\bar{\kappa}$ is some average absorption coefficient, and the $f_i(\lambda)$ are non-dimensional functions of wavelength and each is non-zero only over one relatively narrow band. We make now the mathematical assumption that

$$\int_0^\infty f_i(\lambda) e_{b\lambda} d\lambda \simeq \int_{\Delta\lambda_i} e_{b\lambda} d\lambda = e_{bi},$$

$$\int_0^\infty f_i(\lambda) \vec{q}_\lambda d\lambda \simeq \int_{\Delta\lambda_i} \vec{q}_\lambda d\lambda = \vec{q}_i,$$

$$\int_0^\infty f_i(\lambda) I_{0\lambda} d\lambda \cong \int_{\Delta\lambda_i} I_{0\lambda} d\lambda = I_{0i}; \; i = 1, N; \tag{6}$$

where $\Delta\lambda_i \equiv \int_0^\infty f_i(\lambda) d\lambda$ defines the width of the "i"-th band.

This approximation will be nearly always good for the first integral. Monochromatic flux and integrated intensity, however, depend strongly on monochromatic optical thickness. Their approximate expressions will certainly be accurate if the bands can be approximated by boxes of constant absorption coefficient $\bar{\kappa}$ and varying widths $\Delta\lambda_i$. Thus, integrating equation (1) over all bands and over all windows:

$$\nabla \cdot \vec{q}_B = \nabla \cdot \sum_{i=1}^{N} \vec{q}_i \simeq \bar{\kappa} \sum_{i=1}^{N} (4e_{bi} - I_{0i}) = \bar{\kappa}(E_B - I_B) \tag{7}$$

$$\nabla \cdot (\vec{q} - \vec{q}_B) = 0. \tag{8}$$

It follows then, from equations (4) and (8) that

$$\nabla \cdot \vec{q}_B = S(\vec{r}). \tag{9}$$

Also, integrating equations (2) and (3) over all bands yields

$$\nabla I_B \simeq -3\bar{\kappa} \vec{q}_B, \tag{10}$$

and

$$2\vec{q}_{Bw} \cdot \vec{n}_w = \frac{\epsilon_w}{2 - \epsilon_w} [E_{Bw} - I_{Bw}], \tag{11}$$

---

[1] Associate Professor of Mechanical Engineering, Rensselaer Polytechnic Institute, Troy, N. Y. 12181. Member ASME.

Contributed by the Heat Transfer Division for publication in the JOURNAL OF HEAT TRANSFER. Manuscript received by the Heat Transfer Division May 7, 1979.

where it was assumed that the walls are gray. Equations (7, 9–11) constitute the same set encountered when using the differential approximation for gray media, and are readily solved even for two and three-dimensional cases. After E_B has been calculated, the temperature distribution is immediately deduced as $E_B(T) = 4\sum_{i=1}^{N} e_{bi}(T)$.

In order to determine the overall radiative heat transfer rates, the fluxes through the optical windows must be determined independently by standard methods; i.e.,

$$\vec{q} = \vec{q}_{Tr} + \vec{q}_B - \sum_{i=1}^{N} q_{Tr,i} \qquad (12)$$

where $\vec{q}_{Tr}$ is the heat flux encountered in a transparent medium.

Illustrative Example

To compare with the simple exponential kernel approximation used by Greif [6] as reported by Sparrow and Cess [1], consider the case of radiative equilibrium ($S = 0$) between one-dimensional black and isothermal parallel plates. Thus

$$\frac{dq_B}{d\tau} = E_B - I_B = 0, \frac{dI_B}{d\tau} = -3q_B, \tau = \int_0^x \bar{\kappa} dx,$$

with

$$\tau = 0: 2q_B = E_{B1} - I_{B1}, \tau = \tau_L: 2q_B = I_{B2} - E_{B2};$$

it follows that

$$\frac{E_B - E_{B2}}{E_{B1} - E_{B2}} = \frac{1}{2} \frac{1 + \frac{3}{2}(\tau_L - \tau)}{1 + \frac{3\tau_L}{4}},$$

and

$$q_B = \frac{1}{4} \frac{E_{B1} - E_{B2}}{1 + \frac{3\tau_L}{4}}.$$

For the transparent case $q_{Tr\lambda} = e_{b\lambda}(T_1) - e_{b\lambda}(T_2)$ so that

$$\frac{q}{\sigma(T_1{}^4 - T_2{}^4)} = 1 - \frac{1}{1 + \frac{4}{3\tau_L}} \frac{\sum_{i=1}^{N} [e_{bi}(T_1) - e_{bi}(T_2)]}{e_{b1} - e_{b2}}. \qquad (13)$$

As is the case for the gray medium, this result from the differential approximation is identical to the one obtained from the exponential kernel approximation [1]. The gray and non-gray case of the illustrative example are compared in [1] for CO_2 at radiative equilibrium and at 1 atm between black plates at 800°R and 1200°R, respectively (using the exponential kernel approach). For optically thick cases ($\tau_L \to \infty$) the nondimensional heat flux in equation (13) tends towards 0.616, while the gray differential approximation tends, of course, towards zero. This is due to the fact that for CO_2 under these conditions the transparent regions between the three major bands constitute the major portion of the wavelength spectrum.

Conclusion

It has been shown that the band absorption of radiating gases can be incorporated into the three-dimensional differential approximation without increasing its complexity. Obviously, utilization of the simple box model for band radiation is somewhat crude. However, the model reduces to the correct optically thin limit as well as the correct opaque-band limit, and can be expected to be reasonably accurate in between.

References

1 Sparrow, E. M. and Cess, R. D., *Radiation Heat Transfer*, Ch. 8, Revised Edition, Brooks/Cole Publication, 1970.

2 Wassel, A. T. and Edwards, D. K., "Molecular Gas Band Radiation in Cylinders," ASME JOURNAL OF HEAT TRANSFER, Vol. 94, 1974, pp. 21–26.

3 Modest, M. F., "Photon-Gas Formulation of the Differential Approximation in Radiative Transfer," *Letters in Heat and Mass Transfer*, Vol. 3, 1976, pp. 111–116.

4 Traugott, S. C., "Radiative Heat-Flux Potential for a Non-Gray Gas," *AIAA Journal*, Vol. 4, No. 3, 1966, pp. 541–542.

5 Simmons, G. M. and Ferziger, J. H., "Non-Gray Radiative Heat Transfer Between Parallel Plates," *International Journal of Heat Mass Transfer*, Vol. 11, 1968, pp. 1611–1620.

6 Greif, R., "Energy Transfer by Radiation and Conduction with Variable Gas Properties," *International Journal of Heat Mass Transfer*, Vol. 7, 1964, pp. 891–900.

A Simple Method for Calculating Radiative Heat Transfer in Rod Bundles with Droplets and Vapor as Absorbing Media

Shi-chune Yao,[1] L. E. Hochreiter,[2] and C. E. Dodge[2]

Introduction

Post dry-out heat transfer in dispersed two-phase flow is a continuing area of interest for thermal design of steam generators, advanced propulsion systems, and particularly light water nuclear reactor safety studies. When the heat generating surface reaches high temperatures, the radiation heat transfer component of the total wall heat flux can become significant [1].

For a rod bundle which does not contain absorbing media the radiative heat transfer can be calculated with moderate efforts [2, 3]. With the presence of droplet and vapor, the radiative heat transfer has been analyzed in [1] and [4]. However, only single tube or parallel plates are considered in these radiation analyses. Even for such a simple geometry, the exact calculations can be very complicated.

Proposed Method

The proposed method relies on combining similar surfaces for the radiative heat transfer calculations and identifying droplets and vapor as groups of absorbing media. The number of equations involved can be greatly reduced if rods with similar properties and operating temperatures are grouped as a single radiative surface, although they are physically separated. Similarly, the droplets and the vapor in the bundle can be grouped respectively.

Various degrees of sophistication can be included in the grouping strategy. The simplest case is to assign all the surfaces, all the droplets, and all the vapor each into one group. This is a lumped model with the bundle considered as a single channel. On the other hand, complex grouping may assign each rod, droplets in each subchannel, and vapor in each subchannel as a individual group, respectively. An optimal grouping will be found inbetween these extremes. Generally, when strong mixing occurs in the bundle, the properties and temperature of the absorbing media will be rather uniform over the bundles. The approach of lumping the media will be reasonable.

In a large bundle, a rod is able to see a number of its surrounding rods. The larger the pitch to diameter ratio, *P/D*, the more neighbors a given rod can communicate with directly. If all the rods are of the same size, a bundle will possess geometric symmetry. In both Figs. 1(*a*) and (*b*), the bundles are symmetric with respect to rod 1. The geometric view factor among rods can be evaluated effectively using the crossed-string method [5]. The typical view factors for square and equilateral triangular bundles are reported in [3].

---

[1] Assistant Professor, Department of Mechanical Engineering, Carnegie-Mellon University, Pittsburgh, PA 15213.

[2] PWR Systems Division, Westinghouse Electric Corporation, Pittsburgh, PA 15230.

Contributed by the Heat Transfer Division of publication in the JOURNAL OF HEAT TRANSFER. Manuscript received by the Heat Transfer Division November 29, 1978.

where it was assumed that the walls are gray. Equations (7, 9–11) constitute the same set encountered when using the differential approximation for gray media, and are readily solved even for two and three-dimensional cases. After E_B has been calculated, the temperature distribution is immediately deduced as $E_B(T) = 4\Sigma_{i=1}^{N} e_{bi}(T)$.

In order to determine the overall radiative heat transfer rates, the fluxes through the optical windows must be determined independently by standard methods; i.e.,

$$\vec{q} = \vec{q}_{Tr} + \vec{q}_B - \sum_{i=1}^{N} q_{Tr,i} \tag{12}$$

where $\vec{q}_{Tr}$ is the heat flux encountered in a transparent medium.

Illustrative Example

To compare with the simple exponential kernel approximation used by Greif [6] as reported by Sparrow and Cess [1], consider the case of radiative equilibrium ($S = 0$) between one-dimensional black and isothermal parallel plates. Thus

$$\frac{dq_B}{d\tau} = E_B - I_B = 0, \frac{dI_B}{d\tau} = -3q_B, \tau = \int_0^x \bar{\kappa} dx,$$

with

$$\tau = 0\text{: } 2q_B = E_{B1} - I_{B1}, \tau = \tau_L\text{: } 2q_B = I_{B2} - E_{B2};$$

it follows that

$$\frac{E_B - E_{B2}}{E_{B1} - E_{B2}} = \frac{1}{2} \frac{1 + \frac{3}{2}(\tau_L - \tau)}{1 + \frac{3\tau_L}{4}},$$

and

$$q_B = \frac{1}{4} \frac{E_{B1} - E_{B2}}{1 + \frac{3\tau_L}{4}}.$$

For the transparent case $q_{Tr\lambda} = e_{b\lambda}(T_1) - e_{b\lambda}(T_2)$ so that

$$\frac{q}{\sigma(T_1{}^4 - T_2{}^4)} = 1 - \frac{1}{1 + \frac{4}{3\tau_L}} \frac{\sum_{i=1}^{N} [e_{bi}(T_1) - e_{bi}(T_2)]}{e_{b1} - e_{b2}}. \tag{13}$$

As is the case for the gray medium, this result from the differential approximation is identical to the one obtained from the exponential kernel approximation [1]. The gray and non-gray case of the illustrative example are compared in [1] for CO_2 at radiative equilibrium and at 1 atm between black plates at 800°R and 1200°R, respectively (using the exponential kernel approach). For optically thick cases ($\tau_L \to \infty$) the nondimensional heat flux in equation (13) tends towards 0.616, while the gray differential approximation tends, of course, towards zero. This is due to the fact that for CO_2 under these conditions the transparent regions between the three major bands constitute the major portion of the wavelength spectrum.

Conclusion

It has been shown that the band absorption of radiating gases can be incorporated into the three-dimensional differential approximation without increasing its complexity. Obviously, utilization of the simple box model for band radiation is somewhat crude. However, the model reduces to the correct optically thin limit as well as the correct opaque-band limit, and can be expected to be reasonably accurate in between.

References

1 Sparrow, E. M. and Cess, R. D., *Radiation Heat Transfer,* Ch. 8, Revised Edition, Brooks/Cole Publication, 1970.

2 Wassel, A. T. and Edwards, D. K., "Molecular Gas Band Radiation in Cylinders," ASME JOURNAL OF HEAT TRANSFER, Vol. 94, 1974, pp. 21–26.

3 Modest, M. F., "Photon-Gas Formulation of the Differential Approximation in Radiative Transfer," *Letters in Heat and Mass Transfer,* Vol. 3, 1976, pp. 111–116.

4 Traugott, S. C., "Radiative Heat-Flux Potential for a Non-Gray Gas," *AIAA Journal,* Vol. 4, No. 3, 1966, pp. 541–542.

5 Simmons, G. M. and Ferziger, J. H., "Non-Gray Radiative Heat Transfer Between Parallel Plates," *International Journal of Heat Mass Transfer,* Vol. 11, 1968, pp. 1611–1620.

6 Greif, R., "Energy Transfer by Radiation and Conduction with Variable Gas Properties," *International Journal of Heat Mass Transfer,* Vol. 7, 1964, pp. 891–900.

A Simple Method for Calculating Radiative Heat Transfer in Rod Bundles with Droplets and Vapor as Absorbing Media

Shi-chune Yao,[1] L. E. Hochreiter,[2] and C. E. Dodge[2]

Introduction

Post dry-out heat transfer in dispersed two-phase flow is a continuing area of interest for thermal design of steam generators, advanced propulsion systems, and particularly light water nuclear reactor safety studies. When the heat generating surface reaches high temperatures, the radiation heat transfer component of the total wall heat flux can become significant [1].

For a rod bundle which does not contain absorbing media the radiative heat transfer can be calculated with moderate efforts [2, 3]. With the presence of droplet and vapor, the radiative heat transfer has been analyzed in [1] and [4]. However, only single tube or parallel plates are considered in these radiation analyses. Even for such a simple geometry, the exact calculations can be very complicated.

Proposed Method

The proposed method relies on combining similar surfaces for the radiative heat transfer calculations and identifying droplets and vapor as groups of absorbing media. The number of equations involved can be greatly reduced if rods with similar properties and operating temperatures are grouped as a single radiative surface, although they are physically separated. Similarly, the droplets and the vapor in the bundle can be grouped respectively.

Various degrees of sophistication can be included in the grouping strategy. The simplest case is to assign all the surfaces, all the droplets, and all the vapor each into one group. This is a lumped model with the bundle considered as a single channel. On the other hand, complex grouping may assign each rod, droplets in each subchannel, and vapor in each subchannel as a individual group, respectively. An optimal grouping will be found inbetween these extremes. Generally, when strong mixing occurs in the bundle, the properties and temperature of the absorbing media will be rather uniform over the bundles. The approach of lumping the media will be reasonable.

In a large bundle, a rod is able to see a number of its surrounding rods. The larger the pitch to diameter ratio, *P/D,* the more neighbors a given rod can communicate with directly. If all the rods are of the same size, a bundle will possess geometric symmetry. In both Figs. 1(*a*) and (*b*), the bundles are symmetric with respect to rod 1. The geometric view factor among rods can be evaluated effectively using the crossed-string method [5]. The typical view factors for square and equilateral triangular bundles are reported in [3].

---

[1] Assistant Professor, Department of Mechanical Engineering, Carnegie-Mellon University, Pittsburgh, PA 15213.

[2] PWR Systems Division, Westinghouse Electric Corporation, Pittsburgh, PA 15230.

Contributed by the Heat Transfer Division of publication in the JOURNAL OF HEAT TRANSFER. Manuscript received by the Heat Transfer Division November 29, 1978.

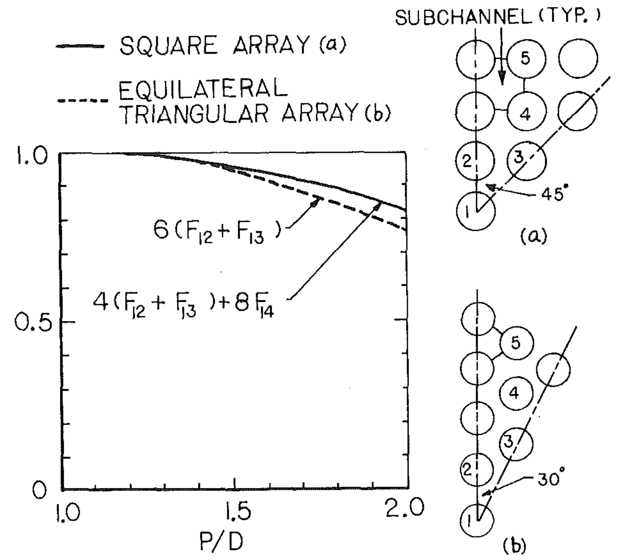

Fig. 1 View factors to selected rods in bundles

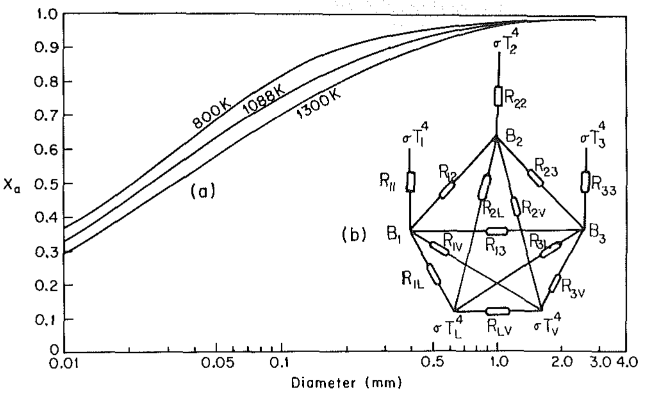

Fig. 2(*a*) Plank mean absorption efficiency of water drops (*b*) A typical electric network for radiative heat transfer of rod bundle

In calculating the radiative heat exchange of a specific rod to the surrounding rods, it is possible to ignore those rods whose view factors are relatively small. For example, as far as rod 1 in Fig. 1 is concerned, only rods 2, 3 and 4 in square bundle and rods 2 and 3 in triangular bundle have to be considered. Fig. 1 shows the total view factors of these counted rods. The counted view factor is 97 percent if P/D equals 1.3, and 90 percent if P/D equals 1.6. Most conventional bundles have P/D less than 1.5 and this simplification is acceptable. Thus, the view factors listed in [3] will be adjusted by normalizing the counted view factors such that their sum is unity. This adjustment implies the thermal radiation effects of the uncounted rods are replaced by the counted rods. The axial radiative heat transfer among the rods in a bundle will be neglected because of the small pitch to diameter ratios.

In the present study, both the droplets and the vapor perform as absorbing media. If their optical thicknesses are much smaller than unity, the absorption of radiation by droplets and vapor can be considered separately, and their radiative properties will be evaluated independently. If the void fraction is high, the absorptivity of droplets can be calculated from the Mie theory which considers radiation interaction with a single droplet. In addition, all the surfaces and media are considered as diffuse and gray.

In a bundle with uniform-sized rods the equivalent mean beam length of a subchannel can be related to the hydraulic diameter of the subchannel by [5]

$$L_m = 0.85\, D_h \tag{1}$$

If the rods in a bundle have slightly different sizes, the hydraulic diameter of the bundle can be used in equation (1) as an approximation. Simplification can be achieved by using the same mean beam length for the absorbing media between any two communicating rods. Since the major portion of the surfaces interacting with a rod is one subchannel away, the mean beam length given by equation (1) can be used as a reasonable estimation while reducing the calculation effort greatly.

Method of Calculation

As the radiative heat flux is of primary concern, the average temperature for group i can be evaluated from the temperature of the constituting rods as

$$T_i = \left[\frac{1}{A_i}\sum_{j=1}^{N_i} A_{ij}T_{ij}{}^4\right]^{1/4} \tag{2}$$

Where A_i is the area of surface group i per unit length of bundle, N_i is the total number of rods in group i, and the subscript ij is for the rod j in surface group i.

The Planck mean absorption coefficient will be used for the optically thin media. If the liquid and vapor are at a temperature considerably lower than that of the rod surfaces, the spectrum of thermal radiation in the bundle will be that corresponding to the surface temperatures. The Planck mean absorption coefficient should also be evaluated at the surface temperature.

The emissivity of the vapor is given as:

$$\epsilon_v = 1 - e^{-a_v L_m} \tag{3}$$

where the a_v is the absorption coefficient of the vapor. If steam is considered as the vapor, the Plank mean absorption coefficient of steam reported in [6] may be used. The reported curve can be fitted by the equation

$$a_v(\text{cm}^{-1}) = 9.84 \times 10^{-5} p\left[18.66\left(\frac{555}{T_w}\right)^2 - \left(\frac{555}{T_w}\right)^4\right] \tag{4}$$

where p is the steam pressure in KP_a, and T_w is the representative wall temperature in K.

The emissivity of a spectrum of droplets at optically thin condition is

$$\epsilon_l = 1 - e^{-\frac{\pi}{4}L_M\int_0^\infty X_a(d)n(d)d^2d(d)} \tag{5}$$

where the $X_a(d)$ is the Plank mean absorption efficiency of the droplets, the n is droplet number density, and the d is the droplet diameter. For the water droplets, the calculated data of [4] are replotted in Fig. 2(a). For water droplets the scattered radiation is predominantly in the forward direction and can be lumped with the transmitted energy. Therefore, the scattering effect can be neglected.

Since the variation of X_a is not too strong if the range of droplet size is not very wide, we can approximate $X_a(d)$ by an averaged value $\overline{X}_a$. It is noticed that the Sauter mean diameter of droplets is defined as

$$d_{32} = \int_0^\infty n(d)d^3dd \Big/ \int_0^\infty n(d)d^2dd \tag{6}$$

Additionally, the void fraction α of the absorbing media is related to droplet size as

$$1 - \alpha = \frac{\pi}{6}\int_0^\infty n(d)d^3dd \tag{7}$$

It is also assumed that the $\overline{X}_a$ can be approximated by the value at Sauter mean diameter.

$$\overline{X}_a = X_a(d_{32}) \tag{8}$$

Substitute (7) into (6), then (6) and (8) into (5), we get

$$\epsilon_l \simeq 1 - e^{-1.5L_mX_a(d_{32})(1-\alpha)/d_{32}} \tag{9}$$

Therefore, the ϵ_l for a spectrum of droplets is related to the property X_a of the droplet at Sauter mean diameter and the void fraction.

The area of each group is the sum of the constituting surface areas. However, the view factors among surface groups have to be derived from the definition of view factor. That is

$$F_{ik} = \int_{A_i} F_{dA_i \rightarrow A_k} dA_i \Big/ A_i \tag{10}$$

where dA_i is a differential area of the area A_i. For a rod bundle, dA_i will be denoted as A_{ij} which is the surface area of the rod j in the surface group i. Substituting the integration by a summation over all the rods in the group i, the view factor between group i and k becomes

$$F_{ik} = \sum_{j=1}^{N_i} F_{A_{ij} \rightarrow A_k} A_{ij} \Big/ A_i \tag{11}$$

Where $F_{A_{ij} \rightarrow A_k}$ is defined as the view factor from the rod j of group i to all the rods which belong to the surface group k. This formulation of the view factor is general even if the rods in each group have different sizes in the bundle. The view factor from any surface to the absorbing media is unity.

With these basic parameters available, the radiative heat transfer can be calculated. For example, a bundle with three surface groups, one droplet group, and one vapor group can be modeled by an equivalent electric network [7]. Assuming gray surfaces with equal emissivity, the network is shown in Fig. 2(*b*) where B is the surface radiosity. The electric resistances R of this network would have the values:

$$R_{ii} = (1 - \epsilon_w)/\epsilon_w A_i,\ R_{ij} = [A_i F_{ij}(1 - \epsilon_l)(1 - \epsilon_v)]^{-1} \tag{12, 13}$$

$$R_{iv} = [A_i(1 - \epsilon_l)\epsilon_v]^{-1},\ R_{il} = [A_i \epsilon_l (1 - \epsilon_v)]^{-1} \tag{14, 15}$$

$$R_{lv} = [A_l \epsilon_l \epsilon_v]^{-1}, \text{ where } i \text{ or } j = 1, 2, 3 \tag{16}$$

The ϵ_w is the surface emissivity and the A_l is the area of the absorbing media per unit length contacting the solid surfaces.

Following the conventional network analysis, equation can be written on each surface radiosity node for conservation of energy flow through the node. A system of three algebraic equations are generated. These equations can be set into matrix form, and solutions of radiosities are obtained by the Gaussian elimination method.

Application of this Method

A sample bundle geometry is shown in Fig. 3 and is taken from the PWR-FLECHT (Full Length Emergency Core Heat Transfer) reflood heat transfer program [8]. The powered inner rods are grouped as surface 1, the outer rods which are relatively cooler due to the cold housing are surface 2, and the nonpowered control rod guide tube thimbles, which locate randomly in the bundle, are surface 3. The vapor and droplets are assumed to be homogeneously distributed throughout the bundle due to the strong mixing of the flow.

Since part of the cold surface boundary lies between rods, the precise description of its surface emissivity is

$$R_{22} = \left[\frac{\epsilon_w A_w}{1 - \epsilon_w} + \frac{\epsilon_w' A_g}{1 - \epsilon_w'}\right]^{-1} \tag{17}$$

where ϵ_w' is the effective emissivity at the gaps, A_w is the total area of the constituting rod surfaces, and the A_g is that of the constituting gaps. Generally, ϵ_w' is higher than ϵ_w due to the radiation cavity effect. However, the ϵ_w of oxidized metal surface is usually high (about 0.8 for oxidized stainless steel). The difference between ϵ_w and ϵ_w' will be relatively small. Equation (12) can be used as a reasonable approximation.

The sample in Fig. 3 is calculated through algebraic manipulation using equations (12–16). The computer time required in a CDC 7600 system is less than 0.1 s. In this problem the geometric parameters are determined as

$A_1 = 97.7$ cm^2/cm $A_2 = 53.8$ cm^2/cm $A_3 = 30.4$ cm^2/cm
$F_{12} = 0.187$ $F_{13} = 0.194$ $F_{23} = 0.213$
$D_h = 1.35$ cm

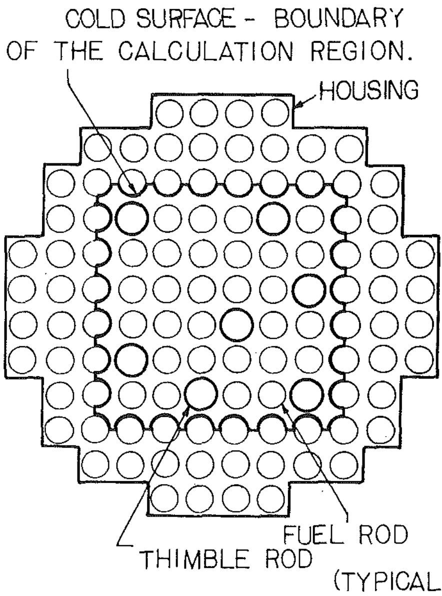

Fig. 3 Geometric configuration of an example bundle (FLECHT 15 × 15)

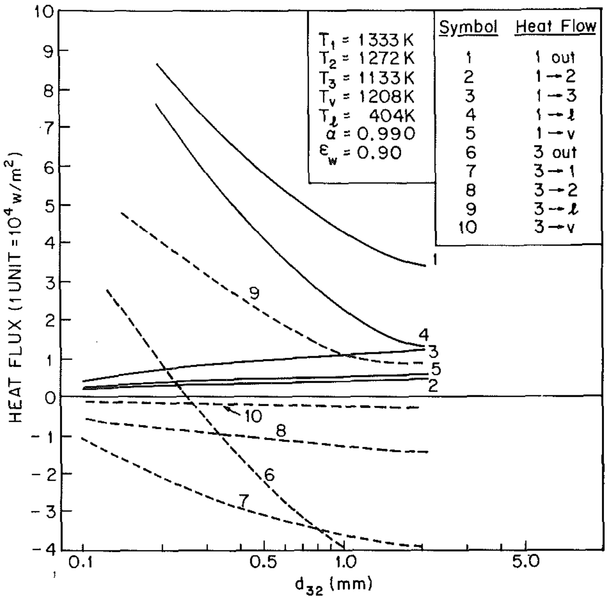

Fig. 4 Heat fluxes among surfaces and media of the sample calculation

Fig. 4 shows the calculated heat fluxes among the surfaces and the absorbing media as a function of the Sauter mean diameter of droplets at a fixed void fraction of the media. The condition is a typical case of slow reflooding. The calculated results cannot be verified with experimental information because each flux component is not measured separately in an experiment. Nevertheless, it is interesting to observe that the cooling of the hot rods is strongly influenced by radiation absorption of droplets when the droplet size is small (see Curve 1). This is the same conclusion reached in [1]. However, the thimble rods will be either cooled or heated in the bundle (see Curve 6) depending upon the size of droplets. At a fixed void fraction, when the droplets are large the thimble rods will be heated by surface radiation from hot rods. When droplets are small the thimble rods are cooled by the droplets which perform as an effective radiation heat sink. As a result, surface to surface radiative transfer can be evaluated effectively using this simple method of calculation.

References

1 Sun, K. H., Gonzalez-Santalo, J., and Tien, C. L., "Calculations of Combined Radiation and Convection Heat Transfer in Rod Bundles Under Emergency Cooling Conditions," ASME JOURNAL OF HEAT TRANSFER, Vol. 88, 1976, pp. 414–420.

2 Naitoh, M., Kawabe, R., and Chino, K., "Analysis of Radiation Heat Transfer in a BWR Fuel Assembly," *Nuclear Engineering and Design,* Vol. 44, 1977, pp. 315–421.

3 Cox, R. L., "Radiative Heat Transfer in Arrays of Parallel Cylinders," ORNL-5329, 1977.

4 Chan, S. H., and Grolmes, M. A., "Hydrodynamically-Controlled Rewetting," *Nuclear Engineering and Design,* Vol. 34, 1975, pp. 307–316.

5 Hottel, H. C., and Sarofim, A. F., *Radiative Transfer,* McGraw-Hill, New York, 1967, p. 31, p. 277.

6 Abu-Romia, M. M., and Tien, C. L., "Appropriate Mean Absorption Coefficients for Infrared Radiation of Gases," ASME JOURNAL OF HEAT TRANSFER, Nov. 1967, pp. 321–327.

7 Oppenheim, A. K., "Radiation Analysis by the Network Method," *Trans. ASME,* May 1956, pp. 725–735.

8 Lilly, G., Yeh, H., Dodge, C., and Wong, S., "PWR FLECHT Skewek Profile Low Flooding Rate Test Series Evaluation Report," WCAP-9183, 1977.

Strongly Implicit Algorithms for Use in Three-Dimensional Natural Convection Studies

D. W. Pepper[1] and R. E. Cooper[1]

Introduction

It is well known that three-dimensional problems are more difficult to solve than two-dimensional problems; the number of unknown transport terms to be solved is greater; the set of boundary constraints is more complicated; and numerical instability as well as time and memory requirements are usually more severe. The three-dimensional strongly implicit procedure (SIP) is a reliable computational scheme that can alleviate some of these restrictions. Three-dimensional algorithms developed here for natural convection in a cubical enclosure are an extension of the two-dimensional algorithms given in [1–6].

Natural convection problems have been successfully analyzed with three-dimensional numerical techniques [7–11]. In most cases, a three-dimensional alternating direction implicit procedure (ADIP) was used for the vorticity and temperature equations, with successive over relaxation (SOR or ADIP) to solve the vector potential equation set. ADIP is a very effective numerical technique. However, ADIP requires a splitting of the time step along with several sweeps of the solution domain to obtain the three-dimensional values of one field variable. Although only a tridiagonal matrix is solved per sweep, the solution time and programming effort increases dramatically as the number of equations increases. SIP solves for an unknown variable without splitting the time step; i.e., the three-dimensional implicit form of the discretized equation is solved only once. In some instances, SIP has been found to require fewer time steps than ADIP and has occasionally given a stable solution where ADIP failed to converge [1]. However, these comparisons have only been made with forward-in-time, centered-in-space (FTCS) differencing; in tests with higher order methods (such as finite element recursion relations or compact schemes), time splitting can be more advantageous than SIP [12].

A set of three-dimensional algorithms, developed from those established in [13] simulates three-dimensional, laminar, natural convection in an enclosed fluid with constant properties. Differential side heating is used with one vertical wall heated and the opposite wall cooled. The top, bottom, and remaining side vertical walls are insulated.

Governing Equations

The equations of motion for laminar natural convection in an enclosure are written in nondimensional form [8, 11] as

$$\frac{\mathrm{Pr}}{\alpha_\omega}\frac{\partial\vec{\omega}}{\partial\tau} = -\nabla x(\vec{\omega} x \vec{U}) - \mathrm{PrRa}(\nabla x \theta \vec{g}) + \mathrm{Pr}\nabla^2\vec{\omega} \tag{1}$$

$$\frac{1}{\alpha_\psi}\frac{\partial\vec{\psi}}{\partial\tau} = \nabla^2\vec{\psi} + \vec{\omega} \tag{2}$$

$$\frac{\partial\theta}{\partial\tau} = -\nabla\cdot(\vec{U}\theta) + \nabla^2\theta \tag{3}$$

where $\vec{\omega}$ is the vorticity vector, $\vec{\psi}$ is the vector potential, θ is the temperature, $\vec{U}$ is the velocity vector, $\vec{g}$ is the gravitational vector, and the terms $\mathrm{Pr}/\alpha_\omega$ and $1/\alpha_\psi\, \partial\psi/\partial\tau$ are fictitious transient terms with $\alpha_\omega = 0.50$ and $\alpha_\psi = 1.0$. Although the true transient solutions are lost, the solutions behave similarly to the transient nature of the flow [11]; the steady-state solution is eventually obtained. This procedure was found to give faster convergence to the steady-state conditions than with an SOR solution to the elliptical form of equation (2).

Equation (2) is usually written as $\vec{\omega} = -\nabla^2\vec{\psi} + \nabla(\nabla\cdot\vec{\psi})$. Assuming incompressibility, the vector potential in the exact solution is solendoidal and $\nabla(\nabla\cdot\vec{\psi})$ vanishes. However, since the numerical solution is inexact, $\nabla\cdot\vec{U}$ will have some nonzero value [8]. In an effort to determine how well divergence was satisfied within the computational domain, $\nabla\cdot\vec{U}$ was calculated throughout the enclosure. Maximum values did not exceed 10^{-4} for $10^3 \leqslant \mathrm{Ra} \leqslant 10^5$.

Vorticity boundary conditions are approximated by assuming vorticity to vary linearly with wall distance [14]. Temperature flux at an adiabatic wall is assumed to be zero. The boundary condition approximations follow those given in [11].

Numerical Method

The equations of motion are discretized with FTCS approximations for the derivative terms. This discretization creates a sparse matrix banded by seven diagonal elements. SIP alters this matrix into a series of upper and lower matrices, which can be solved efficiently by Gaussian elimination techniques. The discretized form of equation (1) is written as

$$D\phi_{i-1}^{n+1} + F\phi_{i+1}^{n+1} + B\phi_{j-1}^{n+1} + H\phi_{j+1}^{n+1} + Z\phi_{k-1}^{n+1} + S\phi_{k+1}^{n+1} + E\phi^{n+1} = q^n \tag{4}$$

where ϕ_{i-1} is actually $\phi_{i-1,j,k}$ (node locations at i, j, or k being implied), $n+1$ denotes unknown values at the new time step, and $\phi \equiv \vec{\omega}_m$, $\vec{\psi}_m$ or θ_m with $1 \leq m \leq 3$, subscripts 1, 2, and 3 denoting values in the x, y, and z planes, respectively. Equation (4) can be written in matrix form as

$$[M]\{\phi\} = \{q\} \tag{5}$$

where $[M]$ is the sparse coefficient matrix containing seven diagonals, $\{\phi\}$ is the column matrix of unknown values of vorticity, vector potentials, or temperature, and $\{q\}$ is the column matrix of explicitly known values evaluated at the nth time step. The coefficients of $[M]$ and $\{q\}$ are given in Tables 1 and 2.

In order to efficiently solve matrix $[M]$, equation (4) is altered by adding additional terms similar to the procedure used in two-dimensional SIP [6]. This alteration allows matrix $[M]$ to be factored into lower and upper matrices, $[L]$ and $[U]$, which require less calculation time when solved by elimination techniques. Equation (4) is rewritten as equation (4) $+ C[\phi_{i+1\cdot j-1} - \alpha_1(\phi + \phi_{i+1} + \phi_{j-1})]$

$$\begin{aligned} &+ G[\phi_{i-1,j+1} - \alpha_1(-\phi + \phi_{i-1} + \phi_{j+1})] \\ &+ A[\phi_{i+1,k-1} - \alpha_2(-\phi + \phi_{i+1} + \phi_{k-1})] \\ &+ W[\phi_{i-1,k+1} - \alpha_2(-\phi + \phi_{i-1} + \phi_{k+1})] \\ &+ T[\phi_{j+1,k-1} - \alpha_3(-\phi + \phi_{j+1} + \phi_{k-1})] \\ &\quad + P[\phi_{j-1,k+1} - \alpha_3(-\phi + \phi_{j-1} + \phi_{k+1})] = R \end{aligned} \tag{6}$$

---

[1] Savannah River Laboratory, E. I. du Pont de Nemours and Company, Aiken, S. C. 29801.

Contributed by the Heat Transfer Division for publication in the JOURNAL OF HEAT TRANSFER. Manuscript received by the Heat Transfer Division January 2, 1979.

References

1 Sun, K. H., Gonzalez-Santalo, J., and Tien, C. L., "Calculations of Combined Radiation and Convection Heat Transfer in Rod Bundles Under Emergency Cooling Conditions," ASME JOURNAL OF HEAT TRANSFER, Vol. 88, 1976, pp. 414–420.

2 Naitoh, M., Kawabe, R., and Chino, K., "Analysis of Radiation Heat Transfer in a BWR Fuel Assembly," *Nuclear Engineering and Design,* Vol. 44, 1977, pp. 315–421.

3 Cox, R. L., "Radiative Heat Transfer in Arrays of Parallel Cylinders," ORNL-5329, 1977.

4 Chan, S. H., and Grolmes, M. A., "Hydrodynamically-Controlled Rewetting," *Nuclear Engineering and Design,* Vol. 34, 1975, pp. 307–316.

5 Hottel, H. C., and Sarofim, A. F., *Radiative Transfer,* McGraw-Hill, New York, 1967, p. 31, p. 277.

6 Abu-Romia, M. M., and Tien, C. L., "Appropriate Mean Absorption Coefficients for Infrared Radiation of Gases," ASME JOURNAL OF HEAT TRANSFER, Nov. 1967, pp. 321–327.

7 Oppenheim, A. K., "Radiation Analysis by the Network Method," *Trans. ASME,* May 1956, pp. 725–735.

8 Lilly, G., Yeh, H., Dodge, C., and Wong, S., "PWR FLECHT Skewek Profile Low Flooding Rate Test Series Evaluation Report," WCAP-9183, 1977.

Strongly Implicit Algorithms for Use in Three-Dimensional Natural Convection Studies

D. W. Pepper[1] **and R. E. Cooper**[1]

Introduction

It is well known that three-dimensional problems are more difficult to solve than two-dimensional problems; the number of unknown transport terms to be solved is greater; the set of boundary constraints is more complicated; and numerical instability as well as time and memory requirements are usually more severe. The three-dimensional strongly implicit procedure (SIP) is a reliable computational scheme that can alleviate some of these restrictions. Three-dimensional algorithms developed here for natural convection in a cubical enclosure are an extension of the two-dimensional algorithms given in [1–6].

Natural convection problems have been successfully analyzed with three-dimensional numerical techniques [7–11]. In most cases, a three-dimensional alternating direction implicit procedure (ADIP) was used for the vorticity and temperature equations, with successive over relaxation (SOR or ADIP) to solve the vector potential equation set. ADIP is a very effective numerical technique. However, ADIP requires a splitting of the time step along with several sweeps of the solution domain to obtain the three-dimensional values of one field variable. Although only a tridiagonal matrix is solved per sweep, the solution time and programming effort increases dramatically as the number of equations increases. SIP solves for an unknown variable without splitting the time step; i.e., the three-dimensional implicit form of the discretized equation is solved only once. In some instances, SIP has been found to require fewer time steps than ADIP and has occasionally given a stable solution where ADIP failed to converge [1]. However, these comparisons have only been made with forward-in-time, centered-in-space (FTCS) differencing; in tests with higher order methods (such as finite element recursion relations or compact schemes), time splitting can be more advantageous than SIP [12].

A set of three-dimensional algorithms, developed from those established in [13] simulates three-dimensional, laminar, natural convection in an enclosed fluid with constant properties. Differential side heating is used with one vertical wall heated and the opposite wall cooled. The top, bottom, and remaining side vertical walls are insulated.

Governing Equations

The equations of motion for laminar natural convection in an enclosure are written in nondimensional form [8, 11] as

$$\frac{\mathrm{Pr}}{\alpha_\omega}\frac{\partial\vec{\omega}}{\partial\tau} = -\nabla x(\vec{\omega} x \vec{U}) - \mathrm{PrRa}(\nabla x \theta\vec{g}) + \mathrm{Pr}\nabla^2\vec{\omega} \qquad (1)$$

$$\frac{1}{\alpha_\psi}\frac{\partial\vec{\psi}}{\partial\tau} = \nabla^2\vec{\psi} + \vec{\omega} \qquad (2)$$

$$\frac{\partial\theta}{\partial\tau} = -\nabla\cdot(\vec{U}\theta) + \nabla^2\theta \qquad (3)$$

where $\vec{\omega}$ is the vorticity vector, $\vec{\psi}$ is the vector potential, θ is the temperature, $\vec{U}$ is the velocity vector, $\vec{g}$ is the gravitational vector, and the terms $\mathrm{Pr}/\alpha_\omega$ and $1/\alpha_\psi\ \partial\psi/\partial\tau$ are fictitious transient terms with $\alpha_\omega = 0.50$ and $\alpha_\psi = 1.0$. Although the true transient solutions are lost, the solutions behave similarly to the transient nature of the flow [11]; the steady-state solution is eventually obtained. This procedure was found to give faster convergence to the steady-state conditions than with an SOR solution to the elliptical form of equation (2).

Equation (2) is usually written as $\vec{\omega} = -\nabla^2\vec{\psi} + \nabla(\nabla\cdot\vec{\psi})$. Assuming incompressibility, the vector potential in the exact solution is solendoidal and $\nabla(\nabla\cdot\vec{\psi})$ vanishes. However, since the numerical solution is inexact, $\nabla\cdot\vec{U}$ will have some nonzero value [8]. In an effort to determine how well divergence was satisfied within the computational domain, $\nabla\cdot\vec{U}$ was calculated throughout the enclosure. Maximum values did not exceed 10^{-4} for $10^3 \leqslant \mathrm{Ra} \leqslant 10^5$.

Vorticity boundary conditions are approximated by assuming vorticity to vary linearly with wall distance [14]. Temperature flux at an adiabatic wall is assumed to be zero. The boundary condition approximations follow those given in [11].

Numerical Method

The equations of motion are discretized with FTCS approximations for the derivative terms. This discretization creates a sparse matrix banded by seven diagonal elements. SIP alters this matrix into a series of upper and lower matrices, which can be solved efficiently by Gaussian elimination techniques. The discretized form of equation (1) is written as

$$D\phi_{i-1}^{n+1} + F\phi_{i+1}^{n+1} + B\phi_{j-1}^{n+1} + H\phi_{j+1}^{n+1} + Z\phi_{k-1}^{n+1} + S\phi_{k+1}^{n+1} + E\phi^{n+1} = q^n \qquad (4)$$

where ϕ_{i-1} is actually $\phi_{i-1,j,k}$ (node locations at i, j, or k being implied), $n + 1$ denotes unknown values at the new time step, and $\phi \equiv \vec{\omega}_m$, $\vec{\psi}_m$ or θ_m with $1 \le m \le 3$, subscripts 1, 2, and 3 denoting values in the x, y, and z planes, respectively. Equation (4) can be written in matrix form as

$$[M]\{\phi\} = \{q\} \qquad (5)$$

where $[M]$ is the sparse coefficient matrix containing seven diagonals, $\{\phi\}$ is the column matrix of unknown values of vorticity, vector potentials, or temperature, and $\{q\}$ is the column matrix of explicitly known values evaluated at the nth time step. The coefficients of $[M]$ and $\{q\}$ are given in Tables 1 and 2.

In order to efficiently solve matrix $[M]$, equation (4) is altered by adding additional terms similar to the procedure used in two-dimensional SIP [6]. This alteration allows matrix $[M]$ to be factored into lower and upper matrices, $[L]$ and $[U]$, which require less calculation time when solved by elimination techniques. Equation (4) is rewritten as equation (4) $+ C[\phi_{i+1 \cdot j-1} - \alpha_1(\phi + \phi_{i+1} + \phi_{j-1})]$

$$\begin{aligned} &+ G[\phi_{i-1,j+1} - \alpha_1(-\phi + \phi_{i-1} + \phi_{j+1})] \\ &+ A[\phi_{i+1,k-1} - \alpha_2(-\phi + \phi_{i+1} + \phi_{k-1})] \\ &+ W[\phi_{i-1,k+1} - \alpha_2(-\phi + \phi_{i-1} + \phi_{k+1})] \\ &+ T[\phi_{j+1,k-1} - \alpha_3(-\phi + \phi_{j+1} + \phi_{k-1})] \\ &+ P[\phi_{j-1,k+1} - \alpha_3(-\phi + \phi_{j-1} + \phi_{k+1})] = R \qquad (6) \end{aligned}$$

---

[1] Savannah River Laboratory, E. I. du Pont de Nemours and Company, Aiken, S. C. 29801.

Contributed by the Heat Transfer Division for publication in the JOURNAL OF HEAT TRANSFER. Manuscript received by the Heat Transfer Division January 2, 1979.

Table 1 Coefficients of [*M*]

	ω_1	ω_2	ω_3	Ψ_1, Ψ_2, Ψ_3	T
D	$-\Pr/\Delta X^2$	$-\frac{U_{i-1,j,k}}{2\Delta X}-\frac{\Pr}{\Delta X^2}$	$-\frac{U_{i-1,j,k}}{2\Delta X}-\frac{\Pr}{\Delta X^2}$	$-1/\Delta X^2$	$-\frac{U_{i-1,j,k}}{2\Delta X}-\frac{1}{\Delta X^2}$
F	$-\Pr/\Delta X^2$	$\frac{U_{i+1,j,k}}{2\Delta X}-\frac{\Pr}{\Delta X^2}$	$\frac{U_{i+1,j,k}}{2\Delta X}-\frac{\Pr}{\Delta X^2}$	$-1/\Delta X^2$	$\frac{U_{i+1,j,k}}{2\Delta X}-\frac{1}{\Delta X^2}$
B	$-\frac{V_{i,j-1,k}}{2\Delta Y}-\Pr/\Delta Y^2$	$-\frac{\Pr}{\Delta Y^2}$	$-\frac{V_{i,j-1,k}}{2\Delta Y}-\frac{\Pr}{\Delta Y^2}$	$-1/\Delta Y^2$	$-\frac{V_{i,j-1,k}}{2\Delta Y}-\frac{1}{\Delta Y^2}$
H	$\frac{V_{i,j+1,k}}{2\Delta Y}-\frac{\Pr}{\Delta Y^2}$	$-\frac{\Pr}{\Delta Y^2}$	$\frac{V_{i,j+1,k}}{2\Delta Y}-\frac{\Pr}{\Delta Y^2}$	$-1/\Delta Y^2$	$\frac{V_{i,j+1,k}}{2\Delta Y}-\frac{1}{\Delta Y^2}$
Z'	$-\frac{W_{i,j,k-1}}{2\Delta Z}-\frac{\Pr}{\Delta Z^2}$	$-\frac{W_{i,j,k+1}}{2\Delta Z}-\frac{\Pr}{\Delta Z^2}$	$-\frac{\Pr}{\Delta Z^2}$	$-1/\Delta Z^2$	$-\frac{W_{i,j,k-1}}{2\Delta Z}-\frac{1}{\Delta Z^2}$
S	$\frac{W_{i,j,k+1}}{2\Delta Z}-\frac{\Pr}{\Delta Z^2}$	$\frac{W_{i,j,k+1}}{2\Delta Z}-\frac{\Pr}{\Delta Z^2}$	$-\frac{\Pr}{\Delta Z^2}$	$-1/\Delta Z^2$	$\frac{W_{i,j,k+1}}{2\Delta Z}-\frac{1}{\Delta Z^2}$
E	$\frac{\Pr}{\alpha_\omega\Delta\tau}+\frac{2\Pr}{\Delta X^2}+\frac{2\Pr}{\Delta Y^2}+\frac{2\Pr}{\Delta Z^2}$			$\frac{1}{\alpha_\Psi\Delta\tau}+\frac{2}{\Delta X^2}+\frac{2}{\Delta Y^2}+\frac{2}{\Delta Z^2}$	$\frac{1}{\Delta\tau}+\frac{2}{\Delta X^2}+\frac{2}{\Delta Y^2}+\frac{2}{\Delta Z^2}$

Table 2 Coefficients of {*q*}

	$q_i{}^n$	
ω_1	$\phi_{i,j,k}\frac{\Pr}{\alpha_\omega\Delta\tau}$	$+\frac{U_{i,j+1,k}\omega_{2_{i,j+1,k}}-U_{i,j-1,k}\omega_{2_{i,j-1,k}}}{2\Delta Y}$ $+\frac{U_{i,j,k+1}\omega_{3_{i,j,k+1}}-U_{i,j,k-1}\omega_{3_{i,j,k-1}}}{2\Delta Z}$ $+\Pr\mathrm{Ra}\,\frac{\theta_{i,j+1,k}-\theta_{i,j-1k}}{2\Delta Y}$
ω_2	$\phi_{i,j,k}\frac{\Pr}{\alpha_\omega\Delta\tau}$	$+\frac{V_{i+1,j,k}\omega_{1_{i+1,j,k}}-V_{i-1,j,k}\omega_{1_{i-1,j,k}}}{2\Delta X}$ $+\frac{V_{i,j,k+1}\omega_{3_{i,j,k+1}}-V_{i,j,k-1}\omega_{3_{i,j,k-1}}}{2\Delta Z}$ $+\Pr\mathrm{Ra}\,\frac{\theta_{i+1,j,k}-\theta_{i-1,j,k}}{2\Delta X}$
ω_3	$\phi_{i,j,k}\frac{\Pr}{\alpha_\omega\Delta\tau}$	$+\frac{W_{i+1,j,k}\omega_{1_{i+1,j,k}}-W_{i-1,j,k}\omega_{1_{i-1,j,k}}}{2\Delta X}$ $+\frac{W_{i,j+1,k}\omega_{2_{i,j+1,k}}-W_{i,j-1,k}\omega_{2_{i,j-1,k}}}{2\Delta Y}$
Ψ_1	$\omega_{1_{i,j,k}}$	$+\frac{\phi_{i,j,k}}{\alpha_\Psi\Delta\tau}$
Ψ_2	$\omega_{2_{i,j,k}}$	$+\frac{\phi_{i,j,k}}{\alpha_\Psi\Delta\tau}$
Ψ_3	$\omega_{3_{i,j,k}}$	$+\frac{\phi_{i,j,k}}{\alpha_\Psi\Delta\tau}$
θ	$\frac{\phi_{i,j,k}}{\Delta\tau}$	

The coefficients C, G, A, W, T, and P are associated with the additional new unknown values. The influence of these new terms is reduced by subtracting nearly equal terms (in parentheses) adjacent to the new variables. The parameters α_1, α_2, and α_3 vary between $0 \leqslant \alpha_i \leqslant 1$ to account for large variations in ϕ or variable grid spacing. A cyclic set of ten values for α was used in this study [1, 14].

Equation (6) can be rewritten in matrix notation as

$$[M']\{\phi\} = \{q\} \tag{7}$$

where $[M']$ now contains 13 diagonal coefficients. $[M']$ can be factored into the product of a lower and an upper matrix, $[M'] = [L][U]$, each containing four nonzero diagonal elements [14].

The three-dimensional SIP algorithms are based on the [L] and [U] diagonal terms and are given as

$$a = Z'/(1 + \alpha_2 e_{k-1} + \alpha_1 f_{k-1})$$

$$b = B/(1 + \alpha_2 g_{j-1} + \alpha_1 e_{j-1})$$

$$c = D/(1 + \alpha_2 g_{i-1} + \alpha_1 f_{i-1})$$

$$A = ae_{k-1},\ C = be_{j-1},\ G = cf_{i-1}$$

$$W = cg_{i-1},\ T = af_{k-1},\ P = bg_{j-1}$$

$$d = E + \alpha_2(A + W) + \alpha_3(T + P) + \alpha_2(C + G) - ce_{i-1} - bf_{j-1} - ag_{k-1} \tag{8}$$

likewise,

$$e = (F - \alpha_2 A - \alpha_1 C)/d$$

$$f = (H - \alpha_3 F - \alpha_1 G)/d$$

$$g = (S - \alpha_2 W - \alpha_3 P)/d \tag{9}$$

To reduce roundoff errors, the unknown ϕ^{n+1} values are solved in residual form such that

$$[M']\{\Delta\phi^{n+1}\} = \{R\} \tag{10}$$

where $\{R\} = \{q\} - [M]\{q\}$ and $\Delta\phi^{n+1} = \phi^{n+1} - \phi^n$. Equation (10) can be rewritten as

$$[M']\{\Delta\phi^{n+1}\} = [L][U]\{\Delta\phi^{n+1}\} = \{R\} \tag{11}$$

Letting $[U]\{\Delta\phi^{n+1}\} = \{\tilde{V}\}$, equation (11) becomes

$$[L]\{\tilde{V}\} = \{R\} \tag{12}$$

At node point i, j, k, equations (11) and (12) can be written as

$$\tilde{V} = (R - c\tilde{V}_{k-1} - b\tilde{V}_{j-1} - c\tilde{V}_{i-1})/d \tag{13}$$

and subsequently

$$\Delta\phi^{n+1} = \tilde{V}^{n+1} - c\Delta\phi_{i+1}^{n+1} - f\Delta\phi_{j+1}^{n+1} - g\Delta\phi_{k+1}^{n+1} \tag{14}$$

Once $\Delta\phi^{n+1}$ is solved, ϕ^{n+1} can be found. An alternate set of algorithms can be written for odd-numbered time steps (or iterations) [6, 14]. Although the alternating sequence generally improves convergence and stability of the solution (by creating overall symmetry in $[M']$), more core is required. The alternating sequence was not used in this study. The programmed algorithm are available upon request.

A simple test case was conducted with Ra = 10^4 and Pr = 100. For low-to-moderate Rayleigh numbers, the steady-state results are generally of interest. Solutions beyond Ra $\geqslant 10^6$ become unsteady and oscillatory, and require either a fine mesh or more accurate discretization techniques. An 11 × 11 × 11 mesh was used with $\Delta X = \Delta Y = \Delta Z = 0.1$ and $\Delta t = .10$. Steady-state results were obtained in 109 seconds on an IBM 360/195 computer for a residual error of 10^{-2}. Core requirements were 165 K bytes. The Nusselt number, obtained by integrating $\mathrm{Nu} = \int_0^1 \partial\theta/\partial x|_{\mathrm{wall}}\, dz$, is in agreement with the values obtained in the literature, Nu = 2.19. Contour plots and discussions of other test cases are given in [15].

This test case was also solved with ADIP, using the algorithm structure employed in [8]. The velocity potential equations were also solved with false transient terms. Although ADIP required less storage, 155 K bytes, the programming effort was a third larger. The solution converged in 145 seconds. As $\Delta t \rightarrow 0$, ADIP tends to converge more quickly than SIP. For $\Delta t = .2$, ADIP converged in 360 seconds; SIP converged in 95 seconds.

Acknowledgment

The information contained in this article was developed during the course of work under Contract No. AT(07-2)-1 with the U.S. Department of Energy.

References

1 Stone, H. L., "Iterative Solution of Implicit Approximations of Multidimensional Partial Differential Equations," *Society for Industrial and Applied Mathematics Journal, Numerical Analysis,* Vol. 5, No. 3, 1968, pp. 530–558.

2 Bozeman, J. D., and Dalton, C., "Numerical Study of Viscous Flow in a Cavity," *Journal of Computational Physics,* Vol. 12, 1973, pp. 348–363.

3 Jacobs, D. A. H., "A Corrected Upwind Differencing Scheme Using a Strongly Implicit Solution Procedure," *Proceedings of the International Conference on Numerical Methods in Fluid Dynamics,* University of Southampton, England, Sept. 26–28, 1973, pp. 84–98.

4 Lin, C. L., Pepper, D. W., and Lee, S. C., "Numerical Methods for Separated Flow Solutions Around a Circular Cylinder," *AIAA Journal,* Vol. 14, 1976, pp. 900–907.

5 Pepper, D. W., and Harris, S. D., "Numerical Simulation of Natural Convection in Closed Containers by a Fully Implicit Method," *Journal of Fluids Engineering,* Vol. 99, No. 4, 1977, pp. 649–656.

6 Pepper, D. W., and Harris, S. D., "Fully Implicit Algorithms for Solving Partial Differential Equations," *Journal of Fluids Engineering,* Vol. 99, No. 4, 1977, pp. 781–783.

7 Ozoe, H., Yamamoto, K., Churchill, S. W., and Sayama, H., "Three-Dimensional Numerical Analysis of Laminar Natural Convection in a Confined Fluid Heated from Below," ASME JOURNAL OF HEAT TRANSFER, Vol. 98C, 1976, pp. 202–207.

8 Aziz, K., and Hellums, J. D., "Numerical Solution of the Three-Dimensional Equation of Motion for Laminar Natural Convection," *Physics of Fluids,* Vol. 10, No. 2, 1967, pp. 314–324.

9 Ozoe, H., Yamamoto, K., and Sayama, H., "Natural Convection Patterns in a Long Inclined Rectangular Box Heated from Below: Part II. Three-Dimensional Numerical Results," *Int. J. of Heat Mass Transfer,* Vol. 20, 1977, pp. 131–139.

10 Holst, P. H., and Aziz, K., "Transient Three-Dimensional Natural Convection in Confined Porous Media," *Int. J. of Heat Mass Transfer,* Vol. 15, 1972, pp. 73–90.

11 Mallinson, G. D., and de Vahl Davis, G., "Method of the False Transient for the Solution of Coupled Elliptic Equations," *Journal of Computational Physics,* Vol. 12, 1973, pp. 435–461.

12 Long, P. E., and Pepper, D. W., "A Comparison of Six Numerical Schemes for Calculating the Advection of Atmospheric Pollution," presented at the Third Symposium on Atmospheric Turbulence, Diffusion, and Air Quality, Raleigh, N. C., October 19–22, 1976, pp. 181–187.

13 Weinstein, H. G., Stone, H. L., and Kwan, T. V., "Simultaneous Solution of Multiphase Reservoir Flow Equations," *Society of Petroleum Engineering Journal,* June 1970, pp. 99–110.

14 Gosman, A. D., Pun, W. M., Runchal, A. K., Spalding, D. B., and Wolfshtein, M., *Heat and Mass Transfer in Recirculating Flows,* Academic Press, 1969, 260 pp.

15 Pepper, D. W., and Harris, S. D., "Numerical Solution of Three-Dimensional Natural Convection by the Strongly Implicit Procedure," presented at the WAM, San Francisco, CA, Dec. 10–15, 1978, Paper No. 78-WA/HT-10.

Correlations for Natural Convection through High L/D Rectangular Cells

D. K. Edwards,[1] J. N. Arnold,[2] and P. S. Wu[3]

Nomenclature

a = horizontal wave number
b = vertical wave number
D = tilted dimension of heated cell surface (when $\tau > 0$)
k = mode of instability integer
L = length between heated and cooled surfaces
N_1, N_2 = power integral coefficients
Nu = Nusselt number based on L
Ra = Rayleigh number based on L (Grashof-Prandtl number product)
Ra_{cr} = critical Rayleigh number
W = horizontal width of heated cell surface
τ = angle of tilt from H-position

Introduction

Heat transfer with natural convection across rectangular cells occurs frequently in technology and is also of academic interest to workers attempting to solve numerically the full equations of motion for a viscous fluid. Multiple rectangular cells in honeycomb-like arrays have been tested in solar heat collectors for their ability to reduce heat loss from the absorber to the coverglass. Each of the multiple cells considered here has dimensions shown in Fig. 1. In the horizontal heated-from-below position, dimension D is horizontal. We designate this position as the H position for short. In the V position at $\tau = 90$ deg, the heated and cooled surfaces are vertical. By extension, the convective motion which occurs in the H position is called H convection, and that for the V position is termed V convection.

It is the purpose of this note to report new data extending our knowledge of the effect of L/D, W/D, τ, and Ra on Nu for natural convection heat transfer through multiple, high L/D rectangular cells and to put forward correlations of the existing data. Buchberg, et al. [1] have reviewed the need for such information in solar collector design.

There are three bodies of relevant work. One [2–9] is concerned with the value of Ra_{cr}. For the H position, Nu = 1 unless $\mathrm{Ra} > \mathrm{Ra}_{cr}$. The second body of work, [10–15] and [5], is concerned with Nu versus Ra for $\mathrm{Ra} > \mathrm{Ra}_{cr}$ in the H position. The third body [16–20] is concerned with the effect of tilt. Cane, et al. [17] investigated the square cross-section $W/D = 1$ for $L/D = 2, 3, 4$, and 5 at tilts of 0, 30, 45, and 90 deg and correlated their air-in-polyethylene data as

$$\mathrm{Nu} = 1 + 0.89 \cos(\tau - \pi/3)[\mathrm{Ra}/(2420(L/D)^4)]^{2.88 - 1.64 \sin \tau} \qquad (1)$$

Edwards, et al. [16] and Arnold, et al. [18] investigated the rectangle for $L/D \doteq 4$ and $W/D \doteq 2, 4, 8$ using silicone oil in varnished paperboard. The cell side-walls thus offered negligible thermal resistance to conduction normal to them, but high thermal resistance to conduction along them. The paperboard and silicone oil were essentially opaque to heat radiation, the air was transparent, and the polyethylene (with adhesive) was partially absorbing-emitting.

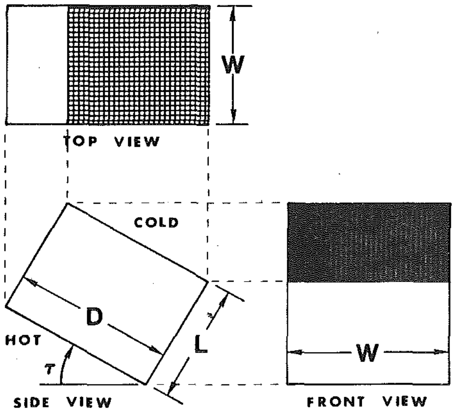

Fig. 1 Size and orientation of a single cell

---

[1] School of Engineering, UCLA, Los Angeles, CA 90024

[2] Presently with Bell Laboratories, Inc., Whippany, NJ 07981

[3] Presently with Hughes Aircraft Company, Canoga Park, CA 91306

Contributed by the Heat Transfer Division for publication in the JOURNAL OF HEAT TRANSFER. Manuscript received by the Heat Transfer Division March 8, 1979.

References

1 Stone, H. L., "Iterative Solution of Implicit Approximations of Multidimensional Partial Differential Equations," *Society for Industrial and Applied Mathematics Journal, Numerical Analysis,* Vol. 5, No. 3, 1968, pp. 530–558.

2 Bozeman, J. D., and Dalton, C., "Numerical Study of Viscous Flow in a Cavity," *Journal of Computational Physics,* Vol. 12, 1973, pp. 348–363.

3 Jacobs, D. A. H., "A Corrected Upwind Differencing Scheme Using a Strongly Implicit Solution Procedure," *Proceedings of the International Conference on Numerical Methods in Fluid Dynamics,* University of Southampton, England, Sept. 26–28, 1973, pp. 84–98.

4 Lin, C. L., Pepper, D. W., and Lee, S. C., "Numerical Methods for Separated Flow Solutions Around a Circular Cylinder," *AIAA Journal,* Vol. 14, 1976, pp. 900–907.

5 Pepper, D. W., and Harris, S. D., "Numerical Simulation of Natural Convection in Closed Containers by a Fully Implicit Method," *Journal of Fluids Engineering,* Vol. 99, No. 4, 1977, pp. 649–656.

6 Pepper, D. W., and Harris, S. D., "Fully Implicit Algorithms for Solving Partial Differential Equations," *Journal of Fluids Engineering,* Vol. 99, No. 4, 1977, pp. 781–783.

7 Ozoe, H., Yamamoto, K., Churchill, S. W., and Sayama, H., "Three-Dimensional Numerical Analysis of Laminar Natural Convection in a Confined Fluid Heated from Below," ASME JOURNAL OF HEAT TRANSFER, Vol. 98C, 1976, pp. 202–207.

8 Aziz, K., and Hellums, J. D., "Numerical Solution of the Three-Dimensional Equation of Motion for Laminar Natural Convection," *Physics of Fluids,* Vol. 10, No. 2, 1967, pp. 314–324.

9 Ozoe, H., Yamamoto, K., and Sayama, H., "Natural Convection Patterns in a Long Inclined Rectangular Box Heated from Below: Part II. Three-Dimensional Numerical Results," *Int. J. of Heat Mass Transfer,* Vol. 20, 1977, pp. 131–139.

10 Holst, P. H., and Aziz, K., "Transient Three-Dimensional Natural Convection in Confined Porous Media," *Int. J. of Heat Mass Transfer,* Vol. 15, 1972, pp. 73–90.

11 Mallinson, G. D., and de Vahl Davis, G., "Method of the False Transient for the Solution of Coupled Elliptic Equations," *Journal of Computational Physics,* Vol. 12, 1973, pp. 435–461.

12 Long, P. E., and Pepper, D. W., "A Comparison of Six Numerical Schemes for Calculating the Advection of Atmospheric Pollution," presented at the Third Symposium on Atmospheric Turbulence, Diffusion, and Air Quality, Raleigh, N. C., October 19–22, 1976, pp. 181–187.

13 Weinstein, H. G., Stone, H. L., and Kwan, T. V., "Simultaneous Solution of Multiphase Reservoir Flow Equations," *Society of Petroleum Engineering Journal,* June 1970, pp. 99–110.

14 Gosman, A. D., Pun, W. M., Runchal, A. K., Spalding, D. B., and Wolfshtein, M., *Heat and Mass Transfer in Recirculating Flows,* Academic Press, 1969, 260 pp.

15 Pepper, D. W., and Harris, S. D., "Numerical Solution of Three-Dimensional Natural Convection by the Strongly Implicit Procedure," presented at the WAM, San Francisco, CA, Dec. 10–15, 1978, Paper No. 78-WA/HT-10.

Correlations for Natural Convection through High L/D Rectangular Cells

D. K. Edwards,[1] J. N. Arnold,[2] and P. S. Wu[3]

Nomenclature

a = horizontal wave number
b = vertical wave number
D = tilted dimension of heated cell surface (when $\tau > 0$)
k = mode of instability integer
L = length between heated and cooled surfaces
N_1, N_2 = power integral coefficients
Nu = Nusselt number based on L
Ra = Rayleigh number based on L (Grashof-Prandtl number product)
Ra_{cr} = critical Rayleigh number
W = horizontal width of heated cell surface
τ = angle of tilt from H-position

Introduction

Heat transfer with natural convection across rectangular cells occurs frequently in technology and is also of academic interest to workers attempting to solve numerically the full equations of motion for a viscous fluid. Multiple rectangular cells in honeycomb-like arrays have been tested in solar heat collectors for their ability to reduce heat loss from the absorber to the coverglass. Each of the multiple cells considered here has dimensions shown in Fig. 1. In the horizontal heated-from-below position, dimension D is horizontal. We designate this position as the H position for short. In the V position at $\tau = 90$ deg, the heated and cooled surfaces are vertical. By extension, the convective motion which occurs in the H position is called H convection, and that for the V position is termed V convection.

It is the purpose of this note to report new data extending our knowledge of the effect of L/D, W/D, τ, and Ra on Nu for natural convection heat transfer through multiple, high L/D rectangular cells and to put forward correlations of the existing data. Buchberg, et al. [1] have reviewed the need for such information in solar collector design.

There are three bodies of relevant work. One [2–9] is concerned with the value of Ra_{cr}. For the H position, Nu = 1 unless $\mathrm{Ra} > \mathrm{Ra}_{cr}$. The second body of work, [10–15] and [5], is concerned with Nu versus Ra for $\mathrm{Ra} > \mathrm{Ra}_{cr}$ in the H position. The third body [16–20] is concerned with the effect of tilt. Cane, et al. [17] investigated the square cross-section $W/D = 1$ for $L/D = 2, 3, 4$, and 5 at tilts of 0, 30, 45, and 90 deg and correlated their air-in-polyethylene data as

$$\mathrm{Nu} = 1 + 0.89 \cos(\tau - \pi/3)[\mathrm{Ra}/(2420(L/D)^4)]^{2.88 - 1.64 \sin\tau} \quad (1)$$

Edwards, et al. [16] and Arnold, et al. [18] investigated the rectangle for $L/D \doteq 4$ and $W/D \doteq 2, 4, 8$ using silicone oil in varnished paperboard. The cell side-walls thus offered negligible thermal resistance to conduction normal to them, but high thermal resistance to conduction along them. The paperboard and silicone oil were essentially opaque to heat radiation, the air was transparent, and the polyethylene (with adhesive) was partially absorbing-emitting.

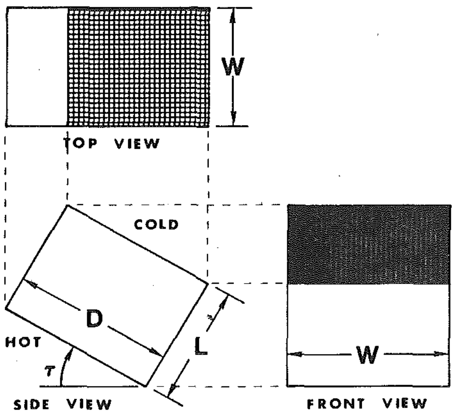

Fig. 1 Size and orientation of a single cell

---

[1] School of Engineering, UCLA, Los Angeles, CA 90024
[2] Presently with Bell Laboratories, Inc., Whippany, NJ 07981
[3] Presently with Hughes Aircraft Company, Canoga Park, CA 91306

Contributed by the Heat Transfer Division for publication in the JOURNAL OF HEAT TRANSFER. Manuscript received by the Heat Transfer Division March 8, 1979.

Data

Additional measurements were made using polyurethane-varnished paperboard honeycombs approximately 0.4 mm thick in silicone oil in the apparatus previously described [5, 16, 18]. Inside cell dimensions were as follows:

L/D	L/W	D/W	D mm	W mm	L mm
8.00	0.88	0.11	4.6	4	36.8
7.91	1.76	0.22	4.6	20.7	36.4
4.46	0.17	0.04	4.8	127.0	21.1
4.11	4.11	1.00	12.3	12.3	50.5

Figs. 2 and 3 show the new results along with others reported previously. The data make it possible to put forward correlations of fairly general applicability.

Data Correlation, *H* Convection

The H data ($\tau = 0$ deg) show Nu = 1 up to Ra_{cr} and then rapid growth in Nu with increasing Ra, typical of behavior predicted by the power-integral formalism [10–15]. This behavior is seen to persist for $\tau = 30$ and 60 deg, there being discernible only a slight increase in Nu above unity below an apparent Ra_{cr}, the slight increase being presumably a feeble V-type motion. Thus the correlation put forward is

$$\text{Nu} = 1 + N_1[1 - \text{Ra}_{cr,1}/\text{Ra}\cos\tau]^{\bullet} + N_2[1 - \text{Ra}_{cr,2}/\text{Ra}\cos\tau]^{\bullet} \tag{2}$$

$$\text{Ra}\cos\tau \le \text{Ra}_{cr,3}, \quad 0 \le \tau \le 60 \text{ deg}$$

$$4 \le L/D \le 8, \quad 1 \le W/D \le 24$$

where

$$\text{Ra}_{cr,k} = (a_k{}^2 + b_k{}^2)^3/a_k{}^2$$

$$a_k{}^2 = a_0{}^2 + b_k{}^2/2, \quad b_k{}^2 = (k\pi + 0.85)^2 \tag{4}$$

$$a_0{}^2 = \left[\frac{8.5}{1 + (1/4)(L/D)} + 15(D/W)^2\right](L/D)^2 \tag{5}$$

$$N_1 = 1.15, \quad N_2 = 1.25$$

The dot notation from Hollands, et al. [19] conveniently denotes that a term is zero unless positive. The values of N_1, N_2 and those in equation (5) are chosen to fit the data. The solid lines on Figs. 2 and 3 are plots of equation (2).

The correlation agrees with the data within ±15 per cent for all seven cells in the H position and 5 out of the 7 in the tilted positions. In two cases of high D/W and relatively low L/D using the H correlation with Ra cos τ is poor. In one case ($L/D = 4.1$, $L/W = 4.1$, $D/W = 1$) the correlation scales a unit value of Nu at $\text{Ra} = 1.5 \times 10^5$ for $\tau = 0$ deg to $\text{Ra} = 3 \times 10^5$ for $\tau = 60$ deg, but the data show Nu = 1.5. In the other case ($L/D = 4.3$, $L/W = 2.0$, $D/W = 0.5$), the correlation overpredicts by 20 percent, because the data at $\tau = 30$ deg do not rise steeply with increasing Ra.

In both cases the poor agreement is thought to be due to an H-V convective interaction. For $D/W = 1$ the H convective roll can equally well line up with axis in the D-direction or the W-direction. With axis in the W-direction, the H roll and V roll have the same character, and as the cell is tilted from 90 deg to 60 deg the motions are compatible. Augmentation of the V convection is seen in the data as τ goes from 90 to 60 deg. For $D/W = 0.5$, the H roll has axis aligned with the short D dimension [2, 3], while the V roll has axis always in the horizontal W direction. As the cell is tilted from $\tau = 0$ to 30 deg, a marked decrease is seen in the data. It is thought that the V-type convection tends to interfere with or damp somewhat the H-type convection. At smaller values of D/W or the higher L/D values, the H type convection is sufficiently robust compared to the V-type convection that H-V interaction has apparently little effect, even at a tilt as high as 60 deg.

Data Correlation, *V*-Convection

The V data display a simple power-law-type behavior. Accordingly the correlation made is

$$\text{Nu} = 1 + \frac{1.1 \times 10^{-4}}{1 + 5(D/W)^4}(D/L)^{4.65}\text{Ra}^{1.3} \tag{6}$$

$$4 \le L/D \le 8, \quad 1 \le W/D \le 24$$

$$1 \le \text{Nu} \le 2, \quad \tau = 90 \text{ deg}$$

This correlation agrees with the data within 15 percent, and in its range of applicability it agrees well with equation (1) for $\tau = 90$ deg and $D/W = 1$ as shown in Fig. 2, even though the fluid Prandtl num-

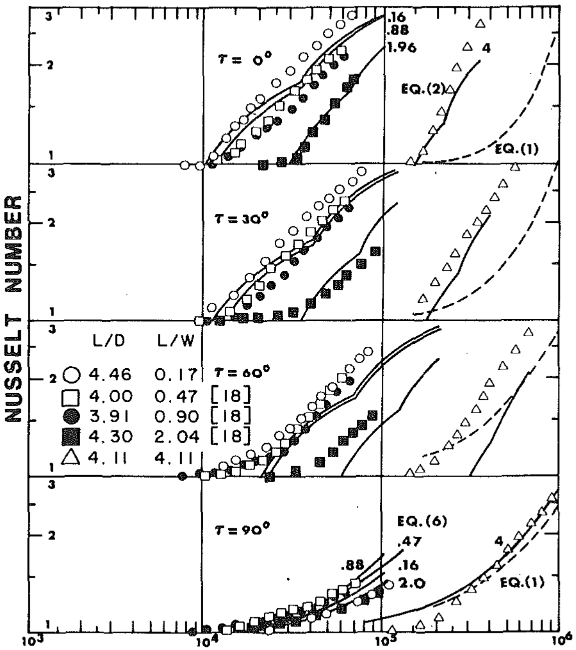

Fig. 2 Experimental data and correlations for $L/D = 4$

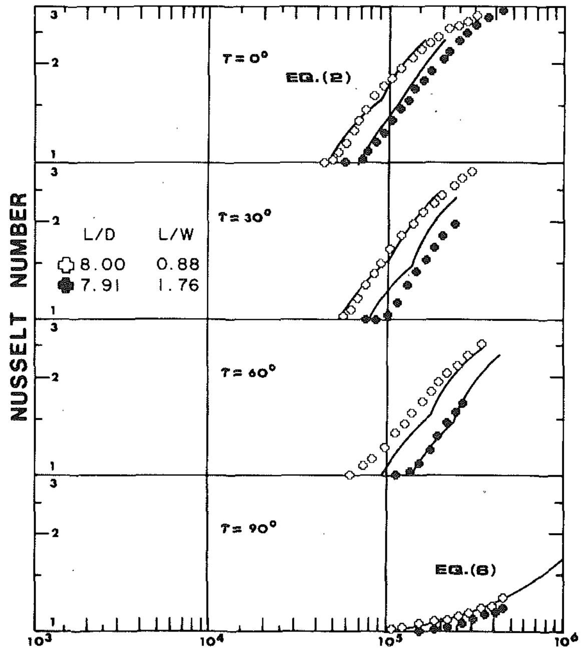

Fig. 3 Experimental data and correlations for $L/D = 8$

bers and radiative properties differ markedly. The agreement of the data with equation (1) does not extend to H-convection, because radiation heat transfer through a transparent fluid tends to isothermalize the cell walls, and shifts the H-curve to higher Ra by a factor of three [20].

One should not apply the correlation of multiple cell V data to a single cell V situation such as that analyzed by Bejan and Tien [21], because in multiple cells vertical heat conduction occurs not just across one cell but through the thin walls to neighboring cells above and below. The conduction reduces the convective heat flux in the L direction by reducing the temperature difference between the positive and negative velocities in the L direction, much like in a balanced counterflow heat exchanger. Thus at high L/D in multiple cells the V convection is strongly damped. By the same token V convection in a single high L/D cell is strongly affected by the thermal conditions on the $L \times W$ surfaces.

Acknowledgment

This work was supported by National Science Foundation Grant ENG 75-22936.

References

1 Buchberg, H., Catton, I., and Edwards, D. K., "Natural Convection in Enclosed Spaces—A Review of Application to Solar Energy," ASME JOURNAL OF HEAT TRANSFER, Vol. 98, 1976, pp. 182–188.

2 Wooding, R. A., "Instability of a Viscous Liquid of Variable Density in a Vertical Hele-Shaw Cell," *Journal of Fluid Mech.*, Vol. 7. 1960, pp. 501–515.

3 Edwards, D. K., "Suppression of Cellular Convection by Lateral Walls," ASME JOURNAL OF HEAT TRANSFER, Vol. 91, 1969, pp. 145–150.

4 Edwards, D. K., and Sun, W. M., "Prediction of the Onset of Natural Convection in Rectangular Honeycomb Structures," Paper 7/62, 1970 International Solar Energy Society Conference, Melbourne, Australia.

5 Sun, W. M., and Edwards, D. K., "Natural Convection in Cells with Finite Conducting Side Walls Heated from Below," *Heat Transfer 1970,* Paper NC2.3, 4th International Heat Transfer Conference, Versailles, France, 1970.

6 Heitz, W. L., and Westwater, J. W., "Critical Rayleigh Number for Natural Convection of Water Confined in Square Cells with L/D from 0.5 to 8," ASME JOURNAL OF HEAT TRANSFER, Vol. 93, 1971, pp. 188–196.

7 Catton, I., "Convection in a Closed Rectangular Region: The Onset of Motion," ASME JOURNAL OF HEAT TRANSFER, Vol. 92, 1970, pp. 186–188.

8 Catton, I., "The Effect of Insulating Vertical Walls on the Onset of Motion in a Fluid Heated from Below," *Int. Journal of Heat Mass Transfer,* Vol. 15, 1972, pp. 665–672.

9 Catton, I., "Effect of Wall Conduction on the Stability of a Fluid in a Rectangular Region Heated from Below," ASME JOURNAL OF HEAT TRANSFER, Vol. 94, 1972, pp. 446–452.

10 Malkus, W. V. R., and Veronis, G., "Finite Amplitude Cellular Convection," *Journal of Fluid Mech.*, Vol. 4, 1958, pp. 225–260.

11 Hollands, K. G. T., "Convectional Heat Transport Between Rigid Horizontal Boundaries after Instability," *Physics of Fluids,* Vol. 8, 1965, pp. 389–390.

12 Catton, I., "Natural Convection in Horizontal Liquid Layers," *Physics of Fluids,* Vol. 9, 1966, pp. 2521–2522.

13 Catton, I., and Edwards, D. K., "Effect of Side Walls on Natural Convection Between Horizontal Plated Heated from Below," ASME JOURNAL OF HEAT TRANSFER, Vol. 89, 1967, pp. 295–299.

14 Edwards, D. K., and Catton, I., "Prediction of Heat Transfer by Natural Convection in Closed Cylinders Heated from Below," *Int. Journal of Heat Mass Transfer,* Vol. 12, 1969, pp. 23–30.

15 Hollands, K. G. T., "Natural Convection in Horizontal Thin-Walled Honeycomb Panels," ASME JOURNAL OF HEAT TRANSFER, Vol. 95, 1973, pp. 439–444.

16 Edwards, D. K., Arnold, J. N., and Catton, I., "End-Clearance Effects on Rectangular-Honeycomb Solar Collectors," *Solar Energy,* Vol. 16, 1976, pp. 253–257.

17 Cane, R. L., Hollands, K. G. T., Raithby, G. D., and Unny, T. E., "Free Convection Heat Transfer Across Inclined Honeycomb Panels," ASME JOURNAL OF HEAT TRANSFER, Vol. 99, 1977, pp. 86–91.

18 Arnold, J. N., Edwards, D. K., and Catton, I., "Effect of Tilt and Horizontal Aspect Ratio on Natural Convection in Rectangular Honeycombs," ASME JOURNAL OF HEAT TRANSFER, Vol. 99, pp. 120–122.

19 Hollands, K. G. T., Unny, T. E., Raithby, G. D., and Konicek, I., "Free Convective Heat Transfer Across Inclined Air Layers," ASME JOURNAL OF HEAT TRANSFER, Vol. 98, 1976, pp. 189–193.

20 Edwards, D. K., and Sun, W. M., "Effect of Wall Radiation on Thermal Instability in a Vertical Cylinder," *Int. Journal of Heat Mass Transfer,* Vol. 14, 1971, pp. 15–18.

21 Bejan, A., and Tien, C. L., "Laminar Natural Convection Heat Transfer in a Horizontal Cavity with Different End Temperatures," ASME JOURNAL OF HEAT TRANSFER, Vol. 100, 1978, pp. 641–647.

Free Convection Heat Transfer from Heated Cylinders Immersed in a Shallow Water Layer

F. P. Incropera[1] and M. A. Yaghoubi[1]

Introduction

Free convection heat transfer from horizontal heated cylinders submerged in bounded, quiescent liquids occurs in sensible energy storage and waste heat dissipation systems. In such applications the existence of finite boundaries and a liquid-air interface can strongly influence heat transfer from the source to the liquid. Although much attention has been devoted to the problem of free convection from horizontal cylinders, little has been done to consider these special effects. Marsters [1, 2] has shown that confining walls can enhance heat transfer from a single horizontal cylinder and arrays of such cylinders, while Yaghoubi and Incropera [3] have shown similar behavior for a single cylinder. However, there exists a need for additional data, and the purpose of this study has been to measure and to correlate heat transfer effects for cylinders submerged in a shallow water layer. Efforts have focused on the effects of water layer depth and the destabilizing temperature difference between the cylinder surface and the air-water interface.

Experimental Conditions

Experiments were performed using test cells with installation of either one heated cylinder midway between the sidewalls or an array of five equidistant cylinders (Fig. 1). If the cylinder length-to-diameter ratio is sufficiently large, the buoyancy induced flows are approximately two-dimensional. The geometrical variables which influence heat transfer from the single cylinder are then the cylinder diameter D, the sidewall spacing W, and the height H_2 of the water layer above the cylinder. In addition to these variables, heat transfer from the array is also influenced by the pitch S'. The distance between the top of the test cell and the air-water interface, h_1, has a negligible effect on interface conditions and hence may be neglected. Moreover, theoretical and experimental results of Marsters [1] suggest that the height of the cylinder above the test cell bottom, h_2, has a negligible effect on heat transfer and may also be neglected. This result has been confirmed by flow visualization studies and temperature measurements [4], which indicate the absence of motion and the existence of highly stable conditions in the fluid layer below the cylinders.

The experiments have concentrated on determining the effect of the water layer height on cylinder heat transfer. For the single cylinder, diameters of 12.7 mm, 19.1 mm and 25.4 mm were considered, and measurements were made for height ratios in the range $3.8 \leq (H_1/D) \leq 30$. For the horizontal array, a single cylinder diameter of 25.4 mm, with a pitch of $S' = 50.8$ mm was considered, the measurements were made for height ratios in the range $3 \leq (H_1/D) \leq 15$. The cylinder length-to-diameter ratio was maintained in excess of 8, while h_1 and h_2 were held at 12.7 mm and 25.4 mm, respectively. For all of the foregoing measurements, the space ratio, W/D, was maintained approximately constant in the range $11 \leq (W/D) \leq 12$. However, additional measurements were made for a single cylinder installed in a long channel, which essentially corresponds to $W/D \rightarrow \infty$.

Each cylinder was machined from copper and drilled along its axis to permit insertion of an electrical heater whose P was measured. The average of three measurements made at the midplane of the cylinder was designated as the cylinder surface temperature, T_c, while the bulk water temperature, T_w, was measured at a point well removed from the cylinders, test cell walls and the air interface. Since the water is

---

[1] Heat Transfer Laboratory, School of Mechanical Engineering, Purdue University, West Lafayette, IN 47906.

Contributed by the Heat Transfer Division for publication in the JOURNAL OF HEAT TRANSFER. Manuscript received by the Heat Transfer Division May 23, 1979.

bers and radiative properties differ markedly. The agreement of the data with equation (1) does not extend to H-convection, because radiation heat transfer through a transparent fluid tends to isothermalize the cell walls, and shifts the H-curve to higher Ra by a factor of three [20].

One should not apply the correlation of multiple cell V data to a single cell V situation such as that analyzed by Bejan and Tien [21], because in multiple cells vertical heat conduction occurs not just across one cell but through the thin walls to neighboring cells above and below. The conduction reduces the convective heat flux in the L direction by reducing the temperature difference between the positive and negative velocities in the L direction, much like in a balanced counterflow heat exchanger. Thus at high L/D in multiple cells the V convection is strongly damped. By the same token V convection in a single high L/D cell is strongly affected by the thermal conditions on the $L \times W$ surfaces.

Acknowledgment

This work was supported by National Science Foundation Grant ENG 75-22936.

References

1 Buchberg, H., Catton, I., and Edwards, D. K., "Natural Convection in Enclosed Spaces—A Review of Application to Solar Energy," ASME JOURNAL OF HEAT TRANSFER, Vol. 98, 1976, pp. 182–188.

2 Wooding, R. A., "Instability of a Viscous Liquid of Variable Density in a Vertical Hele-Shaw Cell," *Journal of Fluid Mech.*, Vol. 7. 1960, pp. 501–515.

3 Edwards, D. K., "Suppression of Cellular Convection by Lateral Walls," ASME JOURNAL OF HEAT TRANSFER, Vol. 91, 1969, pp. 145–150.

4 Edwards, D. K., and Sun, W. M., "Prediction of the Onset of Natural Convection in Rectangular Honeycomb Structures," Paper 7/62, 1970 International Solar Energy Society Conference, Melbourne, Australia.

5 Sun, W. M., and Edwards, D. K., "Natural Convection in Cells with Finite Conducting Side Walls Heated from Below," *Heat Transfer 1970,* Paper NC2.3, 4th International Heat Transfer Conference, Versailles, France, 1970.

6 Heitz, W. L., and Westwater, J. W., "Critical Rayleigh Number for Natural Convection of Water Confined in Square Cells with L/D from 0.5 to 8," ASME JOURNAL OF HEAT TRANSFER, Vol. 93, 1971, pp. 188–196.

7 Catton, I., "Convection in a Closed Rectangular Region: The Onset of Motion," ASME JOURNAL OF HEAT TRANSFER, Vol. 92, 1970, pp. 186–188.

8 Catton, I., "The Effect of Insulating Vertical Walls on the Onset of Motion in a Fluid Heated from Below," *Int. Journal of Heat Mass Transfer,* Vol. 15, 1972, pp. 665–672.

9 Catton, I., "Effect of Wall Conduction on the Stability of a Fluid in a Rectangular Region Heated from Below," ASME JOURNAL OF HEAT TRANSFER, Vol. 94, 1972, pp. 446–452.

10 Malkus, W. V. R., and Veronis, G., "Finite Amplitude Cellular Convection," *Journal of Fluid Mech.,* Vol. 4, 1958, pp. 225–260.

11 Hollands, K. G. T., "Convectional Heat Transport Between Rigid Horizontal Boundaries after Instability," *Physics of Fluids,* Vol. 8, 1965, pp. 389–390.

12 Catton, I., "Natural Convection in Horizontal Liquid Layers," *Physics of Fluids,* Vol. 9, 1966, pp. 2521–2522.

13 Catton, I., and Edwards, D. K., "Effect of Side Walls on Natural Convection Between Horizontal Plated Heated from Below," ASME JOURNAL OF HEAT TRANSFER, Vol. 89, 1967, pp. 295–299.

14 Edwards, D. K., and Catton, I., "Prediction of Heat Transfer by Natural Convection in Closed Cylinders Heated from Below," *Int. Journal of Heat Mass Transfer,* Vol. 12, 1969, pp. 23–30.

15 Hollands, K. G. T., "Natural Convection in Horizontal Thin-Walled Honeycomb Panels," ASME JOURNAL OF HEAT TRANSFER, Vol. 95, 1973, pp. 439–444.

16 Edwards, D. K., Arnold, J. N., and Catton, I., "End-Clearance Effects on Rectangular-Honeycomb Solar Collectors," *Solar Energy,* Vol. 16, 1976, pp. 253–257.

17 Cane, R. L., Hollands, K. G. T., Raithby, G. D., and Unny, T. E., "Free Convection Heat Transfer Across Inclined Honeycomb Panels," ASME JOURNAL OF HEAT TRANSFER, Vol. 99, 1977, pp. 86–91.

18 Arnold, J. N., Edwards, D. K., and Catton, I., "Effect of Tilt and Horizontal Aspect Ratio on Natural Convection in Rectangular Honeycombs," ASME JOURNAL OF HEAT TRANSFER, Vol. 99, pp. 120–122.

19 Hollands, K. G. T., Unny, T. E., Raithby, G. D., and Konicek, I., "Free Convective Heat Transfer Across Inclined Air Layers," ASME JOURNAL OF HEAT TRANSFER, Vol. 98, 1976, pp. 189–193.

20 Edwards, D. K., and Sun, W. M., "Effect of Wall Radiation on Thermal Instability in a Vertical Cylinder," *Int. Journal of Heat Mass Transfer,* Vol. 14, 1971, pp. 15–18.

21 Bejan, A., and Tien, C. L., "Laminar Natural Convection Heat Transfer in a Horizontal Cavity with Different End Temperatures," ASME JOURNAL OF HEAT TRANSFER, Vol. 100, 1978, pp. 641–647.

Free Convection Heat Transfer from Heated Cylinders Immersed in a Shallow Water Layer

F. P. Incropera[1] and M. A. Yaghoubi[1]

Introduction

Free convection heat transfer from horizontal heated cylinders submerged in bounded, quiescent liquids occurs in sensible energy storage and waste heat dissipation systems. In such applications the existence of finite boundaries and a liquid-air interface can strongly influence heat transfer from the source to the liquid. Although much attention has been devoted to the problem of free convection from horizontal cylinders, little has been done to consider these special effects. Marsters [1, 2] has shown that confining walls can enhance heat transfer from a single horizontal cylinder and arrays of such cylinders, while Yaghoubi and Incropera [3] have shown similar behavior for a single cylinder. However, there exists a need for additional data, and the purpose of this study has been to measure and to correlate heat transfer effects for cylinders submerged in a shallow water layer. Efforts have focused on the effects of water layer depth and the destabilizing temperature difference between the cylinder surface and the air-water interface.

Experimental Conditions

Experiments were performed using test cells with installation of either one heated cylinder midway between the sidewalls or an array of five equidistant cylinders (Fig. 1). If the cylinder length-to-diameter ratio is sufficiently large, the buoyancy induced flows are approximately two-dimensional. The geometrical variables which influence heat transfer from the single cylinder are then the cylinder diameter D, the sidewall spacing W, and the height H_2 of the water layer above the cylinder. In addition to these variables, heat transfer from the array is also influenced by the pitch S'. The distance between the top of the test cell and the air-water interface, h_1, has a negligible effect on interface conditions and hence may be neglected. Moreover, theoretical and experimental results of Marsters [1] suggest that the height of the cylinder above the test cell bottom, h_2, has a negligible effect on heat transfer and may also be neglected. This result has been confirmed by flow visualization studies and temperature measurements [4], which indicate the absence of motion and the existence of highly stable conditions in the fluid layer below the cylinders.

The experiments have concentrated on determining the effect of the water layer height on cylinder heat transfer. For the single cylinder, diameters of 12.7 mm, 19.1 mm and 25.4 mm were considered, and measurements were made for height ratios in the range $3.8 \leq (H_1/D) \leq 30$. For the horizontal array, a single cylinder diameter of 25.4 mm, with a pitch of $S' = 50.8$ mm was considered, the measurements were made for height ratios in the range $3 \leq (H_1/D) \leq 15$. The cylinder length-to-diameter ratio was maintained in excess of 8, while h_1 and h_2 were held at 12.7 mm and 25.4 mm, respectively. For all of the foregoing measurements, the space ratio, W/D, was maintained approximately constant in the range $11 \leq (W/D) \leq 12$. However, additional measurements were made for a single cylinder installed in a long channel, which essentially corresponds to $W/D \to \infty$.

Each cylinder was machined from copper and drilled along its axis to permit insertion of an electrical heater whose P was measured. The average of three measurements made at the midplane of the cylinder was designated as the cylinder surface temperature, T_c, while the bulk water temperature, T_w, was measured at a point well removed from the cylinders, test cell walls and the air interface. Since the water is

---

[1] Heat Transfer Laboratory, School of Mechanical Engineering, Purdue University, West Lafayette, IN 47906.

Contributed by the Heat Transfer Division for publication in the JOURNAL OF HEAT TRANSFER. Manuscript received by the Heat Transfer Division May 23, 1979.

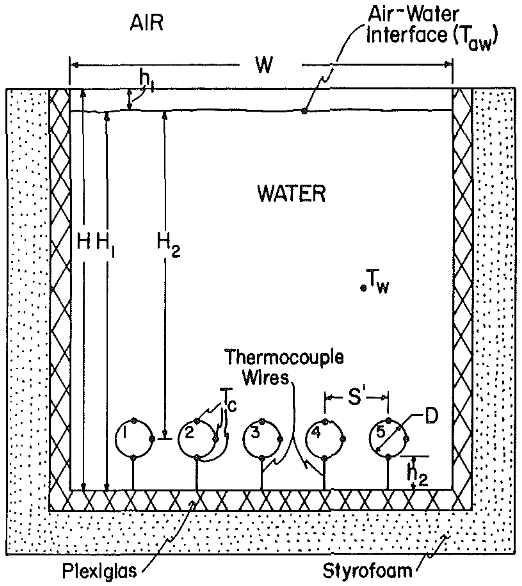

Fig. 1 Schematic of test cell with horizontal array of five cylinders

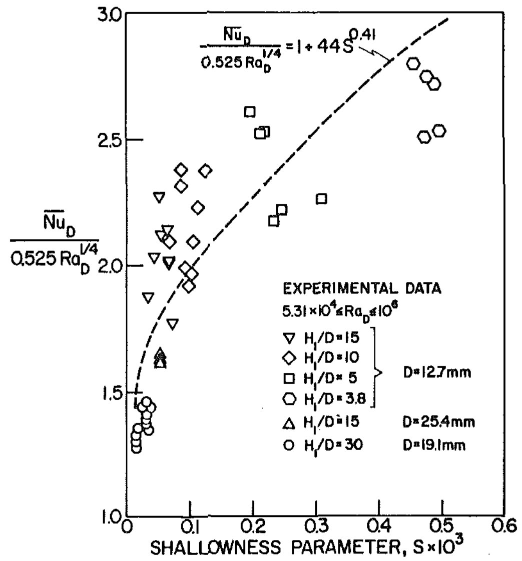

Fig. 2 Nusselt number as a function of shallowness parameter for a single cylinder

known to be characterized by a nearly isothermal core extending from just above the cylinders to just below the air-water interface [4], the value of T_w provides an accurate measure of bulk water conditions. Due to the large temperature gradient which exists at the air-water interface (~700°C/m), the interface temperature, T_{aw}, was inferred from measurements made using a rake of seven thermocouples installed 2.5 mm apart.

Attempts were made to correlate the single cylinder experiments by an expression of the form

$$\overline{\mathrm{Nu}}_D = f(\mathrm{Ra}_D, S) \tag{1}$$

where the average Nusselt number for the cylinder is

$$\overline{\mathrm{Nu}}_D = \frac{\bar{h}D}{k} = \frac{P}{A(T_c - T_w)}\frac{D}{k} \tag{2}$$

The Rayleigh number, which accounts for near field effects, is defined as

$$\mathrm{Ra}_D = \frac{g\beta(T_c - T_w)D^3}{\alpha\nu} \tag{3}$$

and a shallowness parameter, which is intended to account for far field effects, is defined as

$$S = \frac{\beta(T_c - T_{aw})}{H_2/D} \tag{4}$$

This parameter provides a measure of fluid recirculation within the test cell, which may be enhanced by increasing $(T_c - T_{aw})$ and decreasing H_2/D. Attempts were also made to correlate heat transfer results obtained for the horizontal array. Average parameter values were computed for the central three cylinders of the array, rather than for all five cylinders, in order to minimize effects associated with presence of the sidewalls. In this case, however, results were best correlated in terms of parameters defined as

$$\overline{\mathrm{Nu}}_H = \frac{\bar{h}H_2}{k} = \frac{\sum_{i=2}^{4} P_i}{3A(T_c - T_{aw})}\frac{H_2}{k} \tag{5}$$

$$\mathrm{Ra}_H = \frac{g\beta(T_c - T_{aw})H_2^3}{\alpha\nu} \tag{6}$$

All properties appearing in equations (2) to (4) were evaluated at $(T_c + T_w)/2$, while those appearing in equations (5) and (6) were evaluated at $(T_c + T_{aw})/2$.

Results and Discussion

The single cylinder heat transfer measurements are presented in Fig. 2, where the Nusselt number has been normalized with respect to the McAdams correlation for an infinite medium [5] and plotted as a function of the shallowness parameter S. The Nusselt number exceeds that associated with an infinite medium by up to 200 percent, and the excess decreases with decreasing S, where infinite medium behavior is approached as S approaches zero. For the range of conditions in this study, the data are correlated to within ±25 percent by an expression of the form

$$\frac{\overline{\mathrm{Nu}}_D}{0.525\,\mathrm{Ra}_D^{1/4}} = 1 + 44\,S^{0.41} \tag{7}$$

The foregoing results are consistent with the role that recirculation effects are known to play in a finite medium. Flow visualization studies [4] have revealed that recirculation is induced by the plume which rises from the cylinder to the air-water interface, cools as it flows horizontally along the interface, and subsequently descends along the sidewalls. This recirculating flow becomes more pronounced with increasing S, and its effect on heat transfer enhancement is consistent with the results of Marsters [1]. Note, however, that the shallowness parameter accounts only for the effect of the height of the medium, when, in fact, the test cell width W will also influence fluid recirculation. One would expect the enhancement of heat transfer due to recirculation in a finite medium to decrease with increasing W/D. That this is the case has been confirmed by Marsters [1] and by our own measurements of heat transfer from a single cylinder in a long channel ($W/D \to \infty$). These measurements are well corroborated by the standard correlation for an infinite medium [5], indicating the absence of any enhancement.

Measurements were obtained for the horizontal array of cylinders and, when represented in the normalized form, $\overline{\mathrm{Nu}}_D/0.525\,\mathrm{Ra}_D^{1/4}$, the results varied from approximately 1.2 to 1.5. The fact that the Nusselt number exceeds that associated with a single cylinder in an infinite medium is due to plume interaction and recirculation effects and is consistent with previous multiple cylinder studies [6–8]. However, as in these studies, it has been found that the cylinder diameter is not a suitable characteristic length and that the data is better correlated in terms of the dimensionless parameters defined by equations (5) and (6).

Results for the array are plotted in Fig. 3, along with correlations developed for uniform heating from the bottom of a horizontal cavity [9–11]. The experimental results are consistently higher than predictions based on the correlations, but differences diminish with increasing Rayleigh number. This trend is consistent with hydrodynamic conditions observed in a previous study [4]. For small values of H_2 ($\mathrm{Ra}_H \lesssim 10^6$), the plume from each cylinder rises to the interface

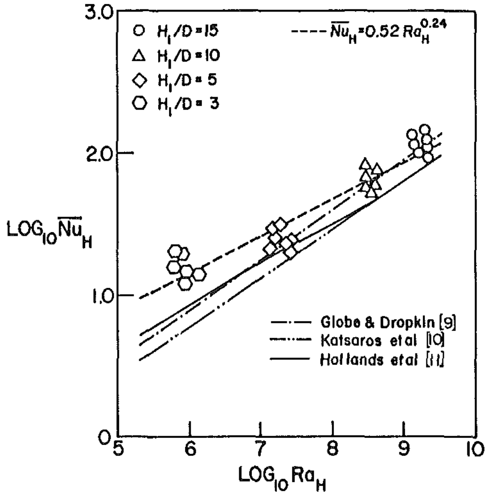

Fig. 3 Nusselt number as a function of Rayleigh number for the horizontal array

and spreads horizontally, until it interacts with an adjoining plume and descends to approximately the level of the cylinders, where it resumes a horizontal motion. The net effect is one of creating similar regions of recirculating flow (cells) between the cylinders. These regions differ from the strongly mixed, nonrecirculating conditions associated with uniform heating from below. Similar discrepancies between results for uniform and nonuniform heating have been reported by Boehm [12], who obtained heat transfer results for stripwise heating which exceeded those associated with uniform heating. With increasing H_2, however, plume oscillations provide for plume interactions below the air-water interface, and the flow becomes highly disordered and more strongly mixed, approaching conditions associated with uniform heating from below.

The data of Fig. 3 are correlated to within ±33 percent by the expression

$$\overline{\mathrm{Nu}}_H = 0.52\,\mathrm{Ra}_H{}^{0.24} \tag{8}$$

which is of the same form as expressions proposed by Globe and Dropkin [9] and Katsaros, et al. [10], except that the exponent of 0.24 is less than their recommended value of 0.33. It should be noted, however, that if the low Rayleigh number results ($\mathrm{Ra}_H \approx 10^6$) are ignored, the remaining data vary approximately as $\mathrm{Ra}_H{}^{1/3}$. It should also be noted that the data of Fig. 3 pertain to a single tube pitch ($S'/D = 2$). Heat transfer from the array will depend upon the pitch, and the departure of results from those associated with uniform heating from below is expected to increase with increasing S'/D.

Summary

Due to recirculation effects, free convection heat transfer from a single cylinder submerged in a bounded layer of water exceeds that associated with an infinite medium by as much as 200 percent. For a fixed test cell width, the data may be correlated to within ±25 percent by an expression which relates the cylinder Nusselt number, $\overline{\mathrm{Nu}}_D$, to the Rayleigh number, Ra_D, and a shallowness parameter, S. Heat transfer from the cylinders of a horizontal array exceeds that associated with an infinite medium by up to 50 percent. For a fixed tube spacing, the data may be correlated to within ± 33 percent by an expression which relates the Nusselt number, $\overline{\mathrm{Nu}}_H$, to the Rayleigh number, $\overline{\mathrm{Ra}}_H$. Additional data for varying test cell width and tube spacing are needed before more general correlations may be developed.

References

1 Marsters, G. F., "Natural Convective Heat Transfer from a Horizontal Cylinder in the Presence of Nearby Walls," *Canadien Journal of Chemical Engineering*, Vol. 53, 1975, pp. 144–149.

2 Marsters, G. F., "Arrays of Heated Horizontal Cylinders in Natural Convection," Thermosciences Rep. 3-71, Dept. of Mech. Eng., Queen's University, Kingston, Canada, 1971.

3 Yaghoubi, M. A. and Incropera, F. P., "Natural Convection from a Heated Horizontal Cylinder Submerged in a Shallow Water Layer," *Proc. Sixth International Heat Transfer Conference*, Vol. 2, NC-15, 1978, pp. 269–274.

4 Incropera, F. P. and Yaghoubi, M. A., "Buoyancy Driven Flows Originating from Heated Cylinders Submerged in a Finite Water Layer," *International Journal of Heat and Mass Transfer*, In Press.

5 McAdams, W. H., *Heat Transmission*, McGraw-Hill, 1954, pp.175–177.

6 Eckert, E. R. G. and Soehngen, E., "Studies on Heat Transfer in Laminar Free Convection with the Zehnder-Mach Interferometer," USAF Tech. Rep. 5747, 1948.

7 Marsters, G. F., "Arrays of Heated Horizontal Cylinders in Natural Convection," *International Journal of Heat and Mass Transfer*, Vol. 15, 1972, pp. 921–933.

8 Tillman, E. S., "Natural Convection Heat Transfer from Horizontal Tube Bundles," ASME Paper No. 76-HT-35, 1976.

9 Globe, S. and Dropkin, D., "Natural Convection Heat Transfer in Liquids Confined by Two Horizontal Plates and Heated from Below," ASME JOURNAL OF HEAT TRANSFER, Vol. 81, 1959, pp. 24–28.

10 Katsaros, K. B., Liu, W. T., Businger, J. A. and Tillman, J. E., "Heat Transport and Thermal Structure in the Interfacial Boundary Layer Measured in an Open Tank of Water in Turbulent Free Convection," *Journal of Fluid Mechanics*, Vol. 83, Part 2, 1977, pp. 311–335.

11 Hollands, K. G. T., Raithby, G. D. and Konick, L., "Correlation Equations for Free Convection Heat Transfer in Horizontal Layers of Air and Water," *International Journal of Heat and Mass Transfer*, Vol. 18, 1975, pp. 879–884.

12 Boehm, R. F. and Alder, R. S., "Natural Convection Arising from Stripwise Heating on a Horizontal Surface," *International Journal of Heat and Mass Transfer*, Vol. 16, 1973, pp. 853–855.

Finite-Difference Solution of Free Convection Problem with Non-uniform Gravity

B. J. Venkatachala[1] and G. Nath[2]

Nomenclature

C_f = local skin-friction coefficient
F = dimensionless stream function
$F''(\xi, 0)$ = surface skin-friction parameter
$F''(0, 0)$ = surface skin-friction parameter at $\xi = 0$
g = local acceleration in the direction opposite of the x-axis
g_0 = gravitational acceleration
G = dimensionless temperature
$G'(\xi, 0)$ = surface heat-transfer parameter
$G'(0, 0)$ = surface heat-transfer parameter at $\xi = 0$
Gr_x = local Grashof number
K = thermal conductivity
Nu = local Nusselt number
Pr = Prandtl number
q = local heat-transfer rate per unit area
T = temperature
T_∞ = ambient temperature
x, y = distances along and perpendicular to the surface
x_0 = distance of leading edge of the plate from the center of rotation
β = bulk coefficient of thermal expansion
ΔT = difference between the surface temperature and ambient temperature, $T_w - T_\infty$
η, ξ = transformed co-ordinates
ν = kinematic viscosity
ρ = density
τ = shear stress at the surface

---

[1] Research Student, Department of Applied Mathematics, Indian Institute of Science, Bangalore, India.

[2] Associate Professor, Department of Applied Mathematics, Indian Institute of Science, Bangalore, India.

Contributed by the Heat Transfer Division for publication in the JOURNAL OF HEAT TRANSFER. Manuscript received by the Heat Division, November 6, 1978.

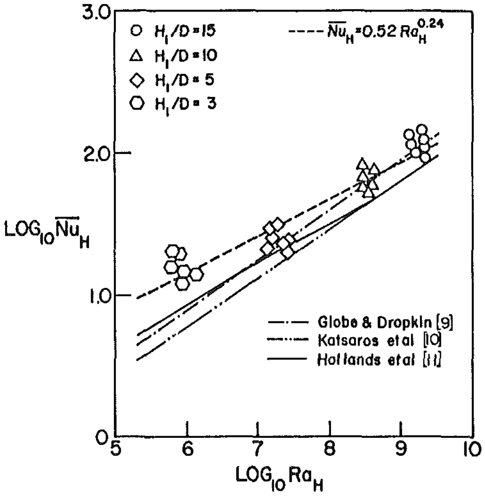

Fig. 3 Nusselt number as a function of Rayleigh number for the horizontal array

and spreads horizontally, until it interacts with an adjoining plume and descends to approximately the level of the cylinders, where it resumes a horizontal motion. The net effect is one of creating similar regions of recirculating flow (cells) between the cylinders. These regions differ from the strongly mixed, nonrecirculating conditions associated with uniform heating from below. Similar discrepancies between results for uniform and nonuniform heating have been reported by Boehm [12], who obtained heat transfer results for stripwise heating which exceeded those associated with uniform heating. With increasing H_2, however, plume oscillations provide for plume interactions below the air-water interface, and the flow becomes highly disordered and more strongly mixed, approaching conditions associated with uniform heating from below.

The data of Fig. 3 are correlated to within ±33 percent by the expression

$$\overline{\mathrm{Nu}}_H = 0.52\,\mathrm{Ra}_H{}^{0.24} \qquad (8)$$

which is of the same form as expressions proposed by Globe and Dropkin [9] and Katsaros, et al. [10], except that the exponent of 0.24 is less than their recommended value of 0.33. It should be noted, however, that if the low Rayleigh number results ($\mathrm{Ra}_H \approx 10^6$) are ignored, the remaining data vary approximately as $\mathrm{Ra}_H{}^{1/3}$. It should also be noted that the data of Fig. 3 pertain to a single tube pitch ($S'/D = 2$). Heat transfer from the array will depend upon the pitch, and the departure of results from those associated with uniform heating from below is expected to increase with increasing S'/D.

Summary

Due to recirculation effects, free convection heat transfer from a single cylinder submerged in a bounded layer of water exceeds that associated with an infinite medium by as much as 200 percent. For a fixed test cell width, the data may be correlated to within ±25 percent by an expression which relates the cylinder Nusselt number, $\overline{\mathrm{Nu}}_D$, to the Rayleigh number, Ra_D, and a shallowness parameter, S. Heat transfer from the cylinders of a horizontal array exceeds that associated with an infinite medium by up to 50 percent. For a fixed tube spacing, the data may be correlated to within ± 33 percent by an expression which relates the Nusselt number, $\overline{\mathrm{Nu}}_H$, to the Rayleigh number, $\overline{\mathrm{Ra}}_H$. Additional data for varying test cell width and tube spacing are needed before more general correlations may be developed.

References

1 Marsters, G. F., "Natural Convective Heat Transfer from a Horizontal Cylinder in the Presence of Nearby Walls," *Canadien Journal of Chemical Engineering*, Vol. 53, 1975, pp. 144–149.

2 Marsters, G. F., "Arrays of Heated Horizontal Cylinders in Natural Convection," Thermosciences Rep. 3-71, Dept. of Mech. Eng., Queen's University, Kingston, Canada, 1971.

3 Yaghoubi, M. A. and Incropera, F. P., "Natural Convection from a Heated Horizontal Cylinder Submerged in a Shallow Water Layer," *Proc. Sixth International Heat Transfer Conference*, Vol. 2, NC-15, 1978, pp. 269–274.

4 Incropera, F. P. and Yaghoubi, M. A., "Buoyancy Driven Flows Originating from Heated Cylinders Submerged in a Finite Water Layer," *International Journal of Heat and Mass Transfer*, In Press.

5 McAdams, W. H., *Heat Transmission*, McGraw-Hill, 1954, pp.175–177.

6 Eckert, E. R. G. and Soehngen, E., "Studies on Heat Transfer in Laminar Free Convection with the Zehnder-Mach Interferometer," USAF Tech. Rep. 5747, 1948.

7 Marsters, G. F., "Arrays of Heated Horizontal Cylinders in Natural Convection," *International Journal of Heat and Mass Transfer*, Vol. 15, 1972, pp. 921–933.

8 Tillman, E. S., "Natural Convection Heat Transfer from Horizontal Tube Bundles," ASME Paper No. 76-HT-35, 1976.

9 Globe, S. and Dropkin, D., "Natural Convection Heat Transfer in Liquids Confined by Two Horizontal Plates and Heated from Below," ASME JOURNAL OF HEAT TRANSFER, Vol. 81, 1959, pp. 24–28.

10 Katsaros, K. B., Liu, W. T., Businger, J. A. and Tillman, J. E., "Heat Transport and Thermal Structure in the Interfacial Boundary Layer Measured in an Open Tank of Water in Turbulent Free Convection," *Journal of Fluid Mechanics*, Vol. 83, Part 2, 1977, pp. 311–335.

11 Hollands, K. G. T., Raithby, G. D. and Konick, L., "Correlation Equations for Free Convection Heat Transfer in Horizontal Layers of Air and Water," *International Journal of Heat and Mass Transfer*, Vol. 18, 1975, pp. 879–884.

12 Boehm, R. F. and Alder, R. S., "Natural Convection Arising from Stripwise Heating on a Horizontal Surface," *International Journal of Heat and Mass Transfer*, Vol. 16, 1973, pp. 853–855.

Finite-Difference Solution of Free Convection Problem with Non-uniform Gravity

B. J. Venkatachala[1] and G. Nath[2]

Nomenclature

C_f = local skin-friction coefficient
F = dimensionless stream function
$F''(\xi, 0)$ = surface skin-friction parameter
$F''(0, 0)$ = surface skin-friction parameter at $\xi = 0$
g = local acceleration in the direction opposite of the x-axis
g_0 = gravitational acceleration
G = dimensionless temperature
$G'(\xi, 0)$ = surface heat-transfer parameter
$G'(0, 0)$ = surface heat-transfer parameter at $\xi = 0$
Gr_x = local Grashof number
K = thermal conductivity
Nu = local Nusselt number
Pr = Prandtl number
q = local heat-transfer rate per unit area
T = temperature
T_∞ = ambient temperature
x, y = distances along and perpendicular to the surface
x_0 = distance of leading edge of the plate from the center of rotation
β = bulk coefficient of thermal expansion
ΔT = difference between the surface temperature and ambient temperature, $T_w - T_\infty$
η, ξ = transformed co-ordinates
ν = kinematic viscosity
ρ = density
τ = shear stress at the surface

---

[1] Research Student, Department of Applied Mathematics, Indian Institute of Science, Bangalore, India.

[2] Associate Professor, Department of Applied Mathematics, Indian Institute of Science, Bangalore, India.

Contributed by the Heat Transfer Division for publication in the JOURNAL OF HEAT TRANSFER. Manuscript received by the Heat Division, November 6, 1978.

ψ = dimensional stream function
ω = angular velocity of rotating plate

Superscript

$'$ = prime denotes differentiation with respect to η

Subscripts

0 = condition at the leading edge
w = condition at the surface
ξ = derivative with respect to ξ

Introduction

Many laminar free convection analyses describing realistic situations do not admit similarity solutions. The nonsimilarity in these cases arises from a number of causes such as non-uniform gravity, thermally stratified fluid, non-uniform surface temperature, etc. In free convection problems, the nonuniform gravity occurs quite frequently. For example, centrifugal gravity fields arise in many rotating machinery applications. The gravity field is also created artificially in an orbital space station by rotation.

The effect of non-uniform gravity due to the rotation of an isothermal plate has been investigated by Lemlich and coworkers [1–3], Catton [4], Lienhard, et al. [5], and Nath [6]. The theoretical studies of this problem have been carried out using momentum integral method or series expansion method or local nonsimilarity method. The integral method is only an approximate method and it is rather difficult to determine the range for which the solution is valid [5]. The series expansion method is laborious to apply and it requires many terms for large x. The local nonsimilarity method [7–9] does not predict accurate results for large x. Hence, it is considered necessary to analyze the aforementioned problem using the finite-difference method.

In this note, a new implicit finite-difference method developed by Keller and Cebeci [10–12] has been used to study the foregoing problem. The results have been compared with those of the series, momentum integral and local nonsimilarity methods [5, 6].

Governing Equations

We consider the effect of the nonuniform gravity field on the steady isothermal laminar free convection flows along (1) an infinite cold plate rotating at ω rad/s in a radial plane with its leading edge beginning at a distance x_0 from the axis of rotation, and (2) a finite hot plate of length x_0, rotating at ω rad/s in a radial plane about the line $x = 0$. The boundary-layer equations in dimensionless form governing the above problem under the assumption that $\beta\Delta T \ll 1$ (i.e., weakly stratified flow) are [5]

$$F''' + 3FF'' - 2F'^2 + (g/g_0)G = 4\xi[F'F_\xi' - F''F_\xi] \qquad (1)$$

$$\mathrm{Pr}^{-1}\,G'' + 3FG' = 4\xi[F'G_\xi - G'F_\xi]. \qquad (2)$$

The boundary conditions are

$$F(\xi, 0) = F'(\xi, 0) = 0,\ G(\xi, 0) = 1,\ F'(\xi, \infty) = G(\xi, \infty) = 0 \qquad (3)$$

where

$$\xi = x/x_0,\ \eta = x^{-1}y(\mathrm{Gr}_x/4)^{1/4} \qquad (4a)$$

$$\psi = (64\,\mathrm{Gr}_x)^{1/4}\nu F(\xi, \eta),\ G = (T - T_\infty)/\Delta T \qquad (4b)$$

$$\mathrm{Gr}_x = g_0\beta\Delta T x^3/\nu^2, \quad \Delta T = T_w - T_\infty. \qquad (4c)$$

The gravity field has been assumed to be of the form [5]

$$g/g_0 = 1 \pm (x/x_0) = 1 \pm \xi. \qquad (5)$$

Here the positive sign is for the cold rotating plate and the negative sign is for the hot rotating plate.

The skin-friction coefficient and Nusselt number can be expressed as [5]

$$C_f = \tau_w/[\rho(\nu/x)^2] = 4(\mathrm{Gr}_x/4)^{3/4}F''(\xi, 0) \qquad (6a)$$

$$\mathrm{Nu} = qx/(K\Delta T) = -(\mathrm{Gr}_x/4)^{1/4}G'(\xi, 0). \qquad (6b)$$

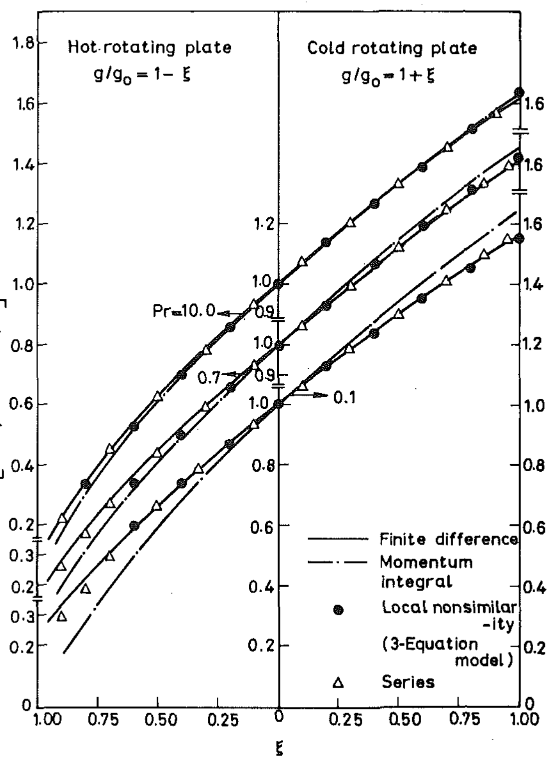

Fig. 1 Comparison of finite-difference solution for skin friction $F''(\xi, 0)/F''(0, 0)$ with other approximate methods

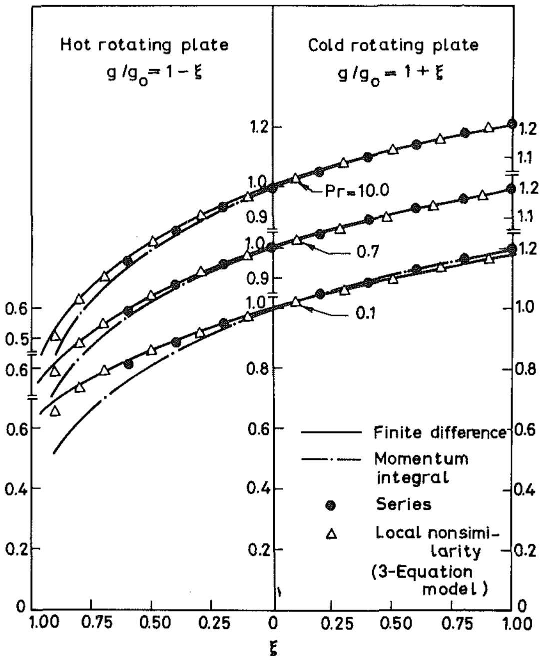

Fig. 2 Comparison of finite-difference solution for heat transfer $G'(\xi, 0)/G'(0, 0)$ with other approximate methods

Results and Discussion

Equations (1) and (2) under conditions (3) have been solved numerically using an implicit finite-difference scheme developed by Keller and Cebeci [10–12]. Since the complete description of the method and its application to boundary-layer problems are available in [10–13], the description of the method is not presented here. For the problem under consideration, we have taken the step size $\Delta\eta = 0.05$ and $\Delta\xi = 0.1$. Further reduction in them changes the results only in the fourth decimal place. In order to test the accuracy of our method, we have compared the similarity results for $F''(0)$ and $-G'(0)$ obtained by putting $\xi = 0$ and $g/g_0 = 1$ in equations (1) and (2) with those tabulated in [5] and found that they agree up to four decimal places.

The comparison of the skin-friction and heat-transfer results ($F''(\xi, 0)/F''(0, 0)$, $G'(\xi, 0)/G'(0, 0)$) obtained by the finite-difference method with those of the momentum integral method, series solution and local nonsimilarity method [5, 6] is given in Figs. 1–2. For a cold rotating plate, the skin-friction and heat-transfer results are found to be in good agreement with those of the series solution, momentum integral and local nonsimilarity methods except for small Prandtl number (Pr = 0.7 or 1) when they differ from those of the momentum integral method and this difference increases as ξ increases. For a hot rotating plate, the finite-difference results differ considerably from the momentum integral results and this difference increases with Pr or ξ. The series solution gives much better results than the momentum integral method. However, the method of series solution is not expected to be valid for large ξ. The finite-difference results are in good agreement with the local nonsimilarity results even for large ξ except when Pr is small. It is also observed from these figures that Pr and g/g_0 have strong effects on $F''(\xi, 0)$ and $G'(\xi, 0)$.

Conclusions

The finite-difference results for a cold rotating isothermal plate under non-uniform gravity have been found to be in good agreement with those of the local nonsimilarity method, series solution and momentum integral method. However, for a hot rotating plate, the momentum integral results differ considerably from the finite-difference results, but the series solution and local nonsimilarity results are comparatively in good agreement with those of the finite-difference method except when the distance from the leading edge is large.

References

1 Lemlich, R., "Natural Convection to Isothermal Flat Plate with Spatially Nonuniform Acceleration," *I.E.C. Fundamentals Quarterly*, Vol. 2, 1963, pp. 157–158.

2 Lemlich, R. and Vardi, J., "Steady Free Convection to a Flat Plate with Uniform Surface Heat Flux and Nonuniform Acceleration," ASME JOURNAL OF HEAT TRANSFER, Vol. 86, No. 4, Nov. 1964, pp. 562–563.

3 Lemlich, R. and Steinkamp, J. S., "Laminar Natural Convection to an Isothermal Flat Plate with a Spatially Varying Acceleration," *AIChE Journal*, Vol. 10, No. 3, 1964, pp. 445–447.

4 Catton, I., "Effect of a Gravity Gradient on Free Convection from a Vertical Plate," *C.E.P. Symposium Series*, Vol. 64, No. 82, 1968, pp. 146–149.

5 Lienhard, J., Eichhorn, R. and Dhir, V., "Laminar Natural Convection under Nonuniform Gravity," ASME JOURNAL OF HEAT TRANSFER, Vol. 94, No. 1, Feb. 1972, pp. 80–86.

6 Nath, G., "Nonsimilarity Solutions of a Class of Free Convection Problems," *Proc. Indian Acad. Sci.*, Vol. 84A, No. 3, Sept. 1976, pp. 114–123.

7 Sparrow, E. M., Quack, H. and Boerner, C. J., "Local Nonsimilarity Boundary-Layer Solutions," *AIAA Journal*, Vol. 8, No. 11, Nov. 1970, pp. 1936–1942.

8 Sparrow, E. M. and Yu, H. S., "Local Nonsimilarity Thermal Boundary Layer Solutions," ASME JOURNAL OF HEAT TRANSFER, Vol. 93, No. 4, Nov. 1971, pp. 328–334.

9 Minkowycz, W. J. and Sparrow, E. M., "Local Nonsimilarity Solution for Natural Convection on a Vertical Cylinder," ASME, JOURNAL OF HEAT TRANSFER, Vol. 96, No. 2, May 1974, pp. 178–183.

10 Keller, H. B. and Cebeci, T., "Accurate Numerical Methods for Boundary Layers. I. Two-Dimensional Laminar Flows," Proceedings of the Second *International Conference on Numerical Methods in Fluid Dynamics*, Lecture Notes in Physics, Vol. 8, Springer-Verlag, New York, 1971.

11 Keller, H. B. and Cebeci, T., "Accurate Numerical Methods for Boundary Layers. II. Two-Dimensional Turbulent Flows," AIAA Journal, Vol. 10, No. 9, Sept. 1972, pp. 1197–1200.

12 Cebeci, T. and Smith, A. M. O., Analysis of Turbulent Boundary Layers, Academic Press, New York, 1974.

13 Venkatachala, B. J., "A Numerical Study of Some Flow and Heat Transfer Problems in Laminar Boundary Layers," Ph.D. Thesis, Indian Institute of Science, Bangalore, July 1978.